# Neoproterozoic to Holocene tectonothermal evolution of the southern Cantabrian Mountains NW Iberia, revealed by apatite fission-track thermochronology

Inaugural-Dissertation
zur
Erlangung der Doktorwürde
der
Fakultät für Chemie und Geowissenschaften
der
Ruprecht-Karls-Universität
Heidelberg,
Deutschland

vorgelegt von
Kevin L. Carrière
aus Windsor Ontario,
Kanada

Ich erkläre hiermit, daß ich die vorgelegte Dissertation selbst verfaßt und mich dabei keiner anderen als der von mir ausdrücklich bezeichneten Quellen und Hilfen bedient habe.

Ich erkläre hiermit, daß ich an keiner anderen Stelle ein Prüfungsverfahren beantragt bzw. die Dissertation in dieser oder anderer Form bereits anderweitig als Prüfungsarbeit verwendet oder einer anderen Fakultät als Dissertation vorgelegt habe.

Heidelberg, den 16. Mai, 2006.

Gutachter 1: **Prof. Dr. Günther A. Wagner**
Forschungsstelle Archäometrie der Heidelberger Akademie der Wissenschaften
am Max-Planck-Institut für Kernphysik
Saupfercheckweg 1, D-69117, Heidelberg
Deutschland

Gutachter 2: **Priv. Doz. Dr. Uli A. Glasmacher**
Geologisch-Paläontologisches Institut
Ruprecht-Karls-Universität
Im Neuenheimer Feld 234, D-69120, Heidelberg
Deutschland

Tag der Promotoinsprüfung: 10. Juli, 2006.


*Delightfully though, the roads never lead where they're supposed to go.*

A *mon oncle Irvin*

**Acknowledgements**

*To arrive at this point has taken a lifetime, some discipline, some focus, but mostly diligence and a self belief. Though this has ultimately been an personal journey, my thanks stretch far. Many, knowingly or not, have impressed a profound and lasting wisdom on which I've drawn upon for guidance in what has thus far been an adventurous path to knowledge. So, though I cannot mention all who've left their impression, I'd like to mention some of those whose efforts have helped in the completion of this work.*

*Thanks Mom and Dad for setting the path to knowledge, and for supporting the adventures in their many forms.*

*Credit goes to the teachers at St. Joseph's Elementary School and Saugeen District Secondary School for laying the educational foundation; special thanks to Mrs. Smith, for seeing potential and pushing me to actualise it; Thanks Mr. Parker for seeding ideas and facilitating an awakening. Thanks to Ernie Abel, for everything I didn't learn in school. My admiration and deepest respect go to Ian Mc Kenzie and John Hopkins for showing what joy can be found in an in earth and environmental science career.*

*To all those I had to leave back home: Jay, Julie, Sandeep, Mike, Andrew, Adam, Kevin, Elan, Damien, Mike, Ange, Rachel, Leslie, Tina, Jeff, Joe, Lorenzo, Graeme, Rich, Roger, Celine, Chuck & Val, Allyson, Calvin, Kirk & Barb, Bob, Gord, Doug & Pam, Geoff, Jeff, Darrin, Don, Duane, Chris, Gerry, Chris, Tom, Laurent & Liz, Don & Karren, Kees and Trent... Aloha.*

*Here's to Thomas, Fabio & Bonsai for just about everything one could think of while in Heidleberg: Friendship, debate, good food, camaraderie, adventure... oh, and thanks for the T-shirt too.*

*To the many who've helped make this study worth while: Susan, Steffen, Annette, Clements, Christine, Jorcham, Frauke, Frederika, Francis, Asher, Kirsten, Gaël, Emmanuel. Ibi, Axel, Birgit, Zbynek, Marta, Fernando, Isabell, Michael, Anja, Jana, Margarita, Carsten, Jochen, Roswitha, Heiko, Tanja, Iris and Sonja: Danke für akkes.*

*To Enno and Stephan... Mahalo.*

*My gratitude to goes to Dale Isler, Istvan Dunkl, Ray Donelick, Richard Ketcham for sounding analytical questions; Gabriel Gutiérrez-Alonso for forwarding papers and instilling motivation for discovering the big picture; Uli Glasmacher for guidence throughout the analysis and interpretation process. I thank Thilo Bechstädt for facilitating peripherals required to conduct this work and for his expedient review of the thesis. I am indebted to the Gratuiertenkolleg-273 and the International Postgraduate Program for their part in funding of research and travel costs associated with the project. I'd like to thank Günther A. Wagner for allocating the topic and work facility at the Forschungstelle Archäometrie der Heidelberger Akademie der Wissenschaften am Max-Planck-Institut für Kernphysik.*

*Thank-you Anna.*

## Abstract

The southern Cantabrian Mountains expose sedimentary rocks having experienced uplift coeval with alpidic, Variscan and in the south, possibly Cadomian orogenic cycles; these rocks are commonly referred to by their Variscan tectonic expressions: the Cantabrian Zone and Narcea Antiform. This thesis yields new experimental and geologic information from 32 AFT samples gathered along N-directed transects in the Cantabrian Zone and Narcea Antiform.

The Cantabrian Zone, a nearly complete Palaeozoic succession has been characterised as the thin-skinned tectonism dominated (Julivert, 1971; Pérez-Estaún et al., 1988), arcuate foreland fold-and-thrust belt. South of the León Line fault system non-metamorphic conditions dominate (e.g. Raven & van der Pluijm, 1986; Aller et al., 2005; Keller & Krumm, 1992; Marschik, 1992; Schneider, 2002; Gasparrini, 2003), to the North anchizone to epizone conditions are recorded (e.g. Aller et al., 1987, 2005; Marschik, 1992). The Narcea Antiform, unconformably overlain by the Palaeozoic succession, represents as a Neoproterozoic sedimentary basement, the Variscan foreland-hinterland transition (e.g. Gutiérrez-Alonso, 1995). Metamorphic conditions increase from anchizone to greenschist facies (e.g. Aller et al., 1987; Martín-Parra, 1990; Keller & Krumm, 1992), coincident with hinterland directed increasing deformation.

Unconformable and deformed, discontinuous Stephanian intramontane basin fills, following major structural lineaments (e.g. León Line, Sabero-Gordón and Conombre-La Urz fault systems) overlay pre-Stephanian successions in both the Narcea Antiform and Cantabrian Zone. At the foreland-hinterland transition, they record anchizone to epizone metamorphic signatures (Aller et al., 2005), while those confined to the Cantabrian Zone infer lowest metamorphic grades (e.g. Marschik, 1992; Ayllón et al., 2003; Frings et al., 2004; Aller et al., 2005).

Experimental results show uranium concentration may be used in the absence of data for more often observed substitutions to the apatite chemical formula [$Ca_{10}(PO_4)_6(F,Cl,OH)_2$] (Elliott, 1994), to predict correlation between AFT grain-ages and their respective $D_{par}$ values.

Graphs constructed for AFT central-age versus geographic parameters latitude and elevation yield negative slopes, indicating a complex elevation dependent cooling profile affected by the interplay between differential topography, recent tectonic activity and time dependent changing geomorphic conditions.

AFT grain-ages from the Narcea Antiform, the Cantabrian Zone and Stephanian basins reveal thermal conditions coeval with the Variscan orogenic cycle may have been insignificant to totally anneal preexisting fission tracks. AFT grain-age subcomponents indicate AFT partial annealing zone (PAZ) conditions in the Narcea Antiform may have prevailed from as early as Neoproterozoic time. Alternatively, many pre-Stephanian Palaeozoic rocks near major structural lineaments yield AFT-grain-age distributions completely annealed following Late Carboniferous (late Variscan) time.

Model time-Temperature (t-T) pathways for nineteen of the thirty-two samples quantitatively estimate the thermal evolution of the southern Cantabrian Mountains. Samples from the Narcea Antiform yield AFT single-grain-age cooling signatures, which when evaluated with respect to their 1σ errors, may be interpreted to signal earliest entry into the AFT-PAZ at Neoproterozoic time, possibly coeval with subduction along Avalonian-Cadomian-Pan African magmatic arc (Gutiérrez-Alonso et al., 2005). Pre-Stephanian cooling in Neoproterozoic samples is lowly constrained. Nevertheless pervasive cooling in these samples occurred coeval with ~ 3.6 km (Veselovsky, 2004; Dietrich, 2005) of pre-Stephanian Palaeozoic sedimentation in the adjacent Cantabrian

Basin. Following a latest Variscan to early post-Variscan thermal pulse to upper-PAZ conditions the Narcea Antiform experienced denudation related cooling and exited the PAZ by as early as the Middle Jurassic.

Palaeozoic rocks in the southern Cantabrian Zone evidence middle- to high-PAZ conditions sustained to between Middle Triassic to Late Jurassic time. Sustained palaeothermal conditions may be associated with a) heat from a locally derived sedimentary cover of between 1 km at ~ 85 ˚ C/km (e.g. Frings et al., 2004) transitioning to that delivered by an assumed ~ 3 - 4 km at 30 ˚C/km, and/or b) the circulation of thermal convection-heated high salinity brines (cf. Ayllon, 2003; Gasparrini et al., in press), possibly of Triassic age (cf. Arche & López-Gómez, 1996).

Rapid late Mesozoic cooling to sub-PAZ conditions coeval with the far field onset of first Atlantic then Biscay rift episodes (Ziegler, 1988), is evidenced in AFT t-T reconstructions. Late Mesozoic-early Cenozoic reheating, coeval with the transitioning interplay between late Biscay rifting, Biscay crustal subduction (Andeweg, 2002), far field onset of alpidic orogenesis (Boillot & Malod, 1988; Andeweg, 2002) and an Early Eocene (alpidic climax) fluid delivered thermal pulse (e.g. Gutiérrez-Alonso et al., 2005) are evidenced in t-T models showing low to middle-PAZ conditions.

Cooling at Latest Palaeogene-Neogene time is dominated by processes initially associated with alpidic shortening and unroofing (Andeweg, 2002). A final heterogeneously delivered thermal reactivation, mostly insignificant to the AFT chronometre, occurs coeval with renewed tectonic activity along the northern Iberian margin (Andeweg, 2002), climaxing by latest Miocene (Messinian) time. Heterogeneous cooling of samples is evidenced from Early Pliocene time. Post-tectonic denudation is interpreted to have become the dominant influence of cooling in the study area.

In light of the absence of extensive Mesozoic or Cenozoic covers in the southern Cantabrian Mountains, AFT t-T models present the only method for time-constrained quantitative estimation of post-Variscan cooling in NW Iberia.

## Zusammenfassung

Im Kantabrischen Gebirge sind Sedimente aufgeschlossen, die während der alpidischen, variszischen und zumindest im Süden evtl. cadomischen Orogenese herausgehoben wurden. Entsprechend ihrer variszischen Entwicklung werden die Gesteine in die Kantabrische Zone und die Narcea Antiform unterteilt. In dieser Dissertation werden neue experimentelle und geologische Informationen von 32 AFT Proben dargestellt, die entlang von N-S Profilen durch die Kantabrische Zone und die Narcea Antiform entnommen wurden.

Die Kantabrische Zone, die im bogenförmigen Falten-und-Überschiebungs-Gürtel des iberischen Teiles des westeuropäischen Variszikums liegt, besteht aus einer nahezu vollständigen paläozoischen Abfolge und ist von „thin-skinned" Tektonik dominiert (Julivert, 1971; Pérez-Estáun et al., 1988). Südlich des León-Störungssystems sind die Gesteine größtenteils nicht metamorph (z.B. Raven & van der Pluijm, 1986; Aller et al., 2005; Keller & Krumm, 1992; Marschik, 1992; Schneider, 2002; Gasparrini, 2003), während nördlich davon anchizonale bis epizonale metamorphe Bedingungen beobachtet werden (z.B. Aller et al., 1987, 2005; Marschik, 1992). Die Narcea Antiform repräsentiert als sedimentäres Grundgebirge den variszischen Vorland-Hinterland-Übergang (z.B. Gutiérez-Alonso, 1995) und wird im Norden von der prästephanen paläozoischen Abfolge diskordant überlagert. Deformation und anchizonale bis grünschieferfazielle Metamorphose nehmen zum Hinterland hin zu (z.B. Aller et al., 1987; Martín-Para, 1990; Keller & Krumm, 1992).

Deformierte intramontane Stephanbecken, die entlang wichtiger tektonischer Lineamente liegen (z.B. León-, Sabero-Gordón- und Conombre-La Urz Störungssystem), überlagern sowohl in der Kantabrischen Zone als auch in der Narcea Antiform diskordant prästephane Abfolgen. Die stephanen Einheiten in der Narcea Antiform zeigen eine anchizonale bis grünschieferfazielle Metamorphose (Aller et al., 2005), während die in der Kantabrischen Zone diagenetisch-anchizonal überprägt sind (z.B. Marschik, 1992; Ayllón et al., 2003; Frings et al., 2004; Aller et al., 2005).

Die experimentellen Ergebnisse zeigen, dass die Urankonzentration in Apatit [$Ca_{10}(PO_4)_6(F,Cl,OH)_2$] (Elliott, 1994) bei fehlenden Daten von anderen Substituenten herangezogen werden kann, um AFT-Kornalter mit Dpar-Werten zu korrelieren.

AFT-Zentralalter korrelieren negativ mit den geographischen Parametern Breitengrad und Höhe. Dies kann als Ergebnis eines komplexen höhenabhängigen Abkühlungsprofils interpretiert werden, welches durch ein Zusammenspiel von räumlich variierender Topographie, jüngerer tektonischer Aktivität und zeitlich wechselnder geomorphologischer Bedingungen beeinflusst wird.

Die AFT-Kornalter in der Narcea Antiform, der Kantabrischen Zone und der Stephanbecken zeigen, dass der Temperatureinfluss während des gesamten variszischen Zyklus für eine vollständige Ausheilung der vorhandenen Spaltspuren zu gering ist. AFT-Kornalter-Komponenten in der Narcea Antiform weisen auf Bedingungen partieller AFT-Ausheilung (PAZ) hin, die seit dem Neoproterozoikum aufrechterhalten wurden. Viele der prästephanen paläozoischen Proben nahe der wichtigen Störungszonen (León und Sabero-Gordón) zeigen AFT-Kornalter, die auf eine vollständige Ausheilung ab dem späten Karbon (spätvariszisch) hindeuten.

Mit modellierten Zeit-Temperatur-Pfaden (t-T) von 19 Proben wird die thermische Entwickung des südlichen Kantabrischen Gebirges diskutiert. AFT-Kornalter von Proben aus der Narcea Antiform weisen Abkühlungssignaturen auf, die bei Berücksichtigung des 1s-Fehlers den frühesten Eintritt in die AFT-PAZ Phase bereits während des Neoproterozoikums belegen. Dies geht zeitlich mit der Subduktion an dem avalonisch-cadomisch-panafrikanischen magmatischen Bogen einher (Gutiérrez-Alonso et al., 2005). Die bis zum Stephan anhaltende Abkühlung der neoproterozoischen Proben ist

nicht eindeutig nachweisbar und ist nicht mit der ~ 3.6 km mächtigen Sedimentation im benachbarten kantabrischen Becken (Veselovsky, 2005; Dietrich, 2005) vereinbar. Einem spätvariszischen bis initialem post-variszischen thermischen Impuls bis zu oberen PAZ-Bedingungen folgt eine mitteljurassische denudationsbedingte Abkühlungsphase in der Narcea Antiform, was aus dem Verlassen der PAZ geschlossen wird.

In den paläozoischen Gesteinen der südlichen kantabrischen Zone werden mittlere bis hohe PAZ-Bedingungen bis zu einer Zeit zwischen mittlerer Trias und spätem Jura aufrechterhalten. Diese Bedingungen sind gebunden an: a) Versenkungswärme durch eine Bedeckung von proximalen Sedimenten, die von 1 km bei maximalen thermischen Bedingungen von ~ 85 ˚C/km (Frings et al., 2004) bis zu angenommenen ~ 3 - 4 km bei einem geothermischen Gradienten von ~ 30 ˚C/km zunimmt und/oder b) die Konvektion von heißen hochsalinaren Solen (cf. Ayllon, 2003; Gasparrini et al., in press), vermutlich triassischen Alters (cf. Arche & López-Gómez, 1996).

Die AFT t-T Rekonstruktion belegt eine rasche spätmesozoische Abkühlung unterhalb der PAZ-Bedingungen, die mit dem Beginn des entfernten Atlantik-, bzw. später Biskaya-Rifts einhergeht (Ziegler, 1988). Eine spätmesozoische-neogene Aufheizung zu unteren bis mittleren PAZ-Bedingungen wird durch die t-T-Modellierung gezeigt. Sie steht im Zusammenhang mit der Abfolge von: Spätphase der Biskaya-Öffnung, Biskaya-Subduktion (Andeweg, 2002), Beginn der alpidischen Orogenese (Boillot & Malod, 1988; Andeweg, 2002) und einem früheozänen thermischen Impuls während der Hauptphase der alpidischen Orogenese (z.B. Gutiérrez-Alonso et al., 2005).

Die darauf folgende Abkühlungsphase während des ausgehenden Paläogens und beginnenden Neogens geht mit alpidischer Einengungs-, Hebungs- und Abtragungsgeschichte einher (Andeweg, 2002). Eine heterogen ausgeprägte jüngste thermische Reaktivierung, meistens nicht erfasst vom AFT-Chronometer, erfolgte vermutlich gleichzeitig mit einer erneuten tektonischen Aktivität entlang des nördlichen iberischen Kontinentalrandes (Andeweg, 2002) während dem ausgehenden Miozän (Messinian).

Seit dem frühen Pliozän ist ein heterogen ausgeprägtes Abkühlen der Gesteine zu verzeichnen. Die post-tektonische Denudation innerhalb des Arbeitsgebiets ist der bestimmende Prozess dafür. Angesichts fehlenden mesozoischen und känozoischen Deckgebirges im südlichen Kantabrischen Gebirge, erscheint die AFT t-T Modellierung als die einzig mögliche Methode für eine zeitgenaue quantitative Bestimmung der post-variszischen Abkühlgeschichte in der nordwestlichen iberischen Halbinsel.

# Contents

# Figures

# Tables

# 1 Introduction

## 1.1 Timing of tectonothermal events in Iberia

The aim of this study is to discern the low- temperature thermal evolution of the southern Cantabrian Mountains, northwest Iberia.

The southern Cantabrian Mountains expose sedimentary rocks having experienced uplift during Alpidic, Variscan and in the S, possibly Cadomian orogenic cycles; these rocks are commonly referred to by their Variscan tectonic expressions: the Cantabrian Zone (CZ) and Narcea Antiform (NA) (figure 1.1-1). The Cantabrian Zone, comprises a nearly complete pre-Stephanian Palaeozoic succession and has been characterised as the thin-skinned tectonism dominated (Julivert, 1971; Pérez-Estaún et al., 1988), arcuate foreland fold-and-thrust belt in the Iberian part of the western European Variscan orogenic belt.

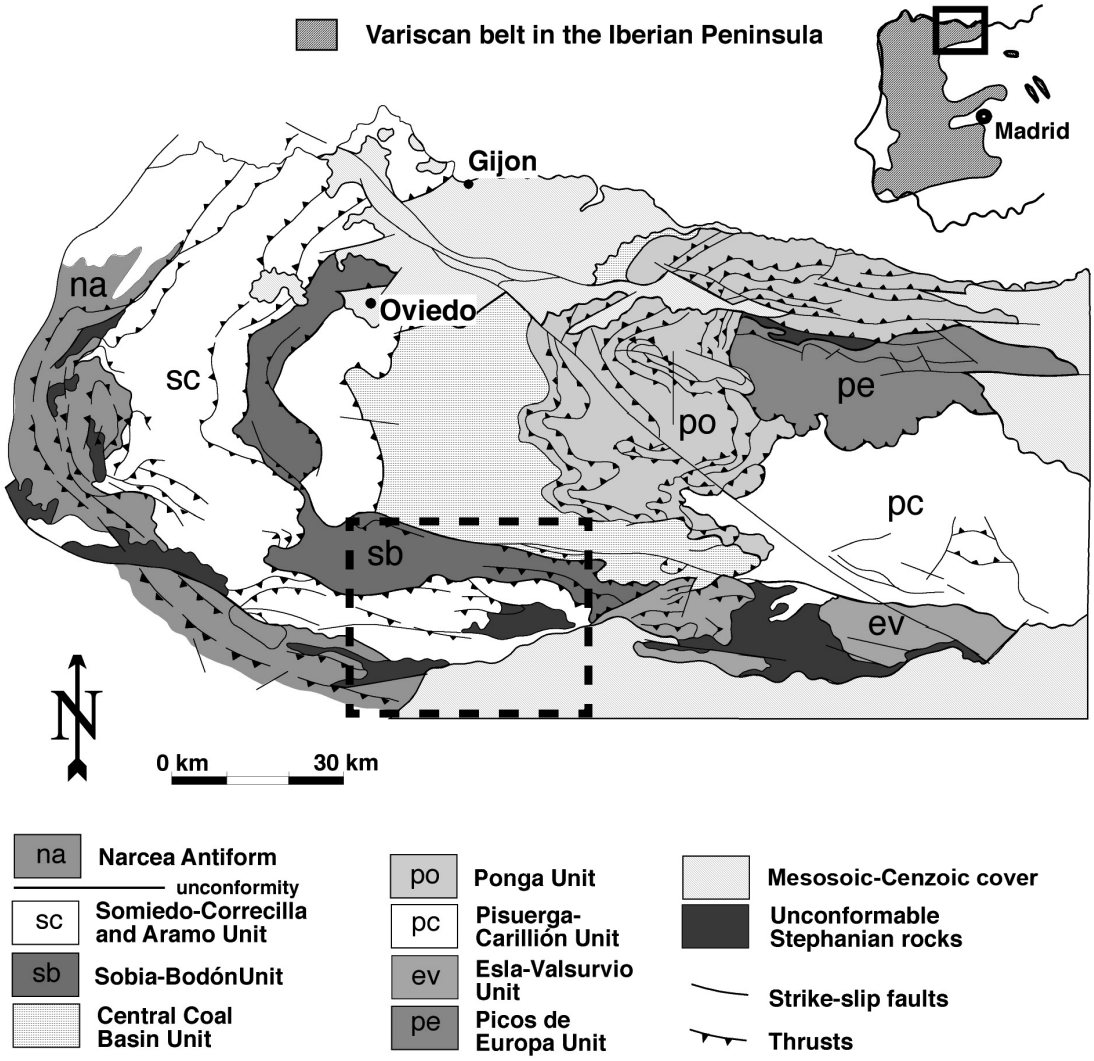


Figure 1.1-1: The Variscan external Cantabrian Zone and its component tectonic units, the transitional Narcea Antiform and Stephanian sedimentary covers (Modified from Julivert, 1971 and Pérez-Estaún et al., 1988). This study's sampling area is marked by the dashed box.

*Introduction*

Bodón and Correcillas units of the Fold and Nappe Province indicate nonmetamorphic conditions (e.g. Raven & van der Pluijm, 1986; Aller et al., 1987, 2005; Keller & Krumm, 1992, 1993; Marschik, 1992; Schneider, 2002; Gasparrini, 2003). The León Line Fault system separates the Fold and Nappe Province from the Central Coal Basin, where along its southern margin, incipient metamorphic conditions are recorded (e.g. Aller et al., 1987, 2005; Marschik, 1992).

The Narcea Antiform's Neoproterozoic turbiditic rocks represent the pre-Variscan Palaeozoic succession's sedimentary basement (e.g. Gutiérrez-Alonso, 1996). The Variscan orogenic foreland-hinterland transition is also recognised in the pervasively deformed antiform. Deformation increases towards the hinterland (e.g. Díaz-García, 2006). Coincident with deformation, metamorphic conditions increase across the antiform from anchizone to greenschist facies (e.g. Aller et al., 1987; Martín-Parra, 1989; Keller & Krumm, 1992, 1993).

Unconformable and deformed, Stephanian intramontane basin fills, following major structural lineaments (e.g. León, Sabero-Gordón and Conombre-La Urz fault systems) overlay pre-Stephanian basements. Stephanian rocks atop those of the foreland-hinterland transition show incipient metamorphic signatures (Aller et al., 2005), while those overlying the Correcillas Unit infer high nonmetamorphic grades (e.g. Marschik, 1992; Frings, 2002; Ayllón, 2003; Ayllón et al., 2003; Frings et al., 2004; Aller et al., 2005).

Mesozoic and Cenozoic accumulations are conspicuously absent over much of this study's sampling area. Discontinuous accumulations of Cretaceous rocks are overturned at the Cantabrian Zone's southern margin. Spatially restricted sediments occur at structural lineaments in the Narcea Antiform. N-sourced Cenozoic accumulations to ~ 3 km in thickness, evidenced in the Duero Basin (e.g. Alonso et al., 1995), are in unconformable contact with underlying basements at the southern margin of the Cantabrian Zone and the western margin of the Narcea Antiform. Highly restricted unconformable accumulations are also evidenced atop basements in the Narcea Antiform (e.g. Martín-Parra, 1989).

Tectonostratigraphic and thermal data from rocks outcropping in the southern Cantabrian Mountains are thus highly suited as a combined natural testing area for understanding the Neoproterozoic to preset, low-temperature tectonothermal evolution of an area succumb to at least two orogenic cycles, yet lacking exposures of cratonic igneous or metamorphic basement.

## 1.2 Apatite fission-track thermochronology in sedimentary settings

Fission-track analysis can be applied to a wide range of geological settings. In collisional settings, fission tracks are used to reconstruct the denudation evolution of mountain belts, help constrain the provenance and amounts of foreland peripheral basins, as well as provides depth-time pathway information for the movement of rocks through the upper kilometres of the Earth's crust (Wagner & van den Haute, 1992); e.g.: Alps (Wagner & Reimer, 1972; Carpéna, 1985; Giger & Hurford, 1989; Rahn & Seward, 2000; Emmerich, 2004; Emmerich et al., 2005), Transantarctic Mountains (e.g. Wagner et al., 1989), Himalayas (e.g. Zeitler, 1985) and Pyrenees (e.g. Fitzgerald et al., 1999; Juez-Larré, 2003). Fission-track studies are also utilised to constrain uplift, denudation and erosion contemporaneous with rift stages in extensional environments, e.g.: Brazilian continental margin (Gallagher & Brown 1997), East Africa Rift (van den Haute, 1984; Wagner et al., 1992).

Fission-track methods, when combined with other dating techniques possessing higher closure temperatures (e.g. K-Ar, Ar-Ar, Rb-Sr and U-Pb) are used to constrain the thermal history of metamorphic and magmatic events in basinal and cratonic settings (e.g. Steven et al., 1979; Andriessen & Reuter, 1994; Carrapa, 2002).

Recently, the fission-track method in combination with the (U-Th)/He low-temperature temperature thermochronometre has been used to decipher the thermal history of rocks at temperatures below the 60 ˚C isotherm (e.g. Juez-Larré, 2003).

Research into the thermal evolution of sedimentary basins has provided many platforms for apatite fission-track (AFT) investigations (Naeser, 1979; Briggs et al., 1981; Naeser et al., 1989; Green, 1989 a). The interest results from the recognition that temperature is amongst the most important geological factors controlling hydrocarbon maturation in sedimentary environments (Wagner & van den Haute, 1992). In a typical sedimentary basin, the maturation of liquid hydrocarbon occurs with significant duration at temperatures between about 60 ˚C and 130 ˚C--the "oil window". Coincidentally the apatite fission-track partial annealing zone (PAZ), which occurs between 60 ˚C and 110 ± 10 ˚C (e.g. Hurford, 1986; Laslett et al., 1987) corresponds almost exactly to the oil window. Conventional thermal indicators such as vitrinite reflectance, clay mineralogy, fluid inclusion and conodont alteration index, record only the maximum temperatures they've experienced, however, due to the constant generation of spontaneous fission tracks through geological time, apatite fission-track analysis is an excellent compliment to the aforementioned thermal indicators (e.g. Arne & Zentilli, 1994; Beardsmore & Cull, 2001), as it provides the unique opportunity to map the thermal evolution through time of a host rock, and correspondingly the maturation history for any hydrocarbons therein contained (e.g. Green, 1989 a).

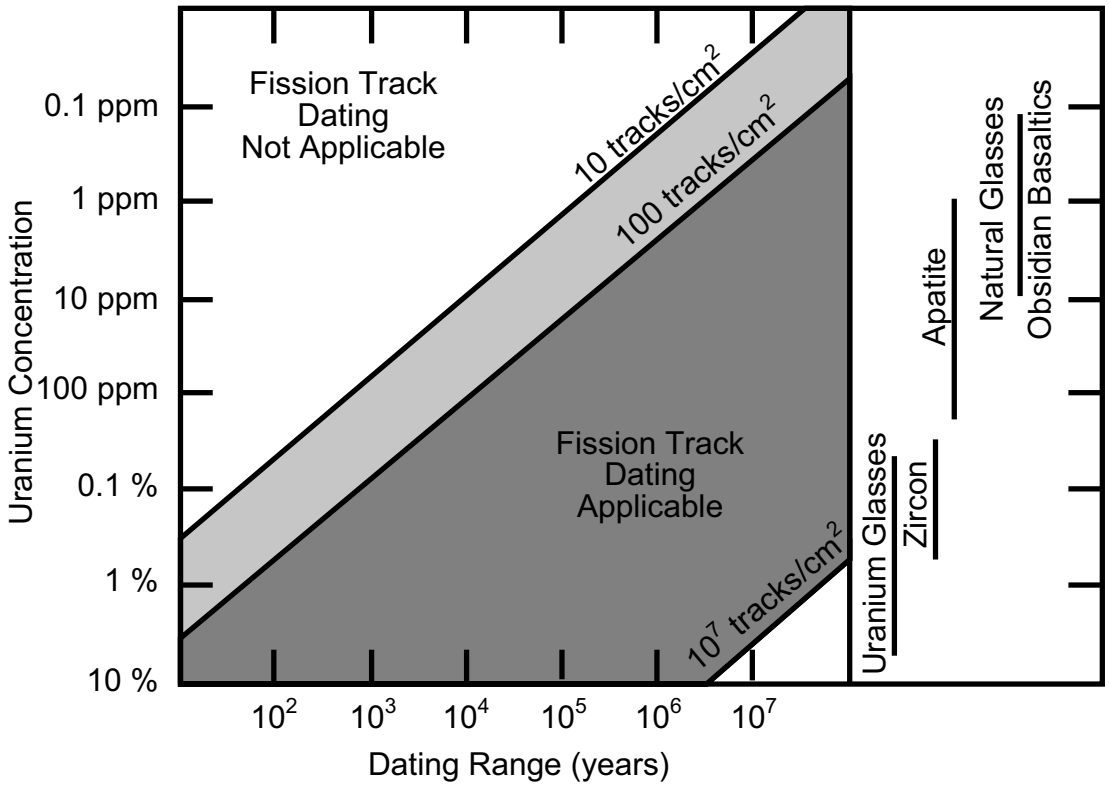


Figure 1.2-1: Potential dating ranges of the fission track method utilising various geological materials according to their uranium concentrations. After Wagner (1978).

Apatite is the only mineral for which the significance of the cooling age can be scrutinised through its track-length distribution. The time span covered by the fission-track dating method is essentially determined by the aerial density of the fission tracks in the investigated material. To acquire a precisely determined age, fission track counts on the order of hundreds to thousands are required. Therefore either samples with sufficient age and/or uranium concentration are required for successful application of the method (Fleischer & Price, 1964; Wagner & van den Haute, 1992). Time-spans to which the various fission-track methods are applicable are depicted in figure 1.2-1. Track densities of at least 10 tracks/cm$^2$ are necessary for dating as lower densities involve unreasonably large errors (Fleischer & Price, 1964). Track densities as high as $10^9$ tracks/cm$^2$ have been counted on replicas of an etched surface (Weiland et al., 1980), however it is not normally recommended to count densities $\geq 10^7$ tracks/cm$^2$ as individual tracks become difficult to discern using an optical microscope and reliability is reduced (Wagner & van den Haute, 1992).

## 1.3 Previous fission-track studies in Iberia

Several fission-track studies have been conducted for the Iberian Peninsula over the last decades. Studies regarding the tectonothermal evolution of the peninsula thus far detail thermal histories reaching back only to the Variscan orogeny.

The oldest AFT age in Iberia is 247 ± 19 Ma (Stapel, 1999), from Lower Triassic sandstones (depositional age 245 Ma) of the Sierra Morena, south-central Iberia. The youngest AFT age 2.7 ± 0.6 (Johnson et al., 1997) comes from rocks of the internal zone of the Betics. To date, the oldest AFT ages garnered from apatites in Variscan Basement are 221 ± 5 Ma (Babero et al., 1998) and 217 ± 6 (Babero et al., 2005) in the Toledo Mountains. An age of 206 ± 9 Ma (Pereira et al., 1998) was garnered from apatite from the Sierra do Caramulo, Portugal. In the Pyrenees Axial Zone, AFT studies reveal ages between 21 ± 3 Ma and 44 ± 4 Ma (Fitzgerald et al., 1999). No AFT data are available for the landward side Iberia's northern margin.

Fission-track analyses of the Portuguese Iberian Massif reveal relatively fast cooling rates (denudation ~ 0.8 mm/y to 1.0 mm/y) during the Variscan orogeny, however, following the initiation of North Atlantic rifting the, rate of cooling at Mesozoic through Cenozoic time slowed in western Iberia (denudation ~ 0.02 mm/y to 0.05 mm/y) (Pereira et al., 1998; Stapel, 1999). Slow cooling, evidenced by AFT ages of ~ 120 Ma and ~ 60 Ma is interpreted to be the result of the restoration of the upper crust geotherm after a thermal pulse, likely related to magmatic event(s) related to the break-up of Pangaea during the Mesozoic (Stapel, 1999).

AFT ages between ~ 130 Ma and ~ 65 Ma (de Bruijne & Andriessen, 2002) from Variscan basement of the Spanish Central System, being roughly coeval with those from western Iberia, are again interpreted to have resulted, at least in part from geothermal fluctuation, but also from the deposition and subsequent erosion of 2 km to 3 km of Triassic to Lower Jurassic sedimentary sequences and a renewed phase of denudation (~ 3 km) related cooling during the Cretaceous (de Bruijne, 2001). Therefore, uplift in the area occupied by the present Spanish Central System and Madrid basin was coeval with extension along the Portuguese Atlantic margin and the Iberian Basin (Juez-Larré, 2003). Late Cretaceous onset of biaxial convergence between Iberia, Africa to the S and Eurasia to the northeast (Pyrenean orogeny) is related to the far field exhumation of the Spanish Central System in association with reactivation of preexisting Variscan lineaments in the lithosphere (de Bruijne, 2001). Miocene to present expression of the Sierra de Guadarrama (Spanish Central System) is associated with the far field effects of Iberian-African plate collision, forming the younger Betic Cordillera of southeast Iberia (de Bruijne & Andriessen, 2002).

Investigation of the lowermost structural unit of the Betic Cordillera (Nevado-Filábride complex) reveals Miocene tectonic denudation progressed W-ward (12 ± 1 Ma in the east, ~ 9 Ma to 8 Ma in the W) as a result of the oblique convergence between Iberia

and the Betic Internal Zone (Johnson, 1997). Andriessen & Zeck (1996), investigating the Alpujárride complex, detail very high cooling rates (150 ˚C/Ma) and an associated high denudation rate between 20 Ma and ~ 17 Ma followed by more subdued cooling thereafter. The youngest ages in the Betics result from Pliocene folding and rapid erosion related denudation (Johnson, 1997).

Mesozoic rift-related thermal signatures also significantly influence the AFT systems from the Catalan Coastal Range. Thermal modelling of fission-track age/length distributions for individual apatite grains here, suggest the possibility for a dominant thermal pulse during Triassic-Early Jurassic, resulting in severe partial annealing conditions and residence thereafter at temperatures slightly above 60 ˚C (Juez-Larré, 2003). The onset of fast cooling during the Palaeogene, registered in AFT systems, is related to between 2 km and 3 km of unroofing associated with the Pyrenean orogeny (Juez-Larré & Andriessen, 2002).

Fitzgerald et al. (1999) report synorogenic exhumation on the order of 12 km to 13 km having occurred in the axial zone during the Eocene in association with the Pyrenean compressional phase. The highest rate of denudation occurring along the southern flank of the axial zone in the Early Oligocene, ceasing in the Middle Oligocene due to the change of convergence accommodation in the Pyrenean double wedge, a product of the collision between Iberia and Europe. Fission-track data from Yelland (1990) modelled by Morris et al. (1998) suggest 1.5 to 2.8 times greater discharge of sediment to the S of the Pyrenees (Erbo Basin) than to the N (Aquitane Basin). The Miocene to present postorogenic denudation of the Pyrenees is estimated to be ~ 2 km to 3 km (Fitzgerald et al., 1999).

An offshore fission-track study of granulites dredged along the Iberian margin of the Bay of Biscay yielded zircon ages of 725 ± 67 Ma (Ortegal Spur) and 284 ± 58 Ma (Le Danois Bank), indicating post-Variscan cooling (Fügenschuh, et al., 2003). Apatite from the Le Danois Bank sample yielded an Early Eocene age of 52 ± 2 Ma, which has been interpreted as the final cooling stage after “Pyrenean” thrust imbrication. In addition Early Cretaceous AFT ages from two other samples dredged from the Danois Bank (138 ± 7 Ma, 120 ± 8 Ma) are interpreted to represent exhumation during rifting (Fügenschuh, et al., 2003). The data evidence a Precambrian high-grade terrane along the northern Iberian margin, extending to the Armorican margin (Fügenschuh, et al., 2003).

## 1.4 Thesis questions and structure

In light of the unique chronometric property available only in the AFT technique, the suite of information from peak metamorphic indicies, and the absence of any quantitative low-temperature thermochronologic study in northwestern Iberia, This study, focusing on AFT central-age and track-length analyses, complemented by AFT time-Temperature (t-T) modelling provides a discrete investigation of the Neoproterozoic to present tectonothermal history of the southern Cantabrian Mountains. Five main questions are addressed:

**1)** Per-grain uranium concentrations are used to address the influence of grain chemistry upon the relationship between AFT single-grain-age and per-grain $D_{par}$ in samples where grain age distributions do not pass the $\chi^2$-test.

**2)** Sample AFT central-age versus their geographic parametres, latitude and elevation are considered, in order to evaluate the influence of differential topography, recent tectonic activity and changing geomorphic conditions over time upon the uplift-enduced denudation profile of the southern Cantabrian Mountains.

**3)** To evaluate the significance and distribution of heating associated with Variscan or later tectonothermal events upon AFT-systems of pre-Carboniferous sedimented rocks in the southern Cantabrian Mountains AFT grain-age and track length data from Neoproterozoic sedimented samples from the Narcea Antiform and pre-Carboniferous sedimented rocks in the Correcillas and Bodón units of the southern Cantabrian Zone were evaluated. Where applicable, their pre-Variscan tectonothermal evolutions were modelled.

**4)** The significance and distribution of heating associated with Variscan or later tectonism in the southern Cantabrian Mountains is evaluated from AFT-systems of late Variscan sedimented coal basins (e.g. southern Central Coal Basin Unit and spatially discontinuous Stephanian coal basins) at or about deep-seated structural lineaments including the Conombre-La Urz, Sabero-Gordón Line and León Line fault systems in the southern Cantabrian Mountains. Where applicable, their pre-Variscan tectonothermal evolutions were modelled.

**5)** In the absence of extensive post-Stephanian sedimentary cover in the southern Cantabrian Mountains, regional sedimentary, tectonic and thermal data were used to constrain new t-T models for the Permian to Holocene low-temperature tectonothermal evolution of the southern Cantabrian Mountains.

To The questions addressed in this thesis, the work is divided into nine chapters:

**Chapter 1:** Introduces the area of interest and provides a brief breakdown of its tectonothermal and stratigraphic setting; describes the state of experimental knowledge regarding AFT low-temperature thermochronology; defines some geological applications of fission-track thermochronology; details current knowledge regarding Iberia's low-temperature tectonothermal evolution; and outlines the objectives of this study.

**Chapter 2:** Provides an overview of the geologic and plate tectonic setting of the study area in the southern Cantabrian Mountains spanning Neoproterozoic to present time.

**Chapter 3:** Outlines the Neoproterozoic, Palaeozoic, Mesozoic and pre-Holocene Cenozoic stratigraphies in the southern Cantabrian Mountains.

**Chapter 4:** Shows the structural evolution of the Narcea Antiform, southern Cantabrian Zone, Central Coal Basin units in the southern Cantabrian Mountains.

**Chapter 5:** Provides a review of the published literature regarding thermal indices and magmatism in and about the Narcea Antiform, southern Cantabrian Zone and the Central Coal Basin units of the southern Cantabrian Mountains.

**Chapter 6:** Introduces the AFT analytical method: Sampling mission, mineral assemblage preparation, sample irradiation, fission-track counting, track-length measurements and t-T modelling techniques.

**Chapter 7:** Discussion the AFT experimental and modelling results from analyses of Neoproterozoic through Palaeozoic aged samples along the southern slope of Cantabrian Mountains as constrained by relevant information garnered from regional stratigraphic, structural and thermal indicies data.

**Chapter 8:** Synthesis of the results presented in previous chapters outlining the tectonothermal evolution of the southern Cantabrian Mountains and their regional context.

**Chapter 9:** Suggests topics for future applications of AFT, apatite (U-Th)/He, $^{40}Ar/^{39}Ar$ and zircon fission-track analysis methods.

# 2 Geologic & plate-tectonic setting

The following pages review geologic and tectonothermal settings in NW Iberia, particularly the southern Cantabrian Zone (sCZ), eastern West Asturian-Leónese Zone (WALZ) and the southeastern part of their suture the Narcea Antiform, in addition to parts of the southern Central Coal Basin will be elucidated. In so doing, this chapter follows in part Veselovsky (2004).

Other comprehensive summaries of the geological evolution of the NW Iberian Massif given for structural characteristics (e.g. Díez-Balda et al., 1990; Martínez-Catalán et al., 1990, 1996; Ribeio et al., 1990; Pérez-Estaún et al., 1991), metamorphism (e.g. Arenas et al., 1986; Martínez & Rölet, 1988; Gil-Ibarguchi and Arenas, 1990) and magmatism (e.g. Bellido-Mulas et al., 1987; Corretgé et al., 1990) amongst others.

## 2.1 European Variscan Belt and orogeny

Weil et al. (2001) describe the European Variscan Belt as a continental scale oroclinal bend extending almost 4000 km from southern Spain to the Carpathian Mountains. In western Europe (figure 2.1-1), it is an example of an orogenic belt lacking exposures of cratonic igneous or metamorphic basement (Fernández-Suárez et al., 2000 a). Morphologically, it is a broad sinuous belt, up to 900 km wide expressing bilateral symmetry. It is interpreted to have developed due to the convergence and collision

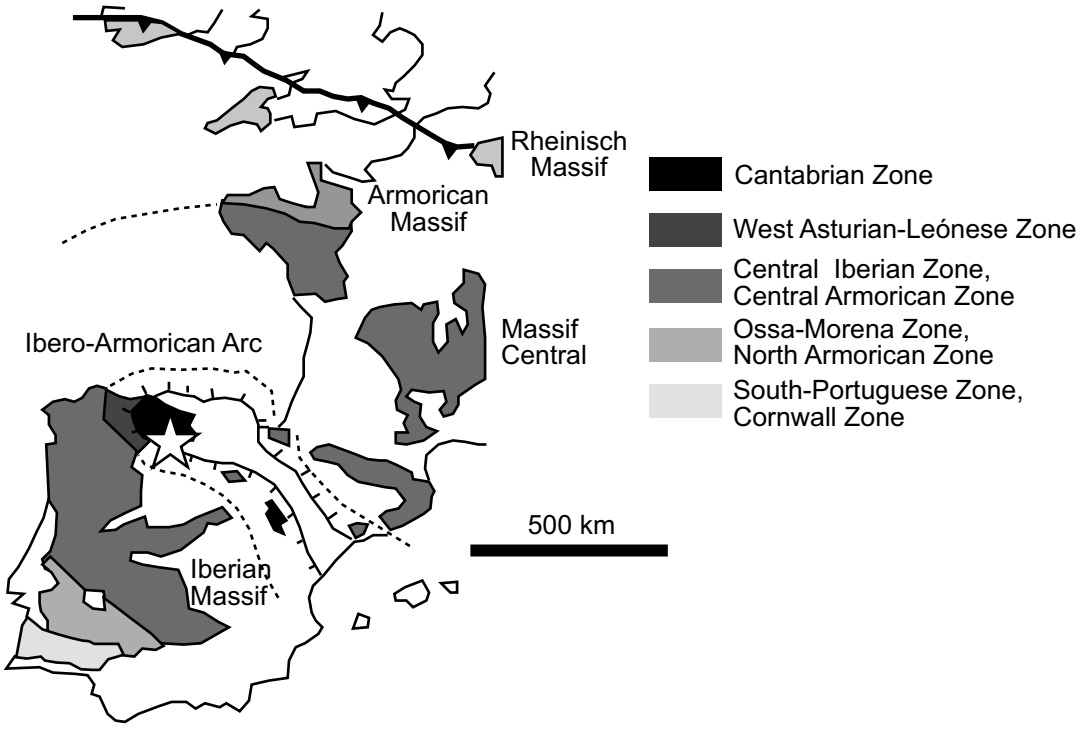


Figure 2.1-1: The Ibero-Armorican Arc with the Cantabrian Zone at its core. Star approximates the location of the sampling area for this study. Modified from Gutiérrez-Alonso et al. (2004 a).

of the palaeocontinents Laurentia/Baltica and Gondwana, in addition to numerous allochthonous terranes, following the closure of at least three oceanic basins (Matte, 1991).

Franke (1992) reported the Variscan Collisional Belt formed during the Late Devonian between 360 and 380 Ma, accompanied by a high-pressure metamorphism event lasting to about 280 Ma (Early Permian) (Fernández-Suárez et al., 2000 a). Mesozoic extension and rifting followed. Cenozoic compression (Andeweg, 2002) transformed the Variscan belt into an alpidic orogen (Cloetingh & Burov, 1996). According to Fernández-Viejo et al. (2000) thickness of the Variscan crust in northwestern Iberia, generally varies from about 30 - 32 km in the internal parts, but reaches down to 47 km under the highest peaks in the most external parts.

## 2.2 Iberian Variscides

The Ibero-Armorican or Asturian Arc is a prominent bend in the western part of the Iberian Variscan Belt (Matte, 1991; Bastida & Aller, 1992; Pérez-Estaún et al., 1994; Ábalos et al., 2002). Lotze (1945) and Julivert et al., (1972) subdivided the Iberian Massif (Variscan Belt's expression in the western half of the Iberian Peninsula) into five zones based on metamorphic, structural and palaeogeographic characteristics, reflecting varying deformation styles.

From the NE to SW the Iberian Massif includes the following zones:
- Cantabrian (external)
- West Asturian-Leónese (internal)
- Central Iberian (including the schistose domain of Galicia-Trás-os-Montes) (internal)
- Ossa Morena (internal)
- South Portuguese (external)

Together, these zones represent a collisional belt in which dismembered ophiolitic units are interpreted to mark a suture (Dallmeyer et al., 1997). The Cantabrian, West Asturian-Leónese and Central Iberian zones each occupy relative autochthonous positions of increasingly metamorphic gradient (Dallmeyer et al., 1997) relative to the chain suture, and display thrust and folds of predominantly N-ward vergence (e.g. Aramburu and Bastida, 1995). In addition to the schistose zone, the Galicia-Trás-os-Montes contains disjunct allochthonous terranes of variable provenance and origin (Arenas et al., 1986; Dallmeyer et al., 1997). Figure 2.2-1 details a roughly E-directed profile through these zones. Highly metamorphosed rocks and granitoids are restricted to the internal zones (Fernández-Suárez et al., 2000 a, b).

The sampling area chosen for this study straddles the transition between internal and external members (hinterland and foreland) of the Variscan orogeny in northwestern Iberia. Figure 2.2-2 provides a detailed overview of the ~ 1500 km$^2$ sampling area.

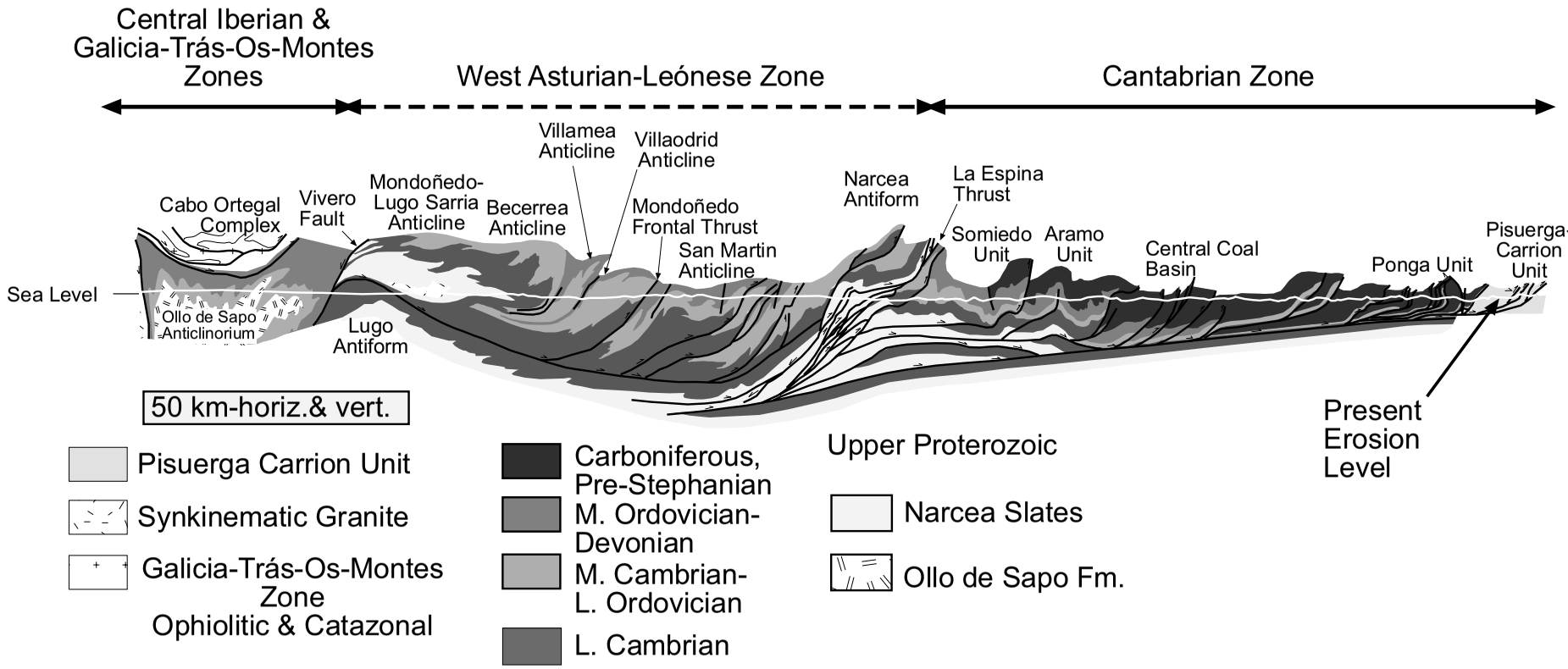


Figure 2.2-1: Geologic cross-section throughout Central Iberian, West Asturian-Leónese and Cantabrian zones of the Iberian Massif (Pérez-Estaún et al., 1991). External-most internal zone sediments of the West Asturian-Leónese Zone were thrust upon rocks of the Cantabrian Zone. The Narcea Antiform, a thick accumulation of Precambrian flysch sediments, represents the transition between these two zones. The Cantabrian Zone is dominated by synorogenic Carboniferous deposits. The Cabo Ortegal Complex and Ollo de Sapo Anticline to the W, define the central part of the Variscan orogen in Iberia.

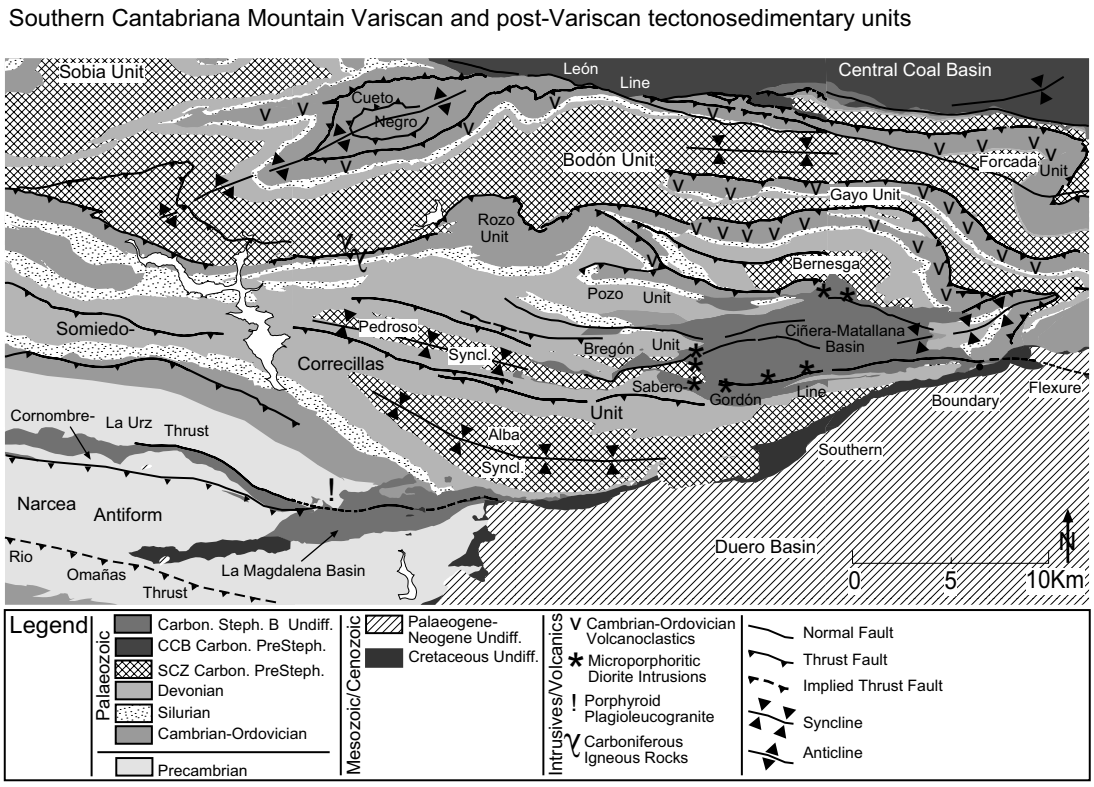


Figure 2.2-2: Sampling area for the assessment of the low-temperature thermochronology of NW Iberia. Area straddles the boundary between internal and external parts of the Variscan orogenic belt in NW Iberia. Analysed area includes the southeastern extent of the Narcea Antiform, the southern Cantabrian (SCZ), and Central Coal Basin (CCB) zones.

## *2.2.1 Timeline for Variscan deformation*

Three diachronous phases of syn-Variscan deformation are recognised in rocks of the Iberian Massif (Dallmeyer et al., 1997). Figure 2.2.1-1 depicts the geotectonic, and metamorphic evolution of the Iberian Massif and includes absolute dates regarding the occurrence of igneous rocks in the Iberian zones.

Deformation and related synorogenic deposition in the innermost zone from about Middle Devonian times is recorded in cooling ages obtained for obduction-related amphiboles in the Morais Ophiolite of the Central Iberian Zone (Dallmeyer & Gil-Ibarguchi, 1990; Quesada, 1991). $^{40}Ar/^{39}Ar$ Dating, combined with X-ray diffraction and electron microprobe analyses enabled Dallmeyer et al. (1997) to constrain the diachronic evolution of main tectonothermal events across the northern Iberian Massif. The three phased diachronic evolution is graphical depicted in figure 2.2.1-2.

Late Silurian/Early Devonian marks the observed beginning of the first metamorphic and deformational episode in the westernmost Galicia-Trás-os-Montes Zone, reaching the Central Iberian Zone in Late Devonian, the West Asturian-Leónese Zone in the Tournaisian, and the Cantabrian Zone in the Serpukhovian. This first deformation event marked the onset of thrust tectonics and the emplacement of thrust sheets in the

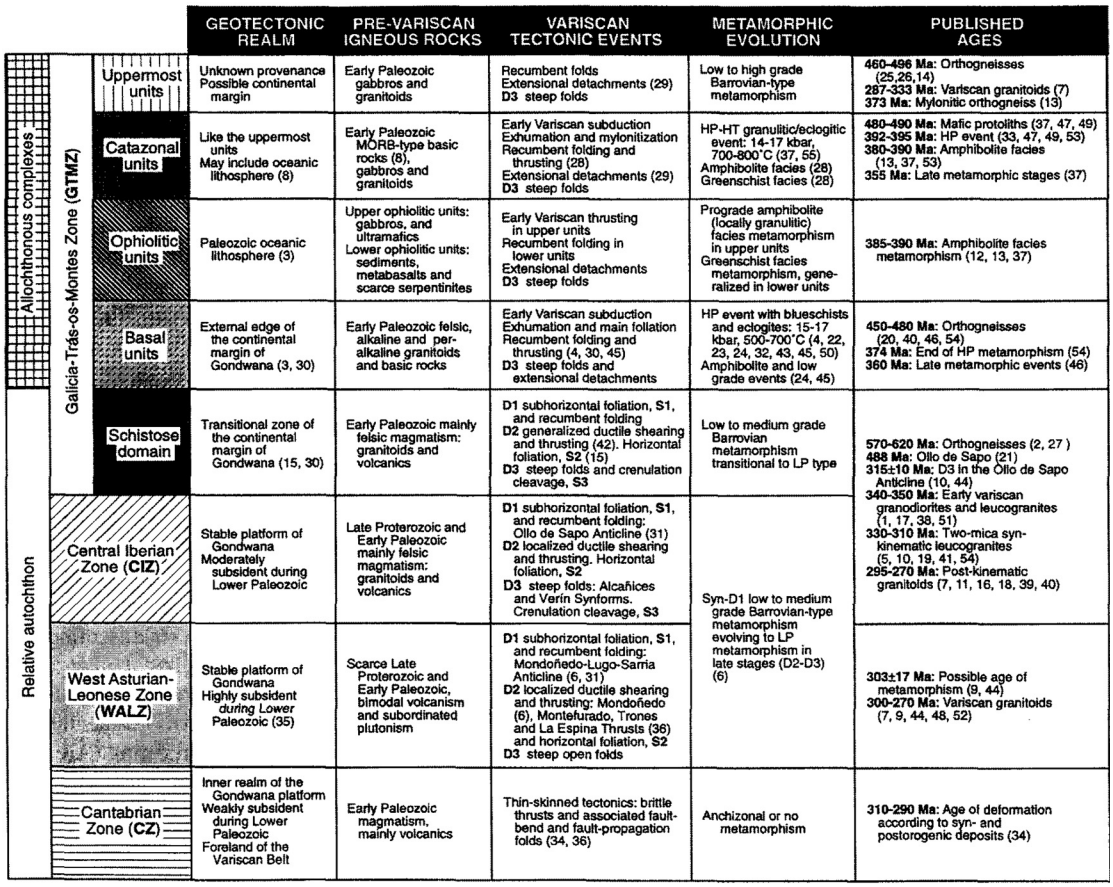

| | | GEOTECTONIC REALM | PRE-VARISCAN IGNEOUS ROCKS | VARISCAN TECTONIC EVENTS | METAMORPHIC EVOLUTION | PUBLISHED AGES |
|---|---|---|---|---|---|---|
| Allochthonous complexes | Galicia-Trás-os-Montes Zone (GTMZ) Uppermost units | Unknown provenance<br>Possible continental margin | Early Paleozoic gabbros and granitoids | Recumbent folds<br>Extensional detachments (29)<br>D3 steep folds | Low to high grade Barrovian-type metamorphism | **460-496 Ma:** Orthogneisses (25,26,14)<br>**287-333 Ma:** Variscan granitoids (7)<br>**373 Ma:** Mylonitic orthogneiss (13) |
| | Catazonal units | Like the uppermost units<br>May include oceanic lithosphere (8) | Early Paleozoic MORB-type basic rocks (8), gabbros and granitoids | Early Variscan subduction<br>Exhumation and mylonitization<br>Recumbent folding and thrusting (28)<br>Extensional detachments (29)<br>D3 steep folds | HP-HT granulitic/eclogitic event: 14-17 kbar, 700-800°C (37, 55)<br>Amphibolite facies (28)<br>Greenschist facies (28) | **480-490 Ma:** Mafic protoliths (37, 47, 49)<br>**392-395 Ma:** HP event (33, 47, 49, 53)<br>**380-390 Ma:** Amphibolite facies (13, 37, 53)<br>**355 Ma:** Late metamorphic stages (37) |
| | Ophiolitic units | Paleozoic oceanic lithosphere (3) | Upper ophiolitic units: gabbros, and ultramafics<br>Lower ophiolitic units: sediments, metabasalts and scarce serpentinites | Early Variscan thrusting in upper units<br>Recumbent folding in lower units<br>Extensional detachments<br>D3 steep folds | Prograde amphibolite (locally granulitic) facies metamorphism in upper units<br>Greenschist facies metamorphism, generalized in lower units | **385-390 Ma:** Amphibolite facies metamorphism (12, 13, 37) |
| | Basal units | External edge of the continental margin of Gondwana (3, 30) | Early Paleozoic felsic, alkaline and peralkaline granitoids and basic rocks | Early Variscan subduction<br>Exhumation and main foliation<br>Recumbent folding and thrusting (4, 30, 45)<br>D3 steep folds and extensional detachments | HP event with blueschists and eclogites: 15-17 kbar, 500-700°C (4, 22, 23, 24, 32, 43, 45, 50)<br>Amphibolite and low grade events (24, 45) | **450-480 Ma:** Orthogneisses (20, 40, 46, 54)<br>**374 Ma:** End of HP metamorphism (54)<br>**360 Ma:** Late metamorphic events (46) |
| Relative autochthon | Schistose domain | Transitional zone of the continental margin of Gondwana (15, 30) | Early Paleozoic mainly felsic magmatism: granitoids and volcanics | D1 subhorizontal foliation, S1, and recumbent folding<br>D2 generalized ductile shearing and thrusting (42). Horizontal foliation, S2 (15)<br>D3 steep folds and crenulation cleavage, S3 | Low to medium grade Barrovian metamorphism transitional to LP type | **570-620 Ma:** Orthogneisses (2, 27 )<br>**488 Ma:** Ollo de Sapo (21)<br>**315±10 Ma:** D3 in the Ollo de Sapo Anticline (10, 44)<br>**340-350 Ma:** Early variscan granodiorites and leucogranites (1, 17, 38, 51)<br>**330-310 Ma:** Two-mica syn-kinematic leucogranites (5, 10, 19, 41, 54)<br>**295-270 Ma:** Post-kinematic granitoids (7, 11, 16, 18, 39, 40) |
| | Central Iberian Zone (CIZ) | Stable platform of Gondwana<br>Moderately subsident during Lower Paleozoic | Late Proterozoic and Early Paleozoic mainly felsic magmatism: granitoids and volcanics | D1 subhorizontal foliation, S1, and recumbent folding: Ollo de Sapo Anticline (31)<br>D2 localized ductile shearing and thrusting. Horizontal foliation, S2<br>D3 steep folds: Alcañices and Verín Synforms. Crenulation cleavage, S3 | Syn-D1 low to medium grade Barrovian-type metamorphism evolving to LP metamorphism in late stages (D2-D3) (6) | |
| | West Asturian-Leonese Zone (WALZ) | Stable platform of Gondwana<br>Highly subsident *during Lower* Paleozoic (35) | Scarce Late Proterozoic and Early Paleozoic, bimodal volcanism and subordinated plutonism | D1 subhorizontal foliation, S1, and recumbent folding: Mondoñedo-Lugo-Sarria Anticline (6, 31)<br>D2 localized ductile shearing and thrusting: Mondoñedo (6), Montefurado, Trones and La Espina Thrusts (36) and horizontal foliation, S2<br>D3 steep open folds | | **303±17 Ma:** Possible age of metamorphism (9, 44)<br>**300-270 Ma:** Variscan granitoids (7, 9, 44, 48, 52) |
| | Cantabrian Zone (CZ) | Inner realm of the Gondwana platform<br>Weakly subsident during Lower Paleozoic<br>Foreland of the Variscan Belt | Early Paleozoic magmatism, mainly volcanics | Thin-skinned tectonics: brittle thrusts and associated fault-bend and fault-propagation folds (34, 36) | Anchizonal or no metamorphism | **310-290 Ma:** Age of deformation according to syn- and postorogenic deposits (34) |

Figure 2.2.1-1: Summary of the geotectonic and metamorphic evolution of the Iberian Variscan orogen (Dallmeyer et al., 1997). Units arranged in their stacking positions with the most external zones towards the bottom.

westernmost part of the Cantabrian Zone as well as the deposition of first flysch turbidites (e.g. Olleros Fm.) from the West Asturian-Leónese Zone (Aramburu & Bastida, 1995). Dallmeyer et al. (1997) recognised E-ward migration of thrust movements in the Cantabrian Zone up to the second phase of deformation. The second episode evidences a similar diachronous character as the preceding phase (figure 2.2.1-2). However, in the second phase older ages in the West (Middle Devonian for the Galicia-Trás-os-Montes Zone), young E-wardly toward the Cantabrian Zone (late Bashkirian to Stephanian). A third stage of deformation is *assumed* by Dallmeyer et al. (1997) to have reached the Cantabrian Zone in the Early Permian. They quantitatively estimate the average propagation rate of the orogenic front was 5 km/Ma, maintaining a hypothetical orogenic shortening of 50 to 75 %, which reflects an average convergence rate of 1 cm/a to 2 cm/a (Veselovsky, 2004).

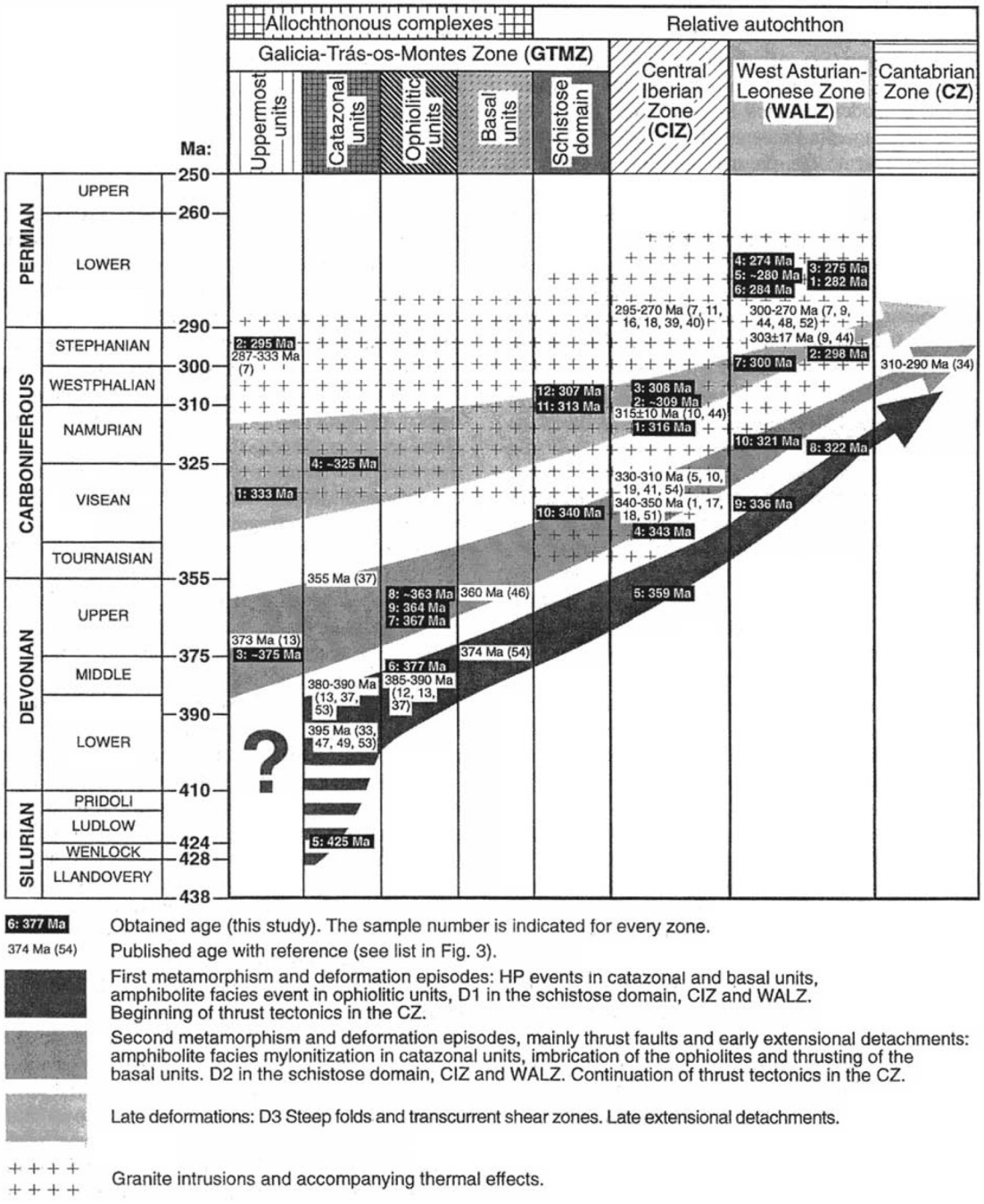


Figure 2.2.1-2: Spatial-temporal diagram showing the diachronic evolution of the Variscan orogen across Iberia (Dallmeyer et al., 1997). Ages are based on $^{40}Ar/^{39}Ar$ ages. Timescale differs from that used in this study. More external zones are placed to the right of the diagram.

## 2.3 Cantabrian Zone

The Cantabrian Zone, NW Spain represents the core of the Ibero-Armorican Arc (Julivert 1971; Pérez-Estaún et al., 1988), an E-wardly directed Variscan foreland fold-and-thrust belt. Local geologic mapping (1:50000 scale) conducted by the Instituto Tecnológico GeoMinero de España (ITGE) is extensive (e.g. Leyva et al., 1984; Lobato et al., 1979; Martín-Parra, 1989; Alonso et al., 1990; Suárez-Rodríguez et al., 1991).

### 2.3.1 Deformation and subdivision

Several E-directed thrust units were emplaced during Carboniferous time and show a tight arcuate trend with concavity trending towards the foreland (Julivert, 1971; Weil et al., 2000). Synorogenic and postorogenic deposits indicate the orogenic push reached the Cantabrian Zone in the Late Carboniferous (Pérez-Estaún et al., 1988; Quesada, 1991). The age of deformation within the Cantabrian Zone is estimated by Dallmeyer et al. (1997) to range between 310 - 290 Ma. (figure 2.2.1-2). The Cantabrian Zone has been subdivided into several domains and units, as depicted in figure 1.1-1.

The first occurrence of unmetamorphosed Palaeozoic sedimentary units E of the basal Narcea Antiform is called the Somiedo-Corecillas Unit of the Fold & Nappe Province (Julivert, 1971). It was emplaced during the late Bashkirian-early Moscovian (Dallmeyer et al., 1997). Deformation propagated E-ward (in the direction of the foreland) and produced the Fold & Nappe Province Sobia-Bodón and Aramo units (see figure 2.3.1-1), the Central Coal Basin (see Aller & Gallastegui, 1995), the Ponga Unit (see Alvarez-Marrón, 1995) and the most easterly Picos de Europa, and Pisuerga-Carrión units (see Pérez-Estaún & Bastida, 1990). Sheets E of the Somiedo thrust were emplaced during early Stephanian (Pérez-Estaún et al., 1988), comprising a time span between 15 and 20 Ma for the emplacement of all units (Dallmeyer et al., 1997).

Two main deformation phases in the Cantabrian Zone are described by Julivert (1971) and Julivert & Marcos (1973):

(i) The first phase was caused by E-trending compression (present day coordinates), producing thrust initiation related to the formation of longitudinal folds, characterised by horizontal fold axes and steep axial surfaces parallel to arc curvature.

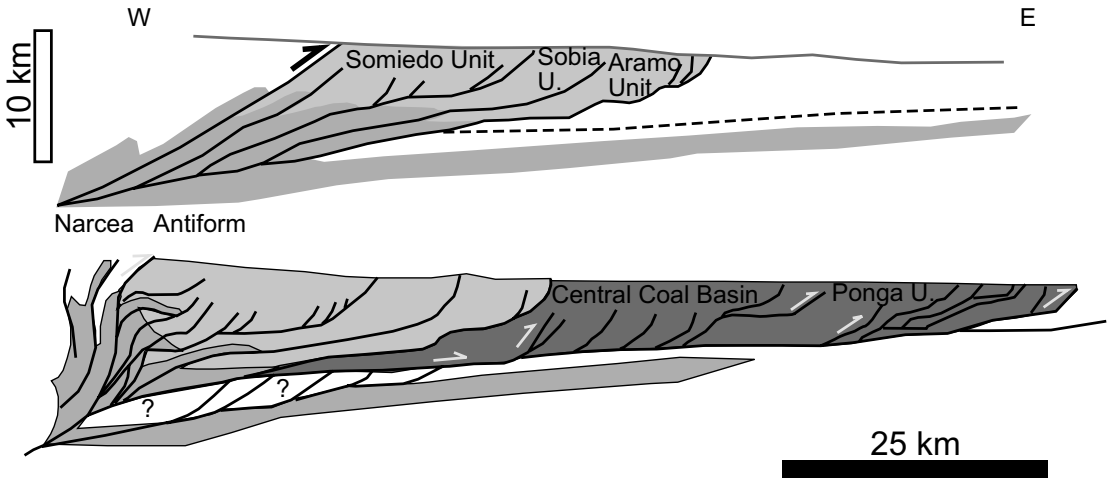


Figure 2.3.1-1: Foreland directed Variscan deformation in Iberia (modified after Pérez-Estaún et al., 1990). Initially the Somiedo, Sobia and Aramo units developed (upper sketch), and were followed temporally by the Central Coal Basin, Ponga units (lower sketch). In both sketches Narcea Antiform sediments are the basement.

(ii) The second phase is interpreted from a radial set of folds with steep fold axes and is commensurate with the final tightening of the Cantabria-Asturias Arc.

Alpidic deformation reactivated many Variscan structures resulting in additional compression with steepened thrusts and faults and increased structural shortening (Alonso et al., 1995). Therefore the present structural setting provides only a partial and distorted view of the Variscan Belt prior to oroclinal bending (Ábalos et al., 2002; Robardet, 2002).

### *2.3.2 Metamorphism and palaeotemperature conditions*

The Cantabrian Zone, the foreland fold-and-thrust belt of the external part of the Iberian Variscan orogeny (see figure 2.2-1), having deformed under a shallow-crustal thin-skinned tectonic regime is essentially considered a nonmetamorphic unit (Julivert, 1971; Pérez-Estaún et al., 1988).

To date, several thermal indicator studies regarding fluid inclusions, illite crystallinity, vitrinite reflectance, and conodont alteration index (CAI) have been published (Brime & Pérez-Estaún, 1980; Brime, 1985; Raven & van der Pluijm, 1986; Aller et al., 1987; Alonso & Brime, 1990; Colmenero & Prado, 1993; Krumm, 1992; Keller & Krumm, 1992, 1993; García-López et al., 1997; Bastida et al., 1999; Brime et al., 2001; Allyón et al., 2003; Frings, 2002; Allyón, 2003; Gasparrini, 2003; Frings et al., 2004; Gasparrini, et al., in press).

In the Cantabrian Zone penetrative cleavage developed only locally and is interpreted as the result of pressure-solution origin (Hirt et al., 1992; García-López et al., 1997; Bastida et al., 1999). Cleavage is independent from the compressional regime (Aller et al., 1987).

Palaeotemperature estimates based on CAI data normalised to the 2000 m depth isotherm at Late Carboniferous time (Raven & van der Pluijm, 1986) for the southern Cantabrian Zone's Correcillas and Bodón units indicate anchizonal conditions with maximum temperatures between 150 - 250 ˚C were reached. However, in the lower part of the Somiedo Unit along the Sabero-Gordón line CAI values indicate maximum temperatures to between 250 - 300 ˚C were reached. N of the León Line, CAI data indicate maximum temperatures reached were in excess of 300 ˚C.

Illite crystallinity values published for this study's sampling area are in relative agreement with the CAI data (e.g. Aller & Brime, 1985; Keller & Krumm, 1992). In the Correcillas and La Sobia-Bodón units (N of the Sabero-Gordón Line in the southern Cantabrian Zone) diagenetic temperatures (≤ 200 ˚C) dominate. The highest metamorphic grades with incipient metamorphic temperatures (> 300 ˚C) were recorded in rocks adjacent to the León Line Fault System (e.g. Aller & Brime, 1985; García-López, 1999) and in Neoproterozoic sedimentary "basement" rocks of the Narcea Antiform (see Martín-

Parra, 1989). Anchizonal conditions prevailed in the Central Coal Basin and in some Stephanian basins (e.g. Raven & van der Pluijm, 1986; Krumm, 1992; Keller & Krumm, 1993; García-López, 1999; Frings, 2002; Ayllón 2003; Ayllón et al., 2003; Frings et al., 2004).

### *2.3.3 Fluid circulation and the thermal evolution of the Cantabrian Zone*

A link between fluid circulation and low-temperature metamorphism in the Cantabrian Zone has been postulated (Allyón, 2003; Gasparrini, 2003; Gasparrini et al., in press; see also: Schneider, 2002). Raven and van der Pluijm (1986) hypothesise hydrothermal fluids, circulated through deep-seated strike-slip faults (primarily the León Line, Sabero-Gordón Line and Ventanielles-Cardaño Line fault system), in association with igneous activity as the central cause of heating. Studies regarding small polymineralic ore deposits (see: Allyón, 2003, and references therein) and large scale dolomitisation mainly affecting Serpukhovian-lower Bashkirian limestones (Spiro et al., 1995; Tornos & Spiro, 2000; Grimmer, 2000; Gómez-Fernández et al., 2000; Gasparrini et al., 2001, 2002; Gasparrini, 2003) also indicate the significance of fault systems or small scale magmatic intrusions on fluid flow. These case studies regarding fluid inclusion and stable isotope investigations represent the only direct evidence of fluid activity in Carboniferous rocks of the Cantabrian Zone. According to Valverde-Vaquero et al. (1999) plutonism of the Peña Prieta and Arcellana stocks took place late in the Variscan orogeny (293 ± 1 and 293 ± 2 Ma respectively: U-Pb dating results), in association with an extensional stress regime. The event is regarded as shallow epithermal, with fluid temperatures ≤ 100 - 300 ˚C and pressure < 500 bar (~ hydrostatic).

### *2.3.4 Narcea Antiform and the West Asturian-Leónese Zone*

The West Asturian-Leónese Zone is differentiated from the Cantabrian Zone by a structural transition composed of an antiformal stack of thrusted Neoproterozoic rocks forming the Narcea Antiform (Lotze, 1945; Julivert, 1971 and Pérez-Estaún et al., 1988, 1991), as shown in figures 1.1-1 and 2.2-2. This Neoproterozoic core evidences the occurrence of at least one complete pre-Variscan orogenic cycle (Fernández-Suárez et al., 1998, 2000 b).

Some authors (e.g. Lotze, 1956; Bouyx 1970; Marcos 1973; Pérez-Estaún, 1978; Nägler et al., 1995) propose the antiform has been affected by a compressive deformation phase in an uppermost Precambrian (Cadomian) orogenic cycle having developed from an Andean-type destructive plate margin about 645 - 540 Ma in the northern Armorican Massif-type area (see also Abalos et al., 2002 and citations therein).

Descriptions of varying detail regarding the stratigraphy of Precambrian rocks in the Narcea Antiform abound (e.g. Pastor-Gomez, 1963, 1969; Farber & Jaritz, 1964; Corretgé & Caprio, 1968; Corretgé, 1969; van den Bosch, 1969 b; Pérez-Estaún, 1973, 1978; Pérez-Estaún & Martínez, 1978; Julivert, 1983 a, b; Valladares et al., 2002 b). Leyva et al. (1984) mapped greywackes and schists in the Neoproterozoic sedimented

Narcea Antiform part of this study's sampling area, Nägler et al. (1995) suggests pelites and greywackes represent the typical lithology. In the study area primary facies are turbiditic and volcaniclasitc rocks with volcanic rocks occurring less frequently (Pérez-Estaún 1973, 1978). Along with the Neoproterozoic pelites and greywackes of the Lug Dome in the West Asturian-Leónese Zone the Narcea antiform represents the oldest rocks exposed in northwest Iberia (Pérez-Estaún et al., 1994; Fernández-Suárez et al., 2000 b).

The estimated total thickness varies for each flank of the antiform. W of the study area Neoproterozoic sediments of the southern flank equivalent, obtain total thickness estimated to > 1500 m (Pérez-Estaún, 1978), ~ 2000 m (Julivert, 1983 b) and ~ 3000 m (Gutiérrez-Alonso et al., 2004 a), those of the northern flank, interpreted as having been deposited as outer deep-sea fans (Valladares et al., 2002 b) reach up to 7000 m but decrease in thickness E-ward (Gutiérrez-Alonso, 1996) to > 1500 m (Martín-Parra, 1989). Uncertainty prevails regarding the age and nature of the underlying basement, as it is only visible in seismic sections (e.g. Fernández-Viejo, 2000).

Regional metamorphic overprint varies. In the Cantabrian Zone, N of the Conombre-La Urz Thrust Fault (shown in figure 2.2-2) it is very low to low, showing newly grown chlorite and an local absence of biotite (Nägler et al., 1995) but increases S-ward. S of the Conombre-La Urz Thrust Fault regional metamorphic indicators show chlorite facies prevails with a localised biotite band (Martín-Parra, 1989). Contact metamorphism of biotite grade also occurs W of the study area (Martín-Parra, 1989).

The West Asturian-Leónese Zone, being the easternmost internal zone of the Iberian Massif, represents the transition between the foreland areas e.g. Cantabrian Zone in the E, and the hinterland e.g. Central Iberian Zone in the W (figure 2.2-1). It is characterised by an upper Proterozoic flyschoid series unconformably overlain by a thick preorogenic Palaeozoic succession of between 5000 to 10000 metres of sediment (Marcos, 1973; Julivert, 1981; Pérez-Estaún et al., 1991; Bastida & Aller 1992; Fernández-Suárez et al., 2000 b). Its tectonic and thermal evolution is similar to that of the Central Iberian Zone (see figures 2.2.1-1 and 2.2.1-2). The West Asturian-Leónese Zone experienced more subsidence during the syn-Variscan extensional phase than adjacent zones. Volcanism and plutonism are present yet scarce in Neoproterozoic sedimentary rocks of the study area, but increase to the W (Dallmeyer et al., 1997; Fernández-Suárez et al., 1998).

### *2.3.5 Ibero-Armorican Arc: origins and genesis*

The Ibero-Armorican Arc is amongst the most conspicuous features of the European Variscan fold belt (figure 2.1-1). It is observable in the western part of the Variscan orogen through France (Britannia) into northern Spain (Kollmeier et al., 2000). In Iberia the core of which consists of a highly curved Cantabria-Asturias Arc, therein lying the Cantabrian Zone of NW Spain. The arc is characterised by foreland-directed concavity with inward-facing structures (Hirt et al., 1992). In the W, the core of the arc is bounded

by the Narcea Antiform. Structurally, the trend varies by ~ 180˚ around the arc. Origin of the arc is debated in the literature (see Veselovsky, 2004 and citations therein). De Sitter (1962) initially proposed the arc resulted from the occurrence of two deformation phases. Julivert (1971) and Julivert & Marcos (1973) assumed the Cantabria-Asturias Arc was a primary, preorogenic feature, having undergone secondary tightening and development of radial folds during the Variscan orogeny. Studies of kinematic indicators and thrust sheet emplacement mechanisms supported this theory with slight modifications regarding the location of the axes of rotation (Julivert & Arboleya, 1984, 1986; Pérez-Estaún et al., 1988). Pérez-Estaún et al. (1988) proposed for the arc, a continual deformation of progressive rotational thrust displacements propagating from W to E (figure 2.3.5-1). Another possibility mentioned in the literature is that of a synorogenic indentation of a rigid block with the resulting curvature of the arc, possibly originating from a unique microplate (Riding, 1974; Matte & Ribeiro, 1975; Lorenz & Nichols, 1984), or from a Gondwanan promontory (Bachtadse & van der Voo, 1986; Martínez-Catalán, 1990).

Recently conducted palaeomagnetic studies, where the declination deviation followed the shape of the arc, indicated a secondary nature of at least half of the present curvature, demonstrating it to be an orocline (Bonhommet et al., 1981; Perroud & Bonhommet, 1981; Perroud, 1986; Hirt et al., 1992; Parés et al., 1994; Stewart, 1995; van der Voo et al., 1997). Parés et al. (1994) ascertained a late tightening of a partially curved (~ 50 %) fold-and-thrust belt, leaving previous structural rotation unknown.

Weil et al. (2000, 2001, 2003) too, using palaeomagnetic data describe three folding phases (see figure 2.3.5-2) on the *assumption* that the present-day curved geometry was caused by the interference of original N-trending structures (first and second folding phases) with a third folding phase later superimposed. The first two phases were dated as Serpukhovian to Stephanian in age, while the later was restricted to the Early Permian. As a result, the direction of overall shortening changed from E in the Carboniferous to N in the Permian (referenced to present-day coordinates). Carey (1955) introduced the theory of oroclinal bending around a vertical axis, which was applied by Weil et al. (2000, 2001, 2003) and Gutiérrez-Alonso et al. (2004 a) in the Cantabrian Zone. Oroclinal bending occurred in the late Stephanian to Early Permian. The oroclinal

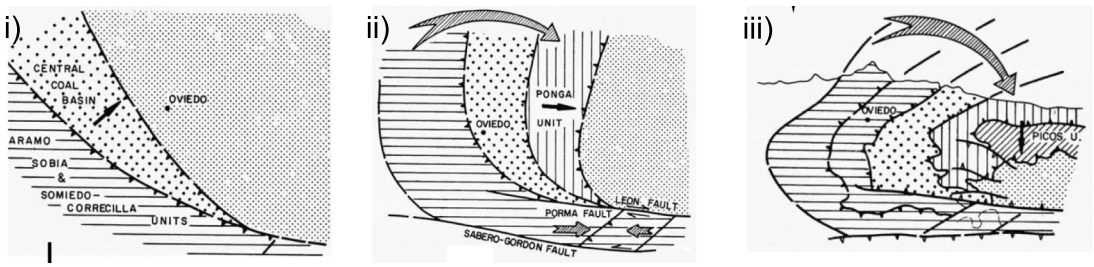


Figure 2.3.5-1: Three stages in the continuous progression of deformation resulting from rotational thrust displacement in NW Iberia (Pérez-Estaún et al., 1988).

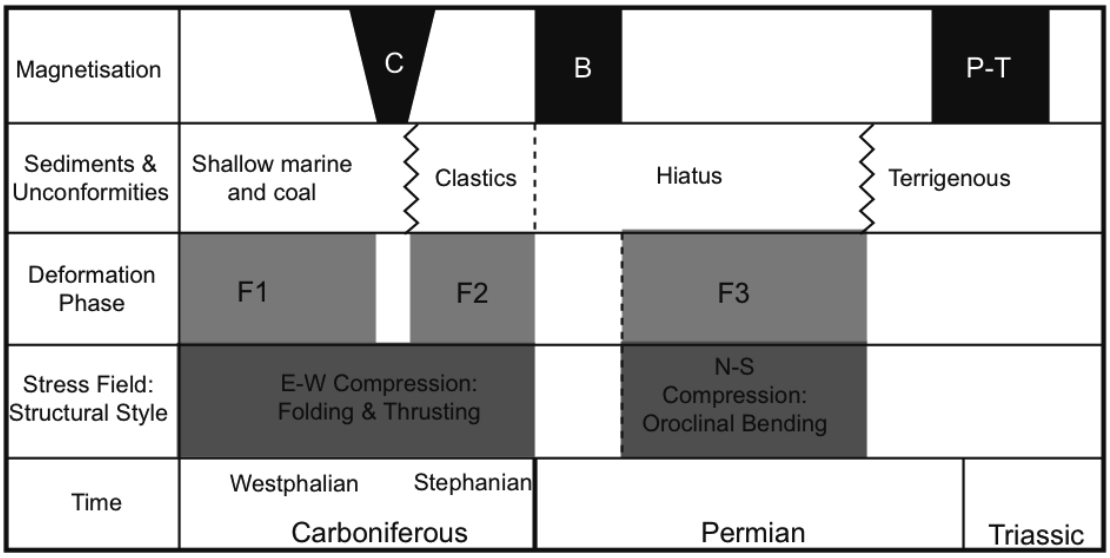


Figure 2.3.5-2: Variscan deformation history of the Cantabrian-Asturian Arc (modified after Weil et al., 2000, 2001, 2003). Depicted are the Asturian Arc's three deformation phases (F1-3), their associated stress fields, sedimentation and remagnetisation history over time. Unconformities are represented by zig-zag lines.

theory elaborated in Weil et al. (2000, 2001) is supported by the analysis of calcite twinning by Kollmeier et al. (2000), where they attribute the E-trending compression to the collision between the Ebro-Aquitaine Massif and the Laurussian margin, followed by a greater, N-directed collision of Gondwana with Laurussia.

Most plutonic intrusions in the Cantabrian, West Asturian-Leónese and northern Central Iberian Zones occurred between approximately 295 and 285 Ma, indicating post-tectonic extension (Fernández-Suárez et al., 2000 b). This posttectonic magmatic event began 10 - 15 Ma earlier in the most internal zones of the Variscan Belt (Dallmeyer et al., 1997). Fernández-Suárez et al. (2000 b) and Gutiérrez-Alonso et al. (2004 a) propose delamination of the lithosphere was a triggering mechanism for the voluminous, orogen-wide, magmatic event. The lithospheric mantle simultaneously thickened below the inner arc and thinned under the outer arc (see figure 2.3.5-3), causing a gravitational instability and resulting in the delamination of the lithospheric root (Figure 2.3.5-4; Gutiérrez-Alonso et al., 2004 a). The final décollement of crust and lithospheric mantle, according to these authors, is evidenced by orogen scale lower crustal melting, widespread magmatism, low pressure-high temperature metamorphism, fluid flow (cf. Gasparrini, 2003; Gasparrini et al., in press) and coeval mineralization. Fernández-Suárez et al. (2000 b) and Gutiérrez-Alonso et al. (2004 a) propose delamination may have began between 319 and 310 Ma under the Central Iberian Zone (50 Ma after the main collision event) culminating between 300 and 290 Ma beneath the entire belt.

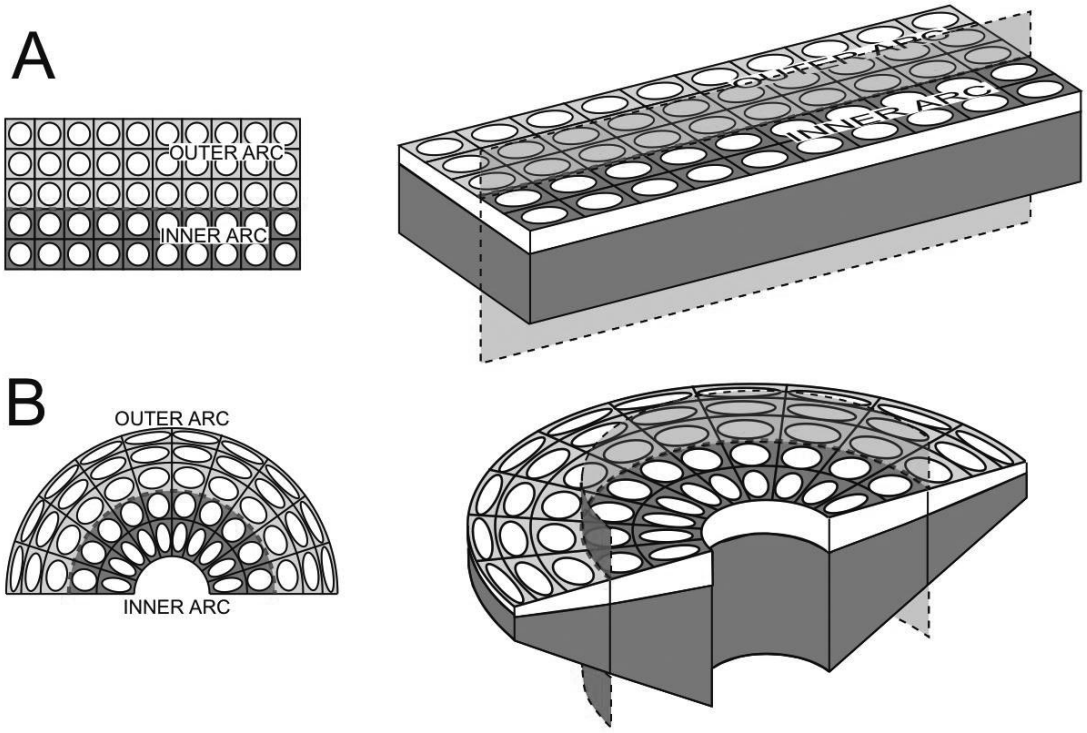


Figure 2.3.5-3: Simplified diagram depicting the effect of lithospheric bending around a vertical axis and the resulting tangential longitudinal strain (Gutiérrez-Alonso et al., 2004 a). The inner arc is characterised by arc-parallel shortening and lithospheric mantle thickening, while the outer arc demonstrates arc-parallel stretching of strain ellipses and thinning (Left: plan view; Right: Three-dimensional representation).

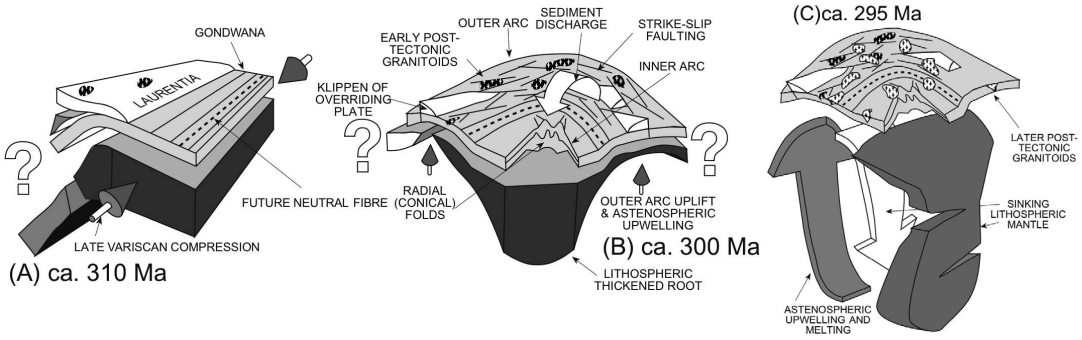


Figure 2.3.5-4: Relationship between post-oroclinal-bending and lithospheric delamination (Gutiérrez-Alonso et al., 2004 a). A) Linear orogenic belt resulting from the collision between Gondwana and Laurentia. B) Oroclinal postcollisional bending. C) Delamination and collapse of the thickened lithospheric root beneath the inner Ibero-Armorican Arc.

## 2.4 Northwestern Iberian palaeographic evolution

### *2.4.1 Neoproterozoic/Cambrian*

U-Pb analysis reveals a complex cratonic Neoproterozoic basement varied in age and composition existed in the European Variscides (Fernández-Suárez et al., 2000 a, 2002 a, b; Gutiérrez-Alonso et al., 2003). Figure 2.4.1-1 shows the Neoproterozoic terrane assemblage that developed on an active Gondwanan margin.

Several models have been proposed regarding its geodynamic evolution during Neoproterozoic time (e.g. Ribeiro et al., 1990; Quesada, 1990). Nägler et al. (1995) interpret the Cantabrian and West Asturian-Leónese zones as parts of an active margin of Gondwana on the basis of juvenile crustal contribution to Neoproterozoic's supposedly synorogenic sedimentary facies. Others cite the maturity of Neoproterozoic-Cambrian sediments and the absence of coeval volcanic rocks as evidence for a Gondwanan passive margin setting in the West Asturian-Leónese Zone (e.g. Beetsma, 1995; Ugidos et al., 1997 a, b, 1999; Valladares et al., 1999, 2000, 2002 a; Bauluz et al., 2000).

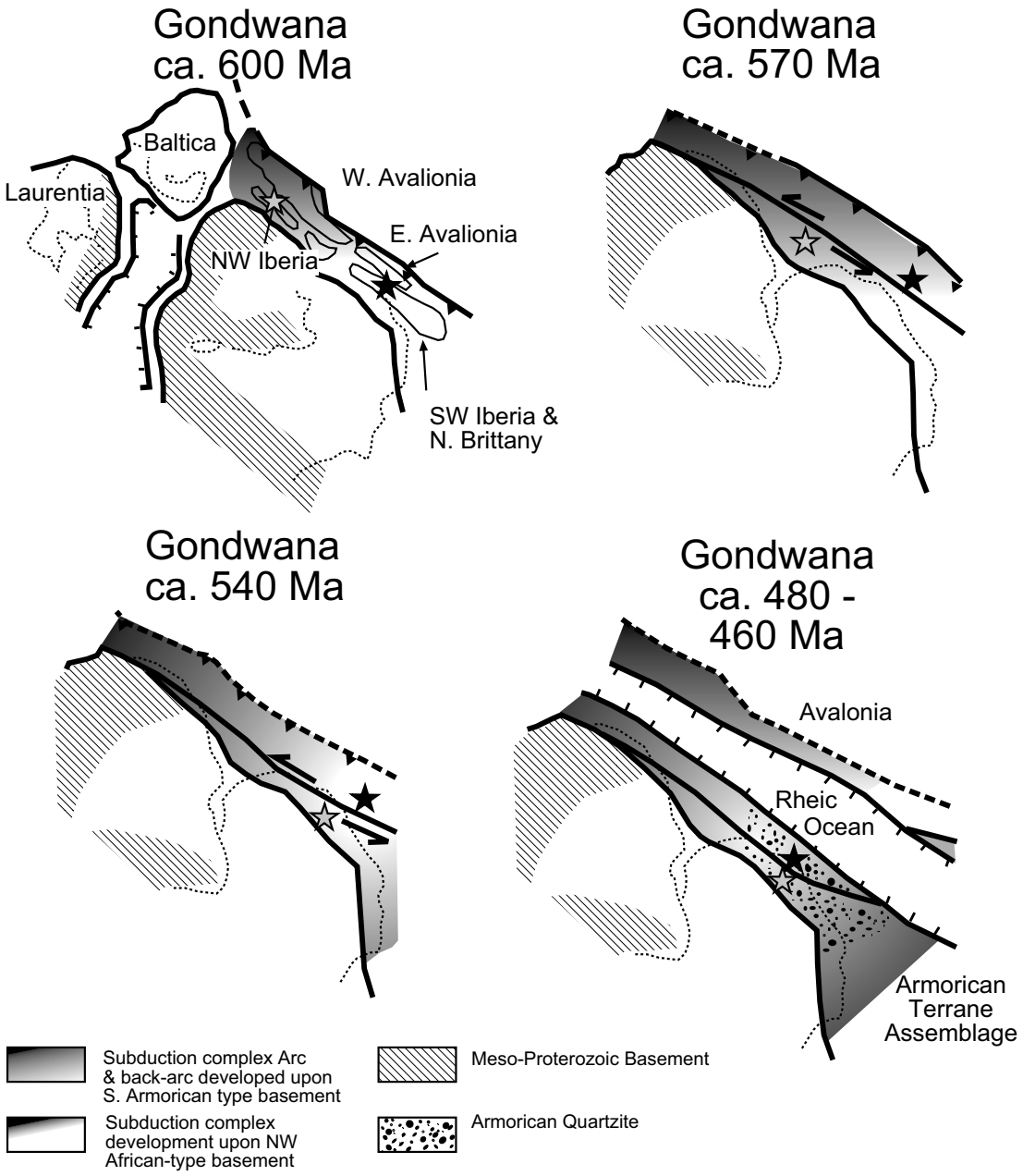


Figure 2.4.1-1: Distribution of Neoproterozoic terranes and early Palaeozoic plate-tectonic evolution at the northern Gondwanan plate margin (ca. 600 Ma to 460 Ma). Stars signify the location of northwest Iberia and Brittany/southwest Iberia. Modified from Fernández-Suárez et al., 2002 a, and Gutiérrez-Alonso et al., 2003.

An angular unconformity in the Narcea Antiform between the Neoproterozoic sediments (Locally Mora Fm.) and lowermost Cambrian (Locally Candana-Herrería Fm.) provides evidence for much debate:

Neoproterozoic below the unconformity has been proposed to have been affected by a compressive deformation phase in an uppermost Precambrian (Cadomian) orogenic cycle (e.g. Lotze, 1956; Bouyx, 1970; Marcos, 1973; Pérez-Estaún, 1978; San José et al., 1990) having developed from an Andean-type destructive plate margin about 645 - 540 Ma in the northern Armorican Massif-type area (Abalos et al., 2002 and citations therein).

Valladares et al. (2002 b), in a review of chemical, isotopic (e.g. Nägler et al, 1995; Fernández-Suárez et al., 1998, 2000 b; Ordóñez, 1998), sedimentary and structural literature for the Iberian Peninsula, proposed the following Precambrian/earliest Cambrian geodynamic setting:

1) Rifting of northern Gondwana into continental blocks at about 1 Ga., with rift related volcanic rocks (1 Ga zircons) and old continental material (≥ 1.9 Ga zircons) entering into basins.

2) Closure of oceans, with Cordilleran-type arc activity and subsequent collision of Gondwanan continental blocks yielding 800 - 640 Ma (e.g. Fernández-Suárez et al., 2000 b) detrital zircons. Early pan-African (Cadomian) events and development of interior orogens (Murphy & Nance, 1991) followed by late pan-African (Cadomian) events, with extensional tectonics, acid magmatism at about 600 Ma, and sedimentation of molasses deposits (Valladares et al., 2002 a)

3) a) Development of an immature passive margin setting and sedimentation of uppermost Neoproterozoic rocks, e.g. the Narcea Gp. (Mora Fm.); b) Erosion of interior orogens, their detritus composing the bulk of the sediments the related Narcea Gp. molasse deposits, as evidenced by $\varepsilon_{Nd}$ and $T_{DM}$ neodymium model ages (figure 2.4.1-2; Nägler et al., 1995). These sediments inherited an abundant recycled relatively-juvenile crust, though with time came an increase in contribution by relatively old basement materials

4) Extension, with relative sea level fall and the formation of the Neoproterozoic-Cambrian "type-one" sequence boundary with basement materials being the main contributors to the Cambrian sedimentary basin (Nägler et al., 1995) and by a scarcity of 800 - 640 Ma zircons (Fernández-Suárez et al., 2000 b); contribution from 600 Ma granites occurring only after the erosion of molasse deposits had been effected.

Contrastingly, Fernández-Suárez et al. (2002 a, b) based on zircons yielding Grenvillian ages (0.9 - 1.2 Ga) and Gutiérrez-Alonso et al. (2003) propose a tectonic setting favouring an Avalonian-Cadomian Arc (west Avalonian terrane) and associated back arc basins

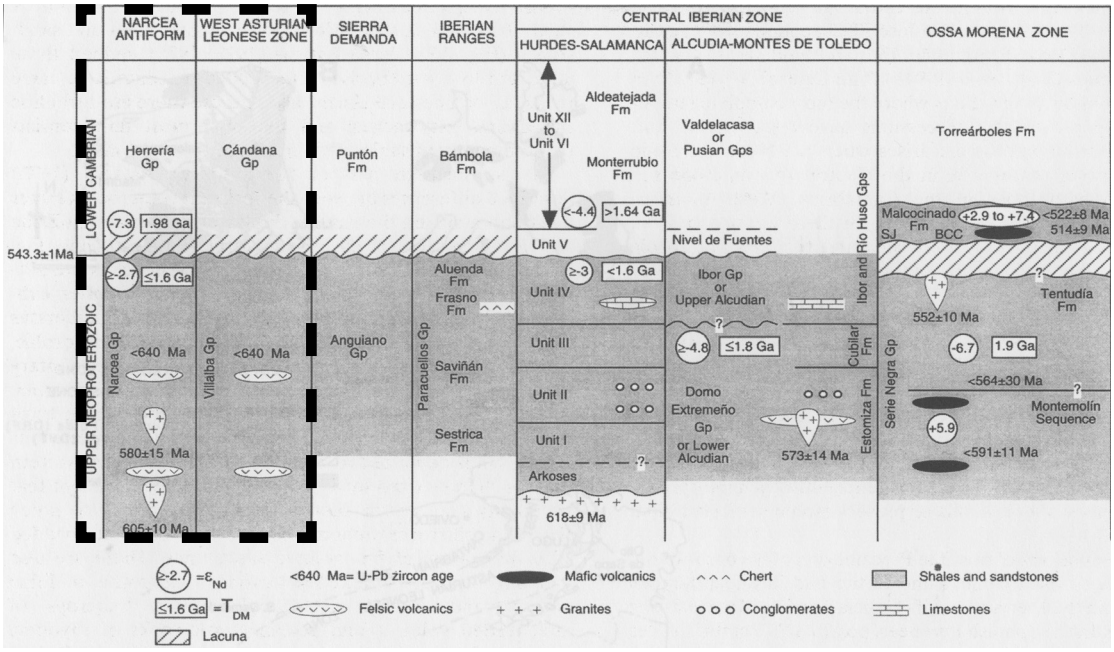


Figure 2.4.1-2: Correlation chart of lithostratigraphic units form the upper Neoproterozoic-lowermost Cambrian across the Spanish Iberian Massif (Valladares et al., 2002). $\varepsilon_{Nd}$ and $T_{DM}$ neodymium model ages after Nägler et al. (1995). Units in this study's sampling area highlighted by the dashed box.

(northwest Iberia and northeast Bohemia) situated closer to the Gondwanan margin (figure 2.4.1-1) for the Neoproterozoic West Asturian-Leónese Zone. The peripheral arc is related to an oblique subduction event on the margin of Gondwana (figure 2.4.1-3). Here, thick deposits of Neoproterozoic sediments were shed into the back arc basins from the arc (Murphy & Nance, 1991), or both the main arc edifice and the margin of Gondwana (Fernández-Suárez et al., 2000 b).

Debate regarding the position of various terranes in the Neoproterozoic abounds in the literature. Veselovsky (2004) provides review of current models:

(i) Nance & Murphy (1996) and Martínez-Catalán et al., (1997), amongst others put Cadomia, Iberia and parts of east Avalonia adjacent to the west African craton. Positioning in this manner is corroborated in part by palaeomagnetic and geologic evidence, indicating the proximity of Iberia and other terranes to northwest Africa (Armorican realm of Tait et al., 1997; Robardet, 2000).

(ii) Fernández-Suárez et al. (2000 a; 2002 a, b) and Gutiérrez-Alonso et al. (2003) contend that northwest Iberia was at a peri-Amazonian position, closer to west Avalonia, Florida and Carolina (South American craton signature), and only southwest Iberia was proximal to the west African craton (northwest African craton signature). They propose a tectonic transfer (strike-slip activity along major transform faults parallel to the Gondwanan margin) prior to the opening of the Rheic Ocean (Figure: 2.4.1-1). This strike-slip motion translated northwest Iberia from an Amazonian realm nearer to the

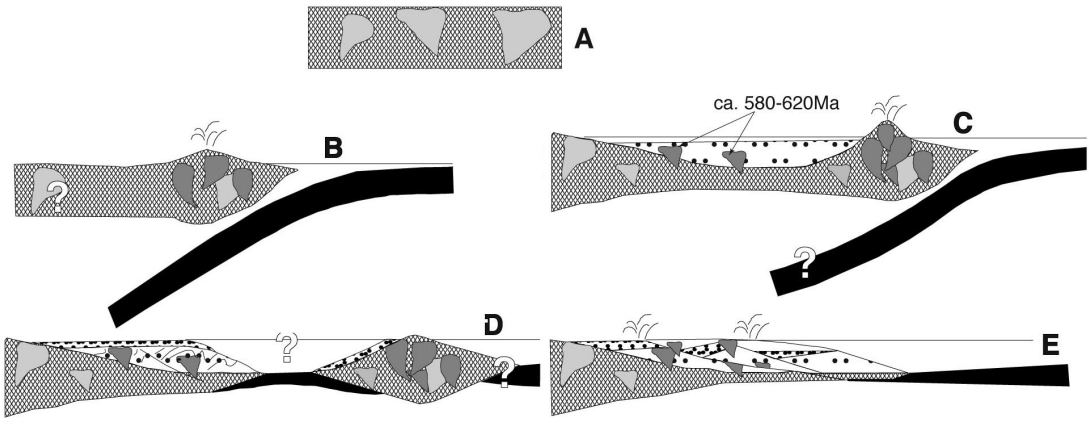


Figure 2.4.1-3: Geologic evolution of the Iberian Peninsula from Proterozoic to early Palaeozoic (after Fernández-Suárez et al., 2000 b). A) Pre-Neoproterozoic cratonic basement. B) Cadomian-Avalonian early magmatic arc (ca. 800-650 Ma). C) Cadomian/Avalonian back-arc. D) Separation of Avalonia from Gondwana-Initiation of the Rheic Ocean. E) Ollo de Sapo Magmatism (ca. 470 Ma).

west African margin, resulting in the Armorican terrane. In this way, the authors justify why peri-Gondwanan terranes with contrasting basement signatures show the same Ordovician Zircon provenance (Armorican Quartzite; see figure Figure: 2.4.1-1).

Subduction and arc magmatism continued until about 560 Ma (Fernández-Suárez et al., 1998, 2000 a). At that time, the arc and back-arc basin developed due to crustal thinning (see figure 2.4.1-3) and enhanced melting of the lower crust (main subduction stage at approximately 650 - 570 Ma; Fernández-Suárez et al., 1998, 2000 a). From the absence of extensive deformation or significant crustal thickening Fernández-Suárez et al. (2000 a; 2002 a, b) interpret subduction was not terminated by a final intercontinental collision. Further extension of the back-arc basin, drift of the Avalonian micro-continent and opening of the Rheic Ocean are suggested as evidence supporting continued subduction (see figure 2.4.1-3; Martínez-Catalán et al., 1997; Fernández-Suárez et al., 1998, 2000 b, 2002 a, b). Robardet et al. (1990) reported the Rheic Ocean (Mid-European Ocean) opened in the late-Middle or early-Late Cambrian. Gutiérrez-Alonso et al. (2003) confined the event to between about 520 - 530 Ma (age of the youngest detrital zircon in the Cambrian arkose) and 460 - 470 Ma (depositional age of the Armorican Quartzite). Platforms developed on both sides of the Rheic Ocean: the Iberian-Armorican platform and the Meguma Platform (Fernández-Suárez et al., 1998, 2002 b). Late-Early Cambrian marks the earliest record for significant tectonic activity at the western Gondwanan margin, increasing in intensity approaching the Early/ Middle Cambrian transition (Bechstädt et al., 1988; Bechstädt & Boni, 1989; Russo & Bechstädt, 1994; Álvaro et al., 2000 a, b). Rifting processes and an extensional regime are interpreted from the mostly terrigenous Lower to Middle Cambrian sediments of the Cantabrian Zone (Marcos, 1973; Pérez-Estaún & Bastida, 1990; Álvaro et al., 2000 a, b).

### 2.4.2 Late Cambrian-Middle Ordovician microcontinent positions

Unlike the relatively highly correlated palaeogeographic positioning information regarding Gondwanan and Laurentian/Baltican cratons during the Late Cambrian-Early to Middle Ordovician, the palaeogeographic position and significance of microcontinents such as Avalonia, Amorica and the proto-Iberian sedimentary rocks are poorly constrained for this time period and the subject of much debate in the literature (e.g. Carls, 1988; Paris & Robardet, 1990; Scotese & McKerrow, 1990; Tait et al., 1997; Robardet, 2000; Robardet et al., 2001; Scotese, 2001):

(i) Tait et al. (1997) and (Fernández-Suárez et al. (2002 a, b) propose Avalonia began drifting from Gondwana and Amorica beginning in the Llanvirn, butting against Baltica during the Silurian, as indicated by calc-alkaline volcanism and the development of endemic faunas. These authors interpret the Tornquist Sea separated Avalonia to the S, from Baltica to the N, whereas the Rheic Ocean opened S of Avalonia and the Iapetus Ocean to the W (relative to present coordinates). The above interpretation is supported in Crowley et al. (2000), where they propose the N-ward migration of Avalonia in the Caradoc resulted in a narrowed Iapetus Ocean and Tornquist Sea.

(ii) Paris & Robardet (1990) interpret from faunal affinities that Avalonia may have been the western promontory of Baltica from at least Middle Cambrian time, hence contradicting the existence of an isolated Avalonian terrane and the Tornquist sea.

### 2.4.3 Ordovician

Three latitudinally distinct continental blocks with marine shelf areas separated by the Iapetus and Rheic Oceans are discerned from faunal analyses (Gondwana, Baltica and Laurentia; Paris & Robardet, 1990; Scotese & Barret, 1990; Witzke, 1990; Robardet, 2000, 2002 and references therein). Laurentia remained at tropical latitudes (Figure 2.4.3-1) through Ordovician time (Paris & Robardet, 1990; McKerrow et al., 1991), north Gondwana at peri-polar latitudes and Baltica at intermediate to high latitudes (Torsvik et al., 1992; Crowley et al. 2000).

At the end of the Ordovician, Baltica drifted N-ward to more temperate palaeolatitudes, resulting in the closure of the Iapetus Ocean (Paris & Robardet, 1990). High palaeolatitudes --between 45˚ N-50˚ N (Paris & Robardet, 1990) and 65˚ N-75˚ N (Tait et al., 1997)-- are inferred from shallow platforms lacking carbonates. Palaeomagnetic data from Iberia (van der Voo, 1993) is in agreement with a high-latitude position for Baltica during the Ordovician.

Thinning and disintegration of the northern Gondwanan margin continued to the Ordovician, when it was marked by extensive two-phase rift-related magmatism, spanning the Central Iberian Zone to France, Corsica and Sardinia (Crowley et al., 2000 and references therein). In the Central Iberian Zone, the magmatism was marked

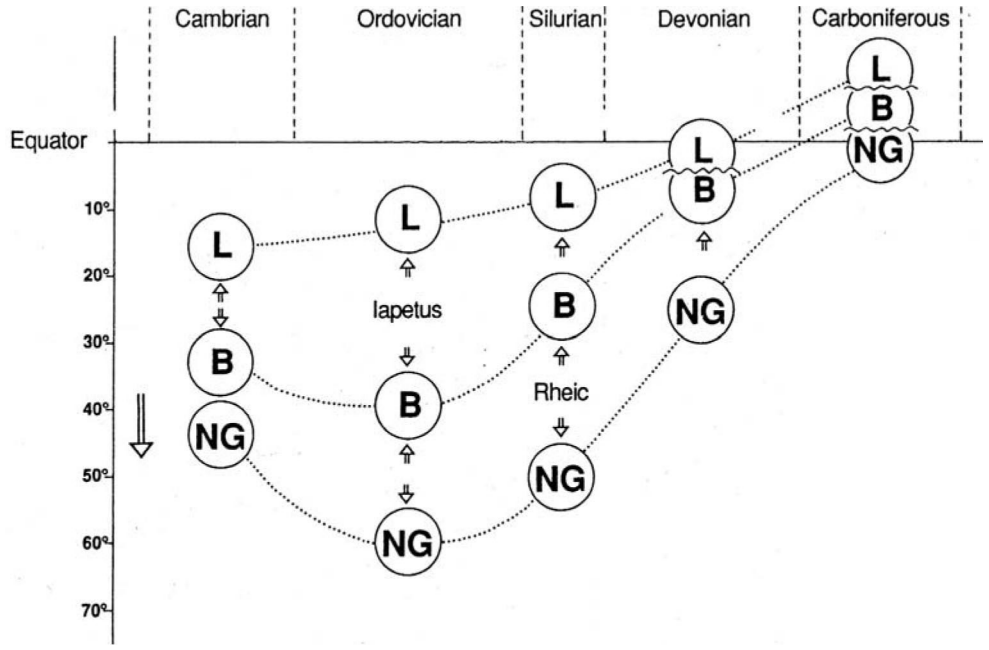


Figure 2.4.3-1: Movements of north Gondwana (NG), Baltica (B) and Laurentia (L) through Palaeozoic time. Wavy lines occurring in Devonian and Carboniferous indicate continental collision (Paris & Robardet, 1990).

by the "Ollo de Sapo" event (figure 2.4.1-3; Dallmeyer et al., 1997: 460 - 490 Ma; Fernández-Suárez et al., 1998: 465 - 520 Ma), where alkaline and perialkaline granites resulted from the fractionation of mantle-derived melts in a proto-rift zone (Crowley et al., 2000).

### *2.4.4 Late Ordovician-Late Devonian microcontinent positions*

Much the same as per Avalonia, debate surrounds the placement of the Armorican terrane and the Tornquist sea (Carls, 1988; Paris & Robardet, 1990; Robardet et al., 1990; Trench & Torsvik, 1991; Tait et al., 1997; Tait, 1999, Robardet, 2000, 2002; Robardet et al., 2001). Opposing models based on palaeomagnetic (Tait, 1999; Tait et al., 2000) and palaeoclimatic & palaeobiogeographic (Paris & Robardet, 1990; Robardet et al., 1990; Paris, 1998) data are summarised in figure 2.4.4-1).

(i) Interpretation of palaeomagnetic data indicates the existence of an Armorican microplate (Iberian, Armorican and Bohemian Massifs; Matte, 2001) or an Armorican Terrane Assemblage (Tait et al., 1997, 2000; Crowley et al., 2000). According to Crowley et al. (2000), the Armorican Terrane Assemblage remained adjacent to Gondwana's northern flank at least until the Arenigian. Between Llanvirnian and Caradocian it detached and quickly moved N-ward and fragmented resulting in its inundation by numerous restricted seaways (Anderle et al., 1995; Franke et al., 1995).

(ii) Contradicting evidence from close Early Ordovician to Devonian faunal affinities (at species level) between northern Gondwana and the Ibero-Armorican realm negate the existence of a broad Prototethys Ocean (3000 km breath at Early Devonian time;

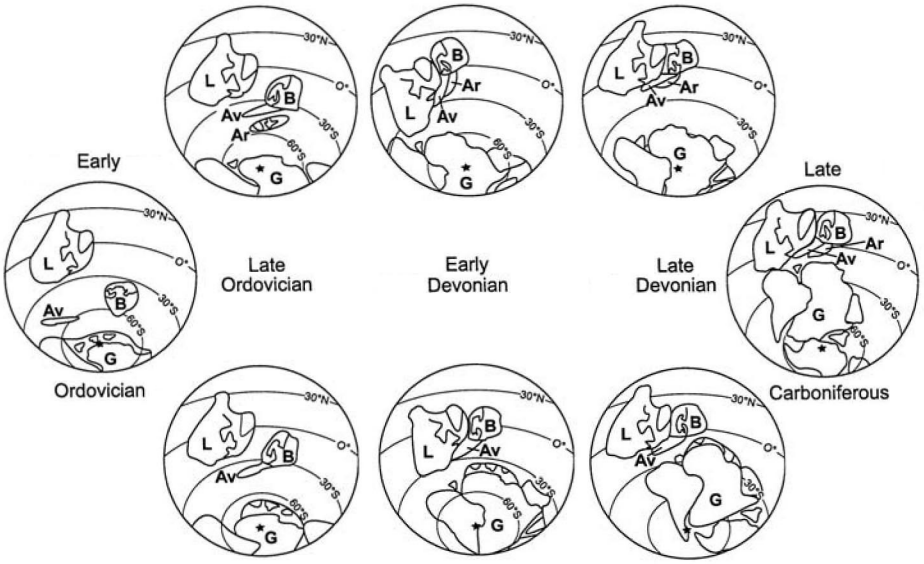


Figure 2.4.4-1: Competing palaeogeographical models of Early Ordovician through Late Carboniferous based on palaeomagnetic data (upper: Tait, 1999 and Tait et al., 2000) or palaeoclimatic and palaeobiogeographical data (lower: Paris, 1998; Paris & Robardet, 1990; Robardet et al., 1990). A-Armorica; Av-Avalonia; B-Baltica; G-Gondwana; L-Laurentia. According to Robardet (2003).

after Tait, 1999) segregating the similar benthic faunal assemblages (Carls, 1988; Paris & Robardet, 1990; Robardet et al., 1990, 2001; Robardet, 2000). Paris and Robardet (1990) propose, a large embayment, the South Armorican Ocean existed in addition to the Iapetus and Rheic oceans. The embayment separated the central Iberian and mid-north Armorican domains for the Cantabrian Mountains and Aquitaine, but never acted as a significant faunal barrier.

Gutiérrez-Marco et al. (2002) and Robardet (2002, 2003) emphasise close sedimentary and palaeobiogeographical affinities between north Gondwana and Iberia/Armorica, rejecting all Armorican microplate theories cited above. Robardet (2002, 2003) declare no wide ocean ever separated north Gondwana's southern Europe from stable Gondwana during the Palaeozoic, nor did one exist in the north Gondwanan region.

### *2.4.5 Silurian*

Following the Late Ordovician, major eustatic transgression immersed large parts of north Gondwana (late Llandovery: Paris & Robardet, 1990; Tait et al., 1997). For the most part, the Silurian represented a quiescent period (Figure 2.4.3-1) relating to the configuration of continents, as there were not much deviation form Ordovician geometries. Baltica/Avalonia drifted to the N, subsequently narrowing the Iapetus Ocean (Paris & Robardet, 1990; Crowley et al., 2000). It is also suggested Baltica and Avalonia collided in the Late Ordovician/Early Silurian prior to the late Llandovery-Early Devonian polyphase collision of Baltica and Laurentia (Mc Kerrow, et al., 1991; Tait et al., 1997, 2000). During the Silurian, north Gondwana was characterised by the

deposition of graptolitic black shales, the deposition lasting longer to the distal NE in regions such as southern Iberia and Sardinia (Paris & Robardet, 1990; Oczlon, 1992). Two contradicting models result from opinions elucidated above:

(i) Robardet (2000, 2002) and Robardet et al. (2001) underscore the function of a "faunal barrier" in the Rheic Ocean throughout the Silurian until the earliest Devonian and the position of the Iberian Peninsula within the proximal shelf of the north Gondwanan province (figure 2.4.4-1; Robardet & Gutiérrez-Marco 2002).

(ii) Opposingly, Tait et al. (1997) identify a narrowing or total closure of the Rheic Ocean between Armorica and the northern continents in the Late Silurian-Early Devonian time, basing their theory on palaeomagnetic data and faunal affinities. However, the diagnostic quality of palaeomagnetic information from Silurian rocks is in question as most measurements are influenced by a later remagnetisation event (van der Voo, 1993). Iberia's position can thus only be estimated to have lied between ~ 50˚ S (latest Ordovician) and 35˚ S (Early Devonian) (Robardet & Gutiérrez-Marco, 2002).

### *2.4.6 Devonian*

The final stages of the diachronous collision between Laurentia and Baltica/Avalonia, in the equatorial-north resulted in the development of the "Old Red Continent" by Early Devonian time (figure 2.4.4-1; Paris & Robardet, 1990). Palaeomagnetic data again contradicts palaeontologic records:

(i) Palaeogeographic reconstructions suggest the closure of all oceans separating Laurentia, Baltica, Avalonia and Armorica by the Middle Devonian (figure 2.4.3-1), and the conclusive formation of the Old Red Continent by the Late Devonian (McKerrow et al., 1991; Torsvik et al., 1992; Tait et al., 1997; Crowley et al., 2000). Palaeomagnetic data supports the theory of a broad ocean then separating Armorica from northern Gondwana (Johnson & Tarling, 1985; Tarling, 1985; Tait et al., 1997).

(ii) Contrastingly, even at the species level, benthic faunal and floral affinities between the Armorican Massif, Iberian Peninsula and the western Algerian Sahara do not support the presence of such an encompassing ocean there between (Carls, 1988; Martínez-Catalán, 1990; Paris & Robardet, 1990; Robardet et al., 1990, 2001; Robardet 2000, 2002). Instead, Robardet et al. (1990) propose the presence of numerous quasi-isolated continental blocks along the northern margin of Gondwana in order to explain the presence of the varied sedimentary and faunal domains in southwestern Europe during early Palaeozoic time. Paris & Robardet (1990) and Oczlon (1992) report the Ibero-Armorican region was still in the warmer regions (30 - 35 ˚S) of the north Gondwanan shelf at Early Devonian time (figure 2.4.4-1); the authors' interpretations arising from the development of carbonate-terrigenous sediments in the Armorican Massif and the Iberian Peninsula.

During the Middle Devonian Gondwana moved to tropical latitudes (figure 2.4.3) enabling the development of reefs (e.g. Santa Lucía, Portilla formations; Veselovsky, 2004: Chapter 2.4.4-1). Palaeontologic and palaeobiogeographic affinities between north Gondwanan regions and the southern margin of Laurussia are evident beginning in the Pragian/Emsian onward (Robardet, 2000, 2002; Robardet et al., 2001). Progressive closure of the Rheic Ocean is indicated by increase of the above mentioned affinities during the Emsian and Middle Devonian.

## *2.4.7 Climax of the Variscan orogen*

The period surrounding the final consolidation of the Variscan orogen was one of continental-scale shearing with transpression acting as an agent for the opening of small oceanic basins (Matte, 1991; Quesada, 1991). Palaeomagnetic data throughout the belt show large-scale differential rotations and deformations (Johnson & Tarling, 1985; Hirt et al., 1992; Tait et al., 1997). Blakey (2004) demonstrates the global consolidation of the orogen using maps based on the *Paleomap Project* (Scotese, 2001). Franke & Engel (1986) and Oczlon (1992) proposed the onset of convergence by Late Devonian (Frasnian/Famennian), evidenced by predominant flysch and greywacke deposition throughout the entire Variscan Belt. The northern margin of Gondwana is interpreted by Oczlon (1992) as being an active continental margin in response to S-ward directed subduction of the Rheic Ocean during Late Devonian time. Palaeomagnetic data reveals the closure of the ocean between the Old Red Continent and Gondwana by Late Devonian time and the initiation of the collision in the Early Carboniferous (Tait et al., 1997). In western Iberia (Cabo Ortegal, Ordenes etc.) high-pressure metamorphic rocks and ophiolites suggest a W-ward subduction (present coordinates system) from 380 - 370 Ma (Figure 2.4.7-1; Martínez-Catalán et al., 1997).

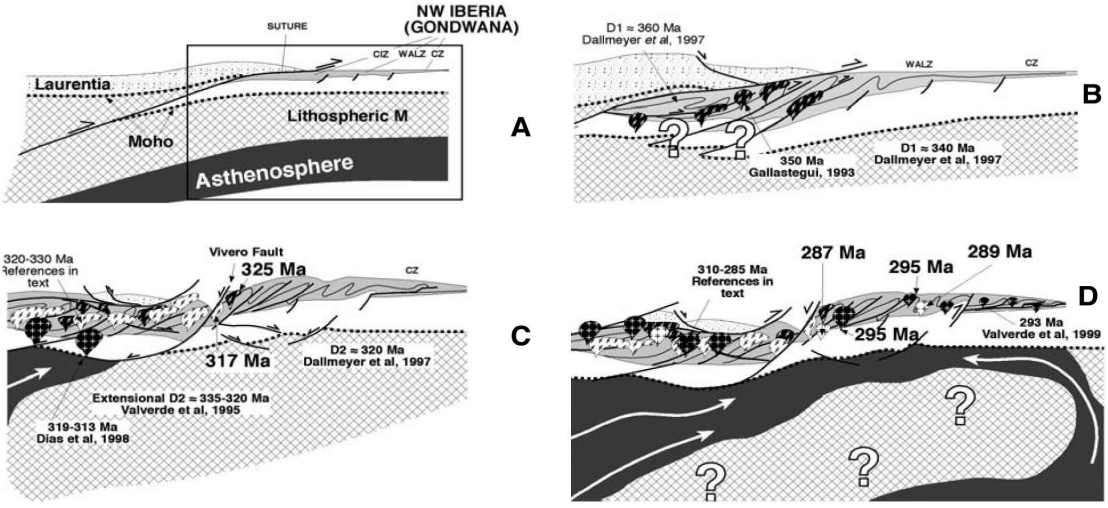


Figure 2.4.7-1: Progressive tectonic evolution of NW Iberia (after Fernández-Suárez et al., 2000 b). A) Pretectonic NW Iberia; B) Early Variscan syntectonic evolution; C) Variscan orogenic Climax; D) Post-Variscan simultaneous oroclinal bending driven extension and compression. Age information from U-Pb dates of granitoids in NW Iberia.

Ophiolitic nappes, marking the suture zone, were stacked during the closure of the Rheic Ocean (Dallmeyer et al., 1997). Subduction of the outer edge of Gondwana occurred after the closure of the Rheic Ocean, deducting the subduction direction from the metamorphic gradient (Martínez-Catalán et al., 1997). Migration of syntectonic granitoids followed the migration of metamorphic stages across the orogen (Fernández-Suárez et al., 2000 b). Underthrusting of continental material propagated (375 - 365 Ma), causing intracontinintal deformation that progressed in the direction of the more external parts of the orogen with time (figure 2.4.7-1). Though occurrences exist, the record shows magmatic activity related to this stage was not widespread in the autochthon of NW Iberia (Fernández-Suárez et al., 2000 b).

### *2.4.8 Pre-Stephanian Carboniferous*

Positioning of the Iberian Peninsula in Early Carboniferous time is lowly constrained (Amler, 2000). Johnson & Tarling (1985) suggest Iberia was part of a terrane, about 20° S of the equator, near the southern margin of Laurussia. Scotese et al. (1979) and Paris & Robardet (1990) place it closer to the northern boundary of Gondwana. Johnson & Tarling (1985) and Tarling (1985) suggest that Britannia (southern border of Laurasia) and Spain (Armorica) collided in the Lower Carboniferous, eventually converging with Gondwana in the Late Carboniferous. Figure 2.4.8-1 details the Silurian to pre-Stephanian Carboniferous migration of Iberia after Blakey (2004).

As seen in figure 2.2-1 there was an E-ward diachronous progradation of Variscan deformation in northwestern Iberia. Several Variscan deformational phases (see Pérez-Estaún et al., 1991; Dallmeyer et al., 1997) represent local responses to regional shortening. In comparing isotopic ratios from different areas within the Iberian Variscan Belt, Dallmeyer et al. (1997) proposed average propagation rates of approximately 5 km/Ma. Migrating intrusion ages recorded by Fernández-Suárez et al. (2000 b) provide supporting evidence to the claim.

### *2.4.9 Stephanian to Early Triassic*

Generally the development of Late Permian-Triassic basins in Iberia was similar to, but not coeval with those in the rest of Europe (López-Gómez et al., 2002). Facies similar to those in European basins are found in Iberia, yet sedimentary ages differ due to the several millions of years required for rift systems to have propagated from the E and NE, resulting in diachronous facies changes (López-Gómez et al., 2002).

Variscan deformation lasted to about 290 Ma (Martínez-Catalán et al., 1997; Dallmeyer et al., 1997), with the final, extensional collapse phase of the Variscan orogeny having taken place during Stephanian B-C into the Permian across much of Iberia. Basin development was coeval with high heat flow, granitic and monzogranitic magmatism, uplift and extension, creating intramontane continental basins along all of Iberia's margins, possibly in conjunction with décollements along former thrust planes (e.g. Demués and San Tirso formations in the Cantabrian Cordillera) (López-Gómez et

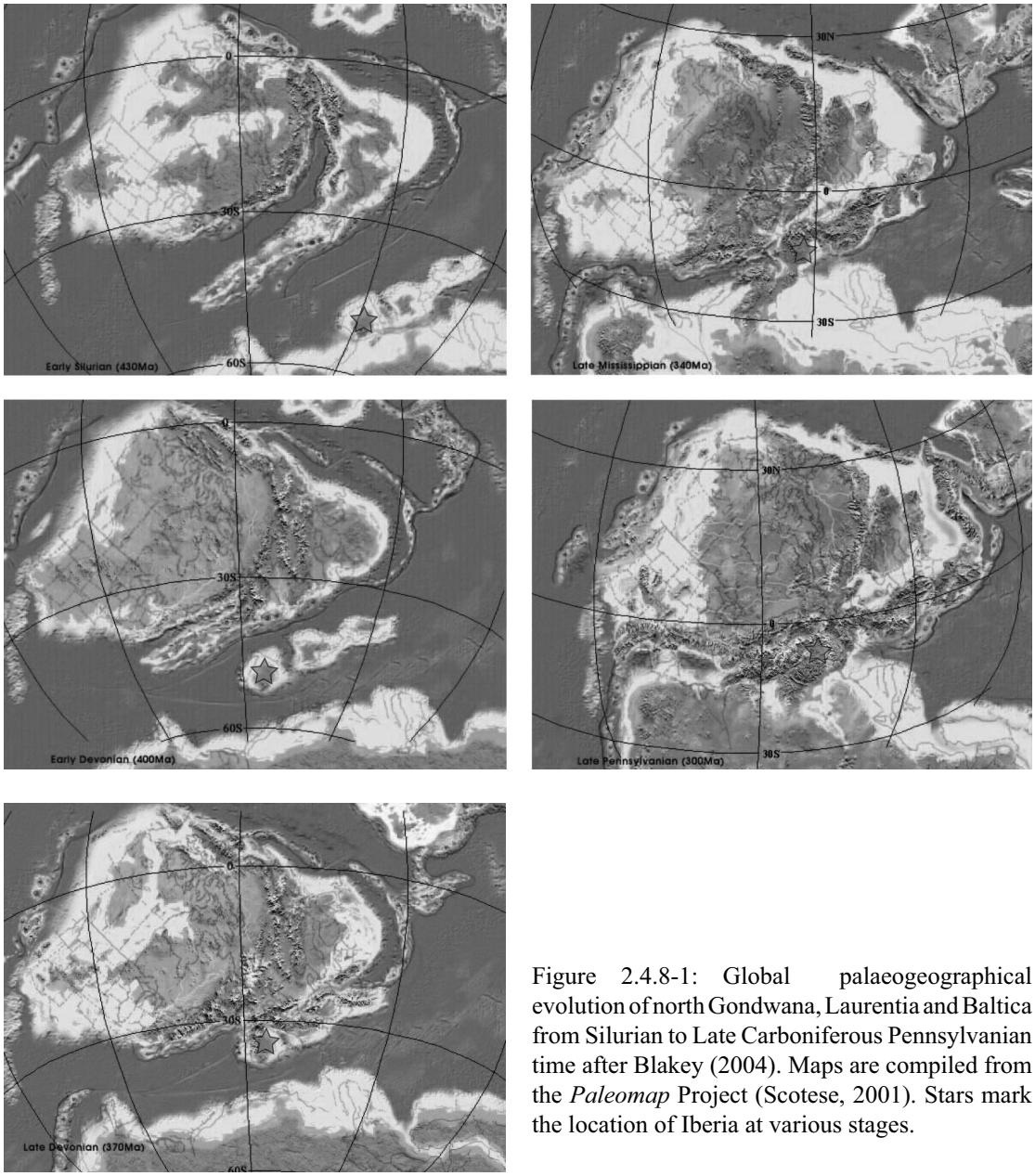


Figure 2.4.8-1: Global palaeogeographical evolution of north Gondwana, Laurentia and Baltica from Silurian to Late Carboniferous Pennsylvanian time after Blakey (2004). Maps are compiled from the *Paleomap* Project (Scotese, 2001). Stars mark the location of Iberia at various stages.

al., 2002). López-Gómez et al. (2002) explain the conspicuous absence of volcanic rocks in many synorogenic basins as a result of low angle boundary faults not reaching the asthenosphere. However in the Cantabrian Cordillera, several outcrops of dioritic dykes and sills intrude, and are folded along with Stephanian sediments of the Ciñera-Matallana Coal basin (Allyón et al., 2003; Allyón, 2003). Though these rocks are not directly dated, associated magmatic activity and ore deposits within the Cantabrian Zone are reported to be of Lower Permian age, between 293 to 262 Ma (Loeschke, 1983; Corretgé & Suárez, 1990; Crespo et al., 2000 and references therein). Denudation eliminated most Stephanian basins, in the Iberian Ranges and along the southern margin of Iberia.

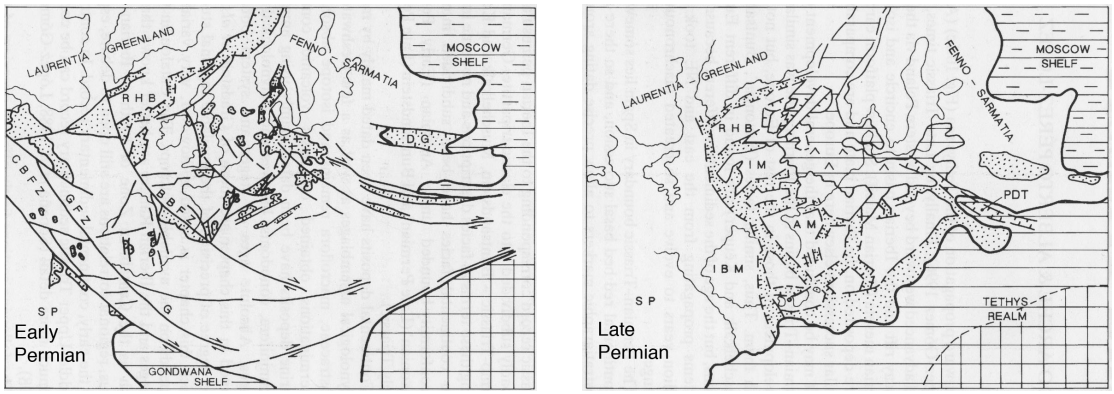


Figure 2.4.9-1: Location and palaeogeographical evolution of the Iberian Peninsula during Permian times (modified from Arche & López-Gómez, 1996).

The Permian-Triassic succession in Spain records the change from a largely compressive tectonic Pangea configuration (e.g. figure 2.4.8-1: Pennsylvanian, 300 Ma) to one dominated by extensional tectonics, continental break-up and the W-ward expansion of the Palaeotethys Ocean (figure 2.4.9-1).

Dextral strike-slip movement and normal faulting dominate in the Iberian Massif. In the final stages of the Variscan orogeny (or the earliest stage of the alpidic history; Doblas et al., 1994 a), Iberia moved W-ward with respect to the Armorican terrane along a dextral strike-slip fault on its northern plate boundary and a sinistral strike-slip fault on its southern plate boundary (e.g. Figure 2.4.9-1: Early Permian); resulting in NE-directed extension in east to northeast Iberia (Ziegler, 1988). As a result of W-ward drift and extension in the late stages of the Variscan orogeny, Permian-Triassic basin development commenced in the Cantabrian-Pyrenean Zone, the Catalonian Coastal Ranges and the Iberian Ranges in association with Permian-Triassic rifting (Martínez-García et al., 1983; Leprevier & Martínez-García, 1990; López-Gómez et al., 2002). In Late Permian time, volcanism is distributed differentially among the various basins. No activity occurred in the Iberian Ranges where basin boundary faults show listric geometries at depths of 13 - 14 km (brittle domain of the lithosphere) (Arche & López-Gómez 1996, 1999). Basaltic flows and dykes appear in the western and central Pyrenees (Valero & Gisbert, 1992; Lucas & Gisbert-Aguilar, 1995), indicative of deep-seated vertical basin boundary faults in the area (López-Gómez et al., 2002). Generally, subsidence rates were high along Iberia's northern margin where over 1500 m of red beds accumulated, but more subdued in the Iberian basin where no more than 300 m are visible (López-Gómez et al., 2002). Uplift, tilting and erosion defines the boundary between Upper Permian and Lower Triassic basins.

## *2.4.10 Mesozoic rifting in Iberia*

Opening of the Atlantic commenced between the Americas and at first Africa, later Iberia, then other parts of Europe, resulting in significant differential motions between these continents (Andeweg, 2002). As a result of ocean spreading between Iberia and North America, a major stage of rifting commenced in the Mesozoic documented by extension related features on all margins of the Iberian microplate (figure 2.4.10-1; Andeweg, 2002).

Following Late Permian erosion, reorganisation of sedimentary basins and palaeoenvironments prevailed from Early to Middle Triassic. Extensional tectonics dominated the eastern half of the Iberian plate, leading to symmetric basin development confined by listric, conjugate faults in the areas of the Iberian Ranges and the Cantabrian-Pyrenees zone, and the development of the Ebro and Tajo basins (López-Gómez et al., 2002). Rifting propagated S-ward along the eastern margin of the Iberian Peninsula in association with extension to create the Catalan-Valencian-pre-Betic Basin (Marzo & Calvet, 1985; Sopeña et al., 1988; Arche & López-Gómez, 1996). Volcanism is not reported, though monzogranitic dykes intruded into the Spanish Central System (González-Casado et al., 1996). With time subsidence decreased throughout the massif. Buntsandstein facies filled basins. Subsidence was episodic. Rifting along the eastern margin was short lived (latest Thüringian to Anisian) and localised to the Iberian Ranges causing graben inversion and local accumulation of up to 650 m of coarsening upward fluvial sequences (Ramos, 1979; García-Royo & Arche, 1987; Pérez-Arlucea, 1985; Arche & López-Gómez, 1999).

Extension produced fault related syn-rift basins (Allen & Allen, 1990) in the areas of the Pyrenees (E-directed), Iberian Ranges (NW-directed) and Catalan-Valencian-pre-Betic area (NE-trending) (López-Gómez et al., 2002), a component of the rift phase having caused the break-up of Pangea (de Bruijne, 2001). Based on the differing orientations of the basins, Arche & López-Gómez (1996) propose the coexistence of two strain fields at this time; one related to the development of the Bay of Biscay and Gibraltar transform faults, the other to an extensional field propagating SW-wardly with time, from the Boreal basin to the Catalan-Valencian-pre-Betic Basin.

From Late Triassic, rifting along the eastern margin turned to a thermally controlled, postrift period starting in the Anisian, and lasted until the Late Jurassic (López-Gómez et al., 2002). During this phase, Iberia maintained contact with Europe, but Africa remained SW, drifting SE along a sinistral strike-slip fault (Malod and Mauffret, 1990). Similarly, Iberia's western boundary with the North American plate was also defined by left-lateral strike-slip and continental rifting, where the North American plate moved SW relative to Iberia (de Bruijne, 2001).

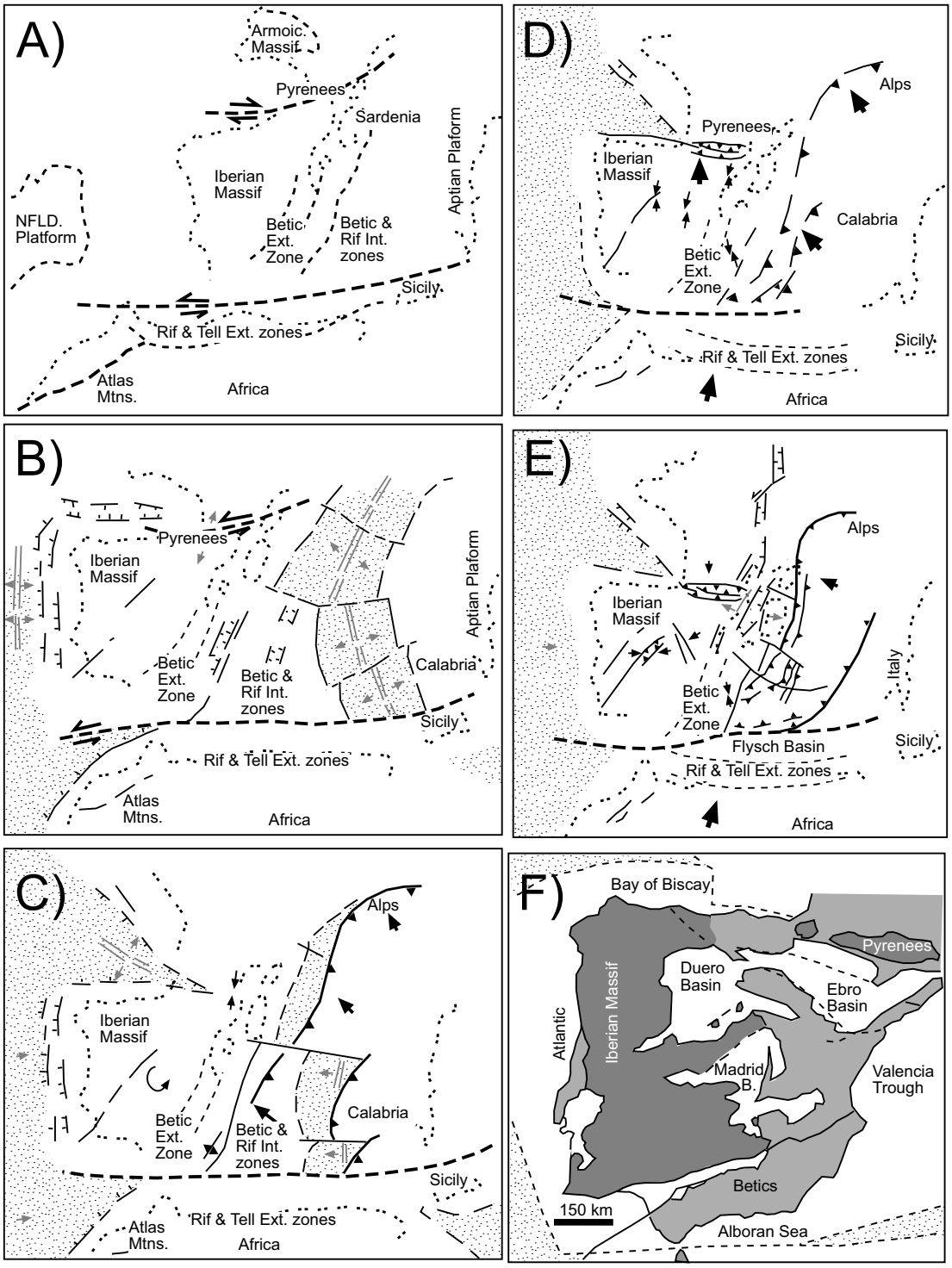


Figure 2.4.10-1: Plate tectonic and palaeogeographic history of Iberia starting following Pangea break-up. A) Early Triassic; B) Late Jurassic to Early Cretaceous; C) Late Cretaceous to Palaeocene; D) Eocene to Early Oligocene; E) Late Oligocene to Middle Miocene; F) Present. Dotted areas define oceanic crust. Oceanic spreading ridges marked by parallel lines. Grey and black arrows respectively show direction of extension and compression. After Sanz de Galdeano (1995), and de Bruijne (2001).

Elsewhere, an extensive yet short lived shallow water carbonate and clastic shelf developed along the southern margin of Iberia, lasting to latest Early Jurrassic, where the onset of rifting along the southern margin disintegrated the carbonate shelf and deepened the basin (Andeweg, 2002). Rifting, there succeeded to thermal subsidence from Late Jurassic through the rest of the Cretaceous (Vera, 1988). Africa moved in a SE-ward trajectory with respect to Iberia (de Bruijne, 2001), initiating the N-trending Ligurian Basin, E of Iberia (Dercourt et al., 1986).

Early Jurassic rifting on the western Iberian margin was followed by a regional hiatus, likely related to the opening of the central Atlantic coinciding with the beginning of oceanic spreading at the Iberian Abyssal Plain at 126 Ma (Whitmarsh & Miles, 1995). Extension continued to the Early Cretaceous. Andeweg (2002) reports the final separation of Galica Bank and Flamish Cap at ~ 118 Ma. Subsequently the area experienced regional scale thermal subsidence (Stapel, 1999).

From Late Jurassic to Early Cretaceous rifting along the east to northeast Iberian margin initiated the Pyrenean Basin and extended the Iberian Basin (Salas and Casas, 1993) in association with the opening of the alpidic coeval Tethys (Andeweg, 2002). Subsidence analysis of the Iberian Basin (van Wees et al., 1998) and thermal modelling (Fernàndez et al., 1995) show several rifting stages in eastern Iberia, primarily in the Permian to Early Triassic and Late Jurassic to Early Cretaceous.

In Early to Middle Cretaceous time, along the northern Iberian margin, extension resulted in the opening of the Bay of Biscay (García-Mondejar, 1989; Verhoef & Srivastava, 1989) at ~ 115 Ma (Andeweg, 2002) continuing to the mid-Late Cretaceous (~ 85 Ma: Ziegler, 1988). Due to rifting of the bay as well as rifting earlier initiated in the Azores region of the North Atlantic (~ 126 Ma; Andeweg, 2002) Iberia commenced a SSW-ward trajectory away from Europe (Savostin et al., 1986; de Bruijne, 2001). Subsequent cessation of motion between the Iberian and African plates coincides with mutual left lateral translation and counter-clockwise rotation (~ 35 °; Ziegler et al., 2001) of the locked plates, resulting in subsequent collision between Iberia and Europe (Andeweg, 2002). As a consequence, inversion and subduction of the Ligurian Basin onto the eastern side of Iberia occured (de Jong, 1990; Sanz de Galdeano, 1995) as well as the formation of the Betic Nappe units (Biermann, 1995).

Nearing the end of the Mesozoic (~ 85 Ma: Ziegler, 1988) the Atlantic propagated N-ward, first via the failed Rockwell Trough, then between Greenland and Ireland, leaving the Bay of Biscay a failed rift (Ziegler, 1988) and freezing Iberia's rotation (Srivastava et al., 1990). In response to the new dynamic setting, Europe rotated in a clockwise fashion about Iberia (Andeweg, 2002). Convergence between Africa and Eurasia brought on compression (the largest phase of which occurring in the Eocene to Early Oligocene) in the internal zones of the Alps (de Bruijne, 2001). Moreover, it inverted the former extensional northern margin of Iberia and induced its subduction under the Eurasian plate via NNE-trending compression. Initiated by this compression were the

W-wardly encroaching Pyrenees (Puigdefàbregas & Souquet, 1986; de Bruijne, 2001; Andeweg, 2002). From the Palaeocene onward, the movement between Eurasia and Iberia became right lateral and transpressive (100 km translation between 42 - 24 Ma: Roest and Srivastava, 1991).

### *2.4.11 Cenozoic compression of Iberia*

Andeweg (2002) reports, the Palaeogene and Neogene are periods dominated by compressional deformation. Inversion of Mesozoic sediments continued related to the ongoing W-ward propagating closure of the Bay of Biscay-Pyrenean Zone (García-Mondejar, 1988). A short-lived S-ward subduction of previously formed Biscay oceanic crust during latest Cretaceous to Early Eocene induced the development of the Cantabrian Cordillera through the formation of S-ward progressing thrust belts and foreland basins (Boillot & Malod, 1988; de Bruijne, 2001; Andeweg, 2002). In the Late Oligocene Iberia reconnected with Eurasia (de Bruijne, 2001). Termination of this subduction coincided with the proposed timing (~ 54 Ma; Savostin et al., 1986) of the separation of rotation poles of Africa and Iberia with respect to Eurasia (Andeweg, 2002).

Compressional forces at the Iberian-Eurasian plate boundary caused the build-up of intraplate compressional stresses, inducing wide scale inversion of Mesozoic basins within the Iberian plate during the Palaeogene (Juez-Larré, 2003), thus forming the Catalan Intraplate Chain (Anadón et al., 1985), Iberian Chain (Álvaro et al., 1979; Guimerà, 1984; Guimerà & Álvaro, 1990) and the Spanish Central System (Vegas et al., 1990; de Bruijne & Andriessen, 2002).

Final Iberian-Eurasian amalgamation in early-Middle Miocene (~ 30 Ma; Andeweg, 2002) coincided with a significant phase of plate boundary activity. The locus of convergence between Africa and Eurasia moved from the Eurasian-Iberian plate boundary (NNW-directed) to that of the Iberian-African boundary (NW-directed) (Dewey et al., 1989; Andeweg, 2002; Juez-Larré, 2003) during the Tortonian (Mazzoli & Helman, 1994), initiating the onset of the Betics orogeny (Roest & Srivastava, 1991; Biermann, 1995; Andriessen & Zeck, 1996; Azañón & Crespo-Blanc, 2000). In addition, the sinistral Azores-Gibraltar Zone between Iberia and Africa (Srivastava et al., 1990) became activated (Andeweg, 2002). Continued E-ward movement of Africa resulted in the extension of eastern Iberia and the opening of the Valencia Trough (Sabat et al., 1995; de Bruijne, 2001; Andeweg, 2002). Initially associated with the Early Oligocene propagation of the Rhine-Bresse-Graben-System, rifting in southern France moved S-ward until it reached the Alborán Domain in the Early Miocene (23 - 20 Ma; Sanz de Galdeano, 1995). Neogene plate tectonics in the region are considered complex and hotly contested (Blanco and Spakman, 1993; Vissers et al., 1995; Lonergan and White, 1997). However, NNW-trending compression still prevails in the Betic Cordillera (de Bruijne, 2001). See Andeweg (2002) or Ziegler et al. (2001) for further reading on the topic.

By the end of the Tortonian (7 Ma), the Alborán Basin became inverted (Lonergan and White, 1997) and the compressive stress regime in the Betic Cordillera changed from NNW to NW (Galindo-Zaldívar et al., 1993), the same as the present-day orientation. Presently, the Iberian Massif displays mountainous relief with an average height of 660 m in association with the presence of an extensive plateau surrounded and penetrated by mountain ranges of the Cantabrian Cordillera, Pyrenees Mountains, Catalonian Coastal Ranges, Iberian Ranges and The Betics (Gutiérrez-Elorza et al., 2002). As a whole, the Iberian Peninsula is presently subducting under the Betic Cordillera and Alborán Basin (Morales et al., 1999).

Cenozoic alpidic orogenesis uplifted the Variscan basement and an undetached Mesozoic cover, forming the Cantabrian Mountains (Pulgar et al., 1995). For detailed review of the Cenozoic tectonic evolution of the Iberian Peninsula see Andeweg (2002); for information regarding alpidic orogenesis in NW Iberia see Alonso et al. (1995); Capote et al. (2002).

# 3 Stratigraphy

This study crosses three stratigraphically distinct units associated with the pre- to syn-Variscan evolution of the northwest Iberian Peninsula: The Narcea Antiform made up of Precambrian turbidites with feldspathic sandstones, arkose, orthogneiss and porphyroid components (Pérez-Estaún & Martínez, 1978) or; the southern Cantabrian Zone, in which rocks evidence a near continuous accumulation of siliceous and carbonaceous sediments spanning pre-Stephanian Palaeozoic time (Veselovsky, 2004; Dietrich, 2005); and the Central Coal Basin, which displays a unique, yet somewhat comparable sedimentary accumulation to that of the southern Cantabrian Zone, however with Silurian and partly even later sedimentation being absent (e.g. Alvarez-Marrón et al., 1990).

Stephanian aged coal bearing accumulations are discontinuously distributed about the external members of the Iberian Arc and in the study area are mainly seen in the south (La Magdalena and Ciñera-Matallana coal basins), yet also obscure the León Line in the northern extent of the study area (Rucayo Basin).

Following a significant stratigraphic gap, Cretaceous sediments outcrop in the southern margin of the study area, and are unconformably overlain by a conspicuous Tertiary succession in the Duero Basin.

## *3.1 Precambrian stratigraphy*

Precambrian rocks are exposed in the southwest corner of the study area in the Narcea Antiform, a broad arc, stretching landward from the Costa Verde northern Spain, to the study area (Julivert, 1971). The Narcea Antiform is considered the sedimentary basement (Gutiérrez-Alonso, 1995), which separates the eastern part of the Western Asturian-Leónese Zone (internal zone: locally along the southern flank the Narcea Antiform) from the Cantabrian Zone (external zone: locally its northern flank) of the Variscan orogeny (Julivert, 1971). Descriptions of varying detail regarding the stratigraphy of Precambrian rocks in the Narcea Antiform are numerous (e.g. Lotze, 1956; de Sitter, 1962; Pastor-Gomez, 1963, 1969; Farber & Jaritz, 1964; Corretgé & Carpio, 1968; Corretgé, 1969; van den Bosch a, b, 1969; Pérez-Estaún, 1973, 1975, 1978; Pérez-Estaún & Martínez, 1978; Julivert, 1981; Valladares et al., 2002 b).

Locally, the monotony of the Precambrian turbidite succession and complex structural setting, including very low angle cleavage (Pérez-Estaún, 1978) and extensive deformation, obscures definition of a stratigraphy valid for the whole area, nevertheless greywackes and schists of the Mora Fm. (Comte, 1959) dominate. Neither an underlying sediment nor basement is evidenced below in the Narcea Antiform (Valladares et al., 2002 b).

The timing of deposition in the northern flank is constrained by upper Neoproterozoic by cyanobacterial spheromorphs (Palacios & Vidal, 1992) *Sphaerocongregus variabilis* and *Palaeogomorphosphaeria caurensis* (see Valladares et al., 2002 b). Correspondingly, outside of the study area, in southern-flank equivalent rocks, detrital zircons provide ages as young as 640 Ma (Fernández-Suarez, 2002 b).

West of the study area Neoproterozoic sediments of the southern flank, obtain total thickness estimated to > 1500 m (Pérez-Estaún, 1978) and ~ 2000 m (Julivert, 1983 a); those of the northern flank, interpreted as having been deposited as outer deep-sea fans (*sensu* Mutti & Ricci Lucchi, 1975) reach to 7000 m but decrease E-ward (e.g Gutiérrez-Alonso, 1996). greater than 1500 m are locally observed (figure 3.1-1 a; Martín-Parra et al., 1989).

An angular unconformity is visible on both flanks of the Narcea Antiform, where in and about the study area, Neoproterozoic Mora Fm. of the Narcea Antiform is differentiated from overlying Lower Cambrian sediments e.g. Herrería Fm. (Comte, 1959), the basal sedimentary unit of the southern Cantabrian Zone (figure 3.1-1 b).

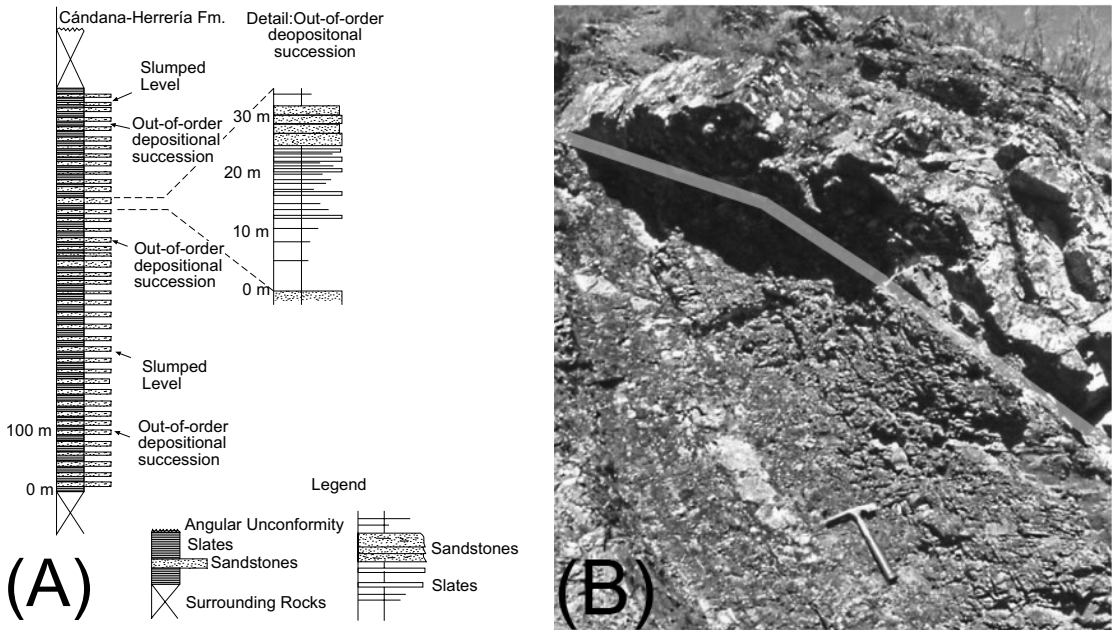


Figure 3.1-1: a) Partial sedimentary column for Neoproterozoic Mora Fm. sediments of the northern Narcea Antiform flank (Cantabrian Zone). Modified from Martín-Parra, (1989). Out-of-order turbidite depositional successions classified with respect to the Nomenclature of Mutti & Ricci Lucchi, (1975); b) Angular unconformity (faded line) defining the boundary between the Mora Fm. (below unconformity) and Herrería Fm. (above unconformity) of the southern Cantabrian Zone; Hammer for scale. Image: courtesy of Thomas Angerer.

## 3.2 Palaeozoic stratigraphy

In the southern Cantabrian Zone member of the study area, the Palaeozoic succession is comprised of two timing constrained depositional cycles with regards to the Variscan orogeny (see figure 3.2-1):
a) Pre-Carboniferous sediments deposited on a clastic-carbonate shelf thickening toward the outer part of the arc (Veselovsky, 2004); b) A Carboniferous succession, marking an abrupt change in sedimentation in conjunction with the onset of the Variscan orogeny and the subsequent transition from a syntectonic to a posttectonic regime (Marcos & Pulgar, 1982).

### *3.2.1 Pre-Variscan Palaeozoic stratigraphy*

Pre-Variscan siliciclastic sediments (Herrería, Oville, Barrios, Formigoso and San Pedro formations) and interspersed hiatuses dominate the Cambrian to Silurian succession. Total thicknesses of the lower Palaeozoic (to Silurian) sedimentary column in the southern Cantabrian Basin are between ~ 1750 and ~ 2925 m (after Veselovsky, 2004). In the Central Coal Basin the Silurian succession is even conspicuously absent (see Alvarez-Marrón et al., 1990).

Carbonates are visible only in the Lower Cambrian Láncara Fm. Beginning with the deposition of the Silurian San Pedro Fm. input of sediments from an elevated area (Cantabrian High) in the northeast of the Southern Cantabrian Basin influenced the development of thicker basinal successions to the SW and their onlap towards the NE. During the Devonian, carbonate formations (La Vid, Santa Lucía, Portilla) were alternately deposited with siliciclastic formations (Esla, Huergas, Nocedo and Fueyo). Devonian thicknesses locally range from ~ 530 – 1750 m (after Veselovsky, 2004). From Middle Devonian (Givetian) time, reef development ceased and the whole of the Cantabrian Zone succumbed to siliciclastic sedimentation (Ermita Fm.) followed by a thin lower Serpukhovian carbonate layer (Alba Fm).

### *3.2.2 Syn-Variscan Palaeozoic Stratigraphy*

In the Cantabrian Zone, the onset of the Variscan orogeny is marked by the deposition of thick synorogenic turbidites (Olleros Fm.), beginning during Serpukhovian time. Expansive carbonate platforms (Val de Teja Fm.) developed across the basin, which in turn were covered by terrigenous sediments (San Emiliano Fm.) from the approaching Variscan orogen. The total thickness of the mainly shallow marine pre-Stephanian Carboniferous succession in the Southern Cantabrian Basin ranges between ~ 1470 and ~ 2850 m (after Veselovsky, 2004).

In the adjacent Central Coal basin, Variscan orogenesis in the study area is marked by the asymmetric Moscovian deposition of 1400 to 3700 m of flysch lithofacies (Lena & Sama groups: after van Ginkel, 1965). In the southernmost Central Coal Basin, the more sandy parts of the basin are composed of: a) marine to paralic mudstones (bottom); b)

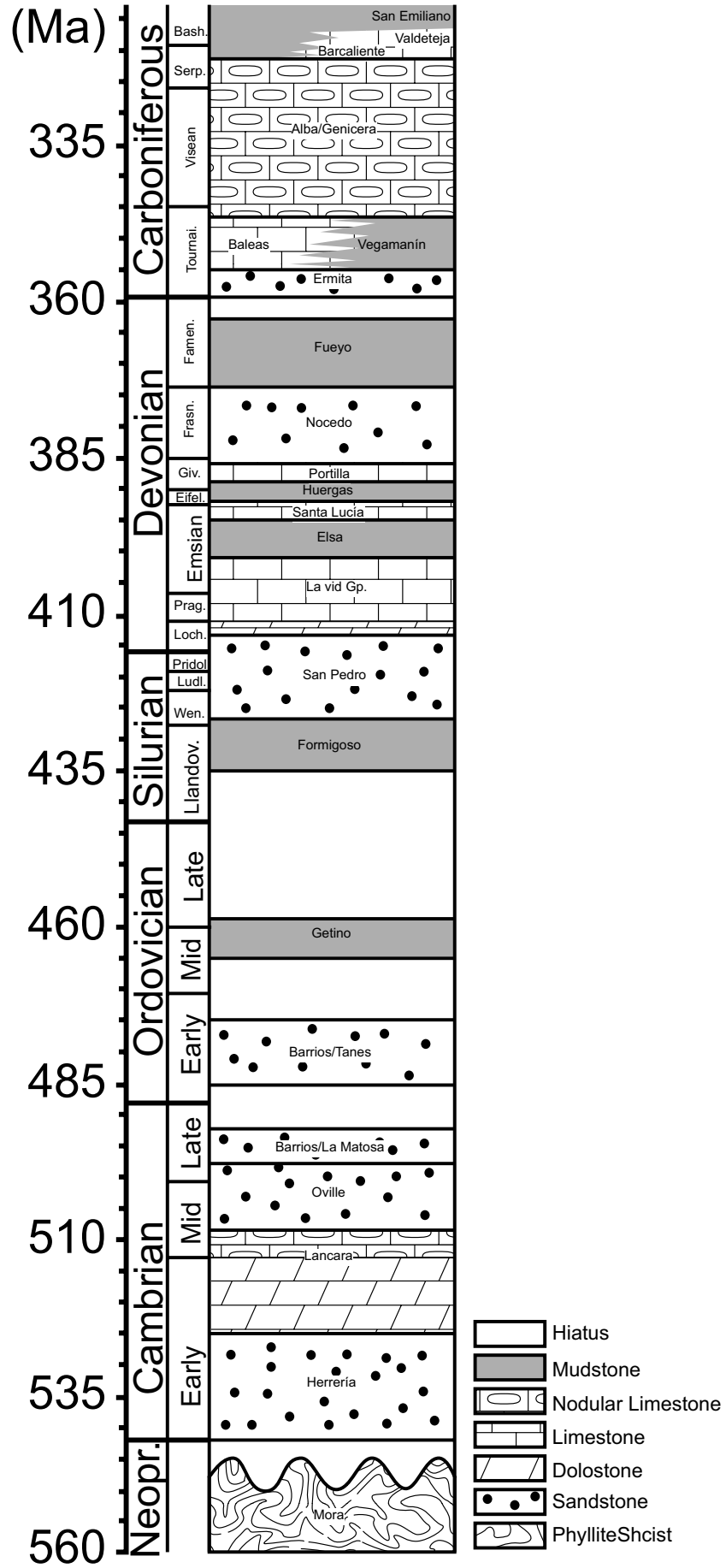


Figure 3.2.1-1: Stratigraphic succession for sediments of the southern Cantabrian Basin for pre-Stephanian Palaeozoic time. White spaces represent stratigraphic gaps. Absolute timescale information from Gradstien et al. (2004). Stratigraphic column modified from Alonso et al. (1991).

paralic limestone and wackestones; c) Paralic to limnic greywackes (top) (Evers, 1967). Lower deposits are roughly comparable to sediments of the San Emiliano Fm while upper deposits (according to van Ginkel, 1965) may already belong to the overlying Sama Group.

## 3.3 Stepahnian Palaeozoic stratigraphy

Stephanian basins in the study area are filled with Stephanian B and C coal bearing rocks. These basins form isolated and elongate coal-fields, roughly aligned along the outer side of the Asturian Arc (Colmenero & Prado, 1993); these strata having been largely associated with intense fracturing processes having taken place during and after the late stages of the Variscan orogeny.

Differentiation of pull-apart and other fault-controlled basins was caused by strike-slip movements along structural lineaments (e.g. León or Sabero-Gordón lines) and is, evidenced by extensive accumulations of molasses deposits (Heward, 1978, Heward & Reading, 1980, Nigman and Savage, 1989, Colmenero & Prado, 1993). In the study area, deposits reach to ~ 1100 m but throughout the arc deposits up to 2500 m in thickness have been recorded (cf. Ayllón, 2003). These deposits rest conspicuously and unconformably over their underlying basements. Heward (1978) suggests in the cases of the La Magdalena and Ciñera-Matallana basins, actual outcrops may represent remnants of more extended palaeobasins. Alluvial fans in fluvial and lacustrine settings are the depositional environments inferred from continental facies association (Colmenero & Prado, 1993). Here, peat swamps expanded mainly on the muddy distal fringes of the fans, in interlobate depressions and along lake margins (Heward, 1978).

### *3.3.1 Ciñera-Matallana Basin geology & stratigraphy*

The Ciñera-Matallana Basin forms an intramontane, E-trending, half-graben structure encompassing 25 km$^2$ (figure 3.3.1-1; Frings et al., 2004). About 1100 m of basin fill are composed of clastic continental rocks: conglomerates, sandstones and shales with intercalated coal seams, all part of a coarsening upwards succession unconformably overlying older strata. Allyón (2003) reports, on the basis of fossil flora, age of the sediments is restricted to Stephanian B. Basin subsidence, controlled by synsedimentary movements along the strike-slip Sabero-Gordón Line fault system (Wagner, 1971; Villegas, 1996) is reflected in significant lateral facies changes and thickness variations in the two basal formations (San Francisco & Pastora) (Allyón, 2003). Tectono-sedimentary conditions stabilised in association with the deposition of the upper succession, as they display relative lateral continuity.

From the works of Wagner (1971), Heward (1978) and Villegas (1996), six formations are identified in the Ciñera-Matallana Basin. Boundary levels are most often marked by coal seams. The formations are discussed below in order from earliest to latest deposition (see also figure 3.3.1-2):

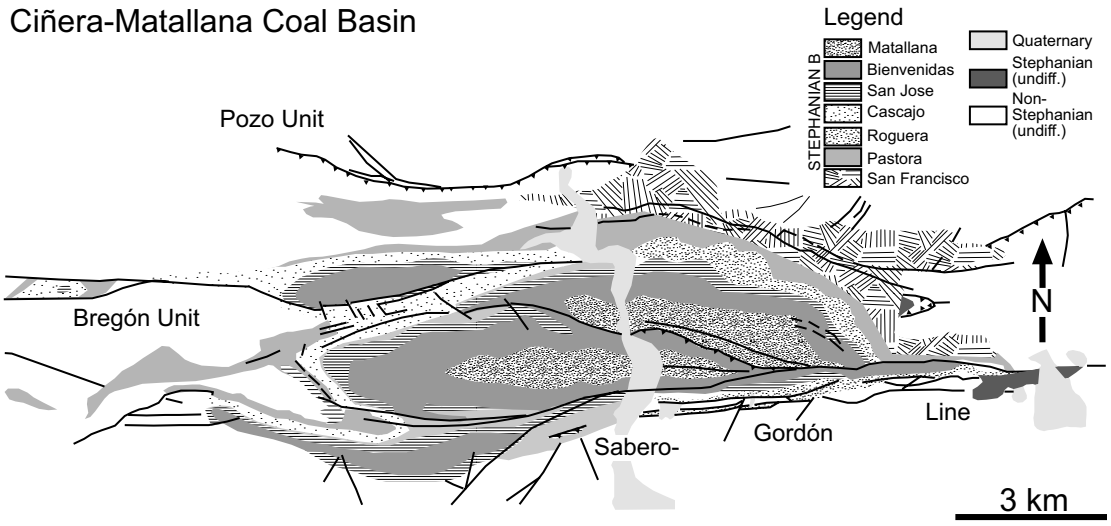


Figure 3.3.1-1: Plan view of the Stephanian B aged Ciñera-Matallana Coal Basin. Modified from Wagner & Artieda (1970), Alonso et al. (1990) and Villegas (1996).

The *San Francisco* Fm. (0 - 400 m) constitutes the first palaeovalley infill during the initial stages of basin formation. It is principally formed by torrential mixed carbonate-clastic-conglomerates with a similar carbonate-iron-sandstone matrix and coarse-grained sandstones (Frings, 2002; Allyón, 2003). Locally some thin coal seams of minor extent and variable thickness occur. This formation is restricted to the northeastern and western margins of the basin.

The *Pastora* Fm. (85 - 200 m) is composed of a swamp facies with significant coal deposits (up to 20 m thick) in the western side of the basin (Allyón, 2003). The deposits intercalate with fluviatile coarse-grained sandstones and conglomerates, in which abrupt lateral facies changes occur. A NE-trending lake formed in the central parts of the palaeovalley, interpreted as the source for organic-rich shales (Wagner, 1971; Méndez-Cicilia, 1985). Allyón (2003) mentions six shale horizons (kaolinitised ash layers) from this formation.

Organic rich shales characterised by the occurrence of *Leaia baenschiana* (phyllopod), fish scales and floating plant debris mark the base of the *Cascajo-Roguera* Fm. (150 - 175 m) (Allyón, 2003). This sand-bearing shale to fine-grained sandstone succession reflects the expansion of the lacustrine facies throughout the basin, and the termination of the significant coal accumulation. In the upper parts of the formation, fluvial (plane parallel and cross-stratified) and swamp facies dominate.

Immature sandstone beds with frequent interbedded organic-rich lacustrine shales all of regular thickness and abundant fossil content characterise the *San José* Fm. (75 - 90 m). Within are five coal seams, four of which at the top of the succession, each between 50 and 60 cm thick. The upper seams form a further exemplary stratigraphic marker, abundant with characteristic fossil flora (Allyón, 2003).

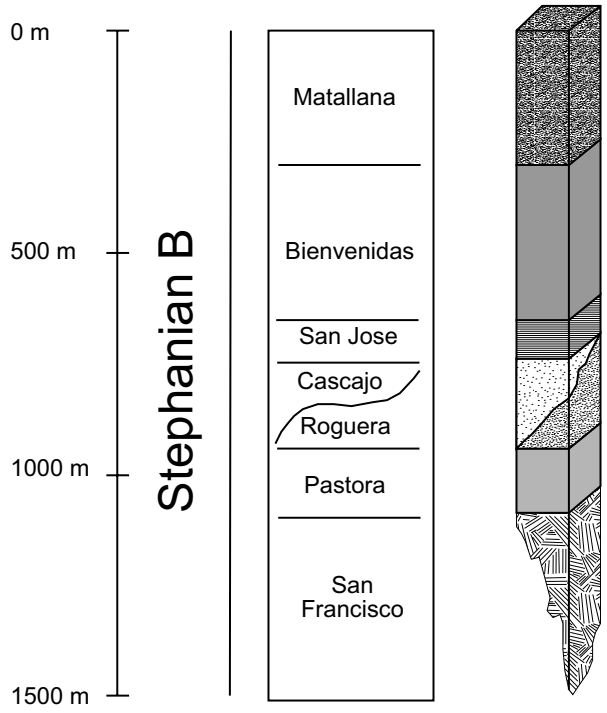


Figure 3.3.1-2: Sedimentary column of differentiated Stephanian sediments in the Ciñera-Matallana Coal basin. Modified from Wagner & Artieda (1970).

The *Bienvenidas* Fm. (350 - 380 m) is composed of a sandstone component, thicker than the underlying formation. The sandstone has a channelled base and contains transported plant debris. Fluvial conglomerates are also common. Five intercalated coal seams between 30 to 120 cm thick are recognised (Allyón, 2003).

The uppermost succession, the *Matallana* Fm. (up to 275 m) is composed of dominantly fluvial facies. Coarse-grained sandstone beds are up to tens of metres in thickness and containing substantial accumulations of plant debris (including tree trunks) alternate with carbonaceous shales, "seat-earth" horizons and some faunal bearing lacustrine levels (Allyón, 2003).

### *3.3.2 La Magdalena Basin stratigraphy*

In the southwestern part of the study area the La Magdalena Coal Field forms an E-W trending, highly tectonised half graben structure. The basin unconformably overlays both Precambrian rocks of the Narcea Antiform and pre-Variscan Palaeozoic strata along the southern margin of the Cantabrian Zone (figure 3.3.2-1).

The coal field is made up of an estimated 1500 m of basin fill composed of clastic continental rocks: conglomerates, sandstones and shales with intercalated coal seams found in three sedimentary units (Leyva et al., 1984). The earliest units result from debris-flow origins composed of paraconglomerates and interbedded coal seams. Paraconglomerate clast constituents are derived from Precambrian aged sediments. The second unit is composed of conglomerates, iron sandstones and shales, sporadically

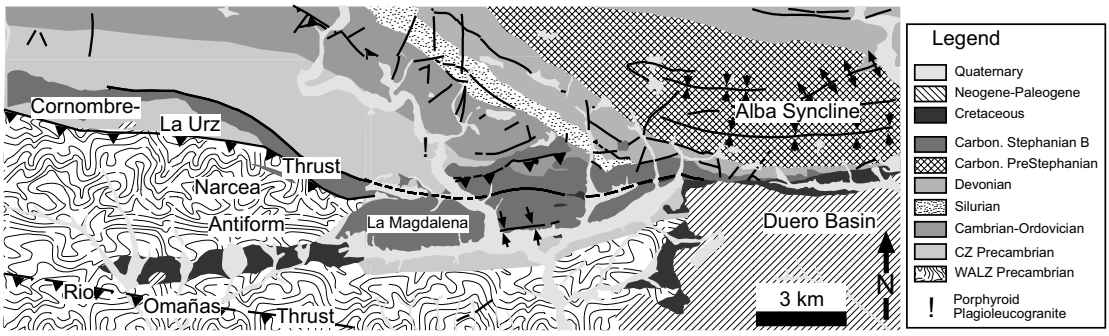


Figure 3.3.2-1: Undifferentiated Stephanian sediments of the La Magdalena Coalfield in their present geologic setting. Modified from Leyva et al. (1984) and Martín-Parra (1989).

deposited in braided corridors of a fluviolacustrine regime. The third unit is composed mainly of canalised iron-sandstones from the distal part of alluvial fan deposits (Leyva et al., 1984; Colmenero & Prado, 1993). Fossil flora constrain the sediments to Stephanian B in age.

### *3.3.3 Rucayo Basin stratigraphy*

The Rucayo basin is fault controlled, and linear trending (E-W). Where it occurs, it obscures the León Line. Three units totalling ~ 220 m in thickness have been realised (figure 3.3.3-1; Alonso et al., 1991). The first unit (~ 80 m) lies unconformably on the underlying Palaeozoic basement. It is composed of quartz conglomerate facies,

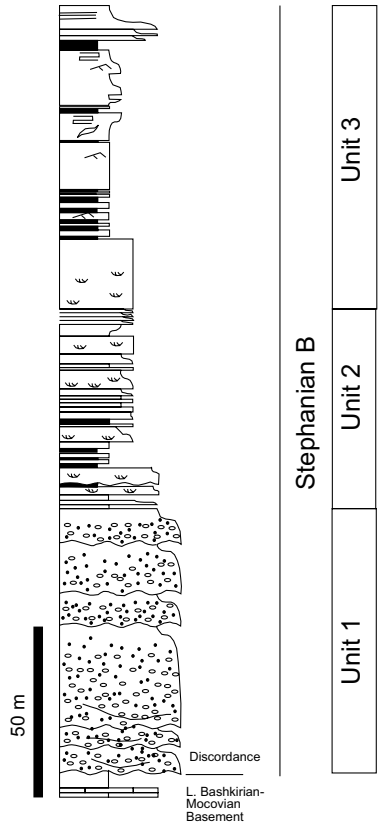


Figure 3.3.3-1: Stephanian Rucayo Basin stratigraphy. Modified from Navarro et al. (1987).

accumulation, which conformably overlay the Utrillas Fm. are associated with Late Cretaceous (Cenomanian) transgression having reached at least into the southernmost parts of the present Cantabrian Mountains. In the southwest corner of the study area isolated accumulations of siliceous sediments reach up to ~ 150 m. Siliceous and carbonate accumulations at the northern margin of the Duero basin together reach to between ~ 150 to ~ 550 m in thickness (figure 3.4-1; e.g. Lobato et al., 1984; Leyva et al., 1984; Martín-Parra, 1989), though E of the sampling area they accumulate up to ~ 1000 m in thickness (Evers, 1967).

## 3.5 Cenozoic stratigraphy

Tertiary sediments are in discordant contact with all Precambrian to upper Mesozoic basements in the study area (e.g. Lobato et al., 1984; e.g. Leyva et al., 1984; Martín-Parra, 1989). Two isolated Neogene aged accumulations of undifferentiated gravels and sands, up to ~ 150 m in thickness cap Precambrian sediments of the Narcea Antiform and its Cretaceous cover in the extreme southwest of this study's sampling area, (Martín-Parra, 1989). Terrigenous sediments with mostly siliceous clasts (see figure 3.5-1) up to ~ 2150 m are evidenced in three systems (Leyva et al., 1984) in the Duero Basin (S of the sampling area).

Locally a coarsening-upwards siliceous succession of up to ~ 750 m (Alonso et al., 1995) is evidenced in the lowermost Palaeogene aged (Leyva et al., 1984) Vegaquemada Fm. The Vegaquemada grades into an additional ~ 1200 m of sandy conglomerates of the La Robla system (Upper Palaeogene (?) to Neogene: see Leyva et al., 1984). An erosional

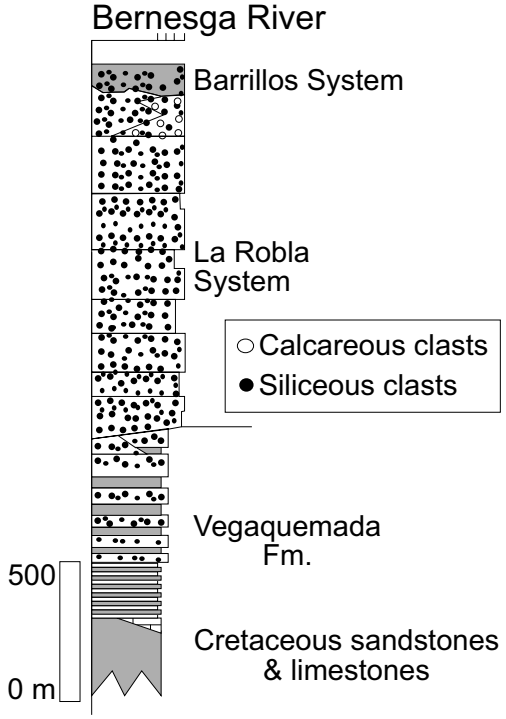


Figure 3.5-1: Stratigraphic section for the Cenozoic sediments of the Duero Basin along the Bernesga River in the south of this study's sampling area. Modified from Alonso et al., 1995.

hiatus defines the boundary between alluvial sands of the La Robla system and a second (Upper Miocene: Leyva et al., 1984) alluvial fan system, the Barillos systems, with total accumulations of ~ 200 m.

The clastic components of these Cenozoic systems were generally supplied from the N to NE (e.g. Alonso et al., 1995; cf. Andeweg, 2002), though Palaeozoic siliceous clasts (e.g. La Robla system) show at least a partial NW source (Alonso et al., 1995). Additionally, at least part of the sandy materials were sourced from the erosion of Cretaceous sands; the La Robla system's characteristics evidence a longitudinal infill of a subsiding trough parallel to the mountain front. For further details of the sedimentation of the margin of the Duero Basin in the study area, see Evers (1967), Lobato et al. (1984), Leyva et al. (1984), Alonso et al. (1995).

which grade heterogeneously and discontinuously to sandstone layers. The second unit (57 m) is composed of fining upwards sandstones and shales with intercalated coal seams. The uppermost succession (83 m) also shows a fining upwards sandstone-shale succession intercalated with coal seams. These successions are interpreted to originate from increasingly distal alluvial fan deposition in a fluvial-lacustrine setting (Alonso et al., 1991). Fossil microflora constrain basin development to Stephanian B times (Horvath, 1985).

## 3.4 Mesozoic stratigraphy

Pre-Cretaceous Mesozoic sedimentary accumulations are conspicuously absent in this study's sampling area. Mixed siliciclastics and carbonates do however outcrop along both the northern and eastern margins of the subaerially exposed parts of the Cantabrian Zone (Aramburu & Bastida, 1995).

Heterogeneously distributed along the southern margin of this study's sampling area, Cretaceous (Albian-Turonian: Leyva et al., 1984) haematite stained quartz sandstones of the Utrillas Fm. unconformably overlay a peneplained erosional surface (Evers, 1967), which in this study's sampling area affects Precambrian rocks of the Narcea Antiform, (e.g. Leyva et al., 1984) and pre-Stephanian Palaeozoic rocks of the southernmost southern Cantabrian Zone (e.g. Lobato et al., 1984), and their Stephanian covers (e.g. Lobato et al., 1984; Leyva et al., 1984; Martín-Parra, 1989). Carbonate sediment

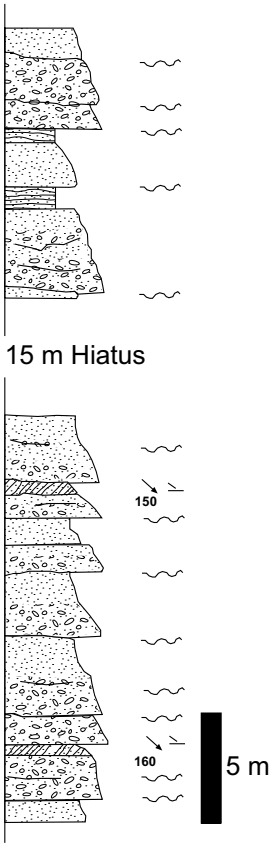


Figure 3.4-1: Cretaceous stratigraphy in the south to southwest of this study's sampling area. Modified from Martín-Parra (1989).

# 4 Structural setting

Structural evolution of geologic entities such as basins and orogenic belts impose characteristic imprints at various scales upon their own thermal evolutions. Structures attributed to late Neoproterozoic (Cadomian: Nägler et al., 1995; Díaz-García, 2006), through Variscan (Julivert, 1971; Pérez-Estaún et al., 1988), to Cenozoic (Alonso et al., 1995; Pulgar et al., 1995; Capote et al., 2002) activity are visible in allochthonous units of the eastern West Asturian-Leónese Zone, the southern Cantabrian Zone, their transitional unit, the Narcea Antiform, the southern Central Coal Basin as well as in Stephanian, and Cenozoic covers. As a result of the complexity imposed by this arrangement, separate treatment of the structural settings for these units is required. The structural setting of the southwestern Cantabrian Mountains is depicted in figure 4-1.

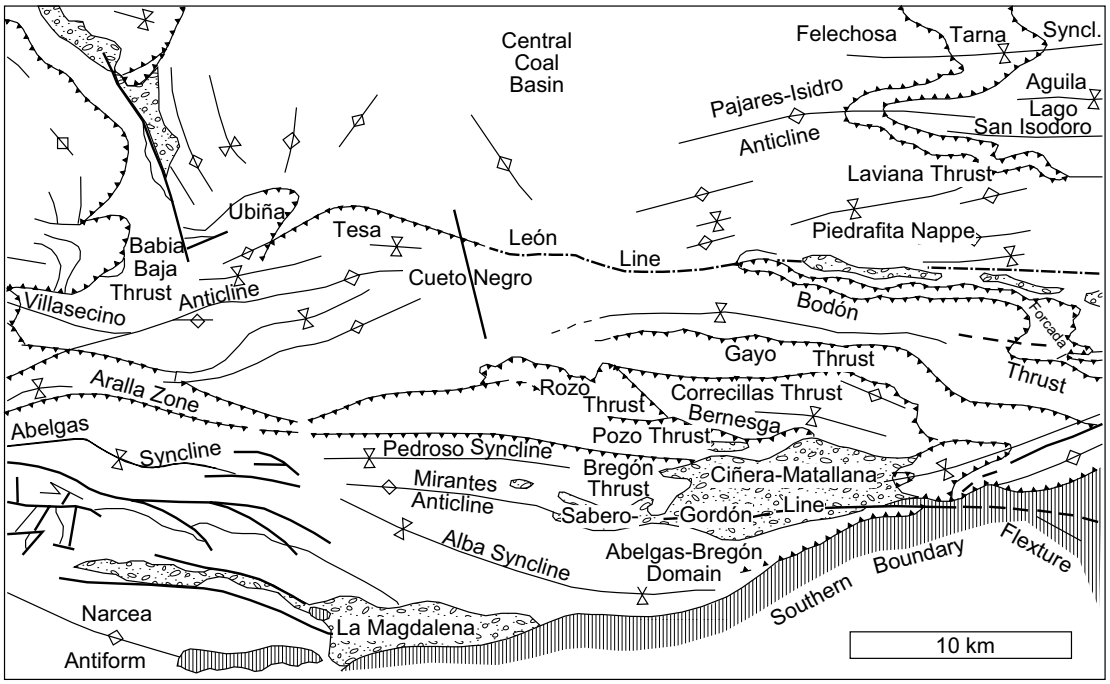


Figure 4-1: Structural overview of the southwestern part of the Cantabrian Mountains including the Precambrian Narcea Antiform; the Palaeozoic southern Cantabrian Zone and Central Coal Basin units and their Stephanian and Mesozoic to Cenozoic covers. Modified from Savage & Boschma, 1980).

## 4.1 Cantabrian Zone

Detailed investigations of the structural setting in the Cantabrian Zone are made by Julivert (1971), Pérez-Estaún et al. (1988, 1991), amongst others. Initial investigations date back to the works of Loetz (1956), de Sitter (1962) and Evers (1967) amongst others. Veselovsky (2004) and Dietrich (2005) each conducted detailed investigations into the evolution of adjacent parts of the southern Cantabrian Basin, in which for pre-Stephanian Palaeozoic strata of the study area, the most recent balanced cross-sections are published. In order to minimise duplication of the cannon of structural

assessments in northwest Iberia, the following pages divulge a brief synopsis of the structural setting initially presented by de Sitter (1962), Wagner, (1966) Evers (1967), Julivert (1971), and Perez-Estaún et al. (1988), amongst others. Summaries by Gasparrini (2003) and Veselovsky (2004) are used as the framework for the following exposition of structural domains in the southern Cantabrian Zone.

The Cantabrian Zone is a system of closely related thrust sheets linked by geometries, kinematics and mechanics (figure 4.1-1; Veselovsky, 2004). Basinal evolution of the southern flank of the Cantabria-Asturian Arc (southern Cantabrian Zone) is characterised by thin-skinned tectonics, with the main detachment horizon located at the base of the Lower Cambrian Lancara Fm. (Julivert, 1971; Pérez-Estaún et al., 1988). Some minor décollement surfaces occur at higher stratigraphies.

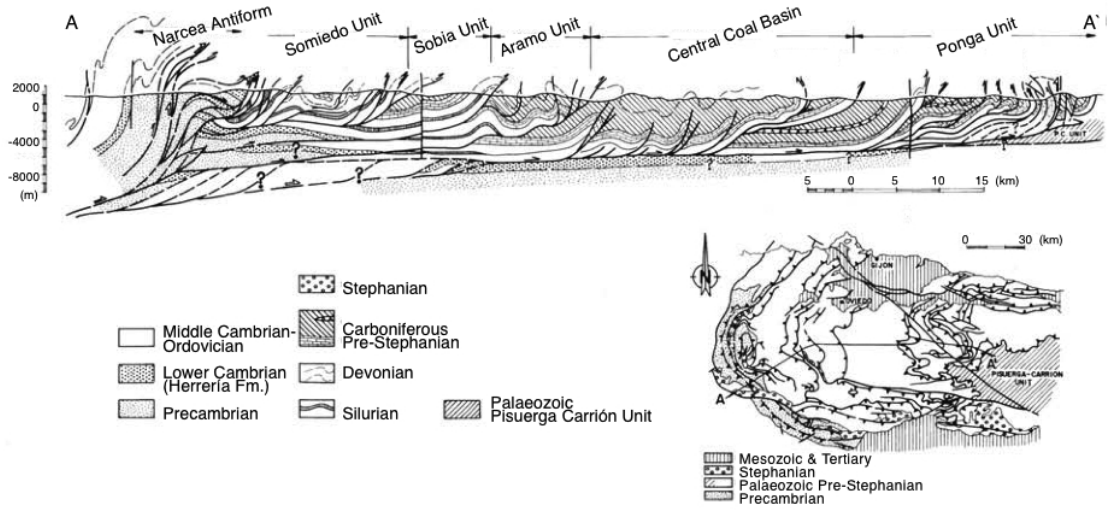


Figure 4.1-1: Geological cross-section through the Cantabrian Zone (after Pérez-Estaún et al., 1994). The deformation style is "thin-skinned". Note the thrusting of the Narcea Antiform onto Cantabrian Zone components. See figure 2.2-1 for the western extension of the cross-section.

During Variscan time, the pre-Stephanian Palaeozoic succession succumbed to strong deformation by imbricate thrusts and cogenetic folds, as well as, late, subvertical faulting (Ábalos et al., 2002). The structural organisation of the Cantabrian Zone results from interference between adjacent thrust sheets, arcuate folds and older radial folds, which cross-cut an older fold set (Julivert, 1971; Julivert & Marcos, 1973). The first fold set, at least partially results from the development of duplexes and antiformal stacks (Alonso, 1987; Pérez-Estaún et al., 1988). Development of hanging-wall ramp anticlines, duplexes and antiformal stacks subsequently hindered the deformation phase (figure 4.1-2; Veselovsky, 2004) resulting in the tightening of existing folds about the arc, and the commencement of folding of individual thrust sheet within the arc (Hirt et al., 1992). Newer folds generally overprinted older ones and as a result were longitudinally oriented with respect to precursor folds and thrusts (Veselovsky, 2004). Radial folds superposed on the above structures are most pronounced at the core of the Cantabrian-Asturian Arc and diminish in amplitude away from the core (Hirt et al., 1992).

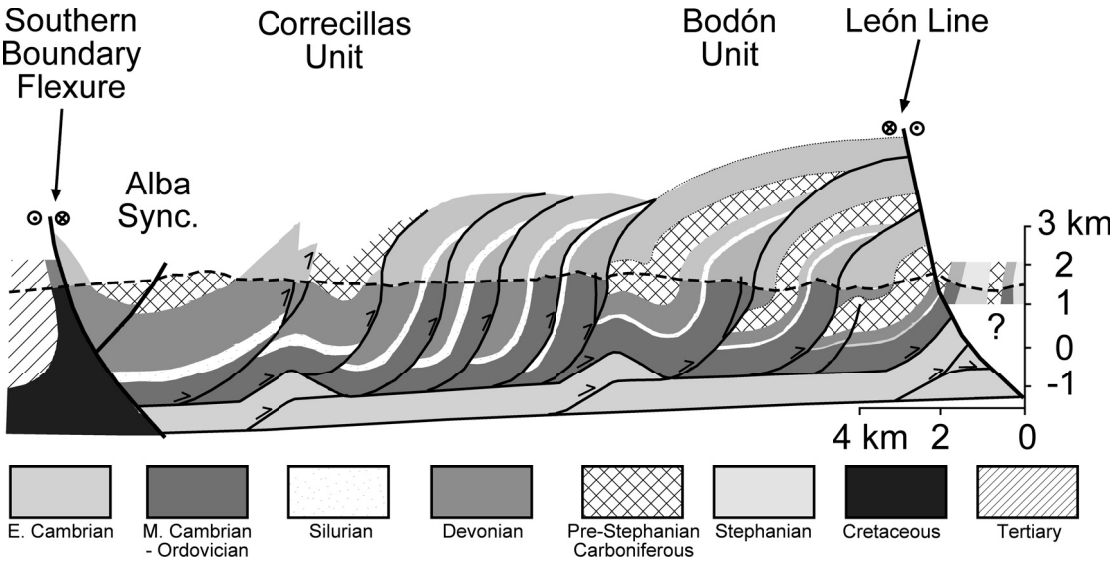


Figure 4.1-2: Balanced cross-section through the southern Cantabrian Zone of the study area. Modified from Veselovsky (2004).

Geometries in the southern Cantabrian Zone exemplify those typical of increased basinal friction (c.f. Mitra, 1986; Nieuwland et al., 2000). They include overlapping ramp anticlines, curved ramps, imbricated thrust sheets, duplexes and anticlinal stacks resulting from a "piggy-back" thrust mechanism with a forward-breaking sequence of individual thrust sheets, and accretion within the basinal Herrería Fm. (Veselovsky, 2004). Pre-Mesozoic structural units present in the southern Cantabrian Mountains of the study area include: The Bodón Unit and the Somiedo-Correcillas Unit, Narcea Antiform and Stephanian basins. Cretaceous covers and the Duero Basin comprise the post-Palaeozoic sediments, in which wholly post-Variscan structures are expressed.

### *4.1.1 Bodón Unit*

The Bodón Unit comprises the Gayo, Bodón and Forcada thrust sheets (figure 4-1; Evers, 1967; Marcos, 1968 a), in which three-kilometre-scale open folds are visible (Veselovsky, 2004). The uppermost Gayo Thrust Sheet is bound by the Correcillas Thrust to the South and the Gayo Thrust to the North where thrusting occurs at the base of the Láncara Fm. Successions in the thrust sheet are over 1700 m thick (Evers, 1967; Lobato et al., 1984). The Bodón Thrust Sheet, in the study area, is between 1900 - 2300 m thick (Evers, 1967). In the East, the Bodón Thrust, separating Bodón and Forcada thrust sheets, occurs at the base of the Hererria Fm. (Julivert, 1971 and references therein); the Bodón Thrust traces the base of the Láncara Fm. in the west. Alonso & Suárez-Rodríguez (1991) assume staircase geometry of the thrust, as tracing the course of the detachment yielded locally difficult. North of Milaró, the Bodón Thrust Sheet is in fault contact with the Moscovian Lena Group of the Central Coal Basin Unit (Gasparini, 2003: Apendix 1). The lowermost Forcada Thrust Sheet is bound to the North by the Forcada Thrust. The nappe's successions are 500 - 800`thick

(Evers, 1967). The Forcada Thrust occurs at the base of the Láncara Fm., and in the East is coincident with the León Line Fault System (Gasparrini, 2003). East of the study area, the Bodón Unit is separated from the Esla Unit by the Porma Fault. To the W the Bodón Unit is named the Sobia Unit.

### *4.1.2 Correcillas Unit*

The Correcillas Unit, separated from the Bodón Unit to the North by the Correcillas Thrust (figure 4-1), is tectonically complex, containing a 1700 - 1900 m thick succession spanning Cambrian to Carboniferous strata (Láncara to Barcaliente fms.) (Evers, 1967) in which three large-scale structural features are regionally recognisable.

In the north of the Correcillas Unit, the Cambrian to Carboniferous succession of the Aralla-Rozo Thrust Sheet is thrust en échelon in an imbricate fashion (Veselovsky, 2004); the top-most sedimentary units are conspicuously absent after likely being sheared, transported away and eroded (pers. com. Dietrich, 2004). This thrust unit suffers a relatively high degree of total shortening (see Veselovsky, 2004: Figure 3.15). The Aralla-Rozo Thrust Sheet is separated form the northern flank of the Abelgas-Bregón Domain--the Perdroso Syncline--by an unnamed thrust fault. The Pedroso Syncline is relatively shallow, and hosts East trending frontal ramps in each flank (Alonso et al., 1990). The Intra-Asturo Facies Line (see Veselovsky, 2004: Figure 3.5), roughly coincident with the Sabero-Gordón Line, separates the northern and southern flanks of the Abelgas-Bregón Domain.

In the Bernesga River area (central part of study area), the southern flank of the Abelgas-Bregón Domain is represented by a broad synclinorium, the Alba Syncline (de Sitter, 1962). Small-scale thrusting and faulting is common, yet this syncline suffered the least amount of shortening in the southern Cantabrian Zone (Veselovsky, 2004). Here the southern margin of the Correcillas Unit (Southern Border Thrust) is represented by Palaeozoic sedimentary rocks thrusted over Mesozoic to Cenozoic infill of the Duero Basin. East of the study area, the Correcillas Unit, is separated from the Esla Unit by the Porma Fault. To the W, the Correcillas Unit is named the Somiedo Unit.

According to de Sitter (1962), for the Luna River and reservoir area (western part of study area), the aforementioned nappes and thrust sheets merge into a broad and complicated synclinorium the amalgamated Abelgas-Bregón Syncline, Precambrian rocks marking its southern flank, Lower Cambrian strata, its northern flank and Lower Carboniferous rocks exposed between the two. North of the Luna Reservoir, the northern flank of this syncline's Cambrian base is thrust over Serphukovian-Moscovian strata of the Somiedo and Bodón Units. Lower Palaeozoic strata narrowly outcropping at the León Line Fault System with Cambrian strata at its base, in fault contact with the Bodón Unit.

### 4.1.3 Out-of-sequence faults in and about the southern Cantabrian Zone

The León Line Fault System, trending East for ~ 150 km, represents the most prominent of many out of sequence faults in the area (figure 4-1). The eastern part of the fault is found continuously in association with Stephanian B deposits in the Rucayo Fm. In the west, the fault system intersects, and for a short stretch (~ 3 - 4 km) is coincident with the Bodón and Forcada thrusts, then diverges NW. The main fault dips steeply subvertical and is associated with extensive local brecciation and small-scale fault propagation. Julivert (1967) proposed initial movement along the León Line occurred during late Moscovian, in association with the structural development of the Central Coal Basin and Ponga units. Initial sinistral strike-slip movement of the León Line with Permian reactivation as a reverse fault has also been proposed (Marcos, 1968 b; Julivert et al., 1971; Marcos et al., 1979; Heward & Reading, 1980) as the fault's palaeo-expression in addition to reactivation in response to later stage movement(s) (e.g. alpidic orogenesis: Pulgar et al., 1999). Other out-of-sequence faults in the southern Cantabrian Zone include the Sabero-Gordón Line Fault System, the Alba Syncline Backthrust and the Southern Border Thrust (Veselovsky, 2004).

## 4.2 Central Coal Basin Unit

The Central Coal Basin Unit presents a wide outcrop of thick, mainly terrigenous synorogenic Carboniferous successions (Aller & Gallastegui, 1995). Adjacent to the León Line Fault System the succession consists of 1400 - 2700 m of Bashkirian to Kasimovian Lena Group flysch deposits, in a WNW trending marginal basin with the greatest subsidence having taken place East of Canseco (Evers, 1967). The structural setting here is highly complex with several folded anticline/syncline pairs and crossfolded structures (figure 4-1; Evers, 1967). Asymmetric folding of the syn-Variscan orogenic flysch deposits, towards the central folding axis, results in Northward dipping axial planes (Evers, 1967). Most fold axes plunge variably towards the W as a result of W-ward increase in thickness of the Lena Group (Evers. 1967). The main structures in the area adjacent to the León Line Fault System (Piedrafita Unit: after Evers, 1967) are related to East trending folds in the underlying Laviana Thrust Sheet (after Julivert, 1971), a Cambrian to Middle Ordovician sequence exposed in the eastern margin of the basin (e. g. Pérez-Estaún & Alvarez-Marrón, 1990).

At the eastern margin of the Central Coal Basin Unit, adjacent to the Ponga Unit, ~1000 m of Bashkirian-lowest Moscovian flysch deposits of the Fresnedo Fm. conformably overlie ~ 500 m of laminated limestones of the Barcaliente Fm. (Serphukovian) (Pérez-Estaún & Alvarez-Marrón, 1990). In the study area, at the eastern margins of the Laviana Thrust sheet, the Laviana Thrust (Pérez-Estaún & Alvarez-Marrón, 1990) marks the contact between Central Coal Basin and Ponga units. Locally the Barcaliente Fm. is in fault contact with Barrios Fm. along the Vegarada (normal), Cebolledo (normal) and Cofiñal (reverse) faults (Pérez-Estaún & Alvarez-Marrón, 1990). Lena Group flysch deposits conformably overly the Fresnedo Fm. flysch (Pérez-Estaún & Alvarez-Marrón,

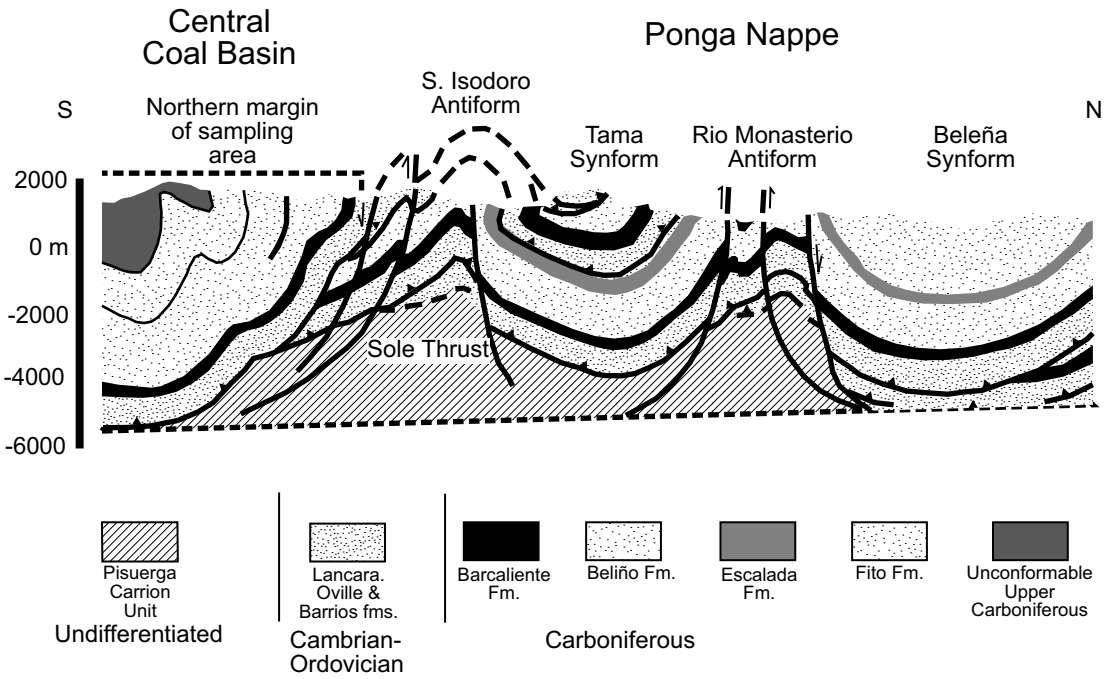


Figure 4.2-1: Geological cross-section through the southeastern Central Coal Basin and southern Ponga Nappe units of the Cantabrian Zone. Modified from Alvarez-Marrón (1995).

1990). Complex synformal/antiformal geometries and crossfolds, as discussed above, prevail both the vicinity of the Laviana Thrust Sheet and in the Ponga Unit (figure 4.2-1; See also Pérez-Estaún & Alvarez-Marrón, 1990: Figure 11; Alverez-Marrón, 1995).

## 4.3 Intramontane and fault-controlled basins (Ciñera-Matallana, La Magdalena and Rucayo basins)

Stephanian Ciñera-Matallana, Rucayo and La Magdalena basins are strike-slip fault controlled basins in the southern flank of the Cantabrian Mountains. They occur within a belt of isolated Stephanian A-C basins (each between 5 and 175 km$^2$ in area), all of which having complex depositional and tectonic histories; where sedimentation began in the Sabero Basin (~ 20 km East of study area: Ayllón, 2003), commenced progressively later for each basin to the W (Heward, 1978). These strike-slip fault related basins, especially the Ciñera-Matallana Basin, are positioned in key sites for unravelling the geological and thermal development during the late stages of the Variscan orogeny (García-López, 1999), and the transition to Permian crustal extension and volcanism (Fernández-Suárez, 2000 b).

### *4.3.1 Ciñera-Matallana Basin*

Details of the structural setting of the Ciñera-Matallana Basin are contained within the unpublished doctoral theses of Méndez-Cecilia (1985) and Villegas (1996), in addition to treatments by Evers (1967) and Wagner (1971). Frings (2002) and Ayllón (2003) each provide updated summaries of the structural setting in the basin. The account presented here follows principally the work of Ayllón (2003) and references therein.

The Ciñera-Matallana Basin is a small intramontane basin (25 km$^2$) located at the southern border of the Cantabrian Mountains in the Correcillas Unit, having developed as a fault-related pull-apart type during latest Variscan time (Frings et al., 2004).

The present limits of the Ciñera-Matallana Basin, similar to other Stephanian basins of the Asturian unconformity (Evers, 1967), are mostly tectonically controlled (figure 4.3.1-1; Frings, 2002; Ayllón, 2003); hence, the present basin morphology does not reflect its initial shape (Ayllón, 2003). In the western half of the basin are three synclines with S-dipping axial planes and shallow, E-oriented axes, plunging in an E-direction (figure 4.3.1-1; Wagner, 1971; see also Frings, 2002; Ayllón, 2003). Synclines are separated by weak anticlines having formed along pre-existing, thoroughly faulted, horst blocks (Ayllón, 2003). The structure of the basin simplifies to the E. Synclines merge into a large synclinorium with shallower dipping limbs (Frings, 2002; Ayllón, 2003). Fault planes preferentially strike East.

Compressive/transpressive deformation, metre- to decametre-scale thrust and folds evolved, either in association with Variscan (Wagner & Artieda, 1970; de Sitter, 1962) and/or alpidic (Villegas, 1996) tectonism.

Coal beds acted as detachment zones, evidenced by extensive shearing in the Pastora Fm. Locally, slip also occurred at discordant surfaces between Stephanian and older Palaeozoic rocks. Reactivation of the Sabero-Gordón Line Fault System during Miocene alpidic uplift of the Cantabrian Mountains resulted in further deformation of this and other Stephanian basins (Alonso et al., 1995; Villegas, 1996; Pulgar et al., 1999). For the most part, S-dipping thrusts are considered to have formed during this latest deformation phase (Villegas, 1996).

### *4.3.2 La Magdalena Basin*

Published work regarding the structure of the La Magdalena Basin is scarce. Heward (1978) mentions a general similarity of this basin with those of the Ciñera-Matallana and Sabero (see Ayllón, 2003) basins. The La Magdalena Basin is comprised of an estimated ~ 1500 m (figure 4.3.2-1; Leyva et al., 1984) of Stephanian B (e.g. Wagner, 1970) brackish marine horizons, alluvial fan and lacustrine deposits, interrupted by thin coal seams and thick conglomerate horizons (Heward, 1978), in fault bound, and/or unconformable contact with underlying Precambrian to Upper Devonian sediments.

The structure of the La Magdalena basin is that of a relatively tightly folded, E-W striking syncline with a failed southern limb due to Northward directed overthrusting by a block of Precambrian aged sedimentary rocks from the Narcea Antiform from the South (Leyva et al., 1984 b; cf. Wagner, 1970), whilst its northern flank has likely been thickened by a number of minor thrust faults which repeat parts of the Stephanian B succession (Wagner, 1970). The orientation of the basin is related to the Cornombre-La Urz Fault, possibly originating previous to the second-phase Variscan deformation

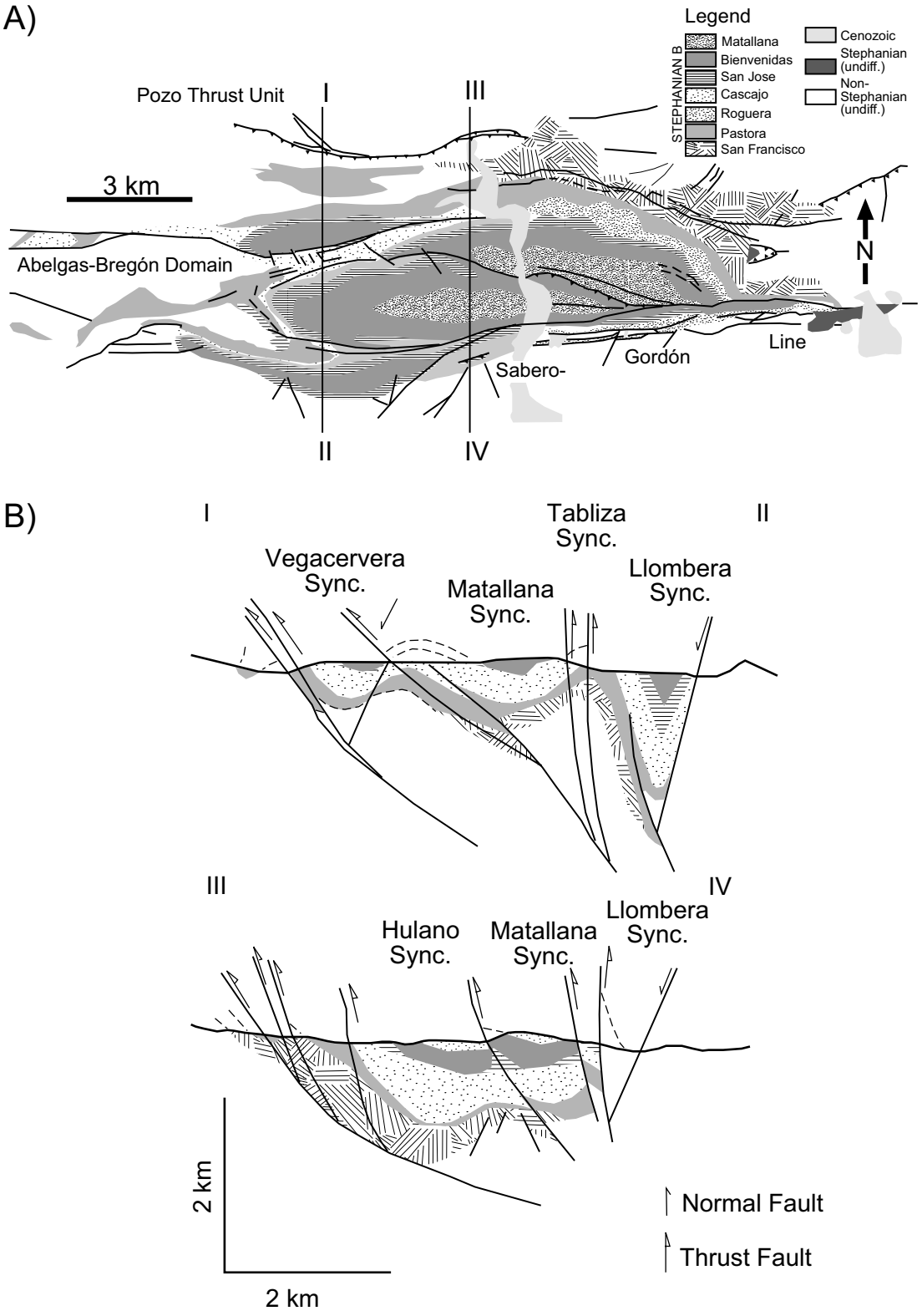


Figure 4.3.1-1: Structural Setting of the Ciñera-Matallana Coal Basin. A) Surficial distribution of the structures and sedimentary units. B) Cross-sections in the western limb of the basin. Modified from Villegas, 1996 and Ayllón, 2003.

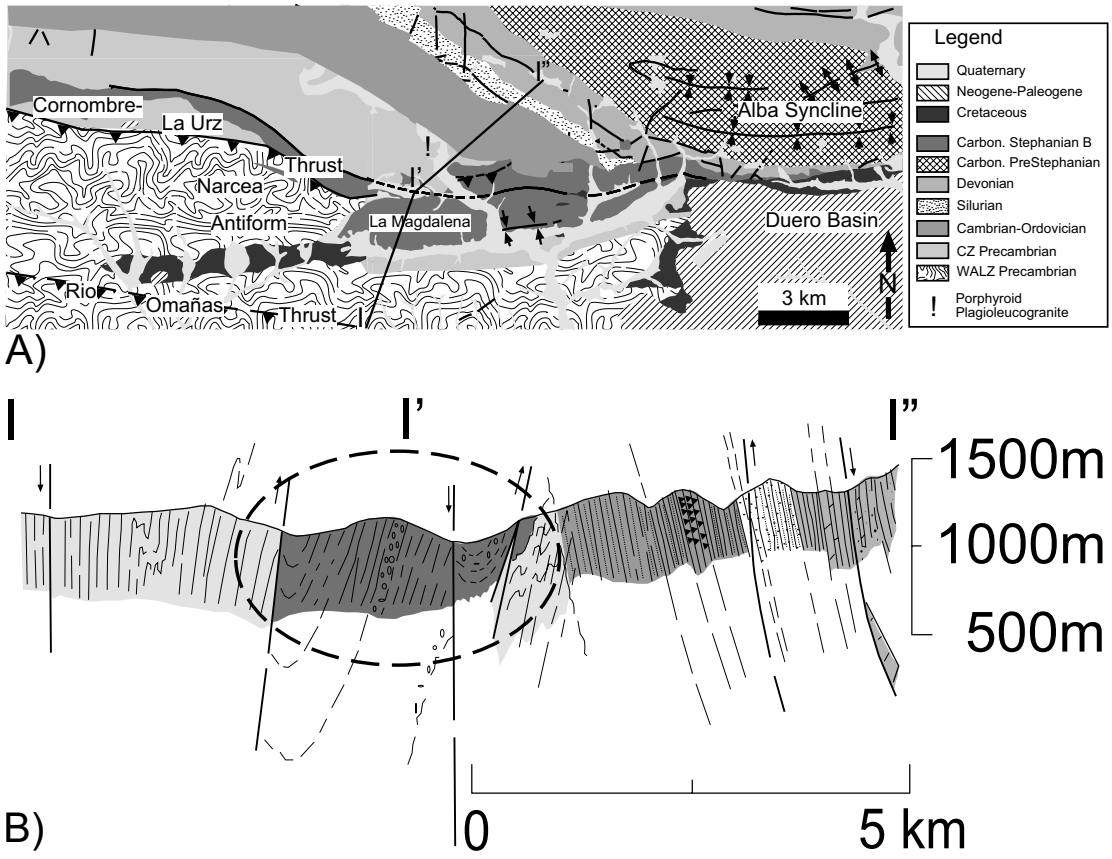


Figure 4.3.2-1: Structural of the La Magdalena Basin. A) Spatial distribution of the La Magdalena Coalfield with respect to the regional geological context. B) Cross-section through the southwest of the study area inclusive of the Narcea Antiform, La Magdalena Coalfield and southernmost Alba Syncline. Dashed circle defines the limits of the La Magdalena Basin in the cross-section. Map modified from Leyva et al. (1984); Martín-Parra (1989); Alonso et al. (1990). Cross-section modified from Leyva et al. (1984).

(Martín-Parra & Pérez-Estaún, 1989), which further Eastward in the study area may extend as the Southern Border Thrust (c.f. Veselovsky, 2004), both of which showing evidence of post-Variscan reactivation (Leyva et al., 1984).

### *4.3.3 Rucayo Basin*

Little information is available regarding structures in the Rucayo Basin (Rucayo Unit: after Evers, 1967; Canseco Unit: after Alonso et al., 1990) beyond that published by Wagner, (1966) and Evers (1967). Thus, the synopsis given here follows that presented by Evers (1967).

Rucayo Fm. mixed carbonate and clastic deposits including mudstones, sandstones, coal beds and quartz conglomerates of the asymmetric Rucayo Basin (Stephanian B: after Alonso, 1990), rest unconformably over Cambrian to Moscovian strata with total thicknesses of 500 m at the type section, to 800 m elsewhere in front of the Forcada up-thrust.

Between Canseco and Rucayo a sharply folded synclinal structure exists, but normally the stratification in the Rucayo Basin is distorted. The contact between the molasse and the underlying rocks is also often difficult to distinguish. The Forcada Thrust Fault, at many places disturbed, marks the southern boundary of the basin. Compaction is interpreted to be unimportant to the structural setting since the bulk of the basin is composed of poorly sorted quartz conglomerates, and only the lowest part consists of thin mudstones and few coal seams (Evers, 1967).

Tectonism was mainly restricted to normal faulting along fundamental weakness zones in the underlying Palaeozoic strata. Development of the basin is associated with faulting at the León Line Fault System. Resulting displacement along the fault was small but locally continued after emplacement (figure 4.3.3-1). Strongly out-wedging conglomerates in the northern limb of the molasses basins suggest at least partial syn-sedimentary movement associated with the fault.

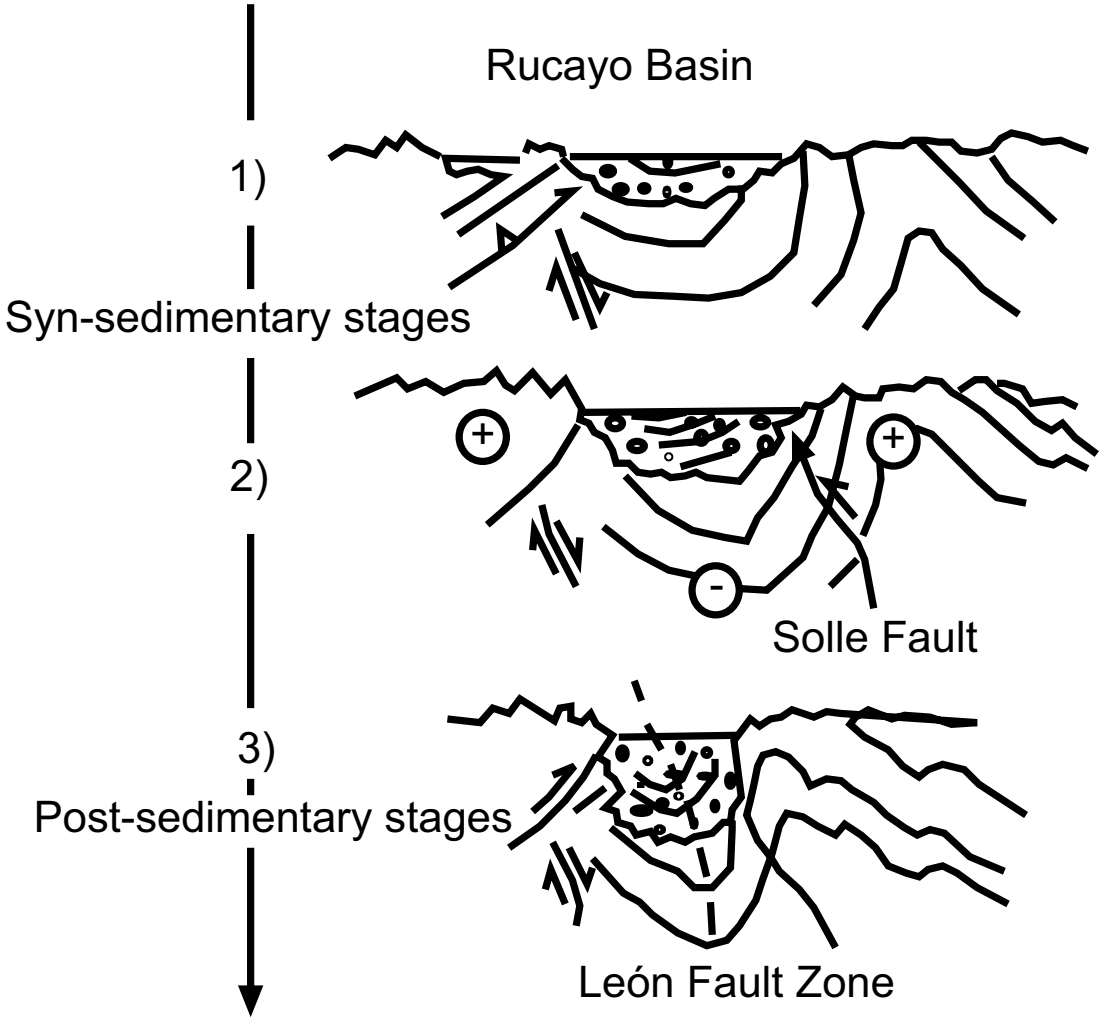


Figure 4.3.3-1: Structural evolution of the Rucayo Basin. Modified from Evers (1967).

Wagner (1966) proposed that Sabero (outside study area) and Rucayo fms. were equally deposited over an extensive, tectonically unrestricted region, and that post-depositional, compressive tectonism followed by a long period of erosion might have exclusively created the basin. Evers (1967) rejects Wagner's (1966) hypothesis based on first order evidence summarised above, instead favouring an intramontane fault controlled origin.

## 4.4 Narcea Antiform

The eastern West Asturian-Leónese Zone consists of a succession of Precambrian metasedimentary rocks (Julivert, 1978). Pérez-Estaún (1973, 1978) defines three units: a lowermost interbedded porphyritic volcanic rock, sandstone and phyllitic slate complex; a turbiditic phyllitic slate and greywacke complex; all overlain by a phyllitic slate and interbedded sandstone unit (Mora Fm.: after Comte, 1959). The estimated total thickness is > 1500 m (Liñan et al., 2002) as the true basement does not outcrop in the area. These metasediments exist locally in the eastern arm of the Narcea Antiform, a broad arc stretching landward from the Costa Verde of northern Spain, to the study area (Julivert, 1971), which separates the West Asturian-Leónese Zone (Variscan internal zone) from the Cantabrian Zone (Variscan external zone) (Lotze, 1945).

Locally, the boundary between northern and southern flanks of the Narcea Antiform is defined as the Cornombre-La Urz Thrust Fault (see figure 4.3.2-1 A); Perez Estaún, 1971; Narcea Fault: after Julivert, 1971). Precambrian rocks of the northern flank (Cantabrian Zone) are overthrusted by the southern flank (West Asturian-Leónese Zone).

Structurally, Precambrian Mora Fm. in each flank display characteristic differences evidencing a discordant tectonic setting visible along the whole Narcea Antiform (Lotze, 1956; de Sitter, 1962; Matte, 1968; Martín-Parra, 1989). The southern flank has been proposed to have been affected by a compressive deformation phase in an uppermost Precambrian (Cadomian) orogenic cycle (Lotze, 1956; Valladares et al., 2002 and citations therein; cf. Fernández-Suárez et al., 2000 b; Díaz-García, 2006), which developed as an Andean-type destructive plate margin about 645 - 540 Ma in the northern Armorican Massif type area (Ábalos et al., 2002 and citations therein).

In the study area, Cadomian orogenesis is inferred by foliation and deformation in the metasediments (Lotze, 1945; Matte, 1968; Marcos, 1973; cf. Díaz-García, 2006), and the existence of abundant volcanic and volcanoclastic rocks in adjacent areas of the West Asturian-Leónese Zone flank of the Narcea Antiform (Martín-Parra, 1989; cf. Fernández-Suárez et al., 2000 b). Contrastingly, in the northern flank, Northward dipping internal sedimentary structures (Pérez-Estaún, 1975; Leyva, 1984) in Neoproterozoic rocks discordantly overlain by Lower Cambrian Herrería Fm. are maintained (see figure 3.1-2: lower unit).

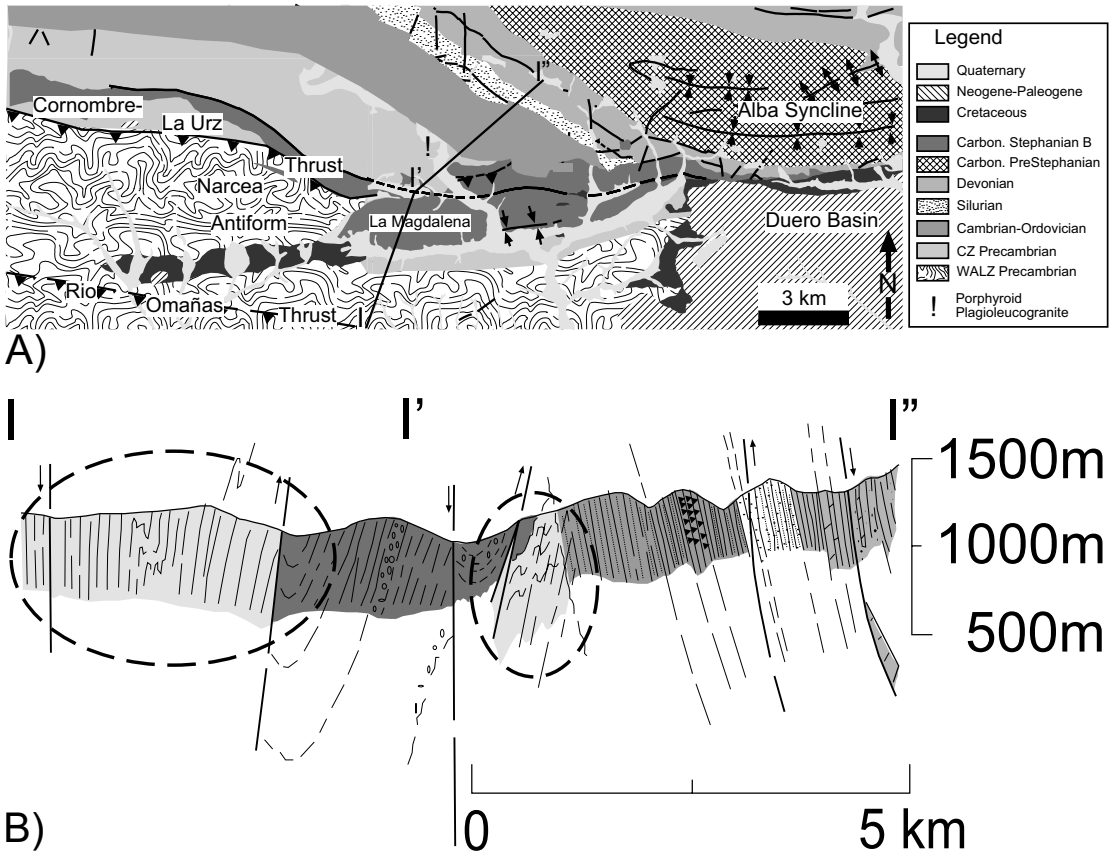


Figure 4.4-1: Structural setting of the Narcea Antiform. A) Regional geological context. B) Cross-section through the southwest of the study area inclusive of the Narcea Antiform, La Magdalena Coalfield and southernmost Alba Syncline. Dashed circles define the limits of the northern and southern flanks of the Narcea Antiform in the cross-section. Map modified from Leyva et al. (1984); Martín-Parra (1989); Alonso et al. (1990). Cross-sectction modified from Leyva et al. (1984).

### *4.4.1 Variscan associated deformation*

Marcos, (1973) defined three principal deformation phases of the Variscan orogeny for the West Asturian-Leónese Zone. Locally, evidence regarding Variscan $D_1$ and $D_2$ deformation phases in the southern flank of the Narcea Antiform is difficult to discern (Martín-Parra & Pérez-Estaún, 1989), though after Pérez-Estaún (1978), Pulgar (1980 a, b) and Bastida (1980), deformation in the southern flank of the Narcea Antiform may include:

a) Asymmetrical $D_1$ folds, which towards the external zone of the cordillera, were accompanied by a penetrative $S_1$ axial plane foliation; b) $D_2$ related thrusts with curved hinges and crenulations (deformation extending Southward from major thrust faults for ~ 2 km (see Martín-Parra, 1989: Figure 18) and $D_3$ deformation, which resulted in local replication and amplification of previous structures, giving rise to long-wavelength folds with subvertical axial planes, as well as the plate-wide arcuate shape of the Iberian Massif (c.f. Gutiérrez-Alonso et al., 2004 a) and the resulting arcuate structure of the southern limb of the Narcea Antiform (Leyva et al., 1984); c) "kinkband" and "chevron" type folds, and fractures affect the subhorizontal layering (Martín-Parra, 1989).

The intensity of Variscan deformation in the northern limb of the Narcea Antiform was much lower than in the southern limb (Martín-Parra, 1989). Here, only localised penetrative cleavage occurs in association with $D_1$ deformation. Foliation does not develop. Locally, $D_2$ deformation in Mora Fm. of the northern flank of the Narcea Antiform is not discernable. However, thrusts associated with $D_2$ deformation may lie under the Matallana Basin (Leyva et al., 1984), or in association with fractures affecting the syncline in the Ricocastrillo de Ordás Area (Pérez-Estaún, 1975), ~ 18 km W along the Bernesga river. $D_2$ structures affecting the Mora Fm. are evidenced in the Riello Map sheet (Martín-Parra, 1989). In the northern flank of the Narcea Antiform, just as in the southern flank, $D_3$ deformation served to amplify any previous structures and superpose the large-scale arcuate structure on Mora Fm. of the Narcea Antiform (Leyva et al., 1984).

## 4.5 Post-Variscan structures

The Duero basin is a foreland basin associated with Southward thrusting of the Cantabrian Mountains beginning with the Pyrenean collision (Alonso et al., 1995). Periodical reactivation of the northern margin in Cenozoic times is recorded in the distribution of alluvial fan sediments along the rim of the basin.

Figure 4.5-1 summarises the response to Variscan and post-Variscan tectonism in the south to southwest of this study's sampling area. Peneplanation of pre-Cretaceous rocks show they were affected by regional erosion, likely in association with denudation driven uplift of northwest Iberia prior to Late Cretaceous extension and transgression marked by sedimentation. Locally, alpidic structures across the southern margin of the Cantabrian Mountains and in the Duero Basin run parallel to the schistosity in Precambrian sediments and follow a parallel slip sense as Variscan attributed thrusts to movements; thus reactivating and overprinting the Variscan and earlier structures, as well and possibly initiating new structures.

Early Cenozoic (Palaeogene) sediments of the Duero Basin, south of the Ciñera-Matallana Basin are inclined to subvertical or overturned by Southward thrusted Palaeozoic basement of the Cantabrian Mountains, indicating a North trending compressional setting prevailed during the pre-Holocene Cenozoic (Alonso et al., 1995). Neogene sediments show an absence of foreland deformation, being horizontally bedded and undisturbed. Thus, the significance of foreland deformation is limited with respect to the Duero Basin's structural development (Andeweg, 2002). Straight river valleys (e.g. Barrios, Cureño) flowing into the northern Duero Basin, by their surficial expressions, suggest a structural control. However, Andeweg's (2002) investigation of cliffs actively eroded by the Pisuerga and Arlanzon rivers, East of this study's sampling area, yielded not a single deformation related structure.

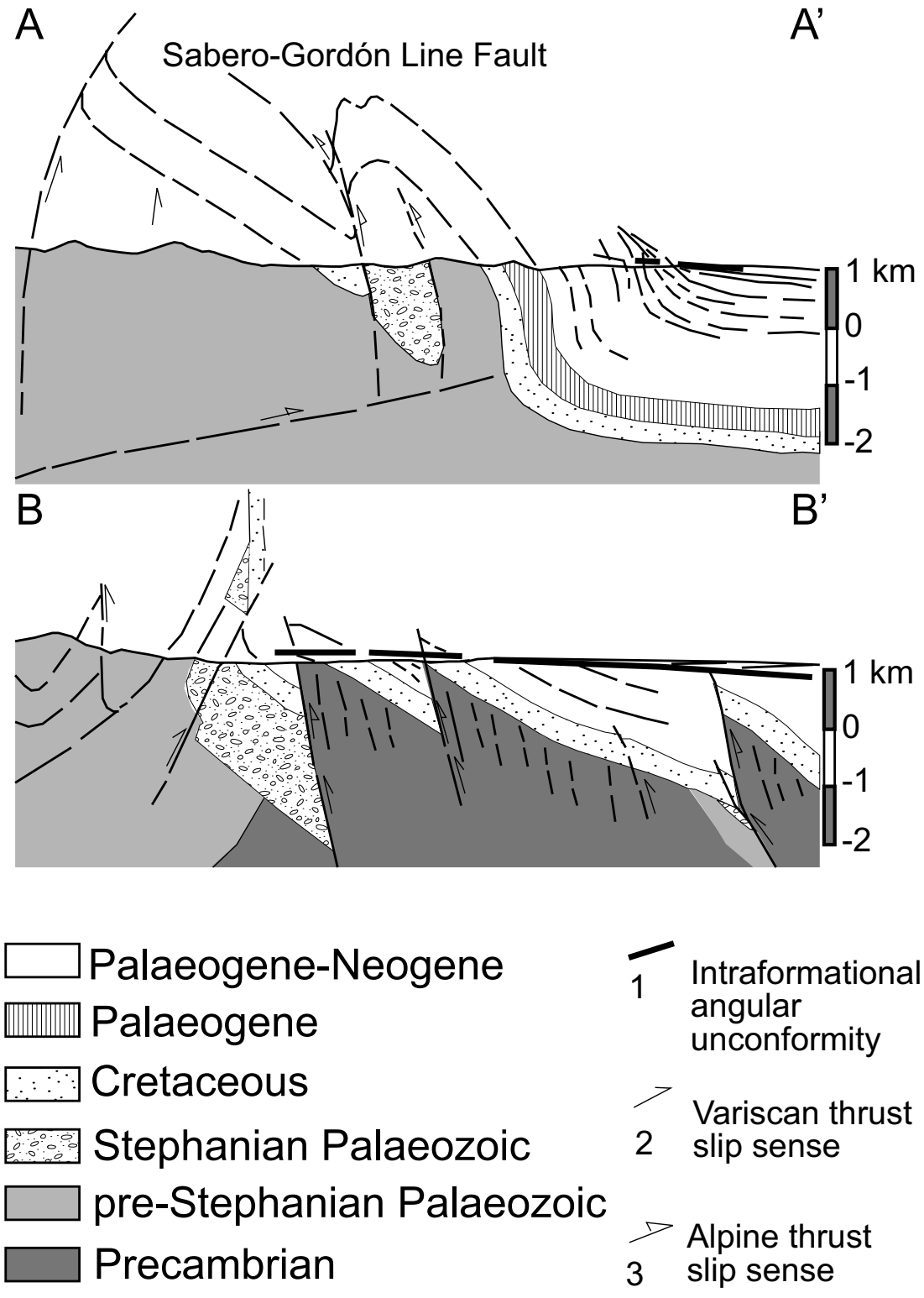


Figure 4.5-1: Cross-sections through the northern border of the Duero Basin, modified from Alonso et al., (1995). Cross-section A-A': between Porma and Esla rivers, 10 km East of this study's sampling area. Cross-section B-B': Along the Barrios River in the southwest of this study's sampling area. Basin geometry markedly differs along the 30 km distance which marks the southern boundary of this study's sampling area.

Seismic reflection (ESCI-N2) through the Cantabrian Cordillera and the northern Duero Basin (figure 4.5-2; Pulgar et al., 1995) also shows that deformation is limited in extent and is concentrated along the southern border of the range. Though loading of the "Iberian" plate under the Cantabrian Cordillera is estimated to be significant (Alonso et al., 1995), an absence of evidence for flexural bending of the "Iberian" plate indicates the crust under the Cantabrian Cordillera and the Duero Basin is either exceptionally strong, transmitting stress to internal regions of Iberia (cf. de Bruijne & Andriessen, 2002), or the basement is extremely weak, resulting in localised isostatic compensation (Andeweg, 2002).

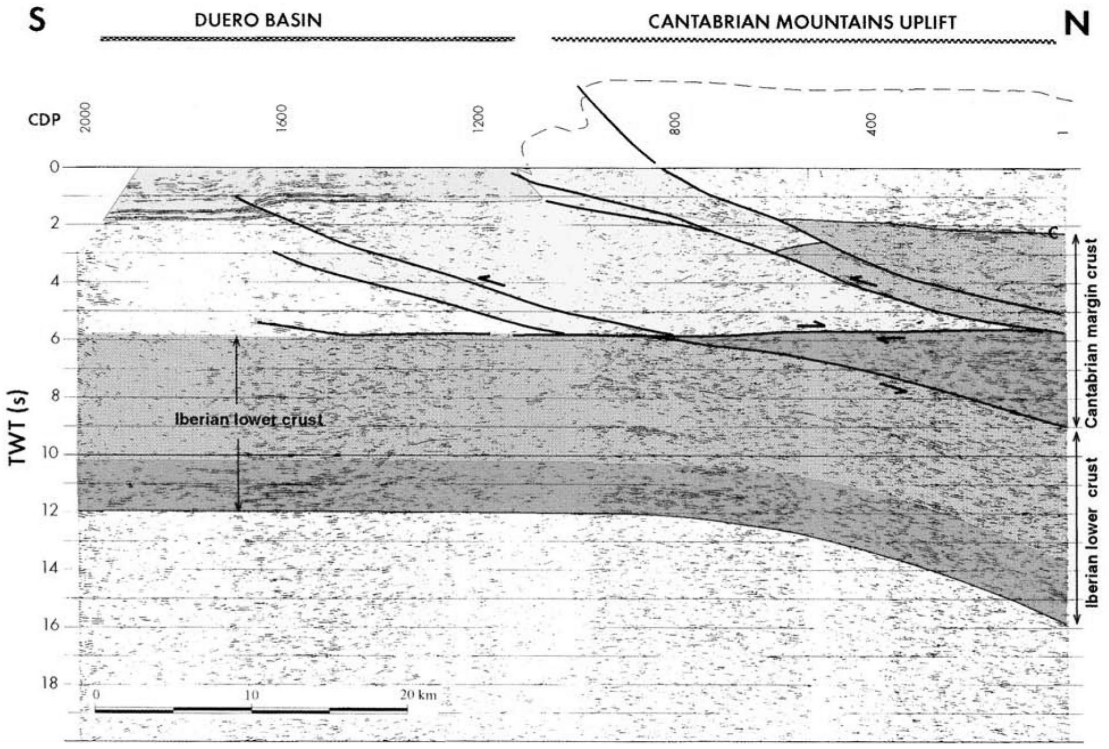


Figure 4.5-2: Deep crustal section seismic reflection line ENCI-N2 showing the alpidic thickening of the lower crust under the Cantabrian Mountains. The Duero Basin (upper left) is recognised from the highly-defined reflectors in the subsurface (Pulgar et al., 1995). Décollment of the Palaeozoic succession is recognised in the right of the image. After Pulgar et al. (1995).

# 5 Metamorphism, peak thermal indicies and mineralisation in northwestern Iberia

## 5.1 Volcanism

Evidence of volcanism in the Narcea Antiform and West Asturian-Leónese Zone is sparse but increases W-wardly (Dallmeyer et al., 1997; Fernández-Suárez et al., 1998). Suárez-Rodrígues et al. (1991) recognised a 16 cm inter-stratigraphic volcanic level, which occurs in the northern flank of the Narcea Antiform, NW of Salce (W of this study's sampling area). The volcanic level shows signs of intense hydrothermal alteration, masking original textures and mineralogical components (Gallastegui, 1991). Scarce, primary textures infer a porphyroid volcanic event, with secondary minerals having altered from mafic parent material. This volcanic event may be linked to the provenance of volcanic components in sandy layers of the Mora Fm. (cf. Martín-Parra, 1989) where volcanic fragments are calcite replaced (Gallastegui, 1991).

Regionaly, alkaline rocks of volcanic origin, attributed to continental rifting (Heinz et al., 1985), occur in Middle Cambrian to Lower Ordovician parts of the Cantabrian Zone's Palaeozoic succession (Evers, 1967; Gallastegui-Suárez, 1990; Gallastegui, 1991), as well as in the Ponga Nappe (Gallástegui-Suárez, 1990) less than 1 km from sample 91. Lower Palaeozoic volcanic rocks also occur in the Silurian succession (Evers, 1967; Gallastegui-Suárez, 1990: Rocas Ígneas). In the sampling area, Lowermost Palaeozoic occurrences include large, upper mantle to lower crust derived (Loeschke & Zeidler, 1982) dolerite sils (10-100 m thick) prevailing in the top of the Oville Fm. to Barrios Fm, deformed together with their sedimentary host rocks (Evers 1967; Gallastegui-Suárez, 1990, Gallastegui, 1991), and pyroclastic rocks consistent of stratified tuffites also found in the Oville Fm. (Evers, 1967). Concentrations of chlorite, plagioclase and leucoxene absent lapilli, likely attributed to subaerial volcanism, occur in Upper Silurian San Pedro Fm. (Evers, 1967). An important phase of alkaline volcanism also occurred in the Permian (Corretgé and Suárez, 1990).

## 5.2 Plutonism

Plutonism in the Narcea Antiform and West Asturian-Leónese Zone is scarce, but increases W-wardly (Dallmeyer et al., 1997; Fernández-Suárez et al., 1998) Precambrian constrained magmatism is not directly evidenced in the study area.

At least two phases of Variscan associated plutonism are evidenced in the Iberian block of the West European Variscan Belt (Dallmeyer et al., 1997: Figure 2.2.1-2). In Iberia, the earliest syn-Variscan granitoids are restricted to more external zones of the West European Variscan Belt (Figure 5.2-1 A; Dallmeyer et al., 1997; Fernández-Suárez et al., 2000 b). In parts of the West Asturian-Leónese Zone external to the study area, tonalite-granodiorite-monzogranite (TGM) plutons, resulting from lower crustal melting with variable incorporation of mantle-derived material, appear coeval with regional

$D_2$ deformation at about 325 Ma (Fernández-Suárez et al., 2000 b). Emplacement of volumetrically much more pervasive leucogranite plutons (mantle derived material incorporating some crustal melts; Figure 5.2-1 B) follows shortly after at about 320 - 310 Ma (Fernández-Suárez et al., 2000 b). Hence, in the West Asturian-Leónese Zone total syn-Variscan magmatic emplacement, required about 15 Ma.

Post-Variscan, TGM granitoid stocks are found throughout the West European Variscan Belt including the Cantabrian Zone (Figure 5.2-1 C). TGM dominate by volume over posttectonic leucogranites (Figure 5.2-1 D). In general, granitoids appear in conjunction with some rare ultramafic and mafic to intermediate dykes of mantle derived origin incorporating varying degrees of crustal contamination (Galán & Suárez, 1989; Suárez et al., 1992; Galán et al., 1996). Ultramafic and mafic to intermediate dykes, by volume, are most often associated with the Cantabrian Zone. These magmatics most often appear as discrete small posttectonic plutons. The largest granitoid stocks occur in the Pisuerga-Carrión Unit (e.g. Peña Prieta stock) (Gasparrini, 2003; Gasparrini et al., in press). Granodioritic to gabbroic stocks occurring in the westernmost Cantabrian Zone (e.g. Arcellana and Carlés stocks: Somiedo-Corecillas & Aramo units) are often confined to deep-seated, laterally extensive late Variscan faults (Loeschke, 1982; Corretgé & Suárez, 1990; Gallastegui et al., 1990).

Post-Variscan magmatic emplacement in the West Asturian-Leónese Zone is again two-staged. Post-Variscan TGM granitoids appear at about 295 - 290 Ma (earliest Permian), followed by leucogranitic emplacement at about 290 - 285 Ma (Fernández-Suárez et al., 2000 b). Total post-Variscan emplacement in the West Asturian-Leónese Zone, required about 10 Ma.

In the sampling area, TGM granitoids occur in and across different levels of the Upper Carboniferous San Emiliano Fm. (Gallastegui, 1991 a, b) and in the Stephanian Ciñera-Matallana basin (Wagner & Artieda, 1970; Méndez-Cecilia, 1985; Gallastegui, 1991 b). Porphyroid leucogranites occur as undated dykes and sills in the northern flank of Narcea Antiform (Leyva et al., 1984) and in the Aralla-Rozo Thrust Unit (Gallastegui, 1991) of the southern Cantabrian Zone.

Little geochronologic information exists for igneous activity recognised in the study area. However, the age of posttectonic (TGM) granitoids are generally about 290 - 295 Ma in the Cantabrian Zone (Valverde-Vaquero et al., 1999), coeval with significantly more voluminous occurrences in the West Asturian-Leónese Zone (Fernández-Suárez et al, 2000 b) and the Central Iberian Zone (Serrano-Pinto et al., 1987; Valverde-Vaquero et al., 1995; Villaseca et al., 1995; Yenes et al., 1996). The post-Variscan age of TGM granitoids in the Cantabrian Zone is exemplified by U-Pb dates of Peña Prieta (approximately N 43° 01' 00", W 4° 44' 45") and Arcellana (N 43° 23' 15", W 6° 15' 50") granitoid stocks yielding 293 ± 2 and 293 ± 1 Ma respectively (Valverde-Vaquero et al., 1999). Frings et al. (2004: after Fernández-Suárez, 1998) estimate the age of

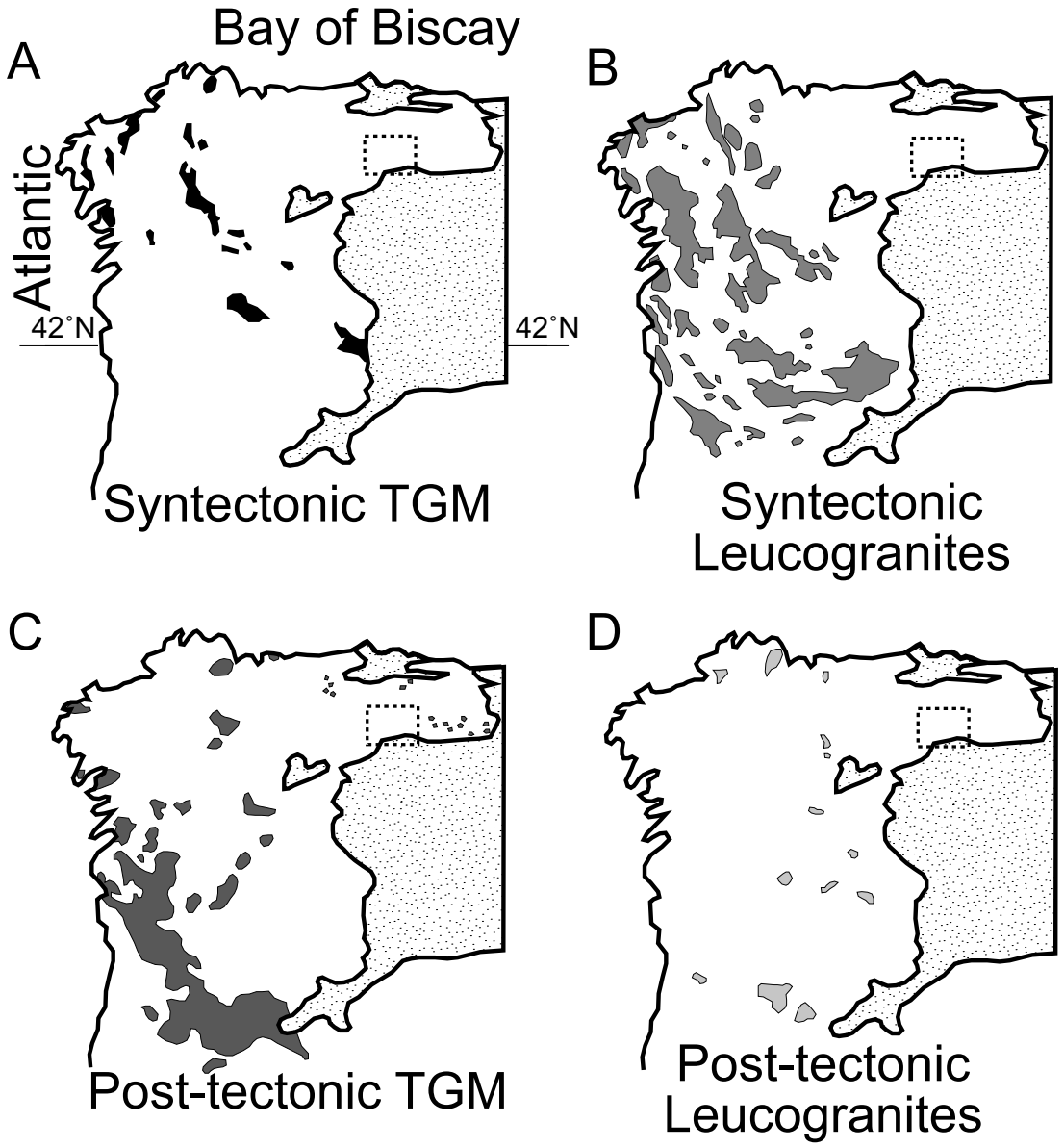


Figure 5.2-1: Distribution of syn-tectonic and posttectonic plutonism in the western Iberian Peninsula. Dashed box represents this study's sampling area. Modified from Fernández-Suárez et al. (2000 b).

dykes and folded sills in the Ciñera-Matallana Coal Basin to be between 295 - 286 Ma. Their emplacement, being posttectonic (Fernández-Suárez, 1998), or synsedimentary is still unclear (Frings, 2004).

## 5.3 Metamorphism in Precambrian sediments of the Narcea Antiform

Greenschist grade regional metamorphism, having reached the Precambrian Mora Fm. in both flanks of the Narcea Antiform, is evidenced by regional chlorite and restricted biotite mineral assemblages (Martín-Parra, 1989; cf. Leyva et al., 1984) and anchizone- (Pérez-Estaún, 1973; Aller et al., 1987; Aller et al., 2005) to epizone (Martín-Parra, 1989; Keller & Krumm 1992, 1993) illite crystallinity values. However, controversy surrounds the timing of the regional metamorphic event, either developing synkinematically with Variscan deformation (e.g. Matte, 1968; Pérez-Estaún, 1978; Leyva et al., 1984; Aller et al., 1987), or predating Variscan deformation (e.g. van Staalduinen, 1973; Savage & Boschma, 1980). The centre of debate is a slaty cleavage, which van den Bosch (1969 a, b) and van Staalduinen (1973) reported to have extended into the lowermost 30 m of the Lower Cambrian Herrería Fm. of the Cantabrian Zone; van Staalduinen (1973), inferring Variscan reactivation of a pre-Variscan cleavage from its stratigraphic restriction. Savage and Boschma, (1980) noted the multiple cleavage development to be cut off at the angular unconformable contact with the Herrería Fm. in the southwestern part of this study's sampling area.

In the northern flank of the Narcea Antiform, Precambrian rocks show chlorite and muscovite / sericite micas (most abundant phase: quartz + (muscovite / sericite) + albitite after: Martín-Parra, 1989; cf. Leyva et al., 1984), rare biotite blasts (Pérez-Estaún, 1978), are considered to be synkinematic with respect to principal schistosity ($S_1$) (Pérez-Estaún, 1978; Martín-Parra, 1989). The mineral assemblages support the hypothesis of a regional metamorphism having reached anchizone to epizone temperatures (figure 5.3-1; Leyva et al., 1984; Keller & Krumm, 1992, 1993). Martín-Parra et al. (1989) proposed

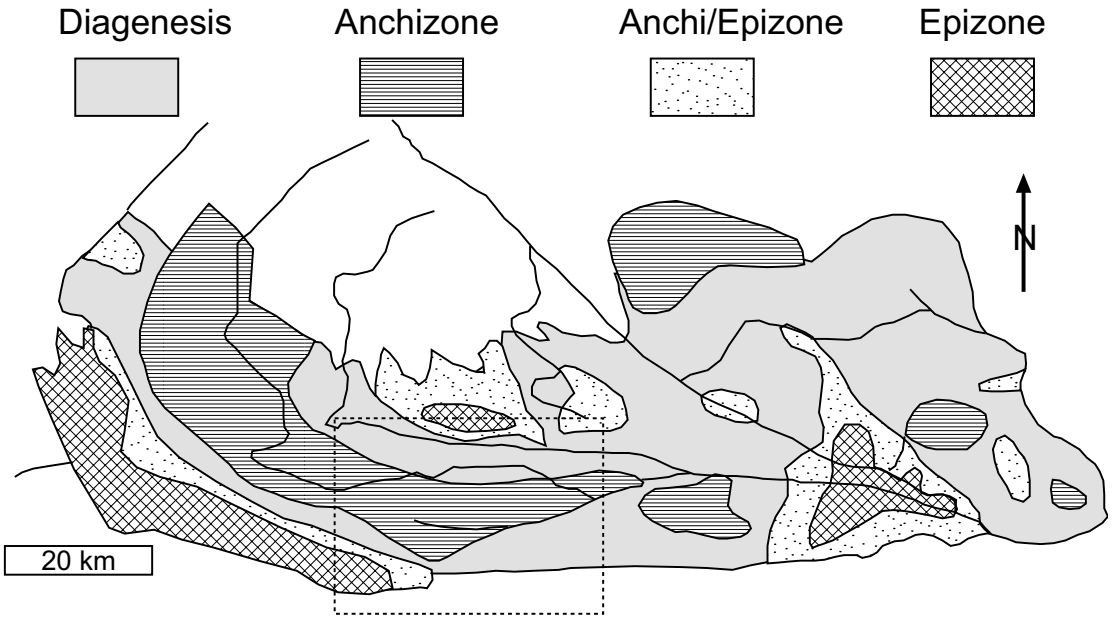


Figure 5.3-1: Distribution of the metamorphic grade in the Cantabrian Zone and adjacent areas. Dashed box represents this study's sampling area. Modified from Keller & Krumm (1993).

an association of temperatures reached with $D_1$-Variscan deformation. Occurrences of these minerals diminish approaching the Precambrian-Cambrian unconformity (Martín-Parra, 1989).

In the southern flank of the Narcea Antiform, a chlorite zone mineral association (most abundant phase: quartz + chlorite + (muscovite / sericite) + albite after: Martín-Parra, 1989; cf. Nägler et al., 1995) generally coincides with an intermediate type, low pressure, low- to very-low-grade prograding regional metamorphism (e.g Capdevila, 1967, 1969; Pérez-Estaún, 1978; Matas et al., 1982; Martín-Parra, 1989) sensu Winkler (1979).

In addition, a laterally extensive biotite zone is latitudinally restricted to the S of the Rio Omaños Thrust Fault for ~ 2 - 4 km (Martín-Parra, 1989). The primary mineral phase is quartz + muscovite + chlorite + biotite + albite. Low- to very-low-grade regional metamorphism is associated with $D_1$- and $D_2$-Variscan deformation phases, climaxing in the latter phase (Pérez-Estaún, 1978). Biotite zone associated metamorphism is coincident with $D_1$-Variscan deformation (Pérez-Estaún, 1978).

To the W of this study's sampling area, three facies of contact metamorphism, restricted to the rocks of West Asturian-Leónese Zone, inclusive of parts of the southern flank of the Narcea Antiform, are mapped in rocks of the Riello Map-Sheet (Martín-Parra, 1989). The facies correspond to: recrystalised contact chlorite, contact biotite, and contact biotite and andalusite. As mapped these facies do not appear to extend into the study area. According to Martín-Parra (1989), contact facies are likely associated with a $D_3$ metamorphism phase having occurred in late to post-Variscan time coeval with subsurface TGM-type granitoid intrusions prevalent in other parts of the West Asturian-Leónese Zone (see figure 5.2-1: C).

Published illite crystallinity values mapped across Precambrian rocks of the southern (Pérez-Estaún, 1973, 1978; Martín-Parra, 1989: Figure 33) and northern (Martín-Parra et al., 1989: Figure 33; Keller & Krumm, 1992, 1993) limbs of the Narcea Antiform, indicate lower epizone to greenschist facies metamorphic conditions prevailed on both sides of the Conombre-La Urz Thrust Fault (cf. Capdevila, 1967, 1969; cf. Pérez-Estaún, 1978), with metamorphic grade in the southwesternmost extent of this study's sampling area increasing S-ward from upper anchizone in Mora Fm. in contact with Herrería Fm. to greenschist facies (Figure 5.3-1; Martín-Parra, 1989; Keller & Krumm, 1993). In the sampling area, anchizone values are restricted to the uppermost Mora Fm. of the northern flank of the Narcea Antiform (Martín-Parra, 1989; Aller et al., 2005) suggesting a change in crystallinity domain. New illite crystallinity data (Angerer pers. com., 2005) suggest the lower crystallinity boundary may actually be at the diagenesis-anchizone transition in rocks at the Precambrian-Cambrian unconformity.

## 5.4 Metamorphism in Cantabrian Zone pre-Stephanian Palaeozoic rocks

The state of metamorphism in the Cantabrian Zone has been widely studied, considering illite crystallinity (e.g. Galán et al., 1978; Brime & Pérez-Estaún, 1980; Brime, 1981, 1985; Aller & Brime, 1985; Aller et al., 1987, 2005; Alonso & Brime, 1990; Marschik, 1992; Keller & Krumm 1992,1993; Gutiérrez-Alonso & Nieto, 1995; García-Lopéz et al., 1997, 1999; Bastida et al., 1999; Brime et al., 2001; Frings, 2002), conodont alteration index (e.g. Raven & van der Pluijm, 1986; García-Lopéz et al., 1997, 1999; and Bastida et al., 1999; Aller et al., 2005), fluid inclusions (e.g. Ayllón, 2003; Ayllón et al, 2003; Gasparrini, 2003; Gasparrini et al. in press) and vitrinite reflectance (e.g. Schneider, 2002). Where studies spatially coincide, boundaries between metamorphic facies, as ascertained by illite crystallinity and conodont alteration indices (e.g. Raven & van der Pluijm. 1986; García-Lopéz et al., 1999; Aller et al., 2005), are highly correlated.

In northern Iberia (including the southern Cantabrian Zone), Variscan metamorphism reached peak conditions during Late Carboniferous (Capdevila, 1967; Julivert, 1981) (late Bashkirian to Moscovian: van der Pluijm & Kaars-Sijesteijn, 1984; cf. Dallmeyer, et al., 1997; cf. Weil et al., 2000, 2001) time; final emplacement occurring into the early Stephanian (Dierendonk et al., 1984; cf. Dallmeyer, et al., 1997; Weil et al., 2000, 2001). Nonetheless, a metamorphic overprint is for the most part absent in Palaeozoic rocks of the Cantabrian Zone (e.g. Keller & Krumm, 1992, 1993; Nägler et al., 1995). In the Luna River area (western part of the study area), rocks show primary clastic fabrics (euhedral quartz crystals) and detrital biotites, but lack newly grown chlorite. Keller & Krumm (1993), using clay mineral assemblages classify Cantabrian Zone strata of the Luna and Bernesga river valleys in the kaolinite domain (cf. Gutiérrez-Alonso, 1996).

### *5.4.1 Illite crystallinity palaeothermal record*

In the Los Barrios de Luna area of the southern Cantabrian Zone, the Cambrian-Ordovician succession (Herrería, Láncara, Oville fms.) is characterised by illite crystallinities indicating diagenesis (e.g. Brime, 1985; Marschik, 1992) to anchizone (e.g. Aller, 1987; Brime, 1981, 1985; Keller & Krumm, 1992, 1993) conditions. Typical signatures include, marked decrease in peak breadth from the Lower Cambrian (Herrería Fm.) towards the Lower Ordovician (Barrios Fm.) and the repetition of the metamorphic gradient below and above thrust planes (e.g. Aller, 1987; Brime, 1981; Keller & Krumm, 1992, 1993; cf. Raven & van der Pluijm, 1986). Marschik (1992) reported highest metamorphic grades (upper anchizone) having occurred in Lower Cambrian Láncara Fm., at zones of highly tectonised imbricate thrusts (basal thrust of the Correcillas Unit) near Láncara de Luna, and NE of Aralla, conspicuously close to a Carboniferous aged (Alonso et al., 1990) igneous intrusion. Metamorphic repetition cannot be explained by simple burial thermal gradient, as a linear illite crystallinity curve would then be expected (Marschik, 1992; Keller & Krumm, 1992).

Illite crystallinity values for Silurian, Devonian and pre-Stephanian Carboniferous strata of the Abelgas-Bregón Domain and Aralla-Rozo Thrust Sheet in the vicinity of the Luna River and the Bernesga River S of Villamanín de la Tercia, normally do not exceeded diagenesis zone facies (Aller et al., 1987, 2005; Brime, 1981, 1985; Marschik, 1992; Keller and Krumm, 1992). The Cuevas Fm., at Estación de Matallana, S of the Ciñera-Matallana Coal Basin expresses an anomalously anchizonal signature when compared to other pre-Stephanian Carboniferous strata. However, as discussed below, anchizone illite crystallinity values are not uncommon in Stephanian aged sediments of the adjacent Ciñera-Matallana Coal basin (see below; Frings, 2002; Aller et al., 2005). Repetition of the metamorphic gradient again occurs across the Rozo Thrust (Mulhall, 2003).

The Bodón Unit, away from the León Line Fault System, is normally characterised by diagenetic zone conditions (Brime, 1985; Marschik, 1992; Aller et al., 2005). However some noteworthy anomalies also occur in the Upper Carboniferous San Emiliano Fm. including: anchizone values along the Rodiezmo River, W of Poladura de la Tercia in the Bodón Nappe; at the footwall of the Gayo Thrust (or core of a syncline) SSE of Barrio de la Tercia; and in the Bodón Nappe between Cármenes and Almuzara, along the Torio River (Marschik, 1992; cf. Aller et al., 2005).

A unique zone of elevated thermal gradient straddles both sides of the León Line Fault System (García-López, 1999). This unique thermal zone is treated in chapter 5.6.

### *5.4.2 Vitrinite-bituminite reflectance palaeothermal record*

Vitrinite-bituminite reflectance data, in the southern Cantabrian Zone are sparse and not highly documented, except for in the Ciñera-Matallana pull-apart type coal basin.
Average vitrinite reflectance values from Upper Carboniferous San Emiliano Fm. North of Villamanín de la Tercia show bituminous coal grade metamorphism was reached (Mulhall, 2003). Schneider (2002) reported for the type-locality of the Lower Devonian La Vid Group a temperature of 154 ˚C, following burial diagenesis, as calculated from bituminite reflectance measurements.

In consideration of the stratigraphic thickness of basinal sediments overlying the La Vid Group of up to ~ 2570 to 3680 m (respectively after Brime et al., 2001; Golonka et al., 1994), Schneider (2002) further concluded that a geothermal gradient of 25 ˚C/km (Golonka et al., 1994) or even 35 ˚C/km (Brime et al., 2001) applied to pre-Stephanian Palaeozoic sedimentary rocks of the southern Cantabrian Zone were not supported by the 154 ˚C temperature. Instead a gradient of at least 45 ˚C/km should have been expected.

### *5.4.3 Conodont alteration index palaeothermal record*

Conodonts alteration index (CAI) values from Devonian to Stephanian strata in the southern Cantabrian Zone are relatively uniformly distributed over large areas (see figure 5.4.3-1; Raven & Van der Pluijm, 1986; Aller et al., 2005). Treatment of data is made here for the southern Cantabrian Zone excluding the Ciñera-Matallana coal basin and parts of the Bodón and Forcada thrust sheets lying within approximately 2 km S of the León Line.

Palaeotemperatures estimated for L. Carboniferous time at 2000 m depth from CAI values are highest (250 - 300 ˚C) about the Sabero-Gordón Line Fault System. Stephanian strike-slip movement along the fault system has been proposed by Bastida et al. (1976) and Raven (1983). High palaeotemperatures may be linked with Stephanian faulting and/or the W-ward extension of the palaeoboundary for the Stephanian Ciñera-Matallana basin (Raven and van der Pluijm, 1986; cf. Aller et al., 2005).

In the Correcillas Unit, away from the Sabero-Gordón Line Fault System estimated palaeotemperatures decrease to between 200 - 250 ˚C. Nonlinear metamorphic gradients between adjacent thrust units were evidenced (Raven & Van der Pluijm, 1986). The

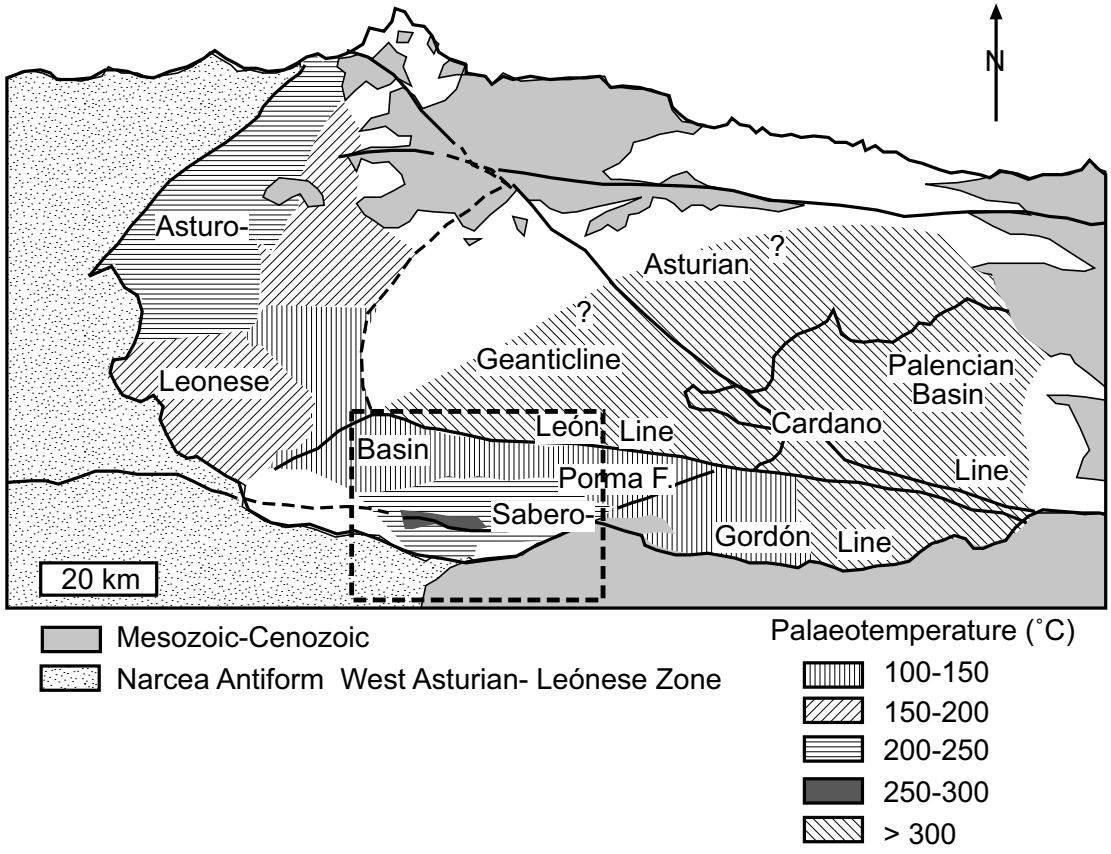


Figure 5.4.3-1: Metamorphic temperatures in the Cantabrian Zone estimated from the variation of conodont alteration index elements. Location of temperature boundaries and major structural elements are depicted. Dashed box defines this study's sampling area. After Raven & Van der Pluijm (1986).

Bodón Unit inclusive of the Gayo and southern parts of the Bodón thrust units is characterised by CAI values indicating ~ 100 - 150 ˚C palaeotemperatures (Raven & van der Pluijm, 1986; Mulhall, 2003; Aller et al., 2005). Palaeotemperature maxima normally follow a linear metamorphic gradient (Raven & van der Pluijm, 1986). A sharp temperature boundary exists between the Bodón and Correcillas units.`

### *5.4.4 Fluid inclusion palaeothermal record*

Microthermometry results for pervasively dolomitised Upper Carboniferous limestones in and about the Bodón Unit in the north and northwest parts of this study's sampling area exhibit modal fluid inclusion temperatures of between 110 to 150 ˚C (Gasparrini, 2003; Gasparrini et al., in press); their distribution showing no spatial correlation. The highest fluid inclusion temperature recorded was 205 ˚C for dolomitised rocks in the vicinity of Cármenes (N 42˚ 57' 45", W 5˚ 34' 30"), along the Torio River Valley. The lowest temperature recorded was 93 ˚C for dolomitised rocks at the Mina Profunda (N 42˚ 57' 59.3, W 5˚ 36'48.5") carbonate hosted Cu mineralisation. Fluid inclusion in cacites which overprint the dolomitised rocks yield values between 100 and 145 . Gasparrini (2003: Table 5) provides a summary of the data.

New microthermometry results from dolomitised limestones in Lower Cambrian Láncara Fm. along the basal thrust of the Correcillas Unit (central southern Cantabrian Zone part of this study's sampling area), indicate maximum fluid inclusion temperatures between 90 and 120 ˚C were reached (pers. com. Lapponi, 2006).

## 5.5 Metamorphism in Stephanian coal basins (Ciñera-Matallana and La Magdalena)

Stephanian pull-apart type coal basins are widely distributed across the Cantabrian and West Asturian-Leónese zones of northwest Iberia (Evers, 1967; Colmenaro & Prado, 1993). In this study's sampling area, Stephanian B sediments are discordant with respect to underlying Neoproterozoic to Upper Carboniferous strata. In the case of the Ciñera-Matallana Basin of the southern Cantabrian Zone, high heat flow conditions (Frings et al., 2004) coincident with, but not limited to localised magmatic activity occurred within surrounding diagenetic to low-temperature metamorphic (anchizone-epizone) environments (Ayllón, 2003). The thermal gradient here is notably higher than that for the surrounding pre- and synorogenic Palaeozoic rocks (e.g. García-Lopéz et al., 1999; Frings et al., 2004; Aller et al., 2005).

Peak palaeotemperatures in the Cinera-Matallana Basin have been attributed to high heat flow coeval with latest Carboniferous to Permian igneous activity (see Ayllón et al., 2003; Frings et al., 2004). Initial magmatic temperatures for dioritic material are estimated to have been between 800 - 850 ˚C, at the contact with coal 603 - 720 ˚C and at the contact with pelitic rocks 507 - 637 ˚C (Méndez-Cecilia, 1985). It is unknown what mechanism was responsible for heat dissipation (Ayllón et al., 2003). According to Méndez-Cecilia (1985) heat may have been transferred by conduction through solid

rock in association with locally subvolcanic TGM-type (see Fernández-Suárez 2000 b) dykes and sills, or after Colmenaro & Prado (1991), by more widespread advection of hydrothermal fluids through various pathways.

### *5.5.1 Illite crystallinity in the Stephanian coal basins*

Illite crystallinity values show heterogeneous metamorphic conditions prevailed in the Ciñera-Matallana Coal Basin (Galán et al., 1978; Marschik, 1992; Keller and Krumm, 1993; Frings 2002; Aller et al., 2005). There is no apparent relation between clay mineral reaction to burial depth (Frings, 2002). Illite crystallinity values measured characterise diagenetic (Galán et al., 1978; Marschik, 1992; Frings, 2002; Aller et al., 2005), anchizone (Galán et al., 1978; Marschik, 1992; Keller and Krumm, 1993; Frings, 2002; Aller et al., 2005), to lower epizone (Marschik, 1992; Frings, 2002; Aller et al., 2005) conditions. The La Magdalena Basin exhibits epizone conditions (Aller et al., 2005). Illite crystallinity values in the basin are generally lower than in the surrounding Precambrian and Palaeozoic successions (García-Lopéz et al., 1999; Aller et al., 2005). In both cases, Stephanian rocks are associated with high coal ranks (e.g. Colmenaro & Prado, 1989).

Using the correlation table of Merriman and Kemp (1996), Frings (2002) estimated temperatures ≤ 200 - 250 ˚C, from the illite crystallinities of samples in the Ciñera-Matallana Basin. Galan et al. (1978) estimated maximum temperatures between 150 - 200 ˚C during Permian time and a palaeogeothermal gradient of 60 ˚C/km under the assumption of 2500 m overburden depth.

### *5.5.2 Vitrinite reflectance in the Ciñera-Matallana Coal Basin*

Thermal maturity in coal seams of the Ciñera-Matallana generally increases with depth (Méndez-Cecilia, 1985; Frings et al., 2004). However, coalification was considered to be at least partly post-folding as maximum vitrinite reflectance values occur in synclines and the minimum values in anticlines (Méndez-Cecilia, 1985). According to Méndez-Cecilia (1985) mean vitrinite reflectance varies from 1.3 % in the uppermost Matallana Fm. to 2.0 % in the Lowermost San Francisco Fm., with the highest value (2.6 %) in the Pastora Fm. This trend of increasing vitrinite reflectance with depth is supported by more recent values published in Frings et al. (2004), for random vitrinite reflectance (%$R_r$) ranging from 1.04 %$R_r$ in the Matallana Fm. to 2.56 %$R_r$ in the Pastora Fm. From the data, and assuming a palaeosurface vitrinite (huminite) reflectance of 0.25 %$R_r$ (equivalent to a palaeosurface temperature of ~ 25 ˚C), Frings et al. (2004) predicted the maximum overburden to be around 1000 m.

Converting vitrinite reflectance to temperature, a palaeogeothermal gradient and overburden depth value of 85 ˚C/km and 1020 m respectively (after Barker & Pawlewicz, 1994), was calculated (Frings et al., 2004) This overburden depth value corresponds

well with measured reflectance values (Frings et al., 2004); the calculated-thermal-gradient is also in agreement with the 70 - 80 ˚C/km proposed by Méndez-Cecilia (1985) for locations away from local contact metamorphism influenced thermal anomalies.

### *5.5.3 Fluid inclusion in the Stephanian coal basins*

Fluid inclusion studies in Stephanian sediments from this study's sampling area are restricted to the Ciñera-Matallana Coal Basin (e.g. Ayllón, et al., 2003; Ayllón, 2003). Fluid inclusion data for the Ciñera-Matallana Basin indicate initial precipitation of minor amounts of calcite. A second generation of low salinity quartz fluid inclusions is also recognised. These inclusions were trapped at temperatures of about 110 - 120 ˚C in the clastic rocks. Progressively higher temperatures (150 - 290 ˚C) are reflected in the formation of quartz inclusions from igneous rocks which intrude the basin. Subsequently fissures in the clastic rocks yield a calcite crystallised from a lower temperature (70 - 80 ˚C) high salinity fluid. Calcites with similar fluid inclusion temperatures are also expressed in the Sabero Basin (Ayllón, 2003), E of this study's sampling area.

### *5.5.4 Previous calculated thermal history of the Stephanian coal basins*

For the modelling of thermal gradients Frings et al. (2004) highlight the importance of having isoreflectance lines, which run parallel or sub-parallel to bedding. However, vitrinite isoreflectance lines calculated by Méndez-Cecilia (1985; see figure 5.5.4-1) cut through the anticline and syncline structures in the coal basin.

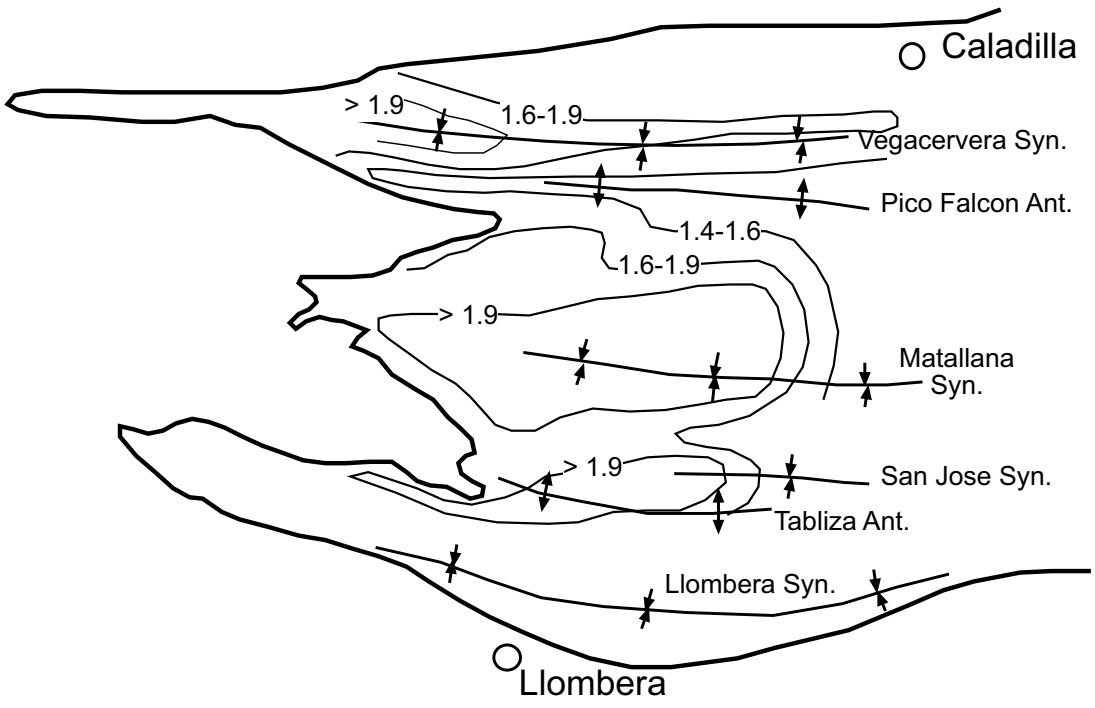


Figure 5.5.4-1: Vitrinite reflectance isoreflectance lines for the western Ciñera-Matallana Coal Basin. After Méndez-Cecilia (1985).

*Thermal indicies and magmatism*

Referring to the isoreflectance data Méndez-Cecilia (1985) and Colmenaro & Prado (1993) proposed a partly post-folding origin for the coalification process. Nevertheless, Frings et al. (2004) propose peak coalification to have occurred more or less contemporaneously with peak burial. This model is base on: a) the strong agreement between regression coefficients for measured $\%R_r$ versus burial depth and calculated palaeogeothermal gradient versus burial; b) correlation between maximum predicted temperature for lowermost Stephanian San Francisco Fm. and the temperature indicated by illite crystallinity results; c) anisotropy of vitrinite reflectance foliation-ellipsoids oriented mainly parallel to bedding with $R_{min}$ normal to bedding; and d) that the geothermal gradient calculated after Barker and Pawlewicz (1994) is in agreement with those of Galán et al. (1978) and Méndez-Cecilia (1985).

Under the assumption maximum coalification reflects peak burial and peak temperature conditions, related to late Variscan magmatic activities, and disregarding the influence of fluid circulation in the basin, Frings et al. (2004), using the kinetic Easy $\%R_o$ approach (Sweeney & Burnham, 1990), calculated a one-dimensional numerical timing constrained burial-temperature model (see Frings et al., 2004: Figure 8), which details two phases of heating: the first and most prevalent pulse coeval with crustal delamination and upwelling of the asthenosphere (Fernández-Suárez, 1998, Fernández-Suárez et al., 2000 b; Gutiérrez-Alonso et al., 2004 a), and its associated late Variscan magmatism (Fernández-Suárez et al., 2000 b, 2002, a, b); the second pulse in association with burial by ~ 1000 m of overburden. This value would be in accordance with the estimated thickness of Cretaceous trangressive sediments (Evers, 1967), although Frings et al. (2004) consider it more likely that the additional overburden resulted instead from additional Stephanian or Lower Permian sedimentation (Frings et al., 2004; cf. Martínez-García, 1990).

The assumption of continued Stephanian-Permian sedimentation is supported by several studies (Comte, 1959; de Sitter, 1962; van Ameron & Van Dillewijn, 1963; Heward, 1978; Martínez-García & Wagner, 1984), which describe the palaeodepositional environment in and about the Ciñera-Matallana Coal Basin as an expansive, highly connected coastal floodplain with alluvial fan and lacustrine sedimentation, depocentres/deep-depressions forming along major structural lineaments, such as the Sabero-Gordón Line Fault System (Frings et al., 2004). The sediments having been subsequently affected by tectonic deformation and erosion, with only the Stephanian successions of the former depocentres being preserved.

## 5.6 Metamorphism along the León Line and southern margin of the Central Coal Basin

### *5.6.1 Illite crystallinity*

A unique zone of elevated palaeothermal gradient straddles both sides of the León Line Fault System (García-López et al., 1999). Extensive cleavage is associated with areas of higher metamorphic grade (Aller et al., 1987). Illite crystallinity values in the study area, North of the León Line Fault System evidence anchizone to epizone metamorphic conditions (Figure 5.6.1-1; Aller & Brime, 1985; Brime, 1985; Marschik, 1992; Aller et al., 2005), with highest metamorphic conditions (after Marschik, 1992; Aller et al., 2005) along the Curueño and Torio river valleys. W of the Torio River, illite crystallinities indicate anchizone-epizone boundary conditions. Aller & Brime (1985) report the highest metamorphic grades (epizone) were reached in the Bashkirian to Kasimovian Sama Group of the extreme southwestern Central Coal Basin, and the Carboniferous of the Aramo Units and Sobia Units, some 5-10 km W of this study's sampling area. Aller & Brime (1985) also report anchizone palaeotemperature conditions dominate the signatures of Carboniferous rocks in the western part of this study's sampling area, on both sides of the León Line.

Illite crystallinity data from the high density sampling strategy adopted by Marschik (1992), for the northernmost parts of the Bodón and Forcada nappes along the León Line, between the Bernesga and Torio River valleys, suggests a positive correlation between metamorphic grade and stratigraphic position. Upper anchizone to incipient

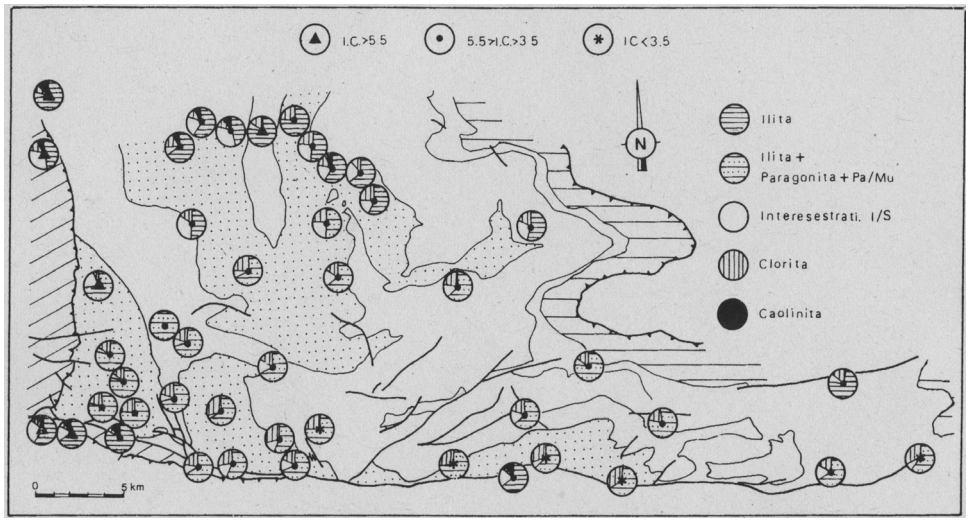


Figure 5.6.1-1: Metamorphic grade of rocks in the southern Central Coal Basin Unit and northernmost southern Cantabrian Zone as gathered from illite crystallinity values (Aller & Brime, 1985). León Line Fault System constrains the southern boundary of the Central Coal Basin.

metamorphic conditions were reached in lower Palaeozoic Láncara Fm. of the hanging wall blocks of the Bodón Thrust, and footwall blocks in Herrería Fm. (see Marschik, 1992), while diagenetic to anchizone conditions are expressed by overlying strata.

Little illite crystallinity data are available for locations along León Line, E of the Torio River Valley in the southern Cantabrian Zone. Aller & Brime (1985) present a single anchizone grade illite crystallinity measurement for Upper Carboniferous sediments in the vicinity of Redilluera (approx. N 42˚ 58' 15" W 005˚ 27' 40"); Aller et al. (2005) present diagenetic to anchizone values for Carboniferous rocks between the Bodón Thrust and the León Line; the highest grade value associated with lower sediments in the hanging wall block of a thrust approximately perpendicular to the León Line. Aller & Brime (1985), and Aller et al. (2005) evidenced anchizone illite crystallinity values for Carboniferous stratigraphies in most areas North of the León Line, including this study's sampling area. However, values presented by Marschik (1992) for the Sama and Lena groups (North of León Line), E of the Torio River valley indicate incipient metamorphic palaeotemperatures were reached.

### *5.6.2 Conodont alteration index*

CAI palaeotemperature estimations for the León Line area (Figure 5.4.3-1; Raven & van der Pluijm 1986, Aller et al., 2005) denote the strong contrast in maximum palaeotemperature between Central Coal Basin and southern Cantabrian Zone units. The distribution of CAI measurements in the southern Central Coal Basin, North of the León Line are scarce, however index values present indicate epizone equivalent temperatures conditions were reached (≥ 310 - 340 ˚C) in Serpukhovian to Stephanian aged rocks. Along the southern margin of the León Line, in this study's sampling area, CAI values show a poorly constrained trend for increasing values towards the W. In the Cureño River Valley area values indicate diagenetic grade (< 70 - 95 ˚C) temperatures were reached in Famennian-Viséan Alba Fm. at Redillura and Ermita Fm. at Rucayo (approximately N 42˚ 57' 30", W 5˚ 20' 20").

The western part of the León Line is not documented, however ~ 1 km S of the line Lower Devonian sediments near Mina Providencia (approx. N 42˚ 58' 30" W 5˚ 36' 10"; see section 5.7) display CAI values of 3.5 suggesting they reached near anchizone temperatures of up to 200 - 230 ˚C. Famennian-Viséan sedimentary rocks stratigraphically overlying, are associated with palaeotemperature maxima in the middle to upper diagenetic range at up to 120 - 155 ˚C (CAI: 3). However Serpukhovian-Stephanian rocks only ~ 2 km W (approx. N 42˚ 58' 3" W 5˚ 34' 05"), S of Pontedo display CAI values of 1.5 suggesting only diagenetic zone palaeotemperatures of up to 50 - 75 ˚C were reached.

## 5.7 Dated mineralisations

Gasparrini (2003) reports on the status of mineralization in Upper Carboniferous carbonates of the northern part of the southern Cantabrian Zone in order to constrain the latest timing of dolomitisation of Upper Carboniferous carbonates. In these mineralisations, U-Pb dates were acquired from Th-free uraninite grains associated with gersdorffite and vaesite in the Mina Profunda of the Bodón Unit (approximately N 42˚ 58' 00", W 5˚ 36' 30") and gersdorffite and pyrite in the Salamón Gold deposit located along a major fault trace at the margin between Ponga and Elsa-Valsurvio units (approximately N 43˚ 56' 50", W 5˚ 07' 50"); the dates being 273 ± 11 and 269 ± 5 Ma respectively (Paniagua et al., 1993, 1996; Crespo et al., 2000). In addition, Pb-Pb dates from galena of Mina Providencia in the Bodón Unit located along an ENE-trending fault associated with the León Line Fault System (cf. Veselovsky, 2004) and Mina Fontún in the Gayo Thrust Unit (approximately N 42˚ 56' 42" W 5˚ 37' 50") yield ages of 271 ± 11 and 269 ± 11 Ma respectively (Paniagua et al., 1993, 1996).

# 6 Apatite fission-track analytical method

## 6.1 History of fission-track thermochronology

Fission-track dating was developed beginning in 1963 by P. Buford Price and Robert M. Walker (see Price and Walker, 1963), as a new method for dating geological materials based on the natural decay by the $^{238}U$ isotope, given the technique relied simply on the count of the individual damage tracks created by the spontaneous fission of $^{238}U$. In a common effort with Robert L. Fleischer several publications on the new dating method were produced, including a list of about 30 mineral phases in which fission tracks had been revealed (Fleischer & Price, 1964).

This was followed by an, often difficult, period of development in which Prof. Dr. Günther A. Wagner, played a leading role in the early advancement of the technique and its geological application (e.g. Wagner, 1966, 1967, 1968, 1969).

Fleischer et al. (1975) published a comprehensive overview of the study of nuclear tracks and their applications, including a chapter on the fission-track dating method. More recently Wagner & van den Haute (1992) published a complete treatise on the technique discussing the fundamental aspects surrounding technique, geological application and interpretation.

Since 1980 international workshops focusing entirely on the fission-track dating and thermochronology have been held, most recently in Amsterdam, 2004, where much light is still shed on the topic. Although fission-track analysis has now gained the status of an accepted method in geological research, it is not yet a 'finished' method and research continues in areas including the effects of the variability of annealing kinetic parametres on track-length shortening (e.g. Carlson et al., 1999; Ketcham et al., 1999; Barbarand et al., 2003).

## 6.2 Principles of nuclear fission

Nuclear fission, one of several modes of disintegration occurring among heavy, unstable (radioactive) nuclides, is a predominantly binary reaction where fission fragments expel each other in opposite directions to create a trail of damage if the fissioning nuclide is a lattice atom of an insulating solid (crystal).
Example fission reactions are:

$^{252}Cf \rightarrow {}^{108}Ru + {}^{140}Xe + 4\ \text{neutrons} + Q$ (spontaneous fission),
$^{235}U + \text{neutron} \rightarrow {}^{236}U \rightarrow {}^{90}Kr + {}^{143}Ba + 3\ \text{neutrons} + Q$ (neutron induced fission),

Where $Q \approx 210$ MeV, is mainly liberated in the form of kinetic energy at $\approx 170$ MeV (Wagner & van den Haute, 1992).

*Analytical method*

Spontaneous fission only occurs with very heavy nuclides of atomic number ≥ 90 and atomic mass ≥ 230. Belonging to the actinide series, most of these nuclides also disintegrated under other processes such as alpha-decay. Only $^{232}$Th and two isotopes of uranium ($^{238}$U & $^{235}$U) occur as primary constituents of natural substances in measurable concentrations. $^{234}$U, $^{231}$Pa and $^{234}$Pa are produced in nature as intermediate members of the $^{235}$U, $^{238}$U, or $^{232}$Th alpha-decay series, however, $^{234}$U is the only intermediate isotope to have significant abundance with respect to its primary parent, as its total half life is greater than $10^5$ a.

Virtually all detected fission events result solely to the fission of $^{238}$U atoms (see table 6.2-1). The relative abundances of the isotopes $^{234}$U, $^{235}$U and $^{232}$Th being too low and/or the spontaneous half-lives being too long to produce any significant amount of spontaneous fission events compared to $^{238}$U.

| Isotope | Relative. abundance (compared to $^{238}$U) | Total half-life (years) | Spontaneous fission half-life (years) |
|---|---|---|---|
| $^{232}$Th | 4[d] | $1.40 \times 10^{10}$[a] | $1.0 \times 10^{21}$[c] |
| $^{234}$U | $5.44 \times 10^{-5}$ | $2.46 \times 10^{5}$[b] | $1.5 \times 10^{16}$[b] |
| $^{235}$U | $7.25 \times 10^{-3}$ | $7.04 \times 10^{8}$[a] | $1.0 \times 10^{19}$[b] |
| $^{238}$U | 1 | $4.47 \times 10^{9}$[a] | $8.2 \times 10^{15}$[b] |
| [a]Steiger & Jäger (1977) | [b]Holden (1989) | [c]Baard et al. (1989) | [d]Geochemical average |

Table 6.2-1: Abundances and half-lives of the four major naturally occurring nuclides suffering spontaneous fission, after Wagner & van den Haute (1992).

### *6.2.1 The latent fission track*

Minerals containing trace amounts of uranium record the spontaneous nuclear fission of the $^{238}$U isotope and the induced nuclear fission of the $^{235}$U isotope, in the form of fission tracks. With regards to $^{238}$U and $^{235}$U isotopes, fission tracks are submicroscopic linear disordered regions in the crystal lattice, formed along the trajectories of the nuclear fragments ejected by the fissioned uranium, nucleus. The intensity of damage can be expected to decrease when moving away from the locus of the uranium atom, which does not coincide with the track centre (Wagner & van den Haute, 1992). Damage to the crystal lattice along a track is gradually to instantaneously restored in association with elevated temperatures, resulting in overall fission-track-length reduction (Wagner & van den Haute, 1992).

## 6.3 Principles of fission-track thermochronology

Fission-track research focuses on the study of the fission-track record in natural crystals and/or glasses, under the guise of determining the geological and/or cooling age, as well as the temperature history of the host lithology containing the crystals and/or glasses.

### 6.3.1 Spatial and aerial density of fission tracks

Fission-track dating is based on assessment of the number of tracks having accumulated in the host crystal or glass since it last cooled below a temperature at which the tracks are retained. Thermal history analysis additionally requires the measurement of the accumulated fission track's lengths in order to reveal the temperature evolution of the rock over the period of time since accumulation of fission tracks began.

The number of accumulated tracks is equal to the number of fission tracks counted per unit volume (spatial track density) since there is a unity relationship between track and fissioned atom. If however an optical revelation technique such as etching of an internal detector surface is used, only those tracks projecting that surface (areal or planar track density) are observable. The calculated spatial track density thus becomes a function of observed areal density.

Wagner and van den Haute (1992) propose a theoretical (model) relation between areal and spatial track density is obtainable assuming:

- homogeneous distribution of fissioned atoms throughout the host volume,
- fission track lengths ($l$) are equal and the locus of the fissioned atom is at the centre of each track ($l = 2R$),
- no preferential direction for fission track formation in the detector.

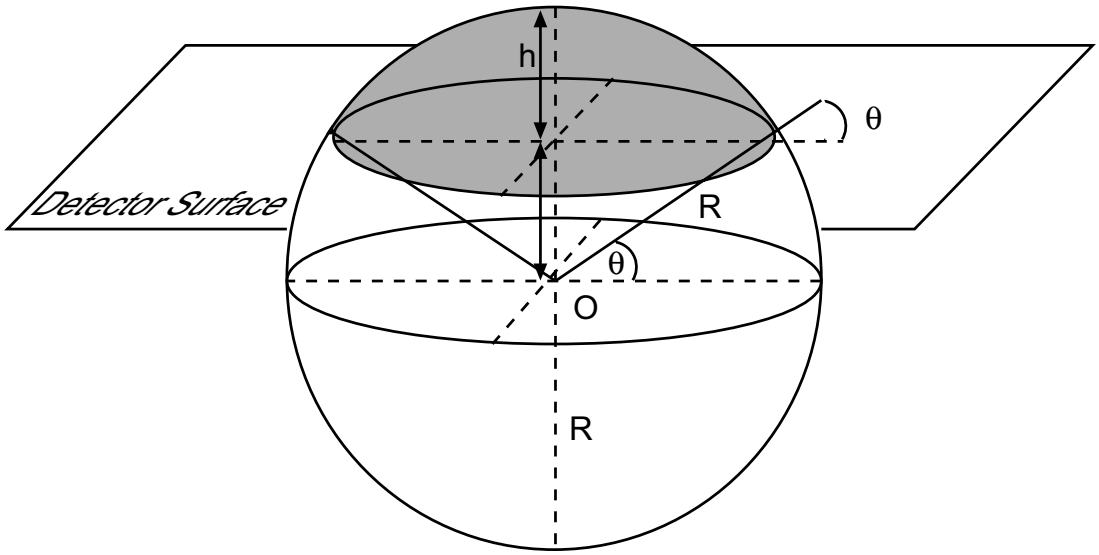


Figure 6.3.1-1: Only those tracks with upper ends falling in the shaded area of the sphere with radius $R$ will intersect the detector surface ($R$ = length of the track of the one fission fragment) when an internal uranium atom at point 0, situated at depth $z$ beneath the detector surface fissions. The probability of a track intersecting the detector surface is given by $2\pi Rh/2\pi R^2$, i.e the area of the shaded sphere zone/the area of the semi-sphere representing all possible track orientations. Figure and caption modified after Wagner & van den Haute (1992).

*Analytical method*

If $N_f$ = the number of fissioned nuclei per unit volume, then the number of nuclei contained by a surface of unit area and elementary thickness *dz* is given by $N_f dz$. If this layer is situated away from the detector surface at distance *z* ($\leq R$) , only tracks dipping $\geq$ arcsin *z*/*R* intersect the surface (Figure 6.3.1-1).

Under the assumption of no preferential direction for track formation in the detector, the probability P(*z*) of a track making the angle $\geq \theta$ = arcsin *z*/*R* is given by the ratio of the investigated surface area (hatched area in figure 6.3.1-1) to that of the surface area of the entire semi-sphere with radius *R* (representing all possible directions), or:

$$P(z) = 2\pi Rh / 2\pi R^2 = R(R - R\sin\theta)/R^2 = (1 - \sin\theta) \qquad (6.1)$$

The number of tracks intersecting the detector surface is thus given by $(1 - \sin\theta) N_f dz$ and the areal track density of the latent tracks $\rho_l$ is obtained from:

$$\rho_l = \int_0^R (1 - \sin\theta) N_f dz = \int_0^R N_f (1 - z/R) dz$$

Which simplifies to:

$$\rho_l = N_f R/2 \quad or \quad \rho_l = N_f l/4 \qquad (6.2a)$$

Where the investigated surface is situated within the volume of the detector, tracks may originate at either side of the surface and their density is given as:

$$\rho_l = N_f R \quad or \quad \rho_l = N_f l/2 \qquad (6.2b)$$

Combination of equations 6.2a and b result in:

$$\rho_l = g N_f R \qquad (6.3)$$

Where *g* represents the geometry factor, and depends on whether the surface is external, g = 1 (or $4\pi$ geometry) or internal g = 0.5 (or $2\pi$ geometry).

The above relationship between spatial and aerial track density is the most highly simplified theoretical approach to understanding the track density problem in track detectors (Wagner & van den Haute, 1992). It is however of fundamental importance as a basis for understanding the fission-track dating method and the idea of measuring track lengths for the interpretation and/or correction of fission-track ages, given all other work conducted in fission-track analysis relies on this relationship (Wagner & van den Haute, 1992). Actual observed fission-track densities and lengths are, nevertheless, highly dependant on the etching method used to reveal latent tracks.

### 6.3.2 Low-temperature fission-track thermochronology

Low-temperature fission-track thermochronology is mostly performed using apatite [$Ca_{10}(PO_4)_6(F,Cl,OH)_2$](Elliott, 1994), a common accessory mineral to most magmatic rocks excluding ultrabasic rocks. The amount of apatite available in siliciclastic sedimentary rocks is generally related to the amount available in the source rock and the amount of sorting of the host sediments prior to lithification, with poorer sorting generally yielding higher concentrations of apatite, though authigenic mineralisation may result in locally higher concentrations of the mineral.

The accumulation of fission tracks in apatite occurs over geological time scales while the system is at or below the critical closure temperature e.g. 110 ± 10 ˚C over 10 Ma (Gleadow & Duddy, 1981). AFT shortening, measurably occurs between 110 ± 10 and 60 ˚C. Shortening is most significantly affected by the single period temperature reached at any given time while the system is open. Stable thermal conditions through any geologically significant time period are more effective in fission-track shortening than episodic conditions. In addition, individual grain annealing kinetics (e.g. grain chemistries including F/Cl ratios, REE incorporation) yield significant control on track annealing in apatites (Donelick, 1993; Barbarand et al., 2003).

## 6.4 Sampling strategy

Sampling for this study spanned siliciclastic sedimentary rocks from the southern Cantabrian Mountains, inclusive of lower Palaeozoic to pre-Stephanian sedimentary rocks of the southern Cantabrian Zone, Upper Carboniferous sedimentary rocks in the southern limb of the Central Coal Basin and Precambrian to Cambrian siliciclastic the central to southern limbs of the far eastern Narcea Antiform. In addition Stephanian, Cretaceous, Palaeogene and Neogene covers were also sampled. Figure 6.4-1 graphically depicts the sampling area and strategy undertaken.

Generally, sampling was concentrated along the lowest points in valleys of the Luna, Bernesga, Torio and Cureño rivers valleys, except for in the Stephanian Ciñera-Matallana Coal Basin, where a sampling strategy similar to that of Frings (2002) was followed. Other anomalous sampling locations are marked in figure 6.4-1.

Sampling for this study involved the collection of one hundred-four samples from which eighty were processed to a point where the presence or lack of significant quantity of apatite could be determined. Thirty-two processed samples yielded enough fission-track-laden apatite grains to measure aerial densities and provide error-constrained AFT ages (see chapter 7). Of the dated samples, twenty yielded at least minimum quantities of confined tracks to produce geologically constrained thermal models.

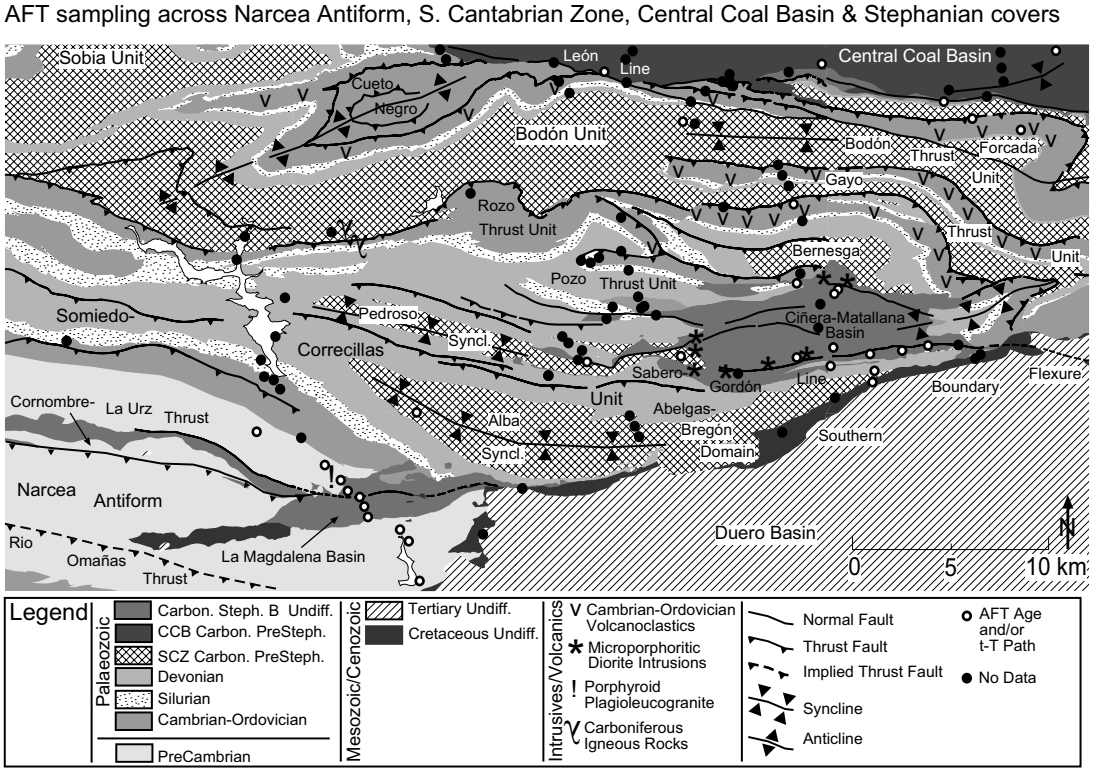


Figure 6.4-1: Overview of the study area with locations of all samples, those yielding fission tracks and barren samples.

## 6.5 Preparation procedure

### *6.5.1 Pre-irradiation preparation*

Depending on rock lithology, between 2 kg and 5 kg of rock material were collected in each sample in order to maximise the possibility for a sufficient yield of apatite grains in the each sample's apatite heavy mineral concentrate. Thereafter, laboratory preparation involved a rigorous process for the concentration of apatite including multiple mechanical techniques, three phases of heavy liquid separation, magnetic separation and hand picking of individual grains (see figure 6.5.1-1).

Following separation, apatite concentrates were embedded in epoxy, ground and polished to 1 µm of grit. Polished mineral concentrates yielding sufficient apatite grains were etched in 5.0 M $HNO_3$ at 20 ºC ± 1 for 20 ± 1 s to make fission tracks visible when investigated under high power optical microscopy (e.g. ~ × 1200).

This study utilises the grain-by-grain External Detector Method (EDM) (Gleadow, 1981; Hurford & Green, 1982) for fission-track age determination (see figure 6.5.1-2). The advantage of this method over that of the grain-population method (described in Wagner & van den Haute, 1992: 6.6.1), being there is no need to count areas of the same

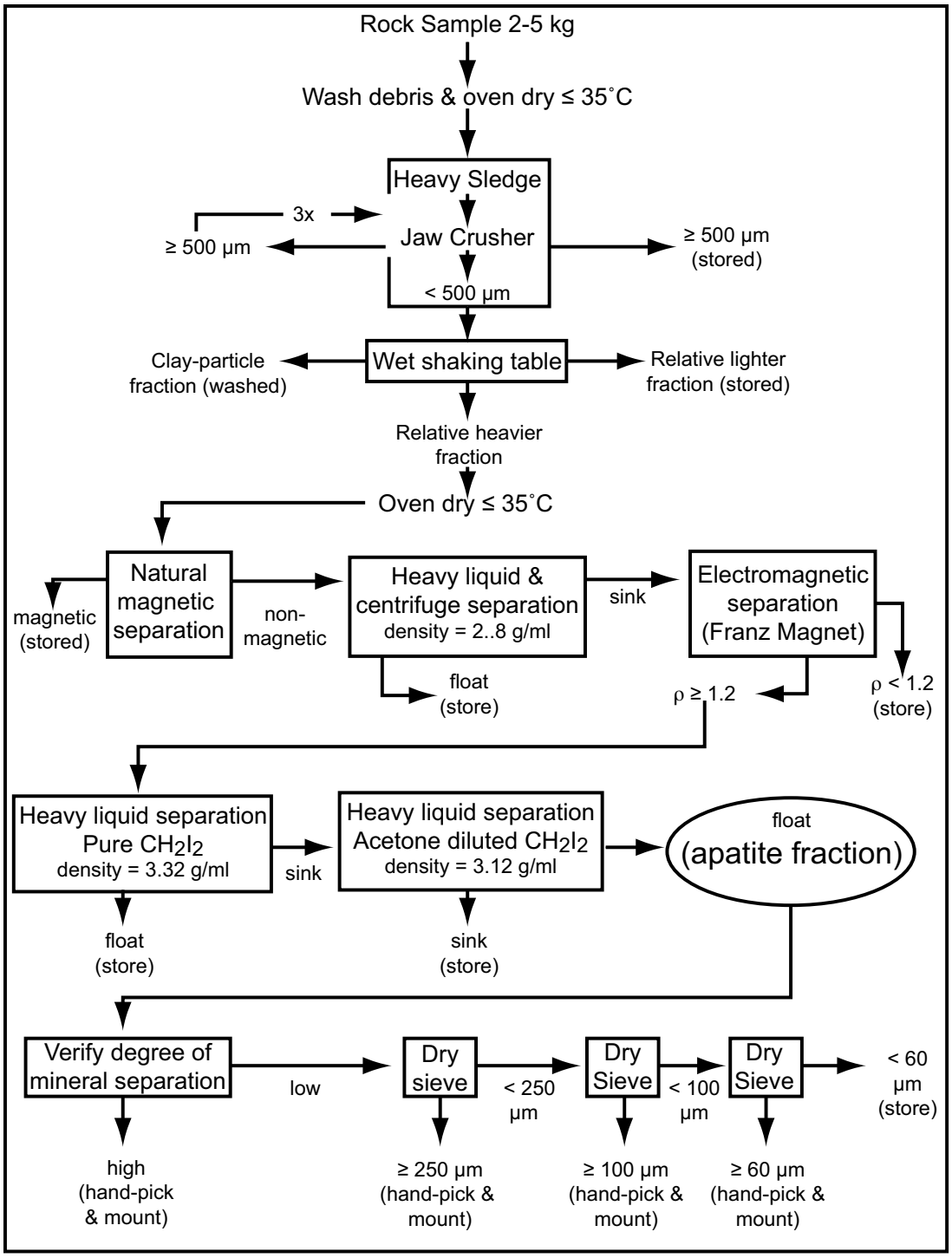


Figure 6.5.1-1: Flow diagram where the different stages of mineral separation are depicted.

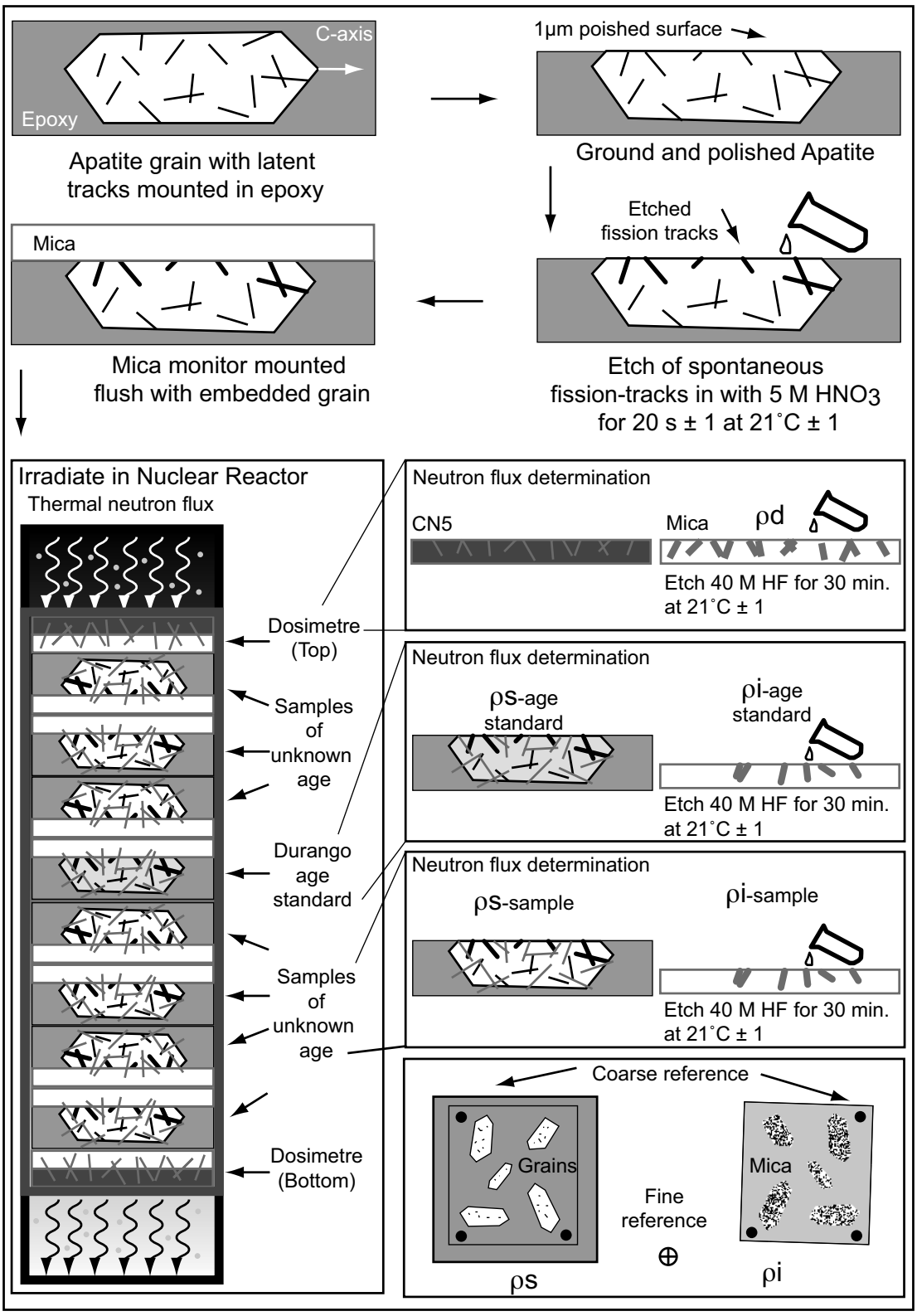


Figure 6.5.1-2: Laboratory procedure for grain-by-grain age determination via the External Detector Method) after Hurford & Carter (1991).

size between each grain. Instead, for each grain and mica pair, the same area is counted in order to determine the aerial track density of both spontaneous and induced fission-tracks within grains. The variability of individual grain-ages can therefore be assessed given each grain yields it own $\rho_s/\rho_i$ ratio (see equations 6.12 a, b) and hence its own age (Wagner & van den Haute, 1992: 3.6.2, 3.8.2).

Samples having yielded sufficient grains exhibiting spontaneous fission-tracks were then each mated together with a ~ 50 μm thick annealed, low-uranium-concentration fission-track detector composed of low opacity mica. In addition, micas were attached to dosimetre glasses[1] with known uranium concentrations in order to provide constraints on the gradient of the neutron fluence samples are subject to during irradiation,. Additionally, they are mounted to similarly polished and etched samples of the Durango AFT age standard (see section 6.8.2), used to solve the ζ-calibrated age equation (see equation 6.21). The final pre-irradiation step involved packing samples, the Durango AFT age standard and dosimetre glasses together in cylindrical irradiation capsules, the minimum dosimetre arrangement required being one at each end of the stack of samples to be irradiated. As a more accurate assessment of the variability of neutron fluence gradient within the capsule was possible, extra dosimetres were also placed within the stack (see figure 6.5.1-2).

### 6.5.2 *Sample irradiation*

Samples were then sent for irradiation in the highly thermalised "Tethys" research reactor facility, operated under the supervision of Prof. Dr. F. De Corte, University of Gent, Gent Belgium. In total, four capsules were sent for this study. Each capsule was irradiated for 16 hours via the highly thermalised neutron channel No. 8. Capsules were inverted midway through the irradiation process to minimise the effect of any potential gradient in neutron fluence through the capsule.

Under the above conditions, close contact between mica and grain surface of the samples and dosimetres permits some induced fission fragments to reach the mica detectors. Following irradiation capsules were left to "cool", or fission-out in a safe location for a period of about one month, as the uranium in the samples became activated due to irradiation. When it was safe to proceed the mated grain/mica pairs were unpacked, each assemblages was perforated with at least two reference marks, then grain/mica assemblages were separated, noting the mica contact surface. To reveal the $^{235}U$ fission event induced etch pits micas were individually etched for at least 30 minutes in a magnetically stirred 40 M HF bath at 21 ± 1 ˚C and three times doused in demineralised water to stop the reaction. Micas were then bathed in 100% ethanol and subject to ~ 10 minutes of heat at ~ 60 - 70 ˚C temperature via conduction heating plate.

1 In this study the Corning CN5 (12 ppm) dosimetre was used as its uranium concentration yields an optimum induced fission-track density (~106-107 tracks/cm$^2$) from the dosimetre ($\rho_d$) when irradiated in a highly thermalised irradiation facility with the procedure described in this chapter.

Final preparation for track counting involved mounting individual grain and mica detector pairs together on standard glass microscope slides. Pairs were oriented such that the reference markers of the polished grain surface and the mated surface of the mica detector were mirrored (see figure 6.5.1-2).

## 6.6 Dating procedure

### *6.6.1 Grain-by-grain external detector method*

For the purpose of this study the ζ-calibrated grain-by-grain external detector method for AFT age determination after Gleadow (1981) and Hurford & Green (1982) is utilised. However, in order to maintain clarity regarding the components involved in the technique, ζ-calibrated AFT age determination is presented in section 6.8.2. and the grain-by-grain track counting method is presented here below.

The advantage of grain-by-grain methods over grain-population methods (described in Wagner & van den Haute, 1992: 3.6.1), being they are the only methods which can be applied when the sample show strong uranium heterogeneity among grains, or is composed of grains with different age as may be the case in detrital settings such as sedimentary basins.

In grain-by-grain methods, there is no need to count areas of the same size between each grain as is done in the grain-population method. Instead the same area is counted in order to determine the aerial density of both spontaneous and induced fission-tracks within grains. The variability of individual grain-ages can therefore be assessed given each grain yields it own $\rho_s/\rho_i$ ratio (see equations 6.12 a, b) and hence its own age (Wagner & van den Haute, 1992: 3.6.2, 3.8.2).

In addition to the external detector method, two alternative methods have been developed (repolish and re-etch). However, given the external detector method is the only grain-by-grain method generally yielding high precisions in AFT applications, description of the alternative grain-by-grain as well as grain-population approaches is restricted to table 6.6.1-1.

The external detector method offers a high degree of flexibility with respect to the grain selection. In this method, grains with spurious defects, anisotropically etched tracks or strongly heterogeneous track distributions can be excluded from the measurement set. Therefore difficult samples can still be analysed. However, if track density is used as a selection criterion a sampling bias may occur (Wagner & van den Haute, 1992).

| | Grain-by-Grain Methods | | | Grain-Population Methods | |
|---|---|---|---|---|---|
| | Same grains used for analysing spontaneous and induced fission-tracks | | | Spontaneous and induced fission-tracks measured in different grains. | |
| Technique for induced track revelation | Repolish, etching | Re-etching grain | Etched external detector method | Polish, etch | Pre-irradiation annealing, polishing, etching |
| Counted tracks | $\rho_s + \rho_i$ | $\rho_i$ or $\rho_s + \rho_i$ | $\rho_i$ | $\rho_s + \rho_i$ | $\rho_i$ |
| Geometry ratio (G) | 1 | 0.5 | 0.5 | 1 | 1[b] |
| Procedural factor (Q) | 1 | ≠1 | ≠1[a] | 1 | 1[b] |
| Relative precision | Moderate | Moderate to high | High | Moderate to low | Moderate |
| Application[c] | Glass | Mica | Apatite, sphene, zircon | Glass | Apatite |

Table 6.6.1-1: Characteristics of fission-track dating procedures (after Wagner & van den Haute, 1992). [a]May be close to unity through careful selection of crystal faces and etching conditions. [b]If annealing does not change the track etching behaviour. [c]Refers to the material to which procedure is most commonly applied.

## *6.6.2 Image calibration*

Though physical area is not required in the grain-by-grain EDM method since identical areas were investigated to determine both spontaneous and induced track densities, it is required in order to determine the track density in the glass monitor or its mica image ($\rho_m$), and is helpful in calculating the uranium concentration of each investigated crystal, the calculation for uranium concentration being a function of the spontaneous ($\rho_s$) and induced ($\rho_i$) fission-track densities measured for each grain in the sample (see equations 6.12 a , b for explanation of $\rho_s$ and $\rho_i$).

Uranium variation between grains in theory bears no variation on individual grain $\rho_s/\rho_i$ ratios, no variation is expected apart from the random variation governed by Poisson statistics alone (Wagner & van den Haute, 1992). Experimental data often show this is not the case and reveal a supplementary variation between $\rho_s/\rho_i$ ratios (Galbraith, 1982).

Therefore, physical calibration of the image was conducted in order to solve for the physical area represented by any single pixel in the 1.4 M-pixel image. In order to calibrate the image, the 40 μm length standard of the Planno Measurement Stantard: CDITG_CAL was twice sampled 30 times along both the X and Y planes using two independently captured images. The mean lengths calculated for any given pixel X-dimension was 0.1 μm, as was the mean length of any given pixel Y-dimensions. The physical area calculated for images captured under this system being 14000.0 $\mu m^2$.

## *6.6.3 Fission track counting*

The grain-by-grain EDM method used here employed mirrored spontaneous and induced fission-track image pairs collected via the *Soft Image Systems Fview-2* high definition (1376 by 1032 pixel), black & white charge-coupled device (CCD) type digital camera. The camera was mounted to an *Olympus BX50* Optical Microscope with an *AutoScan Achsen AS3000B* stage and a 50 × objective attached. Physically

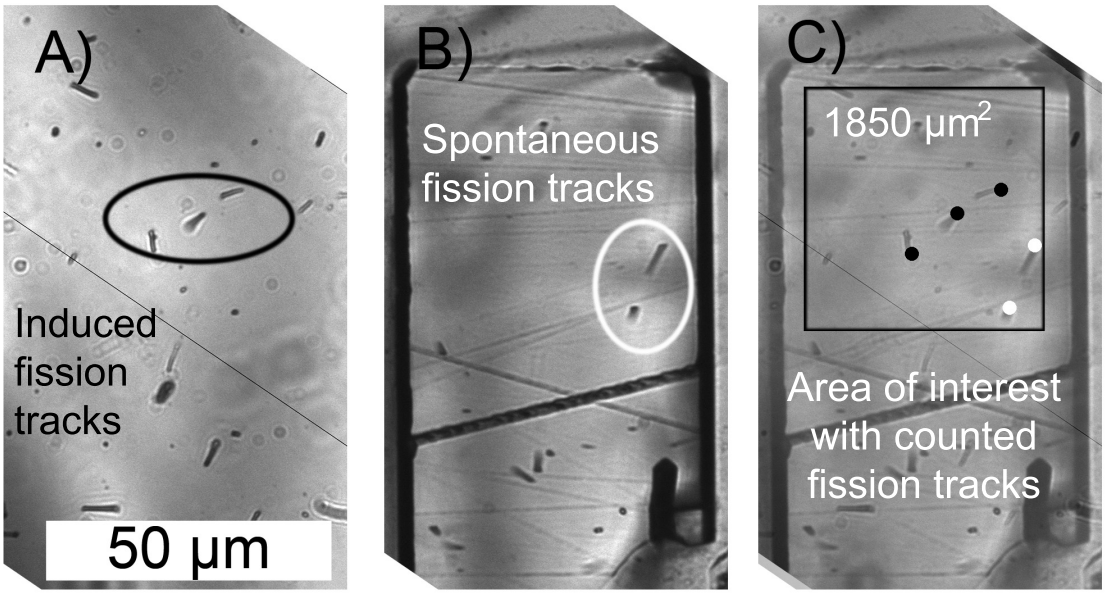


Figure 6.6.3-1: Counting of fission tracks involved overlaying the mica image (a) onto the grain image (b) such that a high precision composite image (c) could be used to resolve the relative location of $^{235}U$ induced fission-tracks with respect to their relevant parent grain. The area of interest is encapsulated by the black square. Black and white dots mark the location of counted $^{235}U$ induced and spontaneous $^{238}U$ fission-tracks respectively.

calibrated image capture was conducted using the *Autoscan's Trackscan 3.0* software and mirrored image pairs (e.g. figure 6.6.3-1) were matched using Adobe Photoshop image processing software. Tracks were counted using a hand-held counting device.

Where possible, upwards of 20 grains were counted for each sample. Only grain with prismatic sections were measured. Where strongly heterogeneous track densities occurred only internally homogeneous subsections were considered for age determination, heterogeneous components being considered as different grains. Induced track densities in dosimetres ($\rho_m$) required for the age determination (see Chapter 6.8.2) were obtained from the weighted mean average track densities of mica dosimetres irradiated along with each sample capsule (minimum arrangement being top and bottom) (see figure 6.5.1-1).

## 6.7 Fission-track age calculation

### *6.7.1 Fundamental age equation*

Fission-track dating, in principle is no different from any other isotopic technique based on the decay of naturally radioactive parent isotope to a stable daughter isotope. Being a first order reaction, the decay occurs at a rate proportional to the number of parent atoms ($N_p$) available at any given time (t), or:

$$dN_p / dt = -\lambda N_p \qquad (6.4)$$

$\lambda$ being the decay-constant, is expressed in $a^{-1}$.

Integration of the above equation while considering that $(N_p)_0$ is the total amount of parent atoms available at time t = 0 results in the equation describing the variation of the number of parent atoms available through time,

$$N_p = (N_p)_0 e^{-\lambda t} \qquad (6.5)$$

In order to solve for time, the quantities generally available to the investigator are the per volume present amount of parent isotope atoms $N_p$ and daughter isotope atoms $N_D$. Thus,

$$(N_P)_0 = N_P e^{\lambda t} \qquad (6.6.a)$$

and considering,

$$N_D = (N_P)_0 - N_P \qquad (6.6b)$$

can be modified to:

$$N_D = N_P (e^{\lambda t} - 1) \qquad (6.6c)$$

the basic equation for the majority of isotopic-dating methods including the fission-track method (Wagner & van den Haute, 1992). In the fission-track method, spontaneous fission-tracks take the place of daughter isotope atoms as the result of decay of $^{238}U$.

The fission constant of naturally radioactive elements provides the basis for the fission-track thermochronological method (Wagner & van den Haute, 1992). $^{232}Th$, $^{235}U$ and $^{238}U$ are the isotopes which posses decay constants significant to geological applications. However, the relative natural abundance of $^{235}U$ being so low and the spontaneous-fissioning half live of $^{232}Th$ being so long, $^{238}U$ is considered the only significant source for spontaneous fissioning (Table 6.2-1, Price and Walker, 1963; Wagner and van den Haute, 1992). Given such, the total production of spontaneous fission events ($N_s$) is proportional to the number of $^{238}U$ available (per unit volume) for fissioning through time:

$$N_s = \left(\frac{\lambda_f}{\lambda_d}\right) \cdot {}^{238}N\left(e^{\lambda_d t} - 1\right) \qquad (6.7)$$

where $\lambda_f$ / $\lambda_d$ is the fixed proportion of the decay constant of $^{238}U$ due to spontaneous fission ($\lambda_f$) in relation to the total decay ($\lambda_d$) (because the natural disintegration of $^{238}U$ not only occurs via spontaneous fissioning but also via $\alpha$-decay, i.e. to $^{206}Pb$ due to $\alpha$-emission)

$\lambda_f$ is limited to between $7.0 \cdot 10^{-17} a^{-1}$ to $8.5 \cdot 10^{-17} a^{-1}$: (Bigazzi, 1981) with $8.46 \cdot 10^{-17} a^{-1}$ (Galliker et al., 1970), obtained via the rotating bubble chamber method, remaining one of the most highly accurate estimations of $\lambda_f$, (Wagner & van den Haute, 1992); $\lambda_d$ is the total decay constant of $^{238}U$ ($1551.10^{-10}$ $a^{-1}$: Wagner & van den Haute, 1992), and $^{238}N$ representing the number of $^{238}U$ atoms.

Because $\lambda_f$ is several orders of magnitude less than the constant for $\alpha$-decay ($1.5 \cdot 10^{-10} a^{-1}$), $\lambda_d$ can be considered to be equal to $\lambda_a$. The above equation when solved for time yields:

$$t = \frac{1}{\lambda_\alpha} \ln\left[1 + \left(\frac{\lambda_\alpha}{\lambda_f}\right) \cdot \left(\frac{N_s}{^{238}U}\right)\right] \qquad (6.8)$$

The time cannot be calculated until the number of $^{238}U$ atoms and the number of spontaneous fissioning events have been determined. The number of $^{238}U$ atoms must be determined per unit volume in each crystal. This is derived from the number of induced tracks counted in an area of the external mica detector ($N_i$) recording the induced fission events while irradiated for a known time in a nuclear reactor such as the Tethys research reactor Gent, Belgium with a fluence ($\phi$) of thermal neutrons.

Spontaneous fissioning events are counted directly under an optical microscope with sufficient magnification. The number of induced fission events recorded in the external mica detector ($N_i$) is calculated from:

$$N_i = {}^{235}N\sigma\phi g \qquad (6.9)$$

Where $^{235}N$ is the number of $^{235}U$ atoms; $\sigma$ is the cross-section for thermal neutron-induced fission of $^{235}U$ ($584.25 \cdot 10^{-24}$ $cm^2$ ($\pm$ 0.19 %): see Wagner & van den Haute, 1992); $\phi$ the neutron fluence (neutrons/$cm^2$); g, the geometry factor, is a constant referring to the initial geometry of the pre-etched internal (1) or external (0.5) surface (section 6.3.1).

In order to determine the number of $^{238}U$ atoms that are in the sample ($^{238}N$), a procedure is used based on fision track counting, assuming the ratio $^{235}U/^{238}U$ (I) = $7.252e \cdot 10^{-3}$ as a constant. This is the case most often encountered on earth, however exceptions such as the site of the Olko Uranium Mine, Gabon, a one time natural nuclear reactor, do exist (Wagner & van den Haute, 1992).

Hence, in most cases, the number of $^{238}U$ atoms is solved from,

$$^{238}N = \frac{N_i}{I\sigma\phi g} \qquad (6.10)$$

Combining equations 6.8 and 6.10 the fission-track age is calculated as:

$$t = \frac{1}{\lambda_\alpha} \ln\left[\left(\frac{\lambda_\alpha}{\lambda_f}\right) \cdot \left(\frac{N_s}{N_i}\right) I\sigma\phi g + 1\right] \qquad (6.11)$$

the fundamental age equation of the fission-track method. The measurement of a fission-track age is now reduced to the ratio of spontaneous and induced track densities and the elucidation of the thermal neutron fluence (Wagner & van den Haute, 1992).

### *6.7.2 Practical age equation*

In equation 6.11 both $N_s$ and $N_i$ are expressed as spatial track densities (tracks per unit volume). Practically though, tracks which intersect the investigated sample surface are those which are counted. Given the theoretical relation between spatial and aerial track densities described in section 6.3.1, and considering the effects of track etching and the systematic observation factor $q \leq 1$, a factor, which aims to account for personal observation biases in track counting (Wagner & van den Haute, 1992), spontaneous and induced track densities can be expressed as:

$$\rho_s = g_s N_s R_s \eta_s f(t)_s q_s, \qquad (6.12a)$$

$$\rho_i = g_i N_i R_i \eta_i f(t)_i q_i, \qquad (6.12b)$$

where:

$g_{s,i}$ = geometry factor,
$R_{s,i}$ = the average etchable range of a fission-track fragment in the investigated material,
$\eta_{s,i}$ = the etching efficiency factor,
$f(t)$ = the etch time factors,
$q_{s,i}$ = the observation factor.

The geometry factor refers to the initial geometry of the pre-etched sample surface, considered constant at 1 for an internal surface, 0.5 for an external surface. The etchable ranges of spontaneous and induced fission-tracks $R_s$ and $R_i$, are practically equal when measured in the same material (Wagner & van den Haute, 1992 and citations therein). The values of $\eta$, $f(t)$ and $q$ are dependant on revelation and observation techniques.

Practically, the age equation, resultant from substitution of equations 6.12 a and b becomes:

$$t = \frac{1}{\lambda_\alpha} \ln\left[\left(\frac{\lambda_\alpha}{\lambda_f}\right) \cdot \left(\frac{\rho_s}{\rho_i}\right) QGI\,\sigma\phi + 1\right] \qquad (6.13)$$

Spatial track densities being are replaced by the observed aerial track densities. The factor $G = g_s/g_i$ refers to the initial geometry ratio of surfaces investigated for counting of spontaneous and induced tracks (normally 0.5 or 1 depending on the procedure used; see table 6.6.1-1). Q is a procedural factor equal to 1 if spontaneous and induced tracks are revealed and counted under identical conditions.

## 6.8 Dating systems

Absolute and calibrated fission-track age determination represent the most commonly used approaches to in fission-track dating. The absolute age approach is conducted as an attempt to directly solve the age equation (6.13) by measuring thermal neutron fluence ($\phi$) (Wagner & van den Haute, 1992). To avoid the explicit determination of $\phi$, the age standard approach, a comparative method based on the reference materials that yield highly constrained geological ages measured with other isotopic methods (K-Ar, Rb-Sr) (Hurford & Green, 1981), have been developed.

### 6.8.1 *Absolute age approach*

If applied properly the absolute approach should lead to correct ages (van den Haute et al., 1988). The major concern of this approach is to accurately quantify $^{235}N\sigma\phi$. This is best achieved through the use of a uranium monitor, and to measure the fission products of the monitor after irradiation (e.g. by $\gamma$-spectrometry). In practice however, the determination of thermal neutron fluence ($\phi$) through the monitoring for another kind of metal (e.g. Au, Co) or glass standard with known uranium concentration, and substituting the value of $\phi$ obtained from the metal or glass into age equation (Wagner & van den Haute, 1992).

However, methodological difficulties attributed to uncertainty about the value of the fission decay constant ($\lambda_f$) and in determining the absolute thermal neutron fluence ($\phi$) (see Hurford & Green, 1982) that formed a part of the absolute fission-track age equation (6.13) were exemplified by a series of conflicting absolute age determinations.

### 6.8.2 $\zeta$-*Calibrated age*

In order to correct for the difficulties attributed to the absolute age approach, Hurford and Green (1983) proposed the calibration of unknown fission-track age determinations versus age standards dated by other radiometric dating techniques known as the $\zeta$-calibration method. From 1988, the fission-track dating community have adopted this

calibration technique (Fleischer et al., 1975; Hurford & Green 1982, 1983; Jonckheere et al., 2000), and it is the method utilised in this study to reveal the fission-track age of each sample.

In the ζ-calibration method, samples of standard with calibrated fission-track ages are irradiated together with standard dosimetres (e.g. CN5, CN2) in order to normalise the spontaneous/induced track ratio to geological time (Hurford & Green, 1983). Hence the unknowns ($\lambda_f$ and $\phi$) are combined in one term, the ζ value, simultaneously solved using the density of spontaneous and induced fissioning events ($\rho_s$ and $\rho_i$) in age standards and their mated mica dosimetres. ζ-calibration values are sensitive to age standard selected, apparatuses used and analysts' personal fission-track recognition biases (Hurford & Green, 1982).

Given a factor $Z = QI\sigma/\lambda_f$ (expressed in the dimension of time), the age equation (6.13) can be rewritten as:

$$t_u = 1/\lambda_\alpha \ln\left[\lambda_\alpha \left(\rho_s/\rho_i\right)_u GZ + 1\right] \qquad (6.14)$$

Z being derived from the analysis of standard of known age ($t_{STD}$) irradiated in the same reactor facility along with the unknown sample ($t_u$), (hence, they share the same $\phi$). and analysed using exactly the same procedure (hence, they share the same Q) follows as:

$$Z = \frac{\left(e^{\lambda_\alpha t_s} - 1\right)}{\lambda_\alpha (\rho_s/\rho_i)_{STD} G} \qquad (6.15)$$

If both the standard and the unknown sample are of a young age, the equation simplifies to:

$t_u = (\rho_s/\rho_i)_u GZ$ *with* $Z = t_{STD}/(\rho_s/\rho_i)_{STD} G$,

or

$$t_u = \frac{\left(\rho_s/\rho_i\right)_u}{\left(\rho_s/\rho_i\right)_{STD}} t_{STD} \qquad (6.16)$$

allowing for the determination of the age of the unknown sample from the ratio of the track density ratios of the unknown sample and the age standard.

ζ-calibration presents a more practical and elaborate alternative to the solving the age equation requiring two steps. Firstly, age standards are repeatedly analysed in combination with glass monitors to establish a calibration factor ζ. Induced fission-track densities ($\rho_m$) of standard glasses (or adjacent mica detectors) are counted as a proxy for ϕ. The ratio between ϕ and $\rho_m$ is:

$$\phi = B\rho_m \qquad (6.17)$$

B, an empirically determined constant expresses the proportionality between ϕ and $\rho_m$ (Fleischer et al., 1975; Wagner & van den Haute, 1992).

The ζ factor (a × $cm^{-2}$) for each glass dosimetre is defined as:

$$\zeta = \frac{\phi\sigma I}{\lambda_f \rho_m} \qquad (6.18)$$

and equation 6.15 can be rewritten as:

$$\zeta = \frac{\left(e^{\lambda_\alpha t_{STD}} - 1\right)}{\lambda_\alpha \left(\rho_s / \rho_i\right)_{STD} G\rho_m} = QI\sigma B / \lambda_f \qquad (6.19)$$

with the ζ-calibration standard error as calculated by Green (1981 a) being:

$$\sigma(\zeta) = \zeta\sqrt{\frac{1}{N_s} + \frac{1}{N_i} + \frac{1}{N_m} + \left[\frac{\sigma\left(t_{STD}\right)}{t_{STD}}\right]^2} \qquad (6.20)$$

where $N_s$, $N_i$ and $N_m$ are the total number of spontaneous, induced and dosimetre-derived tracks respectively. $t_{STD}$ and $\sigma(t_{STD})$ are the age and standard error of the age standard used for the calibration.

The second step involves co-irradiation of the unknown sample with the glass monitor to produce the ζ-calibrated fission-track age, calculated using the following equation (after Hurford & Green, 1983):

$$t_u = \frac{1}{\lambda_\alpha} \ln\left[\lambda_\alpha \left(\frac{\rho_s}{\rho_i}\right)\rho_m G\zeta + 1\right] \qquad (6.21)$$

In this study the dosimetre glass CN-5 with a uranium concentration of 12 ppm (Wagner & van den Haute, 1992) was used to monitor the thermal neutron fluence. The age standard used was Durango apatite (Cerro de Merecado, Mexico), with a K-Ar age of 31.4 ± 0.6 Ma (McDowell & Keizer, 1977). Personal ζ-calbration values are presented in table 6.8.2-1.

| Calibrated personal ζ-value (Durango: 31.4 ± 0.5 Ma) | | | | | | |
|---|---|---|---|---|---|---|
| Irradiation date | Grain Areas | $\rho_s$ ($N_s$) (× $10^6$ tracks $cm^{-2}$) | $\rho_i$ ($N_i$) (× $10^6$ tracks $cm^{-2}$) | $\rho_m$ ($N_m$) (× $10^6$ tracks $cm^{-2}$) | ζ | ± 1 σ |
| 22 08 2003 | 44 | 0.24 (1152) | 1.56( 7614) | 1.37 (10217) | 303.57 | 11.16 |
| 22 09 2003 | 13 | 0.44 (1243) | 2.79 (7931) | 1.19 (13318) | 334.04 | 12.00 |
| 10 11 2004 | 27 | 0.17 (1022) | 1.21 (7278) | 1.30 (22255) | 344.68 | 12.96 |
| 10 12 2004 | 22 | 0.20 (1031) | 1.25 (6526) | 1.22 (15423) | 325.70 | 12. |

Table 6.8.2-1: Calibration of personal ζ-value for Durango apatites in this study. N = number of analysed grains, $\rho_s$, $\rho_i$, $\rho_m$ refer respectively to the spontaneous, induced and dosimetre derived fission-track densities, the number of associated tracks counted in parentheses.

## 6.9 Age formats: (pooled, mean and central-ages)

In order to calculate a reasonable fission-track age of a sample, spontaneous and induced track pairs in at least 20 to 50 grains are usually counted[2]. In a sediment single-grain-ages may vary considerably because individual grains may originate from different sources with diverging thermal histories and/or differing kinetic dispositions. Three methods to calculate a sample fission-track age include: pooled, mean, or central-age.

### 6.9.1 ζ-*Calibrated pooled-age*

Assuming that investigated grains belong to a single homogenous population (based on Poissonian statistics) the ζ-calibrated pooled-age can be calculated by simply substituting the respective sums of spontaneous ($N_s$) and induced ($N_i$) tracks from all investigated grains for the values or $\rho_s$ and $\rho_i$ into the ζ-calibrated age equation (6.21),

$$t_u = \frac{1}{\lambda_\alpha} \ln\left[\lambda_\alpha \left(\frac{\sum N_s}{\sum N_i}\right) \rho_m G \zeta + 1\right] \qquad (6.22)$$

The standard deviation of the ζ-calibrated pooled-age being:

$$\sigma(t_u) = t_u \sqrt{\frac{1}{N_s} + \frac{1}{N_i} + \frac{1}{N_m} + \left[\frac{\sigma(\zeta)}{\zeta}\right]^2} \qquad (6.23)$$

A $\chi^2$ test having been developed (Galbraith, 1981; Green, 1981 a) is applied in order to assess whether the calculated single-grain-ages follow a Poisson distribution or if a supplementary variation exists. The calculation with degrees of freedom = n-1 is:

$$\chi^2 = \Sigma_j \left[\frac{\left(N_{sj} - N'_{sj}\right)^2}{N'_{sj}} + \frac{\left(N_{ij} - N'_{ij}\right)^2}{N'_{ij}}\right] \qquad (6.24)$$

2 Where fewer grains are available the researcher must decide if the number of grains available for counting will reflect a reasonable fission-track age (i.e. if the age will reveal any age information of significance to the study). In this study, where less than 20 grains were available, the minimum number of grains counted to reveal significant age information was ten.

where $N'_{sj}$ and $N'_{ij}$ are the expected spontaneous and induced fission-tracks in the $j^{th}$ grain. Their calculations follow from $N_sN_j/N$ and $N_iN_j/N$, respectively where $N = N_s + N_i$, the total number of spontaneous and induced tracks counted in all grains and $Nj = N_{sj}$ and $N_{ij}$, the number of spontaneous and induced tracks in the $j^{th}$ grain. A value of $P(\chi^2) < 5$ % (i.e. there is less than 5 % probability of finding the calculated $\chi^2$ value) evidences a non-homogeneous single-grain-age distribution (i.e. more than one age population or partially annealed grains with differing annealing responses). In this case the weighted or unweighted mean of the individual $\rho_s/\rho_i$ ratios is taken as an estimate of the overall track-density ratio instead of $N_s/N_i$ and the standard deviation of these ratios serves as a basis for error calculations (Green, 1981 a, Wagner & van den Haute, 1992).

### *6.9.2 ζ-Calibrated mean-age*

The ζ-calibrated mean-age is calculated using the arithmetic mean of all individual spontaneous to induced fission-track density ratios,

$$t_{Mean} = \frac{1}{\lambda_\alpha} \ln\left[\lambda_\alpha \bar{\rho}_{ratio} \rho_m G \zeta + 1\right] \qquad (6.25)$$

where,

$$\bar{\rho}_{ratio} = \frac{\sum \frac{\rho_s}{\rho_i}}{n} \qquad (6.26)$$

and n represents the number of grains investigated. The standard deviation of the ζ-calibrated mean-age being:

$$\sigma(t_{Mean}) = \sqrt{\frac{\sum\left(t_j - t_{Mean}\right)^2}{n-1}} \cdot \frac{1}{\sqrt{n}} \qquad (6.27)$$

$t_j$ representing the fission-track age of the $j^{th}$ grain and The validity of the ζ-calibrated mean-age, as for the ζ-calibrated pooled-age is analysed via the $\chi^2$-test.

### *6.9.3 ζ-Calibrated central-age*

The ζ-calibrated central-age (Galbraith & Laslett, 1993) allows for non-Poissonian variations in the counts of fission tracks. Its precision is directly proportional to the number of induced and spontaneous tracks counted. Thus, it provides for a more robust central tendency of the single-grain-ages, since it forms the weighted mean of the sample (Green, 1981 a; Wagner & van den Haute, 1992). Given such, the ζ-calibrated central-age is more commonly reported than ζ-calibrated pooled-age or ζ-calibrated mean-age.

The ζ-calibrated central-age is reported following equation 6.21 as:

$$t_{Central} = \frac{1}{\lambda_\alpha} \ln\left[\lambda_\alpha(\rho_{ratio})\rho_m G\zeta + 1\right] \quad (6.28)$$

where, the $\rho_{ratio}$ can be represented by:

$$\rho_{ratio} = \frac{\sum w_j \left(\frac{\rho_s}{\rho_i}\right)_j}{\sum w_j} \quad (6.29)$$

The weight of a single grain is represented by:

$$w = \frac{1}{\sqrt{\left(\frac{1}{\rho_s}\right) + \left(\frac{1}{\rho_i}\right)}} \quad (6.30)$$

The standard deviation of the ζ-calibrated central-age is reported as

$$\sigma(t)_{central} = t_{central}\sqrt{\frac{1}{\eta^2(1-\eta)^2\sum w_j} + \frac{1}{N_m} + \left[\frac{\sigma(\zeta)}{\zeta}\right]^2} \quad (6.31)$$

where:

$$\eta = \frac{\sum w_j \left(\frac{\rho_s}{\rho_s + \rho_i}\right)_j}{\sum w_j} \quad (6.32)$$

### 6.9.4 *Dispersion and mixed ages*

Both the $\chi^2$-test (equation 6.24) and dispersion are used as indicators for the presence of mixed single-grain-ages in a sample. As stated in section 6.8.1, if the sample fails the $\chi^2$-test at a nominal value (e.g. $P(\chi^2) < 5$ %) then more than one age population subcomponent is expected. However the $\chi^2$-test is an unweighted test in that it does not consider the 'weight' of the individual grain in the calculation. Age dispersion does incorporate the weight of the sample (Galbraith & Laslett, 1993). However there is no discrete value for dispersion that indicates the boundary between singular statistical age population and mixed age subcomponents.

The complete algorithm to estimate the ζ-calibrated central-age, along with its age dispersion (spread of single-grain-ages) is available in appendix A of Galbraith & Laslett (1993). A ζ-calibrated central-age in combination with a low age dispersion (< 15) represents a relatively good estimation of a homogeneous age population and often pass the $\chi^2$-test. However, samples composite of grains with very low precision

(i.e. low ppm uranium) often fail the $\chi^2$-test, despite yielding low dispersion. An age dispersion of > 40 is taken to strongly indicate the presence of more than one age subcomponent.

Thus samples in this study not passing the $\chi^2$-test (all but two) were tested for age sub-component with the *Binomfit 1.0* mixture modelling program (Brandon, 2002). Thus samples with negative results for mixture modelling were checked for dispersion and if considered high were tested for their variability in the $D_{par}$ annealing kinetic indicator (section 6.13).

## 6.10 Fission-track age visualisation

In order to view a distribution of single-grain-ages and associated standard errors common to one sample with respect to that sample's central value, Galbraith (1990) devised the radial plot to visualise the distribution of single-grain-ages. Here, the AFT age calculation and visualisation program *TRACKKEY version 4.2* (Dunkl, 2002) is utilised to produce the AFT grain-age radial plots (figure 6.10-1).

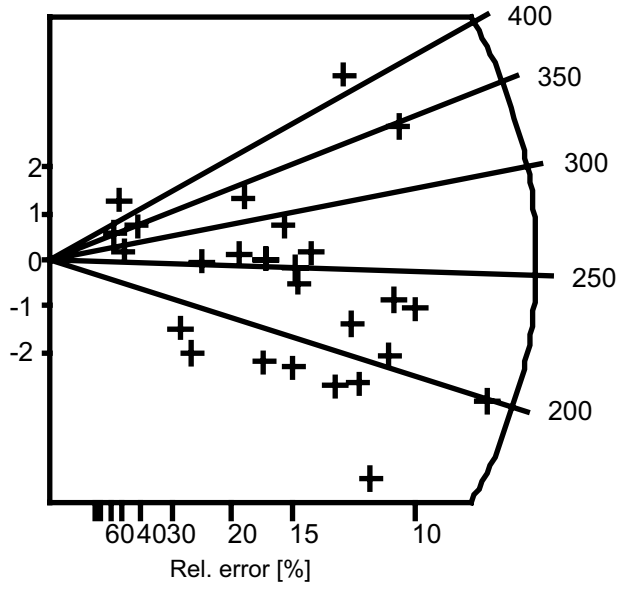


Figure 6.10-1: The *TRACKKEY 4.2* AFT grain age radial plot with the relative error (%) represented in the X-axis; AFT ages are represented in the radial plot with their standard deviation from the mean calculated age depicted on the Y-axis.

The age standardised estimate ($y_j=(z_j-z_0)/\sigma_j$) is represented in the Y-axis. Traditionally, the age's precision ($1/\sigma_n$) is represented in the X-axis (Wagner & van den Haute, 1992). Precision is proportional to the number of spontaneous plus induced tracks in a single grain:

$$\sigma_j = \sqrt{(1/N_s) + (1/N_i)} \qquad (6.33)$$

*TRACKKEY 4.2* represents the precision of AFT grain-ages as a function of their 1σ relative error.

The AFT age is plotted in millions of years (Ma) on the Z-axis, represented as a semicircular ellipse with the central-age occurring at or near the centre or the arc.

The radial plot is used to visualise grain-ages together with their standardised estimates ($y_j$), standard errors ($z_j \pm 1$ or $2\sigma$) and precision ($1/\sigma_j$) values. For any individual grain (X, Y) the corresponding age is acquired by plotting a line from origin ($X_0$, $Y_0$) through ($X_n$, $Y_n$) to the Z axis. Individual $2\sigma$ confidence interval of the single-grain-age may be drawn similarly by extrapolating lines from the origin ($X_0$, $Y_0$) through the grain-age's $\pm 2\sigma$ error (($X_j$, $Y_j$, $Z_j$,$+2\sigma$) and ($X_j$, $Y_j$, $Z_j$, $-2\sigma$)). To avoid displaying all the single grain-ages with their associated $2\sigma$ error bars on the plot, the standard error ($\pm 2\sigma$ ) for the central-age is plotted with respect to the origin, which enables qualitative evaluation of all grain estimate distributions.

## 6.11 Track-length measurement in apatites

Etched fission-tracks in apatite are easily distinguishable from other etchable features such as defects. Reasons for their distinguishability include random orientation, and limited maximum length; in apatite initial track-length ($L_0$) is between about 15.9 µm and 16.5 µm (Green et al., 1986; Gleadow et al., 1986; Donelick et al., 1990) and through the process of partial to total annealing may shorten to 0 µm. over geologic and experimental time scales (Wagner & van den Haute, 1992).

For track-length measurements, only entirely confined lengths parallel to the polished grain surface (i.e. horizontal) are used because only these tracks reveal their complete lengths under conventional microscopic measurement techniques (figure 6.11-1). Confined tracks are those that do not reach the polished mineral surface, but are etched when they intersect another fission track, a crack or a surface-cleavage plane (Green 1981 b). A measurement bias is inherent from this mechanism of track revelation, because longer tracks are more likely than shorter ones to intersect with another track, a fracture or a cleavage plane, and therefore be etched and counted (Wagner & van den Haute, 1992).

Anisotropic track annealing is reported, to be dependant on the tracks orientation to the apatite crystallographic c-axis. Tracks parallel to the c-axis shorten less and etch faster than track perpendicular to the c-axis (figure 6.11-2; Green et al., 1986; Donelick, 1991; Crowley et al., 1991; Donelick et al., 1999; and Ketcham, 2003).

In order to normalise measured fission-track-lengths to their corresponding c-axis parallel value, the crystallographic c-axis of each investigated grain was estimated following the criteria set out in Donelick (1991). There, each grain selected for measurement exhibited (a) linear interface with the epoxy where an inclined prismatic face is intersected by the polished surface and (b) elongate etch pit cross-sections aligned parallel to the c-axis due to bulk etching anisotropy (e.g. Singh et al., 1986).

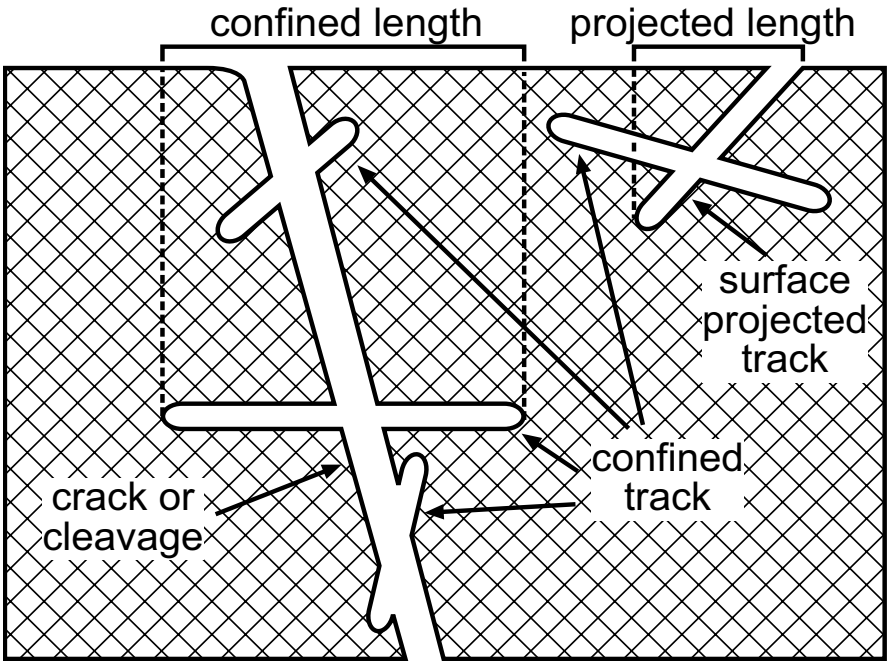


Figure 6.11-1: Observable fission-track types: confined tracks and surface projected tracks. only subhorizontal to horizontal confined tracks were measured for their length parametres. The three confined tracks on the left are TINCLES while that on the right is a TINT. Projected tracks were not measured for their length parametre, instead they were counted apart as partial input to AFT age determination (section 6.7). After Wagner & van de Haute, 1992.

A c-axis parallel annealing correction factor was proposed by Carlson (1990) and Donelick (1991), which quantifies the crystallographic orientation dependence based on the assumption the mean etchable fission-track-length at any angle to the c-axis is given by the corresponding radius of and ellipse with semiaxes equal to the mean-track-lengths parallel and perpendicular to the c-axis. The correction factor allows for the conversion of any c-axis oriented confined-track by measuring the acute to right angle defined by the intersection of that track's length and the c-axis of the grain (figure 6.11-3; Donelick, 1999).

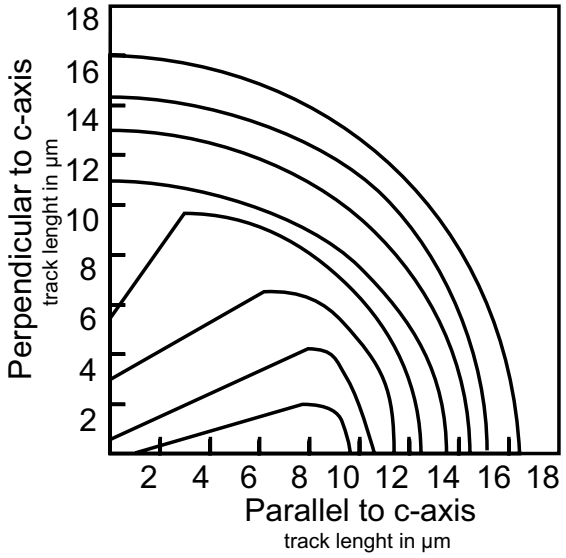


Figure 6.11-2: Model describing the pattern of anisotropic annealing in apatite crystals for different temperatures (after Donelick et al., 1999). Outermost arcs correspond to annealing at cooler temperatures.

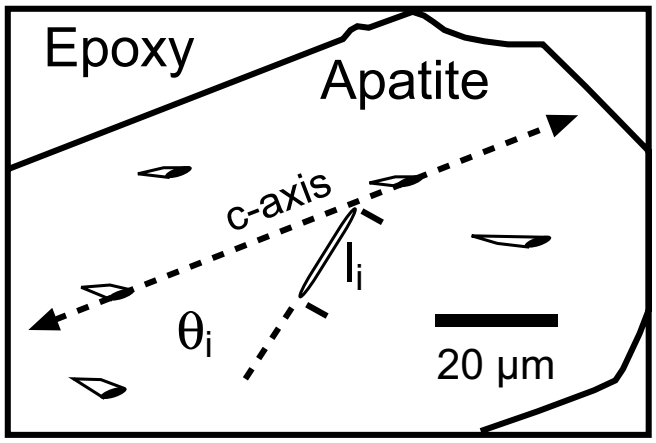


Figure 6.11-3: Schematic representation of an an example apatite crystal yielding confined horizontal and surface projected fission-tracks. Modified after Donelick (1991). The c-axis is estimated by projecting a line through the long-axes of at least two surface projected etch pits. The confined track is measured for its length ($l_i$) and the orientation ($\theta_i$) parametres.

For this study, track-length measurements were conducted "live" using high intensity non-polarised incident light in combination with the hardware outlined in section 6.6.2 under the maximum magnification afforded by the system (200 ×, 100× objective and the 2× magnifier). *Autoscan's Trackscan Easylength* subroutine which makes possible the high precision measurement of both track-in-track (TINT) and track in cleavage (TINCLE) (Bhandari et al., 1971) track types (figure 6.6.4-1) was used to facilitate the measurement and recording of relevant fission-track parametres.

In order to accurately estimate track lengths, image calibration was conducted as per the method described in section 6.6.3, but under 200 × magnification; The X- and Y-pixel dimension values (each 2.5 × $10^{-3}$ µm) input into *Autoscan's Trackscan Easylength* subroutine.

Only those etching revealed tracks entirely localised in the interior of the crystal, and at least subparallel to the grain's polished surface were measured (figure 6.11.4). Estimates of intact $^{235}U$ induced confined track-lengths in apatite exhibit shapes close to the normal distribution with etched initial track-lengths indicating mean values to ~ 16 µm ± 0.8-1 µm (Gleadow et al., 1986; Wagner & van den Haute, 1991: figure 2.24 a). Therefore objects in this study with etched lengths greater than 17 µm were ignored. Also, tracks with lengths shorter than 6 µm were ignored as segmentation of these tracks was often observed; the true length of the segmented fission-tracks being difficult to ascertain.

When available, at least 100 confined track-lengths were measured in order to ensure a statistically representative track-length distribution was obtained (Gleadow et al., 1986). Track-length populations especially those with broad track-length distributions (e.g. bimodal populations, slowly cooled populations) are best represented by large sample numbers ($n > 100$), as smaller counts may not precisely represent the distribution. In this study, unless otherwise stated, track-length distributions are reported by the conventional arithmetic mean AFT length, 1σ standard deviation, number of tracks and a histogram with a 1 µm bin interval (after Green et al., 1986). When track angle relative to c-axis is reported, the polar coordinate plot should be utilised (Carlson, 1990; Donelick et al., 1999).

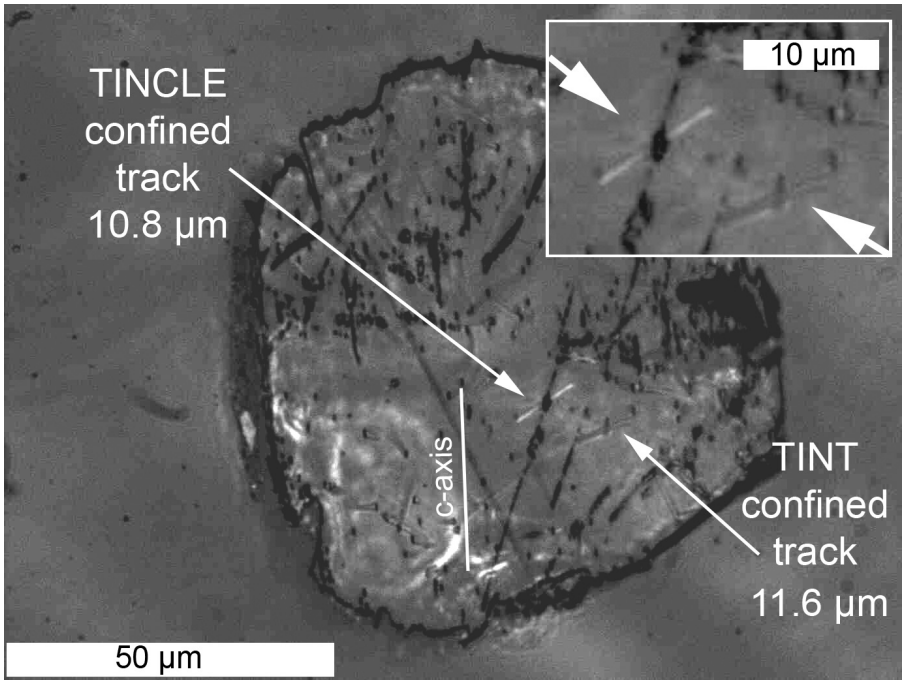


Figure 6.11-4: Measured horizontal confined track-lengths in apatite.

As track-length measurement was conducted separately from track counting for AFT age determination, an image of each grain investigated for its confined track-length(s) was collected under 50 × magnification. The images were collected in order to match confined-track-length data with AFT age data through their grain commonality. Unfortunately, as the gathering of parametres relevant to AFT age determination was conducted in advance of confined-track-length measurement, not every grain yielding measurable confined tracks was analysed for its AFT age relevant parametres. In addition, not every grain having yielded AFT age relevant parametres displayed measurable confined tracks. Consequently, the AFT age and track-length data corresponding to the same grain represent highly reduced count subsets of the data presented in Chapter 7. To eliminate problems in correlating confined track and AFT age relevant parametres, when possible all confined-track-length and AFT age data should be collected simultaneously. Otherwise confined tracks should be measured in advance of the AFT age relevant parametres, since the likelihood of encountering measurable confined tracks in a grain is lower than that of encountering tracks which project a given internal surface of said grain (cf. Wagner & van den Haute, 1992: Chapter 2.4.3).

## 6.12 Fission-track-length and track-density relationship

The probability of fission tracks for intersecting a randomly selected internal grain surface defines the relationship between the statistical distribution (average length and standard deviation) of a fission-track-length population, and that population's spatial (and aerial) fission-track density. The highest probability occurs when the maximum number of tracks in that population exhibit their initial track-length ($L_0$) (Wagner & van den Haute, 1992). However, in combination with the continuous, yet random generation of fission

tracks through time, increased temperatures shorten tracks from their initial lengths to those measured at the time of investigation ($L/L_0$). The reduction of mean-track-length in a population is simultaneously reflected in the reduction from initial track density ($\rho_0$) to that of the measured track density ($\rho/\rho_0$). The relationship holds therefore, that shorter tracks have a lesser probability of intersecting any randomly selected grain surface than their longer complements, and that the track-length distribution and the population density are directly related (Wagner & van den Haute, 1992).
Numerous experimental studies and their extrapolation to geologic time scales have been conducted on the annealing properties of fission tracks in various terrestrial materials; these studies are compiled in Wagner & van den Haute (1992: Appendix B). A series of experiments conducted for Durango apatite (Green, 1988) shows for low degrees of annealing the ratio $(L/L_0):(\rho/\rho_0)$ is 1:1. However the relationship in the ratio changed when $L/L_0$ reached values of ~ 0.65 or less, at which $L/L_0$ became greater than $\rho/\rho_0$. The difference between the ratios was attributed to greater length reduction as a result of track segmentation or break-up during highly evolved stages of annealing. As a result, the probability of intersecting tracks shorter than ~ 11 μm is significantly reduced. The phenomenon of track segmentation was attributed to be the result of the interruption of shorter tracks by zones of annealed crystal. Annealed zones impede the etching agents from penetrating the track fully. Subsequently, the issue has been re-evaluated on the basis of differences in etching rates as the possible mechanism (Donelick et al., 1999).

Given the AFT age is directly related to the fission-track density, only samples having undergone fast cooling across the AFT-Partial Annealing Zone (PAZ: ~ 60 - 110 ±10 ˚C) will approach a geologically significant age for the event. Alternatively, the majority of natural samples investigated in the context of apatite fission-track thermochronology exhibit more complex histories due to slow cooling rates possibly affected by one or more episodes of reheating through time. As a result the reported AFT age becomes younger and a more sophisticated interpretation is required to interpret the age obtained.

## 6.13 Thermal modelling

Thermal modelling is conducted in order to reconstruct the thermal history of a rock sample using the AFT age and the track-length distribution as data sources. Several experimentally based mathematical models have been employed to reproduce the fission-track annealing kinetics for different apatite species including: Durango fluor-chlorapatite (e.g. Laslett et al., 1987; Crowley, 1991; Carlson, 1990), end member fluorapatite and fluor-strontium apatite (e.g. Carlson, 1990; Crowley et al., 1991; Laslett & Galbraith, 1996) and multikinetic models (e.g Ketcham et al., 1999). The above-mentioned kinetic models incorporate the relationship between fission-track shortening and track density reduction under given t-T conditions. Nevertheless, due to the differing nature of these models, their predictions of thermal histories differ significantly, even amongst

models based on the same apatite compositional class. The Crowley (1991) Durango apatite annealing model, for example, significantly underestimates track annealing at high temperatures in comparison to that of the Laslett et al. (1987) model.

The reason for inconsistencies between models is likely due to their inherent basis on data from laboratory experiments, conducted over a short period of time, and extrapolated to geological time scales (Corrigan, 1993). Therefore, small inconsistencies between experimental conditions and results cause significant incongruence upon their extrapolation. As a result, significant envelopes should be employed when modelling in order to safeguard against over-interpretation of the data.

### *6.13.1 Variability of apatite fission-track annealing kinetics*

The apatite-group possesses a wide range of possible chemical compositions. The simplified molecular formula is $[Ca_{10}(PO_4)_6(F,Cl,OH)_2]$ (Elliott, 1994), which may be substituted by numerous elements at its Ca, P, or anion sites (Barbarand et al., 2003); the influence of elemental substitution on annealing kinetics having been demonstrated for Cl, (Crowley et al., 1990; O'Sullivan and Parrish, 1995), Mn, Sr and Fe (Ravenhurst et al., 1993; Burtner et al., 1994; Carlson et al., 1999), rare earth elements (REE) (Carpéna, 1998; Barbarand and Pagel, 2001; Barbarand et al., 2003), OH (Bergman and Corrigan, 1996), $CO_3$ (Ben Ghouma, 1995) and $SiO_2$ (Carpéna, 1998).

Annealing experiments (e.g. Green et al., 1986; Duddy, et al., 1988; Donelick et al., 1990; Carlson, 1990; Carlson et al., 1999; Crowley et al., 1999; Barabarand et al., 2003) evidence chemical composition as the predominant, though poorly understood cause of annealing kinetic variation, especially for that of F-Cl substitution; though the influence of Fe, Mn, Sr, and light REE's have also been evidenced to have effects similar in magnitude to F-Cl on the annealing kinetics of apatites (Carlson et al., 1999; Ketcham et al., 1999; Barbarand et al., 2003); Light REE's displaying an especially significant yet variable effect on the annealing characteristics of near end-member F-apatites (where Cl ~ < 0.1 atoms per formula unit, or about < 0.4 weight percent), the most commonly encountered (Barbarand et al., 2003).

For example, Carlson et al. (1999) demonstrated the differences in fission-track annealing rates amongst fifteen well characterised apatites of differing chemical compositions are at least an order of magnitude greater than discrepancies reported among the mathematical annealing models reported in Laslett et al. (1987), Carslon (1990), and Crowley (1991), when fitted to prior experimental data on Durango apatite, and that the closure temperature for these apatites ranged from 81 to over 200 ˚C.

Proposed kinetic variables for the behaviour of fission tracks in apatite include: Cl-content (Green et al., 1986), ionic porosity (e.g. Carlson, 1990; Dahl, 1997) and c-axis parallel etch-pit diametre ($D_{par}$) (Burtner et al., 1994; Donelick; 1993, 1995, 1997; Sanders, 1998; Barbarand et al., 2003), though most have limited predictive value (Carlson et al., 1999).

$D_{par}$ is not entirely robust, as an increase in OH content may lead to a change in etch figure size without a corresponding change in resistance to annealing (Ketcham et al., 2000). The systematic relationship between Cl concentration and annealing rate falters when Cl is below 0.1 atoms per formula unit (characteristic of near end member Fluorapatite) (Barbarand et al., 2003). Nevertheless $D_{par}$ and Cl have been described as sufficient to characterise the kinetic behaviour of the majority of apatites (Carlson et al., 1999; Barbarand et al., 2003).

Of the proposed indicators mentioned, $D_{par}$ is the most inexpensive and least time-consuming way to characterise the differing annealing kinetics of grains in a sample (de Bruijne, 2001; Barbarand et al., 2003). $D_{par}$ was therefore chosen as the parametre measured to infer kinetic behaviour of apatites investigated from samples in this study.

$D_{par}$ measurements were conducted on all grains yielding an AFT single-grain-age. Their values are depicted in the graphs presented in appendix iii. Where possible, measurements of $D_{par}$ were made in combination with AFT confined-track-lengths.

Donelick (1997) proposed $D_{par}$ values less than ~ 1.75 μm (for apatite etched under conditions of 20 seconds in 5.5 M $HNO_3$ at 21 ˚C) as characteristic of near-end-member fluorapatites. Values of $D_{par}$ greater than ~ 1.75 μm represent the continuum of apatites dominated by Cl and OH anions. As apatites were etched following the method described in Barbarand et al. (2003)--20 ± 1 s in 5.0 M $HNO_3$ at 20 ± 1 ˚C, direct comparison with the Donelick (1993) and Carlson et al. (1999) data sets (amongst others) are impossible.

Barbarand et al. (2003), established a modest level of correlation between Cl content (apfu) and etch-pit length ($D_{par}$) by plotting each against MTL and cell parametre *a*. Increase in etch-pit size generally, though not absolutely, equates with increase in chlorine content, as apatite solubility includes the net affect of *all* elemental substitutions.

Samples throughout this study evidence abundant grains with mean $D_{par}$ values between ~ 0.9 and ~ 2.0 μm. Per-grarin mean $D_{par}$ values seldom approach ~ 2.5 μm and only one measured crystal in sample 26 expresses a mean $D_{par}$ value exceeding 2.5 μm.

Small $D_{par}$ values may result from under etching of the apatites samples (cf. Crowley et al., 1991; Ketcham, 2004). However, given grain etching and track revelation conditions used in this study followed closely that indicated in Barbarand et al. (2003),

the annealing kinetics in apatites from this study are considered to modestly approximate those associated with low (< 0.1 apfu, ~ 0.35 wt%) to zero Cl content apatites. The consideration is made under the assumption apatites from this study, yielding highly variable MTLs (and associated highly variable AFT single-grain-age distributions) and low $D_{par}$ values (< ~ 2.0 μm), represent apatites similarly, or more highly enriched with elemental substitutions than those yielding low (< 0.1 apfu, ~ 0.35 wt%) to zero Cl and low $D_{par}$ values (< ~ 2.0 μm) evidenced in Barbarand et al. (2003).

Geological evidence in support of possible elemental substitution in apatites of the study area is found in the moderate level of whole-rock incorporation of major (wt%) and trace elements, including but not limited to Sm and Nd REEs, evidenced in pre-Permian fine-grained sediments in the Narcea Antiform and southern Cantabrian Zone (Nägler et al., 1995; see also Fernández-Suárez, 1998; Valadarez et al., 2002 b).

### *6.13.2 Modelling procedures*

In order to reconstruct a given host-rock's thermal history from the AFT age and length distribution, two modelling procedures can be employed: forward and reverse modelling. *Forward modelling* results in the generation of a unique AFT age and length distribution from a unique investigator-defined time-Temperature (t-T) path. The resultant data are then compared to AFT data collected from the relevant natural rock sample in order to investigate if the natural data set validates the modelled thermal history. Unique AFT age and track-length distributions are calculated for each sample investigated. *Inverse Modelling* entails the generation of several (hundreds to thousands) of forward models fitting the particular rock sample AFT data and relevant geologic or thermal constraints. In so doing, a random approach (Lutz & Omar, 1991) or a genetic approach (Monte Carlo Algorithm: Gallagher et al., 1991).

An element of consideration when conducting AFT thermal modelling is the "late cooling artifact" (Juez-Larré, 2003). This spurious artefact in thermal modelling results due to very slow annealing of fission tracks at near ambient temperatures (< 60 ˚C) over millions of years (Green et al., 1986; Donelick, et al., 1990; Vrolijk et al., 1992), though not detectable at experimental time scales. Hence, computer models compensate for this track shortening at low-temperatures with late stage cooling. To compensate, the specification of initial-track-length ($L_0$) shorter than 16.3 μm, or the multikinetic annealing model incorporating kinetic parametre data such as etch figure ($D_{par}$) (Burtner et al., 1994; Donelick, 1993), or Cl content (Crowley et al., 1990; O'Sullivan and Parrish, 1995; Carlson et al., 1999; Ketcham et al., 1999; Barbarand et al., 2003) have been used (Ketcham et al., 2000). Though the use of other methods to constrain the > 60 ˚C temperature history, such as (U-Th)/He improve to a great extent the range of the modelling results and therefore limit the possible thermal histories corresponding with the data (Juez-Larré, 2003).

This study uses *AFTSolve* (Ketcham et al., 2000) to reconstruct AFT model thermal histories (figure 6.13.2-1) using the inverse genetic algorithm (Monte Carlo method, e.g. Gallagher et al., 1991). *AFTSolve* allows for selection between mathematical annealing models developed by Laslett et al. (1987), Crowley et al. (1991) or Ketcham et al., (1999) as the basis for its modelled thermal histories.

Given the recent focus on the importance of relationship between apatite composition and annealing kinetics the multikinetic annealing model (Ketcham et al., 2000) was selected to approximate t-T histories of samples in this study. As described above, $D_{par}$ a measure of bulk elemental substitution to apatite's Ca, P, or anion sites was selected as it has been described as adequate to characterise the behaviour of the majority of

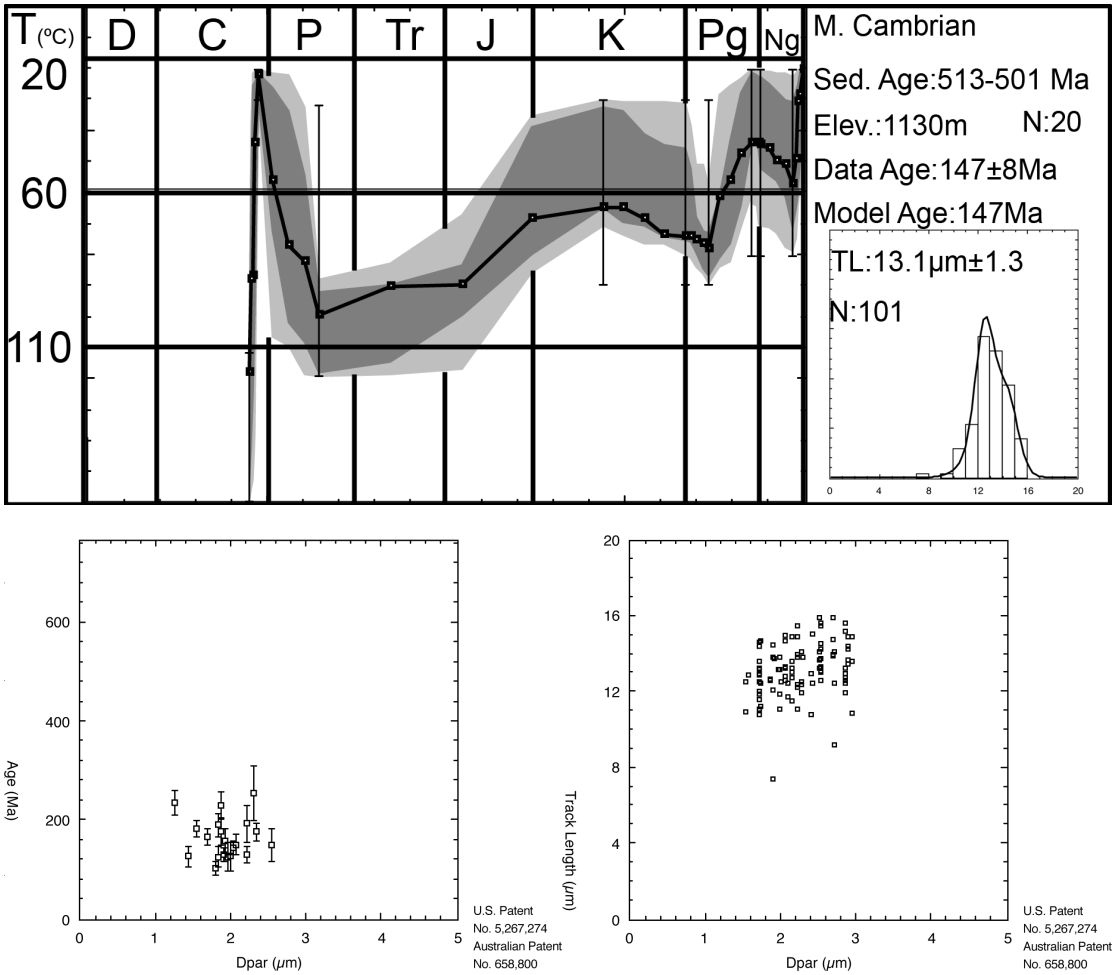


Figure 6.13.2-1: *AFTSolve* uses up to 10 independent temperature-constrained time stops (vertical brackets) in addition to kinetic parametre data (e.g. $D_{par}$) constrained AFT grain-ages and confined-track-length data (lower left and right respectively) to model a host-rock's low-temperature thermal evolution based on a specified modelling algorithm (in this study: Ketcham et al., 1999). t-T models produced for this study were made using c-axis projection corrected confined track-lengths (upper right). Modelled results in the t-T diagram are indicated by three reliability levels (light-grey envelope: all t-T paths with merit function values of at least 0.05, dark grey envelope: all t-T paths with merit function values of at least 0.5, black line: best fit, Ketcham et al., 2000). In this model (D) Devonian, (C) Carboniferous, (P) Permian, (Tr) Triassic, (J) Jurassic, (K) Cretaceous, (Pg) Palaeogene and (Ng) Neogene times are represented. (N) Neoproterozoic, (Cm) Cambrian, (O) Ordovician, (S) Silurian times modelled elsewhere.

apatites (Carlson et al., 1999; Ketcham et al., 1999), and it is the least expensive and time consuming technique available for the estimation of kinetic behaviour (de Bruijne, 2001, Barbarand et al., 2003).

Modelled thermal histories are constrained using tectonic and sedimentary information local to the investigated samples, field observation of structures, data from previous palaeothermal indicator studies, surface morphology and estimations on the local palaeogeothermal gradient. Thus it is of prime interest in this study to determine the tectonic and surface processes having controlled cooling of investigated samples.

In this study, thermal modelling is employed for each sample possible to test the t-T solutions constrained by reported and observed geological evidence, against collected fission-track data for that sample; the measured data representing only a subset of the fission-track record present in the observed grains.

t-T pathway models reported in this study therefore represent the best possible constrained thermal history reconstructions a function of the precision to which the AFT data were collected, present understanding of geologic processes having occurred in the Cantabrian Mountains and understanding of apatite annealing kinetics and modelling technology constraints. As with every model, the calculated t-T pathways absolutely deviate from the true thermal history experienced by the samples, and in so being they are a simplification of reality.

*AFTSolve* allows for the specification of a maximum of ten model path breaks to be placed. While in many instances, this may be sufficient to characterise the evolution of a particular geological body, at least for some samples investigated in this study the geological complexity through time, as represented in the geologic record, is greater than can be characterised by the maximum ten path breaks. In these instances models represent a highly simplified understanding of the known geological history.

Nevertheless, as this study represents the first regional scale fission-track thermochronologic study in the Cantabrian Mountains, models presented here represent new information, which can be used to more highly constrain the thermal evolution of Neoproterozoic through late Palaeozoic sedimentary rocks of the Cantabrian Mountains through time; in so doing better constrain the thermal evolution of northwestern Iberia.

# 7 Apatite fission-track results and discussion

From the 104 field samples collected and 80 processed to a point where the presence or lack of significant quantity of apatite could be determined, thirty-two samples (see figure 6.4-1 for their locations) yielded enough fission-track-laden apatite grains to measure aerial densities and provide error constrained dates. Of the dateable samples, twenty yielded at least minimum quantities of confined tracks to conduct time-Temperature models.

## 7.1 AFT age and track-length measurement results

Table 7.1-1 depicts the results of AFT age (appendices i, ii) and track-length analysis (appendix, ii) for those samples having yielded sufficient fission-track-laden apatite grains to facilitate their investigation. All but two single-grain-age distributions failed the $\chi^2$-test for singularity and homogeneity of population at $P(\chi^2) = 5$ %. The AFT central-age and its error (after Galbraith & Laslett, 1993), which together present a robust weighted mean constrained central tendency of single-grain-ages (Wagner & van den Haute, 1992), are reported.

When samples fail the $\chi^2$-test further analysis may be required in order to extract meaningful age subcomponent clusters. Initially data are qualitatively analysed for thermal history information recorded in the sample fission-track systems. To do so AFT single-grain-age distributions are each plotted radially (e.g. figure 6.10-1) versus their relative errors (appendix ii) and analysed visually to determine any age subcomponents. Additionally when confined-track-lengths were measured, histograms of their distributions accompany the radial plots.

Failure to pass the $\chi^2$-test at $P(\chi^2) = 5$ % may indicate the possibility for divergent AFT kinetics amongst grains in the population. AFT age subcomponents may be attained using a subpopulation clustering technique such as offered in the *Binomfit 1.0* computer program. (Brandon, 2002)

In other cases where a sample grain population contains apatites with a continuum of kinetic expressions, statistical tests may indicate failure when in fact there are no inherent problems with the data (Ketcham et al., 1999) and significant partial annealing of the AFT system(s) in the sample may have been active.

The difficulty in defining subcomponent age clusters is based on the assumption that unique statistically meaningful subcomponent age clusters *actually* exist within the AFT systems (pers. com. Donelick, 2004); as demonstrated by Juez-Larré (2003) this may not always be the case. The meaningfulness of t-T models produced for a given AFT system not passing the $\chi^2$-test may be insignificant unless there is reasonable evidence (annealing kinetic, thermal, tectonic, sedimentary) which constrains its complexity.

| Sample | N Lat. Ellipsoid ED50 | W Long. Ellipsoid ED50 | Elevation (m) | Stratigraphy | Lithology | Formation Age (Ma) | $\rho_s$ (tr/cm$^2$) x 10$^6$ (Ns) | $\rho_i$ (tr/cm$^2$) x 10$^6$(Ni) | P($\chi^2$)% | Dispersion | Central Age (Ma) ± 1$\sigma$ (N Grains) | Arithmetic MTL (µm) (±1s SD) [n tracks] |
|---|---|---|---|---|---|---|---|---|---|---|---|---|
| 25 | 42º49'28.7" | 5º50'38.6" | 1047 | L. Cambrian | SS | 630-518 | 0.62(331) | 0.80(429) | 0 | 0.5 | 192.7 ± 34.6(11) | 10.1(0) [1] |
| 18 | 42º48'22.9" | 5º49'26.9" | 1020 | Neoproterozoic | SS/SH | >542 | 1.81(1973) | 2.05(2234) | 0 | 0.3 | 196.2 ± 17.5(25) | 11.0(2.2) [49] |
| 20 | 42º48'9.4" | 5º49'29.9" | 1020 | Stephanian B | CNGL | 302-301 | 2.02(1331) | 1.89(1248) | 0 | 0.26 | 197.1 ± 16.8(18) | 11.6(2.0) [44] |
| 23 | 42º47'55.1" | 5º49'12.9" | 1010 | Stephanian B | SS/SH | 302-301 | 0.46(184) | 0.80(321) | 0 | 0.52 | 147.1 ± 27.5(13) | 12.4(1.4)[5] |
| 22 | 42º47'50.2 | 5º49'2.3" | 1005 | Stephanian B | CNGL | 302-301 | 1.87(2638) | 2.14(3029) | 0 | 0.25 | 184.9 ± 13.0(25) | 11.2(2.2)[114] |
| 114 | 42º47'33.3" | 5º48'31.0" | 1005 | Stephanian B | CNGL | 302-301 | 0.67(608) | 0.67(613) | 0 | 0.7 | 188.7 ± 39.3(15) | 11.2(2.2)[13] |
| 115 | 42º47'17.2" | 5º48'19.0" | 1000 | Stephanian B | SS/SH | 302-301 | 2.77(3865) | 2.37(3299) | 0 | 0.24 | 242.1 ± 17.3(21) | 9.3(1.42)[94] |
| 104 | 42º45'18.0" | 5º46'20.0" | 1000 | Neoproterozoic | SS/SH | >542 | 1.76(2969) | 1.43(2038) | 0 | 0.21 | 235.0 ±15.2(27) | 11.1(2.1)[112] |
| 105 | 42º46'30.0 | 5º46'55.0" | 970 | Neoproterozoic | SS | >542 | 2.42(2883) | 1.88(2216) | 0 | 0.26 | 262.6 ± 18.0(30) | 11.4(2.1)[102] |
| 106 | 42º46'50.0" | 5º47'5.0" | 970 | Neoproterozoic | SS | >542 | 1.50(2506) | 1.53(2552) | 0 | 0.3 | 196.1 ± 14.6(29) | 10.9(2.0)[109] |
| 84 | 42º58'5.4" | 5º25'57.6" | 1235 | L. Cambrian | CNGL | 542-513 | 0.28(392) | 2.2(3135) | 0 | 0.54 | 27.4 ± 4.8(13) | 15.6(1.6)[2] |
| 83 | 42º57'48.5" | 5º24'12.8" | 1180 | U. Cambrian - Ordovician | VOL/PYRO | 490-468 | 0.88(1991) | 1.58(3054) | 0 | 0.18 | 125.5 ± 7.7(25) | 11.6(1.4)[103] |
| 85 | 42º58'35.4" | 5º26'55.5" | 1355 | Stephanian B | CNGL | 302-301 | 1.88(2965) | 2.14(3386) | 0 | 0.21 | 181.1 ± 12.2(20) | 10.9(2.4)[104] |
| 91 | 43º2'24.8" | 5º28'5.7" | 1525 | M. Bashkir. – Kasimov. | SS | ~316-304 | 0.48(896) | 3.80(7081) | 0 | 0.36 | 29.8 ± 3.4(30) | 12.5(2.2)[56] |
| 97 | 42º59'56.0" | 5º31'27.9" | 1280 | M. Bashkir. – Kasimov. | SS | ~316-304 | 0.54(633) | 1.77(2055) | 0 | 0.77 | 106.3 ± 20.5(20) | 14.9(0.6)[2] |
| 62 | 42º59'55.2" | 5º41'30.5" | 1280 | M. Bashkir. – Kasimov. | SS/SH | ~316-304 | 0.39(480) | 1.72(1487) | 0 | 0.62 | 45.3 ± 6.6(25) | 10.2(3.2)[12] |
| 10 | 42º50'5.1" | 5º46'43.8" | 1240 | Serpukhov. | SS | 326-318 | 1.67(2384) | 1.97(2722) | 0 | 0.4 | 173.9 ± 16.8(25) | 11.5(2.1)[83] |
| 26 | 42º51'27.2" | 5º40'21.5" | 1040 | Bashkir. – Moscov. | SS | 318-307 | 0.12(198) | 0.25(424) | 79.6 | 0.15 | 95.0 ± 9.4(34) | 10.0(1.1)[6] |
| 9 | 42º57'59.3" | 5º36'48.5" | 1610 | U. Devon: Frasnian – Famennian | SS/SH | 385-359 | 0.93(465) | 1.66(827) | 0.1 | 0.28 | 160.7 ± 31.6(14) | 10.9(2.3)[8] |
| 8 | 42º55'45.5" | 5º32'38.1" | 1130 | M. Cambrian | SS | 513-501 | 2.23(2280) | 2.88(2945) | 0 | 0.2 | 157.3 ± 10.4(20) | 11.4(1.9)[101] |
| 3 | 42º53'36.2 | 5º32'16.7" | 1050 | Stephanian B | CNGL | 302-301 | 2.73(455) | 4.14(689) | 1.3 | 0.23 | 141.2 ± 15.3(10) | 11.6(2.1)[11] |
| 72 | 42º51'55.1" | 5º31'1.1" | 1040 | Stephanian B | SS | 302-301 | 0.66(642) | 0.96(941) | 0 | 0.57 | 178.0 ± 23.8(28) | 11.8(1.3)[10] |
| 73 | 42º51'21.7" | 5º31'16.8" | 1040 | Stephanian B | CNGL/SS/SH | 302-301 | 0.76(2288) | 1.09(2298) | 0 | 0.22 | 161.2 ± 10.9(25) | 11.4(1.8)[55] |
| 74 | 42º53'4.4" | 5º30'43.4" | 1105 | Stephanian B | SS | 302-301 | 2.28(1397) | 3.01(1841) | 0.3 | 0.17 | 170.0 ± 10.7(31) | 10.8(1.8)[103] |
| 75 | 42º53'2.4" | 5º30'45.7" | 1060 | Stephanian B | SS/SH | 302-301 | 1.38(278) | 1.72(347) | 65.1 | 0 | 177.1 ± 15.8(20) | 10.4(2.1)[4] |
| 76 | 42º51'46.4" | 5º27'30.2" | 1170 | Stephanian B | SS | 302-301 | 1.72(1008) | 2.27(1112) | 0 | 0.26 | 163.1 ± 13.4(25) | 11.2(2.1)[100] |
| 78 | 42º51'35.6" | 5º28'31.4" | 1150 | Stephanian B | SS | 302-301 | 3.54(2377) | 3.02(2027) | 0 | 0.27 | 255.9 ± 19.8(25) | 11.0(2.0)[102] |
| 79 | 42º51'36.4" | 5º29'42.4 | 1110 | Stephanian B | SS/SH/CNGL | 302-301 | 2.16(1744) | 2.46(1617) | 0 | 0.23 | 162.5 ± 11.7(25) | 11.3(2.1)[101] |
| 80 | 42º50'58.1" | 5º33'9.6" | 1070 | Stephanian B | SS/SH | 302-301 | 3.01(1300) | 2.71(1169) | 0 | 0.31 | 244.9 ± 20.2(30) | 11.4(1.9)[104] |
| 82 | 42º51'38.6" | 5º36'36.5" | 1220 | Bashkir. – Moscov. | SS | 318-307 | 1.87(657) | 2.58(909) | 0 | 0.5 | 174.6 ± 20.1(29) | 10.7(2.3)[101] |
| 110 | 42º51'9.6" | 5º29'44.3" | 1060 | U. Devon.: Famennian | SS | 375-359 | 1.65(1667) | 2.11(2138) | 0 | 0.3 | 181.9 ± 14.1(30) | 11.4(2.0)[103] |
| 111 | 42º51'21.5" | 5º28'51.5" | 1120 | U. Devon.: Frasnian - Famennian | SS | 385-359 | 2.32(1536) | 2.91(1362) | 0.1 | 0.18 | 195.1 ±12.9(25) | 11.5(1.8)[100] |

Table 7.1-1: AFT central-age and mean-track-length results. Lithologies, SS: sandstone; SH: shale; CNGL: conglomerate; VOL/PYRO: volcanic/pyroclastic.

### *7.1.1 Total elemental substitutions and apatite solubility ($D_{par}$)*

Analysis of the $D_{par}$ parametre, the proxy for total elemental substitution in apatite (Barbarand et al., 2003) was made for all grains component of the a) AFT age and b) confined-track-length data listed in Table 7.1-1.

Where grain-age populations failed the $\chi^2$-test, Juez-Larré (2003) opted to model t-T histories of select individual grains yielding sufficient a) projected and induced tracks to calculate their respective AFT ages and b) track-length counts ($n \geq 12$) to model their respective individual thermal histories.

Modelling of individual grains as per Juez-Larré (2003) is not possible for this data set, because the infrequency of encountered confined tracks amongst analysed apatite grains required choosing a data capture technique, which involved the separation of AFT age determination and confined-track-length measurement processes. Thus individual grains yielding track-lengths do not necessarily correspond to those yielding AFT ages.

In cases where multiple AFT age subcomponents are presumed to exist, when sufficient track-length data are collected (normally $n \geq 100$) t-T modelling of individual AFT age subcomponents may proceed using an independent kinetic parametre, (e.g. F, Cl, OH, $D_{par}$) to match $\chi^2$-test passing AFT age yielding grain subcomponents with corresponding confined track yielding grains of similar annealing kinetic expression.

Samples throughout the study evidence abundant grains with mean $D_{par}$ values between ~ 0.9 and ~ 2.0 µm (see appendix iii)--values normally expressed by near end member fluorapatites (cf. Donelick, 1995). Mean $D_{par}$ values seldom approach ~ 2.5 µm--the value generally accepted to represent end member chlorapatites), only one AFT age yielding crystal in sample 10 expresses a mean $D_{par}$ value exceeding 2.5 µm. Correlation between the variability in AFT single-grain-ages and that in their mean per-grain $D_{par}$ values is considered low to almost non-existent (see table 7.1.1-1). Thus discrimination of AFT grain-age subcomponents via the $D_{par}$ annealing kinetic parametre alone remains inconclusive.

$D_{par}$ as an effective independent kinetic parametre to correlate kinetic variability between individual subcomponent AFT age and track-length populations may have been hampered for the following reasons:

1) For many sample apatite assemblages (25, 18, 20, 23, 114-115, 84, 91, 97, 62, 10, 26, 9, 3, 72-73 and 75), confined-track-length counts amounted to less than the minimum value ($n = 100$) required to robustly represent their individual t-T histories, even after exhaustive searches of the mineral assemblage mounts, for confined tracks were made.

| Sample | Pearson (r): Age vs. $D_{par}$ | Sample | Pearson (r): Age vs. $D_{par}$ | Sample | Pearson (r): Age vs. $D_{par}$ | Sample | Pearson (r): Age vs. $D_{par}$ |
|---|---|---|---|---|---|---|---|
| 25 | -0.08 | 105 | 0.12 | 10 | -0.07 | 75 | 0.14 |
| 18 | -0.15 | 106 | 0.03 | 26 | -0.04 | 76 | 0.05 |
| 20 | 0.10 | 84 | 0.07 | 9 | -0.20 | 78 | 0.26 |
| 23 | -0.16 | 83 | 0.38 | 8 | -0.04 | 79 | 0.17 |
| 22 | -0.25 | 85 | 0.30 | 3 | 0.37 | 80 | 0.09 |
| 114 | 0.24 | 91 | 0.26 | 72 | -0.01 | 82 | -0.14 |
| 115 | 0.07 | 97 | 0.00 | 73 | 0.33 | 110 | 0.09 |
| 104 | -0.12 | 62 | 0.48 | 74 | 0.13 | 111 | 0.12 |

Table 7.1.1-1: Per sample correlation coefficients for AFT single-grain-ages versus per-grain mean $D_{par}$. Correlation is considered poor across the data set as no sample yields absolute value of r greater than 0.48.

2) Where both per-sample AFT age yielding grain counts and per-sample total confined track counts summed to values presumed at the time of collection, to have composed populations, which in themselves would have significantly represented model sample t-T histories (e.g. $n \geq 20$ and $n \geq 100$ respectively), the occurrence of significant counts of both $D_{par}$ constrained statistically significant AFT grain-age subcomponents (passing the $\chi^2$-test), and $D_{par}$ coconstrained confined track yielding grain assemblages was conspicuously rare (e.g. sample 74; see below).

3) As introduced in Chapter 6, small $D_{par}$ values may result from under etching of the apatite samples (cf. Crowley et al., 1991; Ketcham, 2004). However, given grain etching and track revelation conditions used in this study followed closely that indicated in Barbarand et al. (2003), the annealing kinetic parametres in apatites from this study are considered to modestly approximate those composed of low (< 0.1 apfu, ~ 0.35 wt%) to zero Cl content (cf. Barbarand et al., 2003). The consideration is made under the assumption apatites from this study, yielding highly variable MTLs (and associated highly variable AFT single-grain-age distributions) and lowly correlated and small $D_{par}$ values (< ~ 2.0 μm) represent apatites similarly, or more highly enriched with elemental substitutions (e.g. REE's) than those yielding low (< 0.1 apfu, ~ 0.35 wt%) to zero Cl and low $D_{par}$ values (< ~ 2.0 μm) evidenced in Barbarand et al. (2003).

Geological evidence in support of possible elemental substitution in apatites of the study area may be found in the moderate level of whole rock incorporation of major (wt%) and trace elements, including but not limited to Sm and Nd REEs, as evidenced in pre-Permian fine grained sediments in the Narcea Antiform and southern Cantabrian Zone (e.g. Nágler et al., 1995; see also Fernández-Suárez, 1998; Valadarez et al., 2002 b). However, in the absence of a robust per-grain elemental compositions investigation sample $D_{par}$ distributions remain unconstrained with respect to other annealing kinetic parametres.

### *7.1.2 Influence of uranium concentration on AFT parametres*

Theoretically, in grain-by-grain fission-track methods, variation in per-grain uranium concentration bears no influence on the individual $\rho_s/\rho_i$ ratios of each grain. Thus no variation of these ratios is expected apart from the random variation governed by Poisson statistics alone (Wagner & van den Haute, 1992). However experimental data have shown this is often not the case and reveal a supplementary variation between $\rho_s/\rho_i$ ratios (Galbraith, 1982).

Apatite composition is complex and variable. Elements such as $Fe^{2+}$, $Mn^{2+}$, $Na^{+}$, $REE^{3+}$ and $Sr^{2+}$ commonly substitute the Ca cation of the apatite crystal formula in ammounts measurable in wt.% (e.g. Carlson et al., 1999; Barbarand et al., 2003). U(IV)+, also commonly substitutes the Ca cation, however normally at values measured at the ppm (μg/g) scale (cf. Carlson et al., 1999). Nevertheless, `` have shown U(VI) substitutes into the Ca1 site in synthetic fluorapatite at concentrations of 2.3 wt.%. To accommodate this substitution the apatite structure significantly distorted such that the Ca1 site approximated octahedral coordination.

Carlson et al. (1999) demonstrated fission-track annealing rates in apatite may be slower in samples with appreciable substitution of Ca by other cations. However, annealing rates are not singularly related to substitution of Ca by other cations, but also complexly depend on a mixing at the halogen site.

To investigate the reasons for the detected supplementary variation in per-grain $\rho_s/\rho_i$ (expressed in this work as AFT single-grain ages) the relationship, between individual apatite etching efficiencies, AFT single-grain ages and their chemical compositions was investigated.

In the absence of data for more substatntial chemical substitutions to the apatite crystal lattice including Cl, F, OH, REE (e.g. Carlson et al., 1999; Barbarand et al., 2003), sample per-grain uranium concentrations (calculated in *TRACKKEY 4.2* (Dunkl, 2002)) were plotted versus sample AFT single-grain ages and their per-grain mean $D_{par}$ values, the proxy for the influence of total elemental substitution upon AFT annealing kinetics (appendix iii) (Barbarand et al., 2003).

Most samples, regardless of their host rocks depositional age, lithology, or geographic position, evidence non-linear trends of variability in AFT single-grain-age and $D_{par}$ inversely related to their per-grain average uranium concentrations (e.g. figure 7.1.2-1; see also appendix iii). Thus, as the per-grain average uranium concentration increased, the variability in both AFT age and $D_{par}$ decreased.

In order to assess the proportion of the variance in AFT age and $D_{par}$ attributed to the variance in uranium concentration, the square of the Pearson's product moment correlation coefficient ($r^2$), and the type of trend best approximating the data distribution

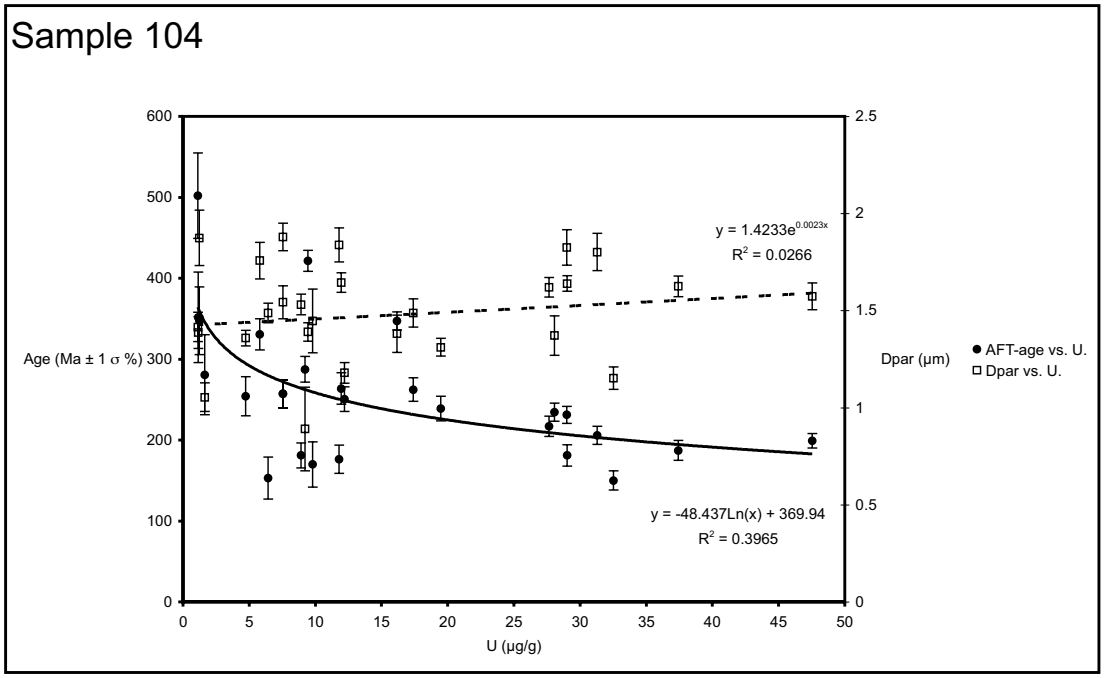


Figure 7.1.2-1: Example graph showing for sample 104 the variability in AFT singl grain age and per-grain $D_{par}$ in relation to per grain uranium concentration. Dependant parametres express increased variability as an inverse function of uranium concentration. In consideration of the calculated $r^2$ value the trend which best fits the AFT age data is an negative slope Log-normal function ($y = -48.437Ln(x) + 369.94$); an exponential function ($y = 1.4233e^{0.0023x}$) best describes the $D_{par}$ constrained data.

were evaluated. Values of $r^2$ for grain-age vs. uranium concentration distributions, as well as that calculated for grain mean $D_{par}$ vs. uranium concentration distributions are listed in table 7.1.2-1. Additionally listed are the arithmetic $\rho_s/\rho_i$ ratios obtained from data listed in table 7.1-1, as well as best fit trend equations for which the $r^2$ values were calculated.

Strong per-sample correlation coefficients ($r^2 \geq \sim 0.50$) between AFT single-grain-ages and their uranium concentrations or mean $D_{par}$ values and their associated uranium concentrations are all but elusive (safe for samples 25 and 111: AFT single-grain-age vs. U). Covariance between AFT single-grain-ages and their uranium concentrations and per-grain mean $D_{par}$ values and their associated uranium concentrations may be described as weak. Nevertheless, there often occurs a curious increase in correlation between the variabilities in AFT single-grain-ages and $D_{par}$ with higher per-grain uranium concentrations (e.g. figure 7.1.2-1; see appendix iii ).

Notable increases in the correlation between AFT single-grain-age variability and that for per-grain mean $D_{par}$ occurs where the per-grain uranium concentrations of at least ~ 20 to ~ 30 ppm are calculated (e.g. Figure 7.1.2-1; see appendix iii). Below this threshold, AFT single-grain-ages and their mean $D_{par}$ values are often lowly correlated

| Sample No. | Arithmetic $\rho_s/\rho_i$ Ratio | Central Age (Ma) ± 1σ (N Grains) | Age vs. U Trend Equation | Age vs.U Correlation Coefficient ($r^2$) | Dpar vs. U Trend Equation | Dpar vs. U Correlation Coefficient ($r^2$) |
|---|---|---|---|---|---|---|
| 25 | 0.76 | 192.7 ± 34.6(11) | $y = 387.82e^{-0.073x}$ | 0.08 | $y = 1.4687x^{0.0403}$ | 0.96 |
| 18 | 0.88 | 196.2 ± 17.5(25) | y = -38.822Ln(x) + 313.27 | 0.11 | y = 0.003x + 1.468 | 0.07 |
| 20 | 1.07 | 197.1 ± 16.8(18) | $y = 159.23x^{0.0571}$ | 0.02 | y = 0.0042x + 1.564 | 0.05 |
| 23 | 0.58 | 147.1 ± 27.5(13) | $y = 315.58x^{-0.437}$ | 0.35 | y = -0.0319Ln(x) + 1.5478 | 0.02 |
| 22 | 0.87 | 184.9 ± 13.0(25) | y = -30.051Ln(x) + 280.297 | 0.18 | $y = 1.675x^{0.011}$ | 0.01 |
| 114 | 1.00 | 188.7 ± 39.3(15) | y = 49.370Ln(x) + 209.979 | 0.05 | y = -1.766E-04x + 1.293E+00 | 0.00 |
| 115 | 1.16 | 242.1 ± 17.3(21) | y = -27.684Ln(x) + 331.758 | 0.12 | $y = 1.814e^{-0.0021x}$ | 0.09 |
| 104 | 1.25 | 235.0 ±15.2(27) | y = -48.437Ln(x) + 369.94 | 0.40 | $y = 1.4233e^{0.0023x}$ | 0.03 |
| 105 | 1.28 | 262.6 ± 18.0(30) | $y = 402.84x^{-0.1492}$ | 0.21 | y = -0.0011x + 1.2351 | 0.03 |
| 106 | 0.98 | 196.1 ± 14.6(29) | y = -33.627Ln(x) + 292.23 | 0.16 | $y = 1.067x^{0.0286}$ | 0.03 |
| 84 | 1.27 | 27.4 ± 4.8(13) | y = -6.2236Ln(x) + 47.165 | 0.18 | $y = 1.1277x^{0.0269}$ | 0.06 |
| 83 | 0.56 | 125.5 ± 7.7(25) | y = -4.9951Ln(x) + 142.89 | 0.01 | y = -0.1125Ln(x) + 1.6409 | 0.10 |
| 85 | 0.88 | 181.1 ± 12.2(20) | $y = 204.18e^{-0.0042x}$ | 0.13 | y = -0.1085Ln(x) + 1.6932 | 0.18 |
| 91 | 0.13 | 29.8 ± 3.4(30) | y = -5.6883Ln(x) + 50.293 | 0.07 | $y = 1.15E+00x^{-3.61E-03}$ | 0.00 |
| 97 | 0.31 | 106.3 ± 20.5(20) | $y = 208.42x^{-0.3925}$ | 0.35 | $y = 1.627e^{-0.0027x}$ | 0.14 |
| 62 | 0.23 | 45.3 ± 6.6(25) | y = -38.687Ln(x) + 163.07 | 0.69 | $y = 1.6438x^{-0.0304}$ | 0.09 |
| 10 | 0.85 | 173.9 ± 16.8(25) | y = -0.316x + 198.713 | 0.00 | y = 0.060Ln(x) + 1.385 | 0.03 |
| 26 | 0.48 | 95.0 ± 9.4(34) | $y = 95.989x^{-0.110}$ | 0.04 | y = -0.073Ln(x) + 1.542 | 0.04 |
| 9 | 0.56 | 160.7 ± 31.6(14) | y = -160.92Ln(x) + 599.27 | 0.30 | $y = 1.7437x^{-0.0179}$ | 0.00 |
| 8 | 0.77 | 157.3 ± 10.4(20) | y = 0.094x + 158.055 | 0.00 | y = -0.166Ln(x) + 2.462 | 0.14 |
| 3 | 0.66 | 141.2 ± 15.3(10) | y = -0.4423x + 172.52 | 0.11 | y = -0.091Ln(x) + 2.054 | 0.21 |
| 72 | 0.69 | 178.0 ± 23.8(28) | $y = 347.07x^{-0.3619}$ | 0.43 | $y = 1.3431e^{-0.0034x}$ | 0.01 |
| 73 | 0.70 | 161.2 ± 10.9(25) | y = -7.6441Ln(x) + 187.66 | 0.06 | y = 0.018Ln(x) + 1.348 | 0.04 |
| 74 | 0.76 | 170.0 ± 10.7(31) | y = -19.23Ln(x) + 246.83 | 0.08 | $y = 1.4158x^{-0.0327}$ | 0.04 |
| 75 | 0.80 | 177.1 ± 15.8(20) | y = -99.654Ln(x) + 466.71 | 0.38 | $y = 1.3435e^{0.0031x}$ | 0.13 |
| 76 | 0.76 | 163.1 ± 13.4(25) | y = -64.745Ln(x) + 378.59 | 0.36 | y = 0.0363Ln(x) + 1.1759 | 0.08 |
| 78 | 1.16 | 255.9 ± 19.8(25) | y = -0.5776x + 295.94 | 0.04 | y = =0.0025x + 1.4249 | 0.11 |
| 79 | 0.88 | 162.5 ± 11.7(25) | y = -0.1634x + 173.91 | 0.00 | y = 0.0018x + 1.4837 | 0.05 |
| 80 | 1.11 | 244.9 ± 20.2(30) | y = -89.004Ln(x) + 543.04 | 0.20 | y = 0.0009x + 1.0924 | 0.02 |
| 82 | 0.72 | 174.6 ± 20.1(29) | y = -138.35Ln(x) + 645.48 | 0.31 | $y = 1.1105x^{0.0549}$ | 0.06 |
| 110 | 0.78 | 181.9 ± 14.1(30) | y = -23.144Ln(x) + 257.88 | 0.06 | y = -0.0776Ln(x) + 1.8784 | 0.08 |
| 111 | 0.80 | 195.1 ±12.9(25) | $y = 392.64x^{-0.2054}$ | 0.64 | y = -0.0038x + 1.8166 | 0.11 |

Table 7.1.2-1: Relationship between variability in per-grain uranium concentrations and dependent AFT parametres single-grain-age and $D_{par}$. Per-sample arithmetic mean $\rho_s/\rho_i$ ratios, and AFT central-ages, errors and grain counts reproduced from table 7.1-1.

($r^2 << 0.50$). Unfortunately though, the highest proportion of grains analysed are for those with uranium concentration values below the ~ 20 to ~ 30 µg/g threshold (see appendix iii).

Though uranium substitution to apatite formula, normally measureable in concentrations of only tens to hundreds of µg/g (e.g. figure 7.1.2-1; appendix iii), its per grain variation amongst apatite crystals in this study may sensitively signal variation in other--often more substantive--chemical substitutions to the Ca cation site of the apatite formula, such as $Fe^{2+}$, $Mn^{2+}$, $Na^{+}$, $REE^{3+}$ and $Sr^{2+}$, and/or F, Cl, OH or REE's to the halogen site; Substitutions to halogen site being strongly correlated to differences in etching efficiencies of fission tracks amongst various apatite crystals (e.g. Carlson et al., 1999; Barbarand et al., 2003).

Thus, in the absence of robust data regarding more substantial and/or effective elemental substitutions to the apatite chemical formula, non-Poissonian variability amongst AFT single-grain ages distributions, may be estimated by evaluating per-crystal uranium correlations and their associated $D_{par}$ values.

## 7.2 Geologic interpretation of the data

A regional overview of the AFT results points to a complex polyphase cooling and denudation history involving the interplay of multiple orogenic cycles, extension, hydrothermal fluid pulses, and regional differential uplift and denudation, spanning Neoproterozoic to Cenozoic times.

### *7.2.1 Pre-, syn- & postdepositional annealing*

Most AFT grain-age distributions exhibit trends associated with continuous differential annealing, composed of partially and totally reset grain-age subcomponnents. Since all samples yield at least partial post-depositional annealing, it cannot be known what the initial recorded single-grain-age distribution was at the time of sedimentation.

The oldest AFT systems evidence cooling from below the 110 ˚C isotherm into the AFT-PAZ beginning from Ordovician to earliest Variscan times. The occurrence of outlier predepositional single-grain-ages, which differ by at least 1σ within AFT systems in uppermost Precambrian to Lower Cambrian samples in the SW of the study area, evidence their individual AFT closure temperatures were likely not reached following cooling after a metamorphic (Cadomian?: Fernández-Suárez et al., 2000 a; cf. Díaz-García, 2006) event in uppermost Neoproterozoic sediments. Predepositional single-grain-ages are also evidenced in Lower Palaeozoic strata located S of the Sabero-Gordón Line.

Apatite grains, which yield AFT ages indicating postsedimentation thermal annealing ($T \geq \sim 110$ ºC ± 10) has occurred consecutively for at least 10 Ma, are the simplest data sets to investigate, as these grains yield no detrital AFT age signal. Hence the AFT t-T histories, from these data sets are readily extractable in consideration of existing kinetic (e.g. $D_{par}$, Cl, Fl, REE), geological (e.g. sedimentary record/tectonic stress field) and thermal indices (e.g. conodont alteration index, illite crystallinity, vitrinite reflectance, fluid inclusion studies) constraints published for the study area.

Apatite grains, with AFT ages predating their host formation's sedimentation (e.g. grains in samples: 9, 10, 20, 25, 78, 80, 110, 114, 115; see appendices i, ii for age distributions; see table 7.1-1 for samples' geographic positions), prove difficult to meaningfully interpret with respect to the thermal regime of their present host rocks unless the low-temperature thermal history information in possible source areas for each grain is highly constrained. These apatite grains have resided in or below the AFT-PAZ since before their residence in their present host rock formations.

In sedimentary settings grains yielding 1σ or 2σ error constrained AFT ages indistinguishable from their host rock's formation age also prove difficult to assess when the age span of formation sedimentation is bound within the error associated with a particular AFT single-grain-age (cf. Juez-Larré, 2003), and/or if the age of

sedimentation is less than 10 Ma. Several grains from samples located in the Stephanian B sedimented coal basins in this study exhibit this phenomenon. They may yield ages influenced by track production in thermal environments, which promoted little to no track annealing, or promoted only partial annealing of tracks while having resided in one or more precursor source areas. Interpretation of the AFT data contained within these grains should be made with extreme caution, normally only when pertinent kinetic, geological and thermal indicators of present and past host environments are highly constrained.

If however, grain-ages and errors fall completely within the formation age for the present host rocks, these grains may be considered to yield AFT ages free of contamination by detrital fissioning signatures; the AFT-clocks of these samples being reset as they have been totally annealed for at least 10 Ma during and/or following the host rock's formation. Modelling of the possible t-T pathways may be conducted for said grains in consideration of existing kinetic, geological and thermal constraints.

### *7.2.2 Anomalous track shortening: authigenic apatite growth and sub-PAZ track shortening*

Authigenic apatite, that has grown during or after sedimentation and lithification (newly grown apatite) has been recognised in sedimentary environments such as areas of active coastal upwelling and deltaic environments (Ruttenberg & Berner, 1993), as well as fluvial sedimentary environments (Bouch et al., 2002), each at temperature ranges characterised by the thermal zone of diagenesis, (less than 200 ºC). Experiments into the size of the authigenic apatite reservoir in such environments shows an increase with depth, indicating continued formation during early diagenesis (Ruttenberg & Berner, 1993). Throughout the southern Cantabrian Zone apatites are crystalised in conodonts (e.g. Raven & van der Pluijm. 1986; Schneider, 2002).

Conspicuously, many Palaeozoic aged samples from the southern Cantabrian Zone, when processed for this study, lacked statistically significant concentrations of dateable apatite grains. The information may provide evidence to support a hypothesis that aggressive fluids active in the southern Cantabrian Zone were responsible for the uptake and redistribution elements including phosphorous following the host rock's deposition. However, constraint of this phosphorous rich fluid circulation remains elusive.

An authigenic origin may also be indicated for apatite crystals in sample 26. These crystals yield extremely low calculated uranium concentrations (2.28 % ± 111 %), and in some cases also show euhedral shapes (see figure 7.2.2-1). Under the assumption these parametres may correspond to the properties of authigenic apatite crystals, this initial, though poorly constrained estimate for fluid circulation and subsequent crystal precipitation would be coincident with the latest Middle to Late Cretaceous (Albian to Turonian) AFT central-age presented of this sample (95.0 ± 9.4 Ma).

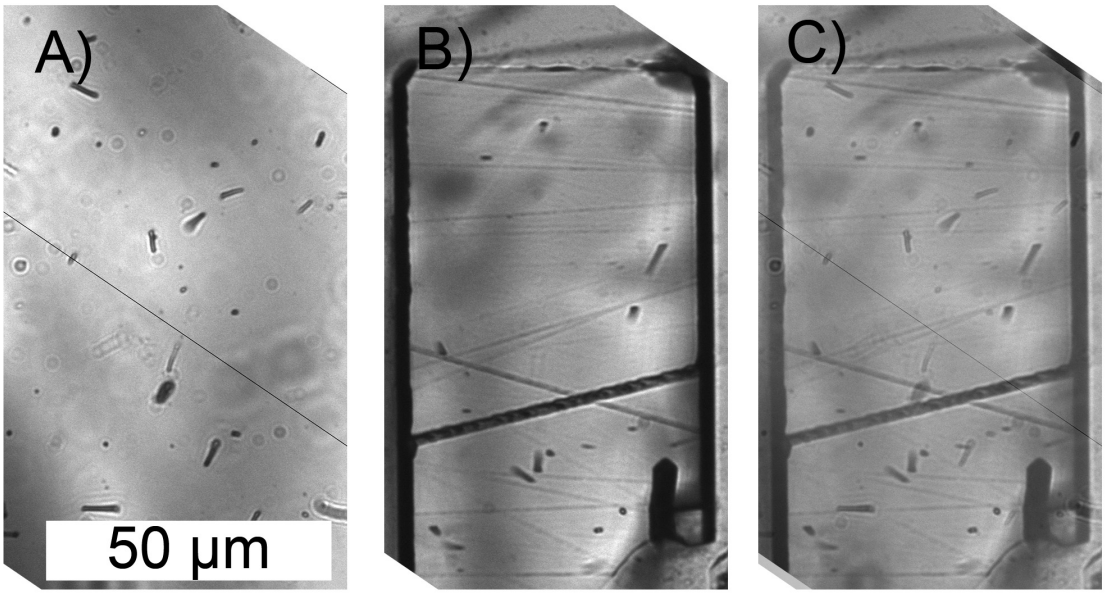


Figure 7.2.2-1: Low density distribution of fission tracks in euhedral apatite crystal from sample 26. A) Mica image of induced $^{235}U$ fission-tracks. B) Spontaneous $^{238}U$ fission-tracks in the euhedral crystal. C) Mica image superimposed over grain image for zonation visualisation and counting purposes.

Elsewhere, in the eastern Bodón Unit, sample 83 (uppermost Cambrian to Ordovician) yields a selection of seven grains, which from their projected induced-fission-track distributions, distinctly fission-track-depleted core and enriched-periphery zonations can be recognised (see figure 7.2.2-2). Spontaneous fission-tracks appear to have occurred in such abundance to have significantly compromised and weakened the peripheral apatite crystal lattice of their host grains. Irradiation of the grains induced additional fission events as evidenced in the $^{235}U$ mica image of figure 7.2.2-2. Combined spontaneous and induced fissioning damage was to such a degree that the rim of the grains disintegrated (see figure 7.2.2-2: b) during post-irradiation sample preparation (i.e. sonic wash). Damage to the periphery zone of the grains inhibited the recognition and counting of spontaneous fission-tracks. The relative overabundance of induced fission-tracks recorded in the mica detector images obscured individual track elucidation.

Mating of the induced fission-track image to their per grain image counterparts (e.g. figure 7.2.2-2), facilitated the precise location of induced tracks distributions to the affected regions of their host grains. The distribution is interpreted to evidence at least two discontinuous uranium zonation phases in the apatite. Given the samples was gathered from volcaniclasitc rocks near the footwall of a thrust in the vicinity of the León Line Fault System (see table 7.1-1 and figure), one can hypothesise the uranium enriched apatite peripheries were formed in association with fracture delivered possibly hydrothermal fluid (cf. Gasparrini, 2003, Gasparrini et al., in press) circulation, coeval with Variscan (Pérez-Estaún et al., 1988) or later (Alonso et la., 1995; Pulgar et al., 1999) orogenic cycles, or postorogenic extension (e.g. Aller et al., 2005).

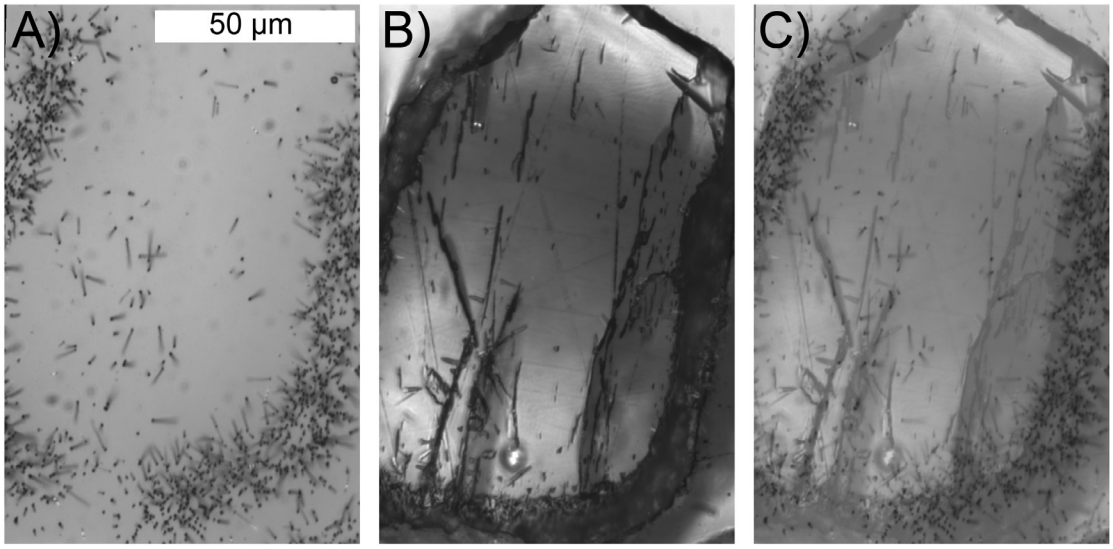


Figure 7.2.2-2:Possible uranium zonation in apatite grain from uppermost Cambrian to Ordovician sediments. A) High density periphery and low-density core of induced $^{235}U$ fission-tracks in mica image. B) Corresponding low density core of spontaneous $^{238}U$ fission-tracks and post-polish broken rim of apatite grain. C) Mica image superimposed over grain image for zonation visualisation and counting purposes.

Nevertheless, the possible occurrence of authigenic apatite in the sedimentary record introduces a significant obstacle to constraining the low-temperature thermochronology of the affected samples. Primarily, these grains are difficult to precisely discriminate unless: (1) some change in one or more kinetic parametres (chemical or crystallographic) becomes apparent; (2) there is a distinct discontinuity between crystal growth phases; and/or (3) correlation can be made between the timing of various fluid circulation phases and the growth zones in the apatites. If only one apatite growth phase is recognisable, as is observed in most analysed grains, the analyst must assume a single source area, unless AFT parametres (e.g. age/track-length distribution, and/or anneling kinetic parametres) can be correlated with thermal information related to possible the source areas. Where zonations they are recognised they must be treated separately from other grain components as their inclusion into the AFT age equation or t-T model will significantly skew the outcome away from a more representative geological solution.

In this study only fission tracks from relative uranium-depleted zones were counted. The AFT central-age of sample 83, inclusive of grains with fission tracks measured in the relatively depleted zonations, is 125.5 ± 7.7 Ma (E. Cretaceous), though individual grains indicate differential kinetic response to cooling into and through their respective AFT-PAZ's beginning from Late Permian-Early Triassic through to Late Cretaceous times, coincident with Triassic rift (e.g. Sanz de Galdeano, 1995) through Late Cretaceous postrift/extension (e.g. Zeigler, 1988).

Low temperature partial annealing introduced in chapter 6 as the "late cooling artifact" may also have played a significant role in the shortening of track lengths and the resultant evolution of AFT-ages in the analysed samples. Immeasurable in laboratory time scales, sub-PAZ shortening occurs proportional to a grain's accumulated residence, over

geologic time scales at temperatures of less than 60 ˚C (Green et al., 1986; Donelick, et al., 1990; Vrolijk et al., 1992). The amount of sub-PAZ annealing in grains yielding AFT ages possibly predating their sedimentation again cannot be estimated. However, in samples with extremely old AFT grain-age subcomponents (e.g. Narcea Antiform: 18, 104 and 105; Ciñera Matallana Basin: 72, 75, 76, 78 and 80; appendices i and ii), sub-PAZ cooling may represent substantial unaccounted-for track shortening.

## 7.3 Geographic parmetre-AFT central-age distribution

The relationship between sample AFT ages and their geographic distributions yields important information regarding tectonic and or geomorphic processes having affected host sediments (e.g. Wagner, 1989). The trend and shape of the AFT age versus geographic position (primarily elevation), yields information useful to the geospatial interpretation of the thermal evolution of the rocks.

In the simplest tectono-sedimentary settings, where sample AFT grain-age distributions represent single populations (i.e. pass the $\chi^2$ test at p = 5.0 %) within a single tectonic unit, have been totally annealed following their sedimentation, the topography above the samples is constant and the rate of exhumation is stable, uplift-induced denudation profiles may exhibit AFT ages which increase with elevation (e.g. Wagner & Reimer, 1972).

Complications to the simple uplift-induced denudation profiles occur for example, due to AFT-PAZ related variable initiation of per-grain AFT-systems, or by surface morphology related disturbed geothermal gradients (Wagner & van den Haute, 1992). Complex profiles may also develop during tectonic stability, very slow uplift, uplift changes, subsidence, or reheating. Fission tracks progressively anneal with depth and temperature in the PAZ, resulting in decreasing age profiles with increasing depth, even in the absence of uplift (e.g. Naeser 1979, Gleadow & Duddy, 1981). In such cases, denudation profiles may exhibit substantial deviation from straight-sloped age/elevation trends (e.g. Wagner & van den Haute, 1992: figure 5.15) and age-elevation slopes no longer represent the uplift rate.

Where uplift-induced denudation profiles are constructed from samples collected over wide geographic areas, variable topography is a relevant influence to the deviation from a simple positive-sloped age-elevation profile (Wagner & van den Haute, 1992). Also, complex age-elevation slopes may be expected from profiles which cross boundaries between recently active thrust units (e.g. Carpéna, 1985).

In regions indicating recent tectonic activity, such as the Cantabrian Mountains, strongly negative-sloped age-elevation profiles (e.g. figure 7.3-1; cf. de Bruijne, 2001) may be evidenced in low closure-temperature thermochronometre sampling regimes (Braun et al., 2006). Where rocks are exhumed at a constant velocity towards the surface through time, their negative slope may be attributed to the effects of changing surface relief.

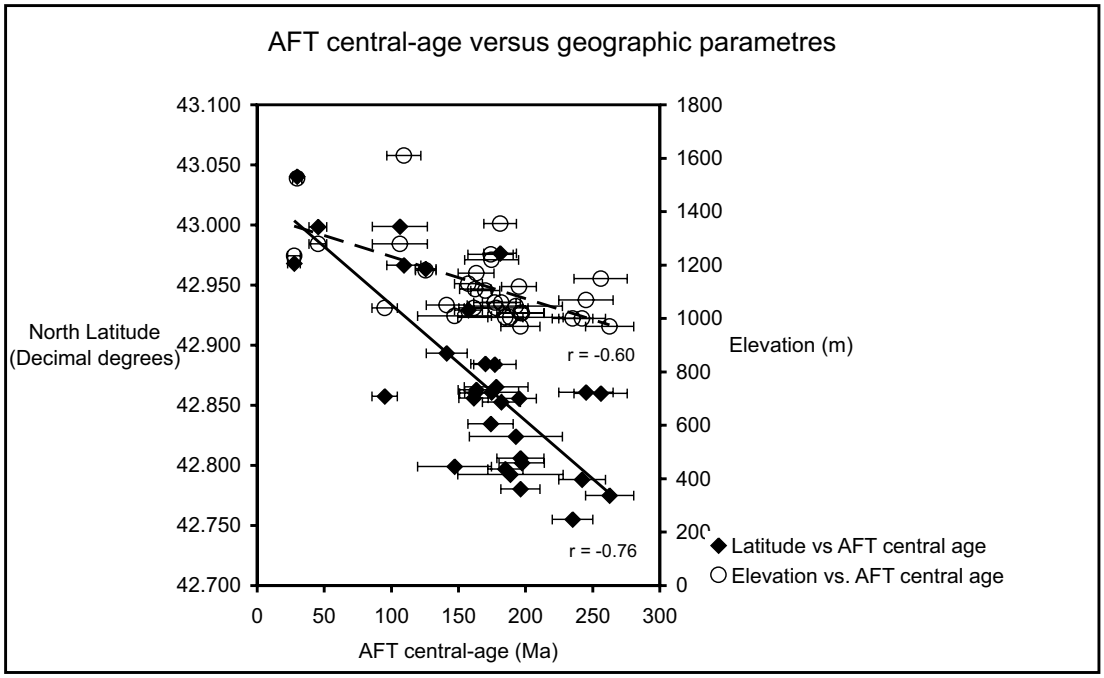


Figure 7.3-1: Chart depicting the relation between sample AFT central-ages, their latitudes and elevations. Strong negative correlations between ages and these geographic data imply the influence of pre-alpidic tectonics was significant to the present expression of surficial morphology. Bars define 1σ errors.

That is, in situations where relief has been substantially reduced in the relatively recent past, the slope of the age-elevation relationship becomes negative if the surface relief has changed between the time the rocks passed through the closure temperature (or for the AFT thermochronometre, entry into the PAZ at 110 ± 10 ˚C) and the time they are exhumed at the surface (Braun, 2002; Braun et al., 2006).

AFT central-age bearing samples in this study follow a synthetic transect through the Cantabrian Mountains which increases in elevation in a roughly N-ward direction. Negative correlation ($r = -0.76$, significant at $p = 0.05$) is evidenced between sample AFT central-ages and their latitude (figure 7.3-1), while a weaker, yet still present positive correlation ($r = 0.31$, significant at $p = 0.05$) between AFT central-ages and longitude also exists. AFT central-ages plotted against their respective elevations (figure 7.3-1) are again strongly negatively correlated ($r = -0.60$, significant at $p = 0.05$). AFT central-ages generally increase (become older) towards the SSW and increase inversely with elevation.

The AFT central-age trend is inverse to pre- to syn-Variscan depositional geometries in the Fold and Nappe Province (e.g. Cantabrian High in the NE, where few sediments were deposited, and the Devonian-Carboniferous basin in the SW where substantial accumulations are present; cf. Veselovsky, 2002). The influence of Variscan forward-breaking (e.g. Pérez-Estaún et al., 1991) thrust tectonics may be evidenced in the series of NE-ward younging AFT central-ages, which inversely reflect the stacking geometry of thrust units in the Fold and Nappe Province (figure 4.1-2) and its Neoproterozoic sedimentary basement.

The similarly oriented palaeostress regime dominant in association with at least the first convergence between Africa and Europe from Late Cretaceous to Early Palaeogene times (e.g. Andeweg, 2002) may also have significantly influenced the central-age distribution of samples in the southern Cantabrian Mountains, as ages continue to young across the León Line into Central Coal Basin. Late Cretaceous to Early Palaeogene convergence initiated the W-ward propagating compression of Pyrenean-Basque-Cantabrian range (e.g. Puigdefabregas & Souquet, 1986), during which occurred the alpidic phase of uplift of the Cantabrian Mountains. Additionally, N-sourced Cenozoic accumulations in the Duero Basin (Alonso et al., 1995) indicate a substantial episode of unroofing (~3 km) in the Cantabrian Mountains occurred coeval with the final convergence of Iberia and Europe.

The negative sloped AFT central-age versus elevation profile (figure 7.3-1) was likely substantially influenced by tectonic and denudation influenced relief reduction in the Cantabrian Mountains coeval with and following Cenozoic final convergence of Iberia and Europe. Nevertheless, AFT central-ages indicate substantial pre-Cenozoic cooling occurred in and about the southern Cantabrian Mountains. The effect of more ancient relief reductions associated with late stages of Variscan and possibly Cadomian (for Neoproterozoic to lowermost Cambrian samples) orogens upon this sample sets cooling profile is complex, and is likely poorly quantifiable within the resolution afforded by this study's sample assemblage. Additionally the absence of post-Stephanian/pre-Cretaceous covers through much of the sampling area precludes elucidation of the effects of latest Palaeozoic-Mesozoic changing regional plate tectonics on the exhumation pathway of the Cantabrian Mountains, evidenced in the present AFT central-age versus geographic parametres. Nevertheless, the negative-slope of the AFT-central-age-elevation profile indicates substantial relief reduction over the sampling area occurred as samples each cooled to the point where entry into their respective AFT-PAZ occurred.

## 7.4 t-T modelling results and interpretation

Across most of the southern Cantabrian Mountains is a conspicuous absence of the post-Carboniferous sedimentary record. AFT t-T modelling provides the only low-temperature chronometre able to quantify post-Stephanian thermal evolution in the area. Thus, even though all samples modelled failed the $\chi^2$-test, the body of literature regarding regional sedimentary, tectonic and palaeothermal conditions in NW Iberia as encapsulated in chapters 2 though 5, in addition to the understanding of apatite annealing kinetics as discussed in Chapter 6, enable t-T modelling to quantitatively represent regional thermal and tectonic evolution of northwest Iberia spanning late Neoproterozoic to present time.

Figure 7.4-1 depicts a chart of the thermal evolution of all modelled samples plotted with respect to available thermal, palaeomagnetic, and magmatic constraints. Details of t-T modelling results for the samples from the southwestern corner of the study area, inclusive of Narcea Antiform Neoproterozoic rocks , southern Cantabrian Zone

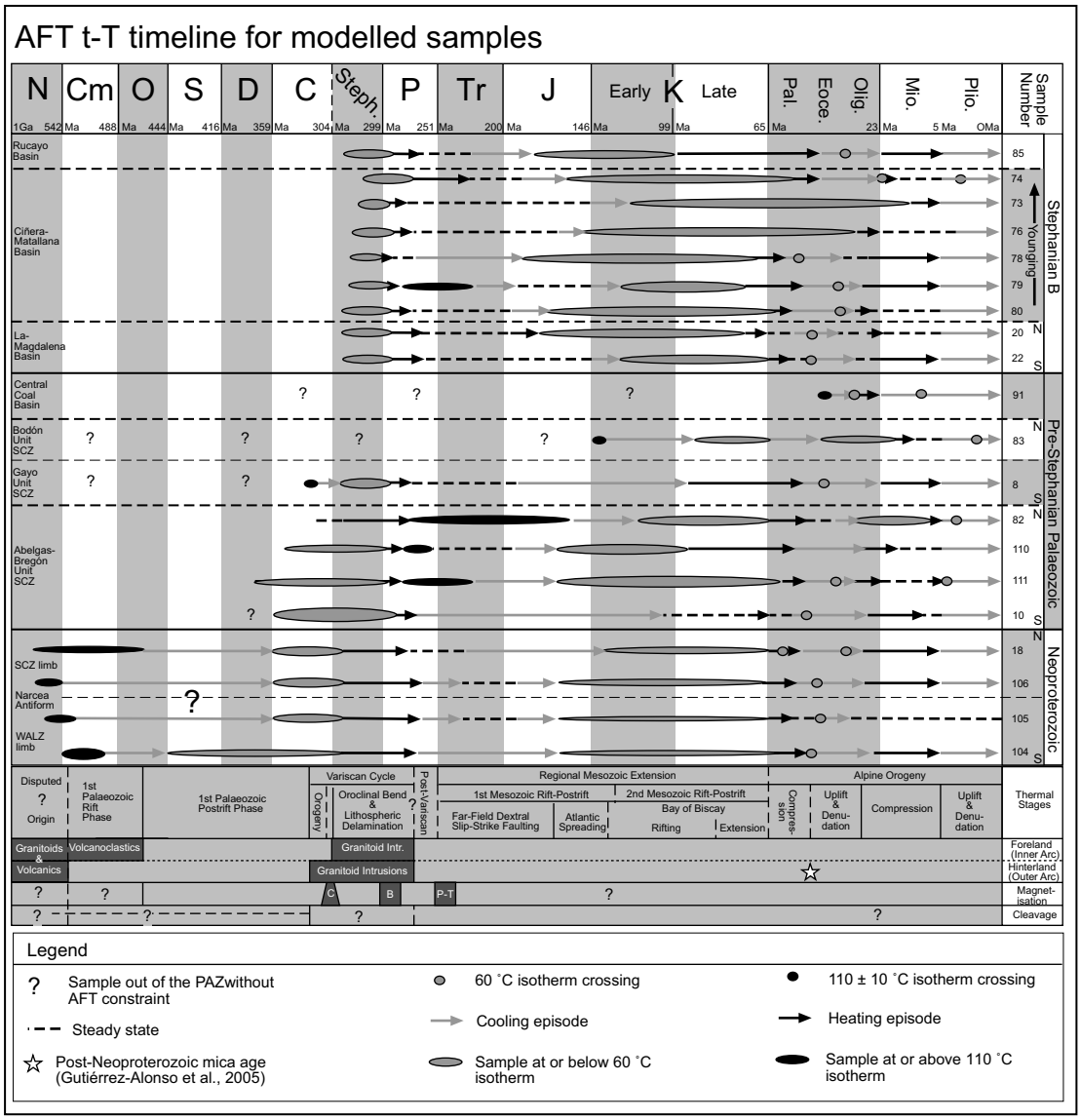


Figure 7.4-1: Timeline depiction of AFT t-T modelling results. Thermal modelling results were obtained from *AFTSolve* program (Ketcham et al., 2000) using the Ketcham et al. (1999) annealing model. Contemporaneous tectonic stages (e.g. Alonso et al., 1995; Sans de Galdeano, 1995; Gibbons & Moreno, 2002; Anderweg, 2002), regional magmatism (e.g. Gallastegui 1990, 1991; Fernández-Suárez, 1998, 2000 a,b; Paniagua et al., 2003; Valverde-Vaquero, 1999, Gutiérrez-Alonso, 2005) , Variscan palaeomagnetic stages (Weil et al., 1999, 2000, 2001) and interpreted timings for cleavage development (e.g Valladares et al., 2002 b; Aller et al., 1987, 2005). Thermal stages, see text. Timescale after Gradstein et al. (2004).

pre-Stephanian Palaeozoic sediments and their La Magdalena Basin Stephanian B cover in the are found in figure 7.4-2. Figure 7.4-3 depicts the modelling results for locations in south-central southern Cantabrian Zone inclusive of the Stephanian B Ciñera-Matallana Basin sediments and its pre-Stephanian Palaeozoic basement. t-T modelling data for pre-Stephanian Palaeozoic to Stephanian B samples collected in the vicinity of the León Line are summarised in figure 7.4-4.

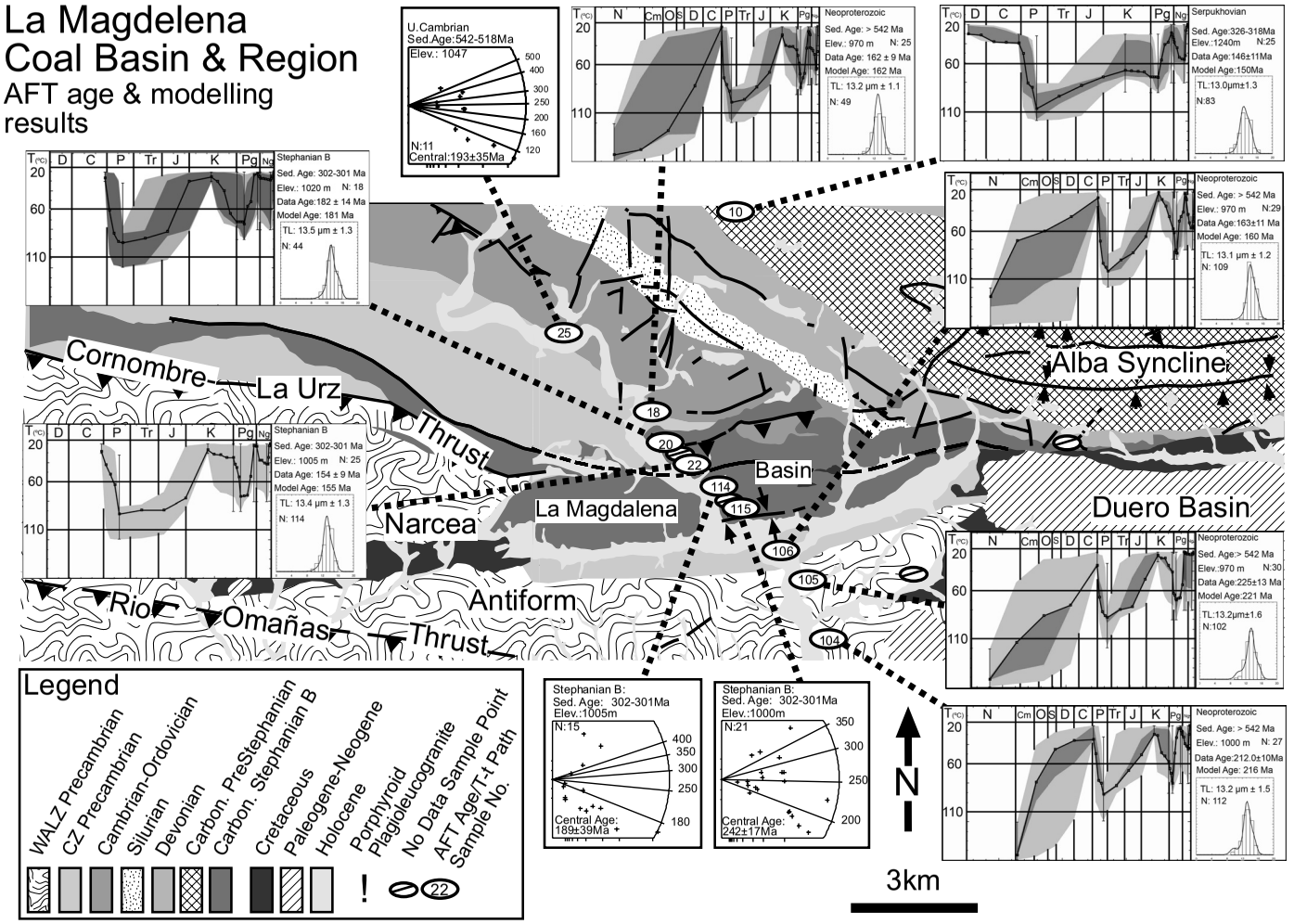


Figure 7.4-2: t-T thermochronology modelling results and AFT age/error plots for the SW of the sampling area, inclusive of Neoproterozoic sediments from the Narcea Antiform, pre-Stephanian Palaeozoic (southern Cantabrian Zone) and Stephanian rocks (La Magdalena Coal Field). See also appendices ii and iv.

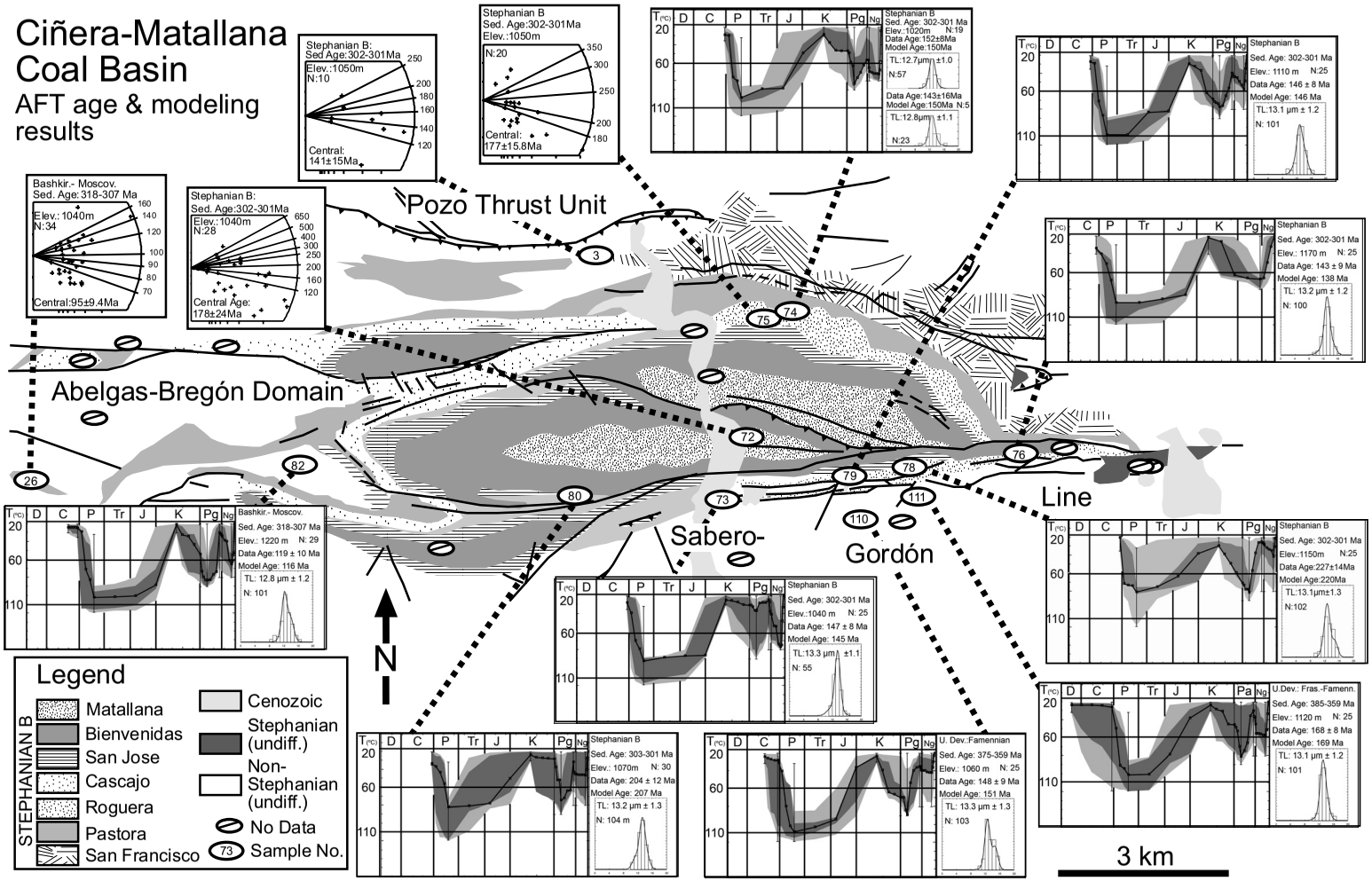


Figure 7.4-3: t-T thermochronology modelling results and AFT age/error plots for the S of the study area inclusive of Stephanian-B sedimented samples from the Ciñera-Matallana Coal Basin and the surrounding southern Cantabrian Zone pre-Stephanian Palaeozoic sedimented sequence. See also appendicies ii and iv.

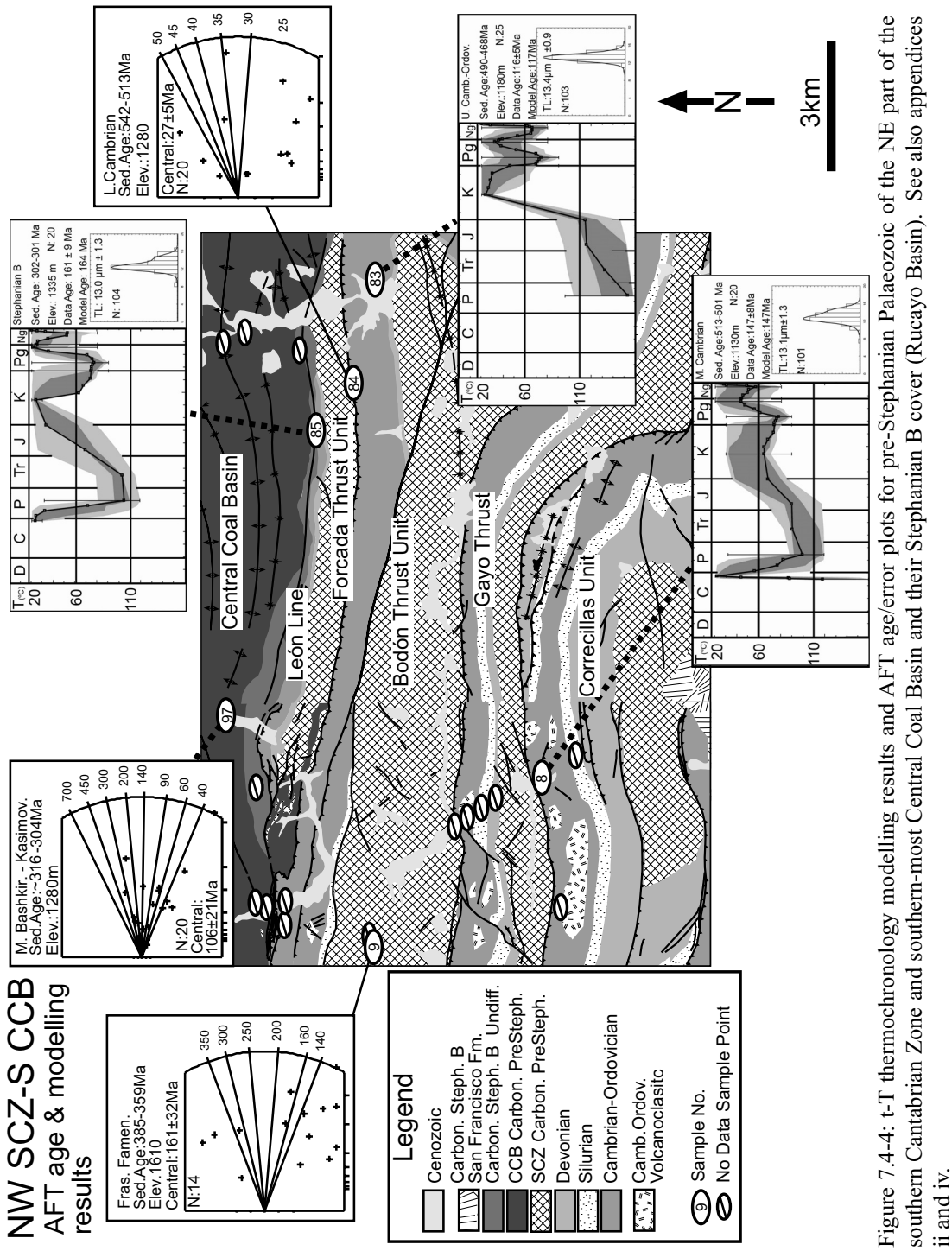


Figure 7.4-4: t-T thermochronology modelling results and AFT age/error plots for pre-Stephanian Palaeozoic of the NE part of the southern Cantabrian Zone and southern-most Central Coal Basin and their Stephanian B cover (Rucayo Basin). See also appendices ii and iv.

### 7.4.1 Pre-Variscan to early Variscan

The oldest rocks sampled in this study correspond to Neoproterozoic metamorphosed sediments of the Narcea Antiform. As has already been mentioned in Chapter 2 speculation regarding the antiform's earliest tectonic and thermal history is highly contested (e.g. Ribeiro et al., 1990; Queseda, 1990; Beetsma, 1995; Nägler et al., 1995; Ugidos et al., 1997 a, b, 1999; Valladares et al., 1999, 2000 2002 a., Bauluz et al., 2000; Díaz-García, 2006).

Evidence for pre-Stephanian Palaeozoic sedimentation over the Narcea Antiform is limited to highly restricted accumulations (< ~ 300 m) of eroded lowermost Cambrian sandstones and carbonates of the Cándana Fm. (Herrería Fm. equivalent) over its southern flank, in the extreme SW of the study area. Along its northern flank a nearly continuous 3.6 km of sediments spanning earliest Cambrian to Kasimovian times represents the pre-Stephanian Palaeozoic sequence. As described in chapters 2 and 3, lowermost Palaeozoic Cándana Fm.-Herrería Fm. sandstones are in non-conformal contact with Neoproterozoic rocks of the Narcea Antiform (see figure 3.1-1 b).

As indicated in Chapters 2 and 5, thermal constraints indicate from high-anchizone (Pérez-Estaún, 1973; cf. Martín-Parra, 1989; Aller et al., 2005) to low greenschist (epizone) facies (Martín-Parra, 1989; Keller & Krumm, 1992, 1993) conditions were reached in Precambrian rocks of the Narcea Antiform. Mid- (Keller & Krumm, 1993) to high-anchizone (Aller et al., 1987, 2005) conditions also evidenced in the lowermost Cambrian sediments at the southern margin of the southern Cantabrian Zone. At least chlorite-grade metamorphism and spatially restricted biotite-grade metamorphism (see Martín-Parra, 1989) are evidenced S of the Rio Omañas Thrust. Additionally, pervasive slaty cleavage exists throughout the Narcea Antiform (e.g. Aller et al., 1987). Cleavage extends in the lower 30 m of the discordantly overlying lowermost Cambrian sediments of the Cantabrian Zone (e.g. van den Bosch, 1969 a, b; van Staalduinen, 1973; Pérez-Estaún, 1973; Aller et al., 1987).

Precambrian deformation having been evidenced locally (e.g. Leyva et al., 1984, Martín-Parra, 1989), its effects with respect to metamorphism and the development of the slaty cleavage is nonetheless highly disputed. Some authors evidence the cleavage and its stratigraphic extent as resulting solely from Variscan activation (Pérez-Estaún, 1987; Leyva et al., 1984; Aller et al., 1987, 2005; Martín-Parra, 1989). Contrastingly, van den Bosch (1969 a, b) and van Staalduinen, (1973) assume the cleavage in the Precambrian sediments of the Narcea Antiform is an entirely Precambrian phenomenon and the cleavage structures in the Lower Cambrian sediments are due to reactivation of the shear system during Variscan time. Keller & Krumm (1993) use the metamorphic jump between Precambrian and Cambrian sediments along with multiple foliation-systems and crenulation cleavage in incorporated neoproterozoic clasts from the basal

Cambrian succession of the southern Cantabrian Zone (e.g. Gutiérrez-Alonso, 2004 b; Díaz-García, 2006) to support a Cambrian to earliest Precambrian deformation related heating event.

As stated in Chapter 6, t-T modelling was conducted using *AFTSolve* (Ketcham, 2000). *AFTSolve* limits t-T models to a maximum of 10 intersection points, suitable for most tectonothermal studys (e.g. Emmerich et al., 2005). This study focusses on the latest Variscan to present thermal history in the Cantabrian Mountains. In order to construct high-resolution thermal models for latest Variscan to present times in samples with pre-Stephanian AFT single-grain-age constituents (e.g. samples 10, 18, 82, 104-106, 110 and 111), t-T histories in these samples remained unconstrained in the modelling program for times beginning with their earliest sedimentation to before Stephanian B time. In order to more highly constrain the pre- to syn-Variscan thermal histories in these samples, t-T constraints of corresponding post-Stephanian components of the samples thermal histories would need to been reduced in frequency, allowing for more early history constraints.

#### *7.4.1.1 Narcea Antiform and lowermost Palaeozoic cover*

Though pre-Stephanian cooling in AFT t-T models from Precambrian samples of the Narcea Antiform (18 and 104-106) remain lowly constrained, though information regarding thermal evolution may still be evidenced in the pre-Stephanian component of their t-T pathways. In the SW of the study area, samples in Precambrian sediments from across both Cantabrian Zone and West Asturian-Leónese Zone limbs of the Narcea Antiform (18, 106 and 104, 105 respectively) as well as lowermost Cambrian sediments (25) of the southernmost Cantabrian Zone succession, each yield heterogeneous AFT single-grain-age components (appendix i & appendix ii) that possibly predate thermal anomalies having occurred coeval with various parts of the Variscan orogenic cycle (e.g. Fernández-Suárez et al., 2000 b; Gutierrez-Alonso et al., 2004 a; Alonso et al., 2005) (see figure 7.4-2) but may be coeval with or even possibly predate the Cadomian (650 - 550 Ma: Plant et al., 2006) orogenic cycle.

Detrital zircon ages (Fernández-Suarez et al., 2000, 2002a,b) and $^{147}Sm/^{144}Nd$ isotopic signatures (e.g. Nägler et al., 1995) in Neoproterozoic rocks of the Narcea Antiform provide evidence for the participation of Mesoproterozoic (Grenvillian s.l.: about 1000 - 1100 Ma) rocks in the source areas for Ediacaran sediments of northwestern Iberia. Nd Model ages ($T_{DM}$) for Neoproterozoic turbidites in this study's sampling area indicate sedimentation there started some time after 1.52 Ga (Mesoproterozoic time), whereas lowermost Cambrian sediments in the sampling area show an $T_{DM}$ of 1.98 Ga, indicating the incorporation Palaeoproterozoic source rocks (Nägler et al., 1995: cf Fernández-Suárez 2000, 2002 a,b).

Gutiérrez-Alonso et al. (2005) present $^{40}Ar/^{39}Ar$ ages in detrital white micas in Neoproterozoic slates (Mora Fm.) and Cambrian sandstones (Herrería equivalent) for locations at the hinge of the Narcea Antiform, NW of this study's sampling area (N 43˚16'11.3" W 6˚27;22.2" and N 43˚ 17'50.2" W 6˚ 25'33.3" respectively). The micas selection being geologically significant as they are unlikely to survive more than one sedimentary cycle, or even long water-borne transport. In Neoproterozoic sediments $^{40}Ar/^{39}Ar$ ages (783.48 ± 3.21 to 590.23 ± 3.21 Ma) show a relatively broad cooling age distribution spanning from pre-Cadomian to Cadomian orogenic cycle. Temperatures never reached the epizone thereafter. $^{40}Ar/^{39}Ar$ ages (1784.60 ± 5.87 to 550.99 ± 3.39 Ma) from Herrería equivalent Cambrian rocks indicate contributions from source rock showing Cadomian, Grenville, and Rio Negro (late Palaeoproterozoic) orogenic signatures. The data are interpreted to represent cooling in a long lived subduction related Cadomian-Avalonian-Pan African magmatic arc (Gutierrez-Alonso et al., 2005). In this study's sampling area peak metamorphism has not been quantitatively dated in the Narcea Antiform or its lowermost Cambrian cover.

AFT analysis provides the only temporally constrained quantitative measure of low-temperature cooling in the eastern Narcea Antiform. Precambrian to earliest Cambrian AFT single-grain-age constituents are evidenced in the AFT grain-age distribution for Neoproterozoic sediments of the Narcea Antiform (see figure 7.4.1.1-1; appendices i, ii), both in the northern block (samples 18), where evidence of a pre-Stephanian Palaeozoic sedimentary cover is absent (e.g. Leyva et al. 1984), and in the southern block (sample 105), where aerially discontinuous accumulations of lowermost Cambrian sediments atop the Narcea Antiform yield to thick accumulations of Cambrian to Devonian sediments along the Narcea Antiform's southern boundary.

Sample 18 shows an AFT grain-age distribution with constituents as old as 675.1 ± 177.9 Ma. In consideration of its 1σ error, this AFT grain-age possibly predates Ediacaran deposition of the turbiditic rocks and may represent low-temperature cooling ages in sediments inherited from a long-lived Cadomian-Avalonian-Pan African magmatic arc system (e.g. Gutiérrez-Aonso et al., 2005). The grain-age distribution for sample 105 yields grains as old as age of 524.3 ± 70.4 Ma, which predates Variscan orogenesis and may represent cooling following at least the Cadomian part of the long-lived Cadomian-Avalonian-Pan African magmatic arc. In consideration of its 1σ error, cooling into the AFT-PAZ from at least as early as Cryogenian time (predating Cadomian orogenesis) is revealed in an AFT single-grain-age of 502.1 ± 264.9 Ma from the southernmost sample in the study (104). In consideration of its 2σ error, sample 106 indicates cooling may have began in Ediacaran time (appendix i & appendix ii), or coeval with Cadomian Orogenesis.

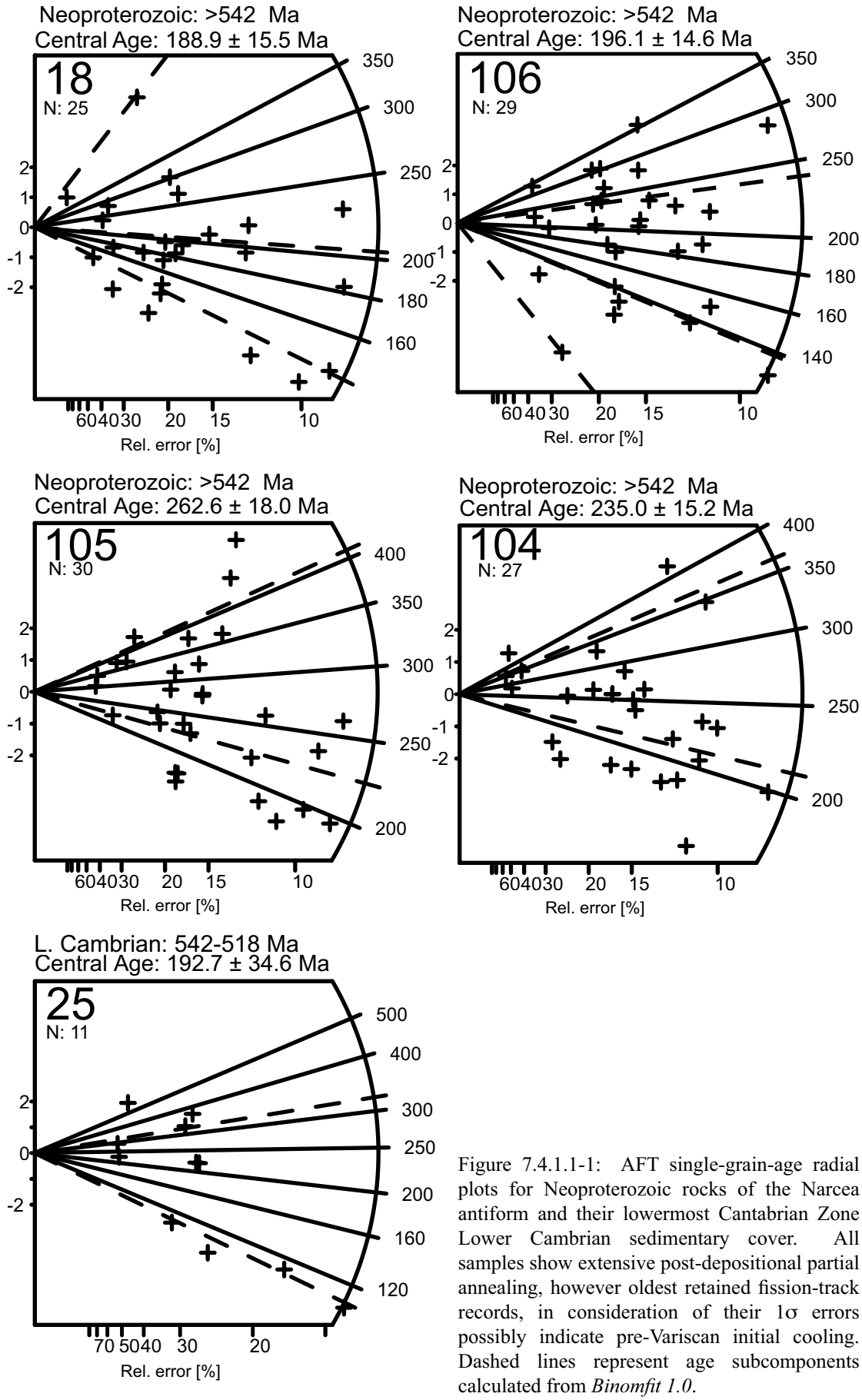


Figure 7.4.1.1-1: AFT single-grain-age radial plots for Neoproterozoic rocks of the Narcea antiform and their lowermost Cantabrian Zone Lower Cambrian sedimentary cover. All samples show extensive post-depositional partial annealing, however oldest retained fission-track records, in consideration of their 1σ errors possibly indicate pre-Variscan initial cooling. Dashed lines represent age subcomponents calculated from *Binomfit 1.0*.

Though significant partial annealing is evident in the AFT grain-age distributions from Neoproterozoic rocks, fission-tracks may never have been significantly annealed (see Gleadow & Duddy, 1981; Wagner, 1986) by the onset of Variscan (e.g. ~ 321 after Dallmeyer et al. 1997), or later (e.g. Alonso et al., 1995, Pulgar et al., 1999) tectonothermal stages.

As no $^{40}Ar/^{39}Ar$ data exist for this study's sampling area the age of cooling after peak metamorphism is elusive. AFT single-grain-age distributions for the eastern Narcea Antiform are interpreted to indicate earliest entry into the AFT-PAZ possibly began as early as Tonian to Ediacaran times. Oldest AFT grain-ages data for samples 18, and 104-106 may therefore be considered approximate the range of $^{40}Ar/^{39}Ar$ data presented for Neoproterozoic slates of the western Narcea Antiform (Gutiérrez-Alonso et al., 2005). Thus oldest AFT single-grain-ages are interpreted to possibly represent cooling which coincides with and/or possibly predates the timing of Cadomian orogenic cycle.

A poorly constrained Precambrian AFT age of 606.5 ± 284.9 Ma (: see figure 7.4.1.1-1; appendices i, ii) is evidenced for one constituent of the Cantabrian Zone's Lower Cambrian Hererría Fm. (sample 25), in discordant contact with the northern limb of the Narcea Antiform. Though highly ambiguous, this age, in consideration of the $^{40}Ar/^{39}Ar$ data presented for Hererría Fm. equivalent rocks in nonconformal contact with the western Narcea Antiform (Gutiérrez-Alonso et al., 2005) is interpreted to point to a detrital signature preserved in the absence of regional heating significant to reset this grain's fission-track system during Cadomian later orogenies or by post-sedimentational burial.

All Neoproterozoic sample t-T models yield broadly constrained time ranges acceptable fit (merit function value of at least 0.05: light grey area in t-T paths) solutions for their pre-Stephanian B constrained thermal pathways. Best fit t-T curves (See figure 7.4-2; appendix iv) produced with the initial cooling assumptions based on oldest AFT age 1σ errors, relaxed by ~ 100 - 150 Ma to account for earliest cooling possibilities, show rapid cooling into the PAZ. Models show cooling may have occurred by Neoproterozoic (104 & 106), Cambrian (105) to Silurian (18) times; thought for sample 18, the good fit solutions (merit function value of at least 0.5: dark grey area in t-T paths) also suggest onset of the cooling may indeed have extend back to Neoproterozoic time. Cooling through the PAZ is indicated in best fit t-T models to have occurred by Silurian (18, 104 and 106) to Early Carboniferous (105) times. Good fit solutions for sample 18 indicate it may also have passed through the PAZ by as Early as Cambrian time. Best fit solutions for the Narcea Antiform samples suggest they reached near-ambient to ambient conditions by Devonian (18, 104 and 106) to latest Carboniferous (105) times. Sample 18's good fit solutions showing near ambient to ambient conditions may have prevailed as early as Early Ordovician time.

Cooling in these samples occurs coeval with ~ 3.6 km of nearly continuous Palaeozoic sedimentation through to Late Carboniferous (Stephanian B) time, evidenced in the adjacent southern Cantabrian Basin (see Veselovsky, 2004), though evidence of post-Neoproterozoic/pre-Stephanian sedimentation atop the Narcea Antiform is restricted to the antiform's southern limb (Leyva et al., 1984), S of this study's sampling area. These accumulations are spatially disjunct, thin (< 200 m) and trend eastward. At the northern margin of the Narcea Antiform, oxidised rocks have been used to infer a subaerial exposed surface prior to burial by the transgressing lowermost Palaeozoic sediments (Lotze, 1956, cf. Díaz-García, 2006). Petrographic and geochemical data (Gutiérrez-Alonso et al., 2004 b) confirm a widespread Precambrian-lowermost Cambrian palaeoweathering surface occurred in these rocks. Clasts similar to those in volcaniclasitc rocks of the adjacent Narcea Antiform are recognised in basal levels of the lowermost Palaeozoic accumulation (Ordóñez et al., 2004). Zircons in stratigraphically equivalent lowermost Precambrian sediments from elsewhere in northwestern Iberia were interpreted as having been recycled from the underlying Narcea Antiform (Fernández-Suárez et al., 2000 a).

In light of local sedimentary, regional geochemical and peak thermal conditions data, the noted AFT age constituents (constrained by 1σ errors) for samples 18 and 105 of the Narcea Antiform and 25 of its lowermost Palaeozoic cover, show values indicating fission tracks in Neoproterozoic AFT systems may never have been significantly annealed (see Gleadow & Duddy, 1981; Wagner, 1986) by the onset of Variscan (Dallmeyer et al., 1997) or later (e.g. Alonso et al., 1995; Pulgar et al., 1999) tectonothermal stages. In these grains fission tracks resistant to annealing may possibly result from their unique fission-track annealing kinetics, more resistive than those normally exhibited in fluor- or even chlorapatites (e.g. Barbarand et al., 2003).

However, fission-track data may support the hypothesis that the Narcea Antiform and its adjacent lowermost Palaeozoic covers likely represent a unique basement high, having remained at shallow burial conditions, less than 110 ± 10 ˚C (or 3.5 to 4 km burial depth in association with lithostatic geothermal gradient of 30 ˚C/km) from at least as late as Middle Devonian time and possibly as early as Neoproterozoic time, coeval with and following a long-lived Cadomian-Avalonian-Pan African magmatic arc (Gutiérrez Alonso et al., 2005; cf. Fernández-Suárez et al., 2000 a; Díaz-García, 2006) and the opening of the Iapetus and Rheic Oceans (e.g. Murphy et al., 2006). That the antiform and lowermost Palaeozoic sediments in non-conformal contact with its margin yield fission tracks resistant to annealing coeval with the accumulation of 3.6 km of pre-Stephanian Palaeozoic rocks in the adjacent southern Cantabrian Basin is interpreted to speak for the eastern Narcea Antiform as acting as a unique Neoproterozoic tectonosedimentary basement high (figure 7.4.1.1-2; cf. Díaz-García, 2006) amongst pervasively subsiding Palaeozoic basins.

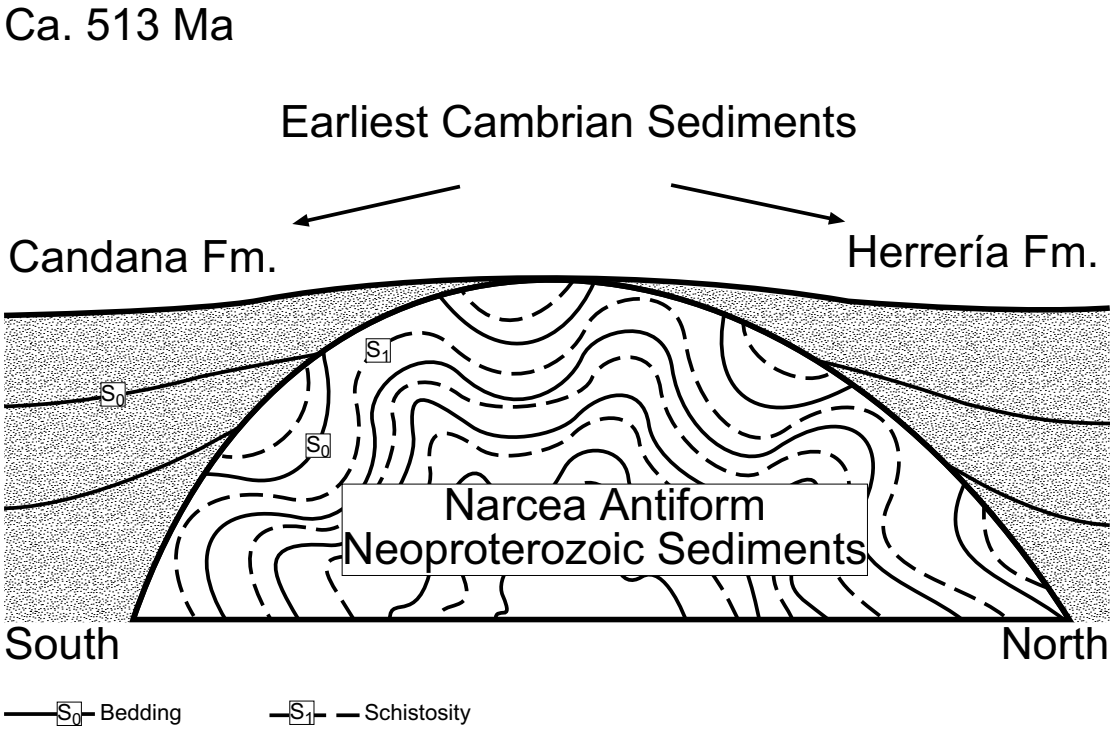


Figure 7.4.1.1-2: Idealised sketch of the palaeogeographic expression of the Narcea Antiform at earliest Cambrian time. Narcea antiform remained as a basement high amongst subsiding Palaeozoic Basins.

### *7.4.1.2 Pre-Variscan signatures in pre-Stephanian upper Palaeozoic rocks of the Fold and Nappe Province.*

Pre-Stephanian Palaeozoic rocks sampled elsewhere in the Cantabrian Zone (see table 7.1-1 and figures 7.4-2 through 7.4-4 for samples and locations), depending on their sedimentary ages and tectonostratigraphic position through time (e.g. Variscan thrust unit-stacking order; see figure 4.1-2), yield varyingly divergent AFT single-grain-age and track-length distributions (see appendix ii).

AFT single-grain-age data in Devonian strata (samples 110 & 111) from along the southern margin of the southern Cantabrian Zone (figure 7.4-3), pre-Stephanian Carboniferous (10 & 82) sediments in the Alba Syncline and Abelgas-Bregón Domain respectively, as well as Devonian rocks (9) of the Bodón Unit (see figure 7.4-4) exhibit AFT grain-age constituents, which possibly predate their host rock's sedimentation, in addition to syn- to postdepositional AFT grain-age constituents (appendices i, ii).

AFT-data from these samples indicate while many grains in Devonian or later sedimented rocks from Fold and Nappe Province tectonostratigraphic units were partially annealed by subsequent thermal events, fission-track distributions in grains with most resistant annealing kinetics were not significantly affected by heating coeval with prograding pre- to syn-Variscan basin development (e.g. Veselovsky, 2004; Dietrich, 2005), or by thermal activation coeval with e.g. Variscan thrust tectonics (e.g. Pérez-Estaún et al., 1988, 1991); late Variscan, Stephanian B-C to Early Permian oroclinal bending

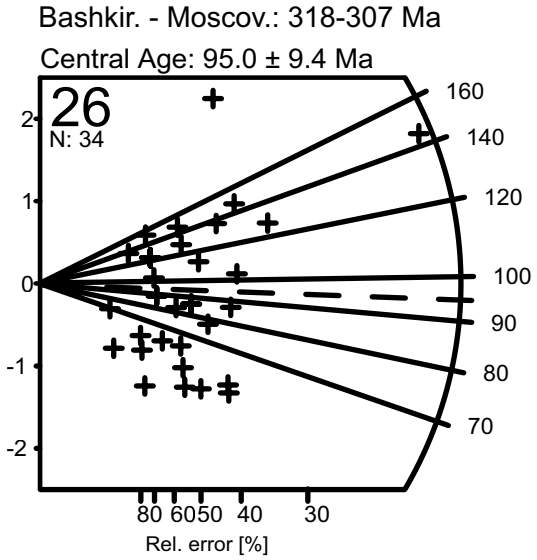


Figure 7.4.1.2-1: AFT single-grain-age distribution for sample 26 The sample is unique amongst pre-Stephanian Palaeozoic rocks in that the grain-age distribution passes the $\chi^2$-test. Its unique grain-age distribution is interpreted to be affected by Mesozoic local fluid flow along the highly tectonised Sabero-Gordón Line, though a possible pre-Variscan signature may still be present. Dashed lines represent age subcomponents calculated using *Binomfit 1.0*.

triggered lithospheric delamination (e.g. Fernández-Suárez et al., 2000 b, Gutiérrez-Alonso et al., 2004 a), or extensional collapse (e.g. Aller et al., 2005); syn- to post-Variscan hydrothermal fluid circulation (e.g. Aller et al., 2005; Gasparrini et al., in press); Atlantic (e.g. Dewey et al., 1973; Ziegler 1988; Sans de Galdeano, 1995) and/or Biscay rifting (e.g. Dewey et al., 1973; Ziegler 1988; Olivet, 1996; Andeweg, 2002); or the effects of the alpidic orogenic cycle (e.g. Alonso et al., 1995; Pulgar et al., 1999).

Uncertainty regarding the thermotectonic evolution of source rocks which supplied sediments to the Devonian or later sedimented pre-Stephanian rocks of the Fold and Nappe Province, southern Cantabrian Zone, precludes detailed evaluation of the predepositional AFT t-T pathways in these samples.

Sample 26 in faulted Middle Bashkirian to Moscovian deposited rocks of the Abelgas-Bregón Domain (see figure 7.4.1.2-1) associated with the Sabero-Gordón Line Fault System, yields a single-grain-age is 279.9 ± 130.5 Ma amongst dominantly post-Variscan AFT single-grain-age constituents. This single age indicates that even in rocks where Variscan or later hydrothermal fluid circulation may have occurred, sufficient thermal conditions (110 ± 10 ˚C for 10 Ma) may never have been reached to significantly anneal the most resistive grain.

Thus, even though there is a significant body of evidence that in pre-Stephanian Palaeozoic rocks of the Abelgas-Bregón Domain heating may have reached anywhere to between upper-diagenetic to anchizone or even epizone conditions (Chapter 5; e.g. Raven & van der Pluijm, 1986; Marschik, 1992; Aller et al., 2005), AFT-data for these rocks suggest thermal conditions in Devonian or later sedimented pre-Stephanian Palaeozoic sediments of the Fold and Nappe Province never reached or exceeded temperatures of 110 ± 10 ˚C for a total of 10 Ma coeval with or following their sedimentation.

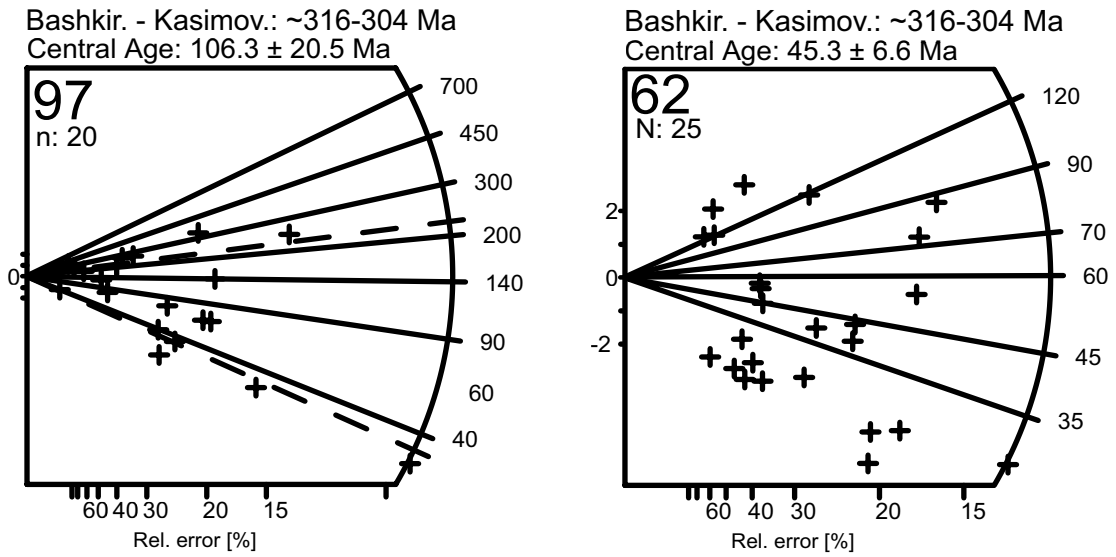


Figure 7.4.1.3-1: AFT single-grain-age distributions for southernmost Central Coal Basin samples (León-Line) showing the effects of differential partial annealing. In consideration of their respective 1σ and 2σ errors oldest AFT grain-ages from samples 97 and 62 may not have been significantly affected by metamorphism coeval with Variscan orogenic or later thermal tectonothermal episodes. Dashed lines represent age subcomponents calculated from *Binomfit 1.0*.

### *7.4.1.3 Detrital AFT signatures in the Central Coal Basin*

Middle Bashkirian-lower to middle Kasimovian sediments of the southern Central Coal Basin, separated from the Fold and Nappe Province, by the León Line Fault System yields three samples of interest to AFT analysis. Samples 97 (figure, 7.4-4) and 62 (see table 7.1-1 for coordinates), were each collected from within 2 km of the León Line. Sample 91 (see table 7.1-1 for coordinates) was collected from the base of a thrust block in the vicinity of the southwestern Ponga Unit; about 1 km of overburden overlay this sample (see figure 4.2-1; Alvarez-Marrón, 1995).

Illite crystallinity (e.g. Aller& Brime, 1985; Marschik, 1992; Aller et al., 2005) and rock cleavage (Aller et al., 1987) data has been used to support the interpretation the southern Central Coal Basin was, at or following late Variscan time, subject to heating between anchizone and epizone conditions with associated peak temperatures ranging upwards from 200 ˚C (e.g. Marshick 1992; Aller et al., 2005). Samples 97 however yields AFT single-grain-ages (figure 7.4.1.3-1) as old as (386.7 ± 335.2 and 334.3 ± 71.3 Ma). In consideration of their 1σ errors, may not have been significantly annealed by heating coeval with the onset of Variscan orogenesis (321 Ma: Dallmeyer et al., 1997); subsequent late to post-Variscan oroclinal bending triggered (Fernández-Suárez et al., 2000 a) lithospheric delamination (Gutiérrez-Alonso et al., 2004 a), or extension collapse (Aller et al., 2005) associated metamorphism in the Cantabrian Zone; post-Variscan hydrothermal extension (Aller et al., 2005); or later thermal events (e.g. Eocene hydrothermal circulation: Gutierrez-Alonso et al., 2005).

The AFT grain-age distribution for sample 62 indicates dominant post depositional partial annealing. All but one grain, when evaluated with respect to their 1σ errors, indicate entry into the PAZ following Variscan orogenic system. Nevertheless, a lowly constrained AFT single-grain-age of 196.2 ± 113.5 Ma, yields a 1σ error constrained earliest-AFT-age of 309.7 Ma. The $D_{par}$ value of 1.8 μm for this grain (appendices i, iii) indicates it is amongst the most resistive to annealing when compared to others in the data set. In consideration of this $D_{par}$ value, the 1σ error constrained AFT single-grain-age may indicate its individual cooling into the AFT-PAZ began following a Moscovian hydrothermal-fluid delivered (cf. Gasparrini 2003) peak metamorphic thermal pulse.

In the absence of temporally quantitative peak metamorphic constraints (e.g. $^{40}Ar/^{39}Ar$ cooling ages) for the timing of latest peak metamorphism in the southern Central Coal Basin, it is here interpreted extensive post-Variscan partial annealing is evidenced in Bashkirian-Kasimovian deposited samples in the southern Central Coal Basin. Nevertheless, Variscan or subsequent heating may not have been significant (110 ± 10 ˚C for 10 Ma) along the León Line to completely anneal all fission tracks having occurred prior to, or coeval with the Variscan orogenic cycle. Unfortunately, low track-length counts in samples 97 and 62 (2 and 12 respectively: see appendix ii) preclude effective modelling and following, the elucidation of their post-sedimentation annealing pathways.

Alternatively, sample 91 in the northernmost Laviana Thrust Sheet at the boundary with the Ponga Unit, expresses an AFT single-grain-age distribution with fission-track systems reset prior to at least Late Cretaceous (Aptian) time in consideration of their 2σ errors. Therefore, no information regarding pre-Variscan to early Variscan cooling is available from this sample. Its cooling history is discussed in Chapter 7.4.7.1.

### *7.4.1.4 Detrital AFT signatures in Stephanian basins*

Several samples from Stephanian B sediments in the La Magdalena and Ciñera-Matallana coal basins yield AFT grain-age components, which when considered with respect of their 1σ errors, may predate the timing of their deposition into these basins (see figure 7.4.1.4-1; appendices i, ii). The La Magdalena basin is speculated to have been sourced from intramontane molasse sediments (Colmenaro & Prado, 1999). Gutiérrez-Alonso et al. (2004 a) envisaged sediments were derived from more internal zones of the Variscan orogenic belt. Nevertheless, the exact source of these sediments is unknown. Rocks of the La Magdalena Basin yield partial annealing AFT grain-age distributions with oldest AFT single-grain-ages of 433.4 ± 177.7 Ma (sample 23), 462.0 ± 153.58 Ma (sample 114), 404.5 ± 39.8 Ma (sample 115) and 417.4 ± 88.0 Ma (sample 115). The Ciñera-Matallana Basin yields oldest AFT single-grain ages of 839.5 ± 384.5 Ma (sample 72), 839.5 ± 194.3 Ma (sample 80). Such old AFT-grain ages are interpreted to speak for source areas, which themselves were either derived of recycled ancient materials, and/

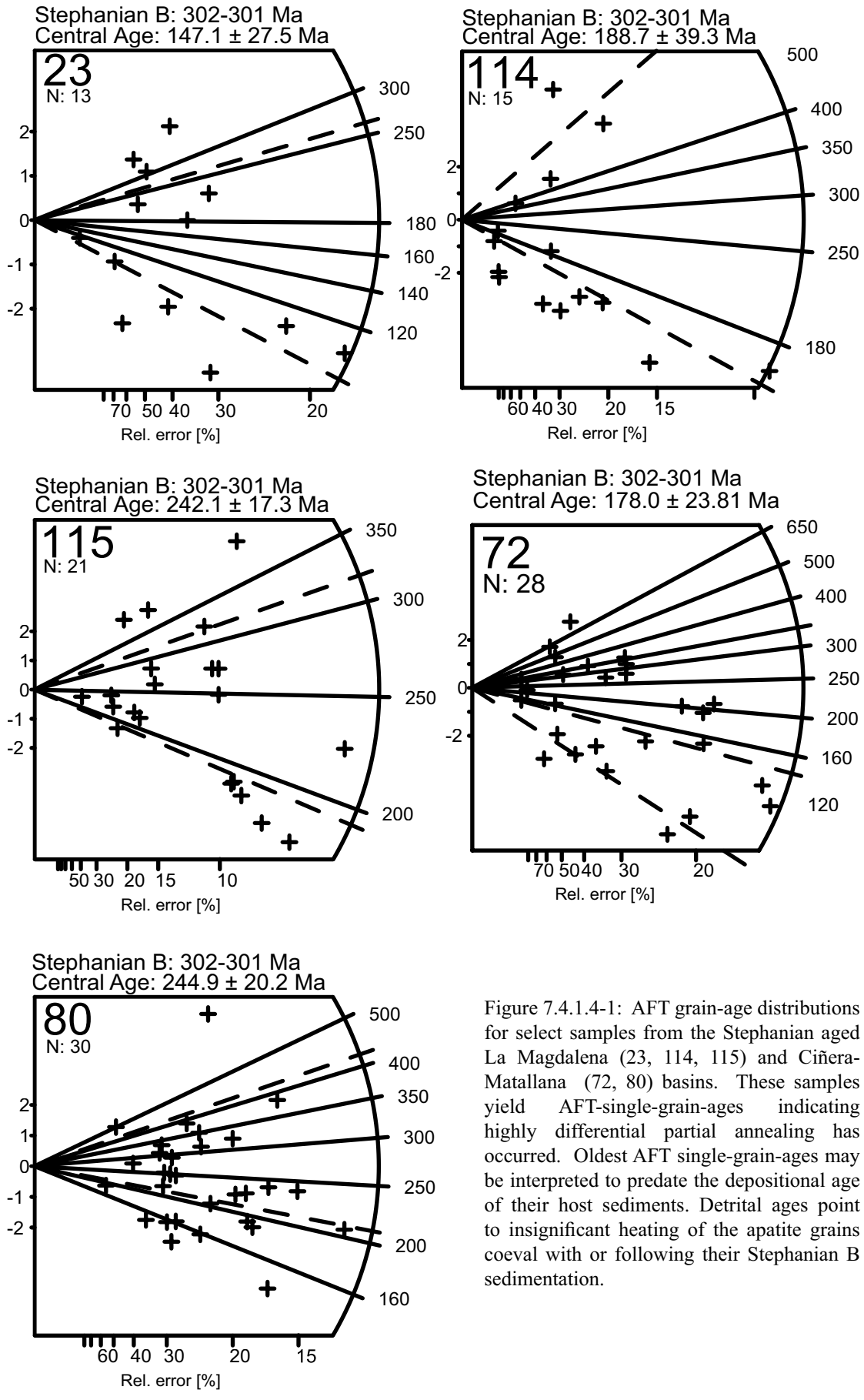


Figure 7.4.1.4-1: AFT grain-age distributions for select samples from the Stephanian aged La Magdalena (23, 114, 115) and Ciñera-Matallana (72, 80) basins. These samples yield AFT-single-grain-ages indicating highly differential partial annealing has occurred. Oldest AFT single-grain-ages may be interpreted to predate the depositional age of their host sediments. Detrital ages point to insignificant heating of the apatite grains coeval with or following their Stephanian B sedimentation.

or were cooled to temperatures below the AFT-PAZ from as early as Mesoproterozoic (in consideration of their 1σ errors) to Palaeoproterozoic (in consideration of their 2σ errors) times.

The Narcea Antiform, interpreted in this study as a possible basement high, and its non-conformal Palaeozoic cover, yield the oldest AFT single-grain-ages in this study apart from those ages described for Stephanian B coal basin sediments. As such, apatites in Stephanian rocks are interpreted to have at least been partially sourced from now eroded upper stratigraphies of the Narcea Antiform and its lowermost Palaeozoic cover.

Some support for the above hypothesis is found in geochemical and isotopic evidence (Nägler et al., 1995) from Neoproterozoic rocks of the SW of this study's sampling area. These rocks incorporated materials with Sm/Nd and $T_{DM}$ signatures, which when expressed as ages, reach to the earliest Mesoproterozoic, at least as old as the most ancient of AFT single-grain-ages calculated for La Magdalena and Ciñera-Matallana Stephanian B samples. U-Pb ages (Fernández-Suárez et al., 2000, 2002 a, b) for detrital zircons, and $^{40}Ar/^{39}Ar$ ages for detrital muscovites (Gutiérrez-Alonso et al., 2005) sampled elsewhere in the Narcea Antiform provide evidence for the participation of Neoproterozoic and Mesoproterozoic rocks in their source areas. Sm/Nd isotopic ratios and Nd crustal residence ages ($T_{dm}$) signatures indicate the participation of Palaeoproterozoic to Neoarchean materials in the source areas of Lower Palaeozoic sediments. These values persist in sediments deposited to Early Ordovician time. Subsequent pre-Stephanian deposits yield isotopic signatures again indicating the incorporation of mostly upper Palaeoproterozoic parent constituents.

Apart from very lowly constrained AFT single-grain-ages (386.7 ± 335.2 and 502.9 ± 347.6 Ma) from middle Bashkirian-Kasimovian rocks from the southern Central Coal Basin (sample 97) and Upper Devonian of the Abelgas-Bregón Domain (110), Neoproterozoic to lowermost Cambrian rocks in the SW of this study's sampling area, are the only pre-Stephanian rocks with 2σ error constrained AFT single-grain-ages indicating they may have initially cooled into the AFT-PAZ as early as Mesoproterozoic time. It is therefore hypothesised that Neoproterozoic to lowermost Cambrian sediments may have acted as significant contributors as source materials for at least the southernmost Stephanian La Magdalena and Ciñera-Matallana coal basins.

### *7.4.1.5 Variscan and later overprints in the Narcea Antiform*

Comparison between the distribution of single-grain-age constituents in Neoproterozoic rocks from the Narcea Antiform reveals samples 106 and to a lesser degree 104 were more significantly affected by Variscan and/or later stage thermal overprints than were samples 18 and 105.

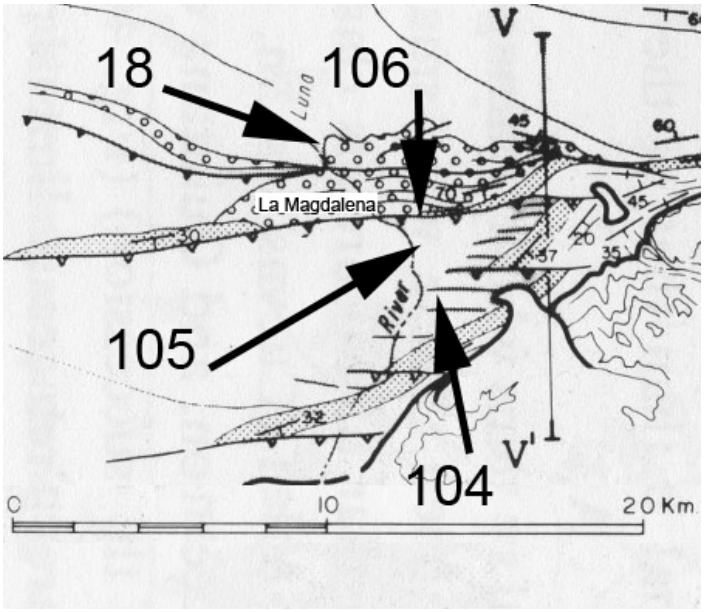


Figure 7.4.1.5-1: Structural map of the southwestern part of this study's sampling area (Alonso et al., 1995) with the location of samples in Neoproterozoic rocks of the Narcea Antiform, S of the La Magdalena Basin. N-ward directed alpidic faults (open triangle marked lineaments) dominate S of the basin.

According to Leyva et al. (1984) a sedimentary boundary occurs in the SW of the sampling area, between pelitic sandstones, in which sample 106 was taken and phylite schists from which 105 and 104 were gleaned. An E-trending Quaternary deposit at the southern margin of the La Magdalena Basin (Figure 7.4.1-2) obscures the connectivity of the Neoproterozoic rock record between samples 106 to the N and 105 to the S. Alonso et al. (1995) map an alpidic N-ward directed thrust (figure 7.4.1.5-1) along the southern margin of the La Magdalena Basin.

The E-striking Rio Omañas Thrust restricts the southern and upper thrust sheets of the Narcea Antiform, regional chlorite and thrust aligned contact biotite zones, increasing in area towards the SW (Martín-Parra, 1989; cf. Díaz-Garcia, 2006). The circulation of fault constrained hydrothermal fluids coeval with Variscan orogenic (Aller et al., 2005), and likely, later thermal events (e.g. Aller et al., 2005; cf. Gutiérrez-Alonso et al., 2005) may have contributed to the partial annealing of the AFT system in the observed grain-age distributions. In consideration of the sedimentological (see Chapter 3), structural (see Chapter 4) and peak thermal indices (see Chapter 5) information for the extreme SW of the study area, the non-linear difference in cooling patterns observed for AFT single-grain-age distributions (appendices i, ii) of sample 106 in the northern (Cantabrian Zone) block and samples 105 and 104 in the southern (West Asturian-Leónese Zone) block, may be explained by differential denudation/erosion following the superposition of the southern block over the northern block (e.g. Díaz-García, 2006).

As AFT single-grain-age constituents dating back to at least Variscan time are present in the northern footwall block (sample 106), superposition can be constrained to have at least occurred coeval with Variscan (e.g. Pérez-Estaún et al., 1988; Dallmeyer et al., 1997) orogenesis and likely also alpidic (e.g. Alonso et al., 1995; Pulgar et al., 1999) deformation. The thrust propagated increase in effective overburden over sample 106 was enough to promote accelerated fission-track annealing and obscure its pre-Variscan

fission-track record. Sample 104, is interpreted to have also been affected by thrust tectonics. At least two E-striking, N-directed alpidic thrusts are evidenced in the S of this study's sampling area (figure 7.4.1-1). The AFT record for sample 104 (appendix ii) exhibits a slightly older age of initial track retention and a more uniform track-length distribution than does sample 106. Sample No. 104 likely suffered less alpidic reheating than 106 due to: 1) its relatively higher position with respect to latest Variscan thermal uplift (sensu Gutiérrez-Alonso et al., 2004 a); 2) it's relative distance from the alpidic orogenic front, which afforded it less shortening than more proximal sampling locations (see figure 7.3-1).

### *7.4.1.6 Variscan overprint in the Fold and Nappe Province, southern Cantabrian Zone*

Total syn- to postdepositional resetting of AFT systems in pre-Stephanian Palaeozoic samples from the southern Cantabrian Zone is only evidenced in Ordovician or earlier deposited rocks in the northeastern Correcillas (sample 8) and eastern Bodón units (samples 83 & 84). AFT central-ages of 157.3 ± 10.4 and 127.5 ± 7.7 Ma were calculated for samples 8 and 83 respectively. These samples incorporate grain-ages as old as 252.3 ± 55.9 Ma (8) and 240.6 ± 59.6 (83) (see appendix i and appendix ii). Thus it may be speculated Cambrian-Ordovician rocks were heated to at least 110 ± 10 ˚C for 10 Ma (cf. Geladow & Duddy, 1981; Wagner 1986) following their deposition.

The AFT grain-age distribution for sample 84 yields no information for pre-Variscan to early Variscan times as fission-track ages, in consideration of their 2σ errors only reveal cooling from Late Jurassic time. Devonian rocks of the Abelgas-Bregón Domain (samples 110 & 111) of the Corecillas Unit and the Bodón Unit (sample 9), as well as syn-Variscan deposited pre-Stephanian Upper Carboniferous rocks (samples 10, 82) exhibit AFT grain-age distributions depicting only partial annealing conditions coeval with the onset of Variscan orogenesis were reached (appendices i, ii).

The Cantabrian Zone's Variscan orogenic expression has been described as a series of forward breaking thrust tectonic units (e.g. Pérez-Estaún, et al., 1991; cf. Veselovsky, 2004). Balanced cross sections for the stacking arrangement of Variscan thrusts (e.g. figure 4.1-2; Veselovsky, 2004; Dietrich, 2005) show the most northerly sheets (e.g. Forcada and Bodón) may have been overthrust by several kilometres of overburden, yet most southerly parts (Alba Syncline, Abelgas-Bregón Domain) show little displacement. The total effective syn-Variscan orogenic overburden thicknesses (occurring for 10 Ma or longer) atop Devonian or later sedimented units across the Fold and Nappe Province was insignificant to reset all measured AFT systems in these samples. Thus, disregarding estimations of non-lithostatic gradients in pre-Stephanain rocks of the Fold and Nappe Province (e.g. at least 45 ˚C: Schneider, 2002; cf. Frings et al., 2004), as AFT data indicate they were temporally not significant to totally anneal pre- to syn-Variscan developed track distributions, less than ~ 3.5 km-4 km of effective overburden under

a lithostatic geothermal gradient (e.g. 30 ˚C/km) must have covered Upper Palaeozoic rocks. Certainty regarding the timing and dimensions of effective overburden covering Lower Palaeozoic rocks of the Fold and Nappe Province remains elusive.

In consideration of their 2σ errors, uncertainties regarding the onset of cooling into the AFT-PAZ for grains yielding earliest AFT ages extends for sample 8 back to 364.1 Ma (Famennian time) and for sample 83 to 359.8 Ma. These ages possibly predate the local maximum age for Variscan orogenesis (e.g. Dallmeyer et al., 1997) by ~ 43 Ma and ~ 39 Ma respectively. The maximum values for the 2σ error constrained AFT single-grain-ages therefore represent the earliest estimate for the onset of far field unroofing in the southern Cantabrian Zone resulting from the E-ward advancing (Dallmeyer et al., 1997) Variscan orogenic front in Iberia. In consideration of 1σ errors the ages postdate Variscan orogenesis. Thus away from the SW corner, it is likely total effective accumulations significant to AFT annealing reached no more than minimum required to promote nearly total to total resetting of AFT thermochronometres coeval with the Variscan orogenic phase.

The AFT t-T model calculated for sample 8 incorporates an earliest AFT system PAZ entry age of 308.2 Ma (late Variscan) reasoned from the grain's 1σ age error, as the entry age did not significantly influence the sample's calculated model goodness of fit parametre (see appendix iv). Therefore the sample is modelled as having passed into the AFT-PAZ at or about the climax of the Variscan orogenesis in the Cantabrian Zone. Sample 83 was modelled as entering the PAZ from Middle Permian time onward as its crystallographic c-axis corrected track-length distribution signalled it was more significantly affected by Permian or later thermal events than by those coeval with Variscan events. Modelling results for these samples will be discussed in the relevant subsequent sections.

### 7.4.2 Late Variscan (Moscovian to earliest Permian)

AFT t-T pathways indicate, following late Variscan compression (at about 310 Ma: Pérez-Estaún et al., 1988), and prior to the emplacement of the latest to early post-Variscan thermal anomaly (e.g. Fernández-Suárez et al., 2000 b; Aller et al., 2005), samples from across the study area were either rapidly cooled (e.g. Narcea Antiform samples 8, 18, 104-106) to ambient conditions (< ~ 40 to ~ 20 ˚C), or remained at near-ambient to ambient conditions (e.g. late Variscan, Serpukhovian-Kasimovian to Stephanian sediment samples) (figures 7.4-1 to 7.4-4). Given the magnitude and breadth of the Variscan orogenic event, spanning Iberia (e.g. Dallmeyer, 1997), Belgium, northern France and southern England (e.g. Ziegler, 1990), late Variscan cooling likely resulted from regional tectonic uplift associated with the E-ward migrating Variscan compressional front (e.g. Dallmeyer et al., 1997).

Rapid transition to between middle to high-PAZ conditions (~80 to ~110 ˚C) by latest Stephanian to Middle Permian (about 304-275 Ma) is evidenced in t-T models for AFT systems with pre- to syn-Variscan age components (all excluding samples 84 & 91). However the occurrence of pre-late Variscan AFT grain-age constituents points to a relatively short lived (< 10 Ma) thermal peak. Mid- to high-PAZ conditions are interpreted to have resulted from the interplay between initial wide-scale, yet heterogeneously distributed, high heat flow conditions (e.g. 150 $mW/m^2$: Frings et al., 2004), and the delivery of supplementary latest Variscan to post-Variscan (Stephanian, Permian and/or Triassic) covers (cf. Wagner, 1966; Evers, 1967). Summaries of the evidence for the regional heterogeneous delivery of high heat flow in the latest to early post-Variscan have been provided in the context of oroclinal bending induced lithospheric delamination (Gutiérrez-Alonso et al. (2004 a) or extensional collapse (Aller et al., 2005) settings.

Latest Carboniferous to Early Permian PAZ-constrained high heat flow in Palaeozoic sediments is evidenced by: a) Anomalously high coal ranks (e.g. Frings et al., 2004), especially near fault systems (e.g. León Line, Sabero-Gordón Line, and Conombre-La Urz thrust), controlling intramontane Stephanian coal bearing basins (e.g. Ciñera-Matallana and La Magdalena); high coal ranks could not have been reached at the depth of burial unless extra heat source was supplied (Colmenaro & Prado, 1992; Gutiérrez-Alonso et al., 2004 a); b) Pervasive dolomitisation of Upper Carboniferous limestones in and about the Bodón Unit of study area, in which fluid inclusion microthermometry data record modal temperatures of between 110 and 200 ˚C (Gasparrini, 2003; Gasparrini et al., in press); significantly higher than those estimated assuming simple burial under lithostatic geothermal gradients. The dolomitisation evidences the circulation of a hot fluid system in latest Variscan (latest Carboniferous to Early Permian) times. New fluid inclusion microthermometry data for early Palaeozoic rocks of the northern Correcillas Unit showing maximum palaeotemperatures of between ~ 90 and ~ 120 ˚C (pers. com. Lapponi, 2006); c) Estimates of the latest to early post-Variscan palaeothermal gradient, which includes amongst others, at least 45 ºC/km (Schneider, 2002) from bituminite reflectance measurements in Lower Devonian rocks in the Abelgas-Bregón Domain and ~ 85 ˚C/km (Frings et al., 2004) calculated from vitrinite reflectance data for the Ciñera-Matallana Coal Basin.

In considering the empirically derived palaeogeothermal gradient for the Ciñera-Matallana basin, Frings et al. (2004) estimate the total overburden relevant to maximum coalification (i.e. at latest to early late Variscan: Stephanian-Permian times) to be in the order of ~ 1 km. The missing sediments attributed to overlying Stephanian to Permian covers, subsequently having been eroded (as sketched in figure 7.4.2-1). That this thickness exceeded ~ 1 km is considered improbable by Frings et al, (2004) in light of the observed regional distribution of Permian covers in the Cantabrian Mountains. Nevertheless, presently there is no way to constrain the maximum palaeothickness of overburden based on sedimentological or structural data (e.g. palinspastic reconstructions).

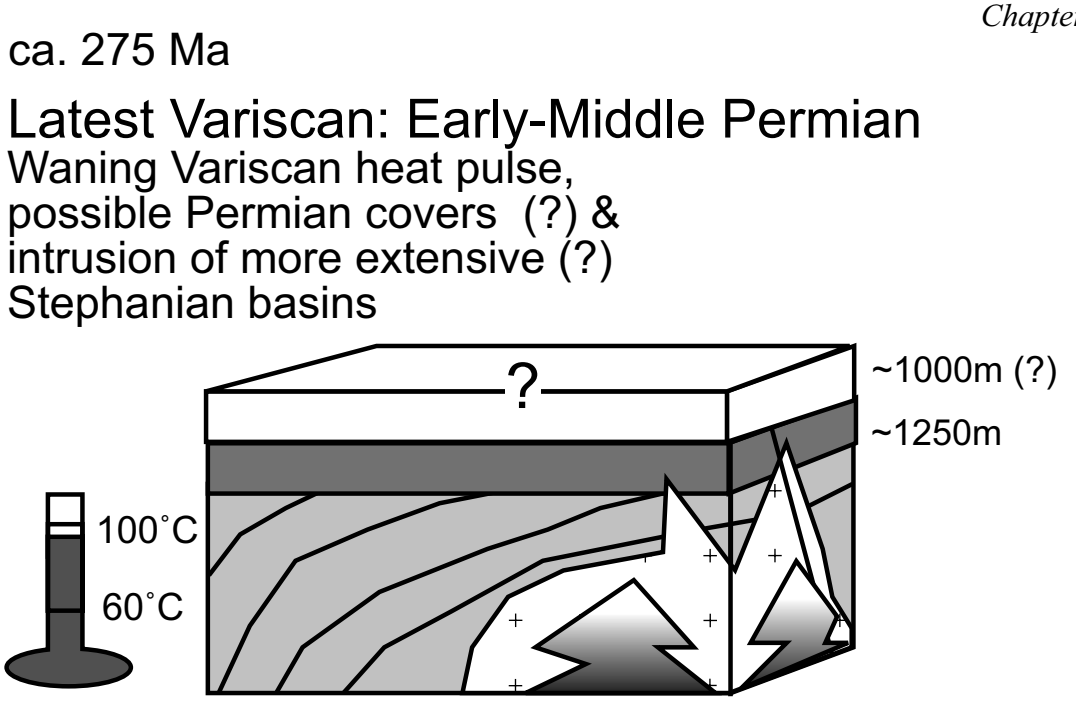


Figure 7.4.2-1: Idealised Early to Middle Permian geologic setting of the southern Cantabrian Mountains as interpreted from AFT t-T models (see figures 7.4-1 through 7.4-4) and constrained by estimates of its late Variscan tectonostratigraphic setting (e.g. Comte, 1959; de Sitter, 1962; van Ameron and van Dillewijn, 1963; Heward, 1978; Martinez-Garcia and Wagner 1984; Martínez-García, 1990), Palaeo-heat flow and thermal data (e.g. Frings, 2002; Ayllón, 2003) and regional tectonic reconstructions (e.g. Gutiérez-Alonso et al., 2004 a; Aller et al, 2005).

Heat in sedimentary settings can be transmitted either by rock-to-rock conduction, or by convection of a fluid passing through micro-, meso-, and macroporosities in the rocks. The effect of contact metamorphic environments, characterised by conductive heat transfer, being often limited in extent, when compared to that of hydrothermal environments (Ayllón, 2003). Fluids in volume are considered to transport heat more efficiently, with wider spread thermal effects (Duddy et al., 1994; Parnell, 1994). Thus, at least in the Ciñera-Matallana Basin and also likely in the La Magdalena Basin, heat was probably rapidly disseminated into the basins via fluids circulating through a network of deep reaching subvertical fractures. Nevertheless, the relative heat conductivity and the porosity/permeability of the sediments/rocks likely placed a strong control on vertical/horizontal dissemination of heat in the basins (e.g. Duddy et al., 1994).

Information gleaned from the Upper Carboniferous dolomites of the Bodón Unit suggests the initial timing and distribution of the maximum heating recorded in fluid inclusions was related to hydrothermal fluid circulation (Gasparrini, 2003) coeval with latest Variscan tectonothermal thermal events (e.g. Fernández-Suárez, et al., 2000 b; Gutiérrez-Alonso et al., 2004 a; Aller et al., 2005). High heat flow in the dolomites was likely associated with favourable porosity permeability conditions in the rocks. Underlying Devonian rocks lack the vuggy porosity of the dolomites. AFT grain-age

distributions for these rocks indicate the delivery of heat associated the circulation of hydrothermal fluid in the region was ineffective to fully anneal all precursor fission-track systems.

Evidence in support of the existence of additional late to post-Variscan deposited sedimentary covers is somewhat evasive. Permian and Triassic sediments are scarce in northwest Iberia and conspicuously absent in this study's sampling area. Local absence of Permian-Triassic rocks hinders a definitive understanding of the latest to post-Variscan/early Mesozoic thermal evolution in the study area. Nevertheless, the magnitude and spatial extent of the Variscan orogeny evokes the possibility for the existence of at least heterogeneously distributed (intramontane) Permian covers across the study area. Under this hypothesis, Stephanian aged basins, probably received higher sediment fluxes than are currently stratigraphically and spatially represented (cf. Evers, 1967; Colmenaro & Prado, 1993).

Comte (1959); de Sitter (1962); van Ameron & van Dillewijn (1963); Heward (1978) and Martínez-García & Wagner (1984) describe the southern Cantabrian Zone as a large, coherent coastal floodplain consisting of alluvial fan and lacustrine sediments, with depocentres/deep depressions having formed along major structural lineaments, such as the Sabero-Gordón line. The sediments subsequently affected by tectonic deformation, eroded, leaving only the Stephanian succession of the former depocentres as evidence. Martínez-García (1990) also predicted Permian covers the have overlain the whole of the Cantabrian Zone. Gutiérrez-Alonso et al. (2004 a) proposed an increased flux of continental molasse sediments were shed from the latest to early post-Variscan, post-lithospheric delamination induced thermally-elevated outer arc (hinterland: West Asturian-Leónese Zone) into the inner arc (foreland: Cantabrian Zone) catchment.

AFT t-T pathways for Palaeozoic samples indicate following the sharp temperature increase at latest Carboniferous to Early Permian times, steady-state mid- to high-PAZ, were sustained through to at least Middle Triassic time (60 Ma; see figures 7.4-2 to 7.4-4). Peak palaeothermal conditions coeval with the coalification of Stephanian rocks have been assumed (e.g. Frings, 2002; Frings et al., 2004) as being directly related to the magmatic activities at late Variscan time, which in the Stephanian basins, were at least partly syntectonic in origin (Ayllón, 2003). Late Variscan magmatism and mineralisation in the Cantabrian Zone has been constrained to Early Permian time (e.g. Paniagua et al., 1993, 1996; Valverde-Vaquero et al., 1999; Crespo, 2000). In order to sustain the modeled mid- to high-PAZ conditions in Palaeozoic rocks of the southern Cantabrian Mountians, the presence of insulating cover may be reasoned. Heating the result of burial equivalent to between 3 to 3.5 km of overburden atop samples 10 (Alba Syncline), 8 (northern Correcillas Unit) and 110 and 111 (southern Correcillas Unit), to more than 4 km in the Bodón Unit (83 in the Bodón Unit) must have occurred coeval with, or shortly following the late Variscan thermal pulse. Overburden thicknesses are estimated in association with geothermal gradients rapidly waning to near lithostatic,

as Lower Palaeozoic rocks at the northern margin of the Correcillas Unit (sample 8), distant from deep-seated structural features (e.g. León & Sabero-Gordón lines) also express model mid-PAZ conditions to at least Early Triassic time.

Regardless of the source of heat to Stephanian aged coal basins and the surrounding country rocks, many AFT systems (72, 75, 76, 78, 80 in the Ciñera-Matallana Basin; 18, 104-106 in the Narcea Antiform; All La Magdalena basin samples; Devonian and most pre-Stephanian Carboniferous samples from the southern Cantabrian Zone and Central Coal Basin) yield single-grain-ages distributions not reset by latest Variscan to early post-Variscan thermal activation. (see appendix ii).

Thus, though evidence of metamorphic conditions (e.g. Chapter 5; Raven & van der Pluijm, 1986; Aller et al., 2005), which constrain Variscan palaeothermal anomalies in this study's sampling area to between at least Late Carboniferous (Serpukhovian to earliest Moscovian) time (e.g. Gasparrini et al., 2003), the transition to between Stephanian and Permian times (e.g. Frings, 2002; Ayllón, 2003; Ayllón et al., 2004; Frings et al., 2004; Gasparrini et al., in press), or even into Late Permian time (e.g. Aller et al., 2005) are reported, to account for the observed AFT grain-age distributions they must have been: (a) heterogeneously and discontinuously distributed, even within Stephanian aged basins; and/or (b) the temporal dimension of peak metamorphic conditions was insignificant (e.g. 110 ± 10 ˚C < 10 Ma) to reset the most annealing resistant of AFT thermochronometres.

### 7.4.3 Post-Variscan (Late Permian-Triassic transition)

As introduced in Chapter 2.4.9 tectonic reconstructions for Late Permian to Triassic indicate, at the end of the Variscan orogenic cycle (e.g. Sanz de Galdeano, 1995; Arche & López-Gómez, 1996), or at the earliest stage of the alpidic history (e.g. Doblas et al., 1994 a), northern Iberia moved W-ward along a dextral strike-slip fault on its northern boundary (with Eurasia) and a sinistral strike-slip fault along its southern plate boundary (figure 2.4.9-1 Early Permian; Arche & López-Gómez, 1996). A NE-directed extension in the Pyrenean block (northeastern Iberia) culminated in a Triassic Rift phase and evolved into the western extension of the Tethys (figure 2.4.9-1 Late Permian; Arche & López-Gómez, 1996). Rifting there forms part of the Triassic to Late Jurassic break-up of Pangea. Permian-Triassic basins formed in the Cantabrian-Pyrenean Zone, the Catalonian Coastal Ranges and the Iberian Ranges, coeval with Permian Triassic rifting (figure 2.4.10 a; Martínez-García et al., 1983; Leprevier & Martínez-García, 1990; López-Gómez et al., 2002). Far field rifting off the western margin of Iberia is also documented to have occurred during the Late Triassic, leaving Iberia unrestrained to the W (figure 2.4.10-1 b).

t-T models for Precambrian rocks of the Narcea Antiform evidence differential though pervasive cooling through Permian and Triassic time (see figure 7.4-1 & 7.4-2). In light of the post-Variscan tectonic setting in northwest Iberia, late Variscan cooling

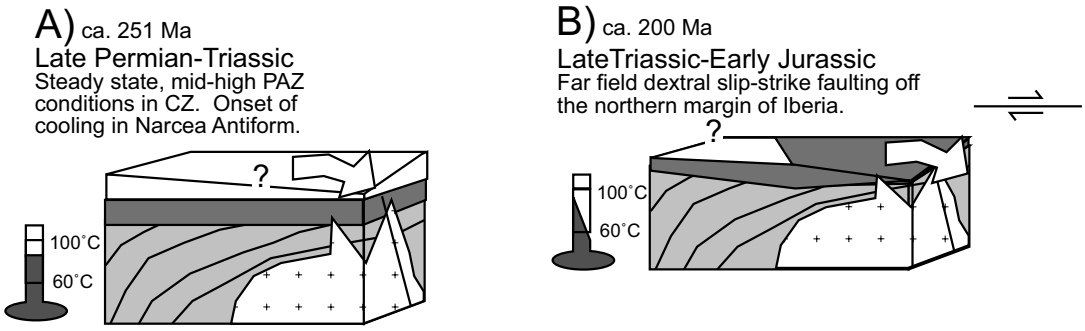


Figure 7.4.3-1: Proposed geologic evolution of the study area at the Palaeozoic-Mesozoic transition during (A) Late Permian-Triassic and (B) Late Triassic-Early Jurassic times. Evolution interpreted from AFT t-T modelling data (see figures 7.4-1 through 7.4-4) and constrained by estimated regional tectonic reconstructions (Doblas et al., 1994; Sanz de Galdeano, 1996).

of the thermally elevated (figure 2.3.5-4 b; cf. Colmenaro & Prado, 1989; Gutiérrez-Alonso et al, 2004 a) Narcea Antiform can be interpreted to have been replaced over time by post-Variscan denudation controlled uplift and cooling; continually shedding overburden, at least locally, into now extinct Permian-Triassic basins of the Variscan Cantabrian Zone.

Upper Triassic evaporites are reported for areas across northern Iberia, in the Central Asturias and Eastern Santander Provinces-Basque Pyrenees and westernmost Western-Central Pyrenees Provinces (López-Gómez et al., 2002). Lower Palaeozoic dolomitsed carbonates in the northern Correcillas Unit indicate maximum temperatures between 90 to 120 ˚C, were obtained in inclusions yielding chemical characteristics of high-salinity brines (Pers. com. Lapponi, 2006). The circulation of high-salinity brines is also evidenced in Upper Carboniferous dolomitised carbonates of the Bodón Unit (Gasparrini, 2003), where fluid inclusions with trapping temperatures between 150 and 200 ˚C are recorded; significantly higher than those estimated assuming simple burial under lithostatic geothermal gradients. As stated in section 7.4.2, Palaeozoic samples of the southern Cantabrian Zone show, following latest Variscan thermal events, rocks remained at mid- to high-PAZ conditions (see figures 7.4-1 through 7.4-4), to at least Middle Triassic time. Thus, sustained thermal conditions may in part be the result of fluid circulation in pervasively subsiding basin(s), in part coeval with regional evaporitic conditions. Proposed palaeogeographic evolution of the sampling area at the time of Palaeozoic-Mesozoic transition, based on literature constrained t-T model reconstructions are presented in figure 7.4.3-1 a and b.

### *7.4.4 Jurassic*

At the beginning of the Jurassic, southern Europe formed a single continental mass open to the E (western Tethys), and Iberia was between 25 ˚N and 35 ˚N. Separated from the Armorican Massif to the N by a trough corresponding to the earliest rift zone of the Bay of Biscay, and to the NW it was separated from the Laurentia-Greenland Plate by an epicontinental sea with a horst and graben structure, later becoming the connection between the North and Central Atlantic (Aurell et al., 2002). Opening of the Bay of Biscay occurred from latest Jurassic into the Campanian (e.g. Dewey et al., 1973).

Early Jurassic palaeogeography in the study area was characterised as a part of the emergent Iberian Massif (figure 7.4.4.-1; Aurell et al., 2002), while surrounding parts of the peninsula comprise the intracratonic basins that formed epicratonic seas. Pulgar et al. (1999) hypothesise restricted deposition of up to between 1 and 2 km of Permian-Triassic-Jurassic sediments may have occurred in the southern Central Coal Basin Unit. However, given no rocks of Jurassic age are exposed in the study area, nor for much of the Cantabrian block outside of the northern part of Asturias, thermal conditions in the study area at Jurassic time remain lowly constrained. Thus, fission-track modelling provides the only applicable temporally constrained low-temperature thermal indicator in the southern Cantabrian Mountains.

In all cases where Jurassic signature are present in t-T pathways (all but sample 91), steepened cooling from between high to middle PAZ conditions to near ambient conditions is depicted (figures 7.4-2 to 7.2-4; appendix iii). Cooling across the study area occurred coeval with the onset of the break-up of the supercontinent Pangea (cf.

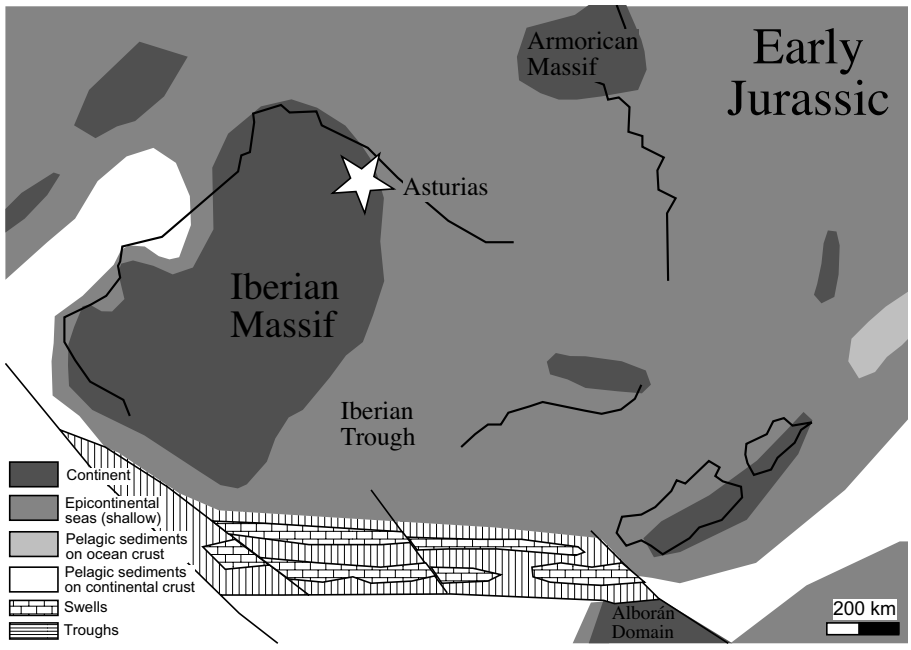


Figure 7.4.4-1: Palaeogeographic and palinspastic reconstructions of the Iberian Microplate for Early Jurassic time, indicating different sedimentary domains of Iberia. Modified from Vera (1998). Star indicates location of sampling area in the southern Cantabrian Mountains.

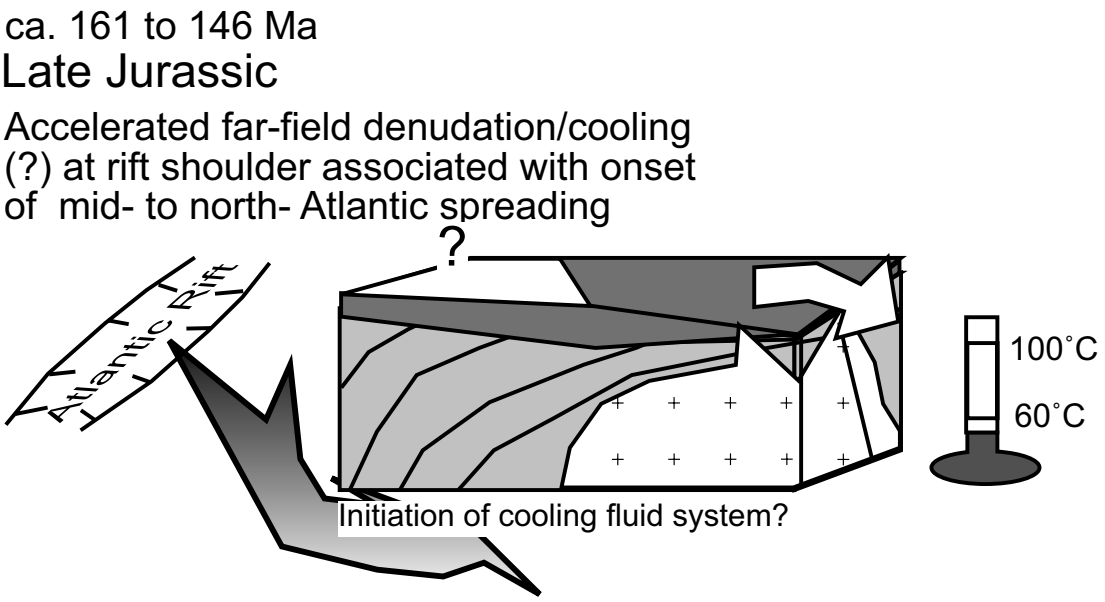


Figure 7.4.4-2: Proposed Late Jurassic evolution of the sampling area as interpreted from AFT t-T modelling data (see figures 7.4-1 through 7.4-4) and constrained by estimates of the Late Jurassic sedimentary accumulations adjacent to the sampling area (Pulgar et al., 1999) and regional tectonic reconstructions (e.g. Dewey et al., 1973; Malod & Mauffret, 1990).

Scotese, 2001); earliest extension and rifting associated with the opening of Atlantic from Late Jurassic time (figure 2.4.10-1 b; e.g. Dewey et al., 1973; Malod & Mauffret, 1990 Sanz de Galdeano, 1995 b; cf. Pedreira, 1998; Stapel, 1999) and the initial stages extension in the Bay of Biscay (e.g. Srivastava et al., 1990; Sans de Galdeano, 1995). Figure 7.4.4-2 depicts the proposed palaeogeographic evolution of the study area for Jurassic time.

The AFT grain-age distribution for the Bashkirian-Moscovian rock sample 26, located at the Sabero-Gordón Fault System (see figure 7.4-3) yields poorly constrained AFT ages exhibiting in part cooling of previously annealed grains (or authigenic apatite formation?) at Jurassic to earliest Eocene times. The unique AFT age spectrum in this sample is considered to record a previously undocumented localised cooling or crystalisation event following a possible fluid circulation along this deep-seated fault system in the southern Cantabrian Zone.

Due to the absence of Jurassic aged geological constraints in the study area, a more exhaustive interpretation of the fission-track t-T history for Jurassic time remains beyond the scope of this thesis. Nevertheless, Jurassic cooling evidenced in the fission-track record from Palaeozoic rocks of the Narcea Antiform may in part represent the onset of denudation following burial conditions from Late Permian through Triassic times following uplift associated with the Variscan orogenic cycles.

### 7.4.5 Early Cretaceous

The near absence of Cretaceous sediments in the southern Cantabrian Mountains precludes any certainty regarding the thermal history of the study area during Cretaceous time. Nevertheless, a two staged pattern of Early Cretaceous (to Albian: 112 to 100 Ma) cooling to between near-ambient and ambient conditions, followed by Late Cretaceous-Eocene heating to mid-PAZ temperatures is unfolded in the AFT record. Early Eocene portions of t-T records are constrained through information from literature regarding local sedimentary and thermal histories (e.g. Ayllón, 2003; Lobato et al., 1984); Cooling data from locations in northwest Iberia (e.g. Gutiérrez-Alonso et al., 2005) and in the offshore (e.g. Fügenschuh, et al., 2003), and regional tectonic reconstructions (e.g. Dewey et al., 1973; Ziegler 1988).

AFT t-T pathways for samples from across this study indicate accelerated cooling initiated from about Late Jurassic time, resulting for the most part in near ambient to ambient conditions, having climaxed at about the Early/Late Cretaceous transition (Aptian: 125 to 112 Ma). Most modelled t-T cooling trajectories for samples across the study area cooled to below the PAZ by Early Cretaceous (Hauterivian) time (~ 136 Ma). Accelerated Early Cretaceous cooling from mid-PAZ conditions, evidenced in t-T models (figures 7.4-1 through 7.4-4), as well as the AFT central-age of 125 ± 8 Ma for sample 83 (see table 7.1-1; appendix: ii), located in uppermost Cambrian-Ordovician volcanoclastic rocks in the Forcada thrust sheet of the Bodón Unit (see figure 4-1), are in agreement with the Early Cretaceous AFT cooling ages (138 ± 7 and 120 ± 8 Ma) from samples dredged from the offshore of the Le Danois Bank, Bay of Biscay. Those data are interpreted to represent exhumation of the Le Danois Bank (Fügenschuh et al., 2003) during earliest Bay of Biscay rifting (figure 2.4.10-1 b). Early Eocene cooling in the study area occurred coeval with progressive Atlantic sea floor spreading, (126 Ma: after Whitmarsh & Miles, 1995); poorly dated extension in shallow western margin of Iberia (e.g. 120 and 60 Ma) interpreted as being the result of restoration of the upper crust geotherm after a thermal pulse related to magmatic events(s) coeval with the onset of Mesozoic break-up of Pangea (Stapel, 1999); separation of the Galicia Bank in the offshore of northwest Iberia from the Flamish Cap at about 118 Ma (Andeweg, 2002); as well as the decrease in the relative sinistral motion between Iberia and Africa (e.g. Ziegler, 1988).

Early Cretaceous components of t-T reconstructions and Early Cretaceous AFT central-ages from this study, therefore likely demonstrate accelerated cooling related to far field extension and resultant tectonic denudation along the western and northern margins of Iberia, with rifting in the Bay of Biscay becoming more important to the end of the Early Cretaceous. Figure 7.4.5-1 depicts the proposed regional tectonosedimentary expression of the southern Cantabrian Mountains as constrained by AFT t-T models.

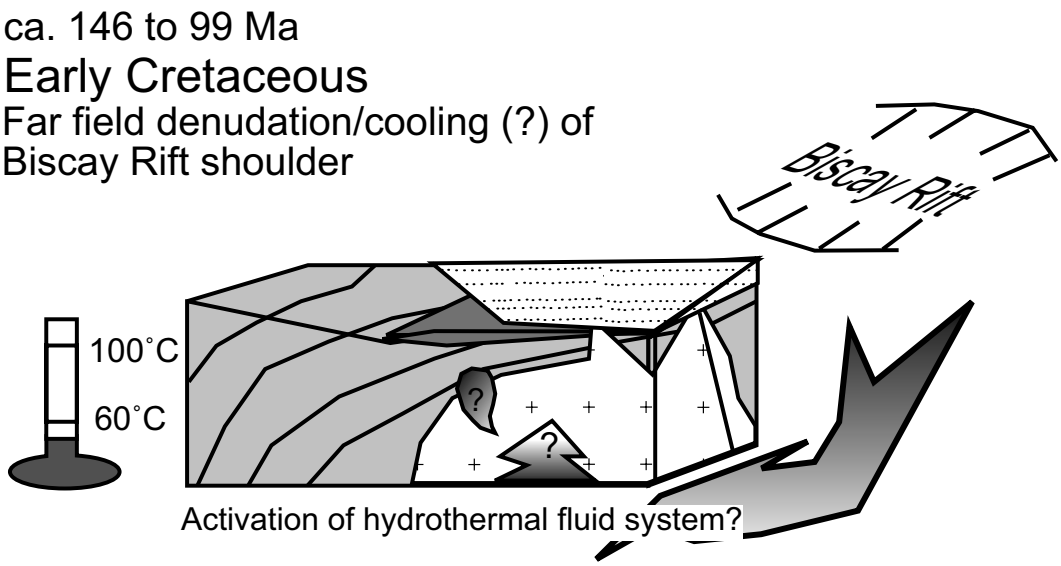


Figure 7.4.5-1: Early Cretaceous evolution of the sampling area as interpreted from AFT t-T modelling data (see figures 7.4-1 through 7.4-4) and constrained by estimates of the sedimentary accumulations in and about the sampling area (e.g. Leyva et al., 1984; Lobato et al., 1984; Ayllón, 2003), estimates of the regional (e.g. Gutiérrez-Alonso et al., 2005) and offshore (Fügenschuh, et al., 2003) thermal evolution and regional tectonic reconstructions (Dewey et al., 1973, Ziegler, 1988).

### *7.4.6 Late Cretaceous*

Regional tectonic reconstructions evidence intense, rift related Cretaceous opening of the Bay of Biscay from about the Aptian-Albian (about 112 Ma) boundary to early Campanian time (about 85 Ma) (e.g. Ziegler, 1988; Olivet, 1996), the subsequent oblique convergence between Europe and Africa (e.g. Savostin et al., 1986; Riecherter & Pletsch, 2000) to the end of the Cretaceous and consequential onset of subduction of the newly formed Biscay oceanic crust (Andeweg, 2002).

Localised cooling, coeval with the transition to Biscay rifting is evidenced along the León Line (e.g. No. 97: 106 ± 21 Ma), which separates epizone metamorphic terrains in the Central Coal Basin from lower grade metamorphic terrains of the southern Cantabrian Zone (Raven & van der Pluijm, 1986), and the Sabero-Gordón Line (e.g. No. 26: 95 ± 9 Ma) in the Abelgas-Bregón Domain, along which up to peak conditions of incipient metamorphic grade have been evidenced (e.g. Raven & van der Pluijm, 1986; Aller et al., 1987, 2005; Marschik, 1992). Additional evidence for localised transitional cooling comes from a lowly constrained AFT central-age of 109 ± 13 Ma, calculated for sample 9 (see table: 7.1-1), located in the Bodón Unit near the "Profunda" dolomite-hosted Cu mineralization site (N 42˚ 57' 59.3", W 5˚ 36' 48.5"). Figure 7.4.6-1 depicts the possible palaeogeographic setting of the study area at Late Cretaceous time.

Regional Late Cretaceous extensional tectonic activity (see figure 2.4.10-1 c) and related sedimentary subsidence are evidenced by the presence of a local depocentre due E of the Ciñera-Matallana Basin (Lobato et al., 1984). There, a shallow marine sequence was deposited at Santonian-Campanian times (85 to 71 Ma), during which

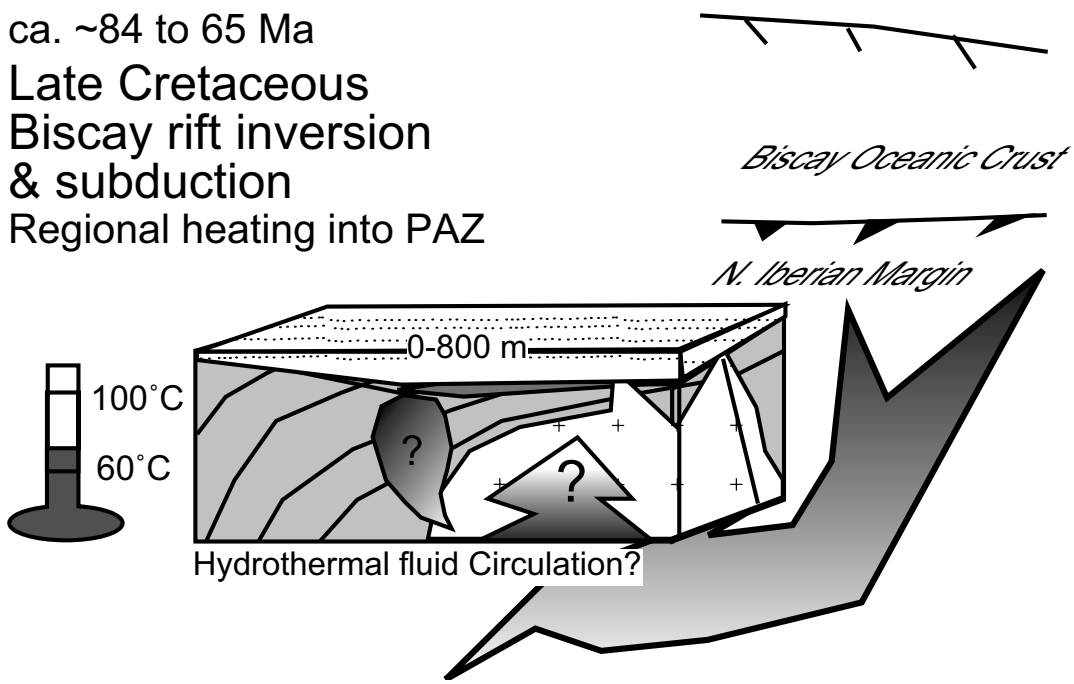


Figure 7.4.6-1: Proposed Late Cretaceous evolution of the sampling area as interpreted from AFT t-T modelling data (see figures 7.4-1 through 7.4-4) and constrained by estimates of the sedimentary accumulations in and about the sampling area (e.g. Evers, 1967; Leyva et al., 1984; Lobato et al., 1984; Ayllón, 2003; Pulgar et al., 1999), and regional tectonic reconstructions (e.g. Dewey et al., 1973; Ziegler 1988; Olivert 1996).

Cretaceous marine waters, are hypothesised to have saturated the Ciñera-Matallana Basin (Ayllón, 2003) and probably also pre-Cretaceous basement in other areas (e.g. Precambrian and pre-Stephanian Palaeozoic lithologies). Reheating, (hydrothermally driven?) to ~ 80 ˚C by latest Cretaceous (Maastrichtian) time is predicted by AFT t-T models for samples S of the León Line.

Direct evidence of Cretaceous sedimentation is restricted to the extreme southern boundary of the southern Cantabrian Mountains. A thin veil of Cretaceous rocks (≤ 150 m) overlay Neoproterozoic to Palaeozoic rocks in the southwestern Cantabrian Mountains (Narcea Antiform) and at the margin between the Duero Basin and the Abelgas-Bregón Domain of the southern Cantabrian Mountains (see figure 4-1).

Evers (1967) and Pulgar et al. (1999) propose Lower Cretaceous clastic, and Upper Cretaceous carbonate sediments up to ~ 1 km in thickness covered the whole of the area now occupied by the southern Cantabrian Mountains. Alternatively, by Late Cretaceous (Santonian-Campanian) time (86 to 71 Ma) the southern Cantabrian Mountains have been considered to have straddled the boundary between coastal-shallow marine and emergent-anorogenic parts of the northwest Iberian Peninsula (Ziegler, 1988; cf. Andeweg, 2002).

As hiatus occur between the clastic and carbonate members of the Cretaceous component of this study's sedimentary record, and between the Cretaceous and subsequent Palaeogene components of the record, it is probable more extensive sedimentary accumulations occurred and were subsequently eroded in association the propagation of alpidic orogenesis in northwestern Iberia.

The interpreted tectonothermal expression is in part supported by a the interplay between pronounced eustacy occurring in the Cretaceous, controlled in part by: a) Atlantic mid-ocean ridge development (Martín-Chivelet et al., 2002); b) subtropical, semi-arid to humid prevailing climate conditions (e.g. Floquet, 1991), having favoured the development of thick deposits of carbonates of both shallow and deep marine settings, across the Iberian Peninsula; c) regional intraplate tectonic activity during the Cretaceous (e.g. Dewey et al., 1973; Ziegler, 1988; Srivastava et al., 1990). However, Late Cretaceous heating represented in the AFT t-T pathways from this study likely also reflect the westernmost expression of the onset of crustal shortening and compression in northwestern Iberia associated with initiation of the Cantabrian arm of the "Pyrenean" alpidic orogenic cycle (cf. Martín-Chivelet et al., 2002).

### *7.4.7 Cenozoic*

The Cantabrian Mountains were emergent by the beginning of Palaeogene time (Andeweg, 2002). Generally thermal subsidence affected the northern margin of Iberia (Espina et al., 1996) at the Cretaceous-Palaeogene boundary. Erosion was dominant along the southern margin of the Cantabrian Mountains (Rincon et al., 1983). AFT t-T modelling data from across the study area shows the onset of cooling from PAZ to near-ambient/ambient conditions occurs coeval with the Cretaceous-Palaeogene boundary and erosion driven denudation of the Cantabrian Mountains.

#### *7.4.7.1 Palaeocene to Early Eocene*

The principle episode of S-ward subduction of the Bay of Biscay under the Iberian margin (see figure 2.4.10-1 d) occurred by Middle Eocene time (e.g. Dewey et al., 1973). Subduction lead to NNW compression (Leprevier & Martínez-García, 1990) along Iberia's northern margin and the onset of uplift of the Cantabrian Mountains (Andeweg, 2002; Pedreira et al., 2003). Coarsening upward alluvial fan sediments with polymict facies, sourced from deep within the Cantabrian Mountains were deposited into the northwestern Duero Basin (Alonzo-Zarza, et al., 2002) (see figure 7.4.7.1-1).

Eocene tectonism including shortening and uplift in the southern Cantabrian Mountains is constrained by the AFT central-age of 45 ± 7 Ma for sample 62 (N 42˚ 59' 55.2", W 4˚ 41' 30.5"; see figure 7.4.1.3-1 and appendix i for grain-age distributions, appendix ii for track-length distribution) located in the NW of the study area, along the León Line fault system in Upper Bashkirian to Moscovian rocks of the southern Central Coal Basin. AFT t-T modelling for sample 91 (N 43˚ 2' 24.8" W 5˚ 28' 5.7" figure

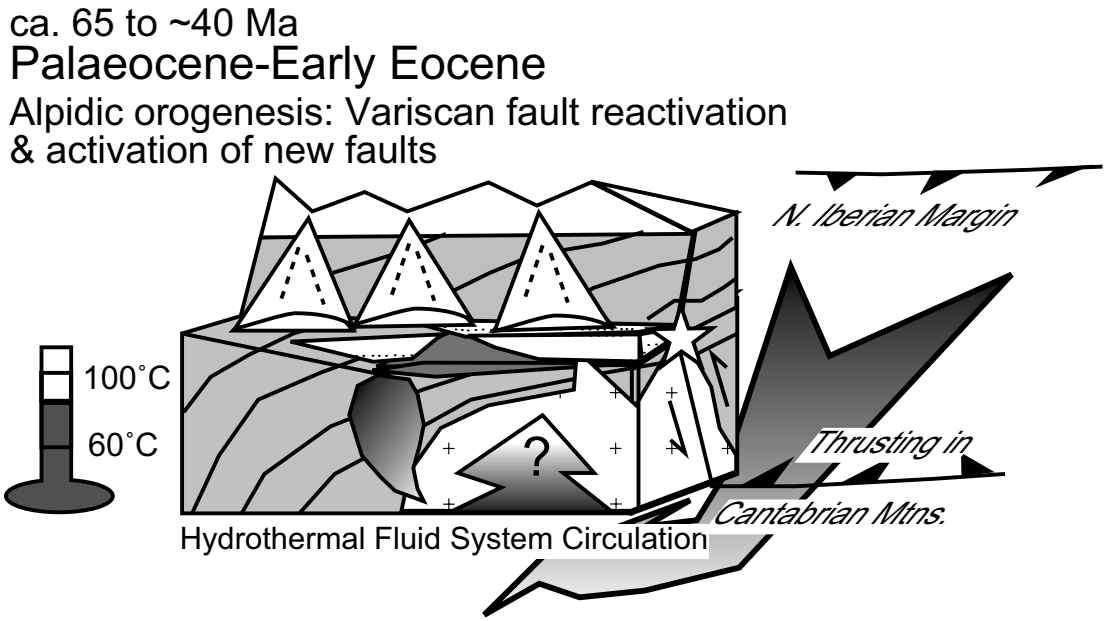


Figure 7.4.7.1-1: Palaeocene to Early Eocene evolution of the southern slope of the Cantabrian Mountains as interpreted AFT t-T models (see figures 7.4-1 through 7.4-4) and constrained by estimates of the sedimentary accumulations in the Duero Basin (e.g. Leyva et al., 1984; Lobato et al, 1984; Alonso et al., 1990, 1995; Alonso-Zarza, 2002). Additional constraint regarding regional thermal activity is provided by Jurado & Riba (1996); Pérez et al. (1996); Andeweg (2002) and Gutiérrez-Alonso et al. (2005).

7.4.7.1-2), located NE of this study's main sampling area indicates the sample initially cooled quickly into and through the PAZ to near ambient conditions (~ 30 ˚C) by about the Middle to Late Eocene (about 40 to 34 Ma).

These data are in relative agreement with the Eocene AFT age (52 ± 2 Ma) for a sample dredged from off-shore in the Bay of Biscay at the Le Danois Bank. There, data are interpreted as the final cooling stage after "Pyrenean" thrust imbrication (Fügenschuh, et al., 2003) distinctly NE of this study's sampling area.

Sample 62's AFT central-age, and sample 91's steep Eocene cooling trajectory are also supported by $^{39}Ar/^{40}Ar$ cooling ages of 44.77 ± 2.02 and 46.70 ± 0.26 Ma (Gutiérrez-Alonso et al., 2005) obtained from white mica grains from two samples in the West Asturian-Leónese Zone (from rocks with Neoproterozoic and lowest Cambrian Formation ages respectively), W of this study's sampling area. The authors propose these ages represent cooling and closure of $^{39}Ar/^{40}Ar$ systems in micas reset by fluid circulation during Eocene uplift of the Cantabrian Mountains (cf. Pedreira et al., 2003); the timing being coeval with subduction of Bay of Biscay oceanic crust (Andeweg, 2002). The Eocene aged AFT and $^{40}Ar/^{39}Ar$ data from across NW Iberia and in the offshore are here interpreted as pointing towards cooling after highly localised expressions of one or more, possibly connected, hydrothermal fluid circulation events in NW Iberia. These events occurred coeval with the collision and S-ward subduction of Bay of

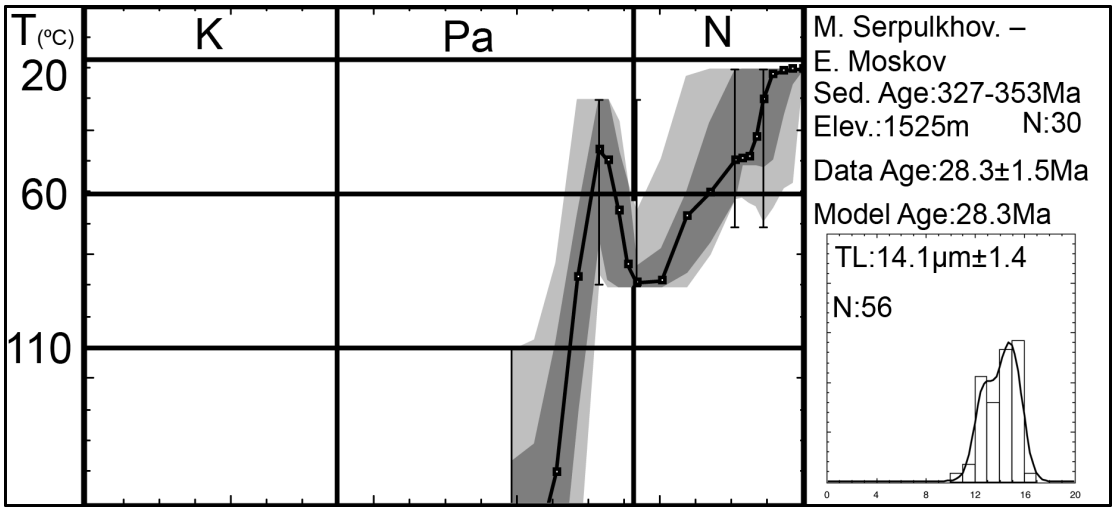


Figure 7.4.7.1-2: AFT t-T model for sample 91 (N 43˚ 2' 2.4", W 5˚ 28' 5.7") located in Middle to Late Carboniferous sediments in the southeastern limb of the Central Coal Basin. The sample yields the youngest cooling trajectory entrance amongst the sample set, recording steep alpidic orogenic related cooling.

Biscay oceanic crust under the northern Iberian margin and led to NNW compression (Leprevier & Martínez-García, 1990) along the northern margin, promoting uplift of the Cantabrian Mountains (Andeweg, 2002; Pedreira et al., 2003).

Nevertheless, under the assumption of a tectonically delivered regionally active hydrothermal (?) fluid circulation system and associated elevated thermal gradient from Late Cretaceous to Middle Eocene times, the Palaocene-Early Eocene AFT t-T model components evidence a scenario where temperature conditions locally reached into the upper PAZ to ~ 90 ˚C. AFT t-T models for samples from S of the León Line Fault System show Palaeocene-Early Eocene pathway segments consistent with proposed heating in the Ciñera-Matallana Basin to between 60 - 100 ˚C (e.g. Ayllón, 2003) delivered from brines originating from the infiltration of Cretaceous marine waters responsible for the delivery of first clastic, then subsequent carbonate sediments to the area. Heat, resulting from alpidic compression associated with the onset of uplift in the Cantabrian Mountains (Pedreira et al., 2003), was locally delivered by the activation of newly formed structures and reactivation of deeply seated, ancient (Variscan ?) structural lineaments e.g. the Sabero-Gordón Line--the main N-ward directed transport thrust in the Ciñera-Matallana Basin (Ayllón, 2003) and the León Line (exemplified by sample 62's Middle Eocene AFT central-age).

### *7.4.7.2 Late Eocene to Early Oligocene*

By latest Eocene to Early Oligocene, active subduction in the Bay of Biscay is evidenced (Andeweg, 2002). Compressional deformation occurs until Late Eocene-Oligocene (Grimaud et al., 1982) to Middle Miocene (Andeweg, 2002), marking the climax period for Cantabrian Mountain uplift (Alonso-Zarza et al., 2002). N-S compression is documented along the Asturian Coast, N of the study area. Regional tectonic compression reactivated NE-trending Variscan faults (Espina et al., 1996) by Late Eocene time, and induced S-ward thrust faulting along the southern Cantabrian border (Pulgar et al., 1999) to Middle Oligocene time.

Palaeo-tectonic-geological reconstruction of the Iberian Peninsula (e.g. Andeweg, 2002) indicate uplift occurred in the SW of this study's sampling area at latest Eocene (Priabonian: about 36 Ma) time. Coincident with regional compression and uplift, a subsequent coarsening upward sequential arrangement of alluvial sediments in the northern Duero Basin were supplied first from the NE in Middle Eocene time, then from the N at about Late Eocene through to Middle Oligocene (Alonso-Zarza et al., 2002). A regional hiatus between Middle and Late Oligocene time is marked in the depositional record of the northern Duero Basin (Alonso-Zarza et al., 2002).

In consideration of the aforementioned constraints, the AFT t-T modelling results express themselves in a complex pattern of cooling coeval with the local climax of alpidic orogenesis in the Cantabrian Mountains (e.g. Andeweg, 2002; cf Alonso et al., 1995; Pulgar et al., 1999). Active shortening and denudation promote cooling to temperatures between near ambient to ambient conditions (see figures 7.4-1 to 7.4-4). Figure 7.4.7.2-1 depicts the local palaeogeographic evolution of the southern slope of the Cantabrian Mountains based on tectonic and sedimentary reconstruction constrained AFT t-T record for Late Eocene-Early Oligocene times.

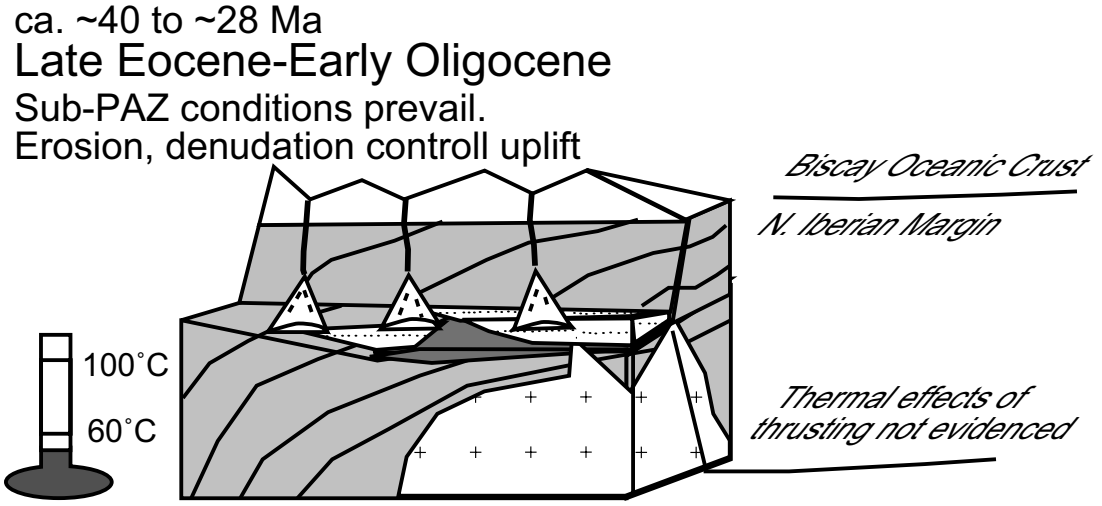


Figure 7.4.7.2-1: Late Eocene to Early Oligocene evolution of the southern slope of the Cantabrian Mountains as interpreted AFT t-T models (see figures 7.4-1 through 7.4-4) and constrained by estimates of the sedimentary accumulations in the Duero Basin (e.g. Leyva et al., 1984; Lobato et al, 1984; Alonso et al., 1990, 1995; Alonso-Zarza, 2002) and regional tectonic models (Andeweg, 2002).

### 7.4.7.3 Late Oligocene to Early Miocene

By Late Oligocene, tectonic activity along the northern Iberian margin was renewed and lasted to ~ 25 Ma (Boillot & Mallod, 1988). As a result were a horst and graben parallel to the margin (Boillot et al., 1979) and the main inversion of the Penas Trough (between the Le Danois Bank and the Asturian Massif) (Zeigler, 1988) (see also figure 2.4.10-1 e). Palaeostress followed a NW trend (Andeweg, 2002), as documented by compression in the Asturian Basin (Leprevier & Martínez-García, 1990). The top of the Le Danois Bank reached near sea level by Early Miocene time (Boillot et al., 1979) coeval with transgressive sedimentation, which occurred along the Asturian margin. The Cantabrian/Asturian coast documents N-S compressional deformation in Eocene Limestones (Andeweg, 2002). The As Pontes, off shore of northern Galicia was subject to strike-slip and thrust fault activity (Huerta et al., 1996). The sedimentary record in the Duero Basin evidences a short lived period of coarsening upwards alluvial fan deposition (figure 7.4.7.3-1; Alonso-Zarza et al., 2002). Continued, yet increasingly quiescent activity is recorded by N to NW sourced, Lower Miocene fining upward alluvial deposits in the northern and northwestern Duero Basin (Leyva et al., 1984; Lobato et al., 1984; Alonso et al., 1995; Alonso-Zarza et al., 2002).

AFT t-T modelling results express highly variable, yet, mostly, insignificant temperature increase (see fig's. 7.4-1 through 7.4-4) coeval with the onset of Oligocene to Early Miocene regional tectonic activity. The onset of quantifiable partial annealing (where temperatures reached ≥ 60 ˚C) is recorded near thrusts in lower Palaeozoic stratigraphies of the Bodón Unit (sample 83: see figure 7.4-4), at or about the Sabero-Gordón Line Fault System (samples 73, 74 and 82: see figure 7.4-3) and in reactivated footwall blocks of the Narcea Antiform (samples 18, 106: see figure 7.4-2).

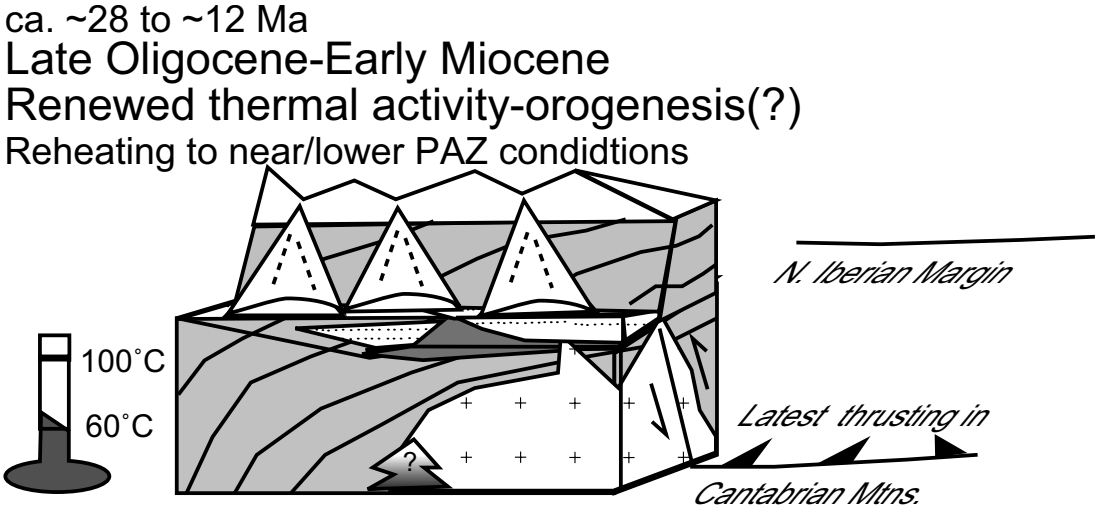


Figure 7.4.7.3-1: Late Oligocene to Early Miocene evolution of the southern slope of the Cantabrian Mountains as interpreted from AFT t-T models (see figures 7.4-1 through 7.4-4) and constrained by estimates of the sedimentary accumulations in the Duero Basin (e.g. Leyva et al., 1984; Lobato et al, 1984; Alonso et al., 1990, 1995; Alonso-Zarza, 2002) and regional tectonic models (e.g. Andeweg, 2002).

#### 7.4.7.4 Late Miocene to earliest Pliocene

From about the latest Miocene to Early Pliocene the establishment of an external drainage system induced a significant sedimentary break and the cessation of sedimentation in the Duero Basin (Alonso-Zarza et al., 2002), thus exhumation/cooling of the adjacent Cantabrian Mountains is no longer evidenced in the Duero sedimentary record.

Though likely present as a significant input to cooling throughout the whole of the alpidic orogenic cycle, from Late Miocene onward, fast denudation and subsequent isostatic crustal movement driven exhumation of the upper crust (cf. Brenet et al., 2001) was probably the dominant factor controlling cooling pathways of AFT systems in many samples from the Cantabrian Mountains to their present expression.

Tertiary palaeoclimatic patterns recorded in Duero Basin sediments evolved from tropical greenhouse-type conditions at Late Cretaceous time, through Palaeocene-Early Eocene times. Aridity increased during the Eocene-Oligocene interval, and lasted through Miocene time (as indicated by evaporite accumulation in the central part of the basin, and *sclerophyllous* forests), favoured by uplift of the surrounding mountains (Alonso-Zarza et al., 2002). Alternating conditions characterised the Middle to Late Miocene palaeoclimate, with two dry Late Miocene intervals occurring about the Aragonian-Vallesian boundary and at Turonian times. Relatively more humid and colder conditions then followed, lasting to the end of the Neogene (Alonso-Zarza et al., 2002).

A salinity crisis affects the whole of the Mediterranean at late Messinian time, from ~ 6 to ~ 5 Ma. The crisis resulted from the closure of the marine passages between the Atlantic and the Mediterranean, caused by one or more near complete to complete deccications of the Mediterranean (Butler, 1999). However within the course of a few million years, strike-slip deformation in the Gibraltar arc reopened the connection between the Atlantic and Mediterranean, flooding the basin shortly thereafter. Deccication is evidenced by a vast and thick layer of anhydrite extending across the Mediterranean. Mechanisms proposed to explain the isolation of the Mediterranean during Messinian have included a 60 m drop in global sea level due to glaciation (e.g. Clauson et al., 1996; Krijsman et al., 1999), and tectonic uplift in the western Mediterranean (cf. Johnson, 1997). Duggen et al., (2003) propose a significant change in the dynamics of subduction and in volcanism, likely resulting from the W-ward migration of the Betic subduction zone between Iberia and Morocco, caused the closure of the marine passages during Messinian time.

The Messinian palaeogeographic evolution of the southern Cantabrian Mountains is lowly constrained with respect to its sedimentological record. Middle to Upper Miocene evaporite accumulations evidenced in other parts of the Duero Basin are not recognised

in the sedimentary record of its northern domain (e.g. Alonso-Zarza et al., 2002). All but the southernmost part of this study's sampling area is considered emergent by Late Miocene time (Andeweg, 2002).

If significant, cooling and humidity associated with Messinian glaciation should also have influenced the observed AFT t-T records, likely promoting uplift and denudation. Instead, AFT models t-T express the climax of Miocene reheating (between sub-PAZ to low-PAZ conditions) occurred at latest Messinian time (see figures 7.4-2 to 7.4-4).

Glacial geomorphic features including U-shaped valleys, cirques, hornes, hanging valleys, glacial deposits and terminal moraines, are recognised in the sampling area (e.g. Marquínez et al., 1991). The age of these features is estimated to coincide with Pleistocene glaciation, obscuring the effect of any previous glacial cycle. The thickness of ice estimated in the region to between 1000 m and 2000 m. However, given in the possibility for glacially related reduction in global mean sea level having caused the Late Miocene salinity crisis (Clauson et al., 1996; Krijsman et al., 1999) in the Mediterranean one should consider the effect of possible glacial overburden at Messinian time to the cooling pathways of samples in the southern Cantabrian Mountains.

The average specific gravity of glacial ice is about 850 to 921 kg/m$^3$ , its thermal conductivity being about 2.1 W/mK (Dreyer, 1974), the average density of lithospheric rock being 2700 kg/m$^3$, the thermal conductivity of siliciclastic sedimentary rocks approaching 7.7 W/mK. It can be assumed that glacial ice has about 1/3 the effect of that of rock when calculating a simple lithostatic geothermal gradient (e.g. 1 km of glacial ice would increase the underlying rock mass by a maximum of ~ 10 ˚C). Assuming 2000 m of glacial ice was atop the Cantabrian Mountains over Messinian times, and regarding the low thermal conductivity of glacial ice as being insignificant to influence the geothermal gradients for rocks in the sampling area, a total increase in temperature of approximately ~ 20 ˚C could be expected with respect to the addition of the Messinian glacial ice. As is evidenced in the t-T reconstructions (figures 7.4-2 to 7.4-4), Miocene heating is highly variable (from insignificant to ~ 80 ˚C).

In consideration of the value of the spontaneous fission $\lambda_f$ in $^{238}U$ ($8.46 \times 10^{-17}$ a$^{-1}$: Galliker et al., 1970) and its corresponding half-life ($t_{1/2} = 8.19 \times 10^{15}$), and the AFT central-ages calculated for the samples (table 7.1-1), and the subsequent duration in which observed fission distributions could accumulate, the likelihood the occurrence of any of the spontaneous $^{238}U$ fission events evidenced in the samples corresponds to Late Miocene times is extremely low. Thus, the analysed AFT systems may not even have the temporal precision to resolve with reasonable certainty the effects of a Messinian constrained (about 2 Ma) heating event on the fission-track record in samples from this study. An integrated AFT/apatite (U-Th)/He approach (e.g. Wolf et al., 1996; Juez-Larré, 2003) to thermochronologic investigation in the sampling area may better constrain low- temperature cooling across the Cantabrian Mountains. The technique was not utilised as samples yielded insufficient apatite grains suitable for analysis.

Continuing regional tectonics is interpreted to have played a more perceptible role than glaciation in shaping the fission-track history of northern Iberia over Late Miocene time. Convergence between African and Eurasian plates has changed to NW direction (Mazzoli & Helman, 1994). Intraplate deformation in Iberia at Late Miocene time occurs similarly to that for Middle Miocene, however less intensely (e.g. Andeweg, 2002). Changes in the North Atlantic's seafloor morphology are related to alpidic orogenesis (Tucholke & McCoy, 1986). The most recent thrusting movements of the Sierras de los Obarenes yield Tortonian (~ 12 to ~ 7 Ma) ages (Jurado & Riba, 1996), and compressional deformation has been constrained to as late as Pliocene time (Cortes Gracia & Casas Sainz, 1997). Similarly compressional deformation, is recognised in offshore sediments of up to Late Miocene age (Ziegler, 1988); deformation being associated with the convergence between Europe and Iberia, and to a lesser degree, the far field effects of African/Eurasian convergence.

Significant tectonic activity is experienced to the E in the northern Pyrenees and southwestern France. Folding of the Jura Mountains initiated in Early Miocene times (Roure & Coletta, 1996) continued to propagate. Uplift of the Massif Central (Bois, 1993) occurred in relation to substantial volcanic activity. Renewed exhumation of the southern Pyrenees began (Fitzgerald et al., 1999), related to exhumation, the excavation of the Ebro Basin lead to increased sediment supply to the Valencia Trough (Andeweg, 2002; cf. Juez-Larré, 2003). The Cerdanya Basin and Conflent Basin (see Andeweg, 2002) each developed along E-striking normal faults in relation to dextral transtensional activity of the NE to ENE trending Tet Fault (HNPC, 1992).

Renewed heating in the southern Cantabrian Mountains was also likely influenced by the far field tectonic activity along Iberia's northern and northeastern margins. The varied signatures of the pre-Pliocene Neogene portion of the cooling curves may speak for differentially expressed, structurally controlled (re)activation of hydrothermal fluid circulation in the Cantabrian Mountains. t-T pathways for samples along major structural lineaments tend to show increased Miocene thermal activity (e.g. Narcea Antiform: 18, 106; Alba Syncline: 10; Abelgas-Bregón Domain: 82, 111; Ciñera-Matallana Basin: 73, 79; Bodón Unit: 83; Rucayo 85); Samples more distant to structural lineaments depict relative thermal quiescence (Narcea Antiform: 104, 105; Abelgas-Bregón Domain: 110; Ciñera-Matallana Basin: 74, 78; Correcillas Unit: 8).

Modelled samples from the La Magdalena (20 and 22) Stephanian basin and the Central Coal Basin Unit (91) do not fit the trend. Both Sample 20 and 91 yield relatively low confined-track-length counts (44 and 56 tracks respectively), their low precisions likely influencing the late portions of their t-T curves. Sample 20, with sufficient AFT age and confined track distributions was only able to yield acceptible t-T passes (merit function of at least 0.05; see Ketcham et al., 2000); the reason for which remains undetermined. Therefore the results from this sample should be interpreted with caution.

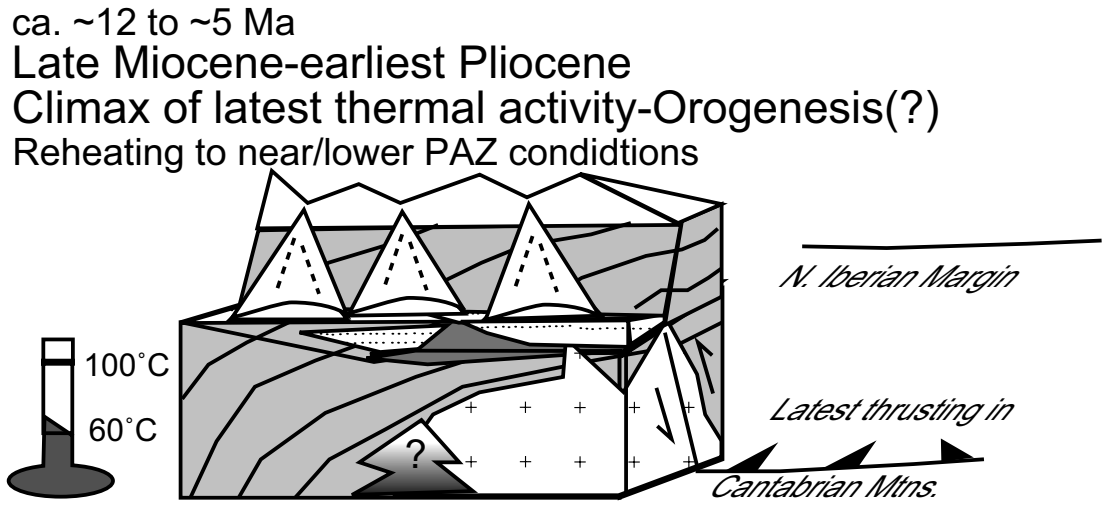


Figure 7.4.7.4-1: Late Miocene to earliest Pliocene evolution of the southern slope of the Cantabrian Mountains as interpreted from AFT t-T models (see figures 7.4-1 through 7.4-4) and constrained by estimates of the sedimentary accumulations in the Duero Basin (e.g. Lobato et al, 1979; Leyva et al., 1984; Alonso et al., 1990, 1995; Alonso-Zarza, 2002) and regional tectonic models (e.g. Andeweg, 2002).

Figure 7.4.7.4-1 depicts the local palaeogeographic evolution of the southern slope of the Cantabrian Mountains based on tectonic and sedimentary reconstruction constrained AFT t-T record for Late Miocene to earliest Pliocene times.

### *7.4.7.5 Early Pliocene to present*

Central Iberia, including parts of the Duero Basin were covered by vast plains of carbonate cemented conglomerates at Early Pliocene time (Andeweg, 2002; cf. Alonso et al., 1995). By Late Pliocene a general uplift in Iberia resulted in uplifted beach sediments along many of the Iberian margins and the erosion of the conglomerate caps. Pervasive uplift, evidenced by compressional structures in Pliocene rocks (Muñoz et al., 1983) affected the central part of the southern Pyrenees. In the northern Pyrenees and southwest France, alkaline volcanic activity in the Massif Central reached its climax at Late Pliocene time (Bois, 1993), coeval with regional basement uplift. The Ebro Basin expresses fracturing and normal faulting in relation to N to NNE trending compression and perpendicular extension (Arlegui Crespo, 1996).

Palaeo-tectono-geologic reconstructions for northwestern Iberia indicate relative tectonic quiescence dominated in the region following Late Miocene time (figure 7.4.7.5-1; Andeweg, 2002). However, in the extreme northwestern Iberia, uplift is still being recorded from about 3 Ma to present (Andeweg, 2002). Rivers in the study area are erosional, not sedimentational (e.g. Alonso et al., 1990; Leyva et al., 1984; Lobato et al, 1984). Marine quaternary sediments in Galicia are now 55 m-60 m above sea level (Vidal Romani, 1989), Helium isotopic ratios reveal recent seismic activity

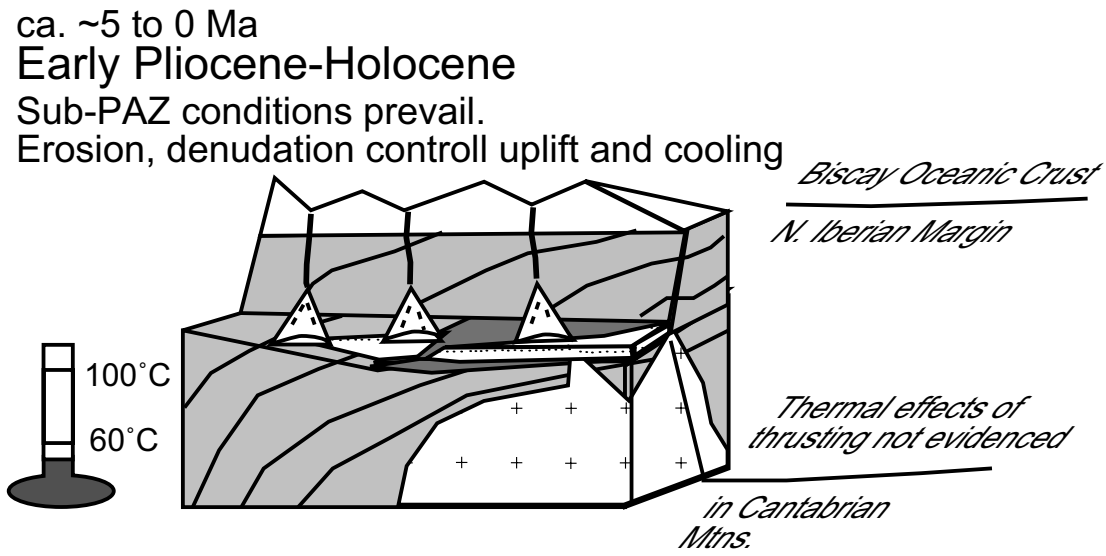


Figure 7.4.7.5-1:Early Pliocene to present evolution of the southern slope of the Cantabrian Mountains as interpreted from AFT t-T models (see figures 7.4-1 through 7.4-4) and constrained by estimates of the sedimentary accumulations in the Duero Basin (e.g. Lobato et al, 1979, Leyva et al., 1984 Alonso et al., 1990, 1995; Alonso-Zarza, 2002) and regional tectonic models (Andeweg, 2002).

in Galicia (Pérez et al., 1996), N-S trending normal faults host significant seismicity in northwestern Iberia (SIGMA, 1998), and recent movements of faults in the Bierzo basin affect Pliocene-Holocene sediments (IGME, 1982).

Patterns expressed in the AFT t-T models for samples from across this study's sampling area exemplify a high degree of heterogeneity amongst individual cooling pathways during post-Miocene times. AFT t-T pathways of individual samples differ due to the thermodynamic and mechanical characteristics of the rocks, influenced by the complex spatial-temporal interplay of geologic factors, which for example include: a) Heterogeneous tectonic activity; resulting from changing stress fields, both within and between tectonic units in the Cantabrian Mountains and adjacent Duero Basin (e.g. Andeweg, 2002); b) Regional/local heat flow heterogeneity (e.g. Čermak & Rybach, 1979) resulting from: i) Heterogeneous crustal expression through time (e.g. Alonso et al., 1995; Pulgar et al., 1995, 1999; Pedreira, et al., 2003); ii) Possible regional to local varied hydrothermal/hydrofrigid fluid circulation, which for this period is undocumented in the study area; iii) Differential thermal conductivity and porosity/permeability characteristics in and between studied rock formations (Duddy et al., 1994). Where for example, poorly conductive/low porosity shaly formations, coals and carbonaceous shales are characterised by high thermal gradients and high heat flow (Uysal et al., 2000), as these lithologies tend to absorb heat and act as a barrier to its transfer to adjacent formations; their low porosities making them impervious to the circulation of heat/cold bearing fluids (Bjørlykke, 1994); c) Individual apatite grain kinetic response to heating/cooling (e.g. Duddy et al., 1988; Carlson et al., 1999; Ketcham et al., 1999, Barbarand et al., 2003).

Nevertheless, due to increasing tectonic quiescence, denudation and related isostatic rebound were likely the dominant influences on regional exhumation and cooling of the Cantabrian Mountains from Pliocene time onwards. Thus, similar to the findings of other fission-track studies conducted for the Central Iberian Ranges (de Bruijne, 2001) and in the Catalan Coastal Ranges (Juez-Larré, 2003), relative relaxation of tectonic activity and palaeoclimate-change controlled denudation, as signalled by post-Miocene sedimentary hiatus of the Duero Basin, from Pliocene time onwards likely took over from tectonic uplift to become the primary factor in controlling orogen-scale regional denudation/cooling evidenced in the post-Miocene fission-track record of the Cantabrian Mountains.

# 8 Conclusions

## 8.1 Experimental conclusions

Thirty-two samples from this study's sampling area yield AFT age and track-length data significant to constrain the low-temperature cooling history of the Cantabrian Mountains from Neoproterozoic to present time. Of those samples, thirty fail $\chi^2$-test ($P(\chi^2) = 5$ %). Those which pass the test were not modelled due to their low track-length counts.

AFT grain-age and per-grain $D_{par}$ distributions are, for most samples, lowly correlated. Low correlation likely indicates complex variability in chemical or crystallographic composition. Variability in $D_{par}$ alone does not adequately predict variability in a sample's AFT grain-age distribution.

Calculated uranium concentration varies significantly amongst individual grains in each sample. Variability in the distribution of both AFT grain-age and $D_{par}$ parametres increased inversely to uranium concentrations. Uranium concentration may be a sensitive indicator of AFT grain chemistry's influence on the correlation between AFT grain-age and annealing kinetic ($D_{par}$) parametres.

Analysed Neoproterozoic to Palaeozoic sediments, yield highly variable $2\sigma$ error constrained AFT grain-age distributions in many cases with pre-, syn- and post-depositional AFT grain-age subcomponents; the spread of the $2\sigma$ error constrained AFT single-grain-ages from all samples extends from Palaeoproterozoic time to present.

AFT grain-age subcomponents yielding possible detrital ages, when evaluated in consideration of the available data regarding sedimentary, tectonic and peak metamorphic conditions are interpreted to indicate the thermal overprints in excess of the upper limit of the AFT-PAZ evidenced in rocks in and about this study's sampling area were never sustained for a duration equivalent to that required for the resetting of AFT systems in all analysed grains e.g. $110 \pm 10$ ˚C for 10 Ma: (Gleadow & Duddy, 1981; Wagner, 1986).

Where AFT ages predating a rock's sedimentation cannot be reasonably negated, the grains, prior to their deposition followed unique and inestimable t-T journeys upon entry into their AFT-PAZ's prior to their deposition in their current host sediment. Thus, these samples carry annealing information which cannot be accounted for in the present geological record.

The introduction of authigenic apatite may also skew understanding of a host sediments AFT age. The formation of authigenic apatite occurs in various geologic settings e.g. cement in fluvial sandstone (Bouch et al., 2002), cave cements (Bartol and Rink, 2002). In the sampling area, it has been recognised as a component of a conodont found in Devonian clastic sediments in the Abelgas-Bregón Domain of the southern Cantabrian Zone (Scheneider, 2002; cf. Raven & van der Pluijm, 1986). Additionally, anomalous Uranium concentrations, bimodal fission-track distributions in grains and anomalous AFT grain-age data of some grains from earliest Cambrian and pre-Stephanian Upper Carboniferous rocks in the Cantabrian Zone, in consideration of the samples' respective geological contexts have been used to infer the existence of authigenic apatite in the sampling area.

Sub-PAZ annealing (Green et al., 1986; Donelick, et al., 1990; Vrolijk et al., 1992), may also have played a significant role in the AFT-age and track-length distributions of the analysed samples; the amount of sub-PAZ shortening being proportional to a grain's accumulated residence time at temperatures below 60 ˚C; the amount of sub-PAZ annealing in grains yielding AFT ages possibly predating their sedimentation again cannot be estimated. However, in samples with extremely old AFT grain-age subcomponents, sub-PAZ partial annealing may represent temporally significant unaccounted for track shortening.

In consideration of the complex interplay of possible reasons for the observed AFT grain-age distributions, samples with central ages not passing the $\chi^2$-test were nevertheless modelled, under the assumption that differential partial annealing resulting from long durations at PAZ conditions, and complex variability in chemical composition signalled by low correlation between Uranium concentrations and $D_{par}$ values in analysed grains accounted for the most significant factors affecting AFT age and track-length distributions.

## 8.2 AFT central-age vs.geographic parametre conclusions

Tectonic and denudation related relief reduction in the Cantabrian Mountains coeval with and following Cenozoic final convergence of Iberia and Europe likely influenced the negative sloped profiles constructed for AFT central-age versus geographic parameters latitude and elevation. Nevertheless, AFT central-ages indicate substantial pre-Cenozoic cooling occurred in and about the southern Cantabrian Mountains. The effect of relief reductions associated with late stages of Variscan and possibly Cadomian (for Neoproterozoic to lowermost Cambrian samples) orogens upon this sample sets cooling profile is complex, and is likely poorly quantifiable within the resolution afforded by this study's sample assemblage.

The absence of post-Stephanian/pre-Cretaceous covers through much of the sampling area precludes elucidation of the effects of latest Palaeozoic-Mesozoic changing regional plate tectonics on the exhumation pathway of the Cantabrian Mountains, evidenced in

the present AFT central-age versus geographic parametres. Nevertheless, the negative-slope of the AFT-central-age-elevation profile indicates substantial relief reduction over the sampling area occurred as samples each cooled to the point where entry into their respective AFT-PAZ occurred.

## 8.3 time-Temperature modelling conclusions

1) AFT data from select Neoproterozoic and pre-Stephanian Palaeozoic samples in the Narcea Antiform and Cantabrian Zone's Fold and Nappe Province and Central Coal Basin units reveal AFT ages, which when evaluated with respect to their 1σ errors indicate post-metamorphic-peak partial annealing was sufficient to reset all but the most AFT annealing-resistant grains. Ancient AFT ages in sample grain-age distributions indicate the thermal effects of Variscan or later orogenic cycles may not have been significant to completely anneal all precursor fission tracks.

Fission tracks in apatite grains from turbiditic sediments in the Narcea Antiform yield AFT ages, which indicate partial annealing following thermal resetting, possibly predating and/or having occurred coeval with a long-lived Cadomian-Avalonian-Pan African magmatic arc system. Lower Cambrian rocks at the margin of the Narcea Antiform, in nonconformal contact with their Precambrian basement, outsited the study area incorporate $^{40}Ar/^{39}Ar$ peak metamorphic cooling ages spanning late Palaeoproterozoic to Neoproterozoic time. In the study area they yield AFT ages which indicate their most resistant grains may never have been totally annealed since at least Neoproterozoic time.

Thus, sampled turbiditic rocks of the Narcea Antiform and their nonconformal lower Cambrian sedimentary cover remained as a basement high, buried by, at most 4 km (assuming a lithostatic geothermal gradient of ~ 30 ˚C/km) following peak-metamorphic conditions possibly in association with earliest (pre-Cadomian: see Gutiérrez-Alonso et al., 2005) cooling in a long-lived subduction related Cadomian-Avalonian-Pan African magmatic arc system (cf. Díaz-García. 2006). Subsequent metamorphic events (e.g. Ordovician-Silurian, Late Carboniferous-Middle Permian) were significant enough only to partially anneal fission-track systems in these samples.

As the exact nature of the low-temperature cooling conditions of the Neoproterozoic turbiditic sediments source rocks are lowly constrained, the pre-Stephanian component of the AFT t-T pathways for samples from the Narcea Antiform show cooling into the AFT-PAZ predates Variscan Orogenesis and may predate the Ediacaran (cf. Gutiérrez-Alonso et al., 2005) timing of their sedimentation. In select pre-Stephanian Palaeozoic samples from the southern Cantabrian Zone's Alba Syncline and Abelgas-Bregón thrust unit, t-T histories predating the onset of Variscan orogenesis are modelled.

*Conclusions*

The source for Stephanian rocks of the Ciñera-Matallana and La Magadalena coal basins may ultimately be traceable to at least the Narcea Antiform as select samples yield 2σ error constrained Precambrian AFT grain-age subcomponents with earliest possible cooling extending as far back as Mesoproterozoic to Palaeoproterozoic times.

2) AFT grain-age distributions from most Devonian or later rocks indicate only partial annealing may have been active coeval with or following their deposition. Total post-depositional annealing of AFT systems is evidenced only in lower Palaeozoic rocks in the northern Correcillas and Bodón units of the Fold and Nappe Province, and the Laviana thrust sheet of the Central Coal Basin; each in the vicinity of major structural lineaments.

3) AFT t-T modelling results indicate, coeval with final stages of the Variscan oroclinal bending triggered lithospheric delamination induced (Fernández-Suárez et al., 2000 a; Gutiérrez-Alonso et al., 2004 a), or extensional collapse (e.g. Aller et al., 2005) in NW Iberia, heating to between middle- to high- PAZ conditions occurred from most samples in the Cantabrian Mountains.

Differential post-Variscan cooling recognised from samples in and across the sampling area can be categorised as follow:

i) t-T models for Neoproterozoic rocks show rapid cooling followed emplacement of the latest Variscan to early post-Variscan thermal pulse. Cooling through the AFT-PAZ was reached at least by Middle Jurassic time. The rate and intensity of cooling is not indistinguishable from that associated with rapid tectonic unroofing.

ii) Modelled pre-Stephanian Palaeozoic samples of the Abelgas-Bregón Domain and Correcillas Thrust Sheet of the Fold and Nappe Province, southern Cantabrian Zone show for time following latest Variscan to early post-Variscan tectonothermal activation, temperatures remained constant in the middle- to high-PAZ to as late as Middle Triassic to Late Jurassic. Even higher temperatures may have been experienced in early Palaeozoic samples from the eastern Bodón Unit and Carboniferous rocks of the Laviana thrust sheet, as these samples do not yield cooling information for latest Variscan to early post-Variscan time.

iii) Stephanian samples in the La Magdalena basin and most samples in the Ciñera-Matallana basin indicate middle-PAZ conditions, having been reached coeval with latest to early post-Variscan time remained constant to at least Middle Triassic time. Stephanian sediments in the Rucayo Basin and one sample in The Ciñera-Matallana Basin indicate high-PAZ to near total-annealing conditions, once having been reached, were steadied to at least Middle Triassic time. Nevertheless AFT systems in these samples were not fully reset by the latest Variscan thermal pulse.

Variability amongst the latest Variscan to earliest post-Variscan portions of t-T paths for Stephanian samples may be attributed to fault delivered differential hydrothermal fluid circulation coeval with final stages of the oroclinal bending triggered lithospheric delamination induced (Gutiérrez-Alonso et al., 2004 a) and/or extensional collapse (e.g. Alonso et al., 2005) in NW Iberia.

4) Interplay between a combination of factors may have acted to maintain these samples at elevated thermal conditions, including:

i) Initial circulation of one or more regional hydrothermal fluid systems, heating rocks in the basin to beyond that caused by burial diagenesis. Microthermometry results in pre-Stephanian upper Palaeozoic (Gasparrini, 2003; Gasparrini et al., in press) and lower Palaeozoic (pers. com Lapponi, 2006) rocks, as well as Stephanian (Ayllón, 2003; Ayllón et al., 2003) rocks of the southern Cantabrian Zone evidence circulation of a low-salinity fluid followed by a high-salinity brine. Fluid inclusion trapping temperatures in both fluids are about the same as the peak temperatures indicated for latest Variscan to early post-Variscan parts of Palaeozoic sample t-T pathways. It is here envisaged the first generation low-salinity brines circulated coeval with the climax of latest Variscan to early post-Variscan oroclinal bending induced lithospheric delamination (Gutiérrez-Alonso, et al., 2004 a), or extensional collapse (e.g. Aller et al., 2005) triggered thermal pulse.

ii) Regional burial of the Palaeozoic succession by Stephanian-Permian-Triassic covers of 1 km in conjunction with peak latest Variscan to early post-Variscan thermal conditions and palaeogeothermal gradients of ~ 85 ˚C/km (Frings et al., 2004), to up to 3 to 3.5 km burial in association with waning post-Variscan palaeogeothermal gradients (to ~ 30 ˚C/km). Since the adjacent Narcea Antiform expressed cooling conditions not indistinguishable from rapid Permian to Mesozoic unroofing, and Stephanian samples in the Fold and Nappe Province, southern Cantabrian Zone yield AFT grain-age subcomponents with earliest cooling signatures similar to those from samples in the possibly lithospheric delamination induced thermally elevated Narcea Antiform (e.g. Gutierrez-Alonso et al., 2004 a), the antiform is envisaged to have possibly provided significant input into the post-Variscan sedimentary basin interpreted (e.g. Wagner 1964) to have covered the southern Cantabrian Zone and Central Coal Basin between Middle Triassic and Early Jurassic times.

iii) Spatially restricted Upper Triassic evaporites recognised elsewhere in northern Iberia may also have extended across the study area prior to their late Mesozoic denudation and erosion. High salinity fluid inclusions trapped in the Palaeozoic succession are interpreted to represent convection-cycled brines, which were preferentially transported along zones of high permeability. High permeability zones include but are not restricted to highly tectonised structural lineaments e.g. Sabero-Gordón (cf. Ayllón, 2003; Ayllón

et al., 2003) and León Lines, the basal thrust under the Láncara Fm. of the Correcillas Nappe (pers. com. Lapponi, 2006) and or macroporosities in the dolomitised parts (Gasparrini, 2003; Gasparrini et al., in press) of the Palaeozoic succession.

5) Late Mesozoic accelerated denudation and erosion of the Permian-early Mesozoic basin is evidenced in the cooling patterns of t-T reconstructions for Neoproterozoic and Palaeozoic successions across all but the most northeastern part of the sampling area. The climax of late Mesozoic cooling was reached by late Early Cretaceous (Aptian) time. Pre-Variscan Palaeozoic sediments from the Alba Syncline and the northern Correcillas Thrust Unit indicate cooling to low-PAZ conditions, all other samples in the Narcea Antiform and Fold and Nappe Province, southern Cantabrian Zone show cooling to between near-ambient to ambient conditions.

Late Mesozoic cooling in the study area is interpreted to result form denudation related to Jurassic far field extension of the Atlantic margin transitioning to Early Cretaceous cooling at distal parts of the early Bay of Biscay rift shoulder. Latest Early Cretaceous cooling evidenced in this study is in agreement with cooling ages from samples dredged from the offshore of the Le Danois Bank (e.g. Fügenschuh et al., 2003).

6) Coeval with Late Cretaceous intensified Biscay rifting, the subsequent oblique convergence between Europe and Africa, the consequential onset of subduction of newly formed Biscay crust under northern Iberia and the onset of westernmost far field expression related to crustal shortening and compression of the Pyrenean alpidic orogenic cycle, t-T reconstructions for samples from across the study area show rocks were progressively reheated to between low- to middle-PAZ conditions.

t-T data indicate the latest Cretaceous to Early Palaeogene (Early Eocene) represents the timing of thermal climax associated with the complex interplay and transition between Biscay rifting, crustal subduction and farfield early-alpedic heating in northwestern Iberia. Cooling after a short lived high-temperature fluid circulation, preferentially delivered along major structural lineaments is evidenced in AFT central-ages and t-T data for samples along the León and Sabero-Gordón lines, at basal-thrusts in the Correcillas and Bodón units, and samples from zones of high porosity such as the dolomitised rocks of the Bodón Unit; these samples are interpreted to have variably suffered under high-PAZ to total annealing conditions.

Timing of the Eocene thermal pulse as documented by this study's fission-track record is in agreement with AFT ages in the offshore and $^{40}Ar/^{39}Ar$ cooling ages from lowermost Palaeozoic rocks in the core of the Iberian Arc; the $^{40}Ar/^{39}Ar$ ages interpreted by Gutiérrez-Alonso et al. (2005) to represent localised fluid circulation associated with the onset of alpidic uplift in the Cantabrian Mountain (Pedreira et al., 2003).

7) AFT t-T data for Late Eocene to Early Oligocene indicate rapid cooling through the PAZ to between near-ambient and ambient conditions occurred coeval with intense westernmost Pyrenean associated alpidic shortening and unroofing of the Cantabrian Mountains. Cooling occurs coeval with deposition of first NE, then N sourced coarsening upward Upper Eocene to Lower Oligocene clastic sediments in the Duero Basin.

t-T data indicate renewed heating in Cantabrian Mountains may have occurred at Late Oligocene time, coincident with renewed tectonic activity along the northern Iberian margin (e.g. Boillot et al., 1979). The climax of the final thermal emplacement occurred by latest Messinian time. In the sampling area renewed heating occurs coevally with a regional hiatus in the Duero Basin sedimentary record, spanning Late Oligocene to earliest Miocene time, followed by lacustrine cycling in the basin recognised to late Messinian time.

Dominantly tectonically-induced heat, which preferentially followed structural lineaments, was heterogeneously delivered in the emergent study area. Low-PAZ conditions were reached in early Palaeozoic rocks of the Bodón Unit, Stephanian sediments at the margins of the Ciñera-Matallana Basin and in the northern limb of the Narcea Antiform. Elsewhere, heating is considered to have been too little to have significantly promoted annealing of fission tracks in the samples.

8) Under the Pliocene to present NW-SE direct stress field in the Cantabrian Mountains (Andeweg, 2002), the far field effect of Pyrenean collision has increasingly diminished. Post-Miocene seismic activity is evidenced in Galicia (Pérez et al, 1996) and faulting there affects Pleistocene to Holocene age marine sediments, as well as Pliocene and Holocene sediments in the Bierzo basin. However, geothermal activity indicators for the southern slope of Cantabrian Mountains show the present gradient as equivalent to lithostatic (Čermak & Rybach, 1979).

Final heterogeneous cooling of samples is evidenced in AFT t-T pathways beginning from Early Pliocene time. As evidenced elsewhere in northeastern (Juez-Larré, 2003) and central (de Bruijne, 2002) Iberia, the quieting but still present Pliocene tectonism over time gave way to climate-change-controlled denudation along the southern slope of the Cantabrian Mountains.

# 9 Future research

## 9.1 Future AFT analyses

Preliminary AFT investigation in the southern Cantabrian Mountains show a highly heterogeneous tectonothermal evolution spanning Neoproterozoic to present time. In all parts of this study's sampling area, high precision AFT analysis can be conducted to better constrain the spatial and temporal dimensions associated with the area's thermal. These studies include:

**Narcea Antiform:** Initial investigation of AFT grain-age distributions in samples from of the Neoproterozoic sediments in the Narcea Antiform and its lowermost Cantabrian Zone Palaeozoic covers reveals these rocks may never have been buried to depths significant to erase possible pre-depositional but post-peak-metamorphim fission-track signatures. The southern margin of the Narcea antiform is unconformably overlain by rocks belonging to the West Asturian-Leónese Zone, noted as having reached high grade metamorphic conditions (Gutiérrez-Alonso, 1996; Díaz-García, 2006). High resolution AFT investigation across both margins of the antiform and its lowermost Palaeozoic covers may help to constrain timing and duration of the metamorphic event in the eastern arm of the Asturian Arc.

**Fold and Nappe Province, southern Cantabrian Zone:** Preliminary investigation of the Fold and Nappe Province, southern Cantabrian Zone yields significant gaps in the AFT record for pre-Stephanian Palaeozoic rocks. Reprocessing the saved bulk rock remains from these samples employing a disk-mill instead of a jaw-crusher may reveal higher concentrations of fission-track bearing apatites to study. Therefore a more highly constrained understanding of the southern Cantabrian Zone's thermal evolution may be achieved.

Vertically oriented Palaeozoic stratigraphies from locations E of the Barrios de Luna dam-site in the Abelgas-Bregón thrust sheet forming highest peaks in the Fold and Nappe Province, southern Cantabrian Zone. Resampling rocks and/or reprocessing samples along the nearly 1000 m of relief may reveal fission-track laden apatites useful in the construction of a denudation profile for the southern Cantabrian Zone. The denudation profile would help to constrain the timing and rate of uplift along the southern slope of the Cantabrian Mountains.

**Central Coal Basin:** Rocks from along the southern slope of the Central Coal Basin indicate they have been heterogeneously metamorphosed to diagenetic, anchizone and epizone conditions. Initial investigation of rocks along León Line indicates peak heating in locations may have been temporally restricted to less than 10 Ma in duration. High

resolution sampling, and/or reprocessing of samples from across the León Line may help to constrain the spatial and temporal dimensions of peak metamorphic conditions along this fault Variscan associated fault.

**Stephanian coal basins:** AFT investigation of The Ciñera-Matallana Coal Basin reveals rocks have been heterogeneously affected by a latest Variscan to early post-Variscan metamorphic event. High resolution sampling at and about intrusion sites in the basin may help to constrain the spatial and temporal dimensions of cooling after intrusion emplacement.

Illite crystallinity data from the northeastern limb of the La Magdalena Basin (Aller et al., 2005) show epizone conditions were there reached, though AFT data from this study indicate the temporal dimension of latest Variscan to earliest post-Variscan peak metamorphic conditions was shorter than required to reset all AFT chronometres in the basin. Grid-type high resolution sampling along and across faults in this basin may help to constrain the spatial and temporal dimensions of cooling after latest Variscan to early post-Variscan thermal emplacement in the basin.

**Mesozoic covers and Cenozoic (Duero) basin:** No AFT data were recorded from Mesozoic or Cenozoic sediments along the southern margin of the southern Cantabrian Mountains. Cretaceous rocks structurally overlain by dolomitised Palaeozoic covers could be sampled to help constrain the timing of the dolomitisation event.

Apatites were not recognised in rocks sampled from the Duero Basin. At its northwestern margin, stratigraphic thicknesses in the Duero Basin increase E-wardly over 30 km to ~ 3 km in thickness. A synthetic bore hole study of AFT ages can be reconstructed from high definition sampling of the rapidly grading sediments. These data may help constrain the timing of alpidic orogenesis in the Cantabrian Mountains.

## 9.2 Other techniques

Apatite (U-Th)/He dating, with a closure temperature of ~ 75 ˚C has been utilised (Wolf et al., 1996) to better constrain the lower limit of cooling in Palaeozoic sediments in northeastern Iberia. Most t-T reconstructions for samples from across this study's sampling area show extensive periods of the sub-PAZ conditions. Apatite (U-Th)/He dating may also help to constrain lowest-temperature cooling along the southern slope of the Cantabrian Mountains. Cooling in Neoproterozoic and upper Palaeozoic sediments extending as far back as latest Jurassic to Early Cretaceous time may be recognised.

$^{40}Ar/^{39}Ar$ dating in detrital micas from westernmost Neoproterozoic and lowermost Palaeozoic sediments belonging to the Cantabrian Zone part of the Asturian Arc yield two ages constraining a high temperature metamorphic fluid circulation event at Eocene time (Gutiérrez-Alonso et al., 2005). As Eocene thermal reactivation is evidenced in AFT t-T reconstruction for samples from this study, high resolution $^{40}Ar/^{39}Ar$ investigation in

the eastern most part of the Narcea Antiform and it lowermost Palaeozoic covers may also quantitatively constrain the timing of peak metamorphic conditions experienced in the SW corner of this study's sampling area.
Zircon apatite studies quantitatively constrain the timing of cooling after having reached near metamorphic to metamorphic conditions between 250 ˚C to 350 ˚C (Wagner & van den Haute, 1992). Rocks from across this study's sampling area, including Neoproterozoic rocks of the Narcea Antiform, rocks from Stephanian Basins and those along the León Line in the Central Coal Basin, yield mineral concentrates with abundant zircon constituents. These rocks also document anchizone to incipient metamorphic conditions were reached. Fission-track analysis of zircon concentrates from this study may constrain the timing of earliest cooling from thermal pulses evidenced across the sampling area.

The integration of quantitative dating analyses to the t-T record of the southern Cantabrian Mountains will help to reconstruct the timing and magnitude of a complex tectonothermal evolution spanning from Neoproterozoic to present time in a corner of the microcontinent showing thermal activity in association with at least two complete orogenic cycles and which still evidences subtle tectonic movement to date.

# References

Ábalos, B., Carreras, J., Druguet, E., Escuder Viruete, J., Gómez Pugnaire, T., Lorenzo Alvarez, S., Quesada, C., Rodríguez Fernández, L.R. and Gil-Ibarguchi, J.I. (2002). Variscan and Pre-Variscan tectonics. In W. Gibbons and T. Moreno, Eds. *The geology of Spain*, p. 155-183. Geological Society, London.

Allen, P.A. and Allen, J.R. (1990). *Basin Analysis.* Blackwell, Oxford.

Aller, J., Bastida, F., Brime, C. and Pérez-Estaún, A. (1987). Cleavage and its relation with metamorphic grade in the Cantabrian Zone (Hercynian of NW Spain). *Sci. Geol. Bull.*, 40, p. 1-8.

Aller, J. and Brime, C. (1985). Deformacion y metamorphismo en la parte sur de la cuenca carbonifera central (NO. de España). *10th annual conference on carboniferous stratigraphy*, 1983, 1, Madrid.

Aller, J. and Gallastegui, J. (1995). Analysis of kilometric scale superposed folding in the Central Coal Basin (Cantabrian Zone, NW Spain). *Journal of Structural Geology*, 17, p. 961-969.

Aller, J., Luz-Valín, M., García-López, S., Brime, C. & Bastida, F. (2005). Superposition of tectono-thermal episodes in the southern Cantabrian Zone (foreland thrust and fold belt of the Iberian Variscides, NW Spain). *Bull. Soc. Géol. France* 176, p. 503-514.

Alonso, J.L. (1987). Sequences of thrusts and displacement transfer in the superposed duplexes of the Elsa Nappe region (Cantabrian Zone, NW Spain). *Journal of Structural Geology* 9(8), p. 969-983.

Alonso, J.I. and Brime, C. (1990). Mineralogy, geochemistry and origin of the underclays of the Central Coal Basin, Asturias, Spain. *Clays and Clay Minerals*, 38, p. 265-276.

Alonso, J.I., Pulgar, J.A., García-Ramos, J.C. and Barba, P. (1995). Tertiary basins and Alpine tectonics in the Cantabrian Mountains (NW Spain). In P.F. Friend and C.J. Dabrio, Eds. *Tertiary Basins of Spain,* p. 214-227. Cambridge University Press.

Alonso, J.I. and Suárez-Rodrígues, A. (1991). Tectónica. In L.R. Rodríguez-Fernández, Ed. *Memoria del mapa geologico de España*, Escala 1:50000, No. 103 (La Pola de Gordón), p. 79-88. ITGE, Madrid.

Alonso, J.L., Suarez, A., Rodriguez, F.L.R., Farias, P. and Villegas, F.J. (1990). *La Pola de Gordón*, 138 p. Instituto Tecnológico GeoMinero de España (ITGE), Madrid.

Alonso-Zarza, A.M., Armenteros, I., Braga, J.C., Muñoz, A., Pujalte, V., Ramos, E., Aguirre, J., Alonso-Gavilán, G., Arenas, C., Baceta, J.I., Carballeira, J., Calvo, J.P., Corrochano, A., Fornós, J.J., González, A., Lúzon, A., Martín, J.M., Pardo, G., Payros, A., Pérez, A., Pomar, L., Rodriguez, J.M. and Villena, J. (2002). Tertiary. In W. Gibbons and T. Moreno, Eds. *The Geology of Spain*, p. 291-334. The Geological Society, London, Bath.

Alvarez-Marrón, J. (1995). Three-dimensional geometry and interference of fault-bend folds: Examples from the Ponga Unit, Variscan Belt, NW Spain. Journal of Structural Geology, 17, p. 549-560.

Alvarez-Marrón, J., Pérez-Estaún, A., Aller, N. and Heredia, N. (1990). *Puebla de Lillo* (79). Instituto Tecnológico GeoMinero de España, Madrid.

Álvaro, J.J., Rouchy, J., Bechstädt, T., Boucot, A.J., Boyer, S., Debrenne, F., Moreno-Eiris, E., Perejón, A. and Vennin, E. (2000 a). Evaporitic constraints on the southward drifting of the western Gondwana margin during Early Cambrian times. *Palaeogeography, Palaeoclimatology, Palaeoecology*, 160, p. 105-122.

Álvaro, J.J., Vennin, E., Moreno-Eiris, E., Perejón, A. and Bechstädt, T. (2000 b). Sedimentary patterns across the Lower-Middle Cambrian transition in the Elsa nappe (Cantabrian Mountians, northern Spain). *Sedimentary Geology*, 137, p. 43-61.

*References*


Álvaro, M., Capote, M. and Vegas, R. (1979). Un modelo de evolución geotectónica para la Cadena Celtibérica. *Acta Geológica Hispanica*, 14, p. 172-177.

Amler, M.R.V. (2000). Paläobiographie von Iberia im Karbon. Progr. 70. Jahrestagung der Paläont. Ges. *Terra Nostra*, Coburg.

Anadón, P., Cabrera, L., Guimerà, J. and Statanach, P. (1985). Paleogene strike-slip deformation and sedimentation along the southeastern margin of the Ebro Basin. In K. Biddle and N. Christie-Blick, Eds. *Strike-slip deformation, basin formation and sedimentation*. Soc. Econ. Paleont. and Mineral, 37, p. 303-318.

Anderle, H.-J., Franke, W. and Schwab, M. (1995). Stratigraphy. In R.D. Dallmeyer, W. Franke and K. Weber, Eds. *Pre-Permian geology of central and eastern Europe.* Springer, p. 99-107.

Andeweg, B. (2002). *Cenozoic tectonic evolution of the Iberian Peninsula, causes and effects of changing stress fields*. Ph.D Thesis. Faculty of Earth and Life Sciences, p. 178. Vrije Universiteit, Amsterdam.

Andriessen, P.A.M. and Reuter, K.J. (1994). K-Ar and fission track mineral age determinations of igneous rocks related to multiple magmatic arc systems along the 23˚S latitude of Chile and NW Argentina. In K.J. Reuter, E. Scheuder and P.J. Wigges, Eds. *Tectonics of the southern central Andes*, p. 141-151. Springer Verlag,

Andriessen, P.A.M. and Zeck, H.P. (1996). Fission-track constraints on timing of Alpine nappe emplacement and rates of cooling and exhumation, Torrox area, Betic Cordilleras, S. Spain. *Chemical Geology*, 131, p. 199-206.

Aramburu, C. and Bastida, F. (1995). *Geología de Asturias*. 314 p, Gijón.

Arche, A. and López-Gómez, J. (1996). Origin of the Permian-Triassic Iberian Basin, central-eastern Spain. *Tectonophysics*, 266, p. 443-464.

Arche, A. and López-Gómez, J. (1999). Tectonic and geomorphic controls on the fluvial styles of the Eslida Formation, Middle Triassic, Eastern Spain. *Tectonophysics*, 315, p. 187-207.

Arenas, R., Gil-Ibarguchi, J.I., González-Lodeiro, F., Klein, E., Martíne-Catalán, J.R., Ortega-Girones, E., Pablo-Maciá, J.G.D. and Peinado, M. (1986). Tectonostratigraphic units in the complexes with mafic and related rocs of the NW of the Iberian Massif. *Hercynica*, 2, p. 87-110.

Arlegui Crespo, L.E. (1996). *Diaclasas, fallas y campo de esfuerzos en el sector central de la Cuenca del Ebro*. Departamiento de Ciencias de la Tierra, p. 308. Universidad de Zaragoza, Zaragoza.

Arne, D. and Zentilli, M. (1994). Apatite fission-track thermochronology integrated with vitrinite reflectance. In P.K. Mukhopadhyay and W.G. Dow, Eds. *Vitrinite reflectance as a Maturity Parameter*, 570, p. 249-268. Amer. Chem. Soc., Washington, D. C.

Aurell, M., Meléndez, G., Olóriz, F., Bádenas, B., Caracuel, J.E., García-Ramos, J.C., Goy, A., Linares, A., Quesada, S., Robles, S., Rodríguez-Tovar, F.J., Rosales, I., Sandoval, J., Suárez de Centi, C., Tavera, J.M. and Valenzuela, M.I. (2002). Jurassic. In W. Gibbons and T. Moreno, Eds. *The geology of Spain*, p. 213-254. The Geological Society, London.

Ayllón, F. (2003). *Mineral, Fluid and Thermal Evolution in Veins from Late Orogenic Coal Basins of the Cantabrian Zone (Variscan, NW Spain)*. Doctoral Thesis. Naturwissenschaftlich-Mathematischen Gesamtfakultät, p. 199. Ruprecht-Karls-Universität Heidelberg, Heidelberg.

Ayllón, F., Bakker, R.J. and Warr, L.N. (2003). Re-equilibration of fluid inclusions in diagenetic-anchizonal rocks of the Cinera-Matallana coal basin (NW Spain). *Geofluids*, 3(1), p. 49-68.

Azañón, J.M. and Crespo-Blanc, A. (2000). Exhumation during a continental collision inferred from the tectonometamorphic evolution of the Alpujarride Complex in the central Betics (Alboran Domain, SE Spain). *Tectonics*, 19(3), p. 549-565.

Baard, J.H., Zijp, W., L. and Nolthenius, H.J. (1989). *Nuclear Data Guide For Reactor metrology*. Kluwer Acad. Publ., Dordrecht.

Babero, L., Carter, A. and Hurford, A.J. (1998). Post-Variscan evolution of the Montes de Toledo area: a preliminary apatite fission track study. *Boletin de la Sociedad Espanola de Mineralogia*, 21, p. 42-43.

Babero, L., Glasmacher, U.A., Villaseca, C., López-García, J.A. and Martín-Romera, C. (2005). Lon-term thermo-tectonic evolution of the Montes de Toledo area (Central Hercynian Belt, Spain): constraints fro apatite fission-track analysis. *International Journal of Earth Sciences (Geologische Rundschau)*, 94, p. 193-203.

Bachtadse, V. and van der Voo, R. (1986). Palaeomagnetic evidence for crustal and thin-skinned rotations in the European Hercynides. *Geophys. Res. Lett.*, 13, p. 161-164.

Barbarand, J., Carter, A., Wood, I. and Hurford, T. (2003). Compositional and structural control of fission-track annealing in apatite. *Chemical Geology*, 198(1-2), p. 107-137.

Barbarand, J. and Pagel, M. (2001 a). Clontrôle de la cinétique de cicatrisation des traces de fission dans les cristaux d'apatite: le rôle de al composition chimique. *C. R. Acad. Sci. Paris*, 332, p. 259-265.

Barker, C.E. and Pawlewicz, M.J. (1994). Calculation of vitrinite reflectance from therma histories and peak temperatures. A comparison of methods. In G. Buntebarth and L. Stegena, Eds. *Palaeogeothermics*, p. 79-93. Springer, Berlin, Heidelberg, New York.

Bastida, F. (1980). Las estructuras de la primera fase herciniana de deformación en la rama N. de la Zona Asturoccidental-Leonesa (N.W. España. *Cuad. Lab. Xeol. Laxe*, 1, p. 173-176.

Bastida, F. and Aller, J. (1992). Rasgos geológicos generales. In C. Aramburu and F. Bastida, Eds. *Geología de Asturias*, p. 27-34.

Bastida, F., Brime, C., García-López, S. and Sarmiento, G.N. (1999). Tectono-thermal evolution in a region with thin-skinned tectonics; the western nappes in the Cantabrian Zone (Variscan Belt of NW Spain). *International Journal of Earth Sciences*, 88, p. 38-48.

Bastida, F., Marcos, A., Arboleya, M.L. and Mendez, I. (1976). La unidad de Peña Corada y su relacion con el manto del esia (Zona Cantabraica, NW de España). *Breviora geologcia Asturica*, 10, p. 49-55.

Bauluz, B., Mayayo, M.J., fernández-Nieto, C. and González-Lopéz, J.M. (2000). geochemistry of Precambrian and Paleozoic silisiclastic rocks from the Iberian Range (NE Spain): implications for source-area weathering, sorting, provenance and tectonic setting. *Chemical Geology*, 168, p. 135-150.

Beardsmore, G.R. and Cull, J.P. (2001). *Crustal heat flow: A guide to measurement and modelling*. 324 p. Cambridge University Press, Cambridge.

Bechstädt, T. and Boni, M. (1989). Tectonic control on the formation of a carbonate platform: the Cambrian of southwestern Sardinia. *Soc. Econ. Paleontol. Mineral. Spec. Publ.*, 44, p. 107-122.

Bechstädt, T., Schledding, T. and Selg, M. (1988). Rise and fall of an isolated, unstable carbonate platform: the Cambrian of southwestern Sardinia. *Geol. Rund.*, 77, p. 389-416.

Beestma, J.J. (1995). *The late Proterozoic/Paleozoic and Hercynian crustal evolution of the Iberian Massif, N Portugal: as traced by geochemistry and Sr-Nd-Pb Isotope systematics of pre-Hercynian terrigenous sediments and Hercynian granitoids*. Vrije Universiteit, Amsterdam.

Bellido-Mulas, F., Gonzalez, L.F., Klein, E., Martinez, C.J.R. and Pablo, M.J.G. (1987). Las rocas graniticas hercinicas del norte de Galicia y occidente de Asturias. Memorias del Insituto Geológico y Minero de España, IGME, Madrid, Spain, 101.

Ben Ghouma, N. (1995). *Etude de l'influence de al composition de l'apatite sur al révélation et le recuit des trace de fission de l'uranium*, p. 257. France Comté University, Besançon, France.

*References*


Bergman, S.C. and Corrigan, J. (1996). Compositional variation of natural apatites subjected to fission track analysis. *International Workshop on Fission-Track dating Abstracts*, p. 7, Gent, Belgium.

Bernet, M., Zattin, M., Garver, J.L., Brandon, M.T. and Vance, J.A. (2001). Steady-state exhumation of the European Alps. *Geology*, 21(1), p. 35-38.

Bhandari, N., Bhat, S.G., Lal, D., Rajagopalan, G., Tamhane, A.S.J. and Venkatavaradan, V. (1971). Fission fragment tracks in apatite: recordable track lenghts. *Earth and Planetary Science Letters*, 3, p. 434-438.

Biermann, C. (1995). The Betic Cordilleras (SE Spain). Anatomy of a dualistic collision type orogenic belt. *Geologie en Mijnbouw*, 41, p. 167-182.

Bigazzi, G. (1981). The problem of the decay constant $\lambda_f$ or $^{238}U$. *Nuclear Tracks*, 5, p. 35-44.

Bjørlykke, K. (1994). Fluid-flow processes and diagenesis in sedimentary basins. *Geofluids: Origin, Migration and Evolution of Fluids in Sedimentary Basins*, 78, p. 127-140.

Blakey, R. (2004). Plate Tectonics and Continental Drift: Regional Paleogeographic Veiws of Earth History, *http://jan.ucc.nau.edu/~rcb7/nat.html*.

Blanco, M.J. and Spakman, W. (1993). The P-wave velocity structure of the mantle below the Iberian Peninsula: evidence for subducted lithosphere below southern Spain. *Tectonophysics*, 221, p. 13-34.

Boillot, G. and Malod, J. (1988). The north and north-west Spanish continental margin: a review. *Rev. Soc. Geol. España*, 1, p. 295-316.

Boillot, G., Dupeuble, P.A. & Malod, J. (1979). Subduction and tectonics on the continental margin off northern Spain. *Marine Geology* 32, p. 53-70.

Bois, C. (1993). Initiation and evolution of the Oligo-Miocene rift basins of southwestern Europe: contribution of deep seismic profiling. *Tectonophysics*, 226, p. 227-252.

Bonhommet, N., Cobbold, P.R. and Perroud, H. (1981). Paleomagnetism and cross-folding in a key area of the Asturian arc (Spain). *Journal of Geophysical Research*, 86(B3), p. 1873-1887.

Bouch, J.E., Hole, M.J., Trewin, N.H., Chenery, S. and Morton, A.C. (2002). Authigenic apatite in a fluvial sandstone sequence; evidence for rare-earth element mobility during diagenesis and a tool for diagenetic correlation. *Journal of Sedimentary Research*, 72(1), p. 59-67.

Bouyx, E. (1970). *Contribution a l'étude des formations Anteordoviciennes de al Meseta Méridionale (Ciudad Real t Badajoz)*. IGME, Madrid.

Brandon, M.T. (2002). Decomposition of mixed grain-age distributions unsing BINOMFIT. *On Track*, 24, p. 13-18.

Braun, J. (2002). Quantifying the effect of recent relief changes on age-elevation relationships. Earth and Planetary Science Letters, 200, p. 331-343.

Braun, J., van der Beek, P., Batt, G. (2006). *Quantitative Thermochronology: Numerical Methods for the Interpretation of Thermochronological Data*. Cambridge University Press.

Briggs, N.D., Naeser, C.W. and McCulloh, T.H. (1981). Thermal history of sedimentary basins by fission-track dating. *Nuclear Tracks*, 5, p. 235-237.

Brime, C. (1981). Postdepositional transformation of clays in Palaeozoic rocks of Nothwest Spain. *Clay Minerals*, 16, p. 421-424.

Brime, C. (1985). A diagenesis to metamorphism transition in the Hercynian of NW Spain. *Mineralogical Magazine*, 49(352), p. 481-484.

Brime, C., García-López, S., Bastida, F., Valín, M.L., Sanz-López, J. and Aller, J. (2001). Transition from diagenesis to metamorphism near the front of the Variscan regional metamorphism (Cantabrian Zone, north-western Spain). *Journal of Geology*, 109, p. 363-379.

Brime, C. and Pérez-Estaún, A. (1980). A Diagenesis-metamorphism transition in the Cabo Peñas region. *Cuadernos do Laboratorio Xeoloxico de Laxe*, 1, p. 85-97.

Burtner, R.L., Nigrini, A. and Donelick, R.A. (1994). Thermochronology of lower Cretaceous source rocks in the Idaho – Wyoming thrust belt. *American Association of Petroleum Geologists Bulletin*, 78, p. 1613-1636.

Butler, R. (1999) How the Mediterranean dried up. *Mercian Geologist*, 15, p. 63-64.

Capdevila, R. (1967). Extensión du metamorphisme regional hercynienne dans le Nord-Ouest de l'Espagne (Galice orientale, Asturies, León). C. R. Somm. *Soc. Géol. France fasc.*, 7, p. 277-278.

Capdevila, R. (1969). *Le métamorphisme régional progresif et les granites dans le segment hercynien de Galice nord-oriental (NW de l'Espagne)*. Scientific and Technical University, Montpellier.

Capdevila, R. and Vialette, Y. (1965). Premières mesures d'âge absolu effectuées par la méthode au strontium sur des granites et micaschistes de la province de Lugo (Nord-Ouest de l'Espagne). *C. R. Acad. Sci. Paris*, 270, p. 2527-2530.

Capote, R., Anton-Muñoz, J., Simón, J.L., Liesa, C.L. and Arlegui, L.E. (2002). Alpine tectonics I: the Alpine system north of the Betic Cordillera. *The Geology of Spain*, p. 367-400. The Geological Society, London.

Carls, P. (1988). The Devonian of Celtiberia (Spain) and Devonian paleogeography of SW Europe. In N.J. McMillan, A.F. Embry and D.J. Glan, Eds. *Devonian of the world; proceedings of the Second international symposium on the Devonian System; Volume I, Regional syntheses*., 1, p. 421-466.

Carlson, W.D. (1990). Mechanisms and kinetics of apatite fission track annealing. *American Mineralogist*, 75, p. 1120-1139.

Carlson, W.D., Donelick, R.A. and Ketcham, R.A. (1999). Variability of apatite fission-track annealing kinetics: I. Experimental results. *American Mineralogist*, 84, p. 1213-1223.

Carpéna, J. (1985). Tectonic interpretation of an inverse gradient of zircon fission-track ages with respect to altitude: alpine thermal history of the Gran Paradiso basement. *Contrib. Mineral. Petrol.*, 90, p. 74-82.

Carpéna, J. (1998). Uranium-235 fission track annealing in minerals of the apatite group: an experimental study. In P. Van den haute and F. De Corte, Eds. *Advances in Fission-Track Geochronology*, p. 81-92. Kluwer Academic Publishers, Dordrecht.

Carrapa, B. (2002). Tectonic evolution of an active orogen as reflected by its sedimentary record: *An integrated study of the Tertiary Piedmont Basin (Internal Western Alps, NW Italy)*, p. 177. Vrije Universiteit Amsterdam, Amsterdam, The Netherlands.

Carry, S. (1955). The orocline concept in geotectonics. *Royal Society of Tasmania Proceedings*, 89, p. 255-288.

Čermak, V. and Rybach, L. (1979). *Terrestrial heat flow in Europe*. 328 p. Springer-Verlag, New York.

Clauzon, G., Suc, J.P., Gautier, F., Breger, A. and Loutre, M.-F. (1996). Alternate interpretation of the Messinian salinity crisis: Controversy resolved? *Geology*, 24(4), p. 363-366.

Clift, P.D., Carter, A. and Hurford, A.J. (1998). 4. Apatite Fission Track Analysis of sites 959 and 960 on the Transform Continental Margin of Ghana, West Africa. In J. Mascle, G.P. Lohmann and M. M, Eds. *Proceedings of the Ocean Drilling Progarm, Scientific Results*, 159, p. 35-41.

Cloetingh, S. and Burov, E.B. (1996). Thermomechanical structure of European continental lithosphere: con straints from rheological profiles and ETT estimates. *Geophys. J. Int*., 124, p. 695-723.

Colmenero, J.R. and Prado, J.G. (1993). Coal basins in the Cantabrian Mountains, north-western Spain. *International Journal of Coal Geology*, 23, p. 215-229.

Comte, P. (1959). Recherches sur les terrains anciens de al Corillère Cantabrique. *Mem. Inst. Geol. Min. España*, 60, p. 440.

*References*


Corretgé, L.G. (1969). El complejo ortoneístico de Pola de Allande (Asturias). *Bol. Inst. Min*, LXXX(4), p. 289-306.

Corretgé, L.G. and Caprio, V. (1968). Los ortoneises básicos de Pola de Allande (Asturias). *Brev. Geol. Asturias*, 12(1), p. 14-16.

Corretgé, L.G. and Suárez, O. (1990). Igneous rocks. Cambrian and Palentian Zones. In R.D. Dallmeyer and E. Martínez-García, Eds. *Pre-Mesozoic Geology of Iberia*, p. 72-79. Springer-Verlag, Berlin.

Corrigan, J. (1993). Apatite fission-track analysis of Oligocene strata in South Texas, U.S.A.: Testing annealing models. *Chemical Geology*, 104, p. 227-249.

Cortes Gracia, A.l. and Casas Sainz, A.M. (1997). Fosas neogenas asociadas a reactivacion de pliegues en el borde sur de la Sierra de Cantabria (Alava-Navarra). *Geogaceta*, 21, p. 81-84.

Crespo, J.L., Moro, M.C., Fadón, O., Cabrera, R. and Fernández, A. (2000). The Salamón gold deposit (León, Spain). *Journal of Geochemical Exploration*, 71, p. 191-208.

Crowley, K.D., Cameron, M. and Schaefer, R.L. (1991). Experimental studies of annealing of etched fission tracks in fluroapatite. *Geochim. Cosmochim. Acta*, 55, p. 1449-1465.

Crowley, Q.G., Floyd, P.A., Winchester, J.A., Franke, W. and Holland, J.G. (2000). Early Palaeozoic rift-related magmatism in Variscan Europe: fragmentation of the Armorican Terrane Assemblage. *Terra Nova*, 12, p. 171-180.

Dahl, P.S. (1997). A crystal-chemical basis for Pb retention and fission-track annealing systematics in U-bearing mineral, with implications for geochronology. *Earth and Planetary Science Letters*, 150(3-4), p. 277-290.

Dallmeyer, R.D. and Gil-Ibarguchi, J.I. (1990). Age of amphibolitic metamorphism in the ophiolitic unit of the Morais allochthon (Portugal): implications for early Hercynian orogenesis in the Iberian Massif. *Journal of the Geological Society of London*, 147, p. 873-878.

Dallmeyer, R.D., Martínez-Catalán, J., Arenas, R., Gil-Ibarguchi, J.I., Gutiérrez-Alonso, G., Farias, P., Bastida, F. and Aller, J. (1997). Diachronous Variscan tec tonothermal activity in the NW Iberian Massif: evidence from 40Ar/39Ar dating of regional fabrics. *Tectonophysics*, 277, p. 307-337.

de Bruijne, C.H. (2001). *Denudation, intraplate tectonics and far field effects; an integrated apatite fission track study in central Spain*. Ph.D thesis, Faculteit der Aardwetenschappen, p. 164. Vrije Universiteit, Amsterdam.

de Bruijne, C.H. and Andriessen, P.A.M. (2002). Far field effects of Alpine plate tectonics in the Iberian microplate recorded by fault related denudation in the Spanish Central System (Central Spain). *Tectonophysics*, 349, p. 161-184.

de Jong, K. (1990). Alpine tectonics and rotation pole evolution of Iberia. *Tectonophysics*, 184, p. 279-296.

de Sitter, L.U. (1962). The structure of the southern slope of the Cantabrian Mountains. *Leidse Geologische Mededelingen*, 26, p. 255-264.

Dercourt, J., Zonenshain, L.P., Ricou, L.E., Kazmin, V.G., Le, P.X., Knipper, A.L., Grandjacquet, C., Sborshchikov, I.M., Boulin, J., Sorokhtin, O., Geyssant, J., Lepvrier, C., Biju, D.B., Sibuet, J.C., Savostin, L.A., Westphal, M. and Lauer, J.P. (1985). Presentation de 9 cartes paleogeographiques au 1/ 20000000000eme s'etendant de l'Atlantique au Pamir pour la periode du Lias a l'Actuel. In Anonymous, Ed. *Paleobiogeographie de la Tethys*, 1; 5, p. 636-652.

Dewey, J.F., Helman, M.L., Turco, E., Hutton, D.H.W. and Knot, S.D. (1989). Kinematics of the western Mediterranean. In M.P. Coward, D. Dietrich and R.G. Park, Eds. *Conference on Alpine tectonics.*, 45, p. 265-283.

Dewey, J.F., Pitman, W.C., III, Ryan, W.B.F. and Bonnin, J. (1973). Plate tectonics and the evolution of the Alpine system. *Geological Society of America Bulletin*, 84(10), p. 3137-3180.

Díaz-García, F. 2006. Geometry and regional significance of Neoproterozoic (Cadomian) structures of the Narcea Antiform, NW Spain. Journal of the Geological Society of London 163, p. 499-508.

Dierendonk, Kriest, J. and Savage, J.F. (1984). On the final emplacement of thrust sheets in the Cantabrian zone. In J.G.M. Raven and B.A. van der Pluijm, Metamorphic fluids and transtension in the Cantabrian Mountains of northern Spain: an application of the conocont colour alteration index. *Geological Magazine*, 123(6), pp. 675.

Dietrich, B. (2005). Numerical modeling as a means to enhance genetic sedimentary basin interpretation: a case study of the southern Cantabrian Basin (NW Spain). *GAEA Heidelbergensis*, 14, 263 p.

Díez-Balda, M.A., Vegas, R. and González-Lodeiro, F. (1990). Central-Iberian Zone. Autochtonous sequences. Structure. In R.D. Dallmeyer and E. Martínez-García, Eds. *Pre-Mesozoic Geology of Iberia*, p. 172-188. Springer-Verlag, Berlin.

Doblas, M., López-Ruiz, J., Oyarzun, R., Mahecha, V., Sanchez-Moya, Y., Hoyos, M., Cebria, J.M., Capote, R., Hernandez-Enrile, J.L., Lillo, J., Lunar, A., Ramos, A. and Sopena, A. (1994 a). Extensional tectonics in the central Iberian Peninsula during the Variscan to Alpine transition. *Tectonophysics*, 238, p. 95-116.

Doblas, M., Oyarzun, R., Sopena, A., Lopez, R.J., Capote, R., Hernandez, E.J.L., Hoyos, M., Lunar, R. and Sanchez, M.Y. (1994). Variscan-late Variscan-early Alpine progressive extensional collapse of central Spain. *Geodinamica Acta*, 7(1), p. 1-14.

Donelick, R.A. (1991). Crystallographic orientation dependence of a mean etchable fission track length in apaptite: An empirical model and experimental observations. *American Mineralogist*, 76, p. 83-91.

Donelick, R.A. (1993). Apatite etching characteristics versus chemical composition. *Nuclear Tracks and Radiation Measurements*, 21, p. 604.

Donelick, R.A. (1995). *A method of fission-track analysis utilizing bulk chemical etching of apatite*. Australian Patent Number 658,800.

Donelick, R.A. (1997). Fact and Fiction Regarding Apatite Fission-Track Annealing Kinetics. *On Track*, 1(14), p. 17-20.

Donelick, R.A., Roden, M.K., Moores, J.D., Carpenter, B.S. and Miller, D.S. (1990). A Etchable length reduction of induced fission tracks in apatite at room temperature: crystallographic orientation effects and 'initial' mean lengths. *Nuclear Tracks and Radiation Measurements*, 17, p. 261-265.

Donelick, R.A., Ketcham, R.A. and Carlson, W.D. (1999). Variability of apatite fission-track annealing kinetics II: Crystallographic orientation effects. *American Mineralogist*, 84, p. 1224-1234.

Dreyer, W. (1974). *Properties of Anisotropic Solid-State Materials: Thermal and Electric Properties*. 295 p. Springer, Wien.

Duddy, I.R., Green, P.F. and Laslett, G.M. (1988). Thermal annealing of fission tracks in apatite, 3. Variable temerature behaviour. *Chemical Geology (Isotope Geoscience Section)*, 73, p. 25-38.

Duddy, I.R., Green, P.F., Bray, R.J. and Hegarty, K.A. (1994). Recognition of the thermal effects of fluid flow in sedimentary basins. In J. Parnell, Ed. *Geofluids: Origin, Migration and Evolution of Fluids in Sedimentary Basins*, 78, p. 325-345.

Duggen, S., Hoernle, K., van den Bogaard, P., Rüpke, L. and Morgan, J.P. (2003). Deep roots of the Messinian salinity crisis. *Nature*, 422, p. 602-606.

Dunkl, I. (2002). TRACKKEY; a windows program for processing fission track data. In S. Martin and R. Polino, Eds. *Fission track analysis; theory and applications.*, 51; 2, p. 453.

Elliott, J.C. (1994). *Structure and chemistry of the apatites and other calcium orthophosphates.* 389 p. Elsevier, Amsterdam.

*References*


Emmerich, A. (2004). *Controlling factors of two Middle Triassic carbonate platforms: Latemar and Rosengarten (Dolomites, Northern Italy)*. Doctoral thesis, Fakultät für Chemie und Geowissenschaften. Universität Heidelberg, Heidelberg, Germany.

Emmerich, A., Glasmacher, U.A., Bauer, F., Bechstädt, T. and Zühlke, R. (2005). Meso-Cenozoic basin and carbonate platform development in the SW-Dolomites unraveled by basin modeling and apatite FT analysis: Rosengarten and Latemar (Northern Italy). *Sedimentary Geology*, 175, p. 415-438.

Espina, R.G., De Vicente, G. and Muñoz-Martin, A. (1996 ). Analisis poblacional de fallas alpinas en el border occidental de la Cuenca Vasco-Cantábria (Cordillera Cantábrica, NO de España). *Geogaceta*, 20, p. 936-938.

Evers, H.J. (1967). Geology of the Leonides between the Bernesga and Porma rivers, Cantabrian mountains (NW Spain). *Geologie en Mijnbouw*, 46(12), 483 p.

Farber, A. and Jaritz, W. (1964). Die Geologie des westasturischen Küstengebietes zuischen San Esteban de Pravia un Ribadeo (N. W. Spanien). *Geol. Jb.*, 81, p. 679-738.

Fernàndez, M., Foucher, J.P. and Jurado, M.J. (1995). Evidence for the multi-stage formation of the south-western Valencia Trough. *Marine and Petroleum Geology*, 12, p. 101-109.

Fernández-Suárez, J., Gutiérrez-Alonso, G., Jenner, G.A. and Jackson, S.E. (1998). Geochronology and geochemistry of the Pola de Allande granitoids (northern Spain); their bearing on the Cadomian-Avalonian evolution of Northwest Iberia. *Canadian Journal of Earth Sciences-Journal Canadien des Sciences de la Terre*, 35(12), p. 1439-1453.

Fernández-Suárez, J., Gutiérrez-Alonso, G., Jenner, G.A. and Tubrett, M.N. (2000 a). New ideas on the Proterozioc-Early Paleozoic evolution of NW Iberia: in sights from U-Pb detrital zircon ages. *Precambrian Research*, 102, p. 185-206.

Fernández-Suárez, J., Dunning, G.R., Jenner, G.A. and Gutierrez-Alonso, G. (2000 b). Variscan collisional magmatism and deformation in NW Iberia; constraints from U-Pb geochronology of granitoids. *Journal of the Geological Society of London*, 157 Part 3, p. 565-576.

Fernández-Suárez, J., Gutiérrez-Alonso, G. and Jeffries, T.E. (2002 a). The Importance of along-margin terane transport in northern Gondwana: Insights from detrital zircon parentage in Neoproterozoic rocks from Iberia and Britany. *Earth and Planetary Science Letters*, 204, p. 75-88.

Fernández-Suárez, J., Gutiérrez-Alonso, G., Cox, R. and Jenner, G.A. (2002 b). Assembly of the Armorica Microplate: a strike-skip terrane delivery? Evidence from U-Pb Ages of detrital Zircons. *Journal of Geology*, 110(5), p. 619-626.

Fernández-Viejo, G., Gallart, J., Pulgar, J.A., Córdoba, D. and Dañobeitia, J.J. (2000). Seismic signature of Variscan and Alpine tectonics in NW Iberia: Crustal structure of the Cantabrian Mountains and the Duero basin. *Journal of Geophysical Research*, 104(B2), p. 3001-3018.

Fitzgerald, P.G., Munoz, J.A., Coney, P.J. and Baldwin, S.L. (1999). Asymetric exhumation across the Pyrenean orogen: implications for the tectonic evolution of a collisional orogen. *Earth and Planetary Science Letters*, 173, p. 157-170.

Fleischer, R.L. and Price, P.B. (1964). Fossil records of nuclear fission. *New Scientist*, 21, 406-408.

Fleischer, R.L., Price, P.B. and Walker, R.M. (1975). Nuclear tracks in solids; principles and applications, University of California Press, Berkeley.

Floquet, M. (1991). La pate-forme nord-castillane au Crétacé supérieur (Espagne). Arrière-pays ibérique de la marge passive basco-cantabrique. Sédimentation et Vie. *Memoires Géologiques de la Université de Dijon*, 14.

Franke, W. (1992). Tectonic evolution of Europe; Phanerozoic structures and events in Central Europe. In D. Blundell, R. Freeman and S. Mueller, Eds. A continent revealed; the European *Geotraverse*. Cambridge University Press.

Franke, W. and Engel, W. (1986). Synorogenic sedimentation in the Variscan belt of Europe. *Bull. Soc. Géol. France*, 1, p. 25-33.

Franke, W., Dallmeyer, R.D. and Weber, K. (1995). Geodynamic evolution. In R.D. Dallmeyer, W. Franke and K. Weber, Eds. *Pre-Permian geology of central and eastern Europe*, p. 579-593. Springer.

Frings, K., Lutz, R., de Wall, H. and Warr, L.N. (2004). Coalification history of the Stephanian Cinera-Matallana pull-apart basin, NW Spain; combining anisotropy of vitrinite reflectance and thermal modelling. *International Journal of Earth Sciences*, 93(1), p. 92-106.

Frings, K.H. (2002). *Paläotemperatur-Anomalien in spät-Variskischen Kohlebecken am Beispiel des Ciñera-Matallana Beckens, Kantabrisches Gebirge, NW Spanien.* Doctoral Thesis. Naturwissenschaftlich-Mathematischen Gesamtfakultät, p. 128. Ruprecht-Karls-Universität Heidelberg, Heidelberg.

Fügenschuh, B., Froitzheim, N., Capdevila, R. & Boillot, G. (2003). Offshore granulites from the Bay of Biscay margins: fission tracks contrain a Proterozoic to Tertiary thermal history. *Terra Nova,* 15, p. 337-342.

Galán, G., Aparicio, A. and Villegas, F.J. (1978). El metamorfismo de muy bajo grado (Anquimetamorfismo) de la Cuenca Carbonífera Ciñera-Matallana, León. *Estudios Geológicos*, 34, p. 505-510.

Galán, G., Pin, C. and Duthon, J. (1996). Sr-Nd isotopic record of multi-stage interactions between mantle-derived magmas and crustal components in a collision context – the ultramafic- granitoids association from Vivero (Herccynian belt, NW Spain). *Chemical Geology*, 131, p. 67-91.

Galán, G. and Suárez, O. (1989). Cortlanditic enclaves associated with calc-alkaline granites from Tapia-Asturias (Hercynian Belt, northwestern Spain). *Lithos*, 23(4), p. 233-245.

Galbraith, R.F. (1981). On statistical models for fission track counts. *Journal of the International Association for Mathematical Geology*, 13(6), p. 471-478.

Galbraith, R.F. (1982). Statistical Analysis of some fission-track counts and neutron-fluence measurements. *Nuclear Tracks and Radiation Measurements*, 11, p. 201-203.

Galbraith, R.F. (1990). The radial plot; graphical assessment of spread in ages. In S.A. Durrani and E.V. Benton, Eds. *Proceedings of the 6th international fission track dating workshop*, 17; 3, p. 207-214.

Galbraith, R.F. and Laslett, G.M. (1993). Statistical Models for mixed fission track ages. *Nuclear Tracks and Radiation Measurements*, 21, p. 459-470.

Galindo-Zaldívar, J., González-Lodeiro, F. and Jabaloy, A. (1993). Stress and palaeostress in the Betic-Rif cordilleras (Miocene to present). *Tectonophysics*, 227, 105-126.

Gallagher, K. and Brown, R. (1997). The onshore record of passive margin evolution. *Journal of the Geological Society*, 154(3), p. 451-457.

Gallagher, K., Sambridge, M. and Drijkoningen, G. (1991). Genetic algorithms: An evolution from Monte Carlo methods from strongly non-linear geophysical optimisation problems. *J. Geophys. Res.*, 18, p. 2177-2180.

Gallastegui, G. (1991 a). Rocas Igneas. In L.R. Rodriguez-Fernández, Ed. *Memoria del mapa geológico de España, Escala 1:50000, No. 102 (Los Barrios de Luna)*, p. 90-96. ITGE, Madrid.

Gallastegui, G. (1991 b). Rocas Igneas. In: L. R. Rodriguez-Fernández, Ed. *Memoria del mapa geológico de España, Escala 1:50000, No. 103 (La Pola de Gordón),* p. 89-103. 2 (MAGNA). ITGE, Madrid.

Gallastegui, G., Heredia, N., Rodríguez-Fernández, L.R. and Cuesta, A. (1990). El stock de Peña Prieta en el contexto del magmatismo de la Unidad del Pisuerga-Carrión (Zona Cantábrica, N de España). *Cuad. Lab. Xeol. Laxe*, 15, p. 203-217.

Gallástegui-Suárez, G. (1990). Rocas Igneas. In A. Pérez-Estaún and J. Alvarez-Marrón, Eds. *Memoria del mapa geológico de España, Escala 1:50000, No. 102 (La Pola de Gordón)*, p. 45. ITGE, Madrid.

Galliker, D., Hugentobler, E. and Hahn, B. (1970). Spontane Kernspaltung von $^{238}U$ und Am,. *Helv. Phys. Acata*, 43, p. 593-606.

García-López, S., Bastida, F., Brime, C., Aller, J., Valín, M.L., Sanz-López, J., Mendez, C.A. and Méndez.-Álvarez, J.R. (1999). Metamorphic episodes in the Cantabrian Zone and their structural context. *Trabajos de Geología*, 21, p. 177-187.

García-López, S., Brime, C., Bastida, F. and Sarmiento, G.N. (1997). Simultaneous use of thermal indicators to analyse the transition from diagenesis to metamorphism: an example from the Variscan Belt of north-west Spain. *Geological Magazine*, 134, p. 323-334.

García-Mondejar, J. (1988). Plate reconstruction of the Bay of Biscay. *Geology*, 24, p. 635-638.

García-Royo, C. and Arche, A. (1987). El Triásico de la región Nuévalos-Cubel (Zaragoza). Sedimentación en un sector del bordre de la cuenca del surco Molina-Valencia. *Cuadernos de Geología Ibérica*, 5, p. 575-605.

Gasparrini, M. (2003). *Large-scale hydorthermal dolomitisation in the southwestern Cantabrian Zone (NW Spain): causes and controls of the process and origin of the dolomitising fluids.* Doctoral Thesis. Naturwissenschaftlich-Mathematischen Gesamtfakultät, p. 203. Ruprecht-Karls-Universität Heidelberg, Heidelberg.

Gasparrini, M., Bakker, R., Bechstädt, T. and Boni, M. (2002). Massive hydrothermal dolomitization in the Cantabrian Zone (NW Spain): a Permian to Triassic event promoted by extensional tectonics? In F. Roure and R. Swennen, Eds. *AAPG-IFP Hedberg Conference*, p. s18, Palermo.

Gasparrini, M., Bechstädt, T. and Boni, M. (2001). Large scale hydrothermal dolomitization in the Southern Cantabrian Zone (NW Spain). In R. Cidu, Ed. *Water-Rock Interaction 2001*, 1, p. 165-168. Swets & Zeitlinger Publishers.

Gasparrini, M., Bechstädt, T. & Boni, M. (*in press*). Massive Hydrothermal Dolomites in the Southwestern Cantabrian Zone (Spain) and its relation to the Late Variscan Evolution. *Marine and Petroleum Geology*.

Giger, M. and Hurford, A.J. (1989). Tertiary intrusives of the Central Alps: their Tertiary uplift, erosion, redeposition and burial in the south-alpine foreland. *Eclogae Geol. Helv.*, 82/3, p. 857-866.

Gil-Ibarguchi, J.I. and Arenas, R. (1990). Metamorphic evolution of the Allocthonous Complexes from the northwest of the Iberian Peninsula. In R.D. Dallmeyer and E. Martínez-García, Eds. *Pre-Mesozoic Geology of Iberia*, p. 237-246. Springer-Verlag, Berlin.

Gleadow, A.J.W. (1981). Fission track dating methods: What are the real alternatives? *Nuclear Tracks and Radiation Measurements*, 3, p. 3-14.

Gleadow, A.J.W. and Duddy, I.R. (1981). A natural long-term track annealing experiment forapatite. *Nuclear Tracks*, 5, p. 169-174.

Gleadow, A.J.W., Duddy, I.R., Green, P.F. and Lovering, J.F. (1986). Confined fission track lengths in apatite: a diagnostic tool for thermalhistory analysis. *Contributions to Mineralogy and Petrology*, 94, p. 405-415.

Golonka, J., Ross, M.I. and Scotese, C.R. (1994). Phanerozoic paleogeographic and paleoclimatic modeling maps. In A. F. Embry, B. Beauchamp and D. J. Glass Eds., *PANGEA: Global Environments and Resources, Can. Soc. Petrol. Geol., Memoir 17*, p. 1-48.

Gómez-Fernández, F., Both, R.A., Mangas, J. and Arribas, A. (2000). Metallogenensis of Zn-Pb Carbonate-Hosted mineralisation in the south-eastern region of the Picos de Europa (Central Northern Spain) province: geologic, fluid inclusion and stable isotope studies. *Economic Geology*, 95, p. 19-40.

González-Casado, J.M., Caballero, J.M., Casquet, C., Galindo, G. and Tornos, F. (1996). palaeostress and geotectonic interpretation of the Alpine cycle onset in the Sierra de Guadarrama (eastern iberia-Central System) based on evidence from epysyenites. *Tectonophysics*, 262, p. 213-219.

Gradstein, F.M., Ogg, J.G., Smith, A.G., Agterberg, F.P., Bleeker, W., Cooper, R.A., Davydov, V., Gibbard, P., Hinnov, L., House, M.R., Lourens, L., Luterbacher, H.-P., McArthur, J., Melchin, M.J., Robb, L.J., Shergold, J., Villeneuve, M., Wardlaw, B.R., Ali, J., Brinkhuis, H., Hilgen, F.J., Hooker, J., Howarth, R.J., Knoll, A.H., Laskar, J., Monechi, S., Powell, J., Plumb, K.A., Raffi, I., Röhl, U., Sanfilippo, A., Schmitz, B., Shackleton, N.J., Shields, G.A., Strauss, H., Van Dam, J., Veizer, J., van Kolfschoten, T. and Wilson, D. (2004). *A Geologic Time Scale 2004*. 500 p. Cambridge University Press.

Green, P.F. (1981 a). A new look at statistics in the fission track dating. *Nuclear Tracks*, 5, p. 77-86.

Green, P.F. (1981 b). 'Track-in-Track' length measurements in annealed apatites. *Nuclear Tracks*, 5, p. 121-128.

Green, P.F. (1988). The relationship between track shortening and fission track age reduction in apatite: combined influences of inherent instability, annealing anisotropy, length bias and system calibration. *Earth and Planetary Science Letters*, 89, p. 335-352.

Green, P.F., Duddy, I.R., Gleadow, A.J.W. and Lovering, J.F. (1989 a). Apatite fission track analysis as a palaeotemperature indicator for Hydrocarbon Exploration. In N.D. Naeser and T. McCulloh, Eds. *Thermal History of Sedimentary Basins - Mehtods and Case Histories*, p. 181-195. Springer-Verlag, New York.

Green, P.F., Duddy, I.R., Gleadow, A.J.W., Tingate, P.R. and Laslett, G.M. (1986). Thermal annealing of fission tracks in apatite. 4. Quantitative modelling techniques and extension to geological timescales. *Chemical Geology (Isotope Geoscience Section)*, 79, p. 155-182.

Green, P.F., Duddy, I.R., Laslett, G.M., Hegarty, K.A., Gleadow, A.J.W. and Lovering, J.F. (1989 b). Thermal annealing of fission tracks in apatite: 4. Quantitative modelling techniques and extension to geological timescales. *Chemical Geology (Isotope Geoscience Section)*, 79, p. 155-182.

Grimaud, S., Boillot, G., Collette, B.J., Mauffret, A., Miles, P.R. and Roberts, D.B. (1982). Western Extension of the Iberian-European plate boundary during the Early Cenozoic (Pyrenean) convergence: a new model. *Marine Geology*, 45, p. 63-77.

Grimmer, J.O.W. (2000). *Fluidassozierte Brekzien als Monitor dolomitisierender und dedolomitisierender Lösungströme in der Kantabrischen Zone (Nordspanien)*. Doctoral Thesis. Naturwissenschaftlich-Mathematischen Gesamtfakultät, Ruprecht-Karls-Universität, Heidelberg 148 p.

Guimerà, J. (1984). Paleogene evolution of deformation in the north-eastern Iberian Peninsula. *Geol. Mag.*, 121, p. 413-420.

Guimerà, J. and Alvaro, M. (1990). Structure et évolutoin de la compression alpine dans al Chaîne Ibérique et al Chaîne côtière catalane (Espagne). *Bull. Soc. Géol. France*, 6(2), p. 339-348.

Gutiérrez Marco, J.C., Robardet, M., Rábano, I., Sarmiento, G.N., San José-Lancha, M.A. and Herranz-Araújo, P. (2002). Ordovician. In W. Gibbons and T. Moreno, Eds. *The Geology of Spain*, p. 31-49. Geological Society, London.

Gutiérrez-Alonso, G. (1996). Strain partitioning in the footwall of the Somiedo Nappe: structural evolution of the Narcea Tectonic Window, NW Spain. *Journal of Structural Geology*, 18(10), p. 1217-1229.

Gutiérrez-Alonso, G. and Nieto, F. (1995). Variaciones de la "cristalinidad" de la mica blanca y otros parametros cristaloquimicos a traves del antiforme del Narcea (orogeno Varisco del NO de Iberia). *Studia Geologica Salmanticensia*, 31, p. 63-86.

*References*


Gutiérrez-Alonso, G., Fernández-Suárez, J., Jeffries, T.E., Jenner, G.A., Turbrett, M.N., Cox, R. and Jackson, S.E. (2003). Terrane accretion and dispersal in the northern Gondwana margin. An Early Paleozoic analogue to a long-lived active margin. *Tectonophysics*, 365, p. 221-232.

Gutiérrez-Alonso, G., Fernández-Suárez, J. and Weil, A.B. (2004 a). *Orocline triggered lithospheric delamination. GSA Special Paper 383*, p. 121-131. Geological Society of America.

Gutiérrez-Alonso, G., Blanco, J.A., Macfarlane, A. and Fernázndez-Suárez, J. (2004 b). Paleometeorización vs. Paleoalteración en la superficie de discordancia Proterozoico-Cámbrico en el Antiforme del Narcea. Geogaceta, 33, p. 7-10.

Gutiérrez-Alonso, G., Fernázndez-Suárez, J., Collins, A.S., Abad, I. and Nieto, F. (2005). Amazonian Mesoproterozoic basement in the core of the Ibero-Armorican Arc: $^{40}Ar/^{39}Ar$ detrital mica ages complement the zircon's tale. Geology, 33(8), p. 637-640.

Gutiérrez-Elorza, M., García-Ruiz, J.M., Goy, J.L., Gracia-Prieto, F.J., Gutiérrez-Santolalla, F., Martín, C., Martín-Serrano, A., Pérez-Gonzalez, A., Zazo, C. and Aguirre, E. (2002). Quaternary. In W. Gibbons and T. Moreno, Eds. *The Geology of Spain*. The Geological Society, London. p. 335-366.

Heinz, W., Loeschke, J. and Vavra, G. (1985). Phreatomagmatic volcanism during the Ordovician of the Cantabrian Mountains (NW Spain). *Geologische Rundschau*, 74(3), p. 623-639.

Heward, A.P. (1978). Alluvial fan and lacustrine sediments from the Stephanian A and B (La Magdalena, Ciñera-Matallana and Sabero coalfields), northern Spain. *Sedimentology*, 25, p. 451-483.

Heward, A.P. and Reading, H.G. (1980). Deposits associated with a Hercynian to late Hercynian continental strike-slip system. Cantabrian Mountains, northern Spain. In P.F. Ballance and H.G. Reading, Eds. *Sedimentation in oblique-slip mobile zones*, 4, p. 105-125.

Hirt, A.M., Lowrie, W., Julivert, M. and Arboleya, M.L. (1992). Paleomagnetic results in support of a model for the origin of the Asturian Arc. *Tectonophysics*, 213(3-4), p. 321-339.

HNPC. (1992). Geologia dels Paisos Catalans II, Geologia II, p. 548. *Enciclopedia Catalana S.A.*, Barcelona.

Holden, N.E. (1989). Total and spontaneous fission half-lives for uranium, plutonium, americium and curium nuclides. *Pure Appl. Chem.*, 61, p. 1505-1510.

Horvath. (1985). *Apprts de la palynologie à la stratigraphie du Carbonifère moyen de l'Unité structuale de La Sobia-Bodón (Zone Cantabrique-Espagne)*. Université des Sciences et Techniques de Lille (Inédita).

Huerta, A., Parés, J.M., Cabrera, L., Ferrus, B. & Sáez, A. 1996. Deformación contractiva del margen noroeste ibérico: Implicaciones tectónicas del estudio paleomagnético de la Cuenca de As Pontes (NW España). *Geogaceta,* 20, p. 939-942.

Hurford, A.J. (1986). Standardizatoin of fission trackdating calibration: results of the questionaire distributed by International Union of Geologcial Sciences Subcommission on Geochronology. *Nuclear Tracks and Radiation Measurements*, 11, p. 329-333.

Hurford, A.J. and Carter, A. (1991). The role of fission track dating in discrimination of provenance. In C. Morton Andrew, S.P. Todd and P.D.W. Haughton, Eds. *Developments in sedimentary provenance studies.*, 57, p. 67-78.

Hurford, A.J. and Green, P.F. (1981). Standards, dosimetry and the uranium-238 $\lambda_f$ decay constant: a discussion. *Nuclear Tracks*, 5, p. 53-61.

Hurford, A.J. and Green, P.F. (1982). A users' guide to fission track dating calibration. *Earth and Planetary Science Letters*, 59, p. 343-354.

Hurford, A.J. and Green, P.F. (1983). The zeta age calibration of fission-track dating. *Chemical Geology*, 41(4), p. 285-317.

IGME. (1982). *Vega de Espinareda (126)*. Instituto Geológico y Minero de España, Madrid.

Johnson, C., Harbury, N. and Hurford, T.J. (1997). The role ofextension in the Miocene denudation of the Nevado-Filabride Complex, Bedic Cordillera (SE Spain). *Tectonics*, 16, p. 189-204.

Johnson, G.A.L. and Tarling, D.H. (1985). Continental convergence and closing seas during the Carboniferous. *10. Congr. Internat. Stratigr. Géol. Carbonifère*, p. 163-168, Madrid.

Jonckheere, R., van den Haute, P., De Corte, F. and Wagner, G.A. (2000). Fission track age calibration - the next generation. *9th International conference on fission-track dating and thermochronology*, p. 187-188, Lorne (Australia).

Juez-Larré, J. & Andriessen, P.A.M. (2002). Post Late Paleozoic tectonism in the southern Catalan Coastal Ranges (NE Spain), assessed by apatite fission track analysis. *Tectonophysics,* 349, p. 113-129.

Juez-Larré, J. (2003). *Post Late Paleozoic tectonothermal evolution of the northeastern margin of Iberia, asessed by fission-track and (U-Th)/He analysis: a case history from the Catalan Coastal Ranges*. Ph.D. Thesis, Faculty of Earth and Life Sciences, p. 200. Vrije Universiteit, Amsterdam.

Julivert, M. (1967). *La ventana del ro Monasterio y la terminacion meridional del manto del Ponga. Geologa de la region de mantos al E. de la cuenca carbonfera central (cord. Cantabrica)*. Trabajos de Geologia, Universidad de Oviedo 1, p. 1-26.

Julivert, M. (1971). Decollement tectonics in the Hercynian Cordillera of Northwest Spain. *American Journal of Science*, 270(1), p. 1-29.

Julivert, M. (1978). Hercynian orogeny and Carboniferous palaeogeography in north-western Spain: a model of deformation-sedimentation relationships. *Zeitschrift der Deutschen Geologischen Gesellschaft*, 129, p. 565-592.

Julivert, M. (1981). A cross-section throught the northern part of the Iberian Massif. *Geol. en Mijnbouw.*, 60, p. 107-128.

Julivert, M. (1983 a). *Los tiempos Precambricos y Paleozoicos; El ciclo Hercinico; Generalidades. Precambrian and Paleozoic; Hercynian cycle; general*. Inst. Geol. y Miner. Espana, Madrid.

Julivert, M. (1983 b). Proyecto no 5; Correlacion de los acontecimientos pre-variscicos y variscicos en las Cordilleras Mediterraneo-Alpinas. Project No. 5; Correlation of Prevariscan and Variscan events of the Alpine-Mediterranean mountain belts. *Boletin Informativo - PICG*, 8, p. 17-18.

Julivert, M. and Arboleya, M.L. (1984). An geometrical and kinematical approach to the nappe structure in an arcuate fold belt: the Cantabrian nappes (Hercynian chain, NW-Spain). *Journal of Structural Geology*, 6(5), p. 499-519.

Julivert, M. and Arboleya, M.L. (1986). Areal balancing and estimate of areal reduction in a thin-skinned fold-and-thrust belt (Cantabrian Zone, NW Spain): constraints on its emplacement mechanism. *Journal of Structural Geology*, 8, p. 407-414.

Julivert, M. and Marcos, A. (1973). Superimposed folding under flexural conditions in the Cantabrian zone (Hercynian cordillera, northwest Spain. *American Journal of Science*, 273, p. 353-375.

Julivert, M., Marcos, A. and Truyols, J. (1972). L'evolution paleogeographique du nord-ouest de l'Espagne pendant l'Ordovicien-Silurien. Paleogeographic evolution of northwestern Spain during the Ordovician-Silurian. *Bulletin de la Societe Geologique et Mineralogique de Bretagne*. Serie C, 4(1), p. 1-7.

Jurado, M.J. and Riba, O. (1996). The Rioja area (westernmost Ebro Basin): a ramp valley with neighbouring piggybacks. In P.F. Friend and Dabrio, C.J., Ed. *Tertiary basins of Spain, the stratigraphic record of crustal kinematics*, 6, p. 173-182. Cambridge University Press.

Keller, M. and Krumm, S. (1992). Evidence of an Upper Ordovician themo-metamorphic event in the SW-corner of the Cantabrian Mountains (N-Spain). *Estudios Geol.*, 48, p. 289-296.

Keller, M. and Krumm, S. (1993). Variscan versus Caledonian and Precambrian metamorphic events in the Cantabrian Mountains, Northern Spain. *Zeitschrift der Deutschen Geologischen gesellschaft*, 144, p. 88-103.

Ketcham, R.A. (2003). Observations on the relationship between crystallographic orientation and biasing in apatite fission-track measurements. *American Mineralogist*, 88, p. 817-829.

Ketcham, R.A., Donelick, R. and Donelick, M.B. (2000). AFTSolve: A program for multi-kinetic modeling of apatite fission-track data. *Geological Materials Research*, 2(1 (electronic)), p. 1-32.

Ketcham, R.A., Donelick, R.A. and Carlson, W.D. (1999). Variability of apatite fission-track annealing kinetics: III. Extrapolation to the geological time scales. *American Mineralogist*, 84, p. 1235-1255.

Kollmeier, J.M., van der Pluijm, B.A. and van der Voo, R. (2000). Analysis of Variscan dynamics; early bending of the Cantabria-Asturias Arc, northern Spain. *Earth and Planetary Science Letters*, 181(1-2), p. 203-216.

Krijgsman, W., Hilgen, F.J., Raffi, I., Sierro, F.J. and Wilson, D.S. (1999). Chronology, causes and pregression of the Messinian salinity crisis. *Nature*, 400, p. 652-655.

Krumm, S. (1992). *Polyphase thermal evolution of the southern Cantabrian Mountains and its relationship to deformation, nappe tectonics and sedimentation*. Department of Geology. University of Erlangen, Erlangen.

Laslett, G.M. and Galbraith, R.F. (1996). Statistical modelling of thermal annealing of fission tracks in apatite. *Geochim. Cosmochim. Acta*, 60, p. 5117-5131.

Laslett, G.M., Green, P.F., Duddy, I.R. and Gleadow, A.J.W. (1987). Thermal annealing of fission-tracks in apatite, 2. A quantitative analysis. *Chemical Geology (Isotope Geoscience Section)*, 65, p. 1-13.

Leprevier, C. and Martínez-García, E. (1990). Fault development and stress evolution of the post-Hercynian Asturian Basin (Asturias adn Cantabria, northwestern Spain). *Tectonophysics*, 184, p. 345-356.

Leyva, F., Matas, J. and Rodríguez-Fernández, L.R. (1984). *La Robla*. Instituto Geologico y Minero de Espana (IGME), Madrid, Spain. 98 p.

Leyva, F., Matas, J. and Rodríguez-Fernández, L.R. (1984). (1984 b). Tectónica. In L.R. Rodríguez-Fernández, Ed. *Memoria del mapa geologico de España, Escala 1:50000, No. 129 (La Robla)*. IGME, Madrid, p. 67-83.

Liñán, E., Gozalo, R., Palacios, T., Gamez-Vintaned, J.A., Ugidos, J.M. and Mayoral, E. (2002). Cambrian. In W. Gibbons and T. Moreno, Eds. *The geology of Spain*. The geological Society, London, p. 16-30.

Lobato, L., García-Alcalde, J.L., Sánchez de Posada, L.C., Truyols, J. and Villegas, F. (1984). *Hoja del Mapa Geológico Nacional de España (1:50000), Memoria 104 (Boñar)*. IGME, Madrid, 77 p.

Loeschke, J. (1983). Igneous and pyroclastic rocks in Devonian and Lower Carboniferous strata of the Cantabrian Mountains (NW Spain). *Neues Jahrbuch für Geologie und Paläontologie. Abhandlungen*, 8, p. 495-504.

Loeschke, J. and Zeidler, N. (1982). Early Palaeozoic sills in the Cantabrian Mountains (Spain) and their geotectonic environment. *Neues Jahrbuch für Geologie und Paläontologie. Abhandlungen*, 7, p. 419-439.

Lonergan, L. and White, N. (1997). Origin of the Betic-Rif mountain belt. *Tectonics*, 16, p. 504-522.

López-Gómez, J., Arche, A. and Pérez-López, A. (2002). Permian and Triassic. In W. Gibbons and T. Moreno, Eds. *The Geology of Spain*. The Geological Society, London, p. 185-212.

Lorenz, F. and Nicholls, I. (1984). Plate and intraplate processes of Hercynian Europe during the Late Palaeozoic. *Tectonophysics*, 107, p. 25-56.

Lotze, F. (1945). Zur Gliederung der Varisciden der Iberischen Meseta. *Geotektonische Forschungen*, 6, p. 78-92.

Lotze, F. (1956). Das Präkambrium Spaniens. *Neues Jb. Geol. Paläont. Mh.*, 8, p. 373-380.

Lutz, T.M. and Omar, G.I. (1991). An inverse method of modelling thermal histories from apatite fission track data. *Earth and Planetary Science Letters*, 104, p. 181-195.

Malod, J.A. and Mauffret, A. (1990). Iberian plate motions during the Mesozoic. *Tectonophysics*, 184, p. 261-278.

Marcos, A. (1968 a). Nota sobre el significado de la "Leon Line." *Brev. Geol. Asturias*, 3, p. 1-5.

Marcos, A. (1968 b). La tectónica de la Unidad de la Sobia Bodón. *Trabajos de Geología*, 2, p. 59-87.

Marcos, A. (1973). Las series del Paleozoico inferior y la estructura herciniana del occidente de Asturias (NW de España). *Trabajos de Geología*, 6, p. 3-113.

Marcos, A., Kullmann, J. and Schönenberg, R. (1979). Facies differentiation caused by wrench deformation along a deep-seated fault system (León Line, Cantabrian Mountains, North Spain) – Discussion and reply. *Tectonophysics*, 60, p. 303-309.

Marcos, A. and Pulgar, J.A. (1982). An approach to the tectonostratigraphic evolution in the Cantabrian Foreland thrust and fold belt, Hercynian Cordillera of NW Spain. *Neues Jahrbuch für Geologie und Paläontologie*, 163(2), p. 256-260.

Marschik, R. (1992). *Der Übergand von der Diagenese zur sehr neidergradigen Metamorphose im externen Varistikum (Kantabrische Zone), NW Spanien*. Diplom Arbeit. Mineralogisch-Petrographischen Institut. Universität Hedelberg, Heidelberg.

Martín-Chivelet, J., Berastegui, X., Rosales, I., Vilas, L., Vera, J.A., Caus, E., Gräfe, K.U., Mas, R., Puig, C., Segura, M., Robles, S., Floquet, M., Quesada, S., Ruiz-Oritz, P.A., Fregenal, M.M.A., Salas, R., Arias, C., Garcia, A., Martin, A.A., Melendez, M.N., Chacon, B., Molina, J.M., Sanz, J.L., Castro, J.M., Garcia-Hernandez, M., Carenas, B., Garcia-Hidalgo, J., Gil, J. and Ortega, F. (2002). Cretaceous. In W. Gibbons and T. Moreno, Eds. *The geology of Spain*, p. 255-293. The Geological society, London.

Martín-Parra, L.M. (1989). *Riello*. 119 p. Instituto Geologico y Minero de Espana (IGME), Madrid.

Martínez, F.J. and Rölet, J. (1988). Late Palaeozoic metamorphism in the northwestern Iberian Peninsula, Brittany and related areas in SW Europe. In A.L. Harris and D.J. Fettes, Eds. *The Caledonian – Appalachian Orogen*, Special Publication 38. Geological Society, London, p. 611-620.

Martínez-Catalán, J. (1990). A non-cylindrical model for the northwest Iberian allochthonous terranes and their equivalents in the Hercynian belt of Western Europe. *Tectonophysics* 179, p. 253-272.

Martínez-Catalán, J., Arenas, C., Diaz-Garcia, F., Rubio-Pascual, F., Abati, J. and Marquinez, J. (1996). Variscan exhumation of a subducted Paleozoic continental margin: the basal units of the Ordenes Complex, Galicia, NW Spain. *Tectonics*, 15, p. 106-121.

Martínez-Catalán, J.R., Arenas, R., Díaz-García, F. and Abati, J. (1997). Variscan acretionary complex of northwestern Iberia: Terrane correlation and succession of tectonothermal events. *Geology*, 25(12), p. 1103-1106.

Martínez-Catalán, J.R., Pérez-Estaún, A., Bastida, F., Pulgar, J.A. and Marcos, A. (1990). Structure: West-Asturian-Leonese Zone (Part III). In R.D. Dallmeyer and E. Martínez-García, Eds. *Pre-Mesozoic Geology of Iberia*, p. 103-114. Springer-Verlag, Berlin.

Martínez-García, E. (1990). Stephanian and Permian basins. In R.D. Dallmeyer and E. Martínez-García, Eds. *Pre-Mesozoic geology of Iberia*, p. 39-54. Springer-Verlag, Berlin New York Heidelberg.

*References*


Martínez-García, E. (1991). Hercynian syn-orogenic and post-orogenic successions in the Cantabrian and the Palentian zones (NW Spain). *Gionale di Geología*, 53, p. 209-228.

Martínez-García, E. and Wagner, R.H. (1984). The post-Asturian marine basin of late Stephanian age in Northwest Spain. In H.J. Geldsetzer Helmut, W. Nassichuk Walter, S. Belt Edward and W. Macqueen Roger, Eds. *Part 1, Atlantic Coast basins; Part 2, Paleogeography and paleotectonics; Part 3, Sedimentology and geochemistry.*, 9; 3, p. 508-516.

Martínez-García, E., Wagner, R.H., Lobato, L., Fernández, L. and Alonso, S.L. (1983). El carbonifero de la Region Oriental (Pisuerga-Carrion). In C. Martínez-Diaz, Ed. *Carbonifero y Permico de Espana*, p. 116-132. IGME.

Marzo, M. and Calvet, F. (1985). *El Triásico de los Catalánides*. Institut d'Etudis Ilerdencs, Lleida.

Matas, J., Abejaro, V., Fernández, L. and Fernández, P. (1982). *Noceda*. Instituto Geologico y Minero de España (IGME),, Madrid, Spain. 63 p.

Matte, P. (1968). La structure de la virgation hercynienne de Galice (Espagne). *Revue de Géologie Alpine*, 44, p. 155-280.

Matte, P. (1991). Accretionary history and crustal ev olution of the Variscan Belt in Western Europe. In R.D.J. Hatcher and L. Zonenshain, Eds. *Accretionary tectonics and composite continents*, 196 (3-4), p. 309-337. Elsevier.

Matte, P. (2001). The Variscan collage and orogeny (480-290) and the tectonic definition of the Armorica Microplate; a review. *Terra Nova*, 196 (3-4), p. 122-128.

Matte, P. and Ribeiro, A. (1975). Forme et orientation de l'episode de déformation dans la virgation hercynienne de Galice. Rélations avec le plissement et hypothèse sur la génèse de l'arc Ibero-Amoricaine. *Académie de Sci. cpmtes Rendus*, 280, p. 2825-2828.

Mazzoli, S. and Helman, M. (1994). Neogene patterns of relative plate motion for Africa-Europe: some implications for recent central Mediterranean tectonics. *Geologische Rundschau*, 83, p. 464-468.

McDowell, F. and Keizer, R.P. (1977). Timing of mid-Tertiary volcanism in the Sierra Madre Occidental between Durango City and Mazatlan, Mexico. *Geol. Soc. Am. Bull.*, 88, p. 1479-1487.

McKerrow, W.S., Dewey, J. and Scotese, C.R. (1991). The Ordovician and Silurian development of the Iapetus Ocean. *Palaeontology*, 44, p. 165-178.

Méndez-Cecilia, A.J. (1985). *Estudio de la evolución de los carbones de la cuenca Ciñera-Matallana, León*, Doctoral Thesis, p. 269. University of Oviedo, Oviedo.

Merriman, R.J. and Kemp, S.J. (1996). Clay minerals and sedimentary basin maturity. *Mineralogical Society Bulletin*, 111, p. 7-8.

Mitra, S. (1986). Duplex structures and imbricate thrust systems: geometry structural position and hydrocarbon potential. *AAPG Bulletin*, 70(2), p. 131-160.

Morales, J., Serrano, I., Jabaloy, A., Galindo-Zaldívar, J., Zhao, D., Torcal, F., Vidal, F. and González-Lodeiro, F. (1999). Active continental subduction beneath the Betic Cordillera and the Alboran Sea. *Geology*, 27, p. 735-738.

Morris, R.G., Sinclair, H.D. and Yelland, A.J. (1998). Exhumation of the Pyrenean orogen: implications for sediments discharge. *Basin Research*, 10(1), p. 69-85.

Mulhall, C.M. (2003). *On metamorphism in the southern Cantabrian Zone*. e-mail to Schneider J.

Muñoz, J.A., Puigdefàbregas, C. & Fontboté, J.M. (1983). El Ciclo Alpino y la estructura tectonica del Pirineo. In: Libro Jubilar J.M. Ríos, Geologia de España II. IGME, Madrid, p. 185-205.

Murphy, J.B. and Nance, R.D. (1991). Supercontinent model for the contrasting character of Late Proterozoic orogenic belts. *Geology*, 19, p. 469-472.

Murphy, J.B., Gutiérez-Alonso, G., Nance, N.D., Fernández-Suárez, J., Keppie, J.D., Quesada, C., Strachan, R.A., Dostal., J. (2006). Origin of th Rheic Ocean: Rifting along a Neoproterozoic Structure? *Geology*, 34 (5), p. 325-328.

Mutti, E. and Ricci Lucchi, F. (1975). Turbidite Facies and facies associations. In E. Mutti, Ed. *Examples of turbidites facies and facies associations from selected formations of northern Apennines. IX International congress of Sediemntology: Guidebook.*, A-II, p. 21-36, Nice.

Naeser, C.W. (1979). Fission-track dating and geologic annealing of fission tracks. In E. Jäger and J.C. Hunziker, Eds. *Lectures in Isotope Geology*, p. 154-169. Springer-Verlag, Heidelberg.

Naeser, N.D., Naeser, C.W. and McCulloh, T.H. (1989). The application of fission-track dating in the depositinal and thermal history of rocks in sedimentary basins. In N.D. Naeser and T.H. McCulloh, Eds. *Thermal History of Sedimentary Basins*, p. 157-180. Springer-Verlag, New York.

Nägler, T.F., Schäfer, H.-J. and Gebauer, D. (1995). Evolution of the Western European continental crust: implication s from Nd and Pb isotopes in Iberian sediments. *Chemical Geology (Isotope Geoscience Section)*, 121, p. 345-357.

Nance, R.D. and Murphy, J.B. (1996). Basement isotopic signatures and Neoproterozoic paeogeography of Avalonian-Cadomian and related Peri-Gondwanan Terranes of the circum-North Atlantic. In R.D. Nance and M. Thompson, Eds. *GSA, Special Paper, 304*, p. 109-120.

Navarro, D., Muñoz, J.L. and Santos, J.A. (1987). *Investigatión Geológico-minera del Estefaniense de los sectores de Canseco-Rucayo y Reyero-Salamón (León). Segunda Fase*. Fondo documental del ITGE, 125 p.

Nieuwland, D.A., Leuschner, J.H. and Gast, J. (2000). Wedge equilibrium in fold-and-thrust belts: prediction of out-of-sequence thrusting based on sandbox experiments and natural examples. *Geologie en Mijnbouw/Netherlands Journal of Geosceinces*, 79(1), p. 81-91.

Nijman, W. and Savage, J.F. (1989). Persistent basement wrenching as controlling mechanism of Variscan thin-skinned thrusting and sedimentation, Cantabrian Mountains, Spain. In P. Matte and H.J. Zwart, Eds. *Palaeozoic plate tectonics with emphasis on the European Caledonian and Variscan belts*, 169, p. 281-302. Elsevier.

O'Sullivan, P.B. and Parrish, R.P. (1995). The importance of apatite composistion and single-grain ages when interpreting fission track data from plutonic rocks: a case study from the Coast Ranges, British Columbia. *Earth and Planetary Science Letters*, 132, p. 213-214.

Oczlon, M.S. (1992). Gondwana and Laurussia before and during the Variscan Orogeny in Europe and related areas. *Heidelberger Geowissenschaftliche Abhandlungen*, 53, p. 159.

Olivet, J.L. (1996). La cinématique de la plaque ibérique. *Bulletin des Centres de Recherches Exploration-Production Elf-Aquitaine*, 20, p. 131-195.

Ordóñez, B. (1998). *Geochronological studies of the Pre-Mesozoic basement of the Iberian Massif: the Ossa Morena zone and the Allochthonous Complexes within the Central Iberian zone*. Eidgenössische Technische Hoschschule, Zürich.

Palacios, T. and Vidal, F. (1992). Lower Cambrian acritarchs from Northern Spain: the Precambrian-Cambrain boundary and biostratigraphic implications. *Geological Magazine*, 129, p. 421-436.

Paniagua, A., Fonteboté, L., Fenoll Hach-Alí, P., Fallick, A.E., Moreiras, D.B. and Corretgé, L.G. (1993). Tectonic setting, mineralogical characteristics, geochemical signatures and age dating of a new type of epithermal carbonate-hosted, precious metal-five element deposit: the villamanín area (Cantabrian Zone, northern Spain). In P. Fenoll Hach-Alí, J. Torres-Ruiz and F. Gervilla, Eds. *Current research in geology applied to ore deposits, 2nd biennal SGA Meeting*, p. 531-534, Granada.

*References*


Paniagua, A., Rodríguez-Pevida, L.S., Loredo, J., Fonteboté, L. and Fenoll Hach-Ali, P. (1996). Un yacimiento de Au en carbonatos del Orógeno Hercínico: el área de Salamón (N León). *Geogaceta*, 20(7), p. 1605-1608.

Parés, J., van der Voo, R., Stakamatos, J. and Pérez-Estaún, A. (1994). Remagnetizations and postfolding oroclinal rotations in the Cantabrian/Asturian arc, norther Spain. *Tectonics*, 13(6), p. 1461-1471.

Paris, F. (1998). Early Palaeozoic palaeobiogeography of northern Gondwana regions. *Acta Univ. Carolinae-Geol.*, 42, p. 473-483.

Paris, F. and Robardet, M. (1990). Early Paleozoic palaeobiogeography of the Variscan regions. *Tectonophysics*, 177, p. 193-213.

Parnell, J. (1994). *Geofluids: Origin, Migration and Evolution of Fluids in Sedimentary Basins, GSA Special Publication 78*. Geological Society of America, 374 p.

Pastor-Gomez, V. (1963). *Mapa Geológico de España 1:50000.* Hojas y Memorias números 129 (La Robla), y 160 (Benavides). Inst. Geol. Min. Esp.

Pastor-Gomez, V. (1969). *Mapa geológico de Espana 1:50000*. Hoja y Memoria número 129 (Riello), Inst. Geol. Min. Esp.

Pedreria, D., Pulgar, J.A., Gallart, J. and Díaz, J. (2003). Seismic evidence of Alpine crustal thickening and wedging from the western Pyrenees t the Cantabrian Mountains (north Iberia). *Journal of Geophysical Research*, 108(B4 2204).

Pereira, A.J.S.C., Carter, A., Hurford, A.J., Neves, L.J.P.F. and Godinho, M.M. (1998). Evidence for unroofing history of Hercynian granitoids in central Portugal derived from Late Palaeozoic and Mesozoic sedimentary zircons. In P. Van den haute and F. De Corte, Eds. *Advances in Fission-Track Geochronology*, 10, p. 173-186. Kluver Academic Publishers, Dordrecht.

Pérez, N.M., Nakai, S., Wakita, H., Albert Bertrán, J.F. and Redondo, R. (1996). Preliminary results on $^{3}He/^{4}He$ isotopic ratios in terrestrial fluids from Iberian peninsula: seismotectonic and neotectonic implications. *Geogaceta*, 20, p. 830-833.

Pérez-Arlucea, M. (1985). *Estratigrafía y sedimentología del Pérmico y Triásico en el sector Molina de Aragón-Albarracín (provincias de Guadalajara y Teruel)*. Complutense University, Madrid.

Pérez-Estaún, A. (1973). Datos sobre la sucesión estratigráfica del Precámbrico y la estructura del extremo Sur del Antiforme del Narcea (NW de España). *Brev. Geol. Asturias*, 17(1), p. 5-16.

Pérez-Estaún, A. (1975). *La estratigrafía y la estructura de la rama sur de la Zona Asturoccidental-Leonesa (W. de León, NW de España)*. Universidad Oviedo, Oviedo.

Pérez-Estaún, A. (1978). Estratigrafía y estructura de la rama sur de la Zona Asturoccidental-Leonesa. *Mem. Inst. Geol. Min. España*, 92, 149 p.

Pérez-Estaún, A. and Alvarez-Marrón, J. (1990). Tectónica. In L.R. Rodríguez-Fernández, Ed. *Memoria del mapa geológico de España, Escala 1:50000, No. 79 (Puebla de Lillo)*, p. 28-45. ITGE, Madrid.

Perez-Estaun, A. and Bastida, F. (1990). Structure: Cantabrian Zone. In R.D. Dallmeyer and E. Martínez-García, Eds. *Pre-Mesozoic geology of Iberia*. Springer.

Pérez-Estaún, A., Bastida, F., Alonso, J.I., Marquínez, J., Aller, J., Alvarez-Marrón, J., Marcos, A. and Pulgar, J.A. (1988). A thin-skinned tectonic model for an arcuate fold and thrust belt: the Cantabrian Zone (Variscan Ibero-Amorican Arc). *Tectonics*, 7(3), p. 517-537.

Pérez-Estaún, A., Bastida, F., Martínez Catalán, J.R., Gutiérrez Marco, J.C., Marcos, A. and Pulgar, J.A. (1990). West Asturian Leonese Zone, Stratigraphy. In R.D. Dallmeyer and E. Martínez-García, Eds. *Pre-Mesozoic Geology of Iberia*, p. 92-102. Springer-Verlag, Berlin.

Pérez-Estaún, A. and Martínez, F.J. (1978). El Precámbrico del antiforme del Narcea en el sector de Tineo-Cangas de Narcea (NW de España). *Trabajos de Geología*, 10, p. 367-377.

Pérez-Estaún, A., Martinez-Catalán, J.R. and Bastida, F. (1991). Crustal thickening and deformation sequence in the footwall to the suture of the Variscan belt of northwest Spain. *Tectonophysics*, 191, p. 243-253.

Pérez-Estaún, A., Pulgar, J.A., Banda, E. and Álvarez, M.J. (1994). Crustal structure of the external variscides in northwest Spain from deep seismic reflection profiling. *Tectonophysics*, 232, p. 91-118.

Perroud, H. (1986). Paleomagnitic rotations in the Variscan mountain belt. *Tectonics*, 5(2), p. 205-214.

Perroud, H. and Bonhommet, N. (1981). Palaeomagnetism of th eIbero-Amorican arc and the Hercynian orogeny in Western Europe. *Nature*, 292, p. 445-447.

Plant, J.A., Whittaker, A., Demetriades, A., de Vivo, B., Lexa, J. (2006). *The Geological and Tectonic Framework of Europe*. http://www.gsf.fi/publ/foregsatlas/articles/Geology.pdf

Price, P.B. and Walker, R.M. (1963). Fossil tracks of charged particles in mica and the age of minerals. *Journal of Geophysical Research*, 68(16), p. 4847-4862.

Puigdefàbregas, C. and Souquet, P. (1986). Tecto-sedimentary cycles and depositional sequences of the Mesozoic and Tertiary from the Pyrenees. *Tectonophysics*, 129, p. 173-203.

Pulgar, J.A. (1980 a). Las fases de replegamiento hercinianas en la Zona Asturoccidental-Leonesa (N. W. de España). *Cuad. Lab. Xeol. Laxe*, 1, p. 165-171.

Pulgar, J.A. (1980 b). Análisis e interpretatción de las estructuras originadas durante las fases de prelegamiento en la zona Asturoccidental-Leonesa (Cord. Hercínica, N. W. España). *Geotectónica*. Universidad Oviedo, Oviedo.

Pulgar, J.A., Alonso, J.I., Espina, R.G. and Marín, J.A. (1999). The alpine deformation in the Variscan basement of the Cantabrian Zone. *Trabajos de Geología*, 21, p. 283-294.

Pulgar, J.A., Pérez-Estaún, A., Gallart, J., Álvarez-Marrón, J., Gallastegui, J., Alonso, J.I. and ESCIN-Group. (1995). The ESCI-N2 deep seismic reflection profile: a traverse across the Cantabrian Mountains and adjacent Duero basin. *Revisita de la Sociedad Geológica de España*, 8(4), p. 383-394.

Quesada, C. (1990). Precambrian successions in SW Iberia: Their relationship to Cadomian orogenic events. In R.S. D'Lemos, R.A. Strachan and C.G. Topley, Eds. *The Cadomian Orogeny, Special Publication 51*, p. 353-362. The Geological Society, London.

Quesada, C. (1991). Geological constraints on the Paleozoic tectonic evolution of the tectonostratigraphic teranes in the Iberian Massif. *Tectonophysics*, 185, p. 225-245.

Rahn, M. and Seward, D. (2000). A revised study of the exhumation of the Central Alps: first results from a compilation of more than 500, published and new apatite fission track analyses. Fission track 2000; *9th International conference on fission-track dating and thermochronology*, p. 275-276, Lorne (Australia).

Rakovan, J., Reeder, R.J., Elzinga, E., Cherniak, D., Tait, C.D, Morris, D.E. (2002). Crystal Chemistry of U(VI) In Apatite Determined by X-Ray Absorption Spectroscopy. *Annual Meeting of the Geological Society of America, 2002, Abstracts*. Session 138, Paper No. 138-4.

Ramos, A. (1979). Estratigrafía y paleogeografía del Pérmico y Triásico al oeste de Molina de Aragón (Província de Guadalajara). *Seminarios de Estratigrafía*, 6.

Raven, J.G.M. (1983). Conodont biostratigraphy and depositional history of the Middle devonian to Lower Carboniferous in the Cantabrian zone (Cantabrian Mountains, Spain). *Leidse Geologische Mededelingen*, 52, p. 265-339.

Raven, J.G.M. and van der Pluijm., B.A. (1986). Metamorphic fluids and transtension in the Cantabrian Mountains of northern Spain: an application of the conocont colour alteration index. *Geological Magazine*, 123(6), p. 673-681.

Ravenhurst, C.E., Roden, M.K., Willet, S.D. and Miller, D.S. (1993). Dependence of fission track annealing on apatite crystal chemistry. Nuclear Tracks and Radiation Measurements, 21, 622.

Reichter, K.R. and Pletsch, T.K. (2000). Evidence of a synchronous circum-Iberian subsidence event and its realtion to the African-Iberian plat convergence in the Late Cretaceous. *Terra Nova*, 12, p. 141-147.

Reis, A.C. (1979). Variscan metamorphism and K-Ar dates in the Variscan fold belt of S Brittany and NW Spain. *Journal of the Geological Society of London*, 136, p. 89-103.

Ribeiro, M.L., Quesada, C. and Dallmeyer, R.D. (1990). Geodynamic evolution of the Iberian Massif. In R.D. Dallmeyer and E. Martínez-García, Eds. *Pre-Mesozoic Geology of Iberia*, p. 399-409. Springer-Verlag, Berlin.

Riding, R. (1974). Model of the Hercynian fold belt. *Earth and Planetary Science Letters*, 245, p. 125-135.

Rincon, R., Vilas, L., Arias, C., Garcia-Quintana, A., Mas, J.R., Alonso, A. and Melendez, N. (1983). El Cretacio de las Cordilleras Intermedias y borde de las Meseta. In J.M. Ríos, Ed. *Geologia de España*, 2, p. 79-103. IGME, Madrid.

Robardet, M. (2000). An alternative approach to consider the Variscan belt in SW Europe: The pre-orogenic paleogeographical constraints. *Basement Tectonics*, 15, p. 23-26, A Coruña.

Robardet, M. (2002). Alternative approach to the Variscan Belt in southwestern Europe: Preorogenic paoaeobiogeographical constraints. In J.R. Martínez-Catalán, R. Hatcher, R. Arenas and F. Díaz-García, Eds. *The building of the late Paleozoic basement*, 364, p. 1-15.

Robardet, M. (2003). The Armorica 'microplate': fact or fiction? Critical review of the concept and contradictory palaeobiogeographical data. *Palaeogeography, Palaeoclimatology, Palaeoecology*, 195, p. 125-148.

Robardet, M. and Gutiérrez-Marco, J.C. (2002). Silurian. In W. Gibbons and T. Moreno, Eds. *The Geology of Spain*, p. 51-66. The Geological Society, London.

Robardet, M., Paris, F. and Plusquellec, Y. (2001). Comment on "New Early Devonian paleomagnetic data from NW France: Paleogrography and implications for the Armorican microplate hypothesis" by J. Tait. *Journal of Geophysical Research*, 106(B7), p. 13307-13310.

Robardet, M., Paris, F. and Racheboeuf, P.R. (1990). Palaeogeographic evolution of southwestern Europe during early Palaeozoic times. In W.S. McKerrow and C.R. Scotese, Eds. *Palaeozoic palaeogography and biogeography: Memoir 12*, p. 411-419. Geological Society of London, London.

Roest, W. R. and Srivastava, S.P. (1991). Kinematics of the plate boundaries between Eurasia, Iberia and Africa in the North Atlantic from the late Cretaceous to the present. *Geology*, 19, p. 613-616.

Roure, F. and Coletta, B. (1996). Cenozoic inversion structures in the foreland of the Pyrenees and Alps. In P. A. Ziegler and F. Horvath, Eds. Peri-Tethys Memoir 2: S*tructure and Prospects of Alpine Basins and Forelands*, 170, p. 173-209, Paris.

Russo, A. and Bechstädt, T. (1994). Evolución sedimentológica y paleogeográphica de la formación Vegadeo (Cámbrico Inferior-Medio) en la zona entre Visuña u Piedrafita do Caurel (Lugo NO de España). Rev. *Soc. Geol. España*, 7, p. 299-310.

Ruttenberg, K.C. and Berner, R.A. (1993). Authigenic apatite formation and burial in sediments from non-upwelling, continental margin environments. *Geochimica et Cosmochimica Acta*, 57(5), p. 991-1007.

Sabat, F., Roca, E., Muñoz, J.A., Verges, J., Santanach, P., Sans, M., Masana, E., Estevez, A. and Santisteban, C. (1995). Role of extension and compression in the evolution of the eastern margin of Iberia: the ESCI-Valencia Trough seismic profile. *Rev. Soc. Geol. España*, 8, p. 431-448.

Salas, R. and Casas, A. (1993). Mesozoic extensional tectonics, stratigraphy and crustal evolution during the Alpine cycle of the eastern Iberian basin. *Tectonophysics*, 228, p. 33-55.

San José, M.A., Pieren, A.P., García-Hidalgo, J.F., Vilas, L., Herranz, P., Peláez-Pruneda, J.R., Vilas-Minondo., L. and Perejón, A. (1990). Autochthonous sequences in the Central Iberian Zone: ante-Ordovician stratigraphy. In R.D. Dallmeyer and E. Martínez-García, Eds. *Pre-Mesozoic Geology of Iberia*, p. 147-159. Springer-Verlag, Berlin.

Sanders, C.A.E. (1998). *Tectonics and Erosion; competitive forces in a compressive orogen. A fission track study of the Romanian Carpathians*. Vrije Universiteit, Amsteredam.

Sanz de Galdeano, C.M. (1995). Tertiary tectonic framework of the Iberian Peninsula. In P.F. Friend and C.J. Dabrio, Eds. *Tertiary Basins of Spain, the stratigraphic record of crustal kinematics*, 6, p. 9-14. Cambridge University Press.

Savage, J.F. and Boschma, D. (1980). Geological maps of the southern Cantabrian Mountains (Spain). *Leidse Geologische Mededelingen*, 50(2), 75 p.

Savostin, L.A., Sibuet, J., Zonenshain, P., Le Pichon, X. and Roulet, M. (1986). Kinematic evolution of the Tethys belt from the Atlantic Ocean to the Pamirs since Triassic. *Tectonophysics*, 123, p. 1-35.

Schneider, J. (2002). *Spätdiagenetische Prozesse in den Karbonaten der unterdevonischen La Vid Gruppe, Kantabrisches Gebirge (NW Spanien)*. Doctoral Thesis, Geologisch Paläontologisches Institut, p. 113. Ruprecht-Karls-Universität Heidelberg, Heidelberg.

Scotese, C.R. (2001). *Atlas of Earth History, Volume 1, Paleogeography*, PALEOMAP Project, Arlington, Texas, 52 p.

Scotese, C.R., Bambach, R.K., Barton, C., van der Voo, R. and Ziegler, A. (1979). Palaozoic base maps. *J. Geol.*, 87(3), p. 217-277.

Scotese, C.R. and Barrett, S. (1990). Gondwana's movement over the South Pole during the Palaeozoic: Evidence from lithological indicators of climate. In W.S. McKerrow and C.R. Scotese, Eds. *Palaeozoic palaeogeography and biogeography*, 12, p. 75-85, London.

Scotese, C.R. and McKerrow, W.S. (1990). Revised world maps and introdution. In W.S. McKerrow and C.R. Scotese, Eds. *Palaeozoic palaeogeography and biogeography*, 12, p. 1-21, London.

Serrano-Pinto, M., Casquet, C., Ibarrola, E., Corretgé, L.G. and Portugal-Ferreira, M. (1987). Síntese geocronológica dos groanitoides do Maciço Hespérico. In F. Bea, A. Carnicero, J.C. Gonzalo, López-Plaza and M.D. Rodríguez-Alonso, Eds. *Geología de los granitoides y rocas asociadas del Macizo Hespérico*, p. 69-86. Rueda, Madrid.

Singh, S., Singh, D., Sandhu, A.S., Singh, G. and Virk, H.S. (1986). A study of track etch anisotropy in apatite. *Nuclear Tracks*, 12, p. 927-930.

Sopeña, A., López, J., Arche, A., Pérez-Arlucea, M., Ramos, A., Virgili, C. and Hernando, S. (1988). Permian and Triassic rift basins of the Iberian Peninsula. In W. Manspeizer, Ed. *Triassic-Jurassic Rifing*, 22, p. 757-786. Elsevier, Amsterdam.

Spiro, B., Tornos, F. and Shepherd, T.J. (1995). Stable Isotope characterisation of barren and mineralised tardi-Hercynian hydrothermal carbonates in the Cantabrian Zone (N Spain). In J. Pasava, B. Kribek and K. Zak, Eds. *Mineral Deposits: from their origin to environmental impacts*, p. 75-78. Balkema, Rotterdam.

Srivastava, S.P., Roest, W.R., Kovacs, L.C., Oakey, G., Levesque, S., Verhoef, J. and Macnab, R. (1990). Motion of Iberia since the Late Jurassic: Results from detailed aeromagnetic measurements in the Newfoundland Basin. *Tectonophysics*, 184, p. 229-260.

Stapel, G. (1999). *The nature of isostasy in western Iberia*. Ph.D. Thesis. Faculty of Earth Sciences, Department of Tectonics. Vrije Universiteit, Amsterdam.

Stapel, G., Cloetingh, S. and Pronk, B. (1996). Quantitative subsidence analysis of the Mesozoic evolution of the Lusitanian basin. *Tectonophysics*, 266, p. 493-507.

Steiger, R.H. and Jäger, E. (1977). Subcomission on geochronology: convention on the use of decay constants in geo- and cosmochronology. *Earth and Planetary Science Letters*, 36, p. 359-362.

Steven, T.A., Cunningham, C.G., Naeser, C.W. and Mehnert, H.H. (1979). Revised stratigraphy and radiometric ages of volcanic rocks and mineral deposits in the Marysvale area, West-Central Utah. *U.S. Geol. Surv. Bull.*, 1469, p. 1-40.

Suárez, O., Cuesta, A., Corretgé, L.G. and Fernández-Suárez, J. (1992). Spinel-bearing inclusions in calc-alkaline granitoids of the Cantabrian and West Asturian Leonese zones, Hercynian Iberian Belt. *Bulletin de la Societe Geologique de France, Huitieme Serie*, 163(5), p. 611-623.

Suárez-Rodrígues, A., Heredia, N., López-Díaz, F., Toyos, J.M., Rodríguez-Fernández, L.R. and Gutiérrez, G. (1991). *Los Barrios De Luna (102)*. Instituto Tecnológico GeoMinero de España.

Suppe, J. (1983). Geometry and kinematics of fault-bend folding. *American Journal of Science*, 283, p. 684-721.

Sweeney, J.J. and Burnham, A.K. (1990). Evaluation of a simple model of vitrinite reflectance based on chemical kinetics. *AAPG Bulletin*, 74, p. 1559-1570.

Tait, J. (1999). New Early Devonian paleomagnetic data from NW France: Paleogeography and implications for the Armorican microplate hypothesis. *Journal of Geophysical Research*, 104(B2), p. 2831-2839.

Tait, J., Bachtadse, V., Franke, W. and Soffel, H. (1997). Geodynamic evolution of the European Variscan fold belt: palaeomagnetic and geological constraints. *Geol. Rundschau*, 86, p. 5865-598.

Tait, J., Schätz, M., Bachtadse, V. and Soffel, H. (2000). Palaeomagnetism and Palaeozoic palaeogeography of Gondwana and European terranes. In W. Franke, V. Haak, O. Oncken and D. Tanner, Eds. *Orogenic Processes: Quantification and Modelling in the Variscan Belt.*, 179, p. 21-34. Geologyical Society, London.

Tarling, D.H. (1985). Carboniferous reconstructions based on palaeomagnetism. *Dixieme Congres Int. de Stratigraphie et de Geologie du Carbonifère*, p. 153-161, Madrid.

Tornos, F. and Spiro, B. (2000). The geolology and isotope geochemistry of the talc deposit of Puebla de Lillo (Ccantabrian Zone, Northern Spain). *Economic Geology*, 95, p. 1277-1296.

Torsvik, T., Smethurst, M., van der Voo, R., Trench, A., Abrahamsen, N. and Halvorsen, E. (1992). BALTICA: a synopsis of Vendian-Permian palaeomagnetic data and their palaeotectonic implications. *Earth Sci. Rev.*, 33, p. 133-152.

Trench, A. and Torsvik, T. (1991). A revised Palaeozoic apparent polar wander path for southern Britain (eastern Avalonia). *Geophys. J. Int.*, 104, p. 227-233.

Tucholke, B.E. and McCoy, F.W. (1986). Paleogeographic and paleobathymetric evolution of the North Atlantic Ocean. In P.R. Vogt and B.E. Tucholke, Eds. *The Geology of North America. The western North Atlantic region*, p. 589-602. Geological Society of America.

Ugidos, J.M., Armenteros, I., Barba, P., Valladares, M.I. and Colmenero, J.R. (1997 a). Geochemistry and petrology of recycled orogen-derived sediments: a case study from Upper Precambrian siliciclastic rocks fo the Central Iberian Zone, Iberian Massif, Spain. *Precambrian Research*, 84, p. 163-180.

Ugidos, J.M., Valladares, M.I., Barba, P., Armenteros, I. and Colmenero, J.R. (1999). Geochemistry and Sm-Nd isotope systematics on the Upper Precambrian-Lower Cambrian sedimentary successions in the Central Iberian Zone, Spain. *Journal of Conference Abstracts*, 4, pp. 1021.

Ugidos, J.M., Valladares, M.I., Recio, C., Rogers, G., Fallick, A.E. and Stephens, W.E. (1997 b). Provenance of Upper Precambrian/Lower Cambrian shales in the Central Iberian Zone, Spain: evidence from a chemical and isotopic study. *Chemical Geology*, 136, p. 55-70.

Uysal, I.T., Glikson, M., Golding, S.D. and Audsley, F. (2000). the thermal history of the Bowen basin, Queensland, Australia; vitrinite reflectance and clay mineralogy of Late Permian coal measures. *Tectonophysics*, 323, p. 105-129.

Valladares, M.I., Barba, P. and Ugidos, J.M. (2002 b). Precambrian. In W. Gibbons and T. Moreno, Eds. *The Geology of Spain*, p. 7-16. The Geological Society London.

Valladares, M.I., Barba, P., Ugidos, J.M., Colmenero, J.R. and Armenteros, I. (2000). Upper Neoproterozoic-Lower Cambrian sedimentary successions in the Central Iberian Zone (Spain): sequence stratigraphy, petrology and chemostratigraphy. Implications for other European zones. *Journal of Earth Sciences*, 89, p. 2-20.

Valladares, M.I., Ugidos, J.M., Barba, P., Armenteros, I. and Colmenero, J.R. (1999). Upper Proterozoic-Lower Cambrian shales in the Central Iberian Zone: Chemical features and implications for other per-Gondwanan areas. *Journal of Conference Abstracts*, 4, p. 1021-1022.

Valladares, M.I., Ugidos, J.M., Barba, P. and Colmenero, J.R. (2002 a). Contrasting geochemical features of the Central Iberian Zone shales (Iberian Massif, Spain: Implications for ht eevolution of Upper Proterozoic-Lower Cambrian sediments and their sources in other Peri-Gondwana areas. *Tectonophysics*, 352, p. 121-132.

Valverde-Vaquero, P., Cuest-Fernández, A., Gallastegui, G., Suárez, O., Corretgé, L.G. and Dunning, G.R. (1999). U-Pb dating of late-Variscan magmatism in the Cantabrian Zone (northern Spain). *EUG X*, p. 101, Strasbourg.

van Ameron, H.W.J. and van Dillewijn, J. (1963). Note préliminaire sur le basin houiller de Ciñera-Matallana. *Leidse Geologische Mededelingen*, 29, p. 303-312.

van den Bosch, W.J. (1969 a). Geology of the Luna-Sil Region, Cantabrian Mountains (NW Spain). *Leidse Geologische Mededelingen*, 44, p. 137-225.

van den Bosch, W.J. (1969 b). The relationship between orogenesis and sedimentation in the SW part of the Cantabrian mountains (NW Spain). *Leidse Geologische Mededelingen*, 44, p. 227-233.

van den haute, P. (1984). Fission-track ages of apatites from the Precambrian of Rwanda and Burundi: relationship to East African rift tectonics. *Earth and Planetary Science Letters,* 71, p. 129-140.

van den Haute, P., Jonckheere, R. and De Corte, F. (1988). Thermal neutron fluece determination for fission-track dating with metal activation monitors: a re-investigation. *Chemical Geology (Isotope Geoscience Section)*, 73, p. 233-244.

van der Pluijm, B.A. and Kaars-Sijpesteijn, C.H. (1984). Chlorite-mica aggregates; morphology, orientation, development and bearing on cleavage formation in very-low-grade rocks. *Journal of Structural Geology*, 6(4), p. 399-407.

van der Voo, R. (1993). *Paleomagnetism of the Atlantic, Tethys and Iapetus oceans*. Cambridge University Press.

van der Voo, R., Stakamatos, J.A. and Parés, J.M. (1997). Kinematic constraints on thrust-belt curvature from syndeformational magnetizations in the Lagos del Valle syncline in the Cantabrian Arc, Spain. *Journal of Geophysical Research*, 102, p. 10105-10119.

van Ginkel, A.C. (1965). Carboniferous fusulinids from the Cantabrian Mountains (Spain). *Leidse Geologische Mededelingen*, 34, p. 1-225.

van Staalduinen, C.J. (1973). Geology of the area between the Luna and Torio rivers, southern Cantabrain Mountains, NW Spain. *Leidse Geologische Mededelingen*, 49(2), p. 167-205.

van Wees, J.D., Arche, A., Beijdorff, C.G., López Gómez, J. and Cloetingh, S.A.P.L. (1998). Temporal and spatial variations in tectonic subsidence in the Iberian Basin (eastern Spain): inferences from automated forward modelling of high-resolution stratigraphy (Permian-Mesozoic). *Tectonophysics*, 300, p. 285-310.

Vegas, R., Vazquez, J.T., Suriñach, E. and Marcos, A. (1990). Model of distributed deformation, block rotations and crustal thickening for the formation of the Spanish Central System. *Tectonophysics*, 184, p. 367-378.

Vera, J.A. (1988). Evolución de los sistemas de depósito en el margen ibérico de la Cordillera Bética. *Revisita de la Sociedad Geológica de España*, 1, p. 373-391.

Vera, J.A. (1998). El Jurásico de la Cordillera Bética: estado actual de conocimientos y problemas pendientes. *Cuadernos de Geología Ibérica*, 24, p. 17-42.

Verhoef, J. and Srivastava S.P. (1990). Correlation of sedimentary basins across the North Atlantic as obtained from gravity and magnetic data and its relation to the early evolution of the North Atlantic. In A.J. Tankard, H. Balkwill and H.G. Miller Eds. *Extensional tectonics and stratigraphy of the North Atlantic margins*, Am. Ass. Petroleum Geologists special memoir, p. 131-147.

Veselovsky, S. (2004). *Intigrated numerical modelling of a polyhistory basin, Southern Cantabrian Basin (Palaeozoic, NW-Spain)*. Doctoral Thesis. Naturwissenschaftlich-Mathematischen Gesamtfakultät, p. 243. Ruprecht-Karls-Universität Heidelberg, Heidelberg.

Vidal Romaní, J.L. (1989). *Galicia. Mapa del Cuaternario de España*, p. 95-104. ITGME, Madrid.

Villaseca, C., Eugercios, L., Snelling, N., Huertas, M.J. and Castellon, T. (1995). Nuevos datos geocronologicos (Rb-Sr, K-Ar) de granitoides hercinicos de la Sierra de Guadarrama. *Revista de la Sociedad Geologica de Espana*, 8(3), p. 137-148.

Villegas, F.J. (1996). *Exploración e investigación de un nuevoyacimento de carbón en la cuenca minera Ciñera-Matallana (León)*. Doctoral Thesis, Complutense University, Madrid. p. 417.

Virgili, C., Sopeña, A., Ramos, A., Arche, A. and Hernando, S. (1983). El relleno posthercinico y el comienzo de la sedimentación mesozoica. In Anonymous, Ed. Libro Jubilar J.M. Rios; *Geología de España*, 2, p. 25-36.

Vissers, R.L.M., Platt, J.P. and van der Wal, D. (1995). Late orogenic extension of the Betic Cordillera and the Alboran Domain: A lithospheric view. *Tectonics*, 14, p. 786-803.

Vitorello, I. and Pollack, H.N. (1980). On the variation of continental heat flow with age and the thermal evolution of continents. *J. Geophys. Res.*, 85(b2), p. 983-995.

Vrolijk, P., Donelick, R., Queng, J. and Cloos, M. (1992). Testing models of fission track annealing in apatite in a simple thermal setting: site 800, leg 129. In R. Larson, Y. Lancelot, A. Fisher, L. Abrams, R. Behl and others, Eds. *Proc. Ocean Drilling Program, Sci. Results*, 129, p. 169-176.

Wagner, G.A. (1964). Stephanian floras in NW Spain, with special reference to the Westfalian D-Stephanian A boundary. *C. R. V. Congr. Int. Str. Geol. Carb.*, p. 835--851, París.

Wagner, G.A.. (1966 ). Altersbestimmung an Tektiten und anderen natürlichen Gläsern mittels Spuren der spontanen Kernspaltung des Uran-238 ("Fission Track"-Methode). *Zeitschrift f. Naturforschung*, 21a, p. 733-745.

Wagner, G.A.. (1967). Fission-track-datierung von Tektiten und Gläsern. *Fortschr. Miner.*, 44, p. 145.

Wagner, G.A.. (1968). Fission track dating of apatites. *Earth and Planetary Science Letters*, 4, p. 411-415.

Wagner, G.A.. (1969). Spuren der spontanen Kernspaltung des Uran-238 als Mittel zur Datierung von Apatiten und ein Beitrag zur Geochronologie des Odenwaldes. *Jb. Miner. Abh*, 110(252-286).

Wagner, G.A. (1978). Archaeological applications of fission track dating. *Nuclear Track Detection*, 2, p. 51-63.

Wagner, G.A., Altherr, R. and Van den haute, P. (1992). Apatite fission-track analysis of Kenyan basement rocks: constraints on the thermotectonic evolution of the Kenya dome. A reconnaissance study. *Tectonophysics*, 204(1-2), p. 93-110.

Wagner, G.A., Gleadow, A.J.W. and Fitzgerald, P.G. (1989). The significance of the partial annealing zone in apatite fission-track analysis: projected track length measurements and uplift chronology of the Transantarctic Mountains. *Chemical Geology (Isotope Geoscience Section)*, 79, p. 295-305.

Wagner, G.A. and Reimer, M. (1972). Fission track tectonics: the tectonic interpretation of fission track apatite ages. *Earth and Planetary Science Letters*, 14, p. 263-268.

Wagner, G.A. and Van den haute, P. (1992). *Fission-Track Dating*. 285 p. Enke, Stuttgart.

Wagner, R.H. (1966). Palaeobotanic dating of Upper Carboniferous folding phases in NW Spain. *Mem. Inst. Geol. Min. España*, 66 p.

Wagner, R.H.. (1970). An Outline of the Carboniferous Stratigraphy of Northwest Spain. *Colloque sur la stratigraphie du carbonifere 55*, p. 429-463.

Wagner, R.H.. (1971). The stratigraphy and structure of the Ciñera-Matallana Coalfield (Province of León, NW Spain). *Trabajos de Geología*, 4, p. 385-429.

Wagner, R.H. and Artieda, J.I. (1970). La Cuenca Minera Ciñera-Matallana. *Hullera Vaso Leonesa*, p. 228.

Weil, A.B., Gutiérrez-Alonso, G. and Fernández-Suárez, J. (2003). Orocline triggered lithosphere delamination. *GSA - Anual Meeting Abstracts*, p. 346, Seattle.

Weil, A.B., van der Voo, R. and van der Pluijm, B.A. (2001). Oroclinal bending and evidence against the Pangea megashear: The Cantabrian-Asturias arc (northern Spain). *Geology*, 29(11), p. 991-994.

Weil, A.B., van der Voo, R., van der Pluijm, B.A. and Pares, J.M. (2000). The formation of an orocline by multiphase deformation; a paleomagnetic investigation of the Cantabria-Asturias Arc (northern Spain). *Journal of Structural Geology*, 22(6), p. 735-756.

Weiland, E.F., Ludwig, K.R., Naeser, C.W. and Simmons, E.C. (1980). *Fission-track dating applied to uranium mineralization*. OF 80-380, U.S. Geological Survey.

Whitmarsh, R.B. and Miles, P.R. (1995). Models of the development of West Iberia rifted continental margin at 40 degrees 30' N deduced from surface and deep-tow magnetic anomalies. *Journal Geophysical Research*, 100, p. 3789-3806.

Winkler, H.G.F. (1979). *Petrogenesis of metamorphic rocks. 5 ed.*, Springer Verlag, New York, p. 384.

Witzke, B.J. (1990). Palaeoclimatic constraints for Palaeozoic palaeolatitudes of Laurentia and Euramerica. In W.S. McKerrow and C.R. Scotese, Eds. *Palaeozoic palaeogeography and biostratigraphy*, 12, p. 57-73.

Wolf, R.A., Farley, K. A., Silver, L.T. (1996). Assessment of (U-Th)/He thermochronometry: the low temperature history of the San Jacinto Mountains, California. *Geology*, 25, p. 65-68.

Yelland, A.J. (1990). Fission-track thermotectonics in the Pyrenean Orogen. *Nuclear Tracks and Radiation Measurements*, 17(3), p. 293-299.

Yenes, M., Gutierrez, A.G. and Alvarez, F. (1996). Dataciones k-ar de los granitoides del area laalberca-bejar (sistema central espanol). *Geogaceta*, 20(2), p. 479-482.

Zeitler, P.K. (1985). Cooling history of the NW Himalaya, Pakistan. *Tectonics*, 4, p. 121-151.

Ziegler, P.A. (1988). *Evolution of the Arctic-North Atlantic and the western Tethys*. AAPG Publications, 198 p.

Ziegler, P.A. (1990). *Geological atlas of Western and Central Europe* - 2nd Ed. Shell Int. Petroleum Mij., Den Haag, 239 p.

ZIEGLER, P.A. 1990. Geological Atlas of Western and Central Europe - 2nd Ed. Shell Int. Petroleum Mij., Den Haag, 239 p.

# Appendix i: AFT age parameters

Parameters of the AFT age calculation program *TRACKKEY 4.2* (Dunkl, 2002):

| 3.3 TK version | Sample: 25 | L. Camb. | Sed. Age: 542-518 Ma | Lith.: SS | | | | | | |
|---|---|---|---|---|---|---|---|---|---|---|
| ζ: | 338.04 | ζ err.: | 12.00 | Apatite | | | | | | |
| Irrad.: | 9/22/2003 | $\rho_d$: | 11.883 | CN_5 | | | | | | |
| Grid Size: | 1 µm² | $N_d$: | 13318 | | | | | | | |
| Crystal | $N_s$ | $N_i$ | Area (µm²) | $\rho_s$ (e5) | $\rho_i$ (e5) | Age (Ma) | ± 1σ | U (ppm) | $D_{par}$ | ± 1se |
| 1 | 30 | 27 | 10049.93 | 2.985 | 2.687 | 219.38 | 58.74 | 2.75 | 1.0 | 0.1 |
| 2 | 38 | 20 | 1818.57 | 20.896 | 10.998 | 370.72 | 103.31 | 11.26 | 2.0 | 0.1 |
| 3 | 19 | 6 | 7866.712 | 2.415 | 0.763 | 606.54 | 284.9 | 0.78 | 1.3 | 0.1 |
| 4 | 51 | 92 | 6958.721 | 7.329 | 13.221 | 110.38 | 19.69 | 13.54 | 1.6 | 0.2 |
| 5 | 29 | 26 | 2282.306 | 12.706 | 11.392 | 220.21 | 60.02 | 11.67 | 2.0 | 0.1 |
| 6 | 23 | 50 | 3297.917 | 6.974 | 15.161 | 91.73 | 23.35 | 15.53 | 1.4 | 0.1 |
| 7 | 15 | 29 | 2534.292 | 5.919 | 11.443 | 103.05 | 32.99 | 11.72 | 1.7 | 0.1 |
| 8 | 32 | 19 | 2477.946 | 12.914 | 7.668 | 329.68 | 96.24 | 7.85 | 1.4 | 0.1 |
| 9 | 8 | 7 | 3699.823 | 2.162 | 1.892 | 225.54 | 117.02 | 1.94 | 1.9 | 0.2 |
| 10 | 9 | 6 | 4496.524 | 2.002 | 1.334 | 294.43 | 155.55 | 1.37 | 1.8 | 0.1 |
| 11 | 77 | 147 | 8274.863 | 9.305 | 17.765 | 104.35 | 15.17 | 18.19 | 1.6 | 0.1 |

| 3.3 TK version | Sample: 18 | Neoproterozoic | Sed. Age:>542 Ma | Lith.: SS | | | | | | |
|---|---|---|---|---|---|---|---|---|---|---|
| ζ: | 303.57 | ζ err.: | 11.16 | Apatite | | | | | | |
| Irrad.: | 8/22/2003 | $\rho_d$: | 13.706 | CN_5 | | | | | | |
| Grid Size: | 1 µm² | $N_d$: | 10217 | | | | | | | |
| Crystal | $N_s$ | $N_i$ | Area (µm²) | $\rho_s$ (e5) | $\rho_i$ (e5) | Age (Ma) | ± 1σ | U (ppm) | $D_{par}$ | ± 1se |
| 1 | 47 | 49 | 5507.718 | 8.533 | 8.897 | 196.52 | 40.82 | 7.9 | 1.7 | 0.1 |
| 2 | 287 | 256 | 5695.673 | 50.389 | 44.946 | 229.11 | 21.54 | 39.91 | 1.6 | 0.1 |
| 3 | 65 | 19 | 3038.805 | 21.39 | 6.252 | 675.1 | 177.93 | 5.55 | 1.3 | 0.1 |
| 4 | 208 | 304 | 5395.717 | 38.549 | 56.341 | 140.79 | 13.76 | 50.03 | 2.0 | 0.1 |
| 5 | 28 | 52 | 8304.178 | 3.372 | 6.262 | 111.06 | 26.37 | 5.56 | 1.3 | 0.1 |
| 6 | 13 | 25 | 7197.306 | 1.806 | 3.474 | 107.28 | 36.91 | 3.08 | 1.5 | 0.3 |
| 7 | 60 | 63 | 6268.208 | 9.572 | 10.051 | 195.15 | 35.98 | 8.92 | 1.4 | 0.1 |
| 8 | 64 | 43 | 5188.171 | 12.336 | 8.288 | 302.43 | 60.74 | 7.36 | 1.4 | 0.0 |
| 9 | 134 | 125 | 3252.625 | 41.197 | 38.43 | 219.25 | 28.51 | 34.12 | 1.3 | 0.1 |
| 10 | 14 | 12 | 1215.555 | 11.517 | 9.872 | 238.26 | 94.17 | 8.77 | 1.8 | 0.0 |
| 11 | 107 | 172 | 3898.338 | 27.448 | 44.121 | 128.14 | 16.51 | 39.18 | 1.3 | 0.1 |
| 12 | 43 | 51 | 4564.579 | 9.42 | 11.173 | 173.06 | 36.43 | 9.92 | 1.7 | 0.1 |
| 13 | 67 | 51 | 2441.669 | 27.44 | 20.887 | 267.67 | 50.77 | 18.55 | 1.4 | 0.0 |
| 14 | 53 | 59 | 4489.085 | 11.806 | 13.143 | 184.23 | 35.56 | 11.67 | 1.7 | 0.0 |
| 15 | 18 | 13 | 1532.212 | 11.748 | 8.484 | 281.8 | 103.13 | 7.53 | 1.5 | 0.0 |
| 16 | 16 | 19 | 2156.822 | 7.418 | 8.809 | 172.85 | 59.02 | 7.82 | 1.7 | 0.1 |
| 17 | 5 | 2 | 1675.087 | 2.985 | 1.194 | 500.18 | 418.92 | 1.06 | 1.6 | 0.1 |
| 18 | 87 | 85 | 4906.214 | 17.733 | 17.325 | 209.49 | 32.93 | 15.38 | 1.5 | 0.1 |
| 19 | 258 | 289 | 4253.883 | 60.65 | 67.938 | 183.1 | 17.16 | 60.32 | 1.8 | 0.2 |
| 20 | 8 | 12 | 9492.159 | 0.843 | 1.264 | 137.22 | 62.85 | 1.12 | 1.3 | 0.1 |
| 21 | 37 | 56 | 3294.321 | 11.231 | 16.999 | 136.01 | 29.28 | 15.09 | 1.6 | 0.1 |
| 22 | 123 | 129 | 4277.843 | 28.753 | 30.155 | 195.37 | 25.72 | 26.78 | 1.3 | 0.1 |
| 23 | 39 | 55 | 4427.484 | 8.809 | 12.422 | 145.86 | 31.03 | 11.03 | 1.3 | 0.2 |
| 24 | 31 | 36 | 1701.363 | 18.221 | 21.16 | 176.7 | 43.82 | 18.79 | 1.6 | 0.0 |
| 25 | 161 | 257 | 4821.623 | 33.391 | 53.302 | 129.03 | 13.87 | 47.33 | 1.6 | 0.1 |

| 3.3 TK version | Sample 20 | Stephanian B | Str. Age: 302-301 Ma | Lith.: CNGL |
|---|---|---|---|---|
| ζ: | 338.04 | ζ err.: | 12.00 | Apatite |
| Irrad.: | 22/9/2003 | $\rho_d$: | 11.883 | CN_5 |
| Grid Size: | 1 μm² | $N_d$: | 13318 | |

| Crystal | $N_s$ | $N_i$ | Area (μm²) | $\rho_s$ (e5) | $\rho_i$ (e5) | Age (Ma) | ± 1σ | U (ppm) | $D_{par}$ | ± 1se |
|---|---|---|---|---|---|---|---|---|---|---|
| 1.001 | 46 | 58 | 5446.2 | 8.446 | 10.65 | 157.35 | 31.59 | 10.91 | 1.4 | 0.1 |
| 1.002 | 89 | 108 | 1851.956 | 48.057 | 58.317 | 163.42 | 24.15 | 59.73 | 1.9 | 0.0 |
| 1.003 | 79 | 58 | 9790.324 | 8.069 | 5.924 | 267.91 | 47.35 | 6.07 | 1.5 | 0.1 |
| 1.004 | 131 | 177 | 5161.172 | 25.382 | 34.295 | 146.96 | 17.77 | 35.12 | 1.6 | 0.1 |
| 1.005 | 214 | 170 | 5422.617 | 39.464 | 31.35 | 247.99 | 27.04 | 32.11 | 2.1 | 0.1 |
| 1.006 | 146 | 85 | 5158.216 | 28.304 | 16.479 | 336.06 | 47.47 | 16.88 | 1.9 | 0.0 |
| 1.007 | 165 | 100 | 3011.79 | 54.785 | 33.203 | 323.15 | 42.62 | 34.01 | 1.1 | 0.1 |
| 1.008 | 44 | 60 | 2316.152 | 18.997 | 25.905 | 145.62 | 29.39 | 26.53 | 1.9 | 0.1 |
| 1.009 | 122 | 102 | 3911.196 | 31.193 | 26.079 | 235.85 | 32.8 | 26.71 | 1.7 | 0.0 |
| 1.01 | 107 | 104 | 3042.877 | 35.164 | 34.178 | 203.39 | 28.98 | 35.01 | 1.5 | 0.1 |
| 1.011 | 9 | 24 | 2682.832 | 3.355 | 8.946 | 74.88 | 29.39 | 9.16 | 1.0 | 0.1 |
| 1.012 | 7 | 8 | 3324.686 | 2.105 | 2.406 | 173.38 | 89.96 | 2.46 | 1.9 | 0.0 |
| 1.013 | 61 | 66 | 3237.91 | 18.839 | 20.384 | 183 | 33.18 | 20.88 | 1.8 | 0.0 |
| 1.014 | 20 | 23 | 3676.323 | 5.44 | 6.256 | 172.32 | 53.06 | 6.41 | 1.7 | 0.1 |
| 1.015 | 11 | 10 | 1173.218 | 9.376 | 8.524 | 217.22 | 95.24 | 8.73 | 1.8 | 0.1 |
| 1.016 | 30 | 35 | 4027.828 | 7.448 | 8.69 | 169.89 | 42.72 | 8.9 | 1.4 | 0.0 |
| 1.017 | 30 | 34 | 1454.829 | 20.621 | 23.37 | 174.82 | 44.25 | 23.94 | 1.9 | 0.1 |
| 1.018 | 20 | 26 | 1213.945 | 16.475 | 21.418 | 152.67 | 45.75 | 21.94 | 1.8 | 0.1 |

| 3.3 TK version | Sample: 23 | Stephanian B | Str. Age: 302-301 Ma | Lith.: SS |
|---|---|---|---|---|
| ζ: | 344.68 | ζ err.: | 12.96 | Apatite |
| Irrad.: | 11/10/2003 | $\rho_d$: | 13.007 | CN_5 |
| Grid Size: | 1 μm² | $N_d$: | 22255 | |

| Cryst | $N_s$ | $N_i$ | Area (μm²) | $\rho_s$ (e5) | $\rho_i$ (e5) | Age (Ma) | ± 1σ | U (ppm) | $D_{par}$ | ± 1se |
|---|---|---|---|---|---|---|---|---|---|---|
| 1 | 14 | 17 | 6503.278 | 2.153 | 2.614 | 182.01 | 66.05 | 2.45 | 1.7 | 0.1 |
| 2 | 3 | 16 | 1110.156 | 2.702 | 14.412 | 41.89 | 26.41 | 13.49 | 1.5 | 0.2 |
| 3 | 8 | 22 | 2136.885 | 3.744 | 10.295 | 81 | 33.58 | 9.63 | 1.5 | 0.2 |
| 4 | 1 | 2 | 446.690 | 2.239 | 4.477 | 111.12 | 136.15 | 4.19 | 1.2 | - |
| 5 | 47 | 98 | 8747.384 | 5.373 | 11.203 | 106.62 | 19.35 | 10.48 | 1.5 | 0.1 |
| 6 | 13 | 47 | 2044.591 | 6.358 | 22.987 | 61.7 | 19.48 | 21.51 | 1.9 | 0.1 |
| 7 | 7 | 7 | 2621.018 | 2.671 | 2.671 | 220.35 | 118.08 | 2.5 | 1.7 | 0.1 |
| 8 | 31 | 64 | 4788.777 | 6.473 | 13.365 | 107.67 | 23.92 | 12.5 | 1.4 | 0.0 |
| 9 | 3 | 7 | 1655.38 | 1.812 | 4.229 | 95.36 | 65.9 | 3.96 | 1.5 | 0.0 |
| 10 | 10 | 7 | 2359.245 | 4.239 | 2.967 | 312.53 | 154.48 | 2.78 | 1.3 | 0.1 |
| 11 | 20 | 20 | 919.656 | 21.747 | 21.747 | 220.35 | 70.19 | 20.35 | 1.4 | 0.2 |
| 12 | 18 | 9 | 1182.414 | 15.223 | 7.612 | 433.41 | 177.71 | 7.12 | 1.2 | 0.0 |
| 13 | 9 | 5 | 5641.955 | 1.595 | 0.886 | 391.36 | 218.8 | 0.83 | 1.8 | 0.0 |

| 3.3 TK version | Sample 22 | Stephanian B | Sed. Age: 302-301 Ma | Lith.: CNGL |
|---|---|---|---|---|
| ζ: | 338.04 | ζ err.: | 12 | Apatite |
| Irrad.: | 9/22/2003 | $\rho_d$: | 11.883 | CN_5 |
| Grid Size: | 1 μm² | $N_d$: | 13318 | |

| Cryst | $N_s$ | $N_i$ | Area (μm²) | $\rho_s$ (e5) | $\rho_i$ (e5) | Age (Ma) | ± 1σ | U (ppm) | $D_{par}$ | ± 1se |
|---|---|---|---|---|---|---|---|---|---|---|
| 1.001 | 59 | 66 | 2783.994 | 21.193 | 23.707 | 177.08 | 32.38 | 24.28 | 1.9 | 0.0 |
| 1.002 | 109 | 87 | 3001.132 | 36.32 | 28.989 | 246.84 | 36.62 | 29.69 | 2.0 | 0.1 |
| 1.003 | 43 | 40 | 4711.395 | 9.127 | 8.49 | 212.36 | 47.29 | 8.7 | 1.7 | 0.0 |
| 1.004 | 34 | 32 | 2236.537 | 15.202 | 14.308 | 209.93 | 52.27 | 14.65 | 1.8 | 0.0 |
| 1.005 | 45 | 42 | 5959.466 | 7.551 | 7.048 | 211.67 | 46.07 | 7.22 | 1.6 | 0.0 |
| 1.006 | 84 | 101 | 7794.541 | 10.777 | 12.958 | 164.91 | 25.09 | 13.27 | 2.1 | 0.0 |
| 1.007 | 54 | 30 | 10210.98 | 5.288 | 2.938 | 351.74 | 81.12 | 3.01 | 1.4 | 0.0 |
| 1.008 | 260 | 222 | 7562.524 | 34.38 | 29.355 | 231.03 | 22.74 | 30.07 | 1.7 | 0.0 |
| 1.009 | 158 | 149 | 6256.942 | 25.252 | 23.814 | 209.53 | 25.12 | 24.39 | 1.7 | 0.1 |
| 1.01 | 43 | 65 | 3381.573 | 12.716 | 19.222 | 131.51 | 26.29 | 19.69 | 1.8 | 0.1 |
| 1.011 | 34 | 26 | 3890.225 | 8.74 | 6.683 | 257.43 | 67.72 | 6.85 | 1.7 | 0.1 |
| 1.012 | 70 | 61 | 9086.065 | 7.704 | 6.714 | 226.45 | 40.52 | 6.88 | 1.6 | 0.0 |
| 1.013 | 220 | 250 | 2834.723 | 77.609 | 88.192 | 174.36 | 17.33 | 90.33 | 1.5 | 0.0 |
| 1.014 | 131 | 272 | 11376.76 | 11.515 | 23.908 | 96.01 | 10.8 | 24.49 | 1.4 | 0.0 |
| 1.015 | 57 | 94 | 6160.575 | 9.252 | 15.258 | 120.65 | 20.73 | 15.63 | 1.9 | 0.1 |
| 1.016 | 396 | 470 | 10121.22 | 39.126 | 46.437 | 167.03 | 12.93 | 47.56 | 1.7 | 0.1 |
| 1.017 | 16 | 21 | 4951.36 | 3.231 | 4.241 | 151.23 | 50.49 | 4.34 | 2.0 | 0.1 |
| 1.018 | 296 | 458 | 7764.767 | 38.121 | 58.984 | 128.51 | 10.67 | 60.41 | 1.9 | 0.1 |
| 1.019 | 169 | 164 | 3685.52 | 45.855 | 44.498 | 203.71 | 23.54 | 45.58 | 1.7 | 0.1 |
| 1.02 | 42 | 52 | 6162.021 | 6.816 | 8.439 | 160.21 | 33.75 | 8.64 | 1.6 | 0.1 |
| 1.021 | 90 | 132 | 4769.071 | 18.872 | 27.678 | 135.5 | 19.17 | 28.35 | 1.8 | 0.0 |
| 1.022 | 56 | 52 | 5636.174 | 9.936 | 9.226 | 212.74 | 41.7 | 9.45 | 2.1 | 0.1 |
| 1.023 | 79 | 53 | 4007.071 | 19.715 | 13.227 | 292.62 | 53.05 | 13.55 | 1.5 | 0.1 |
| 1.024 | 58 | 63 | 4959.571 | 11.695 | 12.703 | 182.3 | 33.84 | 13.01 | 1.7 | 0.1 |
| 1.025 | 35 | 27 | 1983.828 | 17.643 | 13.61 | 255.23 | 66.04 | 13.94 | 1.8 | 0.1 |

| 3.3 TK version | Sample 114 | Stephanian B | Sed. Age: 302-301 Ma | Lith.: CNGL |
|---|---|---|---|---|
| ζ: | 338.04 | ζ err.: | 12.00 | Apatite |
| Irrad.: | 22/9/2003 | $\rho_d$: | 11.883 | CN_5 |
| Grid Size: | 1 μm$^2$ | $N_d$: | 13318 | |

| Crystal | $N_s$ | $N_i$ | Area (μm$^2$) | $\rho_s$ (e5) | $\rho_i$ (e5) | Age (Ma) | ± 1σ | U (ppm) | $D_{par}$ | ± 1se |
|---|---|---|---|---|---|---|---|---|---|---|
| 1 | 11 | 25 | 9765.592 | 1.126 | 2.56 | 87.77 | 31.92 | 2.62 | 1.3 | 0.1 |
| 2 | 27 | 40 | 6005.712 | 4.496 | 6.66 | 134.16 | 33.77 | 6.82 | 1.4 | 0.1 |
| 3 | 2 | 8 | 15122.75 | 0.132 | 0.529 | 50.01 | 39.58 | 0.54 | 1.4 | 0.1 |
| 4 | 3 | 3 | 4854.566 | 0.618 | 0.618 | 197.77 | 161.64 | 0.63 | 1.0 | 0.1 |
| 5 | 2 | 7 | 4712.726 | 0.424 | 1.485 | 57.13 | 45.85 | 1.52 | 1.2 | 0.1 |
| 6 | 66 | 110 | 7142.554 | 9.24 | 15.401 | 119.39 | 19.09 | 15.77 | 1.2 | 0.1 |
| 7 | 17 | 34 | 9575.19 | 1.775 | 3.551 | 99.64 | 29.82 | 3.64 | 1.0 | 0.1 |
| 8 | 202 | 249 | 4024.422 | 50.194 | 61.872 | 160.9 | 16.33 | 63.37 | 1.3 | 0.1 |
| 9 | 40 | 55 | 4197.488 | 9.53 | 13.103 | 144.43 | 30.47 | 13.42 | 1.3 | 0.1 |
| 10 | 95 | 31 | 5176.051 | 18.354 | 5.989 | 587.84 | 123.47 | 6.13 | 1.2 | 0.1 |
| 11 | 18 | 19 | 1613.88 | 11.153 | 11.773 | 187.51 | 62.06 | 12.06 | 1.6 | 0.1 |
| 12 | 10 | 5 | 4042.362 | 2.474 | 1.237 | 389.66 | 213.9 | 1.27 | 1.2 | 0.0 |
| 13 | 31 | 13 | 2164.853 | 14.32 | 6.005 | 461.97 | 153.58 | 6.15 | 1.5 | 0.1 |
| 14 | 2 | 3 | 11521.9 | 0.174 | 0.26 | 132.52 | 121.07 | 0.27 | 1.5 | - |
| 15 | 82 | 11 | 1092.157 | 75.081 | 10.072 | 1346.26 | 435.07 | 10.32 | 1.5 | 0.1 |

| 3.3 TK version | Sample 115 | Stephanian B | Sed. Age: 302-301 Ma | Lith.: SS/SH |
|---|---|---|---|---|
| ζ: | 338.04 | ζ err.: | 12 | Apatite |
| Irrad.: | 9/22/2003 | ρd: | 11.883 | CN_5 |
| Grid Size: | 1 μm2 | Nd: | 13318 | |

| Cryst | Ns | Ni | Area (μm2) | RhoS (e5) | Rhol (e5) | Age (Ma) | ± 1σ | U (ppm) | Dpar | ± 1se |
|---|---|---|---|---|---|---|---|---|---|---|
| 1 | 242 | 262 | 9039.819 | 26.77 | 28.983 | 182.89 | 17.62 | 29.68 | 1.4 | 0.0 |
| 2 | 73 | 34 | 5929.43 | 12.311 | 5.734 | 417.4 | 88 | 5.87 | 1.8 | 0.0 |
| 3 | 360 | 412 | 6077.921 | 59.231 | 67.786 | 173.14 | 14 | 69.43 | 1.4 | 0.0 |
| 4 | 39 | 41 | 3427.852 | 11.377 | 11.961 | 188.26 | 42.67 | 12.25 | 1.5 | 0.1 |
| 5 | 114 | 56 | 4501.172 | 25.327 | 12.441 | 396.41 | 66.29 | 12.74 | 1.8 | 0.1 |
| 6 | 223 | 136 | 7202.446 | 30.962 | 18.882 | 321.18 | 36.86 | 19.34 | 1.8 | 0.0 |
| 7 | 237 | 171 | 6838.394 | 34.657 | 25.006 | 272.51 | 29.1 | 25.61 | 1.6 | 0.0 |
| 8 | 225 | 178 | 9226.296 | 24.387 | 19.293 | 249 | 26.58 | 19.76 | 1.8 | 0.1 |
| 9 | 38 | 31 | 8782.431 | 4.327 | 3.53 | 241.6 | 59.14 | 3.62 | 1.8 | 0.1 |
| 10 | 14 | 12 | 5107.717 | 2.741 | 2.349 | 230.15 | 90.93 | 2.41 | 1.5 | 0.2 |
| 11 | 613 | 539 | 10837.42 | 56.563 | 49.735 | 224.46 | 15.59 | 50.94 | 1.7 | 0.0 |
| 12 | 221 | 159 | 6941.297 | 31.838 | 22.906 | 273.28 | 30.12 | 23.46 | 2.0 | 0.1 |
| 13 | 286 | 325 | 6544.17 | 43.703 | 49.663 | 174.36 | 15.51 | 50.86 | 1.9 | 0.1 |
| 14 | 38 | 34 | 5651.743 | 6.724 | 6.016 | 220.65 | 52.71 | 6.16 | 1.9 | 0.1 |
| 15 | 370 | 178 | 11272.02 | 32.825 | 15.791 | 404.51 | 39.75 | 16.17 | 1.3 | 0.0 |
| 16 | 67 | 62 | 7258.972 | 9.23 | 8.541 | 213.46 | 38.42 | 8.75 | 1.9 | 0.1 |
| 17 | 228 | 239 | 6920.736 | 32.944 | 34.534 | 188.8 | 18.79 | 35.37 | 1.5 | 0.1 |
| 18 | 97 | 67 | 4634.555 | 20.93 | 14.457 | 284.4 | 46.36 | 14.81 | 2.4 | 0.1 |
| 19 | 61 | 55 | 4229.217 | 14.423 | 13.005 | 218.99 | 41.5 | 13.32 | 2.2 | 0.1 |
| 20 | 98 | 74 | 6160.542 | 15.908 | 12.012 | 260.63 | 41.25 | 12.3 | 1.9 | 0.1 |
| 21 | 221 | 234 | 2857.173 | 77.349 | 81.899 | 186.94 | 18.82 | 83.88 | 1.7 | 0.2 |

| 3.3 TK version | Sample 104 | Neoproterozoic | Sed. Age: > 542 Ma | Lith.: SS/SH | | | | | | |
|---|---|---|---|---|---|---|---|---|---|---|
| ζ: | 338.04 | ζ err.: | 12.00 | Apatite | | | | | | |
| Irrad.: | 22/9/2003 | $\rho_d$: | 11.883 | CN_5 | | | | | | |
| Grid Size: | 1 μm² | $N_d$: | 13318 | | | | | | | |
| Crystal | $N_s$ | $N_i$ | Area (μm²) | $\rho_s$ (e5) | $\rho_i$ (e5) | Age (Ma) | ± 1σ | U (ppm) | $D_{par}$ | ± 1se |
| 1 | 120 | 90 | 5297.38 | 22.653 | 16.99 | 262.37 | 37.82 | 17.4 | 1.5 | 0.1 |
| 2 | 81 | 62 | 8416.31 | 9.624 | 7.367 | 257.19 | 44.4 | 7.54 | 1.5 | 0.9 |
| 3 | 254 | 143 | 9059.412 | 28.037 | 15.785 | 347.21 | 38.45 | 16.17 | 1.4 | 0.0 |
| 4 | 206 | 95 | 10323.25 | 19.955 | 9.203 | 421.42 | 54.49 | 9.43 | 1.4 | 0.1 |
| 5 | 103 | 81 | 6802.281 | 15.142 | 11.908 | 250.46 | 38.3 | 12.2 | 1.2 | 0.1 |
| 6 | 76 | 45 | 7940.716 | 9.571 | 5.667 | 330.57 | 63.34 | 5.8 | 1.8 | 0.1 |
| 7 | 24 | 28 | 2924.833 | 8.206 | 9.573 | 169.89 | 47.66 | 9.8 | 1.5 | 0.2 |
| 8 | 177 | 170 | 5566.839 | 31.795 | 30.538 | 205.79 | 23.34 | 31.28 | 1.8 | 0.0 |
| 9 | 101 | 69 | 7674.69 | 13.16 | 8.991 | 287.47 | 46.11 | 9.21 | 0.9 | 0.2 |
| 10 | 10 | 7 | 4387.02 | 2.279 | 1.596 | 280.71 | 138.72 | 1.63 | 1.1 | 0.1 |
| 11 | 85 | 93 | 10693.29 | 7.949 | 8.697 | 181 | 27.95 | 8.91 | 1.5 | 0.1 |
| 12 | 9 | 5 | 4403.606 | 2.044 | 1.135 | 351.74 | 196.61 | 1.16 | 1.4 | 0.1 |
| 13 | 65 | 73 | 6337.166 | 10.257 | 11.519 | 176.39 | 30.76 | 11.8 | 1.8 | 0.1 |
| 14 | 195 | 164 | 5985.989 | 32.576 | 27.397 | 234.48 | 26.28 | 28.06 | 1.4 | 0.1 |
| 15 | 290 | 288 | 6203.175 | 46.75 | 46.428 | 199.13 | 18.09 | 47.55 | 1.6 | 0.1 |
| 16 | 218 | 186 | 6569.608 | 33.183 | 28.312 | 231.19 | 24.58 | 29 | 1.8 | 0.1 |
| 17 | 16 | 9 | 7571.902 | 2.113 | 1.189 | 347.51 | 145.35 | 1.22 | 1.9 | 0.1 |
| 18 | 13 | 5 | 4516.445 | 2.878 | 1.107 | 502.11 | 264.86 | 1.13 | 1.4 | 0.1 |
| 19 | 144 | 131 | 4851.15 | 29.684 | 27.004 | 217.07 | 27.38 | 27.66 | 1.6 | 0.1 |
| 20 | 103 | 85 | 4471.414 | 23.035 | 19.01 | 238.89 | 36.08 | 19.47 | 1.3 | 0.1 |
| 21 | 81 | 62 | 8416.31 | 9.624 | 7.367 | 257.19 | 44.4 | 7.54 | 1.9 | 0.1 |
| 22 | 63 | 47 | 4024.035 | 15.656 | 11.68 | 263.74 | 51.74 | 11.96 | 1.6 | 0.1 |
| 23 | 117 | 128 | 4515.344 | 25.912 | 28.348 | 181.01 | 24.08 | 29.03 | 1.6 | 0.0 |
| 24 | 40 | 31 | 6706.917 | 5.964 | 4.622 | 254.07 | 61.5 | 4.73 | 1.4 | 0.0 |
| 25 | 136 | 180 | 5669.02 | 23.99 | 31.752 | 149.99 | 17.9 | 32.52 | 1.2 | 0.1 |
| 26 | 27 | 35 | 5583.623 | 4.836 | 6.268 | 153.1 | 39.61 | 6.42 | 1.5 | 0.1 |
| 27 | 139 | 147 | 4024.035 | 34.542 | 36.53 | 187.16 | 23.18 | 37.41 | 1.6 | 0.1 |

*AFT age parameters*

| 3.3 TK version | Sample 105 | Neoproterozoic | Sed Age: > 542 Ma | Lith.: SS | | | | | | |
|---|---|---|---|---|---|---|---|---|---|---|
| ζ: | 338.04 | ζ err.: | 12 | Apatite | | | | | | |
| Irrad.: | 22/9/2003 | $\rho_d$: | 11.883 | CN_5 | | | | | | |
| Grid Size: | 1 μm² | $N_d$: | 13318 | | | | | | | |
| Crystal | $N_s$ | $N_i$ | Area (μm$_2$) | $\rho_s$ (e5) | $\rho_i$ (e5) | Age (Ma) | ± 1σ | U (ppm) | $D_{par}$ | ± 1se |
| 1 | 330 | 249 | 8177.544 | 40.354 | 30.449 | 260.82 | 23.88 | 31.19 | 1.2 | 0.1 |
| 2 | 223 | 82 | 5161.468 | 43.205 | 15.887 | 524.27 | 70.37 | 16.27 | 1.2 | 0.0 |
| 3 | 36 | 19 | 3137.208 | 11.475 | 6.056 | 369.73 | 105.71 | 6.2 | 1.2 | 0.1 |
| 4 | 102 | 53 | 6684.943 | 15.258 | 7.928 | 375.37 | 65.02 | 8.12 | 1.1 | 0.3 |
| 5 | 183 | 139 | 2923.027 | 62.606 | 47.553 | 259.13 | 30.65 | 48.7 | 1.3 | 0.0 |
| 6 | 55 | 62 | 4346.637 | 12.653 | 14.264 | 175.75 | 33.18 | 14.61 | 1.2 | 0.0 |
| 7 | 16 | 9 | 1871.483 | 8.549 | 4.809 | 347.51 | 145.35 | 4.93 | 1.3 | 0.1 |
| 8 | 258 | 261 | 2326.006 | 110.92 | 112.21 | 195.53 | 18.59 | 114.92 | 1.1 | 0.0 |
| 9 | 57 | 64 | 2619.048 | 21.764 | 24.436 | 176.43 | 32.77 | 25.03 | 1.2 | 0.1 |
| 10 | 48 | 21 | 2830.125 | 16.96 | 7.42 | 443.45 | 117.15 | 7.6 | 1.2 | 0.0 |
| 11 | 166 | 181 | 4033.79 | 41.152 | 44.871 | 181.61 | 20.61 | 45.96 | 1.0 | 0.1 |
| 12 | 149 | 80 | 6413.957 | 23.231 | 12.473 | 363.61 | 52.12 | 12.77 | 1.0 | 0.1 |
| 13 | 145 | 152 | 5636.207 | 25.727 | 26.968 | 188.8 | 22.98 | 27.62 | 1.2 | 0.0 |
| 14 | 190 | 81 | 6039.181 | 31.461 | 13.412 | 454.68 | 62.58 | 13.74 | 1.2 | 0.0 |
| 15 | 106 | 64 | 8613.641 | 12.306 | 7.43 | 324.34 | 52.69 | 7.61 | 1.4 | 0.0 |
| 16 | 14 | 9 | 6704.568 | 2.088 | 1.342 | 305.08 | 130.82 | 1.37 | 1.2 | 0.1 |
| 17 | 100 | 71 | 4816.548 | 20.762 | 14.741 | 276.84 | 44.14 | 15.1 | 1.2 | 0.1 |
| 18 | 264 | 219 | 4826.237 | 54.701 | 45.377 | 237.67 | 23.39 | 46.47 | 1.3 | 0.1 |
| 19 | 67 | 46 | 2123.485 | 31.552 | 21.663 | 286.08 | 55.77 | 22.19 | 1.1 | 0.0 |
| 20 | 101 | 71 | 2016.673 | 50.082 | 35.206 | 279.55 | 44.48 | 36.06 | 1.3 | 0.1 |
| 21 | 29 | 15 | 6253.658 | 4.637 | 2.399 | 377.04 | 120.7 | 2.46 | 1.5 | 0.0 |
| 22 | 50 | 43 | 3028.294 | 16.511 | 14.199 | 229.4 | 48.44 | 14.54 | 1.4 | 0.0 |
| 23 | 54 | 64 | 3974.226 | 13.588 | 16.104 | 167.27 | 31.51 | 16.49 | 1.0 | 0.1 |
| 24 | 76 | 47 | 2734.004 | 27.798 | 17.191 | 316.84 | 59.92 | 17.61 | 1.4 | 0.0 |
| 25 | 19 | 17 | 4268.516 | 4.451 | 3.983 | 220.65 | 74.1 | 4.08 | 1.0 | 0.0 |
| 26 | 147 | 132 | 3578.774 | 41.076 | 36.884 | 219.87 | 27.56 | 37.78 | 1.3 | 0.1 |
| 27 | 214 | 215 | 10641.73 | 20.11 | 20.203 | 196.87 | 20.33 | 20.69 | 1.4 | 0.0 |
| 28 | 77 | 67 | 3376.45 | 22.805 | 19.843 | 226.78 | 38.78 | 20.32 | 1.5 | 0.3 |
| 29 | 50 | 40 | 2903.484 | 17.221 | 13.777 | 246.28 | 53.01 | 14.11 | 1.0 | 0.2 |
| 30 | 72 | 60 | 8257.192 | 8.72 | 7.266 | 236.61 | 42.25 | 7.44 | 1.2 | 0.2 |

| 3.3 TK version | Sample 106 | Neoproterozoic | Sed. Age: > 542 Ma | Lith.: SS |
|---|---|---|---|---|
| ζ: | 338.04 | ζ err.: | 12 | Apatite |
| Irrad.: | 22/9/2003 | $\rho^d$: | 11.883 | CN_5 |
| Grid Size: | 1 μm² | $N^d$: | 13318 | |

| Crystal | $N_s$ | $N_i$ | Area (μm²) | $\rho_s$ (e5) | $\rho_i$ (e5) | Age (Ma) | ± 1σ | U (ppm) | $D_{par}$ | ± 1se |
|---|---|---|---|---|---|---|---|---|---|---|
| 1 | 169 | 153 | 6343.981 | 26.639 | 24.117 | 218.11 | 25.61 | 24.7 | 0.9 | 0.0 |
| 2 | 87 | 81 | 6240.52 | 13.941 | 12.98 | 212.18 | 33.67 | 13.29 | 1.1 | 0.1 |
| 3 | 298 | 206 | 6807.29 | 43.777 | 30.262 | 284.18 | 27.76 | 30.99 | 1.1 | 0.0 |
| 4 | 115 | 63 | 8500.77 | 13.528 | 7.411 | 356.56 | 57.39 | 7.59 | 1.3 | 0.1 |
| 5 | 59 | 67 | 6354.228 | 9.285 | 10.544 | 174.47 | 31.8 | 10.8 | 1.4 | 0.1 |
| 6 | 149 | 154 | 6338.545 | 23.507 | 24.296 | 191.45 | 23.09 | 24.88 | 1.4 | 0.1 |
| 7 | 58 | 37 | 5294.44 | 10.955 | 6.988 | 307.38 | 65.64 | 7.16 | 1.1 | 0.1 |
| 8 | 101 | 85 | 7368.806 | 13.706 | 11.535 | 234.33 | 35.54 | 11.81 | 1.0 | 0.0 |
| 9 | 54 | 83 | 3429.33 | 15.747 | 24.203 | 129.36 | 23.1 | 24.79 | 1.0 | 0.1 |
| 10 | 201 | 310 | 4228.872 | 47.53 | 73.306 | 128.92 | 12.59 | 75.08 | 1.2 | 0.0 |
| 11 | 118 | 127 | 5122.267 | 23.037 | 24.794 | 183.96 | 24.46 | 25.39 | 1.3 | 0.1 |
| 12 | 65 | 42 | 6119.651 | 10.622 | 6.863 | 303.56 | 61.11 | 7.03 | 1.2 | - |
| 13 | 19 | 11 | 7203.383 | 2.638 | 1.527 | 337.89 | 128.61 | 1.56 | 0.9 | 0.0 |
| 14 | 58 | 47 | 6290.936 | 9.22 | 7.471 | 243.2 | 48.55 | 7.65 | 1.5 | 0.1 |
| 15 | 53 | 75 | 6047.983 | 8.763 | 12.401 | 140.39 | 25.71 | 12.7 | 1.1 | 0.0 |
| 16 | 21 | 21 | 5437.923 | 3.862 | 3.862 | 197.77 | 61.46 | 3.96 | 1.0 | 0.1 |
| 17 | 51 | 42 | 2944.211 | 17.322 | 14.265 | 239.37 | 50.64 | 14.61 | 1.1 | 0.0 |
| 18 | 128 | 112 | 4508.447 | 28.391 | 24.842 | 225.54 | 30.32 | 25.44 | 1.1 | 0.0 |
| 19 | 54 | 59 | 7275.789 | 7.422 | 8.109 | 181.25 | 34.77 | 8.31 | 1.2 | 0.0 |
| 20 | 99 | 70 | 8258.901 | 11.987 | 8.476 | 277.96 | 44.58 | 8.68 | 1.4 | 0.1 |
| 21 | 18 | 58 | 3996.577 | 4.504 | 14.512 | 62.03 | 16.89 | 14.86 | 1.5 | 0.0 |
| 22 | 16 | 14 | 7629.002 | 2.097 | 1.835 | 225.54 | 82.95 | 1.88 | 1.1 | 0.1 |
| 23 | 115 | 167 | 6380.242 | 18.024 | 26.175 | 136.84 | 17.32 | 26.81 | 1.0 | 0.0 |
| 24 | 49 | 47 | 4211.234 | 11.636 | 11.161 | 206.06 | 42.74 | 11.43 | 1.1 | 0.1 |
| 25 | 63 | 47 | 3761.095 | 16.75 | 12.496 | 263.74 | 51.74 | 12.8 | 1.1 | 0.0 |
| 26 | 84 | 81 | 4868.689 | 17.253 | 16.637 | 204.98 | 32.79 | 17.04 | 1.2 | 0.0 |
| 27 | 142 | 187 | 9132.245 | 15.549 | 20.477 | 150.73 | 17.66 | 20.97 | 1.4 | 0.0 |
| 28 | 49 | 83 | 2685.558 | 18.246 | 30.906 | 117.49 | 21.6 | 31.65 | 1.0 | 0.0 |
| 29 | 13 | 23 | 4270.272 | 3.044 | 5.386 | 112.53 | 39.26 | 5.52 | 1.1 | 0.0 |

| 3.3 TK version | Sample 84 | L. Cambrian | Sed. Age: 542-518 Ma | CNGL |
|---|---|---|---|---|
| ζ: | 325.7 | ζ err.: | 12.37 | Apatite |
| Irrad.: | 10/12/2003 | $\rho_d$: | 12.235 | CN_5 |
| Grid Size: | 1 μm² | $N_d$: | 15423 | |

| Crystal | $N_s$ | $N_i$ | Area (μm²) | $\rho_s$ (e5) | $\rho_i$ (e5) | Age (Ma) | ± 1σ | U (ppm) | $D_{par}$ | ± 1se |
|---|---|---|---|---|---|---|---|---|---|---|
| 1 | 3 | 25 | 10733.69 | 0.279 | 2.329 | 23.86 | 14.61 | 2.32 | 1.6 | 0.4 |
| 2 | 28 | 82 | 12472.83 | 2.245 | 6.574 | 67.68 | 15.04 | 6.54 | 1.4 | 0.2 |
| 3 | 31 | 364 | 8263.762 | 3.751 | 44.048 | 16.95 | 3.24 | 43.81 | 1.2 | 0.2 |
| 4 | 6 | 137 | 17105.59 | 0.351 | 8.009 | 8.72 | 3.65 | 7.97 | 1.0 | 0.1 |
| 5 | 53 | 605 | 4861.036 | 10.903 | 124.459 | 17.43 | 2.59 | 123.8 | 1.3 | 0.1 |
| 6 | 10 | 142 | 18425.96 | 0.543 | 7.707 | 14.02 | 4.62 | 7.67 | 1.2 | 0.1 |
| 7 | 76 | 649 | 6903.985 | 11.008 | 94.004 | 23.29 | 2.96 | 93.51 | 1.2 | 0.1 |
| 8 | 10 | 160 | 17289.52 | 0.578 | 9.254 | 12.44 | 4.08 | 9.21 | 1.0 | 0.0 |
| 9 | 36 | 193 | 9163.71 | 3.929 | 21.061 | 37.06 | 6.88 | 20.95 | 1.4 | 0.0 |
| 10 | 3 | 9 | 6503.278 | 0.461 | 1.384 | 66.07 | 44.12 | 1.38 | 1.0 | 0.1 |
| 11 | 9 | 25 | 10484.07 | 0.858 | 2.385 | 71.33 | 27.87 | 2.37 | 1.2 | 0.1 |
| 12 | 124 | 718 | 9984.831 | 12.419 | 71.909 | 34.32 | 3.59 | 71.53 | 1.4 | 0.0 |
| 13 | 3 | 26 | 9814.038 | 0.306 | 2.649 | 22.95 | 14.02 | 2.64 | 1.1 | 0.1 |

| 3.3 TK version | Sample 83 | U. Camb.-Ordov. | Sed. Age: 490-468 | VOL/PYRO |
|---|---|---|---|---|
| ζ: | 344.68 | ζ err.: | 12.96 | Apatite |
| Irrad.: | 10/11/2003 | ρd: | 13.007 | CN_5 |
| Grid Size: | 1 μm² | $N_d$: | 22255 | |

| Crystal | $N_s$ | $N_i$ | Area (μm²) | $\rho_s$ (e5) | $\rho_i$ (e5) | Age (Ma) | ± 1σ | U (ppm) | $D_{par}$ | ± 1se |
|---|---|---|---|---|---|---|---|---|---|---|
| 1 | 93 | 170 | 6187.968 | 15.029 | 27.473 | 121.48 | 16.34 | 25.71 | 1.0 | 0.0 |
| 2 | 30 | 45 | 12054.06 | 2.489 | 3.733 | 147.73 | 35.28 | 3.49 | 1.2 | 0.1 |
| 3 | 138 | 263 | 12612.42 | 10.942 | 20.852 | 116.56 | 13.04 | 19.51 | 1.0 | 0.1 |
| 4 | 100 | 204 | 10109.64 | 9.892 | 20.179 | 108.96 | 13.94 | 18.88 | 1.0 | 0.1 |
| 5 | 86 | 232 | 13735.71 | 6.261 | 16.89 | 82.56 | 10.89 | 15.8 | 1.0 | 0.1 |
| 6 | 39 | 54 | 18353.7 | 2.125 | 2.942 | 159.89 | 34.15 | 2.75 | 1.7 | 0.1 |
| 7 | 27 | 47 | 5806.968 | 4.65 | 8.094 | 127.5 | 31.17 | 7.57 | 1.7 | 0.1 |
| 8 | 55 | 105 | 8749.865 | 6.286 | 12 | 116.36 | 19.87 | 11.23 | 2.0 | 0.0 |
| 9 | 175 | 245 | 7309.948 | 23.94 | 33.516 | 158.16 | 16.78 | 31.36 | 1.2 | 0.1 |
| 10 | 56 | 102 | 5347.14 | 10.473 | 19.076 | 121.91 | 20.8 | 17.85 | 1.2 | 0.1 |
| 11 | 88 | 155 | 10273.87 | 8.565 | 15.087 | 126.02 | 17.5 | 14.12 | 1.4 | 0.0 |
| 12 | 42 | 85 | 12329.95 | 3.406 | 6.894 | 109.82 | 21.13 | 6.45 | 1.1 | 0.1 |
| 13 | 132 | 287 | 16980.78 | 7.773 | 16.901 | 102.28 | 11.44 | 15.81 | 1.0 | 0.1 |
| 14 | 56 | 149 | 10503.78 | 5.331 | 14.185 | 83.7 | 13.5 | 13.27 | 1.1 | 0.1 |
| 15 | 32 | 73 | 9157.142 | 3.495 | 7.972 | 97.52 | 21.01 | 7.46 | 1.4 | 0.1 |
| 16 | 166 | 240 | 4072.76 | 40.759 | 58.928 | 153.21 | 16.54 | 55.14 | 1.4 | 0.1 |
| 17 | 31 | 58 | 922.832 | 33.592 | 62.85 | 118.71 | 26.8 | 58.81 | 1.6 | 0.0 |
| 18 | 125 | 162 | 5675.588 | 22.024 | 28.543 | 170.68 | 21.34 | 26.71 | 1.4 | 0.7 |
| 19 | 112 | 154 | 6180.151 | 18.123 | 24.918 | 161 | 20.92 | 23.32 | 1.2 | 0.0 |
| 20 | 47 | 122 | 7864.04 | 5.977 | 15.514 | 85.78 | 15.09 | 14.52 | 1.3 | 0.1 |
| 21 | 69 | 102 | 9007.04 | 7.661 | 11.324 | 149.88 | 24.05 | 10.6 | 1.5 | 0.1 |
| 22 | 35 | 32 | 5813.537 | 6.02 | 5.504 | 240.62 | 59.57 | 5.15 | 1.7 | 0.1 |
| 23 | 180 | 339 | 8790.855 | 20.476 | 38.563 | 117.94 | 11.77 | 36.08 | 1.3 | 0.1 |
| 24 | 11 | 22 | 5852.951 | 1.879 | 3.759 | 111.12 | 41.25 | 3.52 | 1.8 | 0.2 |
| 25 | 66 | 94 | 6030.313 | 10.945 | 15.588 | 155.5 | 25.67 | 14.59 | 1.7 | 0.0 |

| 3.3 TK version | Sample 85 | Stephanian B | Sed. Age: 302-301 Ma | CNGL |
|---|---|---|---|---|
| ζ: | 325.7 | ζ err.: | 12.37 | Apatite |
| Irrad.: | 10/12/2003 | $\rho_d$: | 12.235 | CN_5 |
| Grid Size: | 1 μm² | $N_d$: | 15423 | |

| Crystal | Ns | Ni | Area (μm²) | $\rho_s$ (e5) | $\rho_i$ (e5) | Age (Ma) | ± 1σ | U (ppm) | Dpar | ± 1se |
|---|---|---|---|---|---|---|---|---|---|---|
| 1 | 147 | 168 | 2942.733 | 49.954 | 57.09 | 172.02 | 20.54 | 56.79 | 1. | 0.1 |
| 2 | 106 | 87 | 8951.96 | 11.841 | 9.719 | 238.3 | 35.69 | 9.67 | 1.5 | 0.2 |
| 3 | 105 | 156 | 5672.255 | 18.511 | 27.502 | 132.73 | 17.53 | 27.36 | 1.6 | 0.1 |
| 4 | 89 | 90 | 5408.231 | 16.456 | 16.641 | 194.08 | 29.97 | 16.55 | 1.3 | 0.1 |
| 5 | 190 | 273 | 12258.51 | 15.499 | 22.27 | 137.2 | 14.01 | 22.15 | 1.0 | 0.1 |
| 6 | 152 | 188 | 12349.82 | 12.308 | 15.223 | 159.11 | 18.42 | 15.14 | 1.1 | 0.1 |
| 7 | 54 | 45 | 10246.98 | 5.27 | 4.392 | 234.76 | 48.25 | 4.37 | 1.6 | 0.2 |
| 8 | 216 | 180 | 12844.66 | 16.816 | 14.014 | 234.76 | 25.39 | 13.94 | 1.4 | 0.1 |
| 9 | 261 | 351 | 4728.573 | 55.196 | 74.23 | 146.48 | 13.25 | 73.84 | 1.2 | 0.1 |
| 10 | 117 | 79 | 3081.174 | 37.973 | 25.64 | 288.53 | 43.48 | 25.5 | 1.4 | 0.1 |
| 11 | 155 | 141 | 3029.148 | 51.17 | 46.548 | 215.39 | 26.42 | 46.3 | 1.3 | 0.2 |
| 12 | 63 | 96 | 9773.491 | 6.446 | 9.822 | 129.44 | 21.58 | 9.77 | 1.4 | 0.0 |
| 13 | 252 | 205 | 9879.859 | 25.506 | 20.749 | 240.38 | 24.46 | 20.64 | 1.4 | 0.2 |
| 14 | 100 | 129 | 8443.653 | 11.843 | 15.278 | 152.63 | 21.18 | 15.2 | 1.4 | 0.1 |
| 15 | 401 | 613 | 7884.864 | 50.857 | 77.744 | 129.04 | 9.68 | 77.33 | 1.1 | 0.0 |
| 16 | 176 | 203 | 8521.758 | 20.653 | 23.821 | 170.47 | 18.76 | 23.7 | 1.3 | 0.0 |
| 17 | 39 | 33 | 8931.826 | 4.366 | 3.695 | 231.27 | 55.43 | 3.68 | 1.7 | 0.0 |
| 18 | 73 | 95 | 8682.616 | 8.408 | 10.941 | 151.31 | 24.27 | 10.88 | 1.3 | 0.1 |
| 19 | 112 | 103 | 7504.98 | 14.923 | 13.724 | 213.09 | 30.24 | 13.65 | 1.6 | 0.2 |
| 20 | 157 | 151 | 6976.49 | 22.504 | 21.644 | 203.9 | 24.55 | 21.53 | 1.5 | 0.2 |

*AFT age parameters*

| 3.3 TK version | Sample 91 | M. Bashkir.-Kasmov. | Sed. Age:~316-304 Ma | SS |
|---|---|---|---|---|
| ζ: | 344.68 | ζ err.: | 12.96 | Apatite |
| Irrad.: | 10/11/2003 | $\rho_d$: | 13.007 | CN_5 |
| Grid Size: | 1 μm² | $N_d$: | 22255 | |

| Crystal | $N_s$ | $N_i$ | Area (μm²) | $\rho_s$ (e5) | $\rho_i$ (e5) | Age (Ma) | ± 1σ | U (ppm) | $D_{par}$ | ± 1se |
|---|---|---|---|---|---|---|---|---|---|---|
| 1 | 9 | 172 | 7147.037 | 1.259 | 24.066 | 11.72 | 4.03 | 22.52 | 1.0 | 0.2 |
| 2 | 23 | 227 | 15069.21 | 1.526 | 15.064 | 22.67 | 5.04 | 14.09 | 1.0 | 0.1 |
| 3 | 18 | 81 | 5058.105 | 3.559 | 16.014 | 49.62 | 13.07 | 14.98 | 1.1 | 0.0 |
| 4 | 13 | 81 | 3704.898 | 3.509 | 21.863 | 35.88 | 10.81 | 20.46 | 1.3 | 0.0 |
| 5 | 19 | 132 | 5793.83 | 3.279 | 22.783 | 32.18 | 7.99 | 21.32 | 1.4 | 0.1 |
| 6 | 15 | 109 | 2942.898 | 5.097 | 37.038 | 30.77 | 8.56 | 34.66 | 1.3 | 0.2 |
| 7 | 45 | 556 | 6076.295 | 7.406 | 91.503 | 18.12 | 2.89 | 85.62 | 1.4 | 0.1 |
| 8 | 4 | 53 | 3678.622 | 1.087 | 14.408 | 16.9 | 8.78 | 13.48 | 1.3 | 0.1 |
| 9 | 22 | 160 | 9130.865 | 2.409 | 17.523 | 30.75 | 7.09 | 16.4 | 1.1 | 0.2 |
| 10 | 36 | 289 | 6385.037 | 5.638 | 45.262 | 27.86 | 5.04 | 42.35 | 1.0 | 0.0 |
| 11 | 6 | 70 | 5806.968 | 1.033 | 12.054 | 19.18 | 8.19 | 11.28 | 1.2 | 0.0 |
| 12 | 55 | 583 | 9459.313 | 5.814 | 61.632 | 21.11 | 3.09 | 57.67 | 1.1 | 0.0 |
| 13 | 112 | 657 | 12349.66 | 9.069 | 53.2 | 38.1 | 4.16 | 49.78 | 1.5 | 0.1 |
| 14 | 51 | 133 | 6831.727 | 7.465 | 19.468 | 85.39 | 14.44 | 18.22 | 1.5 | 0.1 |
| 15 | 24 | 151 | 2522.484 | 9.514 | 59.862 | 35.53 | 7.92 | 56.01 | 1.3 | 0.1 |
| 16 | 43 | 373 | 4729.657 | 9.092 | 78.864 | 25.79 | 4.27 | 73.79 | 1.4 | 0.1 |
| 17 | 25 | 198 | 4926.726 | 5.074 | 40.189 | 28.24 | 6.09 | 37.6 | 1.2 | 0.1 |
| 18 | 51 | 481 | 5498.226 | 9.276 | 87.483 | 23.72 | 3.61 | 81.86 | 1.1 | 0.0 |
| 19 | 28 | 332 | 8552.796 | 3.274 | 38.818 | 18.88 | 3.78 | 36.32 | 1.1 | 0.0 |
| 20 | 13 | 51 | 5590.192 | 2.326 | 9.123 | 56.89 | 17.81 | 8.54 | 1.1 | 0.0 |
| 21 | 11 | 86 | 5990.899 | 1.836 | 14.355 | 28.61 | 9.23 | 13.43 | 1.0 | 0.1 |
| 22 | 14 | 119 | 7357.244 | 1.903 | 16.175 | 26.32 | 7.5 | 15.13 | 1.3 | 0.2 |
| 23 | 37 | 226 | 5550.778 | 6.666 | 40.715 | 36.59 | 6.64 | 38.1 | 1.0 | 0.1 |
| 24 | 22 | 125 | 4617.984 | 4.764 | 27.068 | 39.33 | 9.22 | 25.33 | 0.9 | 0.1 |
| 25 | 64 | 400 | 5242.037 | 12.209 | 76.306 | 35.77 | 5.01 | 71.4 | 0.9 | 0.0 |
| 26 | 27 | 163 | 6477.002 | 4.169 | 25.166 | 37.02 | 7.82 | 23.55 | 1.2 | 0.0 |
| 27 | 15 | 263 | 6733.192 | 2.228 | 39.06 | 12.77 | 3.43 | 36.55 | 1.1 | 0.1 |
| 28 | 10 | 89 | 2870.639 | 3.484 | 31.004 | 25.14 | 8.44 | 29.01 | 1.0 | 0.0 |
| 29 | 38 | 225 | 4269.829 | 8.9 | 52.695 | 37.75 | 6.78 | 49.31 | 1.1 | 0.0 |
| 30 | 46 | 496 | 6207.675 | 7.41 | 79.901 | 20.76 | 3.3 | 74.76 | 1.0 | 0.0 |

| 3.3 TK version | Sample 97 | M. Bashkir-Kasmov. | Sed. Age:~316-304 Ma | SS | | | | | | |
|---|---|---|---|---|---|---|---|---|---|---|
| ζ: | 325.7 | ζ err.: | 12.37 | Apatite | | | | | | |
| Irrad.: | 10/12/2003 | $\rho_d$: | 12.235 | CN_5 | | | | | | |
| Grid Size: | 1 μm² | $N_d$: | 15423 | | | | | | | |
| Crystal | $N_s$ | $N_i$ | Area (μm²) | $\rho_s$ (e5) | $\rho_i$ (e5) | Age (Ma) | ± 1σ | U (ppm) | $D_{par}$ | ± 1se |
| 1 | 132 | 874 | 6937.52 | 19.027 | 125.982 | 30.02 | 3.04 | 125.32 | 1.0 | 0.0 |
| 2 | 32 | 97 | 10778.59 | 2.969 | 8.999 | 65.4 | 13.57 | 8.95 | 1.4 | 0.1 |
| 3 | 7 | 11 | 3133.398 | 2.234 | 3.511 | 125.56 | 60.9 | 3.49 | 1.6 | 0.1 |
| 4 | 16 | 81 | 10226.09 | 1.565 | 7.921 | 39.24 | 10.84 | 7.88 | 1.45 | 0.1 |
| 5 | 13 | 12 | 2708.829 | 4.799 | 4.43 | 212.31 | 85.39 | 4.41 | 1.7 | 0.1 |
| 6 | 21 | 15 | 5286.393 | 3.972 | 2.837 | 273.07 | 92.92 | 2.82 | 1.5 | 0.2 |
| 7 | 4 | 3 | 3447.394 | 1.16 | 0.87 | 260.33 | 199.09 | 0.87 | 1.5 | - |
| 8 | 21 | 56 | 7236.014 | 2.902 | 7.739 | 74.29 | 19.23 | 7.7 | 1.8 | 0.1 |
| 9 | 7 | 18 | 3856.017 | 1.815 | 4.668 | 77.02 | 34.44 | 4.64 | 2.1 | 0.1 |
| 10 | 35 | 105 | 5807.116 | 6.027 | 18.081 | 66.07 | 13.15 | 17.99 | 1.6 | 0.1 |
| 11 | 4 | 2 | 2637.161 | 1.517 | 0.758 | 386.65 | 335.19 | 0.75 | 1.7 | 0.2 |
| 12 | 1 | 5 | 10594.2 | 0.094 | 0.472 | 39.73 | 43.54 | 0.47 | 1.7 | 0.1 |
| 13 | 47 | 308 | 4985.748 | 9.427 | 61.776 | 30.33 | 4.89 | 61.45 | 2.2 | 0.4 |
| 14 | 15 | 140 | 5022.715 | 2.986 | 27.873 | 21.31 | 5.85 | 27.73 | 1.0 | 0.1 |
| 15 | 62 | 36 | 8557.937 | 7.245 | 4.207 | 334.32 | 71.25 | 4.18 | 1.1 | 0.1 |
| 16 | 5 | 5 | 2736.074 | 1.827 | 1.827 | 196.23 | 124.34 | 1.82 | 2.0 | 0.4 |
| 17 | 47 | 66 | 4300.457 | 10.929 | 15.347 | 140.35 | 27.34 | 15.27 | 1.4 | 0.1 |
| 18 | 20 | 113 | 6849.66 | 2.92 | 16.497 | 35.17 | 8.64 | 16.41 | 1.7 | 0.1 |
| 19 | 17 | 12 | 3093.541 | 5.495 | 3.879 | 276.25 | 104.71 | 3.86 | 1.7 | 0.2 |
| 20 | 121 | 96 | 8181.19 | 14.79 | 11.734 | 246.36 | 35 | 11.67 | 1.5 | 0.1 |

*AFT age parameters*

| 3.3 TK version | Sample 62 | M.Bashkir.-Kasimov. | Sed. Age:~316-304 Ma | SS/SH | | | | | | |
|---|---|---|---|---|---|---|---|---|---|---|
| ζ: | 325.7 | ζ err.: | 12.37 | Apatite | | | | | | |
| Irrad.: | 10/111/2003 | $\rho_d$: | 12.235 | CN_5 | | | | | | |
| Grid Size: | 1 μm² | $N_d$: | 22255 | | | | | | | |
| Crystal | $N_s$ | $N_i$ | Area (μm²) | $\rho_s$ (e5) | $\rho_i$ (e5) | Age (Ma) | ± 1σ | U (ppm) | $D_{par}$ | ± 1se |
| 1 | 24 | 123 | 3438.198 | 6.98 | 35.775 | 38.76 | 8.78 | 35.59 | 1.4 | 0.1 |
| 2 | 21 | 35 | 4309.243 | 4.873 | 8.122 | 118.45 | 33.01 | 8.08 | 1.6 | 0.1 |
| 3 | 11 | 11 | 6601.813 | 1.666 | 1.666 | 196.23 | 84.01 | 1.66 | 1.8 | 0.1 |
| 4 | 42 | 153 | 6542.692 | 6.419 | 23.385 | 54.46 | 9.72 | 23.26 | 1.9 | 0.3 |
| 5 | 6 | 6 | 6936.832 | 0.865 | 0.865 | 196.23 | 113.54 | 0.86 | 1.8 | 0.1 |
| 6 | 54 | 124 | 7910.351 | 6.826 | 15.676 | 86.19 | 14.44 | 15.59 | 1.6 | 0.1 |
| 7 | 46 | 124 | 2443.656 | 18.824 | 50.744 | 73.49 | 13 | 50.48 | 1.8 | 0.2 |
| 8 | 6 | 45 | 2719.306 | 2.206 | 16.548 | 26.51 | 11.57 | 16.46 | 1.6 | 0.1 |
| 9 | 9 | 40 | 4655.871 | 1.933 | 8.591 | 44.67 | 16.57 | 8.55 | 1.5 | 0.1 |
| 10 | 25 | 114 | 3711.467 | 6.736 | 30.716 | 43.55 | 9.76 | 30.55 | 1.4 | 0.0 |
| 11 | 9 | 34 | 4315.812 | 2.085 | 7.878 | 52.53 | 19.79 | 7.84 | 1.5 | 0.1 |
| 12 | 7 | 65 | 2667.001 | 2.625 | 24.372 | 21.42 | 8.56 | 24.24 | 1.3 | 0.1 |
| 13 | 9 | 32 | 3731.174 | 2.412 | 8.576 | 55.79 | 21.16 | 8.53 | 1.4 | 0.0 |
| 14 | 14 | 110 | 3474.984 | 4.029 | 31.655 | 25.31 | 7.25 | 31.49 | 1.5 | 0.1 |
| 15 | 4 | 6 | 2148.052 | 1.862 | 2.793 | 131.48 | 85.02 | 2.78 | 1.5 | 0.0 |
| 16 | 5 | 60 | 5302.405 | 0.943 | 11.316 | 16.58 | 7.75 | 11.26 | 1.4 | 0.1 |
| 17 | 25 | 270 | 5651.086 | 4.424 | 47.778 | 18.42 | 3.92 | 47.53 | 1.7 | 0.1 |
| 18 | 5 | 8 | 3400.591 | 1.47 | 2.353 | 123.34 | 70.47 | 2.34 | 1.5 | 0.1 |
| 19 | 3 | 42 | 1760.763 | 1.704 | 23.853 | 14.22 | 8.51 | 23.73 | 1.3 | 0.1 |
| 20 | 8 | 85 | 4499.743 | 1.778 | 18.89 | 18.72 | 6.96 | 18.79 | 1.6 | 0.3 |
| 21 | 26 | 228 | 4125.312 | 6.303 | 55.269 | 22.68 | 4.78 | 54.98 | 1.2 | 0.0 |
| 22 | 33 | 259 | 5045.937 | 6.54 | 51.328 | 25.34 | 4.78 | 51.06 | 1.5 | 0.1 |
| 23 | 65 | 459 | 7009.089 | 9.274 | 65.486 | 28.15 | 3.89 | 65.14 | 1.4 | 0.1 |
| 24 | 17 | 85 | 7305.678 | 2.327 | 11.635 | 39.73 | 10.67 | 11.57 | 1.4 | 0.1 |
| 25 | 6 | 74 | 3494.691 | 1.717 | 21.175 | 16.13 | 6.88 | 21.06 | 1.7 | 0.1 |

| 3.3 TK version | Sample 10 | Serpukhov. | Sed. Age: 326-318 Ma | SS |
|---|---|---|---|---|
| ζ: | 338.04 | ζ err.: | 12 | Apatite |
| Irrad.: | 22/9/2003 | $\rho_d$: | 11.883 | CN_5 |
| Grid Size: | 1 μm² | $N_d$: | 13318 | |

| Crystal | $N_s$ | $N_i$ | Area (μm²) | $\rho_s$ (e5) | $\rho_i$ (e5) | Age (Ma) | ± 1σ | U (ppm) | $D_{par}$ | ± 1se |
|---|---|---|---|---|---|---|---|---|---|---|
| 1 | 91 | 77 | 3416.389 | 26.636 | 22.538 | 233.09 | 37.08 | 23.08 | 1.3 | 0.1 |
| 2 | 48 | 38 | 3258.044 | 14.733 | 11.663 | 248.83 | 54.79 | 11.95 | 1.2 | 0.1 |
| 3 | 127 | 111 | 7487.95 | 16.961 | 14.824 | 225.79 | 30.48 | 15.18 | 1.9 | 0.1 |
| 4 | 255 | 201 | 4356.343 | 58.535 | 46.14 | 249.89 | 25.28 | 47.26 | 2.0 | 0.1 |
| 5 | 8 | 33 | 4382.487 | 1.825 | 7.53 | 48.51 | 19.2 | 7.71 | 1.4 | 0.1 |
| 6 | 26 | 51 | 3559.182 | 7.305 | 14.329 | 101.58 | 24.76 | 14.68 | 1.6 | 0.0 |
| 7 | 568 | 804 | 6355.969 | 89.365 | 126.495 | 140.35 | 9.25 | 129.56 | 1.5 | 0.1 |
| 8 | 26 | 23 | 2500.297 | 10.399 | 9.199 | 223.13 | 64.39 | 9.42 | 1.5 | 0.1 |
| 9 | 17 | 14 | 3194.062 | 5.322 | 4.383 | 239.37 | 86.83 | 4.49 | 1.4 | 0.0 |
| 10 | 135 | 166 | 5040.681 | 26.782 | 32.932 | 161.3 | 19.6 | 33.73 | 1.4 | 0.0 |
| 11 | 32 | 47 | 4983.827 | 6.421 | 9.431 | 135.31 | 31.4 | 9.66 | 1.5 | 0.1 |
| 12 | 118 | 102 | 4696.319 | 25.126 | 21.719 | 228.25 | 31.97 | 22.24 | 2.0 | 0.0 |
| 13 | 20 | 36 | 7817.072 | 2.559 | 4.605 | 110.62 | 31.11 | 4.72 | 1.3 | 0.1 |
| 14 | 111 | 112 | 9231.601 | 12.024 | 12.132 | 196.03 | 27.21 | 12.43 | 1.2 | 0.0 |
| 15 | 117 | 310 | 7074.844 | 16.537 | 43.817 | 75.36 | 8.63 | 44.88 | 1.5 | 0.0 |
| 16 | 54 | 42 | 6437.588 | 8.388 | 6.524 | 253.18 | 52.9 | 6.68 | 1.5 | 0.1 |
| 17 | 58 | 59 | 12553.3 | 4.62 | 4.7 | 194.47 | 36.65 | 4.81 | 1.4 | 0.0 |
| 18 | 22 | 16 | 1644.147 | 13.381 | 9.731 | 270.4 | 89.39 | 9.97 | 1.5 | 0.0 |
| 19 | 44 | 81 | 4099.43 | 10.733 | 19.759 | 108.18 | 20.64 | 20.24 | 1.8 | 0.1 |
| 20 | 15 | 11 | 4622.583 | 3.245 | 2.38 | 268.21 | 106.92 | 2.44 | 2.0 | 0.0 |
| 21 | 17 | 27 | 2009.513 | 8.46 | 13.436 | 125.23 | 39.04 | 13.76 | 1.8 | 0.0 |
| 22 | 135 | 55 | 2876.42 | 46.933 | 19.121 | 475.03 | 77.95 | 19.58 | 1.0 | 0.1 |
| 23 | 199 | 185 | 6660.934 | 29.876 | 27.774 | 212.5 | 23.05 | 28.45 | 2.2 | 0.2 |
| 24 | 99 | 144 | 16317.32 | 6.067 | 8.825 | 136.62 | 18.52 | 9.04 | 1.3 | 0.1 |
| 25 | 42 | 77 | 8506.813 | 4.937 | 9.052 | 108.63 | 21.21 | 9.27 | 1.3 | 0.0 |

## *AFT age parameters*

| 3.3 TK version | Sample 26 | Bashkir.-Moscov. | Sed. Age: 318-307 Ma | SS |
|---|---|---|---|---|
| ζ: | 303.57 | ζ err.: | 11.16 | Apatite |
| Irrad.: | Aug-22-3 | $\rho_d$: | 13.706 | CN_5 |
| Grid Size: | 1 μm² | $N_d$: | 10217 | |

| Crystal | $N_s$ | $N_i$ | Area (μm²) | $\rho_s$ (e5) | $\rho_i$ (e5) | Age (Ma) | ± 1σ | U (ppm) | $D_{par}$ | ± 1se |
|---|---|---|---|---|---|---|---|---|---|---|
| 1 | 10 | 14 | 2546.198 | 3.927 | 5.498 | 146.91 | 61.08 | 4.88 | 1.6 | 0.1 |
| 2 | 2 | 11 | 3661.231 | 0.546 | 3.004 | 37.71 | 29.03 | 2.67 | 1.1 | 0.1 |
| 3 | 9 | 18 | 8311.813 | 1.083 | 2.166 | 103.19 | 42.31 | 1.92 | 1.6 | 0.1 |
| 4 | 5 | 12 | 6496.184 | 0.77 | 1.847 | 86.11 | 45.95 | 1.64 | 1.5 | 0.2 |
| 5 | 13 | 21 | 7306.663 | 1.779 | 2.874 | 127.52 | 45.26 | 2.55 | 1.6 | 0.1 |
| 6 | 6 | 11 | 2812.11 | 2.134 | 3.912 | 112.49 | 57.25 | 3.47 | 1.5 | 0.1 |
| 7 | 3 | 5 | 2590.67 | 1.158 | 1.93 | 123.63 | 90.41 | 1.71 | 1.4 | 0.1 |
| 8 | 5 | 20 | 2608.898 | 1.917 | 7.666 | 51.8 | 25.98 | 6.81 | 1.7 | 0.1 |
| 9 | 3 | 10 | 2552.832 | 1.175 | 3.917 | 62.11 | 40.96 | 3.48 | 1.9 | 0.2 |
| 10 | 3 | 6 | 2107.653 | 1.423 | 2.847 | 103.19 | 73.07 | 2.53 | 1.6 | 0.2 |
| 11 | 1 | 5 | 3035.849 | 0.329 | 1.647 | 41.47 | 45.46 | 1.46 | 1.0 | - |
| 12 | 3 | 7 | 4715.534 | 0.636 | 1.484 | 88.55 | 61.2 | 1.32 | 1.7 | 0.2 |
| 13 | 4 | 13 | 6197.493 | 0.645 | 2.098 | 63.7 | 36.5 | 1.86 | 1.5 | 0.3 |
| 14 | 5 | 8 | 6109.731 | 0.818 | 1.309 | 128.73 | 73.55 | 1.16 | 1.5 | 0.1 |
| 15 | 3 | 7 | 7070.969 | 0.424 | 0.99 | 88.55 | 61.2 | 0.88 | 1.6 | 0.2 |
| 16 | 3 | 4 | 4650.501 | 0.645 | 0.86 | 154.17 | 117.9 | 0.76 | 1.6 | 0.0 |
| 17 | 2 | 8 | 4861.299 | 0.411 | 1.646 | 51.8 | 41 | 1.46 | 1.0 | 0.0 |
| 18 | 3 | 5 | 3171.563 | 0.946 | 1.577 | 123.63 | 90.41 | 1.4 | 0.9 | 0.5 |
| 19 | 4 | 10 | 3421.71 | 1.169 | 2.923 | 82.68 | 49.02 | 2.59 | 1.4 | 0.0 |
| 20 | 3 | 5 | 6595.72 | 0.455 | 0.758 | 123.63 | 90.41 | 0.67 | 1.4 | 0.2 |
| 21 | 8 | 12 | 8010.889 | 0.999 | 1.498 | 137.22 | 62.85 | 1.33 | 1.8 | 0.1 |
| 22 | 6 | 16 | 8238.603 | 0.728 | 1.942 | 77.55 | 37.24 | 1.72 | 1.4 | 0.1 |
| 23 | 5 | 7 | 12393.87 | 0.403 | 0.565 | 146.91 | 86.2 | 0.5 | 1.6 | 0.1 |
| 24 | 2 | 7 | 5830.402 | 0.343 | 1.201 | 59.17 | 47.49 | 1.07 | 1.2 | 0.1 |
| 25 | 8 | 19 | 8051.059 | 0.994 | 2.36 | 87.01 | 36.82 | 2.1 | 2.1 | 0.2 |
| 26 | 38 | 54 | 2690.436 | 14.124 | 20.071 | 144.76 | 31.14 | 17.82 | 1.5 | 0.1 |
| 27 | 7 | 25 | 4554.068 | 1.537 | 5.49 | 57.99 | 24.9 | 4.87 | 1.5 | 0.1 |
| 28 | 7 | 26 | 4227.886 | 1.656 | 6.15 | 55.77 | 23.84 | 5.46 | 1.0 | 0.1 |
| 29 | 1 | 3 | 4175.138 | 0.24 | 0.719 | 68.98 | 79.69 | 0.64 | 2.2 | - |
| 30 | 2 | 3 | 2792.074 | 0.716 | 1.074 | 137.22 | 125.37 | 0.95 | 1.8 | 0.1 |
| 31 | 5 | 12 | 7249.316 | 0.69 | 1.655 | 86.11 | 45.95 | 1.47 | 1.5 | 0.1 |
| 32 | 4 | 17 | 2200.276 | 1.818 | 7.726 | 48.77 | 27.16 | 6.86 | 1.2 | 0.0 |
| 33 | 4 | 15 | 4348.131 | 0.92 | 3.45 | 55.24 | 31.16 | 3.06 | 1.3 | 0.1 |
| 34 | 11 | 8 | 2424.442 | 4.537 | 3.3 | 279.89 | 130.49 | 2.93 | 1.1 | 0.1 |

| 3.3 TK version | Sample 9 | U. Devon.: Fras.-Famm. | Sed. Age: 385-359 Ma | CNGL |
|---|---|---|---|---|
| ζ: | 303.57 | ζ err.: | 11.16 | Apatite |
| Irrad.: | Aug-22-3 | $\rho_d$: | 13.706 | CN_5 |
| Grid Size: | 1 μm² | $N_d$: | 10217 | |

| Crystal | $N_s$ | $N_i$ | Area (μm²) | $\rho_s$ (e5) | $\rho_i$ (e5) | Age (Ma) | ± 1σ | U (ppm) | $D_{par}$ | ± 1se |
|---|---|---|---|---|---|---|---|---|---|---|
| 1 | 53 | 99 | 3153.105 | 16.809 | 31.389 | 110.42 | 19.26 | 27.879 | 1.7 | 0.1 |
| 2 | 67 | 27 | 7784.227 | 8.607 | 3.469 | 496.62 | 114.77 | 3.08 | 1.7 | 0.1 |
| 3 | 65 | 35 | 5969.878 | 9.38 | 5.863 | 324.55 | 71.02 | 5.206 | 2.0 | 0.2 |
| 4 | 28 | 54 | 9275.383 | 3.019 | 5.822 | 106.98 | 25.24 | 5.169 | 2.6 | 0.1 |
| 5 | 53 | 114 | 5452.244 | 9.721 | 20.909 | 96 | 16.37 | 18.565 | 1.6 | 0.0 |
| 6 | 52 | 79 | 4184.006 | 12.428 | 18.881 | 135.5 | 24.74 | 16.765 | 2.4 | 0.2 |
| 7 | 11 | 47 | 3901.967 | 2.819 | 12.045 | 48.51 | 16.35 | 10.695 | 1.5 | 0.1 |
| 8 | 13 | 5 | 1129.863 | 11.506 | 4.425 | 519.4 | 274.04 | 3.929 | 1.3 | 0.1 |
| 9 | 109 | 186 | 8549.84 | 12.749 | 21.755 | 120.78 | 15.28 | 19.317 | 1.8 | 0.1 |
| 10 | 17 | 63 | 5156.64 | 3.297 | 12.217 | 55.89 | 15.42 | 10.848 | 1.4 | 0.1 |
| 11 | 11 | 24 | 2483.07 | 4.027 | 9.665 | 86.11 | 32.57 | 8.582 | 1.4 | 0.0 |
| 12 | 86 | 104 | 4711.592 | 18.253 | 22.073 | 169.78 | 25.58 | 19.599 | 1.6 | 0.1 |
| 13 | 46 | 57 | 299.325 | 15.337 | 19.004 | 165.74 | 33.45 | 16.874 | 1.6 | 0.1 |
| 14 | 68 | 20 | 1771.421 | 38.387 | 11.29 | 671.15 | 172.62 | 10.025 | 1.4 | 0.1 |

| 3.3 TK version | Sample 8 | M. Camb. | Sed. Age: 513-501 Ma | SS |
|---|---|---|---|---|
| ζ: | 303.57 | ζ err.: | 11.16 | Apatite |
| Irrad.: | 22/8/3 | $\rho_d$: | 13.706 | CN_5 |
| Grid Size: | 1 μm² | $N_d$: | 10217 | |

| Crystal | $N_s$ | $N_i$ | Area (μm²) | $\rho_s$ (e5) | $\rho_i$ (e5) | Age (Ma) | ± 1σ | U (ppm) | $D_{par}$ | ± 1se |
|---|---|---|---|---|---|---|---|---|---|---|
| 1 | 199 | 235 | 9539.587 | 20.86 | 24.634 | 173.81 | 18 | 21.87 | 2.4 | 0.3 |
| 2 | 135 | 148 | 2983.034 | 45.256 | 49.614 | 187.03 | 23.37 | 44.05 | 1.9 | 0.2 |
| 3 | 173 | 280 | 7578.224 | 22.829 | 36.948 | 127.27 | 13.23 | 32.81 | 1.9 | 0.3 |
| 4 | 78 | 92 | 6651.359 | 11.727 | 13.832 | 174.01 | 27.59 | 12.28 | 1.9 | 0.0 |
| 5 | 35 | 49 | 6750.6 | 5.185 | 7.259 | 146.91 | 32.99 | 6.45 | 2.6 | 0.0 |
| 6 | 61 | 103 | 5636.322 | 10.823 | 18.274 | 122.05 | 20.26 | 16.23 | 1.9 | 0.1 |
| 7 | 90 | 187 | 5988.288 | 15.029 | 31.228 | 99.36 | 13.3 | 27.73 | 1.8 | 0.0 |
| 8 | 189 | 238 | 8307.101 | 22.752 | 28.65 | 163.13 | 17.06 | 25.44 | 1.7 | 0.1 |
| 9 | 101 | 165 | 3637.353 | 27.767 | 45.363 | 126.1 | 16.64 | 40.28 | 2.2 | 0.2 |
| 10 | 157 | 141 | 3168.18 | 49.555 | 44.505 | 227.58 | 27.79 | 39.52 | 1.9 | 0.0 |
| 11 | 28 | 47 | 4658.449 | 6.011 | 10.089 | 122.76 | 29.68 | 8.96 | 2.0 | 0.5 |
| 12 | 51 | 55 | 3933.498 | 12.966 | 13.982 | 190.08 | 37.65 | 12.42 | 2.2 | 0.2 |
| 13 | 209 | 304 | 4274.099 | 48.899 | 71.126 | 141.46 | 13.81 | 63.15 | 2.1 | 0.1 |
| 14 | 58 | 97 | 6675.714 | 8.688 | 14.53 | 123.21 | 20.98 | 12.9 | 1.5 | 0.1 |
| 15 | 29 | 49 | 2844.33 | 10.196 | 17.227 | 121.96 | 28.95 | 15.3 | 2.0 | 0.2 |
| 16 | 199 | 175 | 4933.722 | 40.335 | 35.47 | 232.33 | 25.65 | 31.49 | 1.3 | 0.1 |
| 17 | 74 | 98 | 3589.547 | 20.615 | 27.301 | 155.21 | 24.62 | 24.24 | 1.9 | 0.0 |
| 18 | 47 | 38 | 4335.65 | 10.84 | 8.765 | 252.31 | 55.87 | 7.78 | 2.3 | 0.1 |
| 19 | 269 | 307 | 4199.82 | 64.05 | 73.098 | 179.76 | 16.5 | 64.91 | 1.6 | 0.2 |
| 20 | 98 | 137 | 2464.381 | 39.767 | 55.592 | 147.12 | 20.25 | 49.36 | 2.1 | 0.2 |

| 3.3 TK version | Sample 3 | Stephanian B | Sed. Age: 302-301 Ma | CNGL |
|---|---|---|---|---|
| z: | 303.57 | Zeta err.: | 11.16 | Apatite |
| Irrad.: | 22/8/2003 | $\rho_d$: | 13.706 | CN_5 |
| Grid Size: | 1 μm² | $N_d$: | 10217 | |

| Crystal | $N_s$ | $N_i$ | Area (μm²) | $\rho_s$ (e5) | $\rho_i$ (e5) | Age (Ma) | ± 1σ | U (ppm) | $D_{par}$ | ± 1se |
|---|---|---|---|---|---|---|---|---|---|---|
| 1 | 124 | 193 | 1261.932 | 98.262 | 152.94 | 132.3 | 16.04 | 135.8 | 1.7 | 0.1 |
| 2 | 32 | 98 | 1703.596 | 18.784 | 57.525 | 67.58 | 14 | 51.08 | 1.4 | 0.1 |
| 3 | 8 | 13 | 495.169 | 16.156 | 26.254 | 126.77 | 57.17 | 23.31 | 1.6 | 0.1 |
| 4 | 21 | 23 | 2161.585 | 9.715 | 10.64 | 187.2 | 56.95 | 9.45 | 2.0 | 0.1 |
| 5 | 9 | 13 | 3097.383 | 2.906 | 4.197 | 142.44 | 62 | 3.73 | 2.0 | 0.1 |
| 6 | 23 | 18 | 550.972 | 41.744 | 32.67 | 260.49 | 82.57 | 29.01 | 1.7 | 0.1 |
| 7 | 59 | 83 | 1493.258 | 39.511 | 55.583 | 146.21 | 25.51 | 49.35 | 1.5 | 0.1 |
| 8 | 78 | 122 | 1667.795 | 46.768 | 73.15 | 131.66 | 19.73 | 64.95 | 2.0 | 0.1 |
| 9 | 22 | 24 | 1655.281 | 13.291 | 14.499 | 187.94 | 55.93 | 12.87 | 1.9 | 0.1 |
| 10 | 79 | 102 | 2572.654 | 30.708 | 39.648 | 159.15 | 24.61 | 35.2 | 1.9 | 0.1 |

| 3.3 TK version | Sample 72 | Stephanian B | Sed. Age: 302-301 Ma | SS |
|---|---|---|---|---|
| ζ: | 344.68 | ζ err.: | 12.96 | Apatite |
| Irrad.: | 10/11/2003 | $\rho_d$: | 13.007 | CN_5 |
| Grid Size: | 1 μm² | $N_d$: | 22255 | |

| Crystal | $N_s$ | $N_i$ | Area (μm²) | $\rho_s$ (e5) | $\rho_i$ (e5) | Age (Ma) | ± 1σ | U (ppm) | $D_{par}$ | ± 1se |
|---|---|---|---|---|---|---|---|---|---|---|
| 1 | 42 | 46 | 1332.597 | 31.517 | 34.519 | 201.48 | 43.68 | 32.3 | 1.0 | 0.0 |
| 2 | 30 | 19 | 4241.665 | 7.073 | 4.479 | 344.56 | 101.88 | 4.19 | 1.2 | 0.1 |
| 3 | 10 | 7 | 1686.385 | 5.93 | 4.151 | 312.53 | 154.48 | 3.88 | 1.1 | 0.1 |
| 4 | 27 | 21 | 906.321 | 29.791 | 23.171 | 281.95 | 82.74 | 21.68 | 1.3 | 0.1 |
| 5 | 12 | 36 | 2266.688 | 5.294 | 15.882 | 74.29 | 24.93 | 14.86 | 1.5 | 0.1 |
| 6 | 7 | 22 | 2157.463 | 3.245 | 10.197 | 70.93 | 30.9 | 9.54 | 1.4 | 0.1 |
| 7 | 3 | 2 | 3859.696 | 0.777 | 0.518 | 327.76 | 299.47 | 0.48 | 1.2 | 0.1 |
| 8 | 24 | 6 | 2733.955 | 8.778 | 2.195 | 839.51 | 384.52 | 2.05 | 0.9 | 0.0 |
| 9 | 32 | 91 | 2204.496 | 14.516 | 41.279 | 78.35 | 16.38 | 38.62 | 1.8 | 0.2 |
| 10 | 2 | 3 | 487.253 | 4.105 | 6.157 | 147.73 | 134.98 | 5.76 | 1.4 | 0.1 |
| 11 | 6 | 8 | 1832.972 | 3.273 | 4.364 | 165.96 | 89.85 | 4.08 | 1.4 | 0.2 |
| 12 | 3 | 18 | 1037.831 | 2.891 | 17.344 | 37.25 | 23.27 | 16.23 | 1.2 | 0.1 |
| 13 | 5 | 13 | 3884.625 | 1.287 | 3.347 | 85.64 | 45.19 | 3.13 | 1.2 | 0.0 |
| 14 | 12 | 4 | 2950.666 | 4.067 | 1.356 | 639.66 | 370.12 | 1.27 | 1.9 | 0.1 |
| 15 | 3 | 3 | 1574.91 | 1.905 | 1.905 | 220.35 | 180.11 | 1.78 | 1.2 | 0.1 |
| 16 | 11 | 25 | 1862.795 | 5.905 | 13.421 | 97.88 | 35.61 | 12.56 | 1.2 | 0.1 |
| 17 | 24 | 40 | 5371.708 | 4.468 | 7.446 | 133.11 | 34.74 | 6.97 | 1.5 | 0.1 |
| 18 | 50 | 57 | 5319.402 | 9.4 | 10.715 | 193.69 | 38.25 | 10.03 | 1.5 | 0.1 |
| 19 | 17 | 11 | 5237.307 | 3.246 | 2.1 | 337.44 | 131.21 | 1.97 | 1.3 | 0.0 |
| 20 | 45 | 66 | 6072.879 | 7.41 | 10.868 | 151.05 | 29.77 | 10.17 | 1.5 | 0.1 |
| 21 | 20 | 16 | 2744.4 | 7.288 | 5.83 | 274.28 | 92.59 | 5.46 | 1.2 | 0.0 |
| 22 | 24 | 92 | 2045.807 | 11.731 | 44.97 | 58.21 | 13.53 | 42.08 | 1.0 | 0.0 |
| 23 | 67 | 132 | 3304.733 | 20.274 | 39.943 | 112.78 | 17.46 | 37.37 | 1.0 | 0.1 |
| 24 | 66 | 116 | 3290.15 | 20.06 | 35.257 | 126.29 | 20.06 | 32.99 | 1.1 | 0.2 |
| 25 | 3 | 2 | 9000.865 | 0.333 | 0.222 | 327.76 | 299.47 | 0.21 | 1.5 | 0.1 |
| 26 | 29 | 20 | 7831.967 | 3.703 | 2.554 | 317.1 | 92.96 | 2.39 | 1.4 | 0.2 |
| 27 | 57 | 60 | 7927.693 | 7.19 | 7.568 | 209.51 | 39.57 | 7.08 | 1.3 | 0.1 |
| 28 | 11 | 5 | 4727.555 | 2.327 | 1.058 | 475.19 | 256.94 | 0.99 | 1.3 | 0.1 |

| 3.3 TK version | Sample 73 | Stephanian B | Sed. Age: 302-301 Ma | SS |
|---|---|---|---|---|
| ζ: | 344.68 | ζ err.: | 12.96 | Apatite |
| Irrad.: | 10/11/2003 | $\rho_d$: | 13.007 | CN_5 |
| Grid Size: | 1 μm² | $N_d$: | 22255 | |

| Crystal | $N_s$ | $N_i$ | Area (μm²) | $\rho_s$ (e5) | $\rho_i$ (e5) | Age (Ma) | ± 1σ | U (ppm) | $D_{par}$ | ± 1se |
|---|---|---|---|---|---|---|---|---|---|---|
| 1 | 29 | 22 | 10733.69 | 2.702 | 2.05 | 288.91 | 82.43 | 1.92 | 1.2 | 0.2 |
| 2 | 88 | 193 | 19956.53 | 4.41 | 9.671 | 101.4 | 13.61 | 9.05 | 1.3 | 0.2 |
| 3 | 51 | 96 | 7061.641 | 7.222 | 13.595 | 118 | 20.94 | 12.72 | 1.1 | 0.1 |
| 4 | 94 | 215 | 17394.63 | 5.404 | 12.36 | 97.27 | 12.59 | 11.57 | 1.2 | 0.1 |
| 5 | 57 | 61 | 16474.97 | 3.46 | 3.703 | 206.13 | 38.78 | 3.46 | 1.5 | 0.1 |
| 6 | 5 | 5 | 8487.106 | 0.589 | 0.589 | 220.35 | 139.61 | 0.55 | 1.7 | 0.1 |
| 7 | 30 | 57 | 886.811 | 33.829 | 64.275 | 116.91 | 26.75 | 60.14 | 1.2 | 0.2 |
| 8 | 56 | 68 | 5524.502 | 10.137 | 12.309 | 182.01 | 33.57 | 11.52 | 1.2 | 0.2 |
| 9 | 144 | 135 | 660.934 | 217.874 | 204.257 | 234.77 | 29.52 | 191.12 | 1.5 | 0.1 |
| 10 | 197 | 243 | 5393.123 | 36.528 | 45.057 | 179.21 | 18.49 | 42.16 | 1.4 | 0.1 |
| 11 | 9 | 22 | 14024.75 | 0.642 | 1.569 | 91.05 | 36.2 | 1.47 | 1.2 | 0.1 |
| 12 | 173 | 266 | 4217.277 | 41.022 | 63.074 | 144.16 | 15.12 | 59.02 | 1.3 | 0.2 |
| 13 | 25 | 28 | 11765.02 | 2.125 | 2.38 | 197.1 | 54.75 | 2.23 | 1.4 | 0.1 |
| 14 | 5 | 5 | 22006.04 | 0.227 | 0.227 | 220.35 | 139.61 | 0.21 | 1.4 | 0.1 |
| 15 | 175 | 236 | 6897.417 | 25.372 | 34.216 | 164.11 | 17.53 | 32.01 | 1.4 | 0.1 |
| 16 | 45 | 61 | 7928.744 | 5.676 | 7.694 | 163.28 | 32.69 | 7.2 | 1.0 | 0.1 |
| 17 | 134 | 137 | 10436.78 | 12.839 | 13.127 | 215.6 | 27.46 | 12.28 | 1.5 | 0.1 |
| 18 | 113 | 177 | 11226.37 | 10.066 | 15.766 | 141.54 | 17.88 | 14.75 | 1.5 | 0.4 |
| 19 | 63 | 82 | 11929.25 | 5.281 | 6.874 | 169.96 | 29.2 | 6.43 | 1.2 | 0.1 |
| 20 | 69 | 135 | 13499.23 | 5.111 | 10.001 | 113.56 | 17.36 | 9.36 | 1.4 | 0.2 |
| 21 | 41 | 54 | 4506.312 | 9.098 | 11.983 | 167.99 | 35.38 | 11.21 | 1.3 | 0.1 |
| 22 | 122 | 144 | 8926.899 | 13.667 | 16.131 | 187.17 | 24.11 | 15.09 | 1.4 | 0.1 |
| 23 | 288 | 328 | 11941.07 | 24.118 | 27.468 | 193.88 | 17.32 | 25.7 | 1.2 | 0.1 |
| 24 | 189 | 205 | 13991.9 | 13.508 | 14.651 | 203.42 | 21.94 | 13.71 | 1.3 | 0.1 |
| 25 | 86 | 139 | 3527.536 | 24.38 | 39.404 | 137.22 | 19.54 | 36.87 | 1.2 | 0.1 |

## *AFT age parameters*

| 3.3 TK version | Sample 74 | Stephanian B | Sed. Age: 302-301 Ma | SS |
|---|---|---|---|---|
| ζ: | 344.68 | ζ err.: | 12.96 | Apatite |
| Irrad.: | 10/11/2003 | $\rho_d$: | 13.007 | CN_5 |
| Grid Size: | 1 μm² | $N_d$: | 22255 | |

| Crystal | $N_s$ | $N_i$ | Area (μm²) | $\rho_s$ (e5) | $\rho_i$ (e5) | Age (Ma) | ± 1σ | U (ppm) | $D_{par}$ | ± 1se |
|---|---|---|---|---|---|---|---|---|---|---|
| 1 | 55 | 86 | 1306.108 | 42.11 | 65.844 | 141.79 | 25.07 | 61.61 | 1.4 | 0.2 |
| 2 | 25 | 26 | 1254.246 | 19.932 | 20.73 | 212.01 | 59.94 | 19.4 | 1.0 | 0.2 |
| 3 | 34 | 46 | 793.252 | 42.862 | 57.989 | 163.59 | 37.52 | 54.26 | 1.6 | 0.3 |
| 4 | 22 | 29 | 655.616 | 33.556 | 44.233 | 167.85 | 47.89 | 41.39 | 1.3 | 0.0 |
| 5 | 45 | 58 | 909.671 | 49.468 | 63.759 | 171.61 | 34.72 | 59.66 | 1.0 | 0.1 |
| 6 | 34 | 36 | 2159.499 | 15.744 | 16.671 | 208.3 | 50.45 | 15.6 | 1.1 | 0.1 |
| 7 | 107 | 91 | 1261.866 | 84.795 | 72.115 | 258.32 | 38.14 | 67.48 | 1.5 | 0.0 |
| 8 | 29 | 27 | 904.711 | 32.054 | 29.844 | 236.37 | 63.86 | 27.92 | 1.3 | 0.2 |
| 9 | 9 | 6 | 1434.137 | 6.276 | 4.184 | 327.76 | 173.2 | 3.91 | 1.4 | 0.3 |
| 10 | 33 | 48 | 1079.15 | 30.58 | 44.479 | 152.3 | 34.93 | 41.62 | 1.4 | 0.1 |
| 11 | 84 | 90 | 1996.342 | 42.077 | 45.082 | 205.89 | 32.21 | 42.18 | 1.2 | 0.0 |
| 12 | 43 | 60 | 1156.828 | 37.171 | 51.866 | 158.68 | 32.28 | 48.53 | 1.0 | 0.0 |
| 13 | 18 | 9 | 1794.297 | 10.032 | 5.016 | 433.41 | 177.71 | 4.69 | 1.4 | 0.1 |
| 14 | 88 | 129 | 3426.702 | 25.681 | 37.646 | 151.13 | 21.68 | 35.22 | 1.2 | 0.2 |
| 15 | 51 | 86 | 4364.028 | 11.686 | 19.707 | 131.58 | 23.79 | 18.44 | 1.1 | 0.0 |
| 16 | 71 | 106 | 741.472 | 95.755 | 142.959 | 148.42 | 23.46 | 133.76 | 1.1 | 0.2 |
| 17 | 69 | 105 | 3123.249 | 22.092 | 33.619 | 145.65 | 23.25 | 31.46 | 1.1 | 0.0 |
| 18 | 128 | 156 | 4907.282 | 26.084 | 31.789 | 181.35 | 22.71 | 29.74 | 1.1 | 0.0 |
| 19 | 28 | 32 | 1513.441 | 18.501 | 21.144 | 193.21 | 50.54 | 19.78 | 1.2 | 0.1 |
| 20 | 43 | 34 | 2984.069 | 14.41 | 11.394 | 277.44 | 64.55 | 10.66 | 1.0 | 0.2 |
| 21 | 12 | 16 | 3028.294 | 3.963 | 5.284 | 165.96 | 63.69 | 4.94 | 1.6 | 0.1 |
| 22 | 20 | 40 | 1208.69 | 16.547 | 33.094 | 111.12 | 30.72 | 30.96 | 1.4 | 0.0 |
| 23 | 1 | 2 | 2220.311 | 0.45 | 0.901 | 111.12 | 136.15 | 0.84 | 1.6 | - |
| 24 | 27 | 61 | 4342.088 | 6.218 | 14.049 | 98.46 | 23.07 | 13.14 | 1.2 | 0.2 |
| 25 | 114 | 160 | 3297.622 | 34.57 | 48.52 | 157.77 | 20.25 | 45.4 | 1.1 | 0.2 |
| 26 | 36 | 60 | 722.587 | 49.821 | 83.035 | 133.11 | 28.52 | 77.69 | 1.5 | 0.2 |
| 27 | 23 | 18 | 939.362 | 24.485 | 19.162 | 280.24 | 88.84 | 17.93 | 1.8 | 0.1 |
| 28 | 78 | 133 | 2187.466 | 35.658 | 60.801 | 130.14 | 19.21 | 56.89 | 1.7 | 0.1 |
| 29 | 19 | 26 | 2042.949 | 9.3 | 12.727 | 161.76 | 49.21 | 11.91 | 1.2 | 0.2 |
| 30 | 36 | 31 | 1156.138 | 31.138 | 26.813 | 255.19 | 63.28 | 25.09 | 1.5 | 0.1 |
| 31 | 15 | 34 | 2259.725 | 6.638 | 15.046 | 98.14 | 30.65 | 14.08 | 1.3 | 0.2 |

| 3.3 TK version | Sample 75 | Stephanian B | Sed. Age: 302-301 Ma | Lith.: SS/SH | | | | | | |
|---|---|---|---|---|---|---|---|---|---|---|
| ζ: | 344.68 | ζ err.: | 12.96 | Apatite | | | | | | |
| Irrad.: | 10/11/2003 | $\rho_d$: | 13.007 | CN_5 | | | | | | |
| Grid Size: | 1 μm² | $N_d$: | 22255 | | | | | | | |
| Crystal | $N_s$ | $N_i$ | Area (μm²) | $\rho_s$ (e5) | $\rho_i$ (e5) | Age (Ma) | ± 1σ | U (ppm) | $D_{par}$ | ± 1se |
| 1 | 5 | 10 | 2010.416 | 2.487 | 4.974 | 111.12 | 61.01 | 4.65 | 1.3 | 0.1 |
| 2 | 3 | 1 | 919.656 | 3.262 | 1.087 | 639.66 | 739.02 | 1.02 | 1.5 | - |
| 3 | 9 | 9 | 853.966 | 10.539 | 10.539 | 220.35 | 104.21 | 9.86 | 2.0 | 0.1 |
| 4 | 3 | 6 | 820.464 | 3.656 | 7.313 | 111.12 | 78.69 | 6.84 | 1.4 | 0.2 |
| 5 | 9 | 14 | 1028.372 | 8.752 | 13.614 | 142.51 | 61.13 | 12.74 | 1.3 | 0.1 |
| 6 | 7 | 5 | 530.773 | 13.188 | 9.42 | 306.42 | 179.8 | 8.81 | 1.3 | 0.1 |
| 7 | 6 | 10 | 381.657 | 15.721 | 26.202 | 133.11 | 68.93 | 24.52 | 1.3 | 0.1 |
| 8 | 5 | 5 | 1175.845 | 4.252 | 4.252 | 220.35 | 139.61 | 3.98 | 1.1 | 0.1 |
| 9 | 9 | 4 | 716.018 | 12.57 | 5.586 | 485.6 | 292.4 | 5.23 | 1.5 | 0.2 |
| 10 | 80 | 111 | 1692.823 | 47.258 | 65.571 | 159.56 | 24.18 | 61.35 | 1.7 | 0.1 |
| 11 | 12 | 12 | 1267.22 | 9.47 | 9.47 | 220.35 | 90.35 | 8.86 | 1.3 | 0.1 |
| 12 | 9 | 13 | 839.235 | 10.724 | 15.49 | 153.35 | 66.75 | 14.49 | 1.5 | 0.1 |
| 13 | 7 | 7 | 1207.442 | 5.797 | 5.797 | 220.35 | 118.08 | 5.42 | 1.4 | 0.1 |
| 14 | 4 | 5 | 684.733 | 5.842 | 7.302 | 176.88 | 118.84 | 6.83 | 1.4 | 0.1 |
| 15 | 18 | 30 | 1376.047 | 13.081 | 21.802 | 133.11 | 40.01 | 20.4 | 1.4 | 0.1 |
| 16 | 32 | 46 | 1118.909 | 28.599 | 41.111 | 154.08 | 35.95 | 38.47 | 1.5 | 0.1 |
| 17 | 13 | 5 | 804.025 | 16.169 | 6.219 | 557.95 | 294.39 | 5.82 | 1.4 | 0.1 |
| 18 | 11 | 14 | 526.963 | 20.874 | 26.567 | 173.76 | 70.32 | 24.86 | 1.3 | 0.0 |
| 19 | 9 | 10 | 1065.158 | 8.449 | 9.388 | 198.65 | 91.59 | 8.78 | 1.3 | 0.1 |
| 20 | 27 | 30 | 1129.206 | 23.911 | 26.567 | 198.65 | 53.24 | 24.86 | 1.6 | 0.2 |

## *AFT age parameters*

| 3.3 TK version | Smaple 76 | Stephanian B | Sed. Age: 302-301 Ma | Lith.: SS |
|---|---|---|---|---|
| ζ: | 344.68 | ζ err.: | 12.96 | Apatite |
| Irrad.: | 10/11/2003 | $\rho_d$: | 13.007 | CN_5 |
| Grid Size: | 1 μm² | $N_d$: | 22255 | |

| Crystal | $N_s$ | $N_i$ | Area (μm²) | $\rho_s$ (e5) | $\rho_i$ (e5) | Age (Ma) | ± 1σ | U (ppm) | $D_{par}$ | ± 1se |
|---|---|---|---|---|---|---|---|---|---|---|
| 1 | 32 | 35 | 2220.311 | 14.412 | 15.764 | 201.75 | 49.94 | 14.75 | 1.1 | 0.1 |
| 2 | 20 | 38 | 4893.882 | 4.087 | 7.765 | 116.91 | 32.6 | 7.27 | 1.4 | 0.1 |
| 3 | 8 | 3 | 3678.622 | 2.175 | 0.816 | 571.64 | 387.62 | 0.76 | 1.2 | 0.1 |
| 4 | 10 | 15 | 1346.638 | 7.426 | 11.139 | 147.73 | 60.57 | 10.42 | 1.1 | 0.1 |
| 5 | 49 | 59 | 959.069 | 51.091 | 61.518 | 183.53 | 36.16 | 57.56 | 1.1 | 0.1 |
| 6 | 25 | 51 | 867.104 | 28.832 | 58.816 | 108.96 | 26.92 | 55.03 | 1.4 | 0.1 |
| 7 | 28 | 53 | 2791.811 | 10.029 | 18.984 | 117.35 | 27.78 | 17.76 | 1.3 | 0.0 |
| 8 | 25 | 37 | 2719.553 | 9.193 | 13.605 | 149.71 | 39.18 | 12.73 | 1.2 | 0.1 |
| 9 | 26 | 59 | 1878.725 | 13.839 | 31.404 | 98.03 | 23.38 | 29.38 | 1.2 | 0.0 |
| 10 | 12 | 8 | 617.483 | 19.434 | 12.956 | 327.76 | 150.12 | 12.12 | 1.4 | 0.1 |
| 11 | 4 | 5 | 1504.294 | 2.659 | 3.324 | 176.88 | 118.84 | 3.11 | 1.0 | 0.0 |
| 12 | 52 | 84 | 1872.156 | 27.775 | 44.868 | 137.29 | 24.79 | 41.98 | 1.5 | 0.1 |
| 13 | 117 | 139 | 4736.226 | 24.703 | 29.348 | 185.97 | 24.39 | 27.46 | 1.2 | 0.1 |
| 14 | 21 | 9 | 1767.052 | 11.884 | 5.093 | 502.9 | 201.28 | 4.77 | 1.3 | 0.1 |
| 15 | 11 | 31 | 2410.811 | 4.563 | 12.859 | 79.05 | 27.91 | 12.03 | 1.2 | 0.0 |
| 16 | 20 | 25 | 1300.656 | 15.377 | 19.221 | 176.88 | 53.49 | 17.98 | 1.2 | 0.2 |
| 17 | 28 | 60 | 2377.966 | 11.775 | 25.232 | 103.77 | 24.08 | 23.61 | 1.2 | 0.1 |
| 18 | 11 | 7 | 2903.484 | 3.789 | 2.411 | 342.96 | 166.34 | 2.26 | 1.2 | 0.1 |
| 19 | 29 | 31 | 1149.569 | 25.227 | 26.967 | 206.36 | 53.89 | 25.23 | 1.3 | 0.2 |
| 20 | 12 | 24 | 2594.742 | 4.625 | 9.249 | 111.12 | 39.51 | 8.65 | 1.4 | 0.0 |
| 21 | 160 | 168 | 2627.587 | 60.892 | 63.937 | 210.02 | 24.55 | 59.82 | 1.5 | 0.0 |
| 22 | 143 | 171 | 1773.621 | 80.626 | 96.413 | 184.78 | 22.1 | 90.21 | 1.3 | 0.2 |
| 23 | 45 | 36 | 1248.104 | 36.055 | 28.844 | 274.28 | 62.22 | 26.99 | 1.6 | 0.0 |
| 24 | 79 | 140 | 2318.846 | 34.069 | 60.375 | 125.26 | 18.26 | 56.49 | 1.2 | 0.0 |
| 25 | 41 | 67 | 3777.156 | 10.855 | 17.738 | 135.73 | 27.41 | 16.6 | 1.4 | 0.1 |

| 3.3 TK version | Sample 78 | Stephanina B | Sed. Age: 302-301 Ma | Lith.: SS | | | | | | |
|---|---|---|---|---|---|---|---|---|---|---|
| ζ: | 344.68 | ζ err.: | 12.96 | Apatite | | | | | | |
| Irrad.: | 10/11/2003 | $\rho_d$: | 13.007 | CN_5 | | | | | | |
| Grid Size: | 1 μm² | $N_d$: | 22255 | | | | | | | |
| Crystal | $N_s$ | $N_i$ | Area (μm²) | $\rho_s$ (e5) | $\rho_i$ (e5) | Age (Ma) | ± 1σ | U (ppm) | $D_{par}$ | ± 1se |
| 1 | 105 | 114 | 1141.621 | 91.974 | 99.858 | 203.22 | 28.56 | 93.43 | 1. | 0.0 |
| 2 | 84 | 60 | 1356.459 | 61.926 | 44.233 | 306.42 | 53.1 | 41.39 | 1.5 | 0.1 |
| 3 | 325 | 257 | 2795.424 | 116.261 | 91.936 | 277.41 | 25.47 | 86.02 | 1.3 | 0.0 |
| 4 | 93 | 54 | 1097.79 | 84.716 | 49.19 | 374.93 | 65.73 | 46.03 | 1.0 | 0.2 |
| 5 | 9 | 4 | 981.026 | 9.174 | 4.077 | 485.6 | 292.4 | 3.82 | 1.5 | 0.1 |
| 6 | 69 | 42 | 1497.396 | 46.08 | 28.049 | 358.12 | 71.41 | 26.24 | 1.4 | 0.1 |
| 7 | 50 | 61 | 2060.11 | 24.271 | 29.61 | 181.17 | 35.25 | 27.71 | 1.3 | 0.1 |
| 8 | 144 | 150 | 934.551 | 154.085 | 160.505 | 211.68 | 25.99 | 150.18 | 1.3 | 0.1 |
| 9 | 200 | 219 | 2429.943 | 82.306 | 90.126 | 201.53 | 21.16 | 84.33 | 1.1 | 0.1 |
| 10 | 41 | 37 | 1538.912 | 26.642 | 24.043 | 243.72 | 56.04 | 22.5 | 1.0 | 0.2 |
| 11 | 50 | 28 | 5573.934 | 8.97 | 5.023 | 388.35 | 92.86 | 4.7 | 2.2 | 0.1 |
| 12 | 15 | 12 | 411.546 | 36.448 | 29.158 | 274.28 | 106.74 | 27.28 | 1.1 | 0.1 |
| 13 | 141 | 78 | 1951.887 | 72.238 | 39.961 | 392.98 | 57.45 | 37.39 | 1.3 | 0.0 |
| 14 | 108 | 91 | 1985.783 | 54.387 | 45.826 | 260.69 | 38.41 | 42.88 | 1.3 | 0.2 |
| 15 | 173 | 128 | 2631.857 | 65.733 | 48.635 | 296.06 | 36.32 | 45.51 | 1.3 | 0.2 |
| 16 | 352 | 297 | 4250.664 | 82.811 | 69.871 | 260.34 | 22.8 | 65.38 | 1.3 | 0.1 |
| 17 | 42 | 42 | 963.093 | 43.609 | 43.609 | 220.35 | 48.81 | 40.8 | 1.4 | 0.3 |
| 18 | 16 | 19 | 1579.788 | 10.128 | 12.027 | 186.05 | 63.53 | 11.25 | 1.3 | 0.2 |
| 19 | 94 | 45 | 2434.394 | 38.613 | 18.485 | 452.02 | 83.74 | 17.3 | 1.6 | 0.1 |
| 20 | 129 | 82 | 4194.631 | 30.754 | 19.549 | 343.33 | 50.23 | 18.29 | 1.4 | 0.1 |
| 21 | 19 | 30 | 9222.83 | 2.06 | 3.253 | 140.43 | 41.52 | 3.044 | 1.7 | 0.1 |
| 22 | 3 | 2 | 6936.83 | 0.432 | 0.288 | 327.76 | 299.47 | 0.27 | 1.2 | 0.1 |
| 23 | 22 | 29 | 1563.414 | 14.072 | 18.549 | 167.85 | 47.89 | 17.356 | 1.2 | 0.0 |
| 24 | 75 | 121 | 6180.085 | 12.136 | 19.579 | 137.46 | 20.87 | 18.32 | 1.2 | 0.0 |
| 25 | 18 | 25 | 1451.742 | 12.399 | 17.221 | 159.41 | 49.65 | 16.113 | 1.6 | 0.1 |

## *AFT age parameters*

| 3.3 TK version | Sample 79 | Stephanina B | Sed. Age: 302-301 Ma | Lith.: SS/SH/ CNGL | | | | | | |
|---|---|---|---|---|---|---|---|---|---|---|
| ζ: | 325.7 | ζ err.: | 12.37 | Apatite | | | | | | |
| Irrad.: | 10/12/2003 | $\rho_d$: | 12.235 | CN_5 | | | | | | |
| Grid Size: | 1 μm$^2$ | $N_d$: | 15423 | | | | | | | |
| Crystal | $N_s$ | $N_i$ | Area (μm$^2$) | $\rho_s$ (e5) | $\rho_i$ (e5) | Age (Ma) | ± 1σ | U (ppm) | $D_{par}$ | ± 1se |
| 1 | 19 | 30 | 2515.915 | 7.552 | 11.924 | 124.97 | 36.96 | 11.86 | 1.4 | 0.3 |
| 2 | 172 | 168 | 6745.016 | 25.5 | 24.907 | 200.83 | 23.14 | 24.78 | 1.5 | 0.2 |
| 3 | 56 | 63 | 3941.381 | 14.208 | 15.984 | 174.71 | 32.8 | 15.9 | 1.2 | 0.1 |
| 4 | 13 | 35 | 2647.294 | 4.911 | 13.221 | 73.58 | 24.07 | 13.15 | 1.1 | 0.2 |
| 5 | 16 | 20 | 2870.639 | 5.574 | 6.967 | 157.45 | 53.16 | 6.93 | 1.5 | 0.0 |
| 6 | 77 | 109 | 3521.624 | 21.865 | 30.952 | 139.23 | 21.42 | 30.79 | 1.5 | 0.0 |
| 7 | 5 | 12 | 3301.235 | 1.515 | 3.635 | 82.49 | 44.02 | 3.62 | 1.5 | 0.0 |
| 8 | 31 | 48 | 3159.674 | 9.811 | 15.191 | 127.41 | 29.77 | 15.11 | 1.9 | 0.1 |
| 9 | 76 | 53 | 2016.673 | 37.686 | 26.281 | 279.56 | 51.19 | 26.14 | 1.5 | 0.2 |
| 10 | 25 | 27 | 1465.964 | 17.054 | 18.418 | 181.89 | 50.98 | 18.32 | 1.3 | 0.1 |
| 11 | 60 | 55 | 3553.483 | 16.885 | 15.478 | 213.77 | 40.76 | 15.4 | 1.9 | 0.1 |
| 12 | 6 | 4 | 4230.416 | 1.418 | 0.946 | 292.14 | 188.92 | 0.94 | 1.3 | 0.1 |
| 13 | 61 | 55 | 939.362 | 64.938 | 58.55 | 217.27 | 41.27 | 58.24 | 1.6 | 0.1 |
| 14 | 135 | 198 | 4230.416 | 31.912 | 46.804 | 134.44 | 15.89 | 46.56 | 1.5 | 0.0 |
| 15 | 41 | 54 | 1070.742 | 38.291 | 50.432 | 149.53 | 31.51 | 50.17 | 1.3 | 0.0 |
| 16 | 102 | 67 | 4657.398 | 21.901 | 14.386 | 296.4 | 48.01 | 14.31 | 1.7 | 0.1 |
| 17 | 34 | 46 | 4742.795 | 7.169 | 9.699 | 145.61 | 33.41 | 9.65 | 1.7 | 0.1 |
| 18 | 173 | 169 | 3091.356 | 55.962 | 54.669 | 200.8 | 23.07 | 54.38 | 1.6 | 0.1 |
| 19 | 70 | 126 | 2555.329 | 27.394 | 49.309 | 109.75 | 16.91 | 49.05 | 1.6 | 0.3 |
| 20 | 92 | 107 | 3113.691 | 29.547 | 34.364 | 169.07 | 24.92 | 34.18 | 1.9 | 0.0 |
| 21 | 158 | 171 | 1405.759 | 112.395 | 121.642 | 181.52 | 21.23 | 121 | 1.9 | 0.0 |
| 22 | 57 | 68 | 3803.432 | 14.986 | 17.879 | 164.88 | 30.29 | 17.78 | 1.3 | 0.0 |
| 23 | 147 | 235 | 2588.173 | 56.797 | 90.798 | 123.44 | 13.84 | 90.32 | 1.4 | 0.1 |
| 24 | 47 | 57 | 2177.284 | 21.587 | 26.179 | 162.23 | 32.58 | 26.04 | 1.7 | 0.1 |
| 25 | 71 | 122 | 3011.215 | 23.579 | 40.515 | 114.92 | 17.73 | 40.3 | 1.5 | 0.1 |

| 3.3 TK version | Sample 80 | Stephanian B | Sed. Age: 302-301 Ma | Lith.: SS/SH | | | | | | |
|---|---|---|---|---|---|---|---|---|---|---|
| ζ: | 344.68 | ζ err.: | 12.96 | Apatite | | | | | | |
| Irrad.: | 10/11/2003 | $\rho_d$: | 13.007 | CN_5 | | | | | | |
| Grid Size: | 1 μm² | $N_d$: | 22255 | | | | | | | |
| Crystal | $N_s$ | $N_i$ | Area (μm²) | $\rho_s$ (e5) | $\rho_i$ (e5) | Age (Ma) | ± 1σ | U (ppm) | $D_{par}$ | ± 1se |
| 1 | 92 | 85 | 627.107 | 146.706 | 135.543 | 238.16 | 36.97 | 126.82 | 1.3 | 0.3 |
| 2 | 62 | 42 | 1677.698 | 36.955 | 25.034 | 322.69 | 65.65 | 23.42 | 1.5 | 0.4 |
| 3 | 52 | 51 | 1014.167 | 51.274 | 50.288 | 224.59 | 45.09 | 47.05 | 1.1 | 0.2 |
| 4 | 96 | 24 | 3147.505 | 30.5 | 7.625 | 839.51 | 194.26 | 7.13 | 1.2 | 0.1 |
| 5 | 45 | 28 | 1538.387 | 29.251 | 18.201 | 350.55 | 85.43 | 17.03 | 1.1 | 0.3 |
| 6 | 19 | 32 | 1510.501 | 12.579 | 21.185 | 131.74 | 38.48 | 19.82 | 1.0 | 0.1 |
| 7 | 24 | 17 | 1415.728 | 16.952 | 12.008 | 308.94 | 98.64 | 11.24 | 1.0 | 0.1 |
| 8 | 43 | 30 | 1891.403 | 22.734 | 15.861 | 313.54 | 75.54 | 14.84 | 0.9 | 0.0 |
| 9 | 14 | 11 | 1447.292 | 9.673 | 7.6 | 279.16 | 112.98 | 7.11 | 1.3 | 0.2 |
| 10 | 73 | 67 | 2420.188 | 30.163 | 27.684 | 239.72 | 41.58 | 25.9 | 1.4 | 0.3 |
| 11 | 56 | 91 | 2338.635 | 23.946 | 38.912 | 136.49 | 23.76 | 36.41 | 1.1 | 0.3 |
| 12 | 25 | 22 | 1614.505 | 15.485 | 13.626 | 249.82 | 73.65 | 12.75 | 1.0 | 0.1 |
| 13 | 22 | 30 | 729.156 | 30.172 | 41.143 | 162.32 | 45.98 | 38.5 | 1.4 | 0.1 |
| 14 | 119 | 127 | 1542.87 | 77.129 | 82.314 | 206.69 | 27.53 | 77.02 | 1.0 | 0.2 |
| 15 | 41 | 23 | 926.225 | 44.266 | 24.832 | 387.69 | 102.08 | 23.23 | 1.2 | 0.2 |
| 16 | 38 | 41 | 1202.121 | 31.611 | 34.106 | 204.48 | 46.7 | 31.91 | 1.4 | 0.2 |
| 17 | 21 | 21 | 1497.725 | 14.021 | 14.021 | 220.35 | 68.52 | 13.12 | 1.1 | 0.2 |
| 18 | 58 | 56 | 2391.104 | 24.257 | 23.42 | 228.08 | 43.61 | 21.91 | 1.0 | 0.3 |
| 19 | 26 | 17 | 1596.259 | 16.288 | 10.65 | 334.02 | 104.96 | 9.96 | 1.1 | 0.3 |
| 20 | 104 | 59 | 1622.535 | 64.097 | 36.363 | 383.49 | 64.2 | 34.02 | 1.0 | 0.3 |
| 21 | 30 | 42 | 1215.259 | 24.686 | 34.561 | 158.16 | 38.29 | 32.34 | 1.0 | 0.2 |
| 22 | 23 | 20 | 991.914 | 23.187 | 20.163 | 252.76 | 77.88 | 18.87 | 1.0 | 0.1 |
| 23 | 28 | 21 | 853.966 | 32.788 | 24.591 | 292.16 | 85.07 | 23.01 | 1.2 | 0.2 |
| 24 | 14 | 6 | 663.466 | 21.101 | 9.043 | 502.9 | 246.14 | 8.46 | 1.1 | 0.3 |
| 25 | 54 | 62 | 1701.363 | 31.739 | 36.441 | 192.34 | 36.55 | 34.1 | 1.0 | 0.2 |
| 26 | 13 | 20 | 1326.932 | 9.797 | 15.072 | 144.08 | 51.62 | 14.1 | 1.1 | 0.1 |
| 27 | 19 | 27 | 1057.604 | 17.965 | 25.529 | 155.84 | 47.04 | 23.89 | 0.9 | 0.1 |
| 28 | 56 | 66 | 1399.19 | 40.023 | 47.17 | 187.44 | 34.8 | 44.14 | 1.0 | 0.2 |
| 29 | 27 | 24 | 991.914 | 27.22 | 24.196 | 247.37 | 70.04 | 22.64 | 1.3 | 0.1 |
| 30 | 6 | 7 | 827.690 | 7.249 | 8.457 | 189.33 | 105.58 | 7.91 | 1.2 | 0.0 |

*AFT age parameters*

| 3.3 TK version | Sample 82 | Bashkir.-Moscov. | Sed. Age: 318-307 Ma | SS/SH |
|---|---|---|---|---|
| ζ: | 344.68 | ζ err.: | 12.96 | Apatite |
| Irrad.: | 10/11/2003 | $\rho_d$: | 13.007 | CN_5 |
| Grid Size: | 1 μm² | $N_d$: | 22255 | |

| Crystal | $N_s$ | $N_i$ | Area (μm²) | $\rho_s$ (e5) | $\rho_i$ (e5) | Age (Ma) | ± 1σ | U (ppm) | $D_{par}$ | ± 1se |
|---|---|---|---|---|---|---|---|---|---|---|
| 1 | 29 | 44 | 1702.677 | 17.032 | 25.842 | 146.07 | 35.38 | 24.18 | 1.9 | 0.1 |
| 2 | 24 | 19 | 1767.052 | 13.582 | 10.752 | 277.1 | 85.75 | 10.06 | 1.4 | 0.1 |
| 3 | 10 | 22 | 420.414 | 23.786 | 52.329 | 101.09 | 38.75 | 48.96 | 1.4 | 0.2 |
| 4 | 45 | 66 | 814.552 | 55.245 | 81.026 | 151.05 | 29.77 | 75.81 | 1.0 | 0.1 |
| 5 | 8 | 7 | 400.707 | 19.965 | 17.469 | 251.22 | 130.37 | 16.35 | 1.2 | 0.1 |
| 6 | 7 | 7 | 413.845 | 16.915 | 16.915 | 220.35 | 118.08 | 15.83 | 1.1 | 0.2 |
| 7 | 36 | 28 | 709.449 | 50.744 | 39.467 | 281.95 | 71.86 | 36.93 | 1.3 | 0.1 |
| 8 | 29 | 36 | 928.852 | 31.221 | 38.758 | 178.09 | 44.95 | 36.26 | 1.0 | 0.1 |
| 9 | 3 | 7 | 1747.345 | 1.717 | 4.006 | 95.36 | 65.9 | 3.75 | 0.9 | 0.1 |
| 10 | 7 | 3 | 276.554 | 25.312 | 10.848 | 502.9 | 347.56 | 10.15 | 1.4 | 0.3 |
| 11 | 12 | 17 | 867.104 | 13.839 | 19.605 | 156.32 | 59.24 | 18.34 | 1.8 | 0.2 |
| 12 | 17 | 20 | 1070.742 | 15.877 | 18.679 | 187.77 | 62.36 | 17.48 | 1.5 | 0.1 |
| 13 | 30 | 48 | 965.638 | 31.068 | 49.708 | 138.6 | 32.69 | 46.51 | 1.6 | 0.2 |
| 14 | 40 | 40 | 1491.156 | 26.825 | 26.825 | 220.35 | 49.98 | 25.1 | 1.5 | 0.1 |
| 15 | 23 | 28 | 1931.277 | 11.909 | 14.498 | 181.55 | 51.56 | 13.57 | 1.1 | 0.1 |
| 16 | 33 | 74 | 1990.397 | 16.58 | 37.179 | 99.19 | 21.11 | 34.79 | 1.2 | 0.1 |
| 17 | 17 | 42 | 1104.9 | 15.386 | 38.012 | 90.1 | 26.13 | 35.57 | 1.3 | 0.1 |
| 18 | 36 | 10 | 959.069 | 37.536 | 10.427 | 760.31 | 273.33 | 9.76 | 1.1 | 0.1 |
| 19 | 13 | 24 | 807.983 | 16.089 | 29.704 | 120.29 | 41.68 | 27.79 | 1.3 | 0.1 |
| 20 | 17 | 4 | 972.207 | 17.486 | 4.114 | 888.52 | 494.93 | 3.85 | 1.3 | 0.2 |
| 21 | 9 | 24 | 919.656 | 9.786 | 26.097 | 83.52 | 32.8 | 24.42 | 1.2 | 0.0 |
| 22 | 12 | 21 | 847.397 | 14.161 | 24.782 | 126.83 | 46.15 | 23.19 | 1.3 | 0.0 |
| 23 | 28 | 14 | 1254.673 | 22.317 | 11.158 | 433.41 | 142.83 | 10.44 | 1.3 | 0.1 |
| 24 | 6 | 29 | 1399.19 | 4.288 | 20.726 | 46.21 | 20.8 | 19.39 | 1.2 | 0.1 |
| 25 | 65 | 99 | 713.718 | 91.072 | 138.71 | 145.52 | 23.89 | 129.79 | 1.5 | 0.0 |
| 26 | 29 | 64 | 4155.529 | 6.979 | 15.401 | 100.78 | 22.89 | 14.41 | 1.3 | 0.0 |
| 27 | 11 | 13 | 551.793 | 19.935 | 23.56 | 186.93 | 76.91 | 22.04 | 1.4 | 0.1 |
| 28 | 22 | 14 | 1648.811 | 13.343 | 8.491 | 342.96 | 117.98 | 7.94 | 1.2 | 0.1 |
| 29 | 39 | 85 | 2384.535 | 16.355 | 35.646 | 102.04 | 20.12 | 33.35 | 1.7 | 0.1 |

| 3.3 TK version | Sample 110 | U. Devon.: Fammenian | Sed. Age: 375-359 Ma | Lith.: SS | | | | | | |
|---|---|---|---|---|---|---|---|---|---|---|
| ζ: | 344.68 | ζ err.: | 12.96 | Apatite | | | | | | |
| Irrad.: | 10/11/2003 | $\rho_d$: | 13.007 | CN_5 | | | | | | |
| Grid Size: | 1 μm² | $N_d$: | 22255 | | | | | | | |
| Crystal | $N_s$ | $N_i$ | Area (μm²) | $\rho_s$ (e5) | $\rho_i$ (e5) | Age (Ma) | ± 1σ | U (ppm) | $D_{par}$ | ± 1se |
| 1 | 17 | 29 | 4572.002 | 3.718 | 6.343 | 130.08 | 40.04 | 5.93 | 1.46 | 0.31 |
| 2 | 69 | 119 | 3765.333 | 18.325 | 31.604 | 128.68 | 20.08 | 29.57 | 1.46 | 0.11 |
| 3 | 61 | 82 | 4042.543 | 15.09 | 20.284 | 164.63 | 28.54 | 18.98 | 1.77 | 0.23 |
| 4 | 61 | 81 | 1675.087 | 36.416 | 48.356 | 166.64 | 28.96 | 45.25 | 1.42 | 0.07 |
| 5 | 83 | 74 | 2527.739 | 32.836 | 29.275 | 246.64 | 40.54 | 27.39 | 1.72 | 0.24 |
| 6 | 3 | 17 | 3133.398 | 0.957 | 5.425 | 39.44 | 24.74 | 5.08 | 1.41 | 0.26 |
| 7 | 13 | 32 | 4046.484 | 3.213 | 7.908 | 90.43 | 29.94 | 7.4 | 1.87 | 0.15 |
| 8 | 21 | 17 | 4580.295 | 4.585 | 3.712 | 271.12 | 89.06 | 3.47 | 1.97 | 0.31 |
| 9 | 15 | 15 | 2627.587 | 5.709 | 5.709 | 220.35 | 80.9 | 5.34 | 1.77 | 0.10 |
| 10 | 14 | 14 | 2483.07 | 5.638 | 5.638 | 220.35 | 83.71 | 5.28 | 2.47 | 0.32 |
| 11 | 45 | 65 | 2496.208 | 18.027 | 26.039 | 153.35 | 30.31 | 24.36 | 1.37 | 0.19 |
| 12 | 39 | 22 | 2207.173 | 17.67 | 9.967 | 385.6 | 103.87 | 9.33 | 1.55 | 0.12 |
| 13 | 41 | 38 | 3429.001 | 11.957 | 11.082 | 237.43 | 54.23 | 10.37 | 1.78 | 0.29 |
| 14 | 81 | 84 | 3172.812 | 25.529 | 26.475 | 212.61 | 34.09 | 24.77 | 1.56 | 0.31 |
| 15 | 63 | 34 | 3444.767 | 18.289 | 9.87 | 402.52 | 87.03 | 9.24 | 1.42 | 0.13 |
| 16 | 14 | 19 | 1280.949 | 10.929 | 14.833 | 163.09 | 57.78 | 13.88 | 1.50 | 0.04 |
| 17 | 44 | 84 | 2758.967 | 15.948 | 30.446 | 116.36 | 22.11 | 28.49 | 1.79 | 0.13 |
| 18 | 71 | 146 | 5385.848 | 13.183 | 27.108 | 108.1 | 16.18 | 25.36 | 1.57 | 0.08 |
| 19 | 31 | 31 | 4495.867 | 6.895 | 6.895 | 220.35 | 56.6 | 6.45 | 1.63 | 0.11 |
| 20 | 21 | 23 | 3539.738 | 5.933 | 6.498 | 201.48 | 61.3 | 6.08 | 1.97 | 0.11 |
| 21 | 41 | 52 | 3928.243 | 10.437 | 13.237 | 174.36 | 37.02 | 12.39 | 1.57 | 0.23 |
| 22 | 97 | 149 | 3686.062 | 26.315 | 40.423 | 144.3 | 19.62 | 37.82 | 1.72 | 0.05 |
| 23 | 59 | 70 | 5630.197 | 10.479 | 12.433 | 186.22 | 33.67 | 11.63 | 1.81 | 0.16 |
| 24 | 31 | 36 | 2651.433 | 11.692 | 13.578 | 190.19 | 47.16 | 12.7 | 1.59 | 0.19 |
| 25 | 80 | 63 | 1340.069 | 59.698 | 47.012 | 278.54 | 48.11 | 43.99 | 1.92 | 0.24 |
| 26 | 80 | 128 | 3586.656 | 22.305 | 35.688 | 138.6 | 20.45 | 33.39 | 1.77 | 0.12 |
| 27 | 53 | 61 | 3415.863 | 15.516 | 17.858 | 191.88 | 36.77 | 16.71 | 1.54 | 0.19 |
| 28 | 61 | 38 | 5334.002 | 11.436 | 7.124 | 350.15 | 73.59 | 6.67 | 1.59 | 0.11 |
| 29 | 200 | 318 | 3783.726 | 52.858 | 84.044 | 139.46 | 13.67 | 78.64 | 1.68 | 0.28 |
| 30 | 158 | 197 | 2148.052 | 73.555 | 91.711 | 177.32 | 20.11 | 85.81 | 1.40 | 0.05 |

*AFT age parameters*

| 3.3 TK version | Sample 111 | Fras.-Fam. | Sed. Age: 385-359 | Lith.: SS |
|---|---|---|---|---|
| ζ: | z344.86 | ζ err.: | 12.96 | Apatite |
| Irrad.: | 10/11/2003 | $\rho_d$: | 13.007 | CN_5 |
| Grid Size: | 1 μm² | $N_d$: | 22255 | |

| Crystal | $N_s$ | $N_i$ | Area (μm²) | $\rho_s$ (e5) | $\rho_i$ (e5) | Age (Ma) | ± 1σ | U (ppm) | Dpar | ± 1se |
|---|---|---|---|---|---|---|---|---|---|---|
| 142 | 260 | 3146.536 | 3146.536 | 0.045 | 0.083 | 121.28 | 13.48 | 77.32 | 1.4 | 0.1 |
| 46 | 48 | 1865.587 | 1865.587 | 0.025 | 0.026 | 211.32 | 44.34 | 24.07 | 2.0 | 0.3 |
| 41 | 45 | 3225.363 | 3225.363 | 0.013 | 0.014 | 201.06 | 44.08 | 13.05 | 2.2 | 0.3 |
| 42 | 32 | 2134.915 | 2134.915 | 0.020 | 0.015 | 287.69 | 68.39 | 14.02 | 1.3 | 0.0 |
| 11 | 9 | 3304.191 | 3304.191 | 0.003 | 0.003 | 268.31 | 121.03 | 2.55 | 1.3 | 0.1 |
| 25 | 23 | 1265.183 | 1265.183 | 0.020 | 0.018 | 239.16 | 69.7 | 17.01 | 1.4 | 0.1 |
| 89 | 104 | 3415.863 | 3415.863 | 0.026 | 0.030 | 189.03 | 28.23 | 28.49 | 1.5 | 0.0 |
| 78 | 106 | 2304.394 | 2304.394 | 0.034 | 0.046 | 162.87 | 25.08 | 43.04 | 1.9 | 0.1 |
| 15 | 14 | 1799.897 | 1799.897 | 0.008 | 0.008 | 235.8 | 88.09 | 7.28 | 2.1 | 0.1 |
| 181 | 286 | 3126.829 | 3126.829 | 0.058 | 0.091 | 140.32 | 14.37 | 85.58 | 1.5 | 0.3 |
| 7 | 3 | 2371.397 | 2371.397 | 0.003 | 0.001 | 502.9 | 347.56 | 1.18 | 1.7 | 0.1 |
| 78 | 72 | 1274.38 | 1274.380 | 0.061 | 0.056 | 238.38 | 40.01 | 52.86 | 1.5 | 0.0 |
| 115 | 135 | 4755.933 | 4755.933 | 0.024 | 0.028 | 188.18 | 24.94 | 26.56 | 1.3 | 0.1 |
| 18 | 11 | 3245.07 | 3245.070 | 0.006 | 0.003 | 356.75 | 137.21 | 3.17 | 1.8 | 0.0 |
| 9 | 9 | 1999.857 | 1999.857 | 0.005 | 0.005 | 220.35 | 104.21 | 4.21 | 2.1 | 0.3 |
| 6 | 5 | 1786.759 | 1786.759 | 0.003 | 0.003 | 263.53 | 159.89 | 2.62 | 1.9 | 0.1 |
| 17 | 17 | 719.630 | 719.630 | 0.024 | 0.024 | 220.35 | 76.05 | 22.1 | 1.7 | 0.1 |
| 54 | 71 | 1405.759 | 1405.759 | 0.038 | 0.051 | 168.27 | 31.06 | 47.26 | 1.8 | 0.1 |
| 63 | 55 | 1812.69 | 1812.690 | 0.035 | 0.030 | 251.78 | 47.45 | 28.39 | 1.8 | 0.0 |
| 47 | 57 | 1839.64 | 1839.639 | 0.026 | 0.031 | 182.23 | 36.57 | 28.99 | 1.3 | 0.1 |
| 86 | 121 | 3124.201 | 3124.201 | 0.028 | 0.039 | 157.38 | 23 | 36.24 | 1.8 | 0.1 |
| 144 | 142 | 2315.101 | 2315.101 | 0.062 | 0.061 | 223.4 | 27.76 | 57.39 | 1.7 | 0.1 |
| 136 | 166 | 4865.191 | 4865.191 | 0.028 | 0.034 | 181.08 | 22.06 | 31.93 | 1.4 | 0.0 |
| 58 | 61 | 1622.535 | 1622.535 | 0.036 | 0.038 | 209.69 | 39.28 | 35.18 | 1.8 | 0.0 |
| 28 | 21 | 2472.231 | 2472.231 | 0.011 | 0.008 | 292.16 | 85.07 | 7.95 | 1.7 | 0.0 |

# Appendix ii: AFT age radial plots & Track-length histograms

AFT age radial plots and confined track-length histograms for samples elucidated in figure 7.1-1. Plots were generated using *TRACKKEY version 4.2* (Dunkl, 2002). Age plots list from top to bottom: a) Sedimentary age of the sample and appropriate absolute age, b) AFT central-age and error, c) Sample identifier, d) Number of grains in which fission-tracks were counted. Dashed lines represent mean values for AFT age subcomponents as calculated using *BINOMFIT version 1.0* (Brandon, 2002). Crosses indicate individual grain ages. X-axis shows the relative error of each grain. The radial-axis shows the age. Y-axis indicates if the sample fits within two standard deviations from the calculated central value.

Confined track-length histograms list from top to bottom: a) Sample identifier, b) Mean uncorrected track-length and error, c) number of tracks for which length measurements were collected. X-axis is the bin (e.g. 6 to >7 μm). Y-axis shows the number of samples in each bin.

L. Cambrian: 542-518 Ma
Central Age: 192.7 ± 34.6 Ma

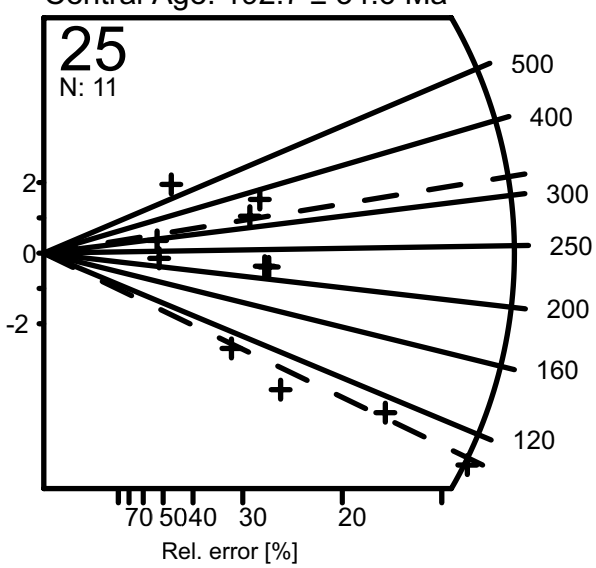


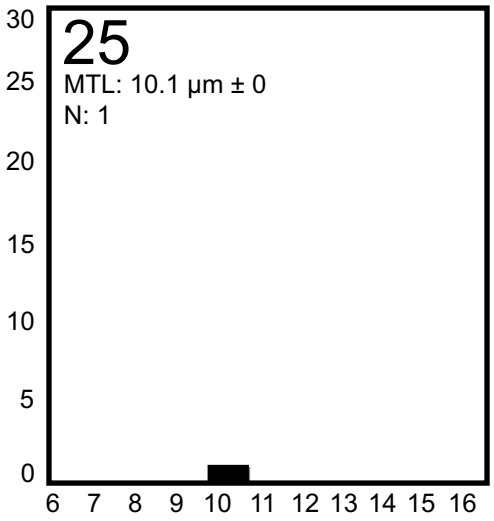


Neoproterozoic: >542 Ma
Central Age: 188.9 ± 15.5 Ma

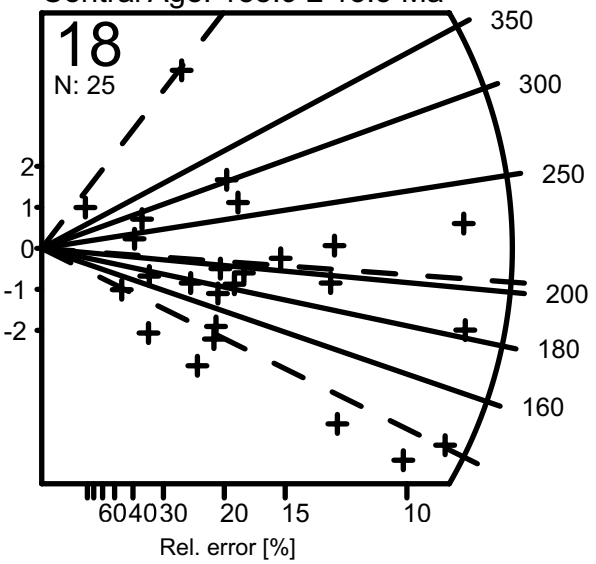


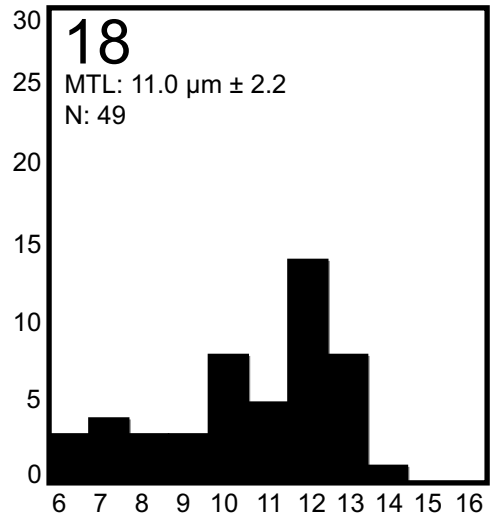


Stephanian B: 302-301 Ma
Central Age: 197.1 ± 16.8 Ma

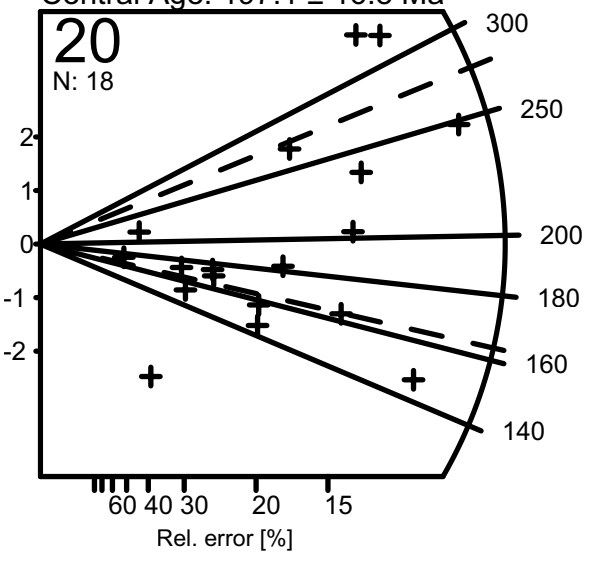


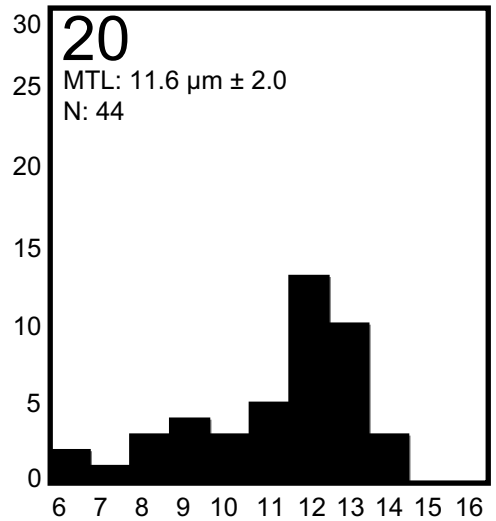

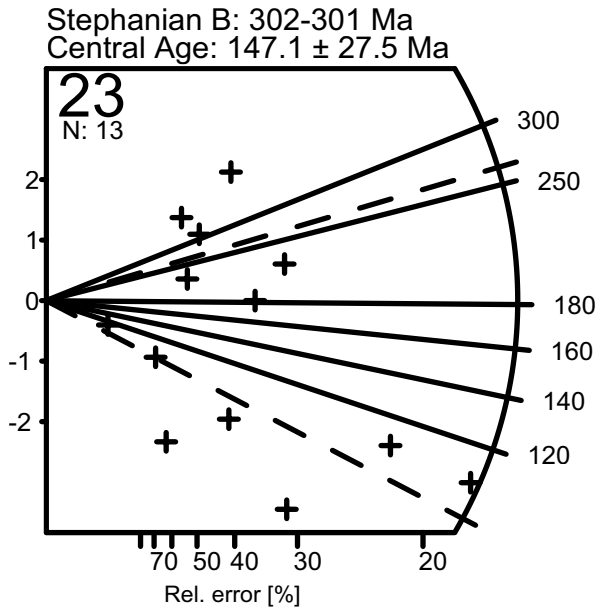
Stephanian B: 302-301 Ma
Central Age: 147.1 ± 27.5 Ma
23
N: 13
300
250
180
160
140
120
2
1
0
-1
-2
70 50 40 30 20
Rel. error [%]

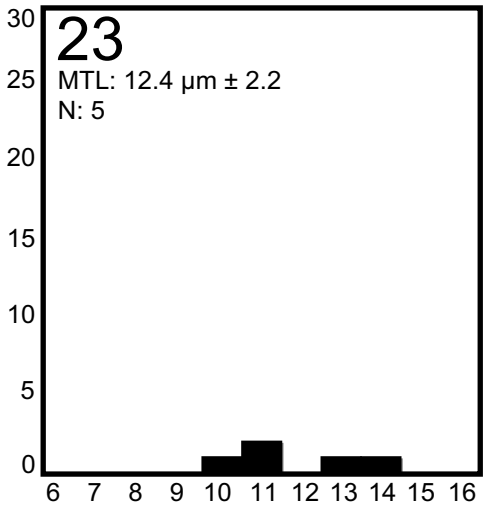
23
MTL: 12.4 µm ± 2.2
N: 5
30
25
20
15
10
5
0
6 7 8 9 10 11 12 13 14 15 16

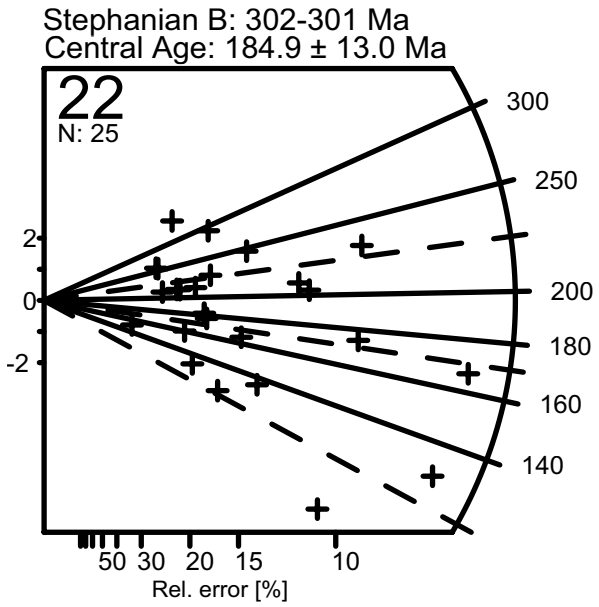
Stephanian B: 302-301 Ma
Central Age: 184.9 ± 13.0 Ma
22
N: 25
300
250
200
180
160
140
2
0
-2
50 30 20 15 10
Rel. error [%]

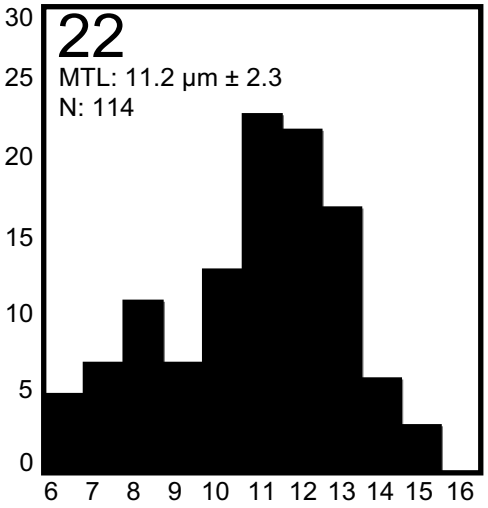
22
MTL: 11.2 µm ± 2.3
N: 114
30
25
20
15
10
5
0
6 7 8 9 10 11 12 13 14 15 16

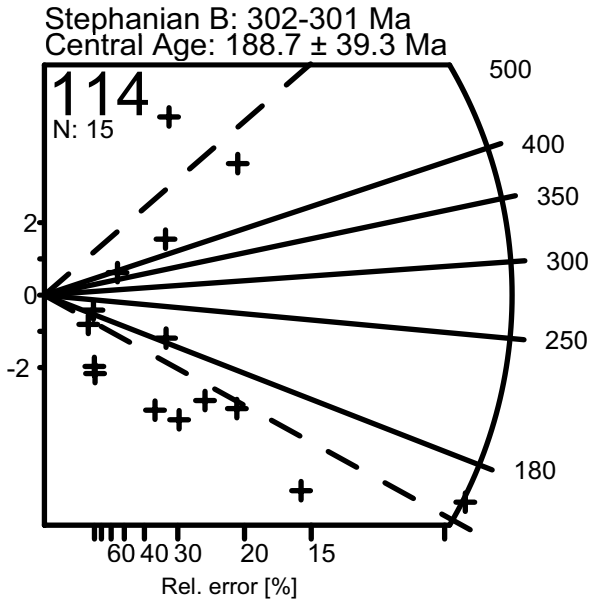
Stephanian B: 302-301 Ma
Central Age: 188.7 ± 39.3 Ma
114
N: 15
500
400
350
300
250
180
2
0
-2
60 40 30 20 15
Rel. error [%]

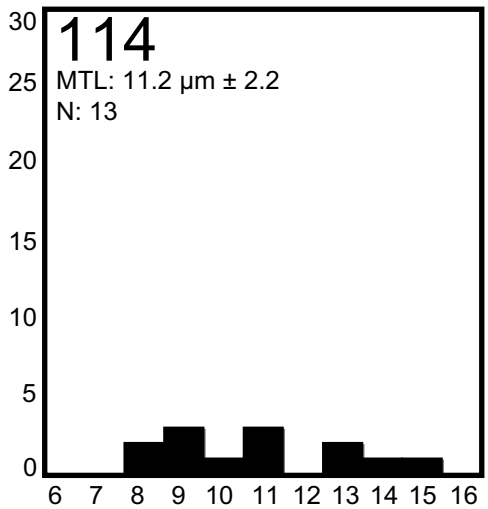
114
MTL: 11.2 µm ± 2.2
N: 13
30
25
20
15
10
5
0
6 7 8 9 10 11 12 13 14 15 16

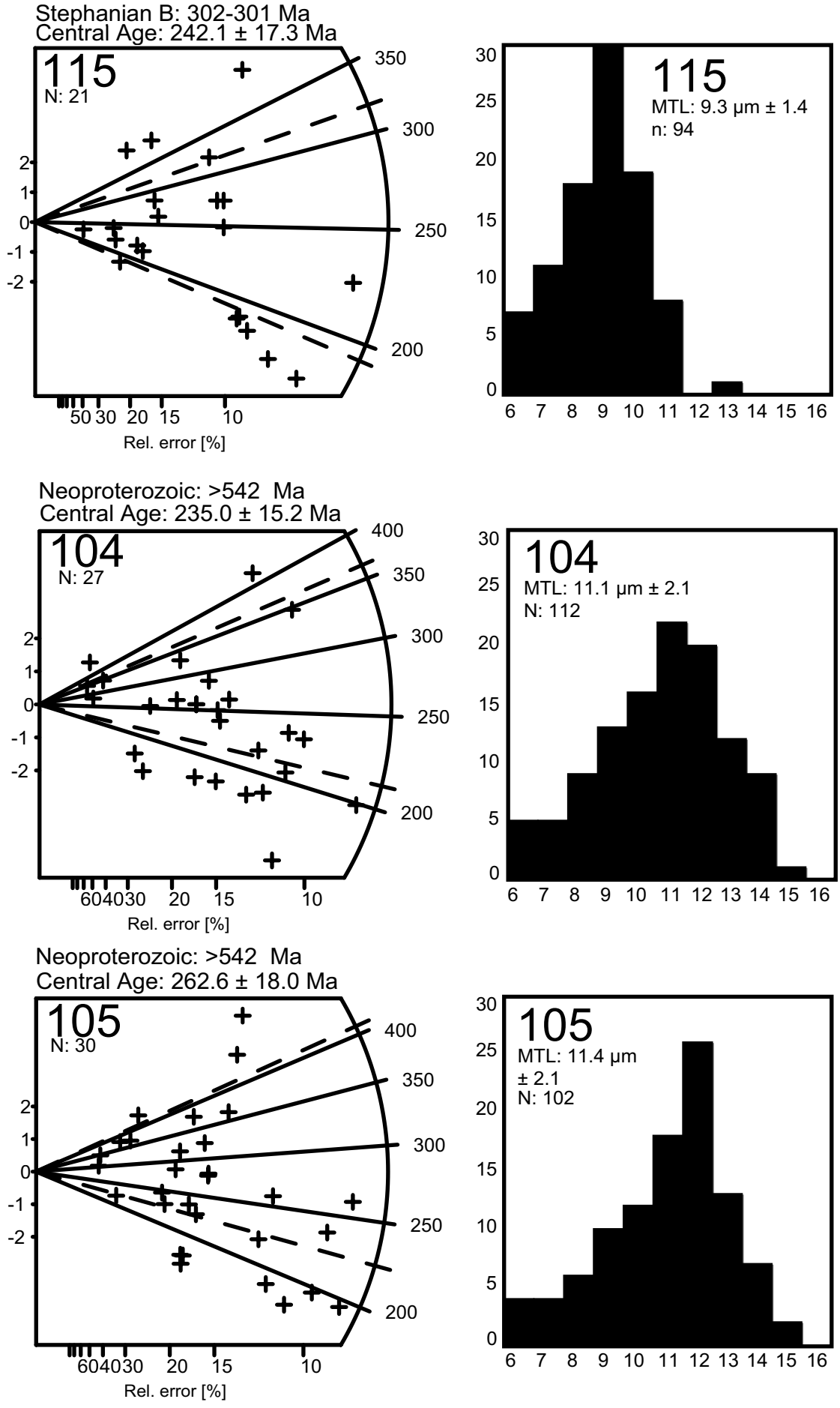
Stephanian B: 302-301 Ma
Central Age: 242.1 ± 17.3 Ma
115
N: 21
350
300
250
200
2
1
0
-1
-2
50 30 20 15 10
Rel. error [%]
115
MTL: 9.3 µm ± 1.4
n: 94
30
25
20
15
10
5
0
6 7 8 9 10 11 12 13 14 15 16
Neoproterozoic: >542 Ma
Central Age: 235.0 ± 15.2 Ma
104
N: 27
400
350
300
250
200
2
1
0
-1
-2
60 40 30 20 15 10
Rel. error [%]
104
MTL: 11.1 µm ± 2.1
N: 112
30
25
20
15
10
5
0
6 7 8 9 10 11 12 13 14 15 16
Neoproterozoic: >542 Ma
Central Age: 262.6 ± 18.0 Ma
105
N: 30
400
350
300
250
200
2
1
0
-1
-2
60 40 30 20 15 10
Rel. error [%]
105
MTL: 11.4 µm
± 2.1
N: 102
30
25
20
15
10
5
0
6 7 8 9 10 11 12 13 14 15 16

Neoproterozoic: >542 Ma
Central Age: 196.1 ± 14.6 Ma

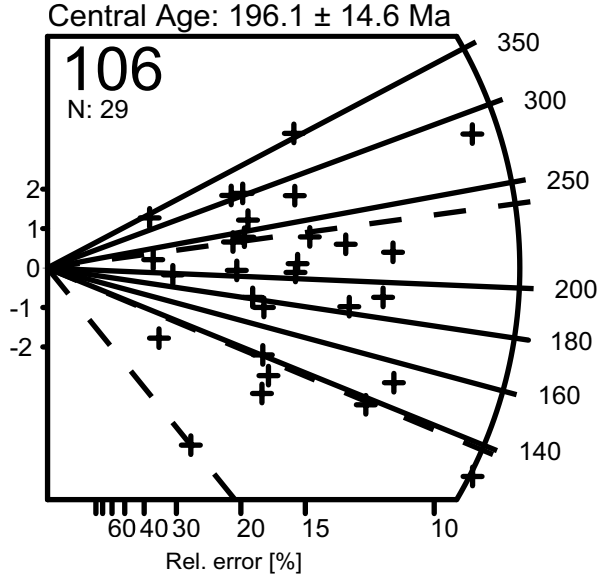


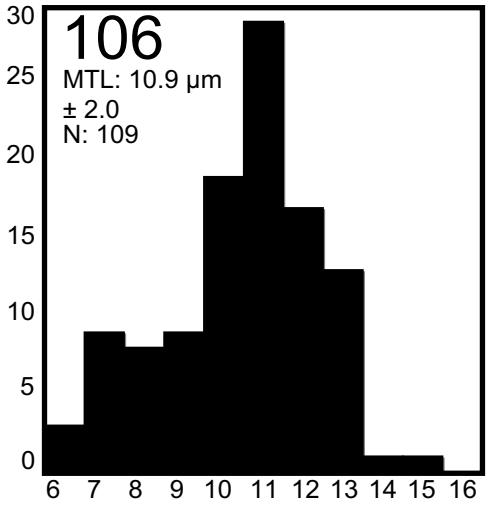


L. Cambrian: 542-518 Ma
Central Age: 27.4 ± 4.8 Ma

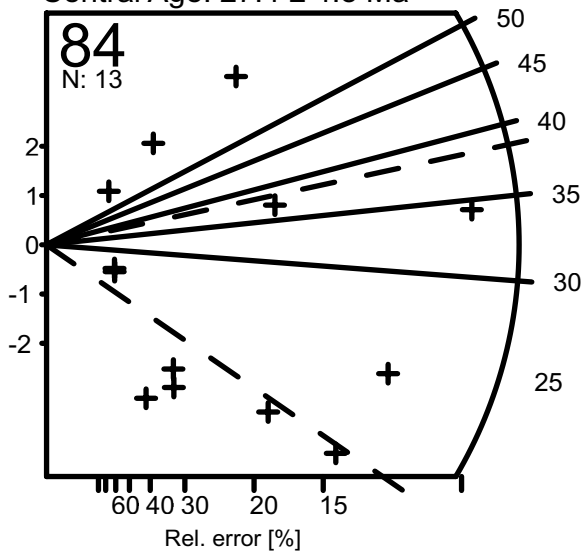


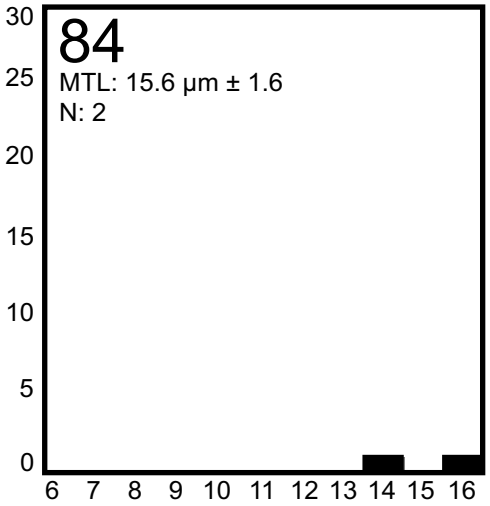


U. Cambrian-Ordovician: 490-468 Ma
Central Age: 125.5 ± 7.7 Ma

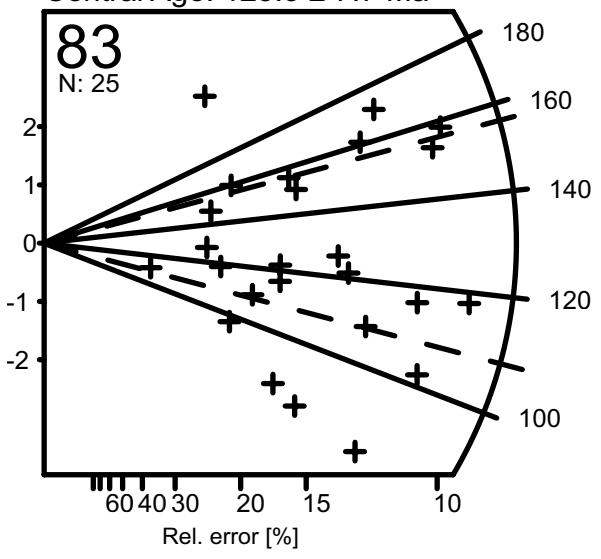


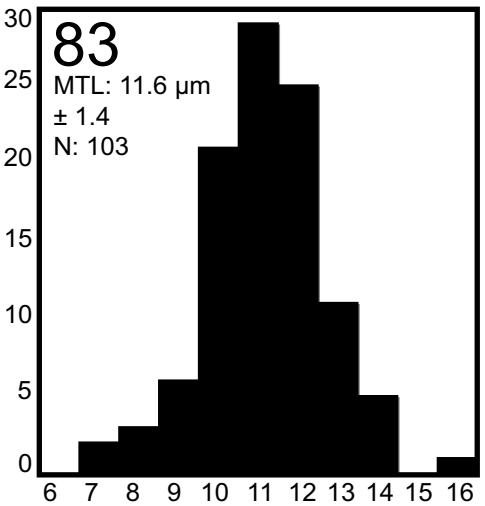

Stephanian B: 302-301 Ma
Central Age: 181.1 ± 12.2 Ma

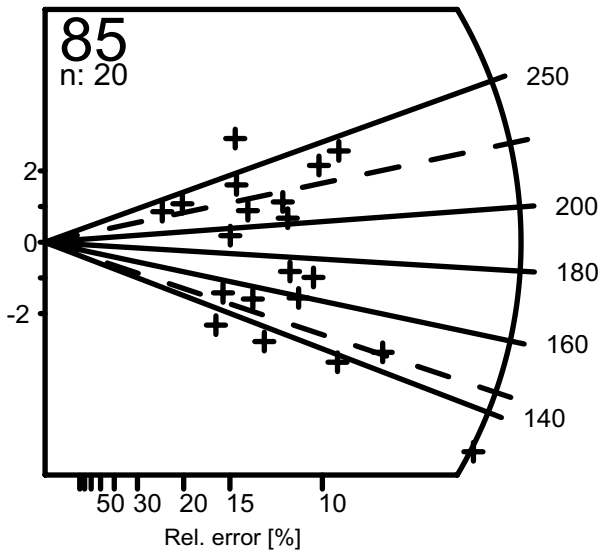


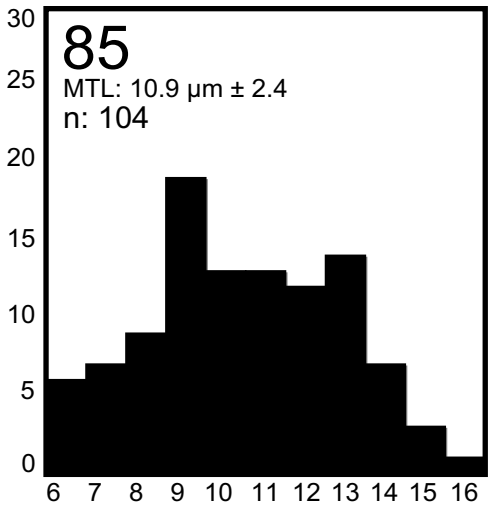


M. Bashkir - Kasimov: ~316-304 Ma
Central Age: 29.8 ± 3.4 Ma

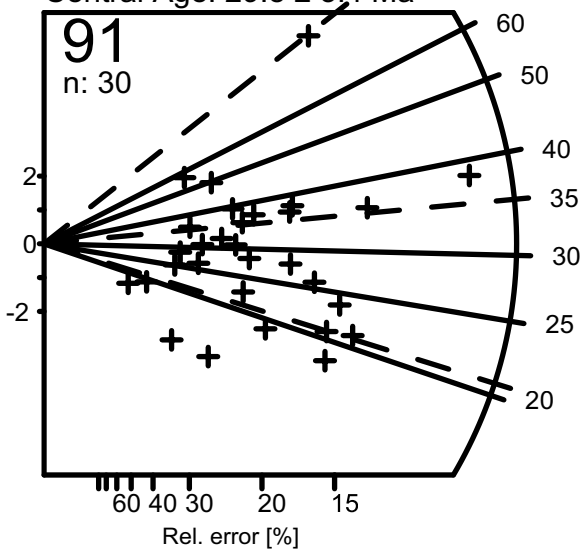


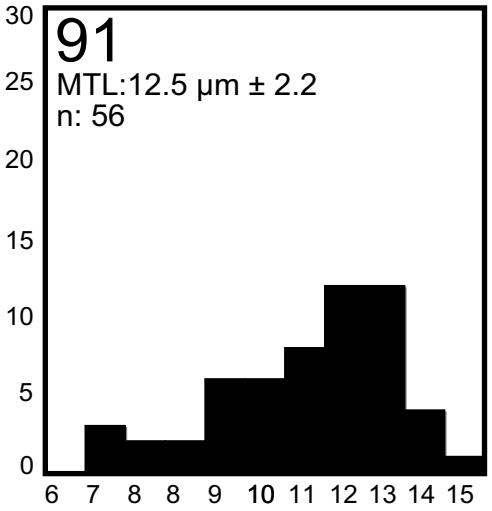


M. Bashkir - Kasimov: ~316-304 Ma
Central Age: 106.3 ± 20.5 Ma

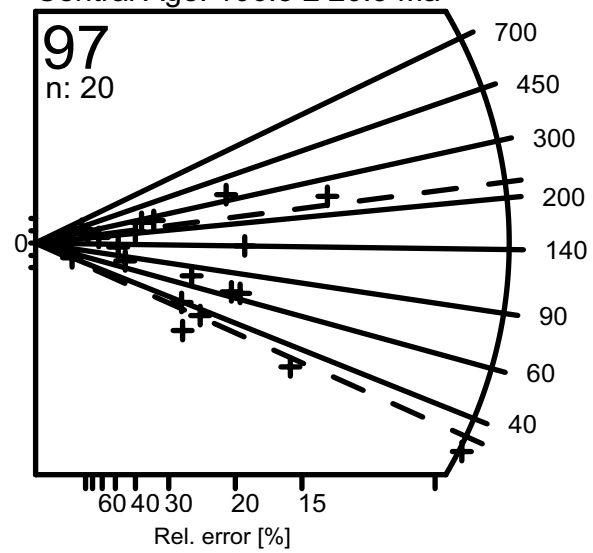


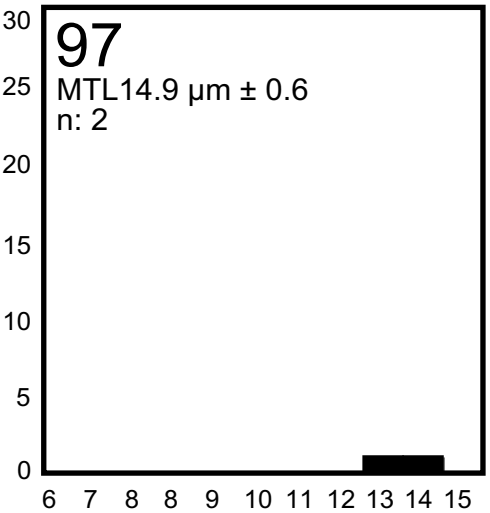

M. Bashkir - Kasimov: ~316-304 Ma
Central Age: 45.3 ± 6.6 Ma

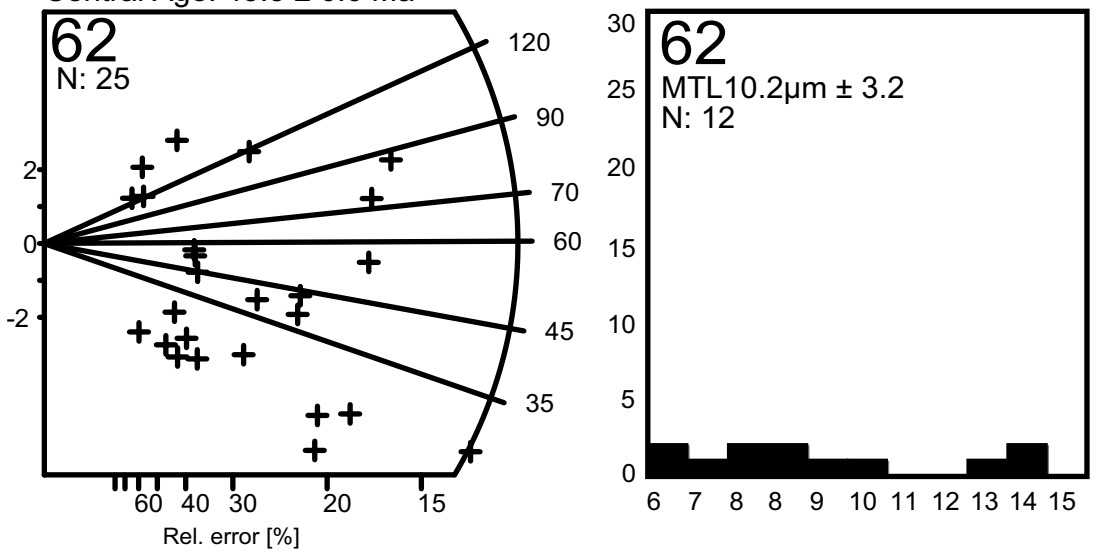


Serpukhov.: 326-318 Ma
Central Age: 173.9 ± 16.8 Ma

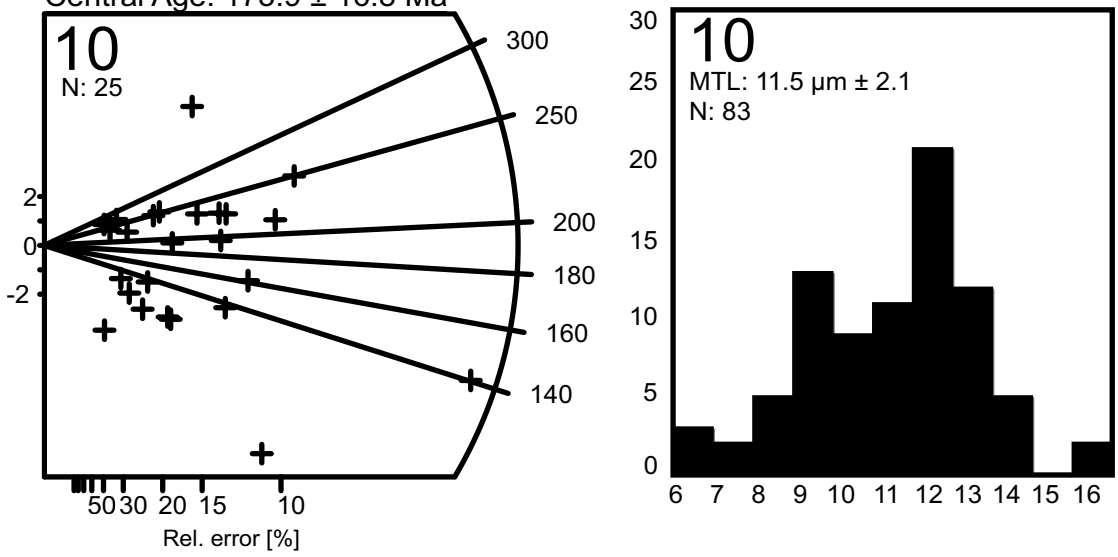


Bashkir.-Moscov.: 318-307 Ma
Central Age: 95.0 ± 9.4 Ma

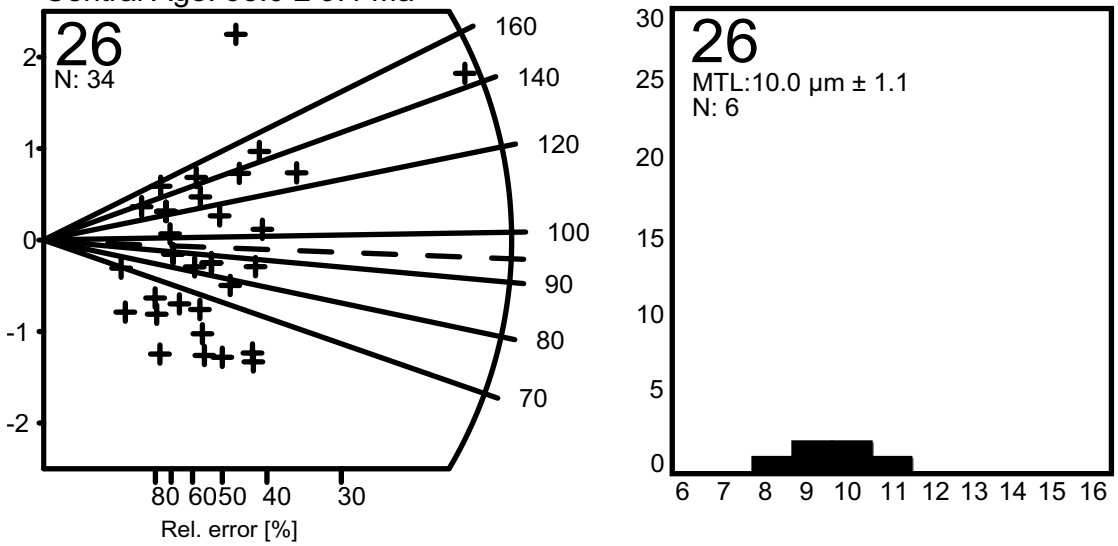

Fras. Fammen.: 385-359 Ma
Central Age: 160.7 ± 31.6 Ma

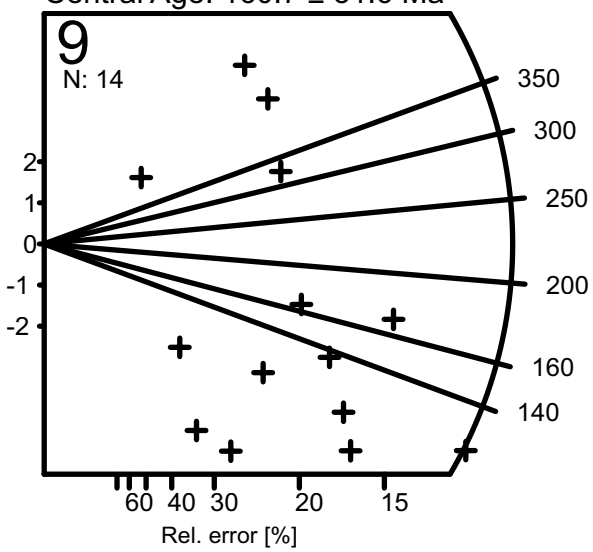


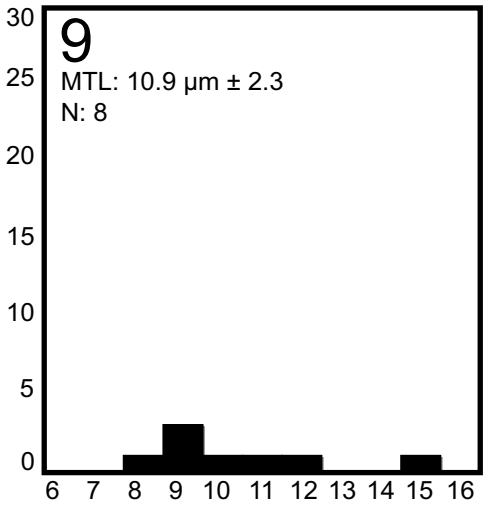


M. Cambrian: 513-501 Ma
Central Age: 157.3 ± 10.4 Ma

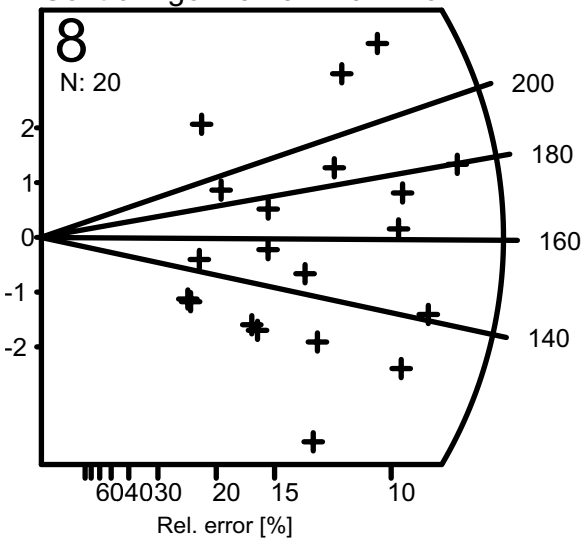


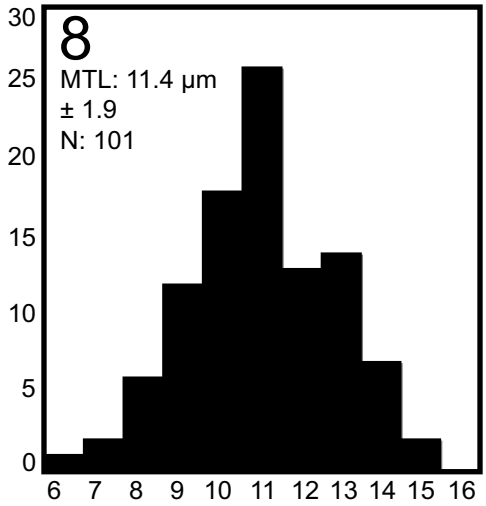


Stephanian B: 302-301 Ma
Central Age: 141.2 ± 15.3 Ma

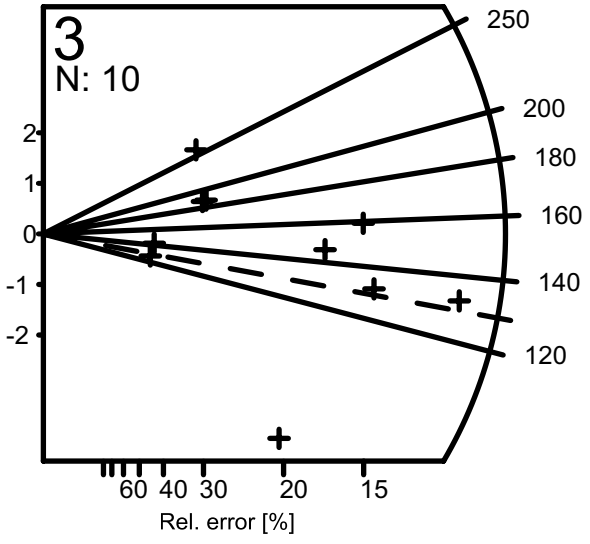


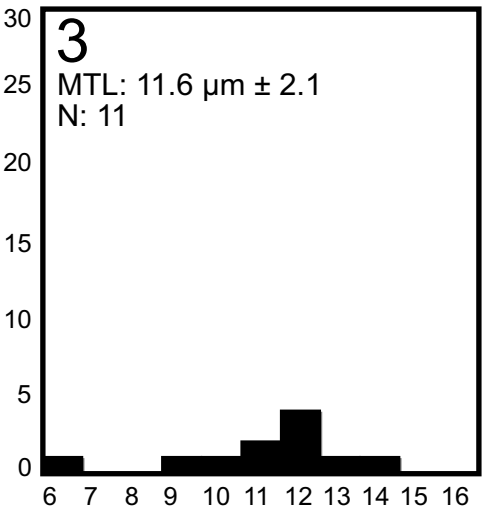

Stephanian B: 302-301 Ma
Central Age: 178.0 ± 23.81 Ma

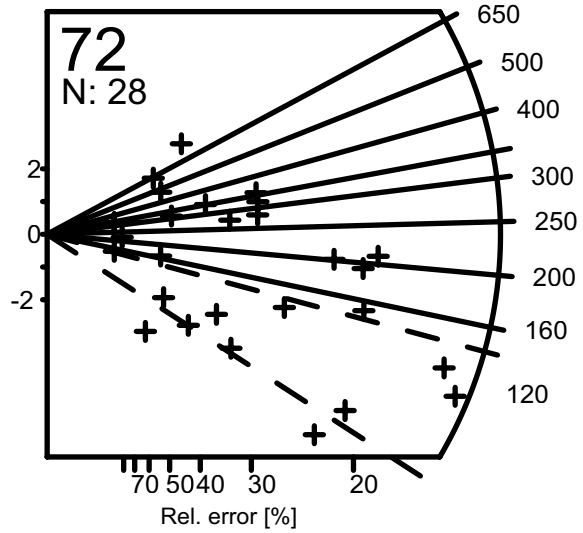


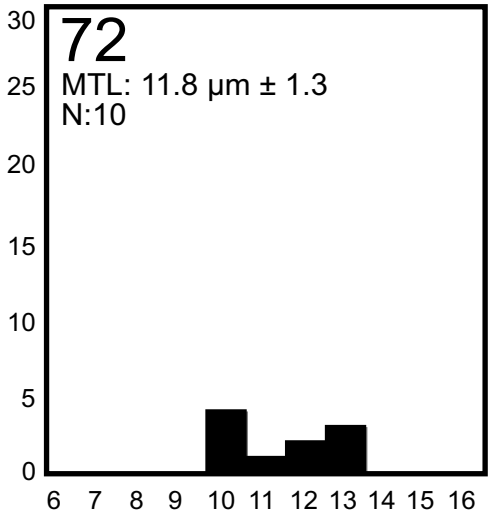


Stephanian B: 302-301 Ma
Central Age: 161.2 ± 10.9 Ma

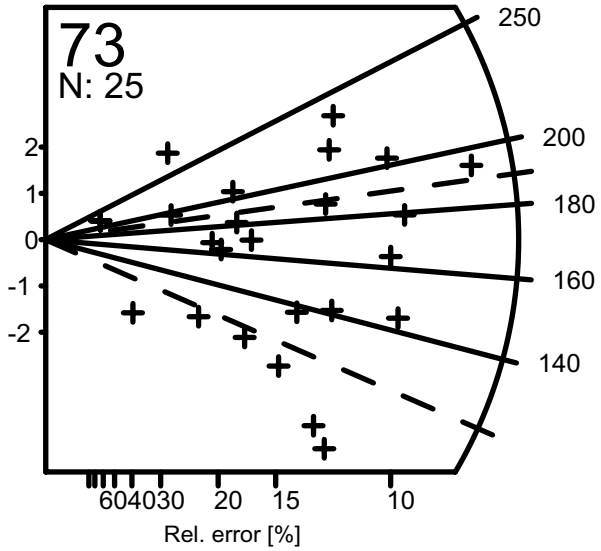


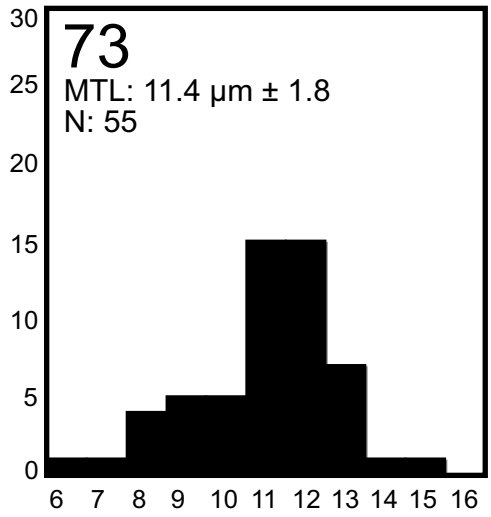


Stephanian B: 302-301 Ma
Central Age: 170.0 ± 10.7 Ma

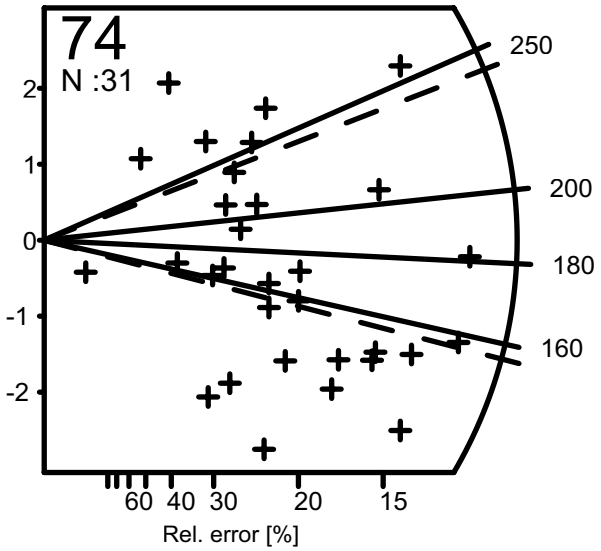


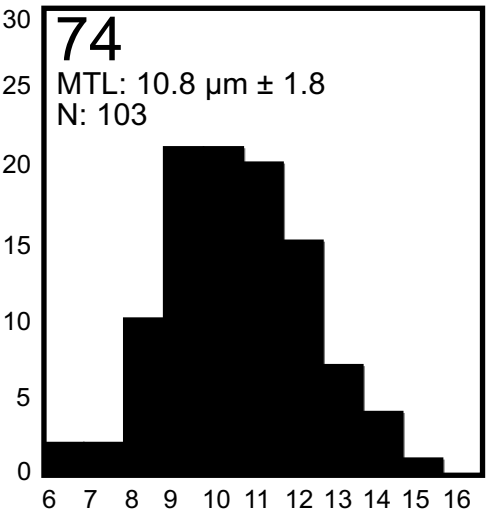

Stephanian B: 302-301 Ma
Central Age: 177.1 ± 15.8 Ma

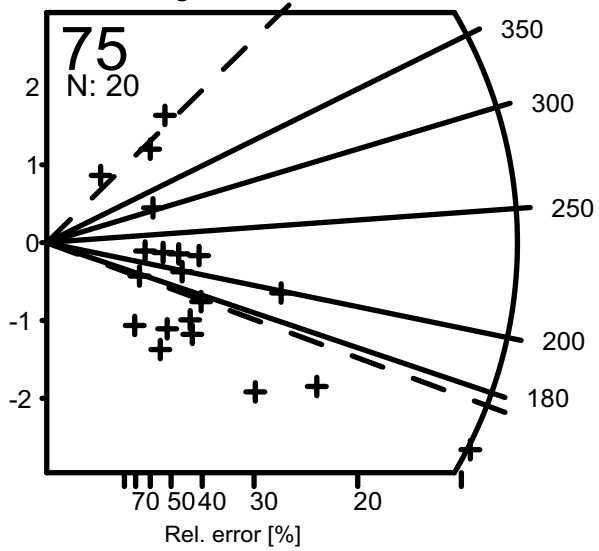


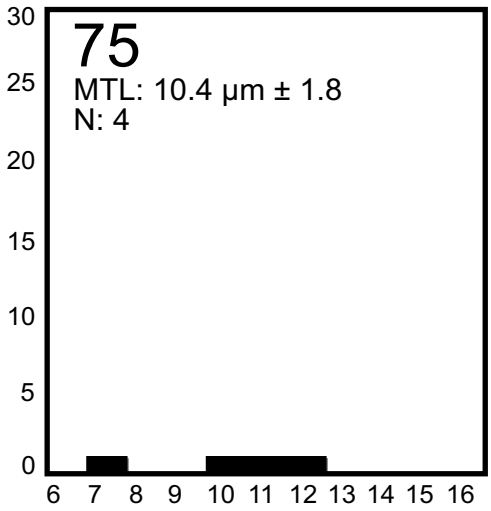


Stephanian B: 302-301 Ma
Central Age: 163.1 ± 13.4 Ma

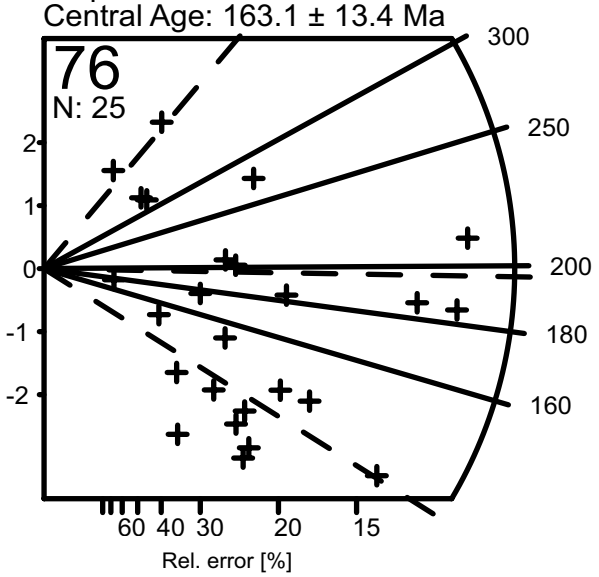


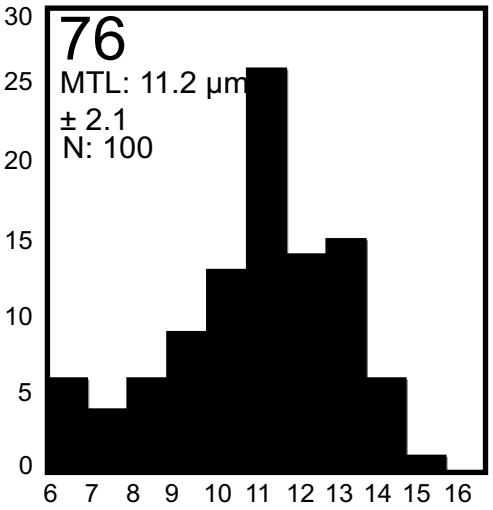


Stephanian B: 302-301 Ma
Central Age: 255.9 ± 19.8 Ma

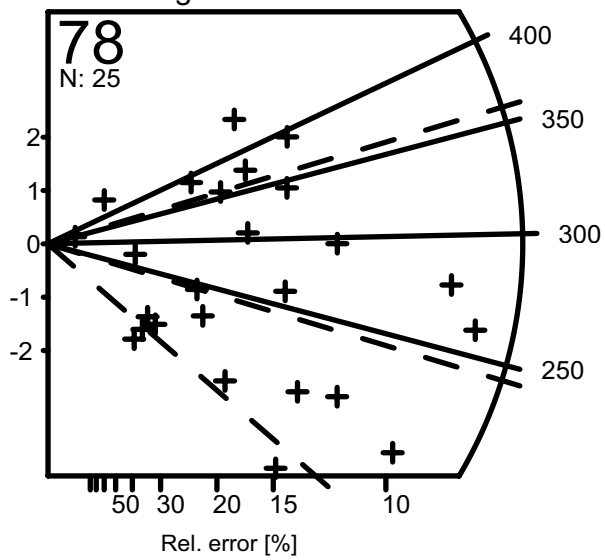


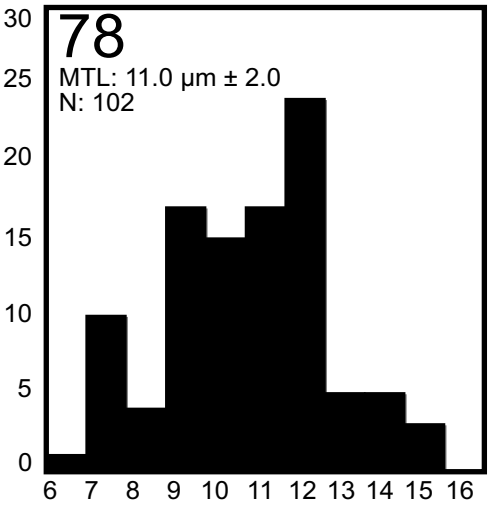

Stephanian B: 302-301 Ma
Central Age: 162.5 ± 11.7 Ma

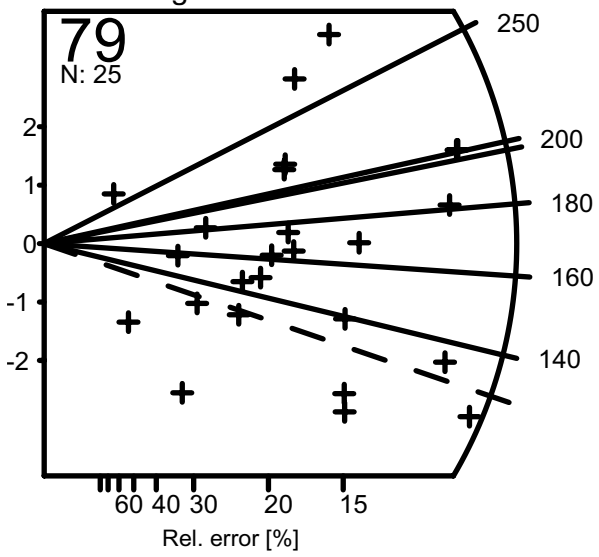


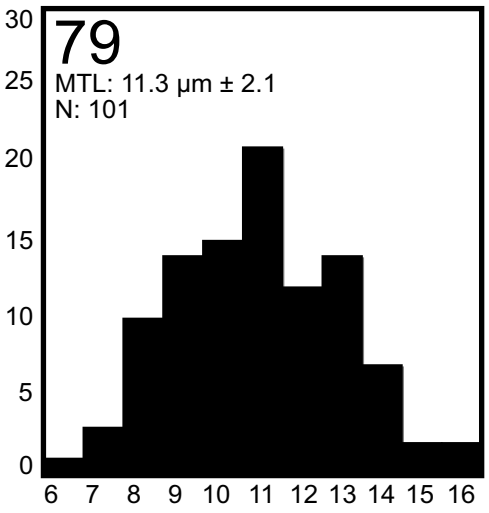


Stephanian B: 302-301 Ma
Central Age: 244.9 ± 20.2 Ma

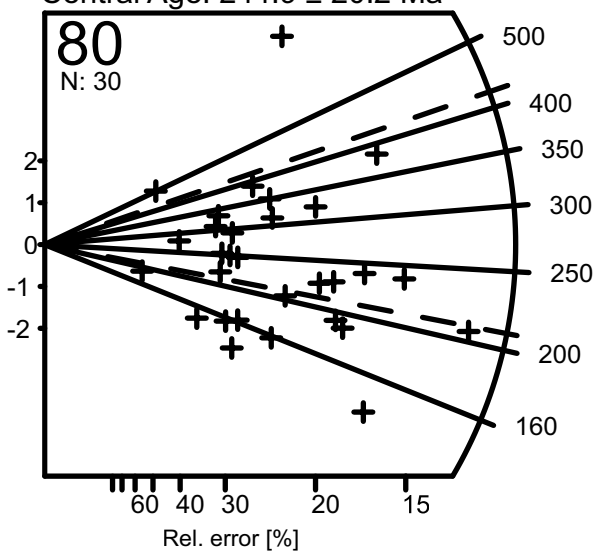


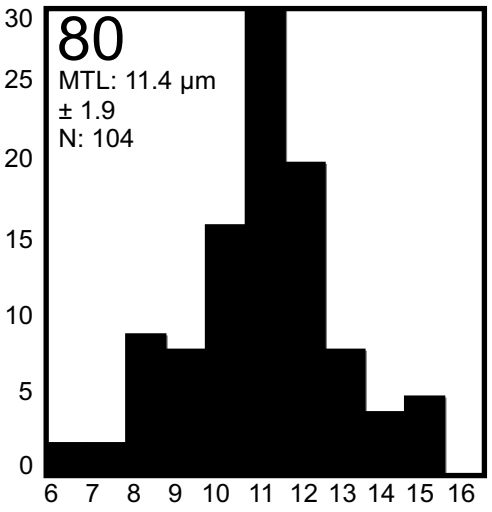


Bashkir.-Moscov.: 318-307 Ma
Central Age: 174.6 ± 20.1 Ma

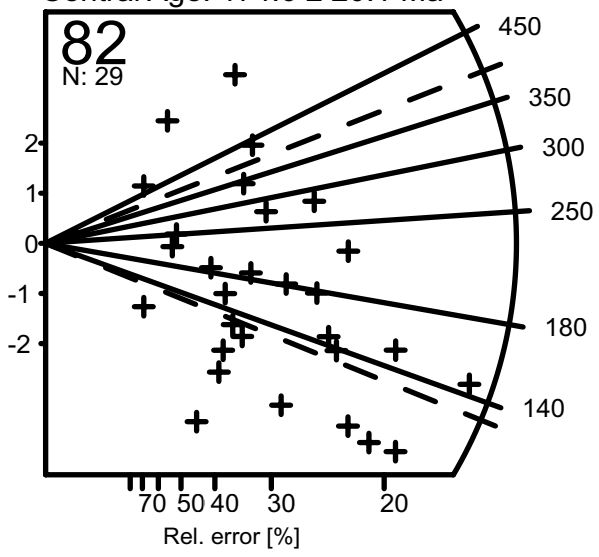


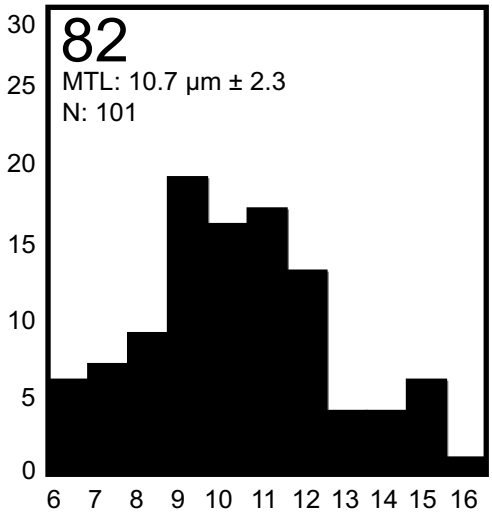

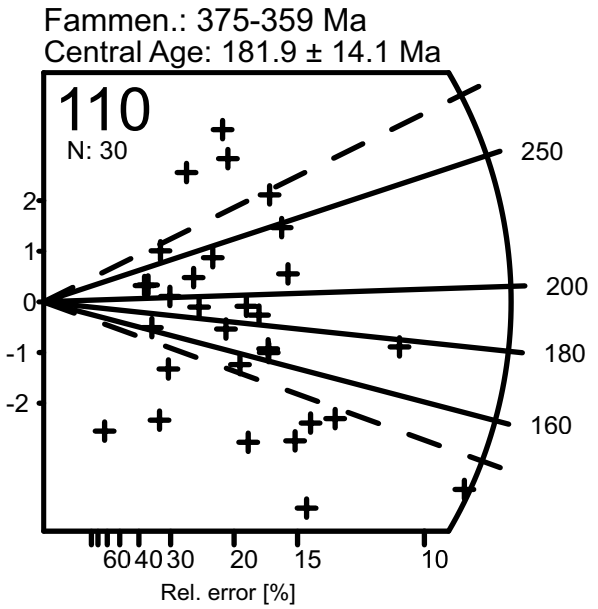
Fammen.: 375-359 Ma
Central Age: 181.9 ± 14.1 Ma
110
N: 30
250
200
180
160
2
1
0
-1
-2
60 40 30 20 15 10
Rel. error [%]

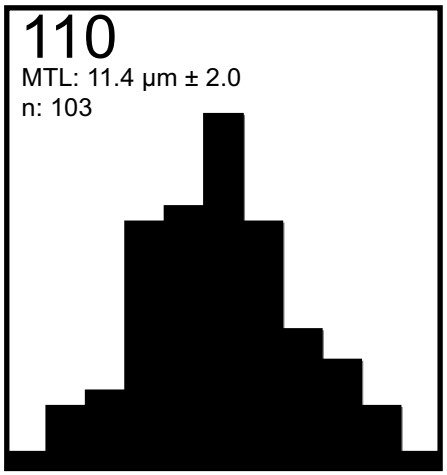
110
MTL: 11.4 µm ± 2.0
n: 103

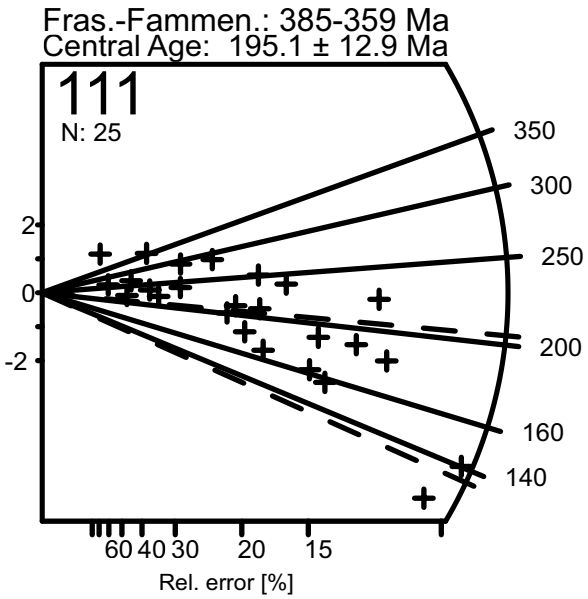
Fras.-Fammen.: 385-359 Ma
Central Age: 195.1 ± 12.9 Ma
111
N: 25
350
300
250
200
160
140
2
0
-2
60 40 30 20 15
Rel. error [%]

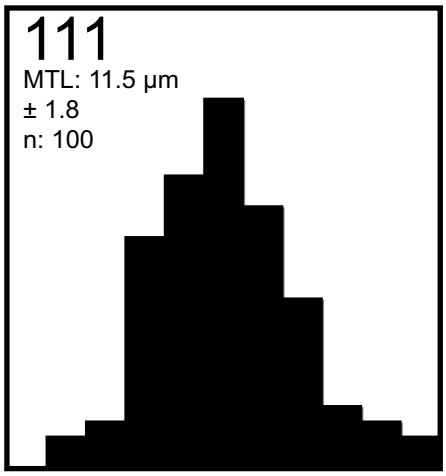
111
MTL: 11.5 µm
± 1.8
n: 100

# Appendix iii: AFT age versus annealing kinetic parameters

Sample 25

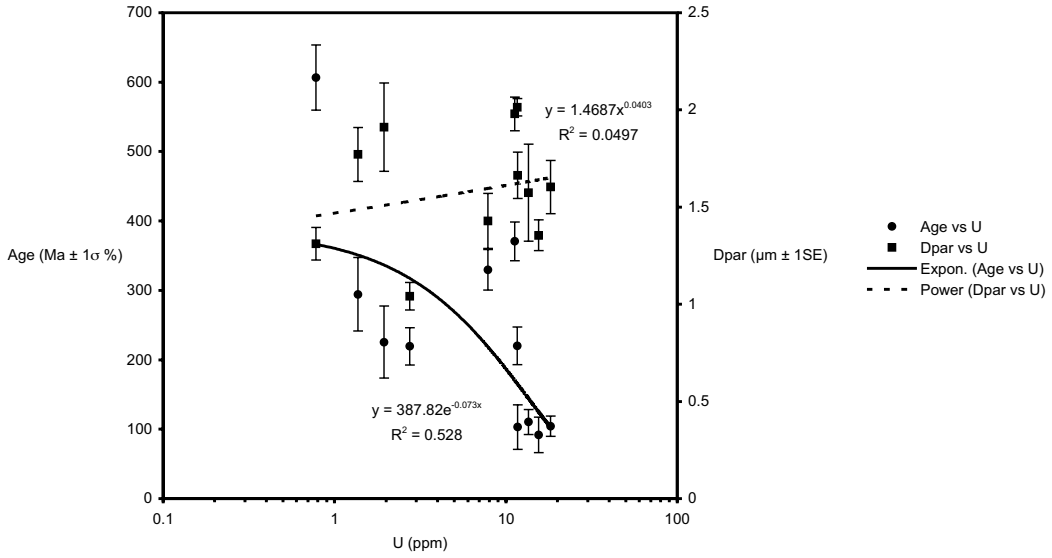


Sample 18

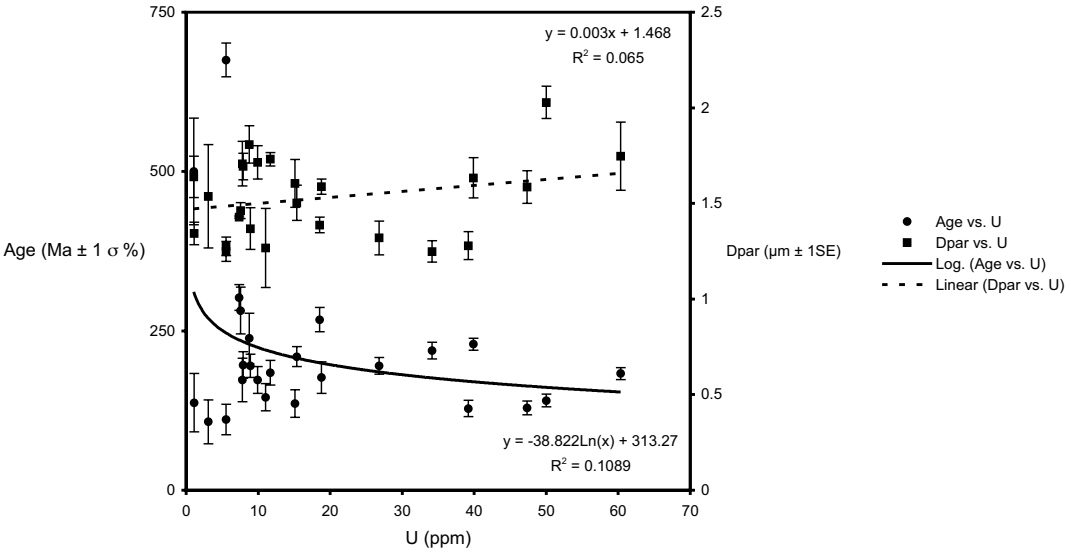

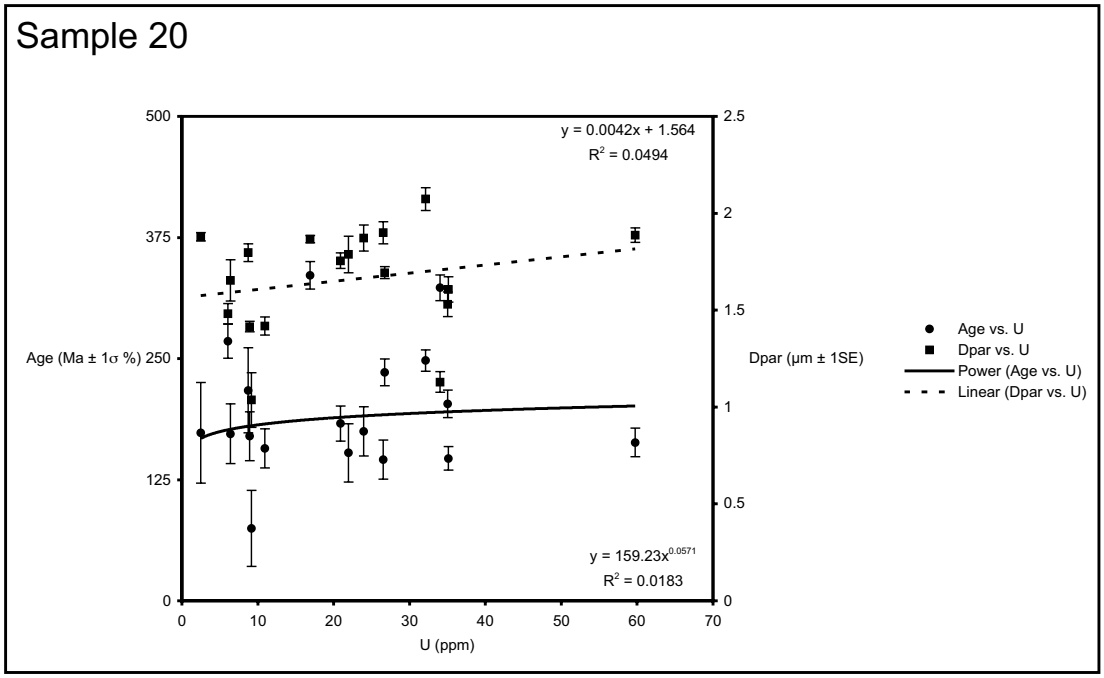
Sample 20
y = 0.0042x + 1.564
R2 = 0.0494
y = 159.23x-0.0571
R2 = 0.0183
Age (Ma ± 1σ %)
Dpar (µm ± 1SE)
U (ppm)
Age vs. U
Dpar vs. U
Power (Age vs. U)
Linear (Dpar vs. U)

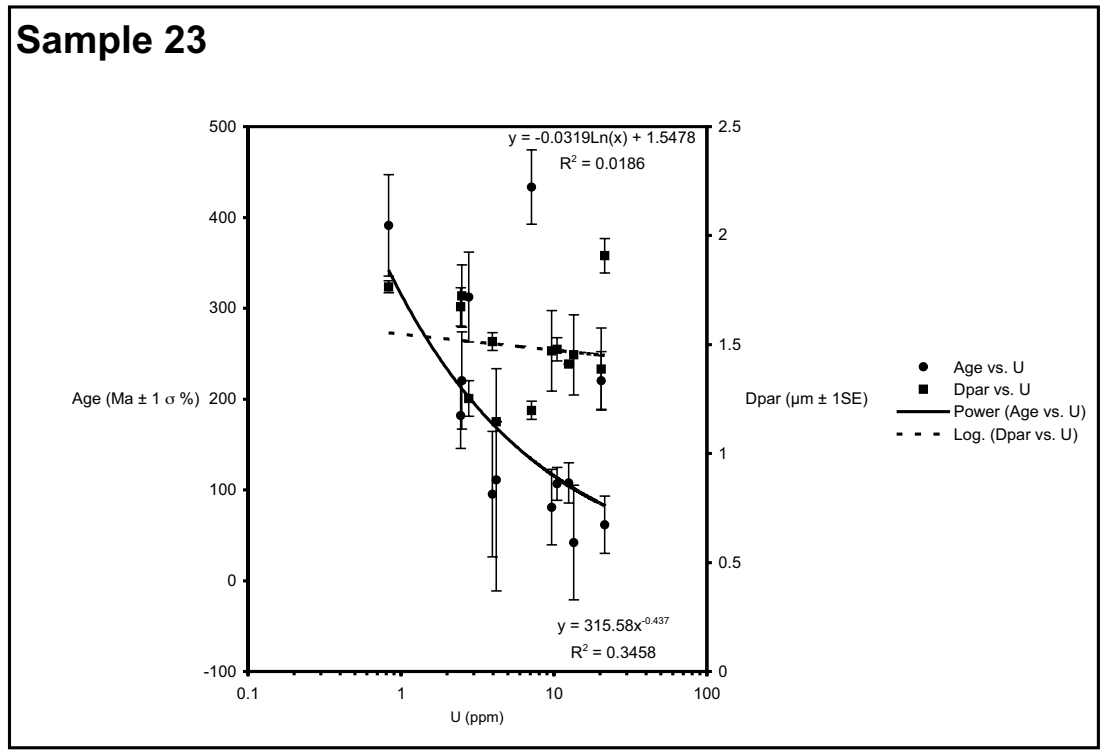
Sample 23
y = -0.0319Ln(x) + 1.5478
R2 = 0.0186
y = 315.58x-0.437
R2 = 0.3458
Age (Ma ± 1 σ %)
Dpar (µm ± 1SE)
U (ppm)
Age vs. U
Dpar vs. U
Power (Age vs. U)
Log. (Dpar vs. U)

## Sample 22

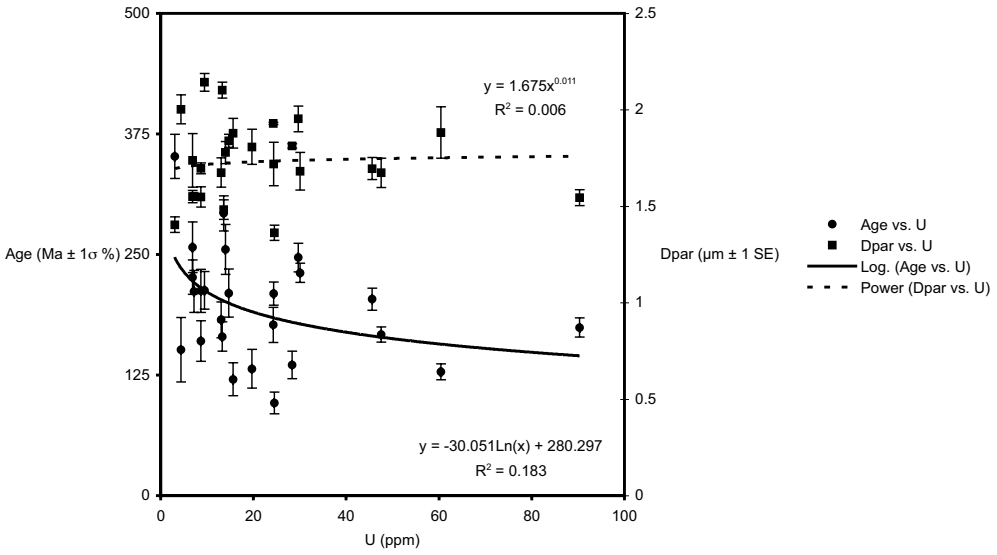


## Sample 114

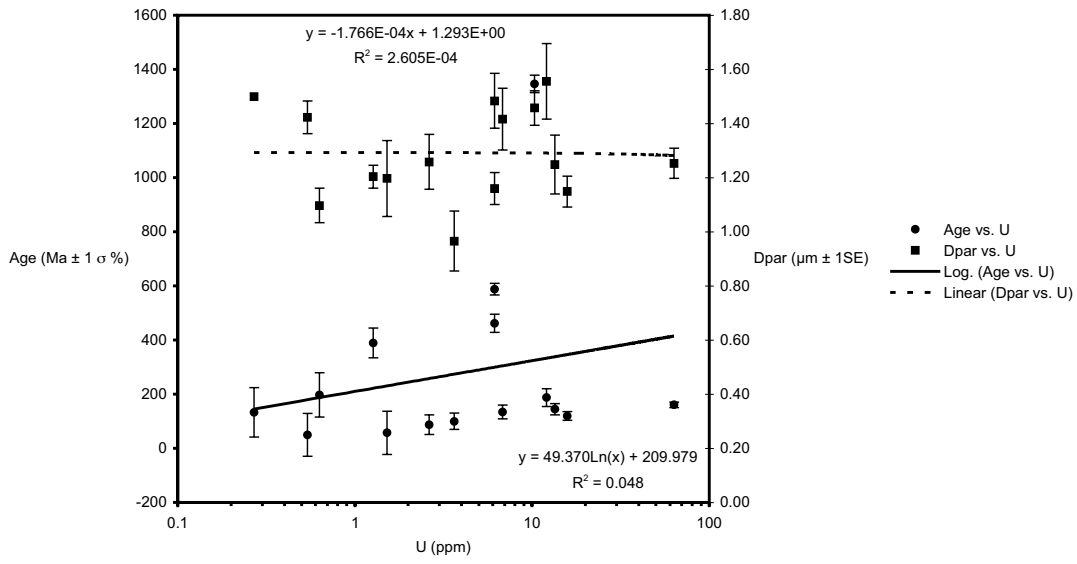

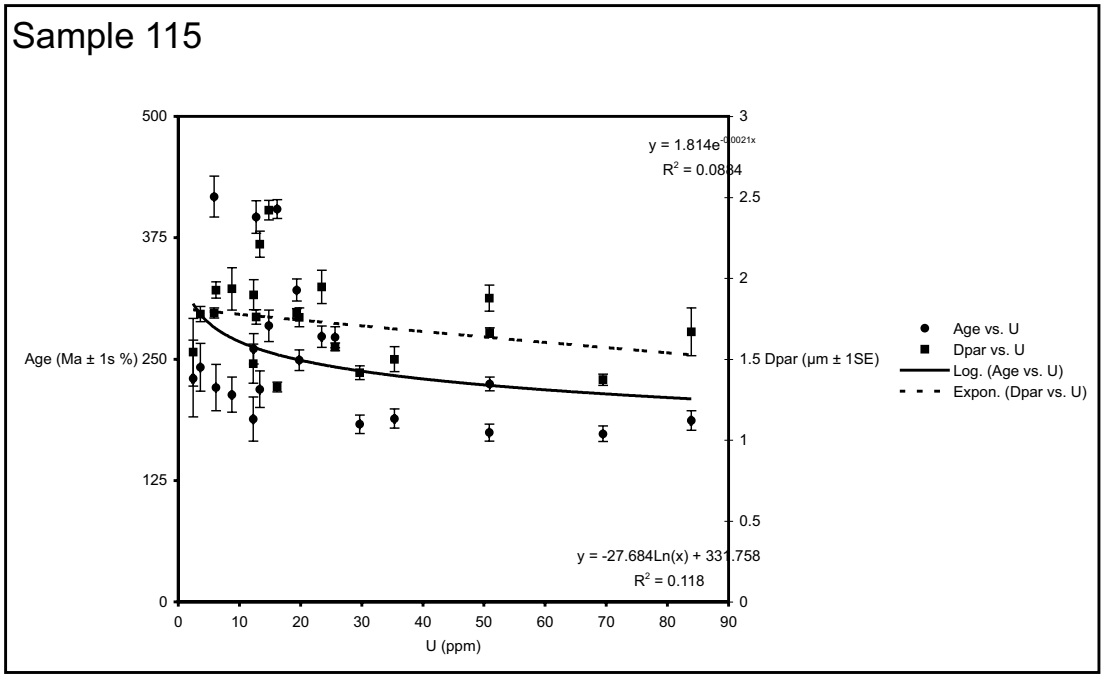
Sample 115
y = 1.814e-0.0021x
R2 = 0.0834
y = -27.684Ln(x) + 331.758
R2 = 0.118
Age (Ma ± 1s %)
Dpar (µm ± 1SE)
U (ppm)
Age vs. U
Dpar vs. U
Log. (Age vs. U)
Expon. (Dpar vs. U)

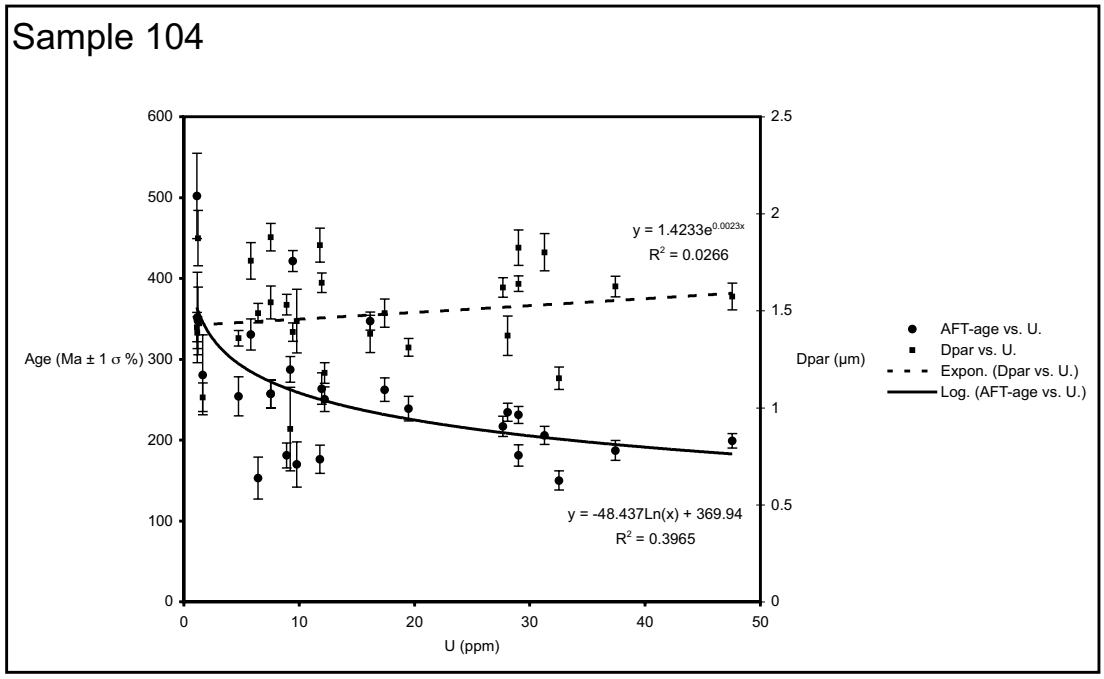
Sample 104
y = 1.4233e0.0023x
R2 = 0.0266
y = -48.437Ln(x) + 369.94
R2 = 0.3965
Age (Ma ± 1 σ %)
Dpar (µm)
U (ppm)
AFT-age vs. U.
Dpar vs. U.
Expon. (Dpar vs. U.)
Log. (AFT-age vs. U.)

## Sample 105

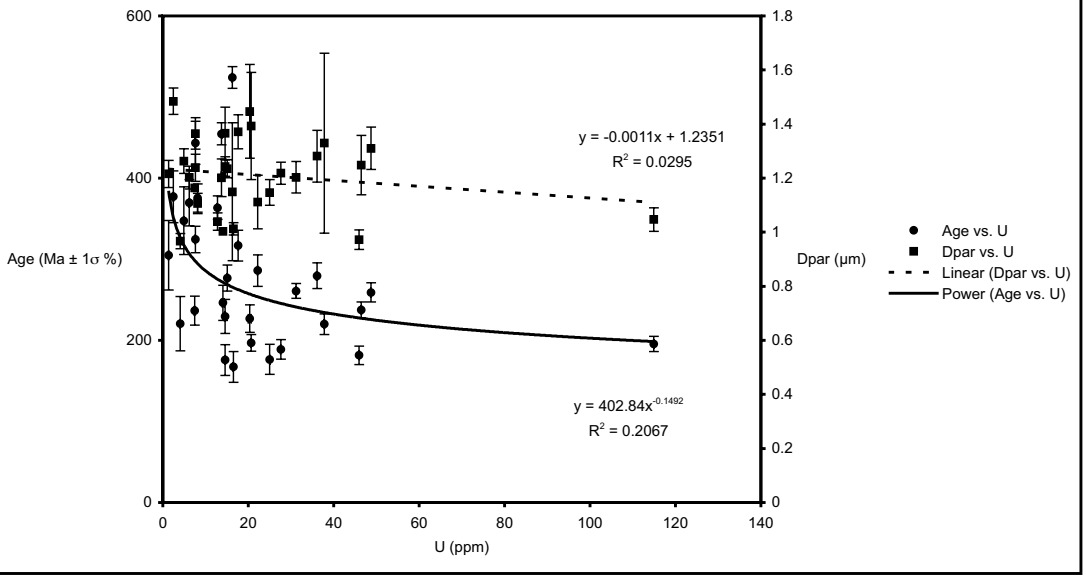


## Sample 106

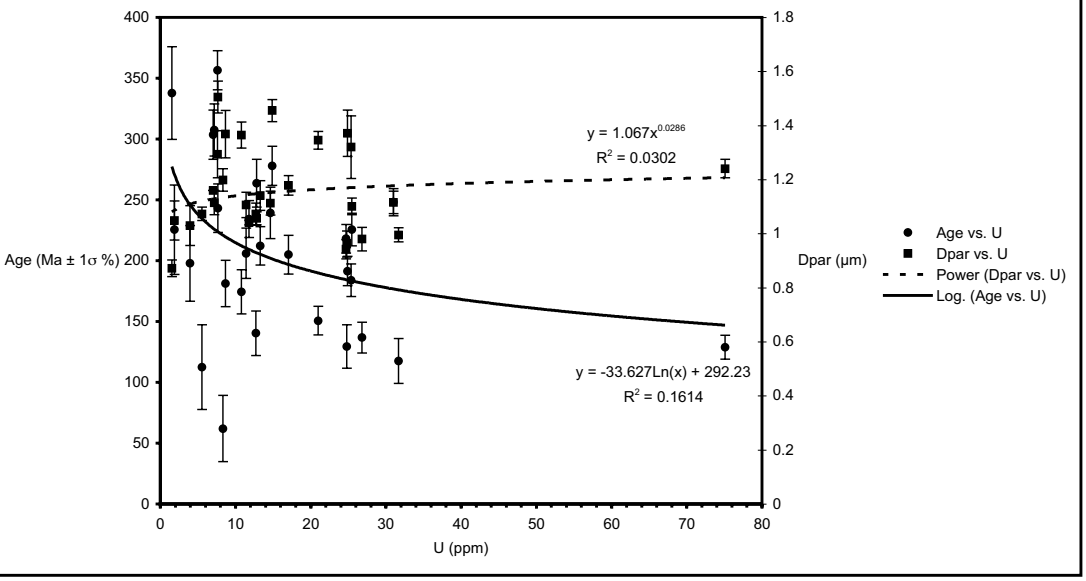

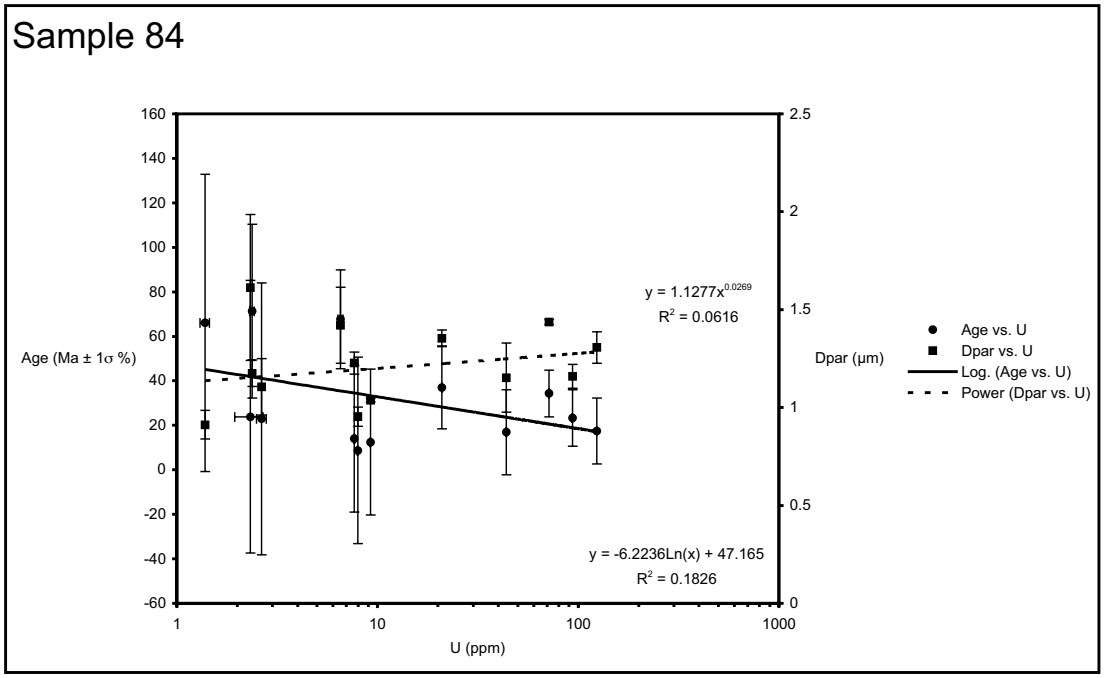
Sample 84
Age (Ma ± 1σ %)
Dpar (µm)
U (ppm)
y = 1.1277x^0.0269
R² = 0.0616
y = -6.2236Ln(x) + 47.165
R² = 0.1826
Age vs. U
Dpar vs. U
Log. (Age vs. U)
Power (Dpar vs. U)

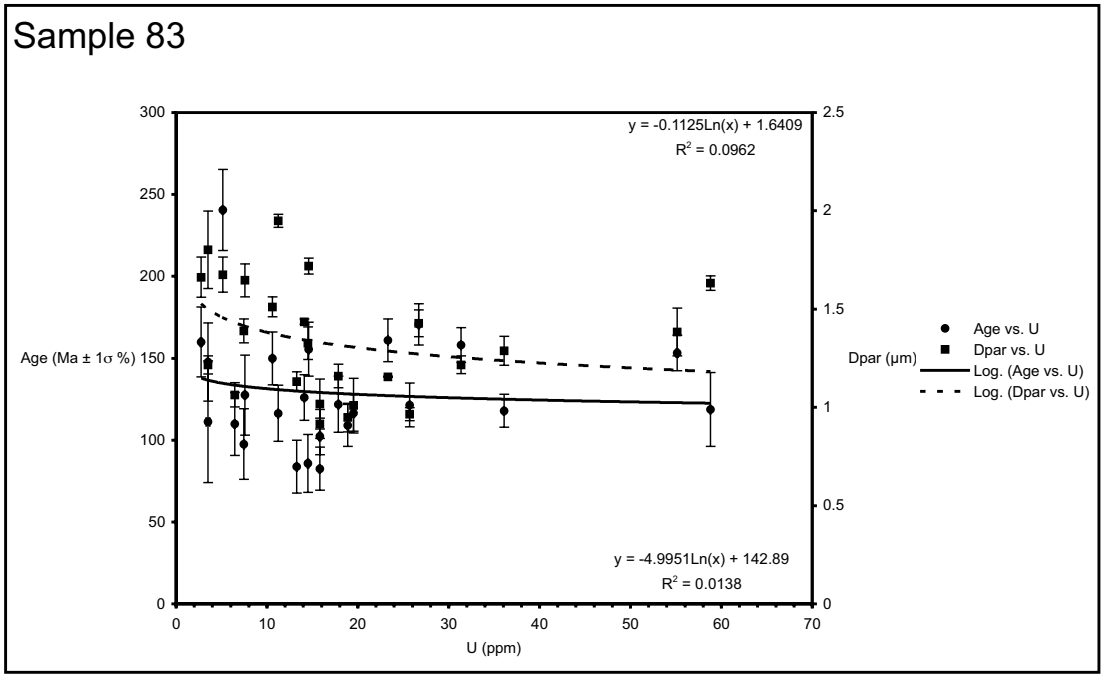
Sample 83
Age (Ma ± 1σ %)
Dpar (µm)
U (ppm)
y = -0.1125Ln(x) + 1.6409
R² = 0.0962
y = -4.9951Ln(x) + 142.89
R² = 0.0138
Age vs. U
Dpar vs. U
Log. (Age vs. U)
Log. (Dpar vs. U)

## Sample 85

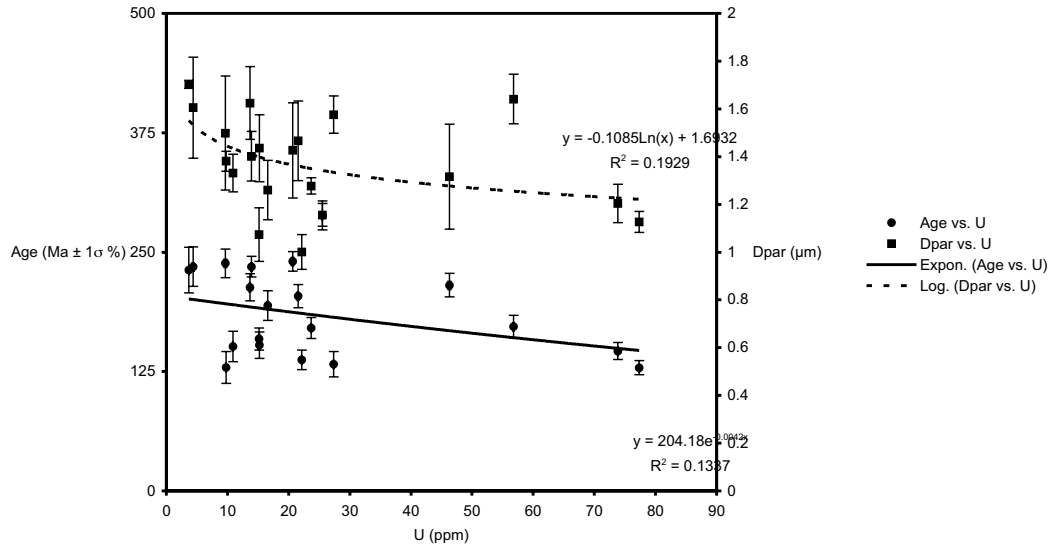


## Sample 91

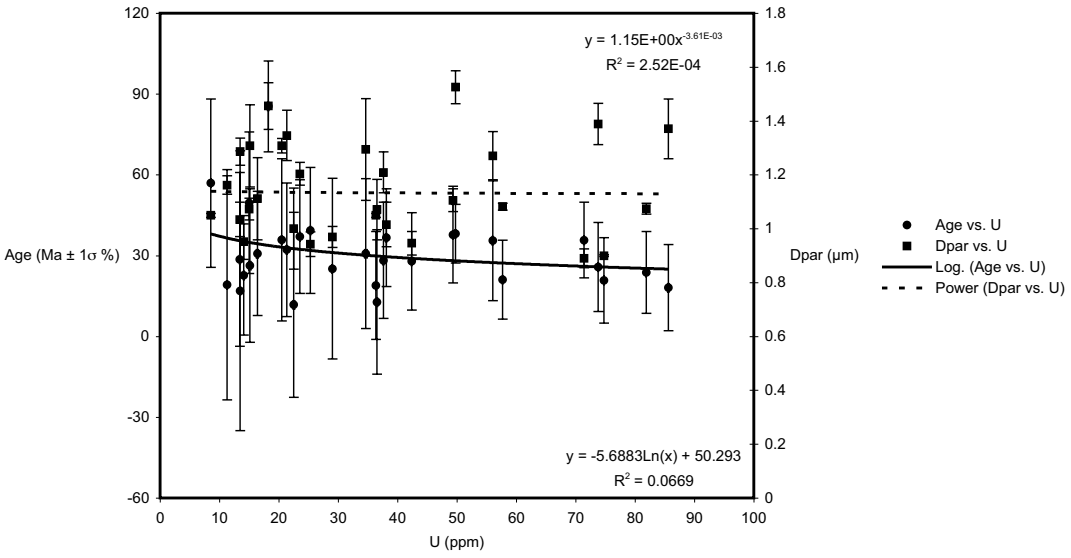

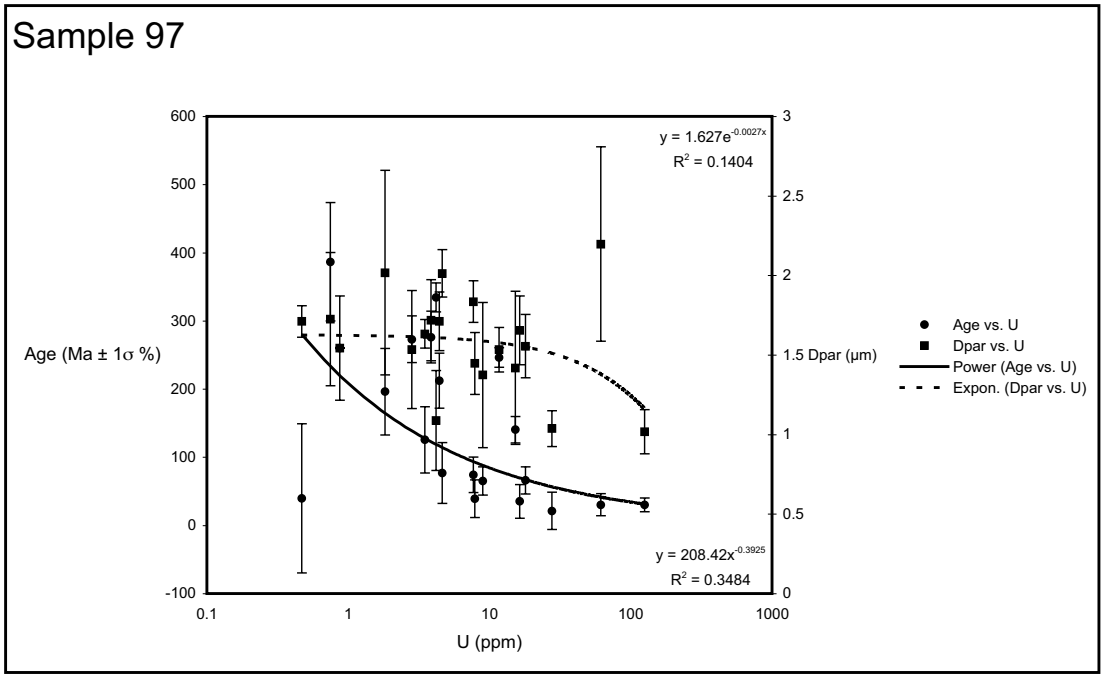
Sample 97
y = 1.627e-0.0027x
R2 = 0.1404
y = 208.42x-0.3925
R2 = 0.3484
Age (Ma ± 1σ %)
1.5 Dpar (µm)
U (ppm)
Age vs. U
Dpar vs. U
Power (Age vs. U)
Expon. (Dpar vs. U)

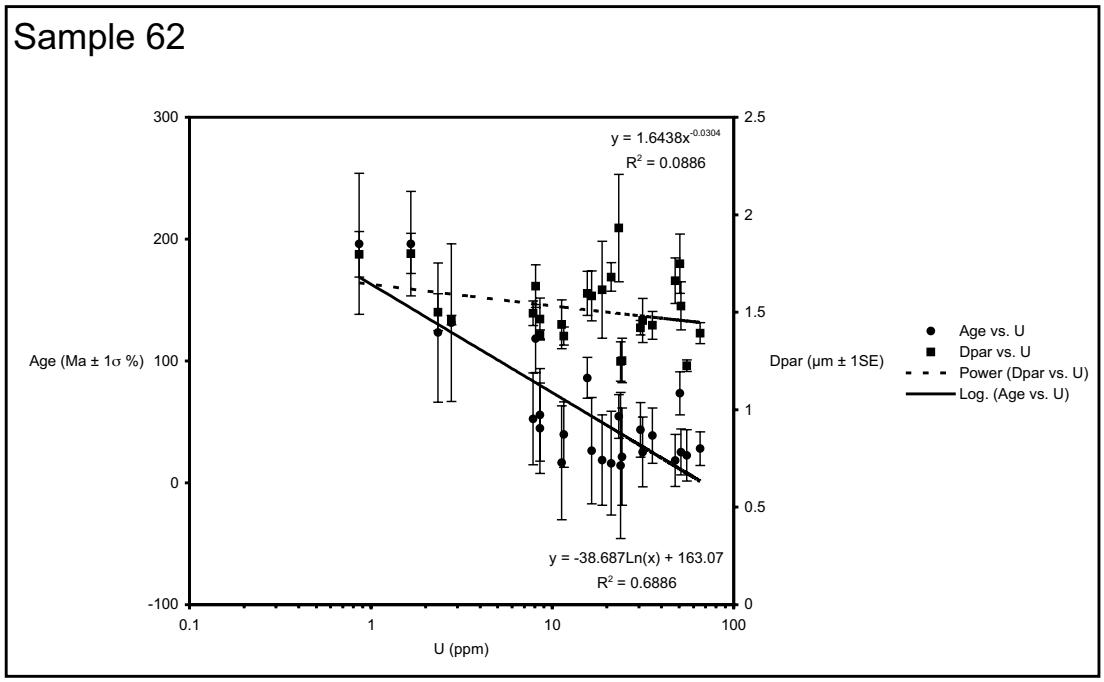
Sample 62
y = 1.6438x-0.0304
R2 = 0.0886
y = -38.687Ln(x) + 163.07
R2 = 0.6886
Age (Ma ± 1σ %)
Dpar (µm ± 1SE)
U (ppm)
Age vs. U
Dpar vs. U
Power (Dpar vs. U)
Log. (Age vs. U)

## Sample 10

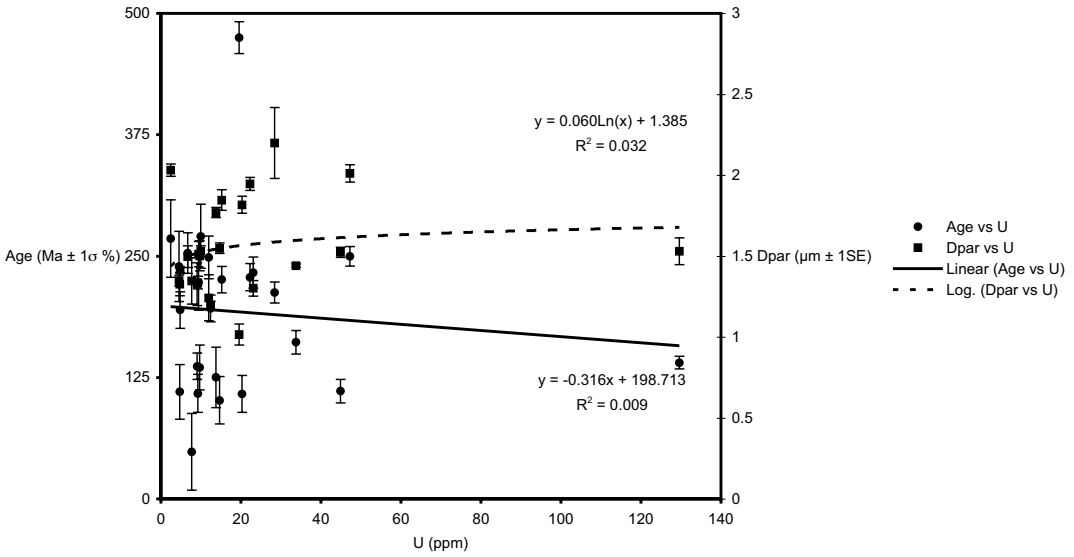


## Sample 26

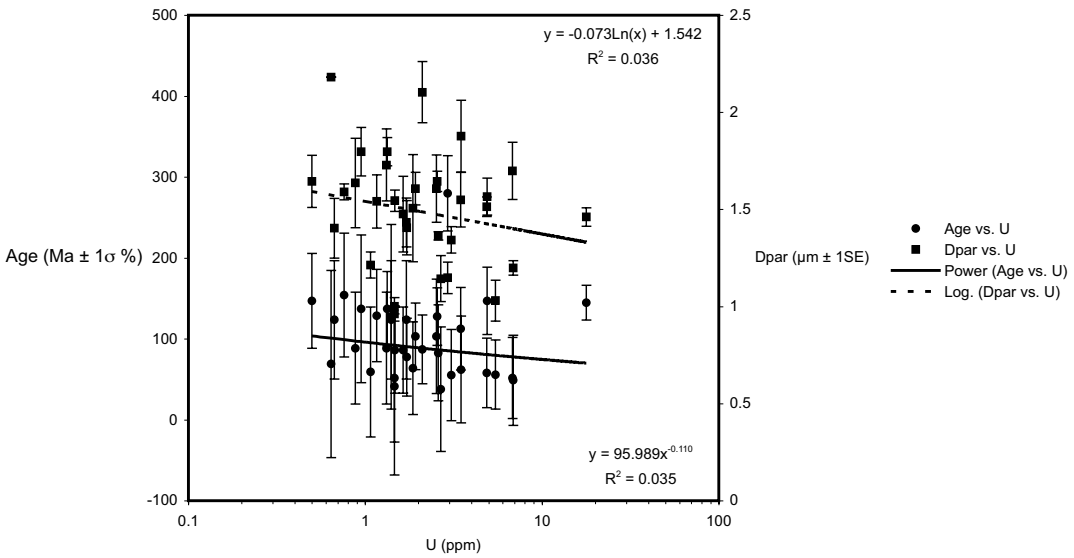

Sample 9

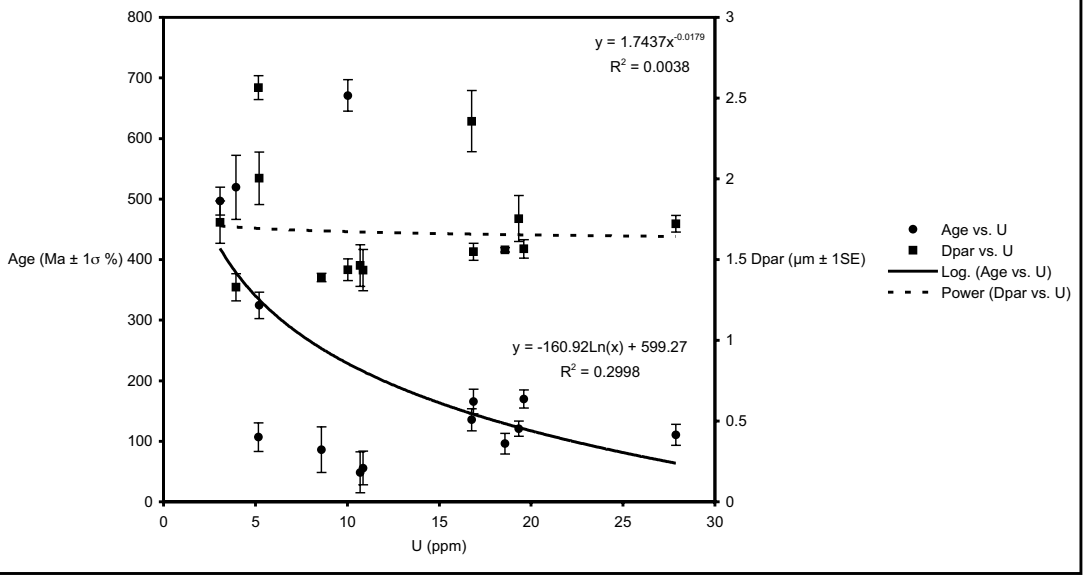


Sample 8

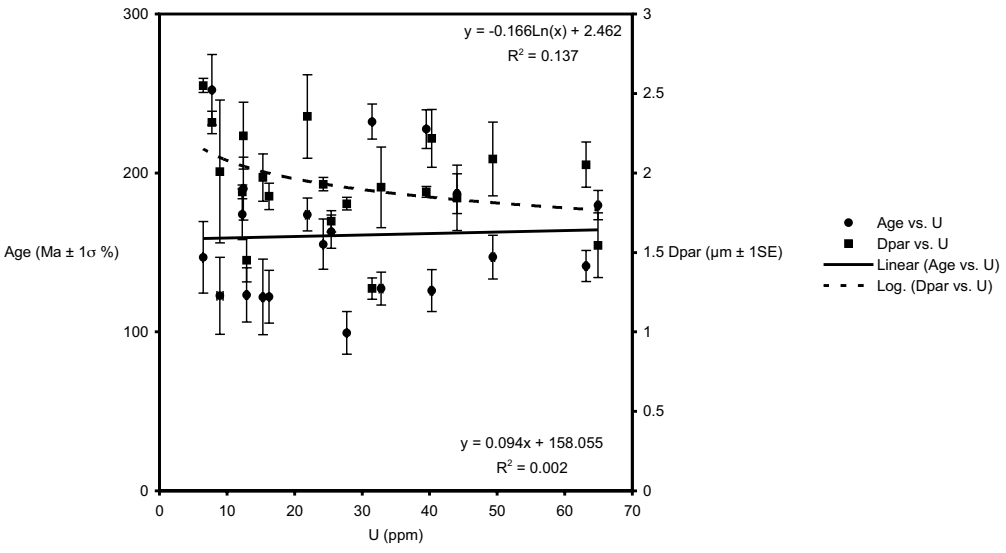

## Sample 3

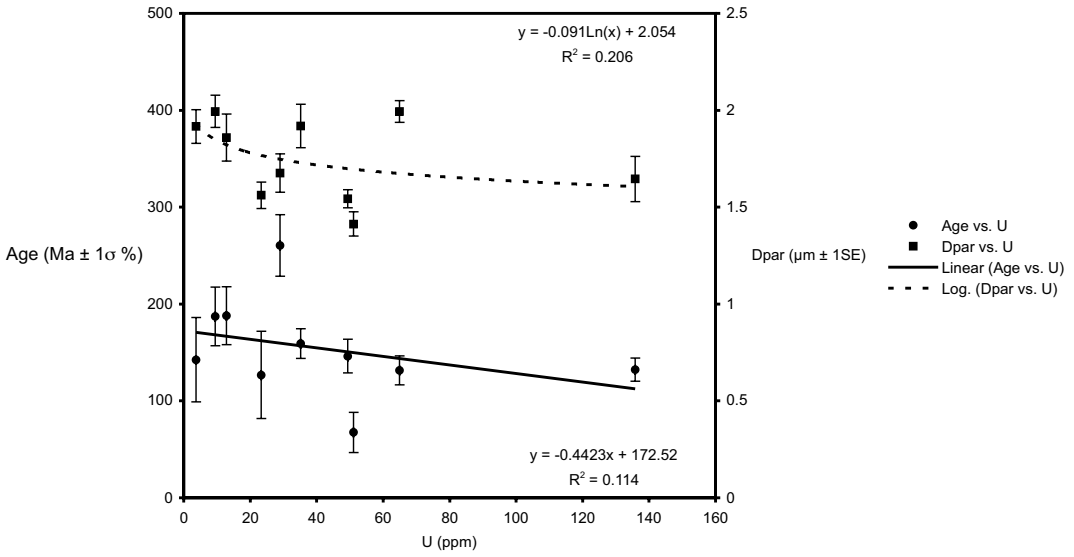


## Sample 72

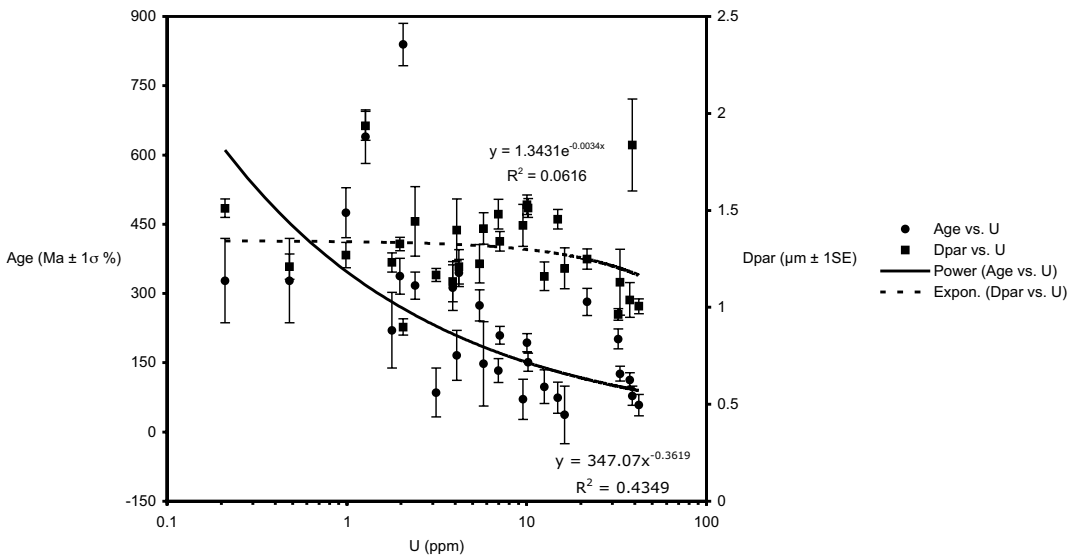

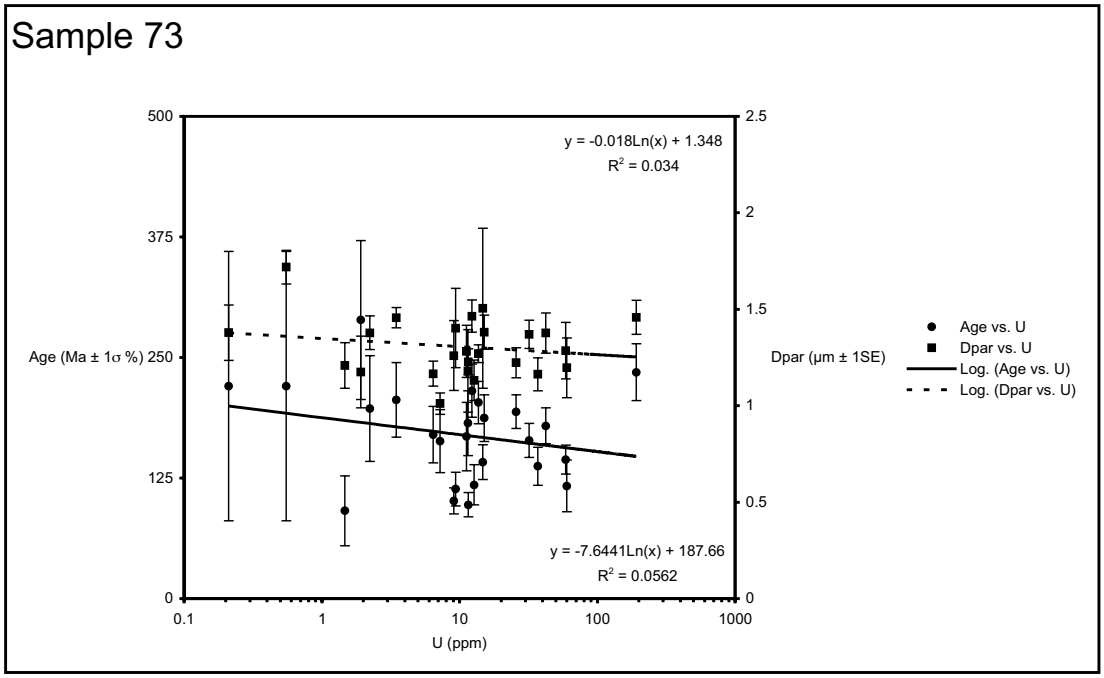
Sample 73
y = -0.018Ln(x) + 1.348
R2 = 0.034
y = -7.6441Ln(x) + 187.66
R2 = 0.0562
Age (Ma ± 1σ %)
Dpar (µm ± 1SE)
U (ppm)
Age vs. U
Dpar vs. U
Log. (Age vs. U)
Log. (Dpar vs. U)

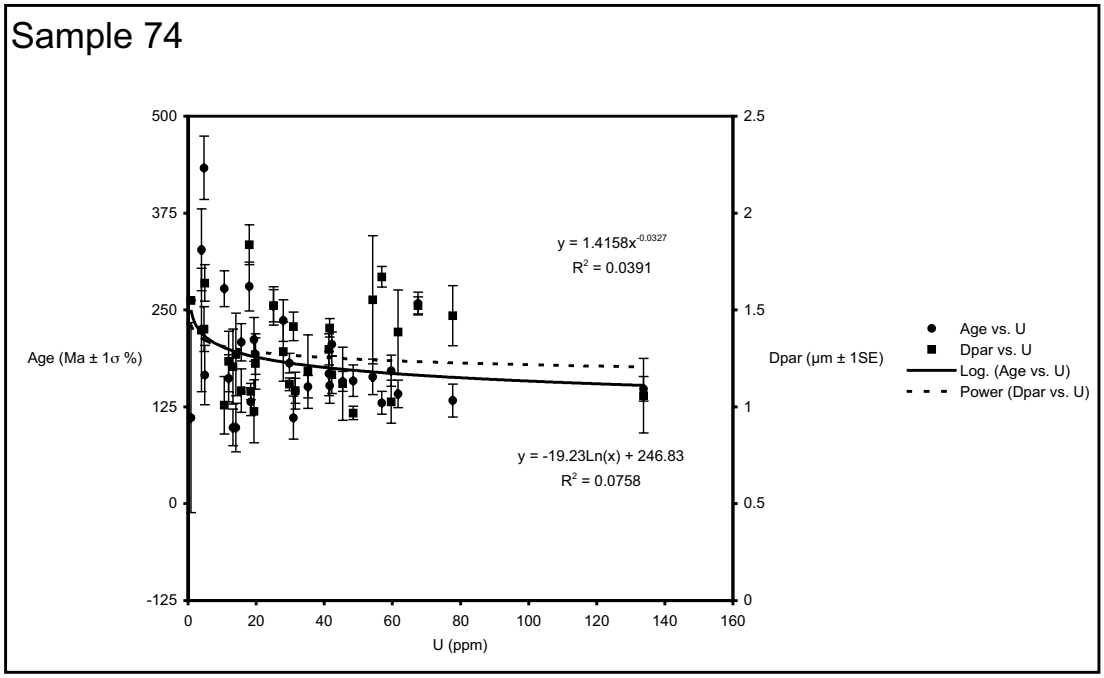
Sample 74
y = 1.4158x-0.0327
R2 = 0.0391
y = -19.23Ln(x) + 246.83
R2 = 0.0758
Age (Ma ± 1σ %)
Dpar (µm ± 1SE)
U (ppm)
Age vs. U
Dpar vs. U
Log. (Age vs. U)
Power (Dpar vs. U)

## Sample 75

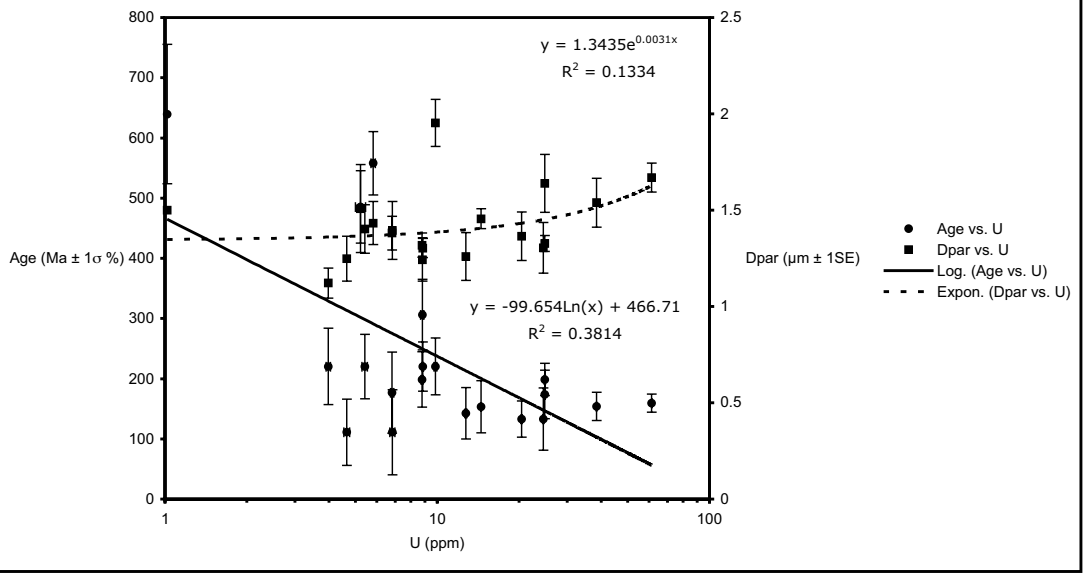


## Sample 76

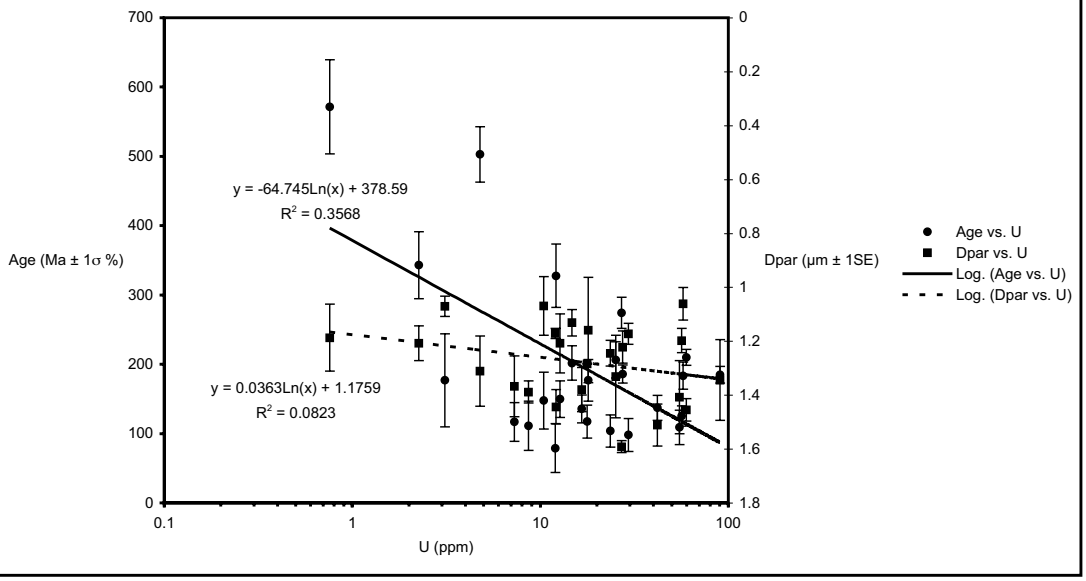

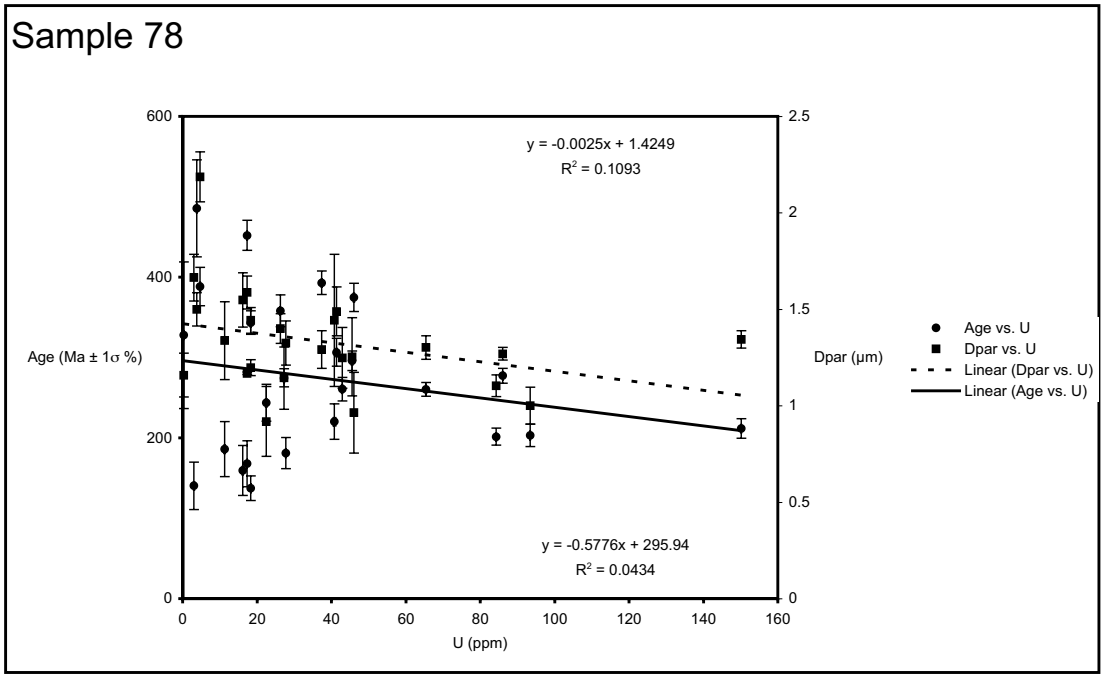
Sample 78
y = -0.0025x + 1.4249
R2 = 0.1093
y = -0.5776x + 295.94
R2 = 0.0434
Age (Ma ± 1σ %)
Dpar (µm)
U (ppm)
Age vs. U
Dpar vs. U
Linear (Dpar vs. U)
Linear (Age vs. U)

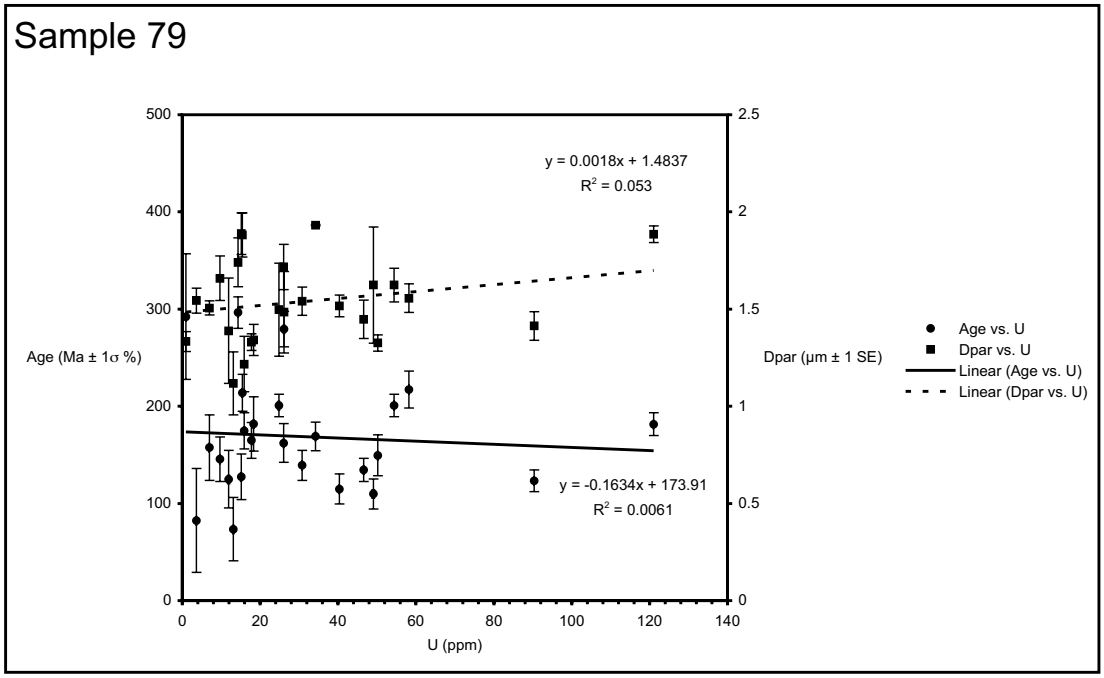
Sample 79
y = 0.0018x + 1.4837
R2 = 0.053
y = -0.1634x + 173.91
R2 = 0.0061
Age (Ma ± 1σ %)
Dpar (µm ± 1 SE)
U (ppm)
Age vs. U
Dpar vs. U
Linear (Age vs. U)
Linear (Dpar vs. U)

## Sample 80

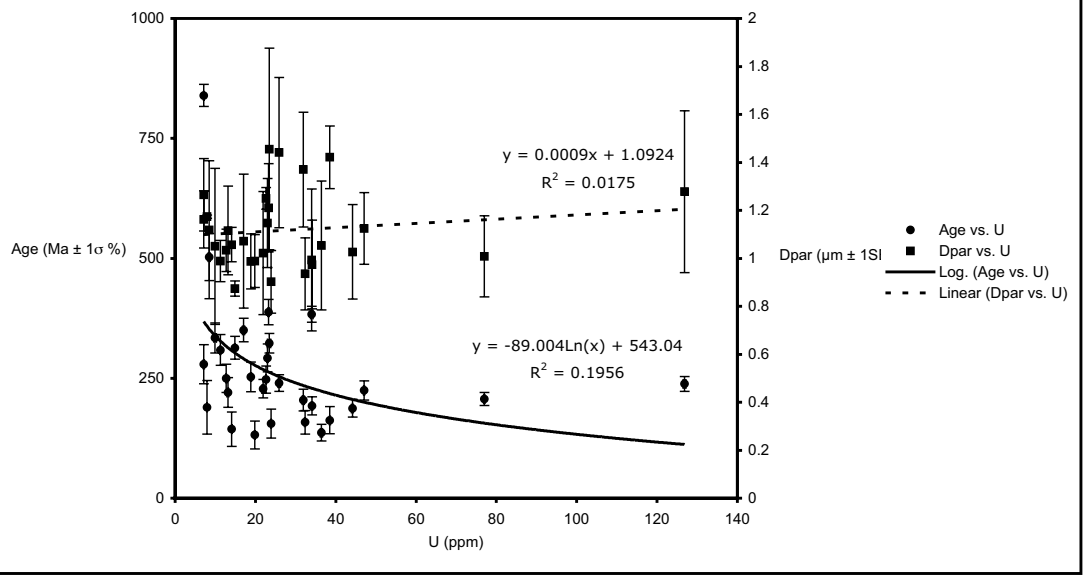


## Sample 82

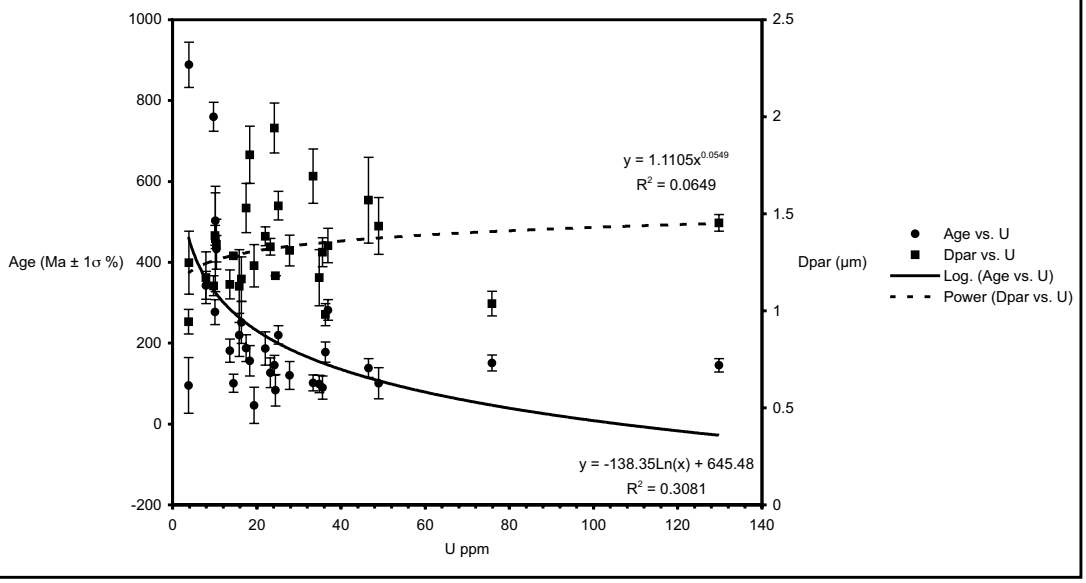

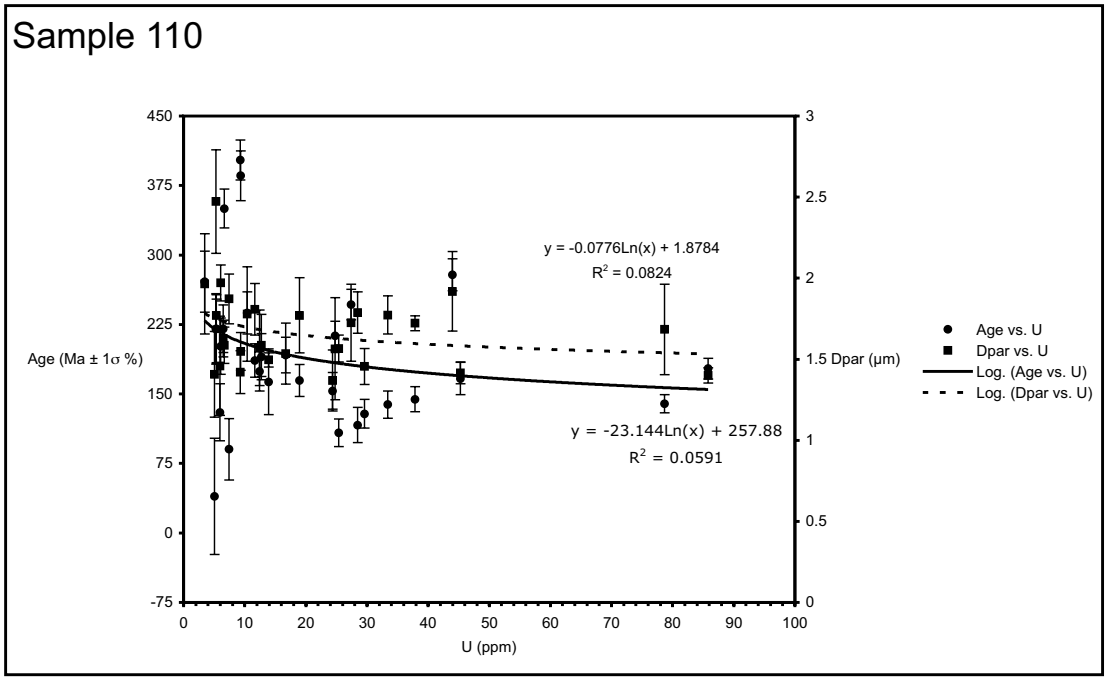
Sample 110
Age (Ma ± 1σ %)
Dpar (µm)
U (ppm)
y = -0.0776Ln(x) + 1.8784
R2 = 0.0824
y = -23.144Ln(x) + 257.88
R2 = 0.0591
Age vs. U
Dpar vs. U
Log. (Age vs. U)
Log. (Dpar vs. U)

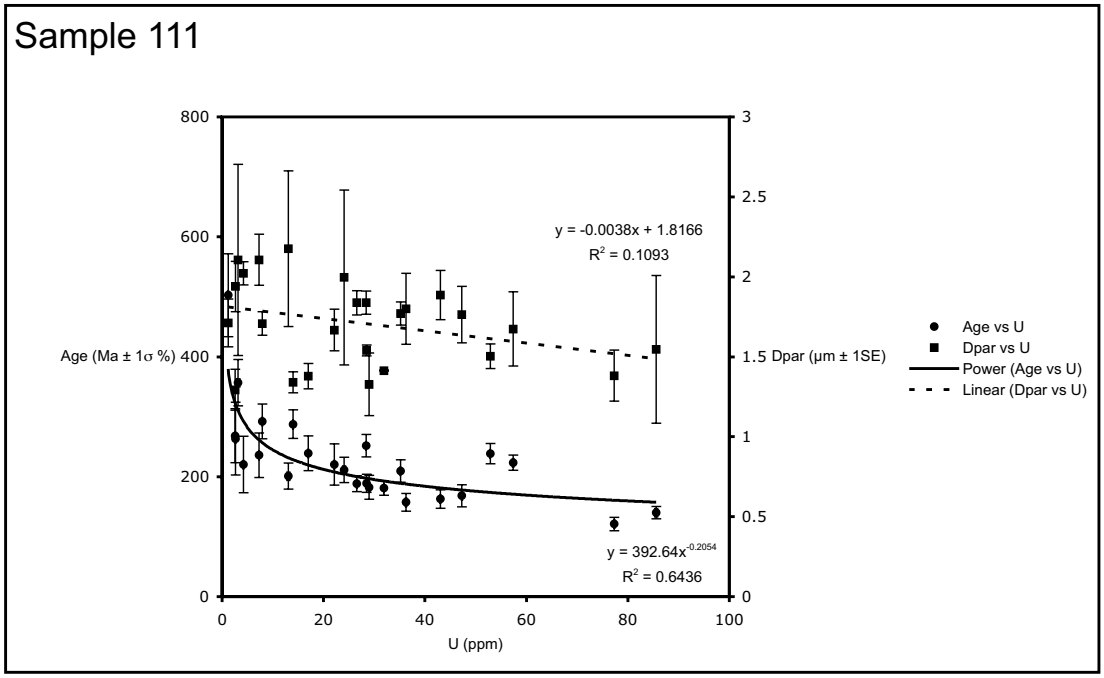
Sample 111
Age (Ma ± 1σ %)
1.5 Dpar (µm ± 1SE)
U (ppm)
y = -0.0038x + 1.8166
R2 = 0.1093
y = 392.64x-0.2054
R2 = 0.6436
Age vs U
Dpar vs U
Power (Age vs U)
Linear (Dpar vs U)

# Appendix iv: *AFTSolve* time-Tempature modelling output

## Sample 18

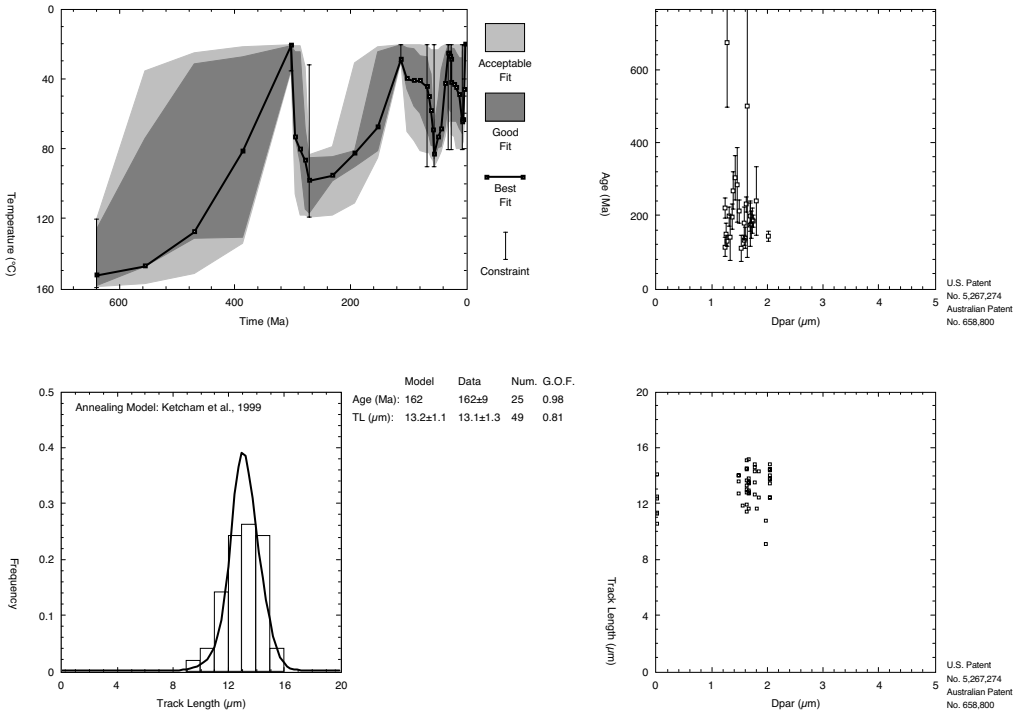


## Sample 20

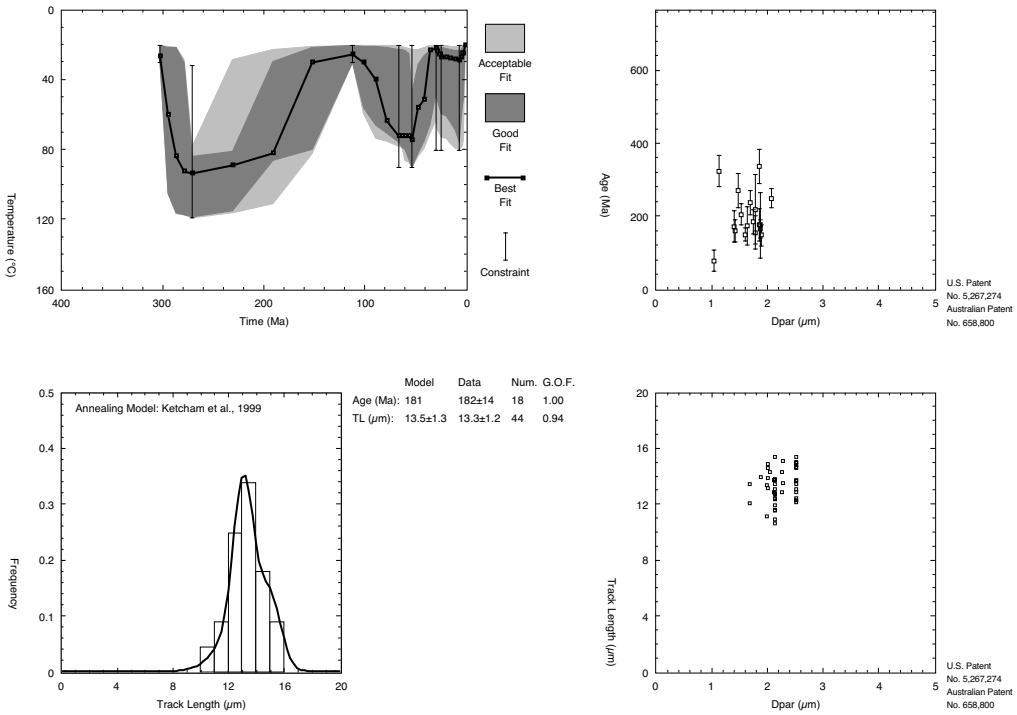

# Sample 104

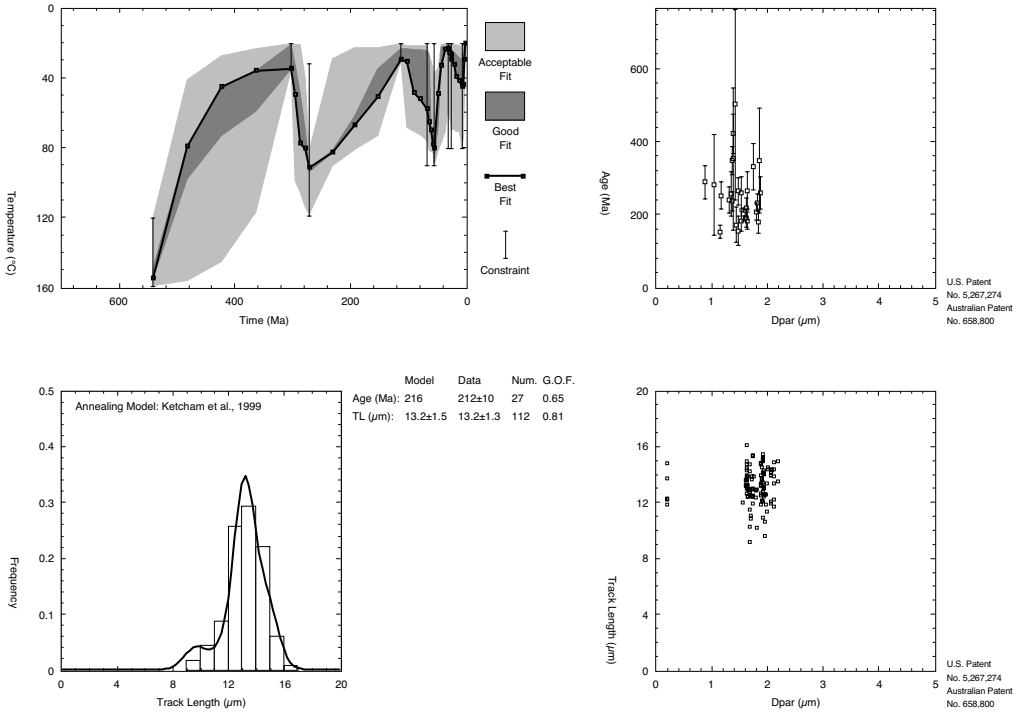


# Sample 105

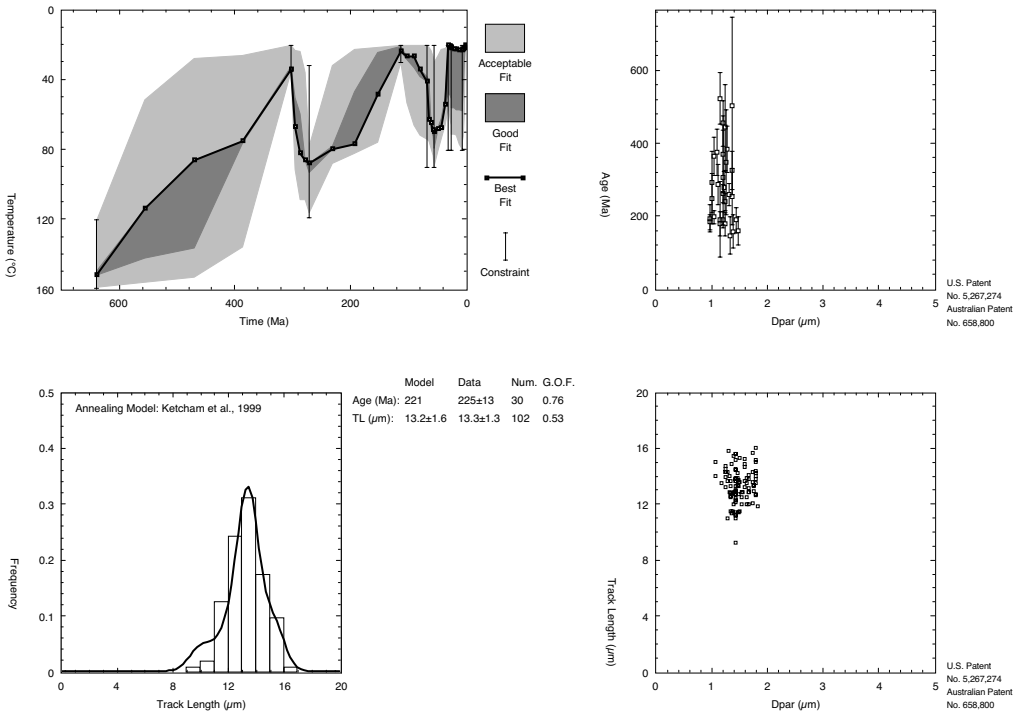

# Sample 106

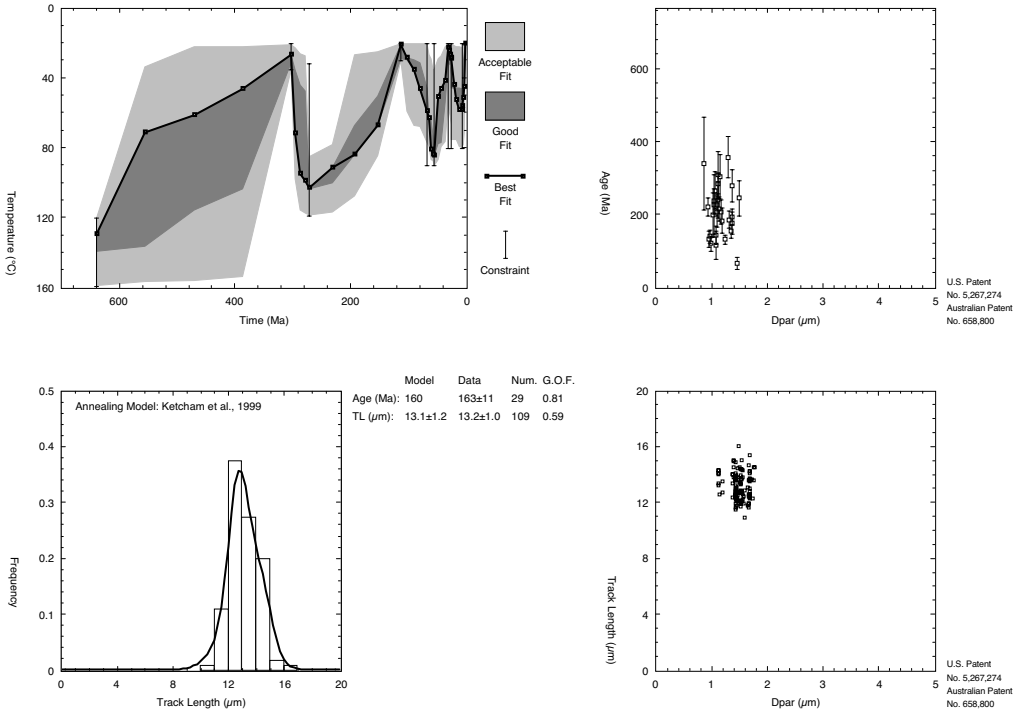


# Sample 83

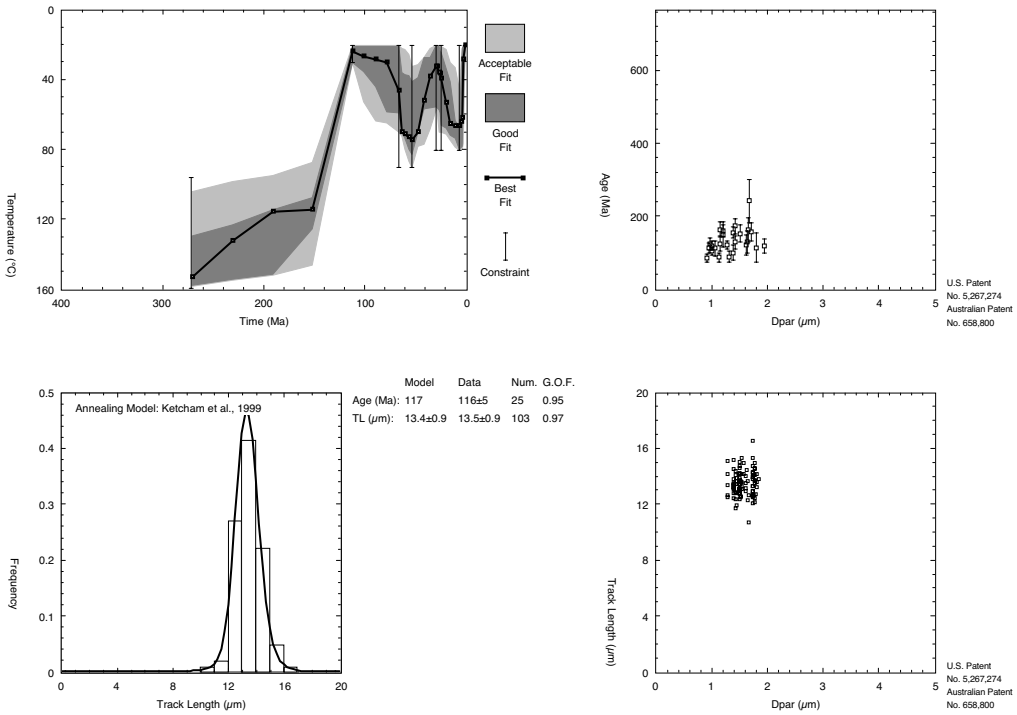

# Sample 85

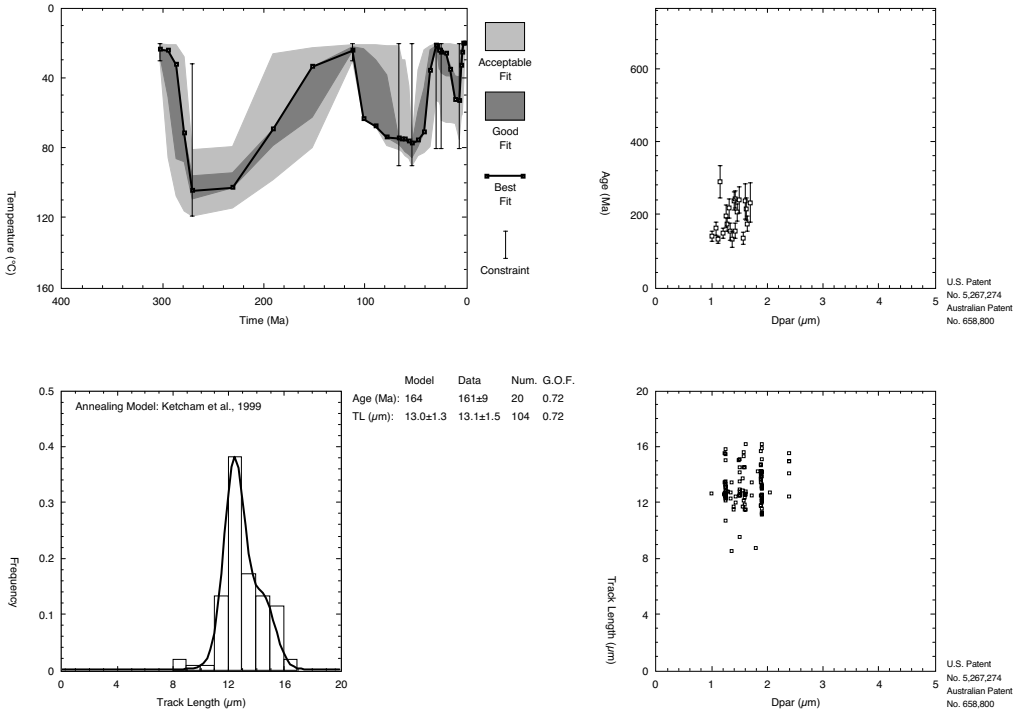


| | Model | Data | Num. | G.O.F. |
|---|---|---|---|---|
| Age (Ma): | 164 | 161±9 | 20 | 0.72 |
| TL (μm): | 13.0±1.3 | 13.1±1.5 | 104 | 0.72 |

# Sample 91

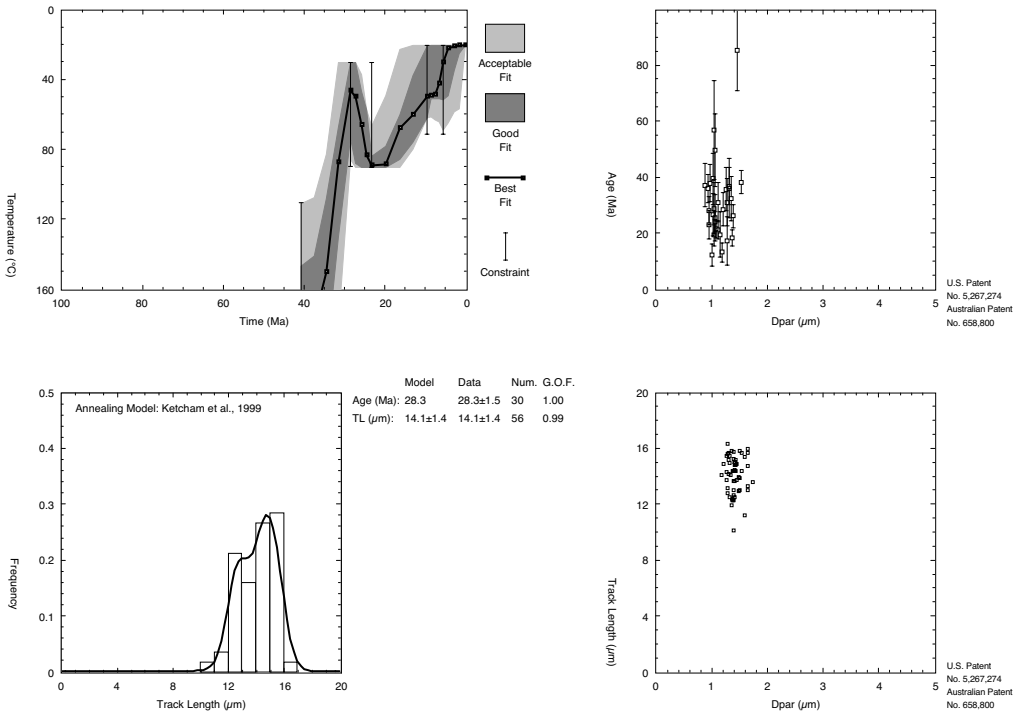


| | Model | Data | Num. | G.O.F. |
|---|---|---|---|---|
| Age (Ma): | 28.3 | 28.3±1.5 | 30 | 1.00 |
| TL (μm): | 14.1±1.4 | 14.1±1.4 | 56 | 0.99 |

# Sample 10

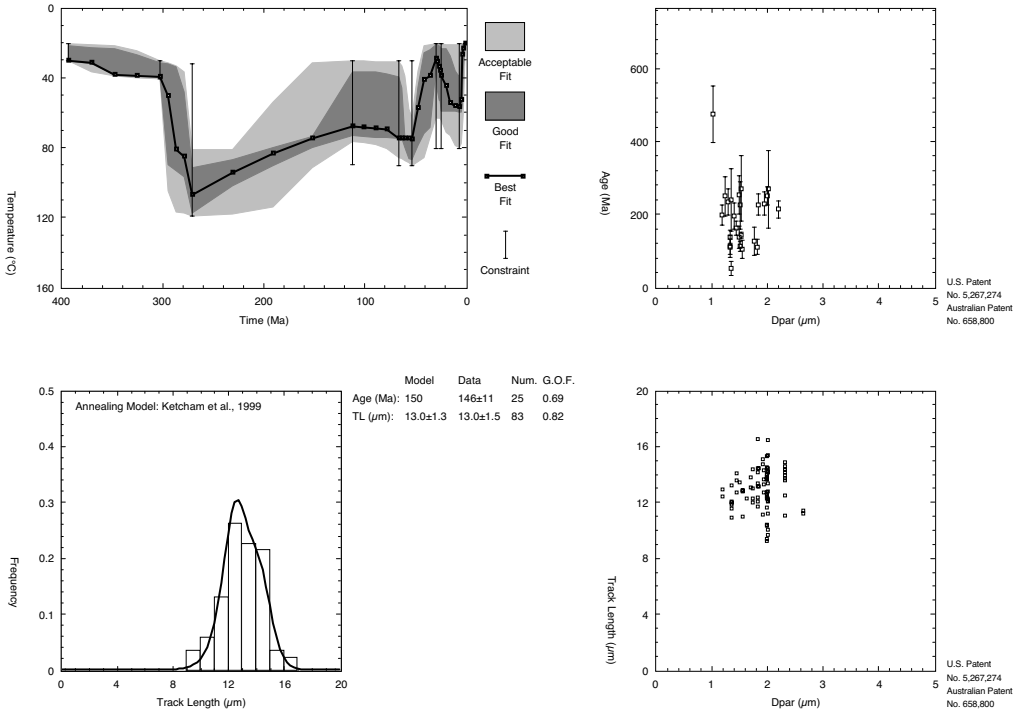


# Sample 8

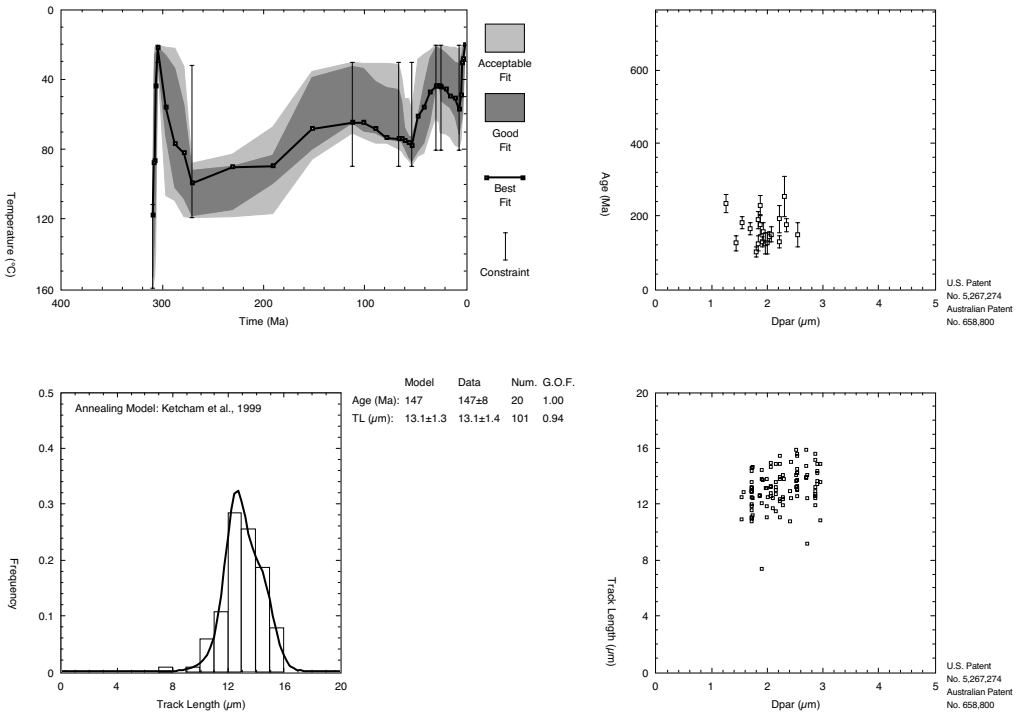

# Sample 73

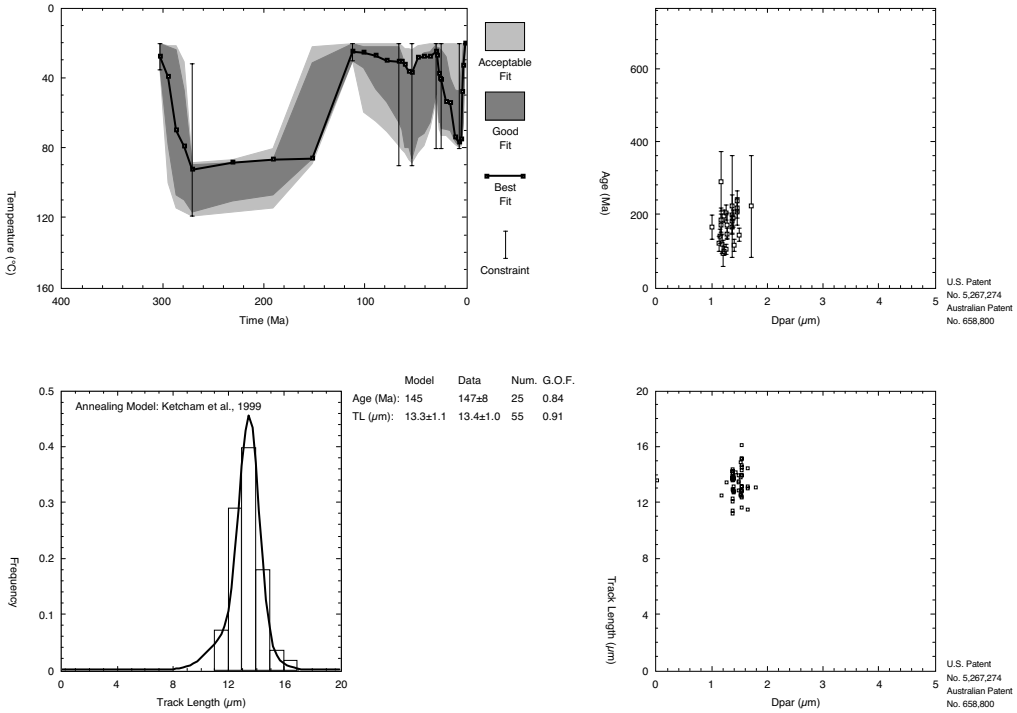


# Sample 74

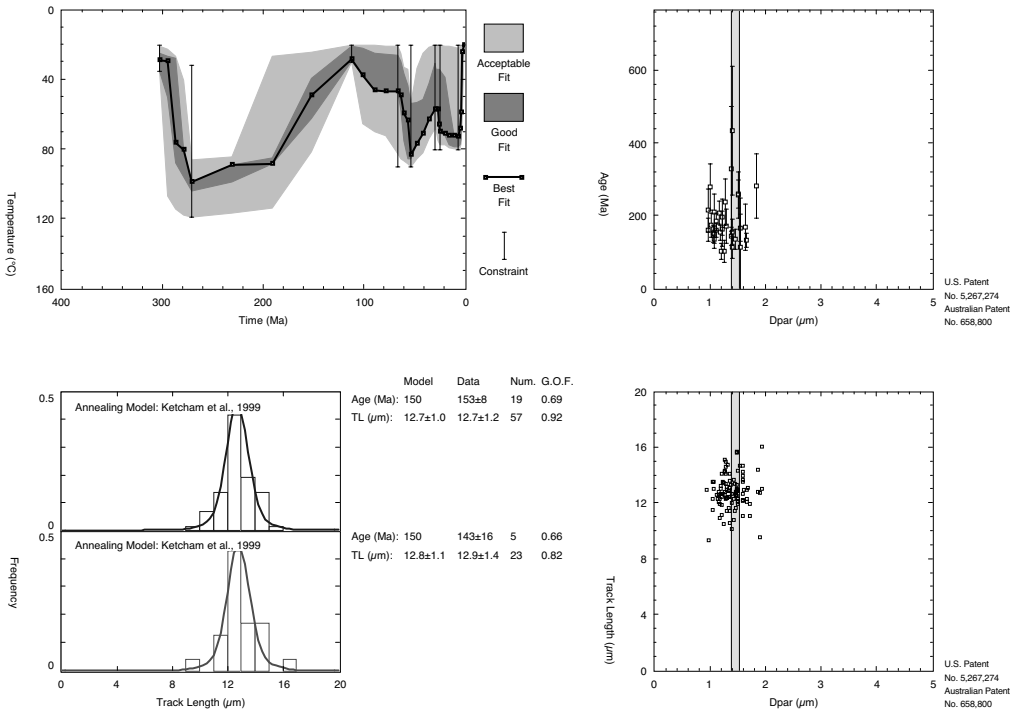

# Sample 76

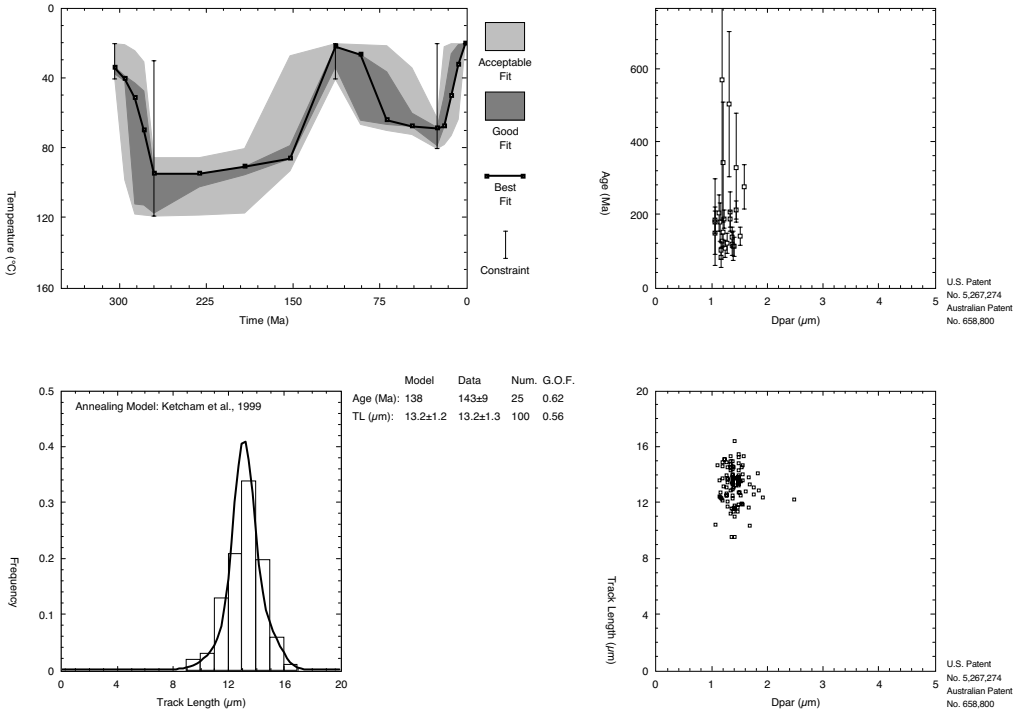


# Sample 78

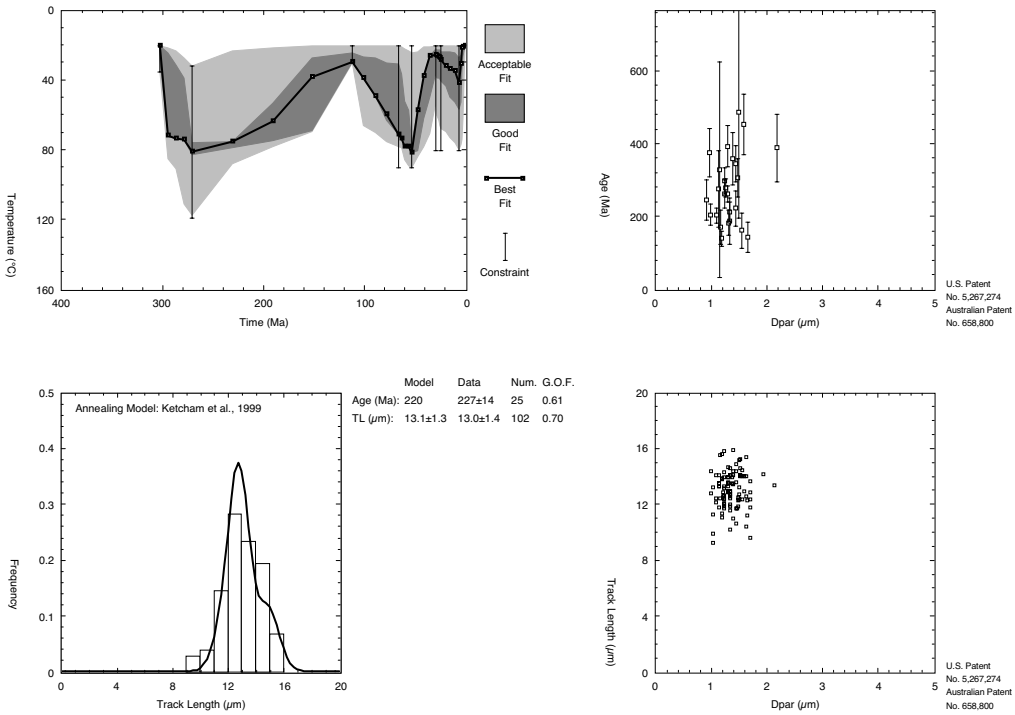

# Sample 79

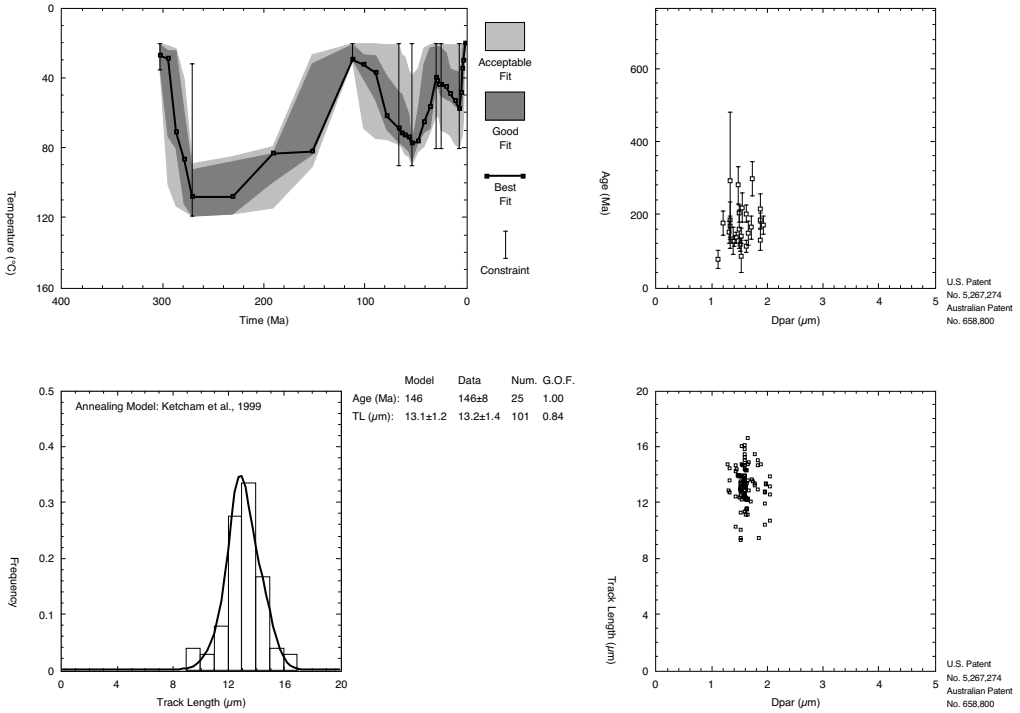


# Sample 80

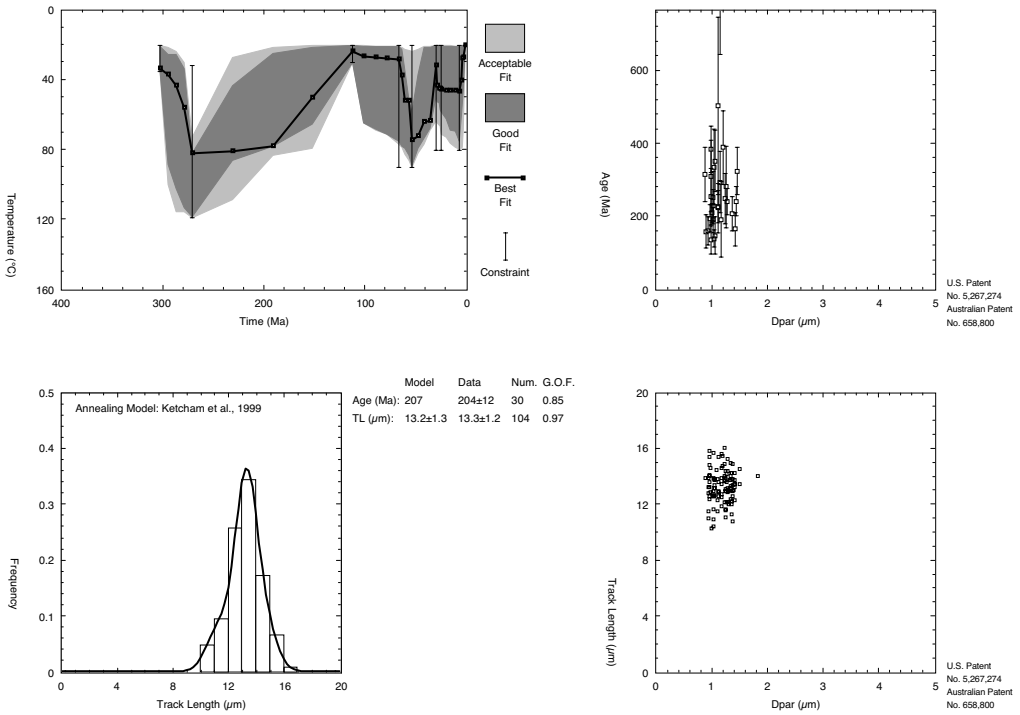

# Sample 82

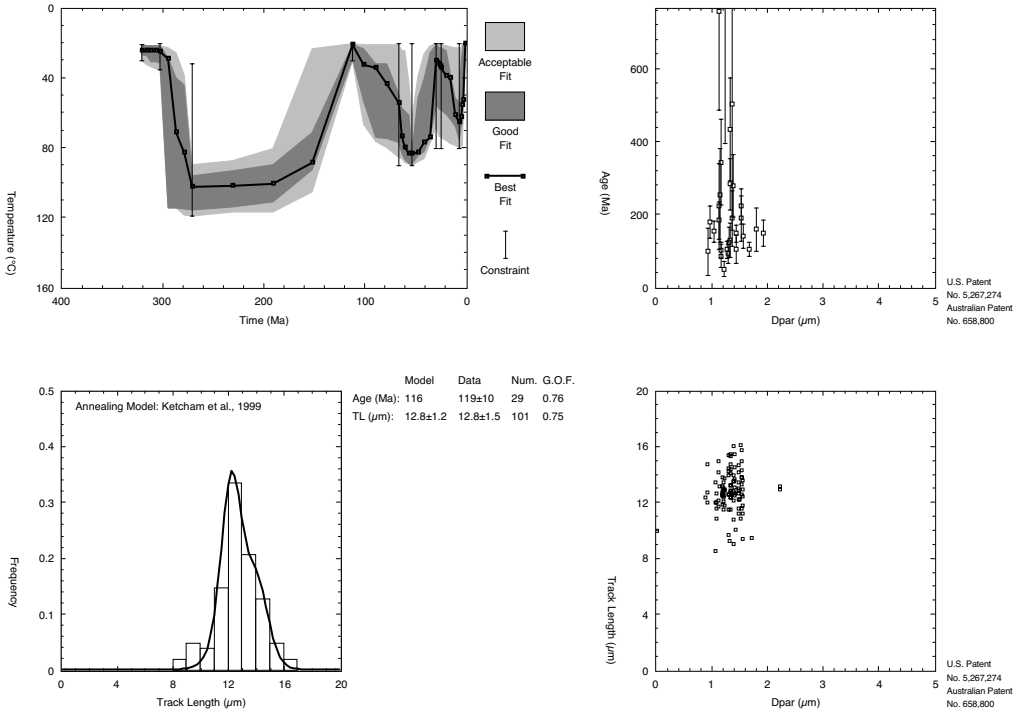


# Sample 110

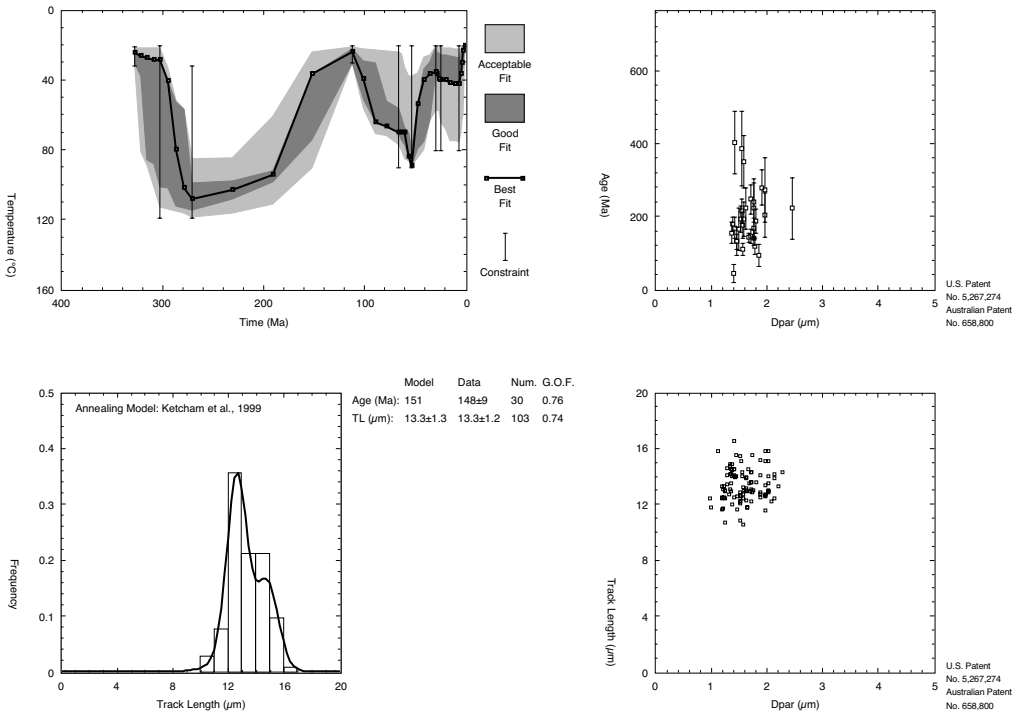

# Sample 111

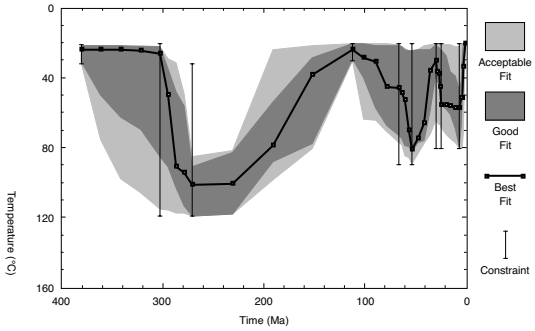


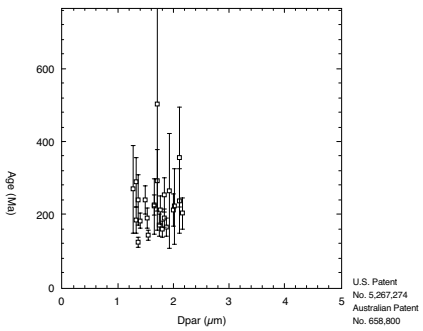


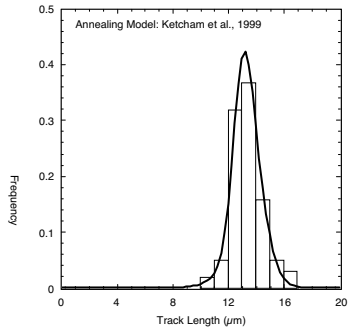


| | Model | Data | Num. | G.O.F. |
|---|---|---|---|---|
| Age (Ma): | 169 | 168±8 | 25 | 0.89 |
| TL (μm): | 13.3±1.1 | 13.4±1.2 | 100 | 0.87 |